

Polyynes

*Synthesis, Properties,
and Applications*

Polyynes

Synthesis, Properties, and Applications

edited by
Franco Cataldo



Taylor & Francis

Taylor & Francis Group

Boca Raton London New York

A CRC title, part of the Taylor & Francis imprint, a member of the
Taylor & Francis Group, the academic division of T&F Informa plc.

Published in 2006 by
CRC Press
Taylor & Francis Group
6000 Broken Sound Parkway NW, Suite 300
Boca Raton, FL 33487-2742

© 2006 by Taylor & Francis Group, LLC
CRC Press is an imprint of Taylor & Francis Group

No claim to original U.S. Government works
Printed in the United States of America on acid-free paper
10 9 8 7 6 5 4 3 2 1

International Standard Book Number-10: 1-57444-512-X (Hardcover)
International Standard Book Number-13: 978-1-57444-512-1 (Hardcover)
Library of Congress Card Number 2005043705

This book contains information obtained from authentic and highly regarded sources. Reprinted material is quoted with permission, and sources are indicated. A wide variety of references are listed. Reasonable efforts have been made to publish reliable data and information, but the author and the publisher cannot assume responsibility for the validity of all materials or for the consequences of their use.

No part of this book may be reprinted, reproduced, transmitted, or utilized in any form by any electronic, mechanical, or other means, now known or hereafter invented, including photocopying, microfilming, and recording, or in any information storage or retrieval system, without written permission from the publishers.

For permission to photocopy or use material electronically from this work, please access www.copyright.com (<http://www.copyright.com/>) or contact the Copyright Clearance Center, Inc. (CCC) 222 Rosewood Drive, Danvers, MA 01923, 978-750-8400. CCC is a not-for-profit organization that provides licenses and registration for a variety of users. For organizations that have been granted a photocopy license by the CCC, a separate system of payment has been arranged.

Trademark Notice: Product or corporate names may be trademarks or registered trademarks, and are used only for identification and explanation without intent to infringe.

Library of Congress Cataloging-in-Publication Data

Polyynes : synthesis, properties, and applications / edited by Franco Cataldo.
p. cm.

Includes bibliographical references and index.

ISBN 1-57444-512-X (alk. paper)

1. Polyynes. 2. Acetylene. 3. Carbynes. I. Cataldo, Franco.

QD305.H8P65 2005
547'.413--dc22

2005043705



Taylor & Francis Group
is the Academic Division of T&F Informa plc.

Visit the Taylor & Francis Web site at
<http://www.taylorandfrancis.com>

and the CRC Press Web site at
<http://www.crcpress.com>

Preface

On 30 and 31 October, 2003, the “Interdisciplinary Meeting on Polyynes and Carbyne” was held in Naples (Italy) at the Osservatorio Astronomico di Capodimonte. I wish to thank Prof. Luigi Colangeli, Dr. John Robert Brucato, Dr. Vito Mennella and Dr. Alessandra Rotundi (all from the Astronomical Observatory) for having contributed to the organization and success of that meeting.

This book has been published as a result of that meeting and many other well known scientists who did not participate in the event were also invited to make contributions to the publication.

Why is there so much enthusiasm for a class of molecules, polyynes, and the related carbon allotrope carbyne? The point is that, with polyynes, inorganic, organic, and polymer chemistry meet. For inorganic chemists the polyynes, and especially carbyne, represent another carbon allotrope. For organic chemists the polyynes chains are the building blocks of new molecules with fascinating properties. For polymer chemists the polyynes are the oligomers of acetylene while carbyne is the corresponding high polymer.

However, the affirmation that the polyynes and carbyne represent a meeting point of different branches of chemistry is far too limiting because polyynes and carbyne are also fields of interest for astrophysicists, astrochemists/astrobiologists as well as flame scientists, biologists, drug designers, materials scientists, mineralogists, geophysicists and so on. The deep and comprehensive knowledge of these molecules and their potential future applications are not the specialist field of a given discipline but instead come from the cooperation and contributions of scientists and specialists from completely different fields.

How can a scientist remain indifferent in light of the fact that carbon chains have been detected by radio astronomers in the molecular clouds present in the interstellar medium or in the circumstellar medium of carbon-rich stars or in the atmosphere of certain bodies of the Solar System such as Titan, Saturn’s giant moon? The wonder increases further when it is realized that about one thousand organic molecules classified as polyynes are produced by plants, fungi, and microorganisms and play a biological role in the biosphere and may be used in the treatment of diseases as antibiotics, anticancer or, more simply, as anti-infective agents.

Is it fascinating to know that the polyynes are considered the key precursors in the formation of polycyclic aromatic hydrocarbons and soot in combustion flames and that a similar mechanism of carbon dust formation can be applied (without flames) to explain the formation and the abundance of elemental carbon in our galaxy. Carbon dust represents about 3% of the



Participants at the Interdisciplinary Meeting on Polyynes held in Naples on 30 and 31 October, 2003, at the Astronomical Observatory of Capodimonte.

From left to right: L. Ravagnan, V. Mennella, L. Kavan, P. Milani, G. Strazzulla, A. Li Bassi, A. Rotundi, W. Kraetschmer, F. Cataldo, J.R. Brucato, Y. Keheyen, L. Colangeli, Xiu Yun Chuan, P. Piseri.

entire mass of our galaxy! And what about the mystery of the source of the diffuse interstellar bands, certain spectral features in the visible and ultraviolet parts of the optical spectrum which may be produced by these carbon chains or related radicals? Polyynes are also recognized precursors in the formation of fullerenes.

What about the claimed synthesis of carbyne reported several times in literature and the uncertain detection of this allotrope in certain meteorites? One important distinction is between carbyne and carbynoid structures. Carbyne remains an ideal structure for the representation of the pure sp-hybridized carbon allotrope. An almost infinite chain of carbon must be a solid, insoluble in any solvent under standard conditions, as they are the other well known allotropes graphite and diamond. On the other hand the carbynoid structures represent any carbon solid which contains polyyne chains, even very long chains, or domains, but stabilized in a matrix of other differently hybridized carbon atoms. Therefore, many publications on the synthesis of carbyne must be interpreted and rationalized in terms of the carbynoid structure concept.

This book represents the first attempt to present an interdisciplinary view on the fascinating subject of polyynes and carbyne. The reason for this renewed enthusiasm for these molecules and chemical structures lies essentially in the significant advancements achieved in recent years with the synthesis of carbon films containing necessarily sp-hybridized carbon chains by sophisticated chemical and electrochemical routes or by more physical but nevertheless successful approaches. Furthermore, polyynes chains were usually difficult to synthesize because of the need of complex multistep synthesis, so that they were regarded more as academic curiosities because of their intrinsic instability. However, it has been found that the polyynes can be easily produced in solution with a simple approach making them available as building blocks. Moreover, it has been demonstrated that the polyynes chains can be stabilized by using appropriate end groups.

The protagonists of these achievements have contributed to this book together with other well known scientists who have also given their own contributions to the development of this field.

We wish to transmit our enthusiasm about this deeply interdisciplinary and fascinating field to the reader, and this modest work represents our attempt.

Franco Cataldo

Editor

Dr. Franco Cataldo is adjunct professor of chemistry at the “Tor Vergata” University of Rome, Italy. He is also the R&D manager in some private research organizations, including the Soc. Lupi Chemical Research Institute. Dr. Cataldo’s research interests are mainly focused on elemental carbon chemistry with special emphasis on polyynes and fullerene chemistry; other fields of interest are macromolecular chemistry and biochemistry, as well as astrochemistry.

Dr. Cataldo has published more than 180 research papers in peer-reviewed international journals of chemistry and is the author of more than 30 patents. He has written two textbooks in Italian and has contributed numerous chapters in multi-authored books.

Dr. Cataldo is member of the editorial board of the journal *Fullerenes, Nanotubes and Carbon Nanostructures*.

Contributors

V.G. Babaev

Faculty of Physics
Moscow State University
Moscow, Russia

Nadia Balucani

Dipartimento di Chimica
Università di Perugia
Perugia, Italy

Luca Banfi

Dipartimento di Chimica e Chimica Industriale
Università degli Studi di Genova
Genoa, Italy

G.A. Baratta

INAF-Osservatorio Astrofisico di Catania
Catania, Italy

Andrea Basso

Dipartimento di Chimica e Chimica Industriale
Università degli Studi di Genova
Genoa, Italy

S. Battiato

Dipartimento di Scienze Chimiche
Università di Catania,
Catania, Italy

C.E. Bottani

INFN-Dipartimento di Ingegneria Nucleare
Politecnico di Milano
Milan, Italy

Igor Burlacov

Department of Mineralogy
Technische Universität Bergakademie Freiberg
Freiberg, Germany

C.S. Casari

INFN-Dipartimento di Ingegneria Nucleare
Politecnico di Milano
Milan, Italy

Franco Cataldo

Soc. Lupi Chemical Research Institute
Rome, Italy

G. Compagnini

Dipartimento di Scienze Chimiche
Università di Catania
Catania, Italy

Wang Chuang Cun

Information Center
Yan Tai University
Yantai-Shan Dong, China

Jean-Baptiste Donnet

Laboratoire de Chimie Physique-ENSCMu
Mulhouse, France

Sergey E. Evsyukov

InstrAction GmbH
Ludwigshafen, Germany

P. Flood

TetraNova Company
Wicklow, Ireland

Giuseppe Guanti

Dipartimento di Chimica e Chimica Industriale
Università degli Studi di Genova
Genoa, Italy

M.B. Guseva

Faculty of Physics
Moscow State University
Moscow, Russia

Taro Hamagami

Institute for Materials Chemistry and Engineering
Kyushu University
Fukuoka, Japan

Robert B. Heimann

Department of Mineralogy
Technische Universität Bergakademie Freiberg
Freiberg, Germany

Dieter Heymann

Department of Earth Sciences
Rice University
Houston, USA

Sergey Horodetsky

Integrity Testing Laboratory Inc.
Markham, Ontario, Canada

Thang Le Huu

Laboratoire de Chimie Physique-ENSCMu
Mulhouse, France

Ralf I. Kaiser

Department of Chemistry
University of Hawaii at Manoa
Honolulu, Hawaii, USA

Yoshiyasu Kato

Division of Chemistry
Graduate School of Science
Kyoto University
Kyoto, Japan

Ladislav Kavan

J. Heryrovský Institute of Physical Chemistry
Academy of Sciences of the Czech Republic
Prague, Czech Republic

Yeghis Keheyan

Istituto per lo Studio dei Materiali Nanostrutturati
Università Roma 1, Dipartimento di Chimica
Rome, Italy

V.V. Khvostov

Faculty of Physics
Moscow State University
Moscow, Russia

Masashi Kijima

Institute of Materials Science
University of Tsukuba
Ibaraki, Japan

Jacob I. Kleiman

Integrity Testing Laboratory Inc.
Markham, Ontario, Canada

Wolfgang Krätschmer

Max-Planck-Institut für Kernphysik
Heidelberg, Germany

Shingo Kuboyama

Department of Applied Science for Electronics and Materials
Kyushu University
Fukuoka, Japan

C. Lenardi

INFM-Istituto di Fisiologia Generale e Chimica Biologica
Milan, Italy

A. Li Bassi

INFM-Dipartimento di Ingegneria Nucleare
Politecnico di Milano
Milan, Italy

P. Milani

INFM-Dipartimento di Fisica
Università degli Studi di Milano
Milan, Italy

Takamasa Momose

Division of Chemistry
Graduate School of Science
Kyoto University
Kyoto, Japan

N.D. Novikov

Faculty of Physics
Moscow State University
Moscow, Russia

Hanae Oulanti

Laboratoire de Chimie Physique-ENSCMu
Mulhouse, France

P. Piseri

INFM-Dipartimento di Fisica
Università degli Studi di Milano
Milan, Italy

L. Ravagnan

INFM-Dipartimento di Fisica
Università degli Studi di Milano
Milan, Italy

Frans J.M. Rietmeijer

Department of Earth and Planetary Sciences
University of New Mexico
Albuquerque, New Mexico, USA

Renata Riva

Dipartimento di Chimica e Chimica Industriale
Università degli Studi di Genova
Genoa, Italy

Alessandra Rotundi

Department of Mathematics and Applied Physics
University of Naples
Naples, Italy

E. Salis

INFM-Dipartimento di Fisica
Università degli Studi di Milano
Milan, Italy

Tadamasa Shida

Kanagawa Institute of Technology
Atsugi, Japan

F. Siviero

INFM-Dipartimento di Fisica
Università degli Studi di Milano
Milan, Italy

G. Strazzulla

INAF-Osservatorio Astrofisico di Catania
Catania, Italy

Yoshito Tobe

Division of Frontier Materials Science
Graduate School of Engineering Science
Toyonaka, Japan

Masaharu Tsuji

Institute for Materials Chemistry and Engineering
Kyushu University
Fukuoka, Japan

Takeshi Tsuji

Institute for Materials Chemistry and Engineering
Kyushu University
Fukuoka, Japan

Loïc Vidal

Institut de Chimie des Surfaces et Interfaces
Mulhouse, France

Tomonari Wakabayasahi

Department of Chemistry
School of Science and Engineering
Kinki University
Higashi-Osaka, Japan

Raymond Wey

Laboratoire de Chimie Physique-ENSCMu
Mulhouse, France

Table of Contents

Preface	iii
Editor	vii
Contributors	ix
 Chapter 1	
Carbon Chain Molecules in Cryogenic Matrices	1
<i>Tomonari Wakabayashi and Wolfgang Krätschmer</i>	
 Chapter 2	
Synthesis and Characterization of Carbynoid Structures in Cluster-Assembled Carbon Films	15
<i>L. Ravagnan, F. Siviero, E. Salis, P. Piseri, P. Milani, C. Lenardi, A. Li Bassi, C.S. Casari and C.E. Bottani</i>	
 Chapter 3	
Epitaxial Growth by D.C. Magnetron Sputtering of Carbyne (Chaoite) Microcrystals on CVD-Deposited Polycrystalline Diamond	37
<i>Robert B. Heimann, Igor Burlacov, Jacob I. Kleiman and Sergey Horodetsky</i>	
 Chapter 4	
Electrochemical Synthesis of Carbyne-Like Materials and Other Nanocarbons	53
<i>Ladislav Kavan</i>	
 Chapter 5	
Synthesis of Carbynoid Structures by the Combustion Flame Method	79
<i>Jean-Baptiste Donnet, Hanae Oulanti, Raymond Wey, Thang Le Huu, Wang Chuang Cun and Loïc Vidal</i>	
 Chapter 6	
Cyclic Polyynes: Generation, Characterization, and Reactions	99
<i>Yoshito Tobe and Tomonari Wakabayashi</i>	

Chapter 7

- Formation of $C_{2n}H_2$ Polyynes by Laser Ablation of Graphite, Coal or C_{60} Particles Suspended in Selected Solvents** 127
*Masaharu Tsuji, Shingo Kuboyama, Takeshi Tsuji
 and Taro Hamagami*

Chapter 8

- Polyynes: Synthesis with the Submerged Electric Arc** 155
Franco Cataldo

Chapter 9

- Polyynes ($C_{2n}H_2$, $n = 2-5$) and Other Products from Laser-Ablated Graphite: A Time-of-Flight Mass Spectroscopic Study in Combination with One-Photon Ionization** 181
*Tomonari Wakabayashi, Yoshiyasu Kato, Takamasa Momose
 and Tadamasa Shida*

Chapter 10

- Polyne-Type Materials** 197
Masashi Kijima

Chapter 11

- Carbon Material with a Highly Ordered Linear-Chain Structure** 219
*V.G. Babaev, M.B. Guseva, N.D. Novikov, V.V. Khvostov
 and P. Flood*

Chapter 12

- Synthesis of Carbynoid Materials by Chemical Dehydrohalogenation of Halogen-Containing Polymers** 253
Sergey E. Evsyukov

Chapter 13

- Ion Irradiation of Solid Carbons** 271
G. Strazzulla, G.A. Baratta, S. Battiato and G. Compagnini

Chapter 14

- Cyanoalkynes and Cyanopolyynes: From Crossed Beam Experiments to Astrochemistry** 285
Nadia Balucani and Ralf I. Kaiser

Chapter 15

- Synthesis of Monocyanopolyynes and Dicyanopolyynes with the Submerged Electric Arc** 323
Franco Cataldo

Chapter 16

Natural Carbynes, Including Chaoite, on Earth, in Meteorites, Comets, Circumstellar and Interstellar Dust	339
--	-----

Frans J.M. Rietmeijer and Alessandra Rotundi

Chapter 17

Structures and Other Properties of Polyynes and their Isomers: Theoretical and Experimental Results	371
--	-----

Dieter Heymann and Franco Cataldo

Chapter 18

Polyynes: Possible Bulk Synthesis and Chemical Properties	425
--	-----

Franco Cataldo

Chapter 19

From Natural to Rationally Designed Artificial Eneidyne: Towards New Anticancer Antibiotics Activable at Will	453
--	-----

Giuseppe Guanti, Luca Banfi, Andrea Basso and Renata Riva

Chapter 20

Polyynes: Simple Synthesis in Solution Through the Glaser Reaction	493
---	-----

Franco Cataldo and Yeghis Keheyan

Abbreviations	499
----------------------------	-----

1 Carbon Chain Molecules in Cryogenic Matrices

*Tomonari Wakabayashi and
Wolfgang Krätschmer*

CONTENTS

1.1 Introduction.....	1
1.2 Matrix-Isolation Experiments of Carbon Vapor	3
1.3 Flashing Carbon	10
1.4 Conclusions	11
References	12

1.1 INTRODUCTION

Carbon is a very remarkable element. It forms various kinds of different bonds not only with other atoms but also with atoms of its own kind. This latter feature can lead to polymers of amazing symmetry of which fullerenes and carbon nanotubes have recently gained much attention [1–5]. Furthermore, one has to realize that the familiar linear sp , triangular sp^2 , and tetrahedral sp^3 bonds are just the limiting cases of carbon orbital arrangements — various intermediate forms exist as well. In fullerenes, for example, the surface curvature suggests a bond intermediate between sp^2 and sp^3 , i.e. a sp^x ($2 < x < 3$) hybridization [6]. It certainly is not an accident that among the elements of the 4th group of the periodic table the versatile carbon — rather than silicon or any other member — forms the basis of life.

It is further remarkable that carbon is the most abundant condensable element in our galaxy. Because of the ease of polymerization, large interstellar molecules and dust particles are very likely formed by carbon or at least may possess a carbon backbone structure. Judging from their optical effects, the interstellar dust particles seem to have a distribution of sizes ranging up to 100 nm or more. Even though their mass fraction (about 1% of the mass of the interstellar matter is locked in grains) seems to be low, they constitute an important ingredient of the interstellar medium [7]. Grains are the sites at which atomic hydrogen converts into molecular H_2 , and thus cosmic dust plays a key role in the chemistry of interstellar clouds.

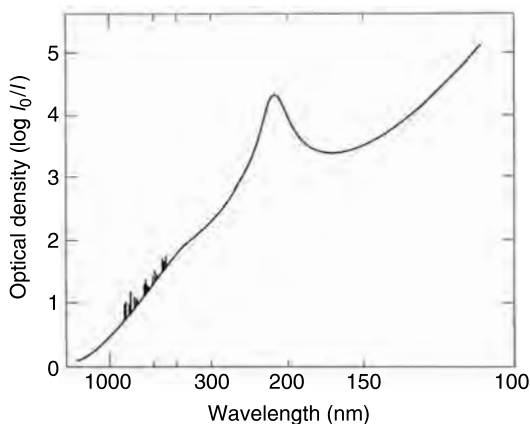


FIGURE 1.1 The average light extinction (*i.e.* scattering plus absorption) of the interstellar medium which consists of a mixture of gas and dust. The extinction is normalized to a column depth of 1 kpc (*i.e.* 3300 light years). Notice the rising continuum which originates from dust particles and on which absorptions are superimposed. The strong and broad feature at about 220 nm is probably produced by graphitic particles, possibly onions [12]. The many narrow features in the UV–vis range are the diffuse interstellar bands (DIBs). The carrier(s) of these are not known. Large polycyclic hydrocarbon molecules and carbon chains have been discussed [14].

Furthermore, grains are efficient infrared (IR) emitters and provide a cooling agent which, in the process of gravitational collapse of interstellar clouds into stars, very much facilitates star formation.

The interstellar medium also hosts grains or molecules which give rise to distinct absorptions in the ultra-violet–visible (UV–vis) range, as shown in Figure 1.1 (adopted from [8]). On a rising continuum which is characteristic for light extinction by small dust particles (the so-called reddening effect) several absorptions are superimposed. These contain information on the chemical composition of at least a certain population of the interstellar particles. The most prominent absorption is a broad feature centered at about 220 nm. In addition, there are plenty of much narrower features, the so-called diffuse interstellar bands (DIBs) which range from the UV to the red. More than 200 DIBs are known today, exhibiting various strengths and widths [9,10]. So far, none of the absorber(s) could be identified. For experimental spectroscopy, the DIBs represent a long-lasting challenge, since the first strong DIBs were already discovered in the 1920s. It is generally assumed that carbon is responsible for both kinds of absorptions: graphitic particles for the 220 nm feature [11,12], and large carbon-based molecules for the DIBs [13,14]. In principle, both hypotheses could be checked by dedicated laboratory experiments. In the case, however, that the nearly collision-free conditions in space are essential for carrier formation

and thus for an understanding of the interstellar absorption, suitable laboratory experiments may turn out to be extremely difficult.

Our approach to reproduce the 220 nm interstellar absorption may serve as an example. We produced graphitic particles by evaporating graphite in a quenching atmosphere of helium at a pressure of a few torr. Under these conditions, the carbon vapour re-condenses to form small particles of about 10 nm size. We collected these particles on substrates and recorded the UV-vis spectra. Naturally, in the process of deposition, the particles heavily clump together, an effect which distorts the absorption spectra in shape, width, and position. These distortions render a direct comparison with the interstellar feature difficult. Strictly speaking, our laboratory approach was thus too simple. One should have aimed at preparing a non-clumped system of free or at least matrix-isolated particles, a much more difficult task (see [15] for the latter approach). Besides an extremely broad absorption at around 220 nm, we also found to our surprise some peculiar absorption features in our samples which were rather unlike to those of graphite particles. These absorptions turned out to originate from fullerenes. Unfortunately, C₆₀ and the other fullerenes did not contribute very much to a better understanding of the carrier of the interstellar 220 nm absorption. However, the existence of closed cage fullerenes stimulated research on other related graphite-like nanostructures. As a result the concept of graphitic onions emerged. It now appears that such particles are good candidates for the 220 nm carrier [12].

Rather puzzling is the fact that the highly ordered fullerene structures form with amazing efficiency through the condensation of carbon vapor, *i.e.* a chaotic high-temperature process. This demands an explanation. What is the build-up process and what are the fullerene precursors? Research on small molecular carbon species may shed some light on this problem.

1.2 MATRIX-ISOLATION EXPERIMENTS OF CARBON VAPOR

Initially, we tried to check the hypothesis that carbon chains may be the carriers of the DIBs and performed some pilot experiments showing that such chains did indeed exhibit strong absorptions in the wavelength range where DIBs are observed. For this purpose we produced carbon vapor by evaporating graphite rods by resistive heating. To measure the carbon molecular spectra, we applied the matrix-isolation technique in which the carbon vapor is co-deposited along with a large excess of a noble gas (usually argon) on a cryogenic substrate (10 K). By this procedure the rather reactive carbon species are trapped within the frozen matrix of the rare gas and remain isolated. Weltner and co-workers introduced this carbon preparation technique in the early 1960s (see [16]). For clarity the principle of matrix-isolation is sketched in [Figure 1.2](#). Compared to gas phase conditions, the matrix allows molecular vibrations but in the cases of concern here

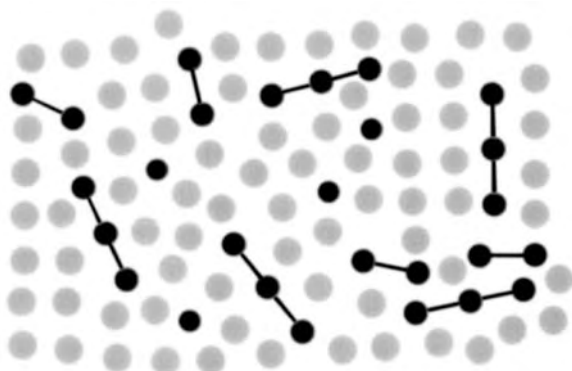


FIGURE 1.2 The principle of matrix isolation. The species to be studied (in our case, carbon vapour molecules shown in black) are co-condensed along with a large excess of noble gas onto a cold (about 10 K for argon) substrate. The highly reactive carbon molecules are trapped in the ice, cannot move, and stay isolated. Only when the matrix is warmed up to its sublimation temperature, can the carbon molecules move and grow to larger chains, and possibly also into rings. We produce the carbon vapor by resistive heating of two contacting graphite electrodes.

allows no molecular rotations. The cryogenic matrix temperature and the absence of molecular rotation considerably simplify the absorption spectra but this comes at a price: compared to the gas-phase spectra, the matrix spectra are considerably broadened and the absorption maxima are shifted in wavelength. These distortions make a detailed comparison to gas phase (e.g. DIB) spectra difficult. The matrix shifts, which depend on the particular spectral line and can go either into the blue or the red, are usually relative moderate ($< 10\%$ in most cases).

Carbon vapor at 3000 K consists of atomic and molecular carbon of the approximate composition C (20%), C_2 (10%), and linear C_3 (70%); the abundance of larger species is rather low ($< 1\%$) [17]. In the range longer than 200 nm, the optical absorption spectrum of carbon vapor matrix-isolated in solid argon is usually dominated by the C_3 molecule with its characteristic relatively sharp and complex structured absorption feature at 410 nm (see [Figure 1.3](#)). This feature, which in the gas phase occurs at 405 nm, originates from the transition from the $^1\Sigma_g$ ground state to the $^1\Pi_u$ electronically excited state. The complicated substructures of the band come from bending vibrations of C_3 in the excited state. In the “as deposited” spectrum of [Figure 1.3](#), which was taken at a window substrate temperature of 10 K, there are indications of other absorptions — a particular example being the broad band centered at about 250 nm. Part of this band belongs to the C_2 molecule (the so-called Mullikan band at 238 nm), but the rest belongs to some other carrier. Maier and co-workers, who deposited mass

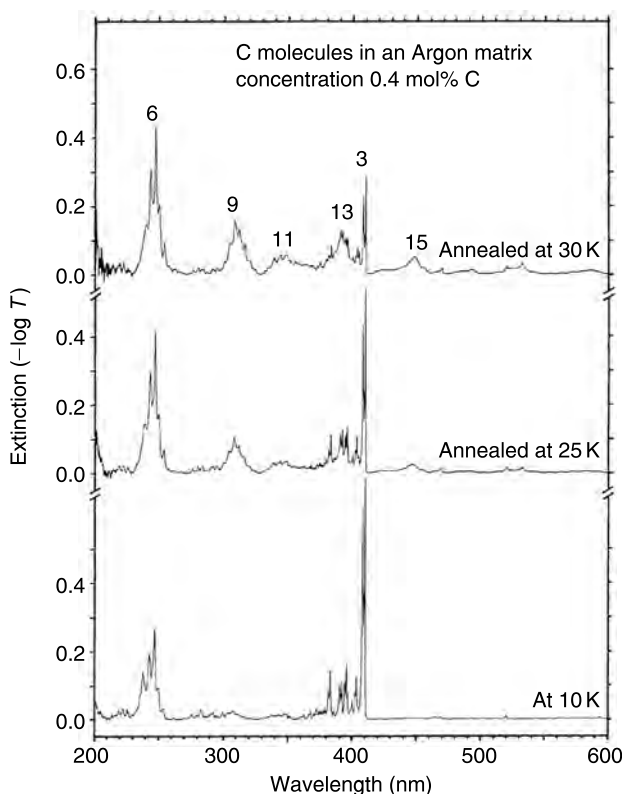


FIGURE 1.3 The UV-vis spectrum of carbon vapor molecules trapped in argon, deposited at 10 K (bottom). In the other spectra the matrix was annealed to the indicated temperature. Notice the decay of the initially intense C_3 absorption at 410 nm with increasing annealing. In the final spectrum the linear species C_n are produced and are indicated by the number of atoms.

selected molecular carbon beams in matrices, could recently identify the carrier of this band as linear C_6 [18,19]. The absorption probably belongs to the dipole allowed and therefore strong $^3\Sigma_g$ ground state to $^3\Sigma_u$ transition. Judging from the abundances in carbon vapor, the C_6 absorption should be weak or absent. Apparently, this molecule forms by a polymerization process, in which the reactive carbon molecules with their unsaturated dangling bonds come together and grow into longer chains according to the scheme $C_m + C_n \rightarrow C_{m+n}$. That such growth occurs is shown by matrix annealing experiments in which the carbon containing matrix (along with the substrate on which the matrix is deposited) is warmed up to a certain temperature (as indicated in Figure 1.3) and afterwards cooled down again to 10 K for recording the spectrum. Clearly, many lines are growing in

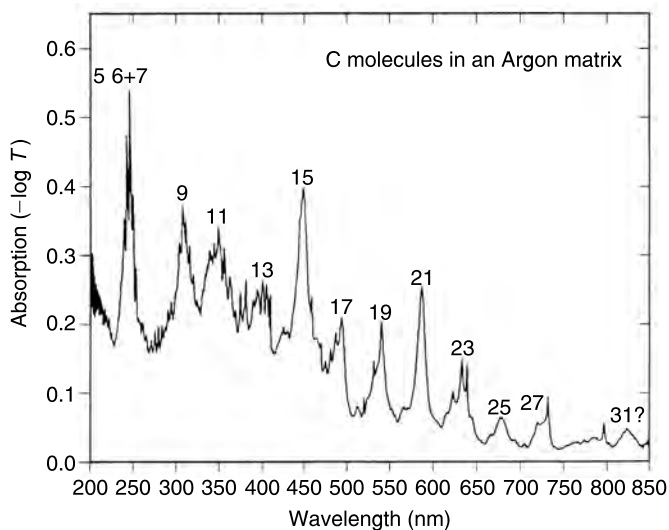


FIGURE 1.4 The UV-vis spectrum of a dense and heavily annealed carbon-bearing matrix. During annealing, the absorptions gradually appear at longer and longer wavelength and seem to belong to longer and longer odd n C_n chains. The regular spacing suggests that the species are linear up to possibly C_{27} .

succession and must belong to successively larger species. The numbers given in the upper spectrum show the size of the carbon molecule which produces the feature. Most of the assignments are based on the already mentioned work of Maier's group. One recognizes in the spectra that the prominent peaks (with the exception of linear C_6) are from species with an odd number of atoms, and that an almost constant increment in wavelength exists in going from one odd carbon molecule to the next. Such a sequence in wavelength is precisely what is expected for linear species. Figure 1.4, which reproduces the spectrum of a heavily annealed matrix, shows the regularities more clearly and suggests that the chains can grow quite large, reaching up to 25 or 27 atoms. We thus conclude that the molecules with an odd number of atoms are linear chains. With the exception of C_6 these odd chains apparently dominate the spectrum, probably because their absorptions (which are $^1\Sigma_g \rightarrow ^1\Sigma_u$ transitions) are more prominent compared to those of their even-atomic partners. It should be remarked that all odd chains have a closed-shell electronic structure in their ground state (*i.e.* are singlet states) and that all even chains have just two electrons in a π orbital which can host four electrons (*i.e.* possess a triplet ground state).

The regularities in the odd chain spectra may be used to predict the wavelength position of the $^1\Sigma_g \rightarrow ^1\Sigma_u$ transition of linear C_3 by extrapolation of the available data. The prediction yields a wavelength of about

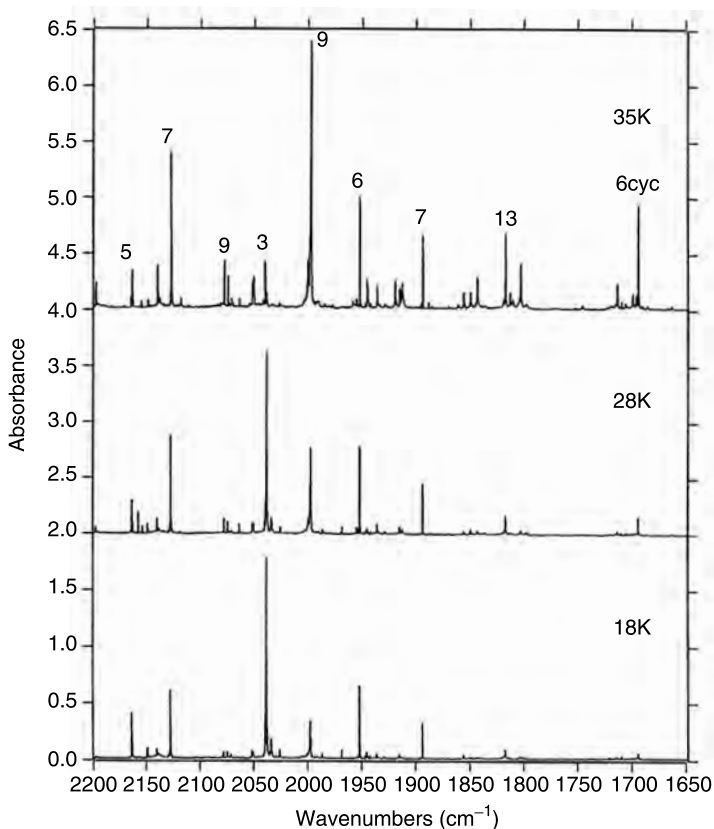


FIGURE 1.5 The IR absorption spectra of carbon molecules trapped in an argon matrix at different states of annealing. Lines that almost all belong to stretching vibrations of linear chains (of symmetry type σ_u) are recognized. The C_n assignments follow the literature. Notice the decrease of the C_3 absorption and the increase of the lines of most of the larger species. A relatively strong absorption at around 1695 cm^{-1} has been assigned to cyclic C_6 [24]. The distribution of IR lines follows no obvious pattern, and the identification in the IR is thus much more difficult as compared to that in the UV-vis range.

180 nm, and indeed we could detect the strong absorption band at that position [20].

The IR spectrum of similarly prepared carbon chains is shown in Figure 1.5. There appears to be no striking regularity in the line positions, quite in contrast to the situation in the UV-vis spectrum. As result of many long-lasting efforts of various research groups, some of which also applied gas-phase laser spectroscopy, assignments to a number of the IR absorptions could be established (see the review [21]). Figure 1.5 shows some of

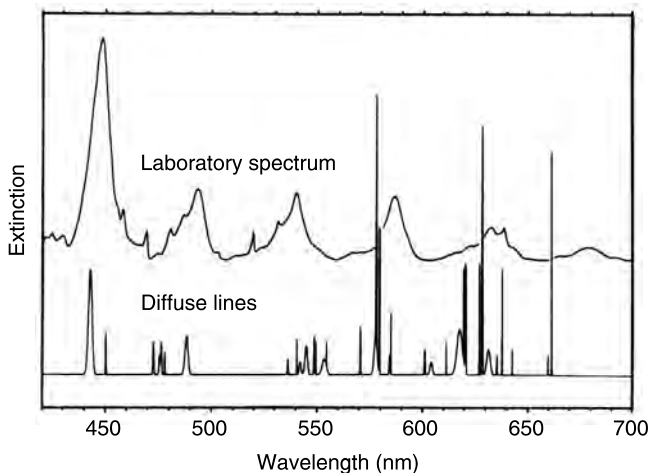


FIGURE 1.6 A comparison of a UV-vis spectrum obtained on matrix-isolated long chains in an argon matrix with the spectrum of the diffuse interstellar bands (DIBs). The matrix spectra are heavily broadened by interaction of the trapped molecule with the matrix. It can be concluded that neutral carbon species and DIB carriers absorb at very similar wavelength. From this finding one may follow the speculation of Douglas [13] that the DIB carriers are carbon chains.

these assignments. For carrier identification, the matrix workers applied ^{12}C – ^{13}C isotopic replacements and analysed the IR spectra of the isotopomers with the help of high level quantum calculations. In the high-resolution gas phase works, the rotational spectra which yield the molecule's moment of inertia were used for the assignments (see e.g. [22,23]). From the matrix data it appears that monocyclic rings also form, as the “ C_6 cyc” line of Figure 1.6 indicates [24]. In view of the floppiness of linear C_3 (with a bending mode at 63 cm^{-1} in the electronic ground state) this species may form readily through conjunction of two C_3 units. Besides cyclic C_6 the linear isomer of C_6 is also present in matrices as could be shown from UV-IR line correlations [25]. The longest chain so far identified by IR laser spectroscopy is linear C_{13} in the gas phase [26]. This result helped to pin down the corresponding absorption in the matrix. At present we are working on the assignments of linear C_{15} and C_{17} in matrices. Our preliminary results suggest that the by far strongest IR absorption of long odd chains is carried by only a few vibrational stretching modes. It appears that the IR spectra of long chains may, after all, exhibit a relative simple regular pattern. This knowledge may be of considerable help for the spectral identification of such species. The complexities in the IR spectra of smaller chains may originate from a transition in the molecular electronic structures. Small chains exhibit more or less constant cumulenenic double bonds, while

longer chains seem to develop bond alternation. The later feature lowers the electronic energy of the chain, an effect related to the familiar Peierls distortion of linear metals (see, e.g. [27]). The bond alternation seems to be accompanied by another feature in the electronic structure which turns out to be greatly responsible for the above-mentioned simplification of the IR spectra of long odd chains. This is a strong increase of the long range coupling between the atoms in the chain, a coupling which extends far beyond the nearest neighbours and which most likely originates from the cloud of delocalized π electrons.

The carbon matrix spectra can be compared with the spectrum of the DIBs. The result is shown in Figure 1.6. It should be realized that the DIBs represent gas-phase spectra while the matrix data are subjected to the various distortions mentioned above. Thus a detailed comparison is difficult. However, some conclusions can be drawn: if the DIB carriers are neutral carbon chains, the chain length should correspond to that of C_{15} or longer. The apparent and not yet well understood onset of DIBs at wavelengths longwards of 440 nm may suggest that shorter chains do not survive photo-destruction or other virulent processes in space. It should be noticed that the grouping of DIBs fits rather well to the odd chain sequence of our matrix spectra. All these arguments support the already otherwise established conjecture of long carbon chains floating in interstellar clouds. We may refer to the discovery of polyynes (e.g. of the family $HC_{2n+1}N$ with $n=0, 1 \dots 5$) made by radio astronomy in observing dense clouds [28]. The polyynes have a carbon chain backbone structure. In the more rarefied interstellar cloud medium where the DIBs are observed, the harsh conditions may destroy the smaller species and strip the larger chain molecules down to their carbon skeleton.

The matrix-isolation experiments we carried out may also have some relevance to the still not well understood problem of fullerene formation. The basic question is: How can such complicated molecules form with such extreme efficiency? Fullerene yields far exceeding 10% have been reported [29]. The initial steps of carbon condensation can be studied with matrix-isolation techniques in a kind of slow motion, and the process can even be stopped at will by cooling down. Basically, chains and monocyclic rings seem to form initially and these should be regarded as building blocks for further growth. When, during annealing we evaporated the matrix completely (see below) and checked the carbon material remaining on the substrate for fullerenes, the result was always negative. No fullerenes were formed. Apparently, the quenching of carbon vapor must take place in a considerably hotter environment such that not only molecular growth but also molecular rearrangements can take place. The cryogenic matrix environment does not allow major rearrangements. Experiments in which carbon vapor is condensed in a hot noble gas atmosphere indicate that for molecular rearrangements to take place temperatures in the range 1000 K and higher are required [30,31].

1.3 FLASHING CARBON

If the matrix of our samples evaporates completely, the carbon species formed by annealing lose their matrix protection and are “falling dry”. We recently studied the effects which then take place [32]. It might be assumed that in such a situation the sample mainly contains sp carbon molecules which form linear chains or monocyclic rings. Shortly after the “falling dry” phase one observes that the sample emits one or more flashes of light, each of about 100–300 μs in duration. We studied this emission in more detail and found that the accumulated flash spectrum closely resembles a black body emission at about 2500 K. High-speed movies of the flashes show how the light emission ignites at a spot and spreads out over the sample surface. Larger parts of the material can be observed to be blown away. The material remaining on the substrate has a flaky, film-like structure. We think the energy of all these phenomena originates from the conversion of sp into sp^2 carbon bonds, an exothermic process which finally leads to graphite, the most stable form of carbon. The energy loss by radiation amounts to about 0.2–0.4 eV/atom, a figure which appears reasonable compared to the total available transformation energy of about 1.2 eV/atom. The rest energy probably remains in the system in the form of disordered graphitic networks and incomplete transformation.

To check this conjecture we performed Raman spectroscopy of our samples *in situ*, meaning Raman exposure of the sample which remained under vacuum in the cryostat. It is well known that by using Raman spectroscopy the density of vibrational states can be monitored. The Raman spectrum shown in Figure 1.7 originates from a sample in which carbon molecules produced by laser ablation of graphite were trapped in a matrix of solid neon. The upper portion shows the spectrum of the sample annealed to almost flash conditions but then re-cooled to 4 K, and the lower portion shows the spectrum of the same sample warmed up to more than 200 K. Clearly, the peak intensity at around 2100 cm^{-1} , which is characteristic for molecular vibrations of sp carbon atoms decreases in intensity when the sample is warmed up, while the intensity of the “disordered graphite” sp^2 peak around 1500 cm^{-1} increases in intensity (the absolute intensities in both spectra are difficult to compare because the virulent conversion leads to mass loss of the sample). Remarkably, the sp -Raman peak seems to consist of a superposition of two peaks centered at about 2000 and 2200 cm^{-1} . At present we have no explanation for that splitting, but this feature may indicate the presence of strained or otherwise distorted sp bonds.

The Raman data confirm our picture of a conversion of carbon bonds from sp into sp^2 . Of course, both bond arrangements have to be considered as limiting cases which are not strictly realized in our samples. When the matrix is evaporated and the carbon molecules are free to react with each other, the chains or rings formed in the heavily annealed matrix re-arrange

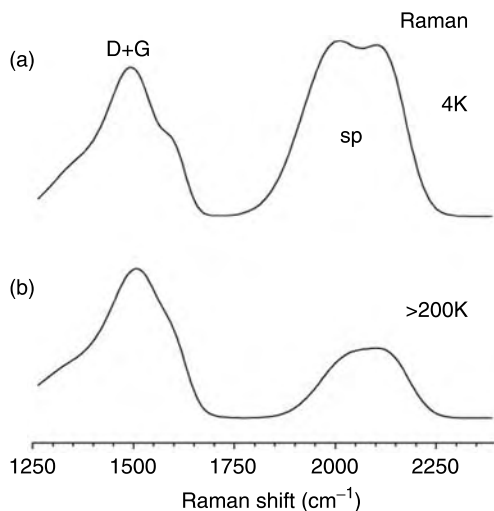


FIGURE 1.7 Raman spectra of matrix samples bearing carbon molecules (532 nm CW laser excitation). Most of the matrix material (neon) had been evaporated by warming up, upon which the sample was cooled down again to 4 K to carry out the measurement (upper spectrum). Then the sample was warmed up to 200 K and the lower spectrum was taken. Notice the decrease in the relative height between the broad peak at 2100 cm^{-1} relative to that at 1500 cm^{-1} . The former displays the abundance of vibrating carbons with sp bonds while the latter displays that of carbons with sp^2 bonds. At some point in the warming process, a virulent but, judging from the Raman data, not entirely complete sp-C to $\text{sp}^2\text{-C}$ transition takes place. This change is accompanied by flashes of light emission.

into disordered graphite-like networks. It may be mentioned that Casari and co-workers obtained similar Raman spectra in their carbon cluster deposition experiments [33]. The sp to sp^2 conversion thus seems to be a very general phenomenon in the growing process from carbon clusters to bulk carbon.

1.4 CONCLUSIONS

The uniqueness of carbon rests on the diversity of the atomic bond types it can assume and the ease by which carbon can polymerize. Upon condensation from the vapor phase into matrices, carbon molecules initially form chains and possibly rings. When these initial species become spatially concentrated, an exothermic conversion into a graphite-like network takes place. Under the cryogenic conditions prevailing during matrix sublimation, the resulting network is highly irregular and distorted. The network seems to still contain sp bonds which gradually disappear upon thermal annealing

to room temperature. The occurrence of carbon chains in space indicates that such conversion processes may also play a role in interstellar clouds, in our early solar system, or in the nuclei of comets.

REFERENCES

- [1] Kroto H.W., Heath J.R., O'Brien S.C., Curl R.F., Smalley R.E. *Nature* **1985**, 318, 162.
- [2] Krätschmer W., Lamb L.D., Fostiropoulos K., Huffman D.R. *Nature* **1990**, 347, 354.
- [3] Iijima S. *Nature* **1991**, 354, 56.
- [4] Dresselhaus M.S., Dresselhaus G., Eklund P.C. *Science of Fullerenes and Nanotubes*, Academic Press, 1996, ISBN 0-12-221820-5.
- [5] Saito R., Dresselhaus G., Dresselhaus M.S. *Physical Properties of Carbon Nanotubes*, Imperial College Press, 1998, ISBN 1-86094-093-5.
- [6] Haddon R.C. *Acc. Chem. Res.* **1992**, 25, 127.
- [7] Ney E.P. *Science* **1977**, 195, 541.
- [8] Huffman D.R. *Adv. Phys.* **1977**, 26, 129.
- [9] Tielens A.G.G.M., Snow T.P. (Editors), *The Diffuse Interstellar Bands*, Kluwer Academic Publishers, 1995, ISBN 0-7923-3629-1.
- [10] Jenniskens P., Desert F.X., *Astron. Astrophys. Suppl.* **1994**, 106, 39.
- [11] Draine B.T. *Interstellar Dust*, IAU Symposium No. 135, L.J. Allamandola and A.G.G.M. Tielens (Editors), Kluwer Academic Press, 1989, pp. 313–326 ISBN 0-7923-0449-7.
- [12] Chhowalla M., Wang H., Sano N., Teo K.B.K., Lee S.B., Amaratunga G.A.J. *Phys. Rev. Lett.* **2003**, 90, 41.
- [13] Douglas A.E. *Nature* **1977**, 269, 130.
- [14] Krätschmer W. *Astrophysics and Space Science* **1986**, 128, 93.
- [15] Schnaiter M., Mutschke H., Dorschner J., Henning Th., Salama F. *Astrophys. J.* **1998**, 498, 486.
- [16] Weltner W. Jr., van Zee R.J. *Chem. Rev.* **1989**, 89, 1713.
- [17] Zavitsanos P.D., Carlson G.A. *J. Chem. Phys.* **1973**, 59, 2966.
- [18] Maier J.P. *Chem. Soc. Rev.* **1997**, 21.
- [19] Grutter M., Wyss M., Riaplov E., Maier J.P., Peyerimhoff S.D., Hanrath M. *J. Chem. Phys.* **1999**, 111, 7397.
- [20] Monninger G., Förderer M., Gürtler P., Kalhofer S., Petersen S., Nemes L., Szalay P.G., Krätschmer W. *J. Phys. Chem. A* **2002**, 106, 5779.
- [21] Van Orden A., Saykally R.J. *Chem. Rev.* **1998**, 98, 2313.
- [22] Heath J.R., Saykally R.J. In: *On Clusters and Clustering*, Reynolds P.J. (Editor), North Holland, 1993, pp. 7–21, ISBN 0-444-89022-X.
- [23] Giesen T.F., Berndt U., Yamada K.M.T., Fuchs G., Schieder R., Winnewisser G., Provencal R.A., Keutsch F.N., Van Orden A., Saykally R.J. *Chemphyschem* **2001**, 4, 242.
- [24] Wang S.L., Rittby C.M., Graham W.R.M. *J. Chem. Phys.* **1997**, 107, 6032.
- [25] Wakabayashi T., Ong A.L., Krätschmer W. In: *Nanonetwork Materials*, S. Saito et al. (Editors), AIP Conference Proceedings, Vol. 590, pp. 513–517 (2001), ISBN 0-7354-0032-6.

- [26] Giesen T.F., Van Orden A., Hwang H.J., Fellers R.S., Provencal R.A., Saykally R.J. *Science* **1994**, 265, 756.
- [27] Kittel C. *Introduction to Solid State Physics*, 5th Edition, Wiley & Sons, 1976, p. 315, ISBN 0-471-49024-5.
- [28] Bell M.B., Feldman P.A., Kwok S., Matthews H.E. *Nature* **1982**, 295, 389.
- [29] Parker D.H., Wurz P., Chatterjee K., Lykke K.R., Hunt J.E., Pellin M.J., Hemminger J.C., Gruen D.M., Stock L.M. *J. Am. Chem. Soc.* **1991**, 113, 7499.
- [30] Smalley R.E. *Acc. Chem. Res.* **25**, 98 (1992).
- [31] Ishigaki T., Suzuki S., Kataura H., Krätschmer W., Achiba Y. *Appl. Physics A* **2000**, 70, 121.
- [32] Wakabayashi T., Ong A.L., Strel'nikov D., Krätschmer W. *J. Phys. Chem. B* **2004**, 108, 3686.
- [33] Casari C.S., Li Bassi A., Ravagnan L., Siviero F., Lenardi C., Piseri P., Bongiorno G., Bottani C.E., Milani P. *Phys. Rev. B* **2004**, 69, 075422.

2 Synthesis and Characterization of Carbynoid Structures in Cluster-Assembled Carbon Films

*L. Ravagnan, F. Siviero, E. Salis, P. Piseri,
P. Milani, C. Lenardi, A. Li Bassi, C.S. Casari
and C.E. Bottani*

CONTENTS

2.1	Introduction	15
2.2	Experimental	17
2.3	Experimental Results	21
2.3.1	Film Morphology	21
2.3.2	Raman Characterization of the As-Deposited Carbon Films	22
2.3.3	Gas Exposure	24
2.3.4	Thermal Stability	28
2.4	Discussion	29
2.5	Summary and Conclusions	33
	Acknowledgments	33
	References	33

2.1 INTRODUCTION

The combination of sp^3 , sp^2 and sp hybridized atoms can give rise to a large number of carbon allotropic forms and phases, but only carbon solids based on all sp^3 (diamond) and sp^2 (graphite, fullerene) hybridization are well known and characterized [1]. In addition there are innumerable transitional forms of carbon where sp^2 and sp^3 hybridization bonds co-exist in the same

solid such as in amorphous carbon, carbon black, soot, cokes, glassy carbon etc [2–4].

Solids based on sp hybridization, although subject of intense experimental efforts, seem to be the most elusive of the different carbon families [5]. The existence of linear chains of carbon atoms linked by alternating single and triple bonds (polyyne) or double bonds (polycumulene) with stabilizing molecular complexes at the end of the chains, has been recognized in interstellar molecular clouds and can be artificially produced by different chemical routes [6–8].

Polyyne and polycumulene chains are very fragile and reactive: exposure to oxygen and/or water completely destroys these species [5–9]. Isolated carbon chains have been extensively studied only in the gas phase [10–12] or by means of matrix-isolation spectroscopy at very low temperature [13–15]. The high reactivity of unsaturated sp chains and their tendency to undergo chain-chain cross-linking reaction causing the evolution towards an sp^2 phase [7] generated a deep skepticism about the possibility of assembling sp carbon chains to form a pure carbon solid [5].

Despite their fragility, the existence of an elemental carbon solid formed solely by sp chains known as “carbyne” has been proposed by many authors and it has been the subject of controversy [16]. Several results have been published mainly reporting on the crystallographic characterization of this hypothetical material, but no compelling evidence of the existence of the carbyne solid has been provided so far [5].

sp chains synthetic routes are based either on the high pressure and high temperature modification of carbon-based solids [17], or on chemical strategies aiming at the elimination of substituents from a linear organic molecule to end the naked linear carbon backbone [7,18]. This latter strategy includes catalytic dehydropolymerization of acetylene [19], dehydrohalogenation of chlorinated polyacetylene [19], air promoted coupling reaction of dicopper acetylide [20], and electrochemical reductive carbonization of poly(tetrafluoroethylene) [9].

The material obtained with the “chemical” approach is formed by carbon chains separated by reaction byproducts (e.g. alkali metal fluoride) preventing cross-linking reactions between adjacent carbynoid chains and decomposition in a reactive environment [9]. These systems are conceptually similar to the matrix-isolated chains where polyyne and polycumulene species are kept isolated and protected from chain-chain and chain-moisture interaction [21].

Recently, we have shown the possibility of growing a pure carbon amorphous solid containing a significant amount of carbynoid structures by supersonic carbon cluster beam deposition (SCBD) at room temperature and in an ultra-high vacuum (UHV) [22].

SCBD is a technique consisting in the production of a supersonic beam of inert gas seeded by carbon clusters (covalent aggregates with masses ranging from tens to thousands of atoms) by means of an appropriate

source. As a result of the relatively low kinetic energy of the clusters (below 0.2 eV/atom) they are not subjected to relevant fragmentation during the deposition, so that the films obtained retain the memory of the precursor clusters structure. The use of a supersonic beam makes also possible to exploit aerodynamic effects to reduce the beam divergence (leading to high deposition rates) and to control the clusters mass distribution.

In situ Raman spectroscopy on the films has confirmed the presence of polyynes and polycumulenes in a nanostructured sp^2 matrix. These sp hybridized linear carbon structures are metastable even in UHV at room temperature. When exposed to oxygen, the carbon network structure rapidly evolves towards a more common mainly sp^2 amorphous phase, with only a small residual amount of sp linear aggregates [23].

A deeper understanding of the stability of sp carbon structures and of their role in the nanostructured carbon network (abundance, stabilization mechanisms, interconnectivity) would provide a new insight in the physics and chemistry of linear carbon chains and it would address the long-sought opportunity of combining carbon building blocks with different hybridization to produce new forms of carbon with tailored structural and functional properties [1,24].

Raman spectroscopy is one of the techniques of choice for the study of carbon-based materials and for the identification of carbyne [5,25]. The presence of a Raman band at roughly 2100 cm^{-1} , generated by a stretching of the carbon triple bond, is admitted to be one of the strongest arguments in favor of the presence of carbynes [5,9]. Raman spectra of carbynoid materials are characterized by G and D bands in the $1200\text{--}1700\text{ cm}^{-1}$ range as in amorphous carbon and by the presence of the band in the 2100 cm^{-1} region [5,9]. For carbyne-rich materials this band should have an intensity comparable or even greater than the amorphous contribution.

In the following we present a Raman spectroscopy characterization of sp carbon chains embedded in a nanostructured carbon thin film deposited by SCBD. The evolution of sp carbon chains when exposed to different inert or reactive atmospheres (He, N_2 , H_2 and dry air), or when annealed in vacuum at various temperatures up to 200°C , has been followed by monitoring the variation of the Raman peaks associated with polyynes and polycumulenes in order to achieve detailed information about the chemical and thermodynamic stability of these species.

2.2 EXPERIMENTAL

A supersonic beam is schematically described as a gas stream expanding very rapidly from a high pressure region (source), through a nozzle, to a low pressure region. The characteristics of the beam are mainly determined by the size and shape of the nozzle and by the pressure difference between the two regions [26]. Compared to effusive beams used in molecular beam

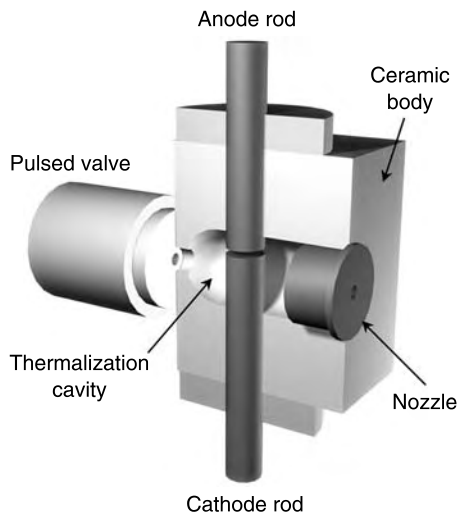


FIGURE 2.1 Three-dimensional view of the cluster beam source (not to scale). The body of the source is sectioned to show the electrodes arrangement in the cavity. Note the asymmetric placement of the gap.

epitaxy, supersonic beams provide higher intensity and directionality allowing deposition with very high growth rates. When a heavy species is diluted in a lighter one (as in the case of clusters diluted in He or another inert gas) and the mixture is expanded, a seeded supersonic beam forms. Seeded supersonic beams are extensively used to cool and to accelerate heavy species [26] such as clusters, and they are particularly attractive for SCBD.

Nanostructured carbon thin films containing carbynoid species were grown by SCBD of carbon clusters produced by a pulsed microplasma cluster source (PMCS, schematically shown in Figure 2.1) [27].

It consists of a ceramic cubic body, in which a cylindrical cavity is drilled. A channel is drilled perpendicular to the axis of the cavity and hosts two rods (electrodes) of the material to be vaporized, facing each other and separated by a gap of about 1 mm. A solenoid pulsed valve injects helium at the pressure of 20 bar through an insulating ceramic nozzle on the back of the cavity. The gap between the electrodes is off-axis, in such a way that the gas flushes on the cathode surface. A removable nozzle with cylindrical shape closes the front of the source.

The principle of operation of the cluster source is as follows: the valve delivers an intense He pulse with an opening time of a few hundreds of milliseconds, thus forming a small high gas density region at the cathode surface. After that, a very intense discharge (hundreds of amperes), lasting for a few tens of milliseconds, is fired between the electrodes by applying a voltage ranging from 500 up to 1500 V. Ionized helium sputters a small area

of cathode surface at the point where the He flux impinges on the electrode. The mixture of helium-vaporized atoms quenches and cluster nucleation takes place. The clusters are then carried out through the nozzle by the supersonic expansion.

The cathode is continuously rotated by means of an external motor in order to allow constant ablation conditions for all pulses and a homogeneous consumption of the rod. Higher deposition rates can be obtained by substituting the simple cylindrical nozzle with a more complex one (called focuser) as described in Reference 28. Exploiting inertial aerodynamic effects [28,29], the focuser reduces the angular semiaperture of the beam from 12° to less than 1° concentrating the cluster on the center of the beam.

The PMCS (Pulse Microplasma Cluster Source) produces a pulsed beam of carbon clusters seeded in helium with a mass distribution, with an approximately log-normal shape peaked around 600 atoms/cluster and extending up to several thousands atoms (Figure 2.2). The kinetic energy of the clusters is of the order of 0.3 eV/atom. Characterization by high resolution time-of-flight-mass spectrometry (TOF/MS) and *in situ* x-ray photoemission spectroscopy indicates that no contaminants (oxygen, nitrogen, hydrogen) are present in the beam and on the deposited films [30].

The PMCS source was mounted in the deposition apparatus CLARA (cluster assembling roaming apparatus) [31], schematically shown in Figure 2.3.

It consists of three differentially pumped vacuum chambers built to UHV specifications and is equipped with a linear TOF/MS.

The first chamber hosts the cluster source, evacuated by two turbomolecular pumps (300 l/s). They are horizontally mounted facing each other, in order to assure the correct operating conditions for the pulsed supersonic

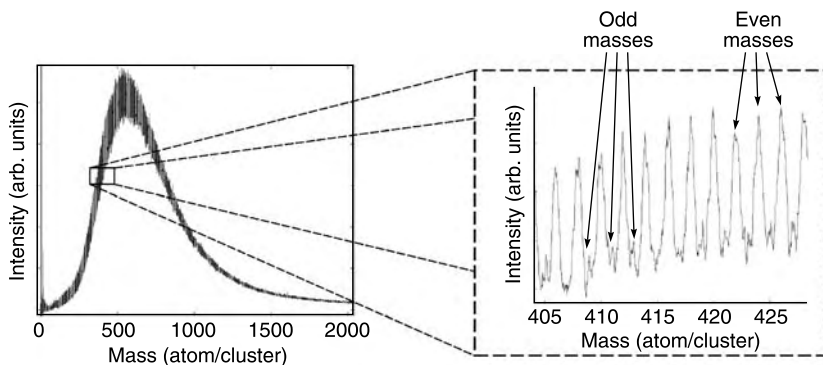
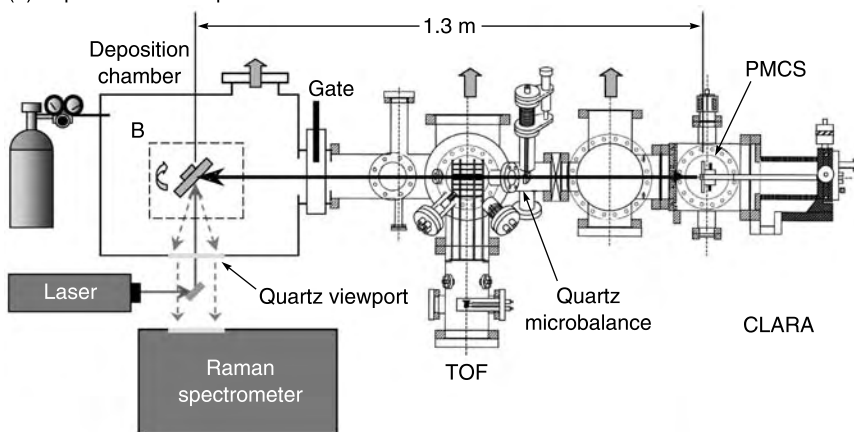
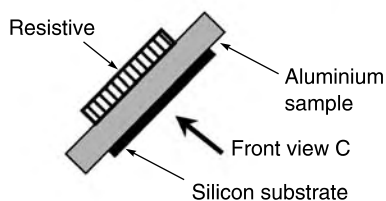


FIGURE 2.2 Mass distribution of the cluster beam measured by a reflectron TOF/MS. The masses are expressed as number of carbon atoms per clusters. As shown in the enlarged windows clusters with both odd and even number of carbon atoms can be observed.

(a) Experimental set up



(b) Substrate upper view



(c) Substrate front view

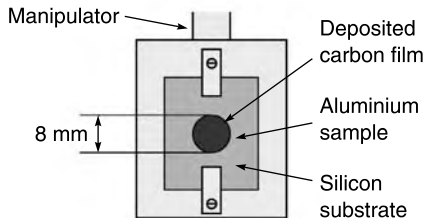


FIGURE 2.3 Schematic representation of the experimental set-up (A). The CLARA apparatus [31] (right) is connected through a gate valve to the deposition chamber (left), where the silicon substrate is placed on a 3-axis translating and z-axis rotating holder. The deposition chamber is equipped with a quartz window through which the Raman laser can be focused on the sample, and a precision leak valve for gas injections. The sample holder is equipped with a resistive heater and a thermo-resistance, for controlled thermal treatment of the sample from room temperature up to 350°C (B). During the deposition the holder intersects the cluster beam, so that a circular spot 200 nm thick and with a diameter of 8 mm is obtained (C).

beam source. The source is mounted on a UHV manipulator connected to the first chamber and an electroformed skimmer is placed in front of the source.

The second chamber is evacuated by a vertically mounted turbomolecular pump. It hosts a Maxtek BHS-150 quartz microbalance in order to monitor the intensity of the cluster beam, and offers the possibility to connect other UHV systems (such as a load-lock chamber and/or an analysis facility). Cluster deposition on a substrate can be performed directly in the second chamber.

A 3 mm pinhole is placed along the apparatus axis, in order to maintain a differential vacuum between the second and the third chamber and to

reduce the size of the beam spot downstream of the apparatus. This chamber hosts a two-stage TOF/MS, developed to be specifically coupled to a supersonic beam of clusters. The chamber can host an electron gun for cluster ionization and a UV grade silica windows to allow cluster ionization by an excimer laser.

The CLARA apparatus is connected through a gate valve to a small UHV deposition chamber, where a silicon substrate is placed on a 3-axis translating and z -axis rotating holder. During the deposition the holder intersects the cluster beam, so that a circular spot 200 nm thick (estimated by means of a quartz microbalance rate measurement) and with a diameter of 8 mm is obtained. The deposition rate is typically 4 nm/min.

After the deposition the holder can be rotated by 90° , thus placing the film in front of a quartz window through which the Raman laser can be focused on the sample. The excitation light is the 532 nm line of a frequency doubled Nd–Yag or the 632.8 nm line of a He–Ne laser. Backscattered light is analyzed by a Jobin-Yvon T64000 spectrometer in triple grating configuration and detected by a liquid nitrogen cooled CCD (Charge Coupled Device) camera. Spectral resolution is below 3 cm^{-1} .

The substrate temperature can be varied after the film deposition up to 350°C by means of a tungsten heater mounted on the sample holder. The final temperature can be reached in a few minutes and it can be kept constant within $\pm 2^\circ\text{C}$ by means of an electronic controller.

The deposition chamber is also equipped with a precision leak-valve and a capacitance manometer in order to allow the introduction of pure gases and a careful control of their pressure.

2.3 EXPERIMENTAL RESULTS

2.3.1 FILM MORPHOLOGY

Films with a density ranging from 1 to 1.4 g/cm^3 can be grown depending on the precursor clusters. Brunauer–Emmett–Teller analysis shows a surface specific area of $665\text{ m}^2/\text{g}$ [32].

The growth of films via SCBD can be viewed as a random stacking of particles as for ballistic deposition [33,34]. The resulting material is characterized by a low density compared to that of the films assembled atom by atom and it shows different degrees of order depending on the scale of observation. The characteristic length scales are determined by cluster dimensions and by their fate after deposition. Carbon cluster beams are characterized by the presence of a finite mass distribution and by the presence of different isomers with different stabilities and relativities. Due to the low kinetic energy of clusters in the supersonic expansion stable clusters can survive to the deposition, while reactive isomers can coalesce to form a more disordered phase [35].

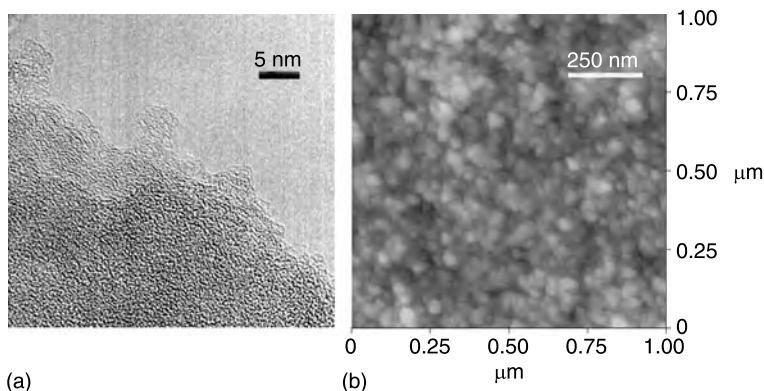


FIGURE 2.4 (a) TEM image of a cluster assembled carbon film showing an amorphous matrix with small closed shell particles and bundles of graphene sheets. (b) Tapping mode AFM topographies at different magnifications of a cluster assembled carbon film with nominal thickness of 700 nm. The scan size is 1000×1000 nm, the vertical color scale is 50 nm.

Transmission electron microscope (TEM) analysis of nanostructured carbon films shows that, at this scale, the morphology is reminiscent of the precursor clusters. TEM micrographs show the presence of an amorphous matrix with small closed shell particles and bundles of graphene sheets (Figure 2.4a). Large onion-like and tubular particles have also been observed.

Surface morphology of nanostructured carbon films has been investigated by atomic force microscopy (AFM) in air (Digital Nanoscope IIIA) operating in tapping mode to avoid scratching of the samples. Figure 2.4b shows typical morphologies of nanostructured carbon films. The observed grains are larger than single clusters in the beam and they result from an aggregation mechanism. The grain size depends on precursor size, and their mean diameter value ranges between 10 and 15 nm.

2.3.2 RAMAN CHARACTERIZATION OF THE AS-DEPOSITED CARBON FILMS

Raman spectra of cluster-assembled carbon films grown in our apparatus and then kept under ambient conditions are characterized by the presence of the so-called G and D bands in the $1300\text{--}1600\text{ cm}^{-1}$ spectral region [36]. Their position and shape can be related to the degree of structural disorder of the film and to the distribution of bond lengths and angle distortions [37]. A weak feature in the $2000\text{--}2200\text{ cm}^{-1}$ spectral region is also present [31]. This feature can be interpreted *a posteriori* as due to sp chains protected from oxidation by the sp^2 carbon matrix (see Figure 2.5).

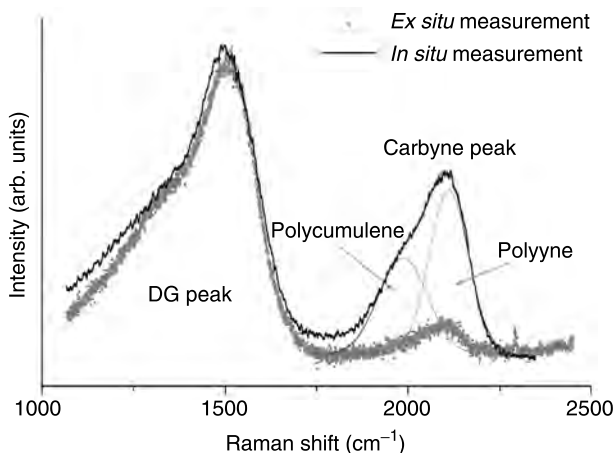


FIGURE 2.5 Raman spectra of cluster-assembled carbon films grown at room temperature. The two spectra were collected *ex situ* (gray) and *in situ* in UHV conditions (black). For the *in situ* spectra we show the two fitting curves of the carbyne peak, identifying the polycumulene (left) and polyynes (right) contributions.

Figure 2.5 shows the comparison between the *ex situ* and *in situ* Raman spectra of two films deposited in the same conditions. A peak at 2100 cm^{-1} dramatically increases in intensity in the *in situ* spectrum (we will refer to it as “C” peak), as shown in Figure 2.5, whereas G and D bands undergo small changes from *ex situ* to *in situ* deposition.

The C peak has a remarkably strong intensity and appears to be structured and composed of a main broad peak at about 2100 cm^{-1} and a weaker shoulder centered around 1800 cm^{-1} , as evidenced by a two-gaussian fit (see Figure 2.5). The peaks at 2100 and 1800 cm^{-1} can be assigned to the vibrational frequencies of the C–C bond in both polyyne and polycumulene chains, respectively [5,9,38]. The relative C peak intensity of the as-deposited carbon, expressed by the ratio between its integrated intensity and the D–G band integrated intensity ($I_{\text{C}}^{\text{rel}} = I_{\text{C}}/I_{\text{D,G}}$), is roughly 45%.

An accurate quantitative determination of the sp content with respect to sp² is not possible by Raman spectroscopy [39], since the actual Raman cross section of linear chains and rings embedded in the carbon amorphous network is not known. Nevertheless, the integrated intensity of the carbyne peak $I_{\text{C}}^{\text{rel}}$ is directly related to the carbyne amount in the network and was thus chosen as the main parameter relating to their evolution. Owing to the amorphous character of the material, gaussian fitting functions have been chosen for the analysis of Raman peaks.

In Figure 2.6 we report the Raman spectra of the cluster-assembled material immediately after deposition in UHV conditions, obtained with different excitation wavelengths (532 nm and 632.8 nm). Using an excitation

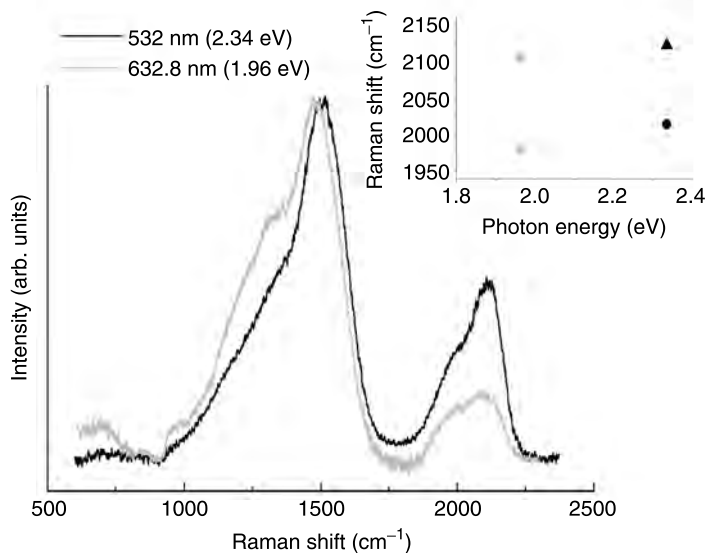


FIGURE 2.6 *In situ* Raman spectra of cluster assembled carbon films obtained with different excitation wavelengths: a frequency-doubled Nd–Yag (532 nm) and a He–Ne (632.8 nm). In the inset: dispersion of polycumulene peak (solid circles) and polyyne peak (solid triangles).

wavelength of 632.8 nm we observe a G peak shift towards a lower frequency (roughly 30 cm^{-1}) and an I_D/I_G increase with respect to the case in which a 532 nm wavelength is used. This reflects the typical dispersion behavior for G and D features in mainly sp^2 amorphous carbon [37]. I_C^{rel} is smaller at 632.8 nm in agreement with the observation on polymeric carbon reported in Reference 9. By varying the laser excitation energy the relative polycumulene/polyyne intensity ratio also varies and it is larger at 632.8 nm than at 532 nm.

2.3.3 GAS EXPOSURE

The sp chains are metastable and have the tendency to undergo cross-linking reactions to form sp^2 phase [7]. In order to characterize the sp metastable decay we have monitored the sp chain stability through the evolution of the C peak intensity, either keeping the sample under UHV for several days (at a pressure of about 2×10^{-9} Torr) or exposing it to different atmospheres (H_2 , He, N_2 and dry air) [40]. In the case of UHV conditions, we have observed a slow decrease of the intensity of both the two components of the C peak and small changes in the shape of the G and D bands. The temporal evolution of I_C^{rel} is well described by an exponential decay plus a constant:

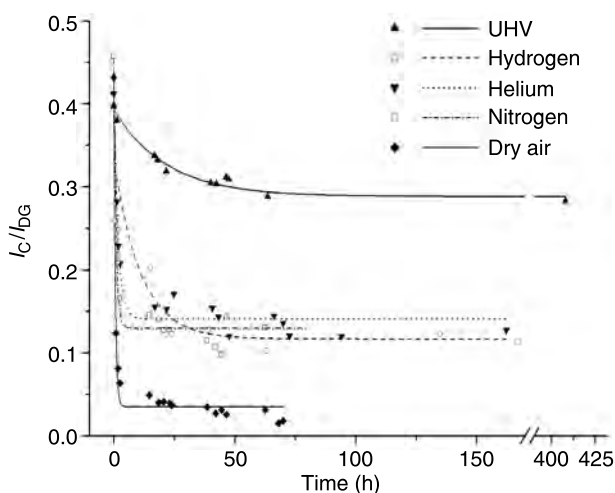


FIGURE 2.7 Decay behavior of the relative C peak intensity as a function of UHV residence time and different gases exposure times.

$I_C^{\text{rel}} = R_0 + R_1 e^{-t/\tau}$ (see Figure 2.7). This provides an estimate of the characteristic decay time constant and of the residual nonreacted fraction of carbynoid structures. A characteristic decay time of the order of 22 h, resulting in a reduction of I_C^{rel} to a 29% of the as-deposited value has been observed (see Table 2.1). It is worth noting that this residual intensity is almost one order of magnitude greater than the intensity measured in *ex situ* samples, and that it remains stable even after 18 days from the deposition.

In order to characterize the effect of gas exposure on polyynes and polycumulenes, we have monitored the evolution of I_C^{rel} in films exposed to the different gases at the pressure of 500 mbar. Figure 2.8 shows the

TABLE 2.1
Fitting Parameters for the Exponential plus a Constant Decay of the Relative C Peak Intensities under Exposure of Different Gases

	R_0	τ (h)
UHV	$28.8 \pm 0.5\%$	22 ± 3
H ₂	$12.0 \pm 0.8\%$	11 ± 3
He	$14.1 \pm 0.3\%$	2.0 ± 0.1
N ₂	$13.0 \pm 0.2\%$	1.0 ± 0.1
Dry air	$3.6 \pm 0.2\%$	0.58 ± 0.03

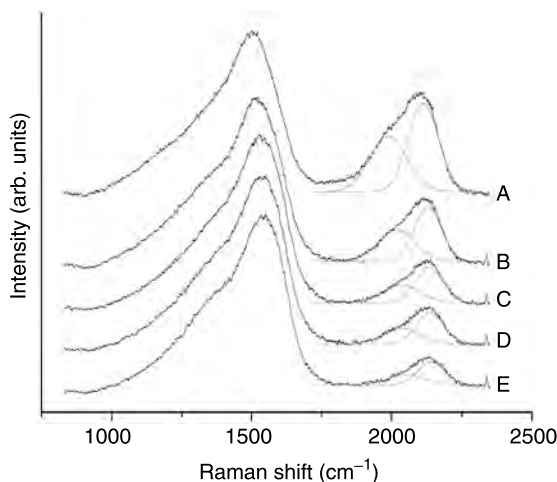


FIGURE 2.8 Raman spectra of a 200 nm thick sample exposed to 500 mbar of molecular nitrogen after different exposure times: as deposited (A), after 50 min (B), 2.5 h (C), 18.5 h (D) and 44.5 h (E). Gaussian fit of the two components of the carbyne peak is also reported.

temporal evolution of the Raman spectrum of a film exposed to N_2 . Similar spectra have been obtained for helium and hydrogen exposure, indicating that the evolution of the polyyne and polycumulene peaks is substantially similar for all these gases. Dry air induces a different behavior, which will be discussed later.

The intensity of the C peak decreases readily following an exponential law and reaching an asymptotic value after a few hours from gas injection (Figure 2.7). Table 2.1 presents the results of the analysis of the evolution of I_C^{rel} , fitted with an exponential decay: the time constants τ and the percentage R_0 of the nonreacted fraction of *sp* chains for the different gas exposures are shown, together with the parameters of the metastable decay in UHV as discussed above.

The gas exposure slightly affects the sp^2 component of the carbon network. Since these changes are not relevant as for the C band, I_C^{rel} can be considered a reliable parameter when following the *sp* component evolution.

The same behavior is qualitatively observed for exposure to helium and molecular hydrogen, and the analysis of the decay time constants and the R_0 for hydrogen, helium and nitrogen shows that the values of R_0 vary of 12–14% for the three gas, while τ is substantially different ($\tau_{N_2} = 1$ h, $\tau_{He} = 2$ h, $\tau_{H_2} = 11$ h). The relative intensity of the polyyne and the polycumulene components remains substantially unchanged during the peak evolution and only a small blue shift is observed for both peaks.

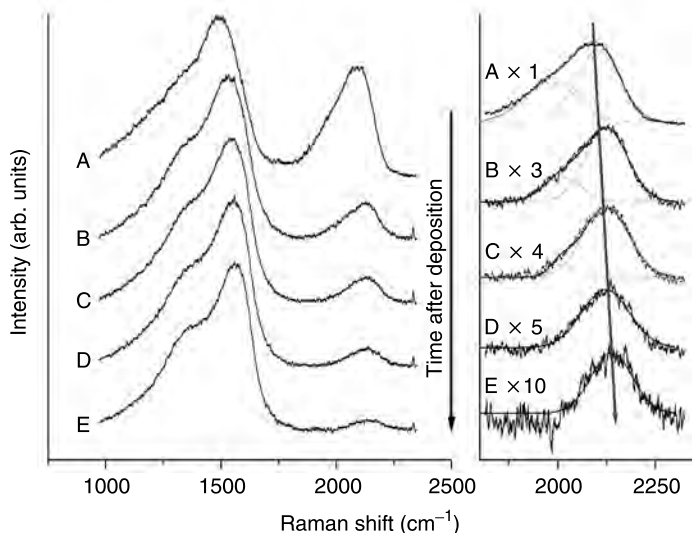


FIGURE 2.9 Left panel: Raman spectra of a 200 nm thick sample exposed to dry air at different time; as deposited (A), after 50 min (B), 2.5 h (C), 15 h (D) and 70 h (E). Right panel: evolution of the corresponding carbyne peak and gaussian fit of its two components. The arrow underlines the blue shift of the carbyne peak occurring during its decay.

This indicates that exposure to a different atmosphere, at the same pressure, mainly affects the kinetics of the decay, while the fraction of sp chains surviving the gas exposure is independent of the specific gas. τ values are found to decrease with increasing mass of the gas molecule: the higher the mass, the faster the decay. The τ trend does not seem to be directly related to the gas molecule size.

A different interaction mechanism is expected, and indeed observed, when the cluster-assembled films are exposed to dry air, since oxygen is known to readily react chemically with carbon chains [7]. Figure 2.9 shows the evolution of the Raman spectrum during exposure to dry air. As reported in Table 2.1, the C peak decay is faster for dry air than for the other gas ($t_{\text{air}} \cong 0.6$ h, with a partial pressure of oxygen of 100 mbar), and the corresponding asymptotic $I_{\text{C}}^{\text{rel}}$ value is significantly smaller ($R_0 \cong 3\text{--}4\%$) and comparable to what observed in *ex situ* measurements.

The relative intensity of the polyynes and polycumulene contributions to the C peak is not constant during dry air exposure. In the right panel of Figure 2.9 the C peak evolution is shown in detail: the polycumulene peak decreases much more rapidly, and roughly 15 h after air injection there is no remaining detectable signal from polycumulenic chains.

2.3.4 THERMAL STABILITY

In order to investigate the thermal stability of sp structures in the carbon network, we have characterized *in situ* the C peak evolution in the Raman spectra of films thermally annealed at different temperatures (up to 200°C), in UHV conditions. For each temperature, starting from room temperature (RT), a series of Raman spectra were acquired at fixed time intervals for a period of several days.

In Figure 2.10 we report the I_C^{rel} evolution as a function of time at RT, 100°C, 150°C, and 200°C. This evolution cannot be fitted by a simple exponential decay; a better description can be obtained by using a sum of two exponential decays with different time constants: $I_C^{\text{rel}} = R_0 + R_1 e^{-t/\tau_1} + R_2 e^{-t/\tau_2}$. The first time constant is of the order of tens of minutes, while the second is of the order of hours. The values of the two decay constants τ_1 and τ_2 and the asymptotic value R_0 are reported in Table 2.2.

We observe threshold effects at different temperatures both for the slow decay constants τ_2 and in the fraction of surviving carbynes after the thermal treatment R_0 . This has a value of roughly 29% after the metastable decay at RT, it drops at 15% at 100°C remaining constant up to 150°C. We observe another drop to 8% at 200°C. This suggests the presence of two activated processes with energy barriers situated between 25 and 40 meV.

On the other hand, τ_2 abruptly decreases when passing from 100°C to 150°C annealing, while only a small decrease is observed at 200°C, when a new energy barrier is presumably being overcome. In the range 100–150°C, instead, a τ_2 decrease suggests that the temperature only affects the decay kinetics.

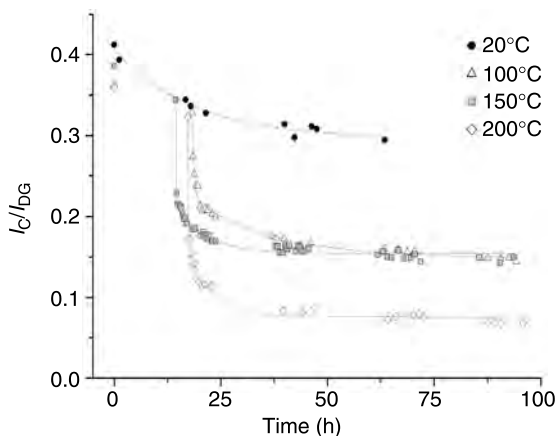


FIGURE 2.10 Decay behavior of the relative C peak intensity during temperature treatment of the sample.

TABLE 2.2

Asymptotic Value and Exponential Decay Times Obtained by Double Exponential plus Constant Fit of the Relative C Peak Intensities for Different Thermal Annealing of the Sample

	R_0	τ_1 (min)	τ_2 (h)
20°C	$29.0 \pm 0.9\%$	—	21 ± 5
100°C	$14.9 \pm 0.5\%$	27.0 ± 2.1	18.3 ± 2.2
150°C	$15.5 \pm 0.3\%$	16 ± 4	6.5 ± 0.9
200°C	$7.6 \pm 0.3\%$	12 ± 3	6.1 ± 1.2

2.4 DISCUSSION

It was widely accepted that polyyne chains can be stabilized in structures where a large interchain distance is maintained by interdispersing foreign materials [7]. Moreover, polycumulene structures have been predicted to be so fragile that the synthesis of a material containing this type of sp chains has been considered extremely difficult if not impossible [5].

Our experiments provide several novel aspects to the scenario of sp chains production and assembling. In cluster-assembled films polyynes and polycumulenes can survive in a sp² carbon matrix at room temperature if oxygen is absent; moreover, they can survive a landing process where the kinetic energy per atom is of several fraction of eV [22].

The presence of the different carbon sp species is confirmed also by the behavior of Raman peaks at different excitation energies [40]. So far, the only reported studies of the carbynoid peak dispersion behavior were performed by Kastner et al. [9] for carbynoid chains obtained by carbonization of PTFE by alkali metals, and by Akagi et al. [41]. Kastner et al. observed a shift of the C–C peak (attributed to polyyne chains) from 1960 to 2080 cm^{−1} when the excitation energy changes from 1.9 to 3.1 eV. This dispersion effect in conjugated systems is explained in terms of a correlation between conjugation length and electronic structure and attributed to a photoselective resonance process [42]. Akagi et al. report a dispersion of the polyyne peak (observed at higher frequencies, roughly 2100–2150 cm^{−1}) of 60 cm^{−1}/eV. We were able to observe a similar dispersion behavior for both spectral contributions (70–80 cm^{−1}/eV for the polycumulene peak, 60 cm^{−1}/eV for the polyyne peak as shown in the inset in Figure 2.6). Moreover, both Akagi et al. and Kastner et al. observed an enhancement of the C peak intensity, relatively to the G+D intensity, of an order of magnitude or more, when changing the excitation source in the same interval. We also observe an enhancement of the overall C peak, but with a larger increase of the polyyne peak with respect to the polycumulene peak. This represents a

further indication of the different electronic structure of the two components of the carbynoid peak.

The interaction with H_2 , N_2 and He causes a decrease of the carbynoid species. Since the decay times are related to the mass of the gas molecules or atoms, we suggest that the gas action is simply mechanic and that the gas species hit the sp chains causing the rearrangement of the metastable structures.

Cluster-assembled carbon film are very porous with a pore diameter peaked at 3–4 nm, as shown by adsorption/desorption isotherm analysis [32]. The gases used in our experiments have a molecular or atomic size much smaller than the average pore size, so it is reasonable to assume that they equally diffuse in the mesoporous film network and interact with the same amount of linear carbon structures. This explains the similar R_0 value observed for the three gases. The time required to reach the asymptotic value of I_C^{rel} is affected by the momentum transferred from the molecule to the film network during collisions, hence by the mass of the gas molecule. We note that H_2 does not seem to chemically interact with sp structures.

A different behavior is observed for the interaction with oxygen where a chemical reaction takes place. In this case we observe a much faster decay and a stronger shortening of the sp chains, as shown by a higher blue shift of the carbyne's Raman peaks, indicating that a sort of chain cleavage is taking place causing the shortening of polynes and polycumulenes (see Figure 2.11). Both theoretical [43] and experimental observations [41] suggest that the vibrational frequency of carbon chains should increase with decreasing length. Moreover, we also observe that the cumulenic fraction is

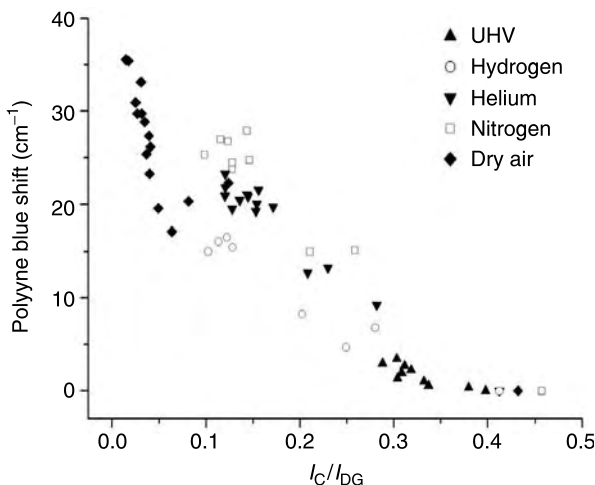


FIGURE 2.11 Blue shift of the polyyne peak for different gas exposure.

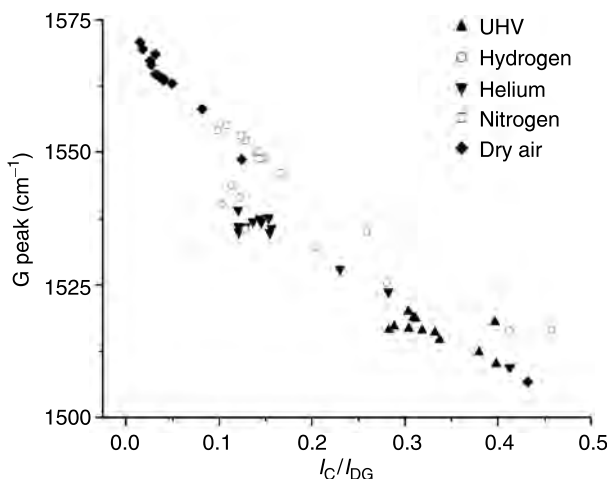


FIGURE 2.12 Blue shift of the G peak versus I_C^{rel} for different gas exposure.

completely destroyed by oxygen exposure, whereas some polyyne chains survive. This confirms the theoretical predictions [38] that cumulenenic chains are less stable with respect to oxygen, and also explains why their contribution in previous *ex situ* Raman spectroscopy studies was not observed.

During exposure to all the gases, a blue shift (up to 60 cm^{-1}) and narrowing of the G peak, and an increase in the I_D/I_G relative intensity were detected. These changes (stronger in the case of oxygen), although not dramatic, seem to indicate a small trend towards ordering of the sp^2 phase [37]. An increase of the D component and a blue shift and narrowing of the G band are also visible in the evolution of the Raman spectra as a consequence of thermal treatments. While sp^2 phase changes during heating are certainly also related to the onset of an ordering (graphitization) process due to annealing, similar changes need an explanation in the case of exposure to oxygen and other gases.

In Figure 2.12 we show the correlation between G peak position and I_C^{rel} . It can be observed that the decreasing of the I_C^{rel} corresponds to a shift of the G peak towards higher frequencies indicating a slight ordering of the sp^2 network. This indicates that a cross-linking mechanism [5,18], proposed for the breaking of both polyyne and polycumulene chains, is taking place leading to the formation of ordered hexagonal sp^2 graphitic domains.

Carbynoid systems obtained from perfluorinated hydrocarbons have shown to decay faster when heated although a systematic characterization of the effect of thermal annealing has not been provided [9]. We observe that moderate thermal heating in UHV conditions strongly affects the decay behavior of the sp chains in nanostructured carbon. The sp phase seems to be

very sensitive to temperature variations even in a small range. The presence of two very different decay times may suggest that the faster one is related to structural rearrangements induced by temperature gradients. The slower one should be related to accelerated cross-linking processes. Two different activation energies should correspond to these two regimes.

Considering the formation and deposition process of carbon clusters by PMCS, it is reasonable to assume that the carbynoid species are formed in the cluster source prior to deposition. The picture coming out from our observations is characterized by relatively fragile sp chains that are quite surprisingly able to survive deposition at kinetic energies per atom, well above the thermal energy measured to induce the sp rearrangement and sp^2 formation.

One possible mechanism for the stabilization of sp chains in the carbon matrix may be the formation of joints between the chain ends and sp^2 island adatoms. Jarrold and co-workers have reported the observation of ball-and-chain dimers formed by fullerenes linked by sp chains obtained by laser desorption of fullerene films [44]. The same type of connections could be formed in our films, rich of fullerene-like fragments [35], thus allowing the stabilization of the carbynoid species. Different type of stabilization sites could be present in our films since we observe a metastable decay of the carbynoid population.

The landing process and the heating process are taking place over two very different time scales. The landing process takes place on a short time scale and the kinetic energy can be efficiently dissipated among a huge amount of degrees of freedom of the substrate and of the cluster itself, especially for large clusters [45]. On the other hand the thermal heating is a process where vibrational modes are statistically populated: the time scale of the process is such that the modes leading to rearrangement can be efficiently populated.

Our results also address another relevant aspect of carbon clusters: that is, the shape and the hybridization of the precursor aggregates. As we have shown, we are depositing particles in a mass range where fullerene-like shape and sp^2 hybridization should be predominant [46,47]. However, an accurate analysis of the mass spectra shows that the contribution of odd clusters is not negligible (Figure 2.2). This suggests that non-fullerene type of clusters could be more abundant than expected even for relatively large clusters. Another possibility, supported by the studies of Jarrold and co-workers [44] is that fullerene like clusters can form complexes with the presence of sp chains.

In any case the survival ability of polyyne and polycumulenes upon landing indicates that they are somehow protected by the aggregate where they have been formed, like a kind of “cushion” capable of absorbing and dissipating the deposition energy and to prevent the cross-linking reactions.

2.5 SUMMARY AND CONCLUSIONS

Our experiments show, unambiguously, that a pure carbon film rich with sp linear chains can be formed by assembling carbon clusters at room temperature under ultra-high vacuum. Polyynes and polycumulene species are present and stabilized in all-carbon metastable structures without the need of hetero-atom terminal groups. Under He, N_2 , and H_2 exposure the amount of sp species reduces exponentially with time depending upon the mass of the gas. For the investigated gases no chemical interactions have been observed.

Oxygen chemically reacts with polyynes and polycumulenes causing an almost complete degradation of these species. Thermal treatments at moderate temperatures also cause a substantial reduction of the sp contents favoring cross-linking reactions. Threshold effects are observed at different temperatures suggesting the presence of activated rearrangement processes.

The existence of a form of solid carbon where carbynoid species can co-exist with sp^2 hybridization has important implications for the achievement of a deeper understanding of the processes leading to the formation of carbon clusters [46], for the synthesis of novel carbon allotropic forms and nanomaterials [1], and for the chemistry of the interstellar medium [12].

The production of a solid consisting of sp^2 and sp hybridized atoms support the theoretical prediction by Baughman et al. [24] about the existence of a layered carbon phase containing sp^2 and sp atoms dubbed graphyne.

Carbyne-containing carbon clusters may also be the vehicle for providing sp chains to different reactions taking place in the interstellar medium, even for conditions considered, up to now, unfavorable for the survival of naked sp chains [8].

ACKNOWLEDGMENTS

We thank L. Kavan, F. Cataldo, T. Wakabayashi, and W. Kraetschmer for insightful discussions. This work has been supported by MIUR under project FIRB "Carbon based microstructures and nanostructure".

REFERENCES

- [1] *Nanostructured Carbon for Advanced Applications*, G. Benedek, P. Milani, V.G. Ralchenko (Editors), NATO ASI Series, Vol. 24, Kluwer Academic Publishers, Dordrecht (2001).
- [2] M.V. Geis, M.A. Tamor, "Diamond and Diamond-like Carbon", in *Encyclopedia of Applied Physics*, Vol. 5, VCH Publishers, Weinheim (1993).
- [3] J. Robertson, *Mater. Sci. Eng. R* **37**, 129 (2002).

- [4] *Carbon Black: Science and Technology*, J.B. Donnet, R.C. Bansal, M.J. Wang (Editors), Dekker, New York (1993).
- [5] R.B. Heimann, S.E. Evsyukov, L. Kavan (Editors), *Carbyne and Carbynoid Structures*, Kluwer Academic Press, Dordrecht (1999).
- [6] H.W. Kroto, J.R. Heath, S.C. O'Brien, R.F. Curl, R.E. Smalley, *Astrophys. J.* **314**, 352 (1987).
- [7] L. Kavan, *Chem. Rev.* **97**, 3061 (1997).
- [8] T. Henning, F. Salama, *Science* **282**, 2204 (1998).
- [9] J. Kastner, H. Kuzmany, L. Kavan, F.P. Dousek, J. Kuerti, *Macromolecules* **28**, 344 (1995).
- [10] R.J. Lagow, J.J. Kampa, H.C. Wei, S.L. Battle, J.W. Genge, D.A. Laude, C.J. Harper, R. Bau, R.C. Stevens, J.F. Haw, E. Munson, *Science* **267**, 362 (1995).
- [11] T. Pino, H. Ding, F. Guethe, J.P. Maier, *J. Chem. Phys.* **114**, 2208 (2001).
- [12] M.C. McCarthy, P. Thaddeus, *Chem. Soc. Rev.* **30**, 177 (2001).
- [13] W. Kraetschmer, N. Sorg, D.R. Huffman, *Surf. Sci.* **156**, 814 (1985).
- [14] A.K. Ott, G.A. Rechtsteiner, C. Felix, O. Hampe, M.F. Jarrold, R.P. Van Duyne, K. Ragavachari, *J. Chem. Phys.* **109**, 9652 (1998).
- [15] J. Szczepanski, J. Fuller, S. Ekern, M. Vala, *Spectrochim. Acta A* **57**, 775 (2001).
- [16] A.G. Whittaker, *Science* **229**, 485 (1985); P.P.K. Smith, P.R. Buseck, *ibid.* **229**, 487 (1985).
- [17] R.B. Heimann, *Diamond Relat. Mat.* **3**, 1151 (1994).
- [18] L. Kavan, J. Kastner, *Carbon* **32**, 1533 (1994).
- [19] Yu. P. Kudryavtsev, R.B. Heimann, S.E. Evsyukov, *J. Mater. Sci.* **31**, 5557 (1996).
- [20] F. Cataldo, D. Capitani, *Mater. Chem. Phys.* **59**, 225 (1999).
- [21] L. Kavan, *Carbon* **5/6**, 801 (1998).
- [22] L. Ravagnan, F. Siviero, C. Lenardi, P. Piseri, E. Barborini, P. Milani, C.S. Casari, A. Li Bassi, C. E. Bottani, *Phys. Rev. Lett.* **89**, 285506-1 (2002).
- [23] E. Barborini, P. Piseri, A. Li Bassi, A. C. Ferrari, C. Bottani, P. Milani, *Chem. Phys. Lett.* **300**, 633 (1999).
- [24] R.H. Baughman, H. Eckhardt, M. Kertesz, *J. Chem. Phys.* **87**, 6687 (1987).
- [25] M. Nakamizo, R. Kammereck, P.I. Walker Jr., *Carbon* **12**, 259 (1974).
- [26] *Atomic and Molecular Beam Methods*, G. Scholes (Editor), Oxford University Press, Oxford (1988).
- [27] E. Barborini, P. Piseri, P. Milani, *J. Phys. D: Appl. Phys.* **32**, L105 (1999).
- [28] P. Piseri, A. Podestà, E. Barborini, P. Milani, *Rev. Sci. Instrum.* **72**, 2261 (2001).
- [29] H. Vahedi Tafreshi, P. Piseri, S. Vinati, E. Barborini, G. Benedek, P. Milani, *Aerosol. Sci. Technol.* **36**, 593 (2002).
- [30] E. Magnano, C. Cepek, M. Sancrotti, F. Siviero, S. Vinati, C. Lenardi, P. Piseri, E. Barborini, P. Milani, *Phys. Rev. B* **67**, 125414 (2003).
- [31] E. Barborini, F. Siviero, S. Vinati, C. Lenardi, P. Piseri, P. Milani, *Rev. Sci. Instrum.* **73**, 2060 (2002).
- [32] C. Lenardi, E. Barborini, V. Briois, L. Lucarelli, P. Piseri, P. Milani, *Diamond Relat. Mat.* **10**, 1195 (2001).
- [33] P. Milani, S. Iannotta, *Cluster Beam Synthesis of Nanostructured Materials*, Springer, Berlin (1999).

- [34] A.L. Barabasi, H.E. Stanley, *Fractal Concepts in Surface Growth*, Cambridge University Press, Cambridge (1995).
- [35] D. Donadio, L. Colombo, P. Milani, G. Benedek, *Phys. Rev. Lett.* **83**, 776 (1999).
- [36] P. Milani, M. Ferretti, P. Piseri, C.E. Bottani, A. Ferrari, A. Li Bassi, G. Guizzetti, M. Patrini, *J. Appl. Phys.* **82**, 5793 (1997).
- [37] A.C. Ferrari, J. Robertson, *Phys. Rev. B* **61**, 14095 (2000).
- [38] J. Kürti, C. Magyar, A. Balázs, P. Rajczy, *Synth. Met.* **71**, 1865 (1995).
- [39] A.C. Ferrari, J. Robertson, *Phys. Rev. B* **64**, 075414 (2001).
- [40] C.S. Casari, A. Li Bassi, L. Ravagnan, F. Siviero, C. Lenardi, P. Piseri, G. Bongiorno, C.E. Bottani, P. Milani, *Phys. Rev. B* **69**, 075422 (2004).
- [41] K. Akagi, M. Nishiguchi, H. Shirakawa, Y. Furukawa, I. Harada, *Synth. Met.* **17**, 557 (1987).
- [42] H. Kuzmany, *Pure Appl. Chem.* **57**, 235 (1985).
- [43] N. Breda, G. Onida, G. Benedek, G. Colò, R.A. Broglia, *Phys. Rev. B* **58**, 11000 (1998).
- [44] A.A. Shvartsburg, R.R. Hudgins, R. Gutierrez, G. Jungnickel, T. Frauenheim, K.A. Jackson, M.F. Jarrold, *J. Phys. Chem. A* **103**, 5275 (1999).
- [45] R.D. Beck, P. St. John, M.M. Alvarez, F. Diederich, R.L. Whetten, *J. Phys. Chem.* **95**, 8402 (1991).
- [46] R.E. Smalley, *Acc. Chem. Res.* **25**, 98 (1992).
- [47] H.W. Kroto, K. McKay, *Nature* **331**, 328 (1988).

3 Epitaxial Growth by D.c. Magnetron Sputtering of Carbyne (Chaoite) Microcrystals on CVD-Deposited Polycrystalline Diamond

*Robert B. Heimann, Igor Burlacov,
Jacob I. Kleiman and Sergey Horodetsky*

CONTENTS

3.1	Introduction	37
3.2	Proposed Epitaxy of Carbyne on Diamond	39
3.3	Equipment	42
3.3.1	Chemical Vapor Deposition (CVD) Reactor	42
3.3.2	D.c. Magnetron	43
3.4	Deposition and Characterization of Carbyne.....	45
3.5	Conclusions.....	49
	Acknowledgments	50
	References	50

3.1 INTRODUCTION

One of the most controversial research topics in modern carbon science concerns the thermodynamically stable existence of an sp-hybridized linear carbon chain allotrope called carbyne [1]. Acceptance by the scientific community of this alleged carbon allotrope as the “third form of carbon” would be much easier if single crystals of carbyne existed which were large enough to permit determination of their crystal structure by x-ray

diffraction and synchrotron radiation, respectively, and vibrational spectroscopic techniques including infrared and Raman scattering. This study was undertaken in an attempt to satisfy the demand for such “larger” carbyne single crystals.* Successful growth of carbyne crystals would move the different structural models proposed for carbyne from inspired speculations to undeniable reality.

Several theories have been advanced to explain the co-existence of conjugated triple bonds (polyyne-type isomer) and cumulated double bonds (cumulene-type isomer) in close proximity without the expected explosive collapse of the linear structure towards graphene sheets. To stabilize the sp-hybridization obviously “spacers” are required to keep the parallel neighboring chains (“pencil-in-box” model of the carbyne structure) apart beyond the van der Waals radius of the carbon atom. Such spacers were found to be metal atoms such as potassium [3], iron [4], copper [5] or rhenium [6], bulky alkyl or aryl groups [7], end-capping CO molecules [8] or alkali metal fluorides [9,10]. Recently, strongly linear 1-D “carbon nano-wires” consisting of long carbon chains of more than 100 atoms were produced and inserted into, and hence stabilized by, a multiwalled carbon nanotube (MWNT) [11].

Nevertheless, the inability of researchers to synthesize carbyne single crystals large enough to conduct structural analyses has hampered the general acceptance of carbyne as the expected sp-hybridized carbon allotrope. Why carbyne stubbornly resists forming crystals of suitable size and purity is a matter of contention at present. It may be that the kinks postulated as a precondition of termination of the otherwise infinite carbon chain [12] introduce statistical short range order in the $\langle 00.1 \rangle$ direction parallel to the chains. Consequently, the idea of a paracrystalline nature of carbyne was advanced [13], which is thought to prevent the formation of a long range-ordered 3-D structure. This conjecture is consistent with the fact that, so far, only more or less 2-D thin films of carbyne, produced by either chemical dehydrohalogenation of halogenated polymers [14,15] or condensation of carbon vapor obtained from laser ablated [16] or sputtered [17] graphite surfaces, has led to a reasonably well-ordered nano-to-microcrystalline carbyne structure. It is in this context that the contribution by Onuma et al. [17,18] take on specific significance. The hot tungsten filament used by these authors acts as a mean to crack longer carbon chains and clusters, respectively, into much smaller C_n units that are thought to reassemble easily in the linear carbyne structure at the substrate surface. This techniques has been applied in the present study, with modifications introduced to provide a polycrystalline diamond template to stabilize epitaxially the growing carbyne structures [2,19]. This epitaxially mediated

*Credit should be given here to Dr. Arthur Whittaker, 20753 Exhibit Court, Woodland Hills, CA 91367, USA who provided the senior author (R.B.H) with the idea of epitaxial growth of crystalline carbyne on diamond [2].

stabilization of the carbyne structure is indeed a novel approach: the interaction of carbon atoms of the strained reconstructed diamond (111) surface with terminating carbon atoms of the carbyne sheet may prevent the collapse of the sp -hybridized bonds to sp^2 -hybridized bonds, *i.e.* graphene sheets. Since a polycrystalline diamond surface would provide a large range of configurational surface energies as opposed to a single crystal diamond surface, CVD-deposited small diamond crystals on a single crystal (100) Si surface are particularly effective for achieving stabilization of carbyne by an epitaxial mechanism.

3.2 PROPOSED EPITAXY OF CARBYNE ON DIAMOND

Figure 3.1 shows a non-reconstructed ideal (111)-(1×1) surface of diamond with the three lattice vectors $\langle 211 \rangle$, $\langle 112 \rangle$ and $\langle 121 \rangle$ that form a triangular network with a unit mesh size of $0.252 \times 0.252 \text{ nm}^2$. Shown also is the unit cell (shaded) with side lengths $a_0/\sqrt{2}$ and $(\sqrt{3}/\sqrt{2})a_0$. Superposed on this lattice network is a network of carbon rings (heavy dots and lines) that corresponds to the (00.1) plane of carbyne with a lattice constant of either $a_0 = 0.895 \text{ nm}$ (chaoite) [20] or 0.892 nm (α -carbyne) [21].

The solid dots at the corners (denoted 1 and 2) and in the center (denoted 3) of the hexagonal rings are the projections of carbon atom chains that extend perpendicular to the (00.1) plane of carbyne and also (111) of diamond. The lengths of these chains are variable but are presumably between $4 < n < 6$, where n is the number of carbon atoms. A reasonable lattice match justifying the assumption of epitaxial relations will be obtained if the lattice vector $\langle 10.0 \rangle$ of carbyne ($a_{0(\text{carb})}$) is rotated by 30° away from the lattice vector $\langle 211 \rangle$ of diamond. In this case three of the six carbon atoms of the planar ring (positions 2) will (almost) coincide with the carbon atom positions of the (111)-(1×1) plane of diamond whereas the remaining three carbon atoms (position 1) are occupying the centers of gravity of the (empty) triangular unit meshes. The chain positions 3 are also situated in the middle of the triangles. The mismatch of the lattices of diamond and carbyne is 2.3% for chaoite and 2.0% for α -carbyne. This model has been generated under the assumption that the carbon chains in the carbyne structure have a distance of 0.297 nm , consistent with the van der Waals radius of the sp -hybridized carbon atom.

Even though the mismatch of the host and guest lattices appears to be rather small it can be expected that the orientation of an epitaxial film growing in thickness will increasingly deteriorate with increasing lattice strain. This will eventually lead to cross-linking of the carbon chains forming strong σ -bonds and consequently the formation of graphitic carbon. Hence a non-reconstructed (111)-(1×1) plane of diamond may not be an ideal 2-D host lattice for carbyne epitaxy. An improvement could be achieved by considering the formation of a warped or buckled reconstructed

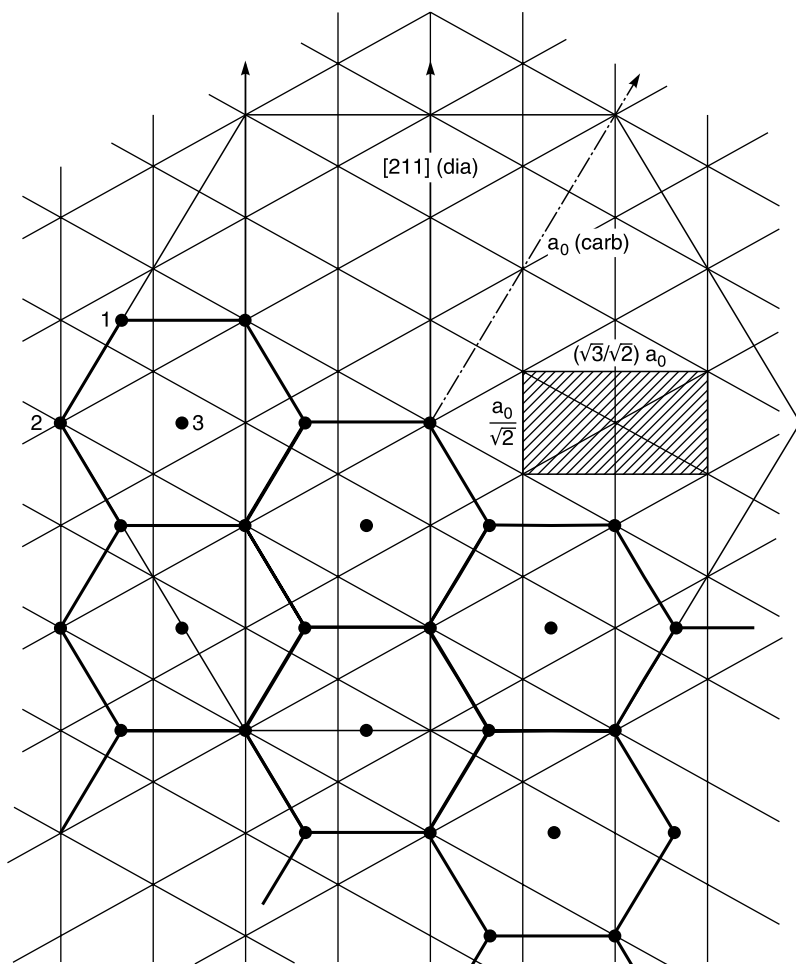


FIGURE 3.1 Proposed epitaxial relationship between a non-reconstructed (111)-(1 \times 1) diamond surface (triangles) and a 2-D hexagonal (00.1) net of carbyne

(2 \times 2)(2 \times 1) surface of diamond that is stable in vacuum at 1000°C [22]. Under these conditions hydrogen atoms or OH groups stabilizing the free carbon “dangling” bonds perpendicular to the (111) plane of diamond will be desorbed and the carbon atoms near the surface will undergo significant topological changes towards formation of a buckled surface. This surface will consist of raised (A,A',B) and lowered (C,C') rows of carbon atoms relative to the unreconstructed (1 \times 1) surface (Figure 3.2).

Owing to the compressed topology of the reconstructed diamond surface the lattice mismatch is thought to decrease. The carbon atom chains 1 and 2 of carbyne coincide rather closely with the atom positions A' of the top layer

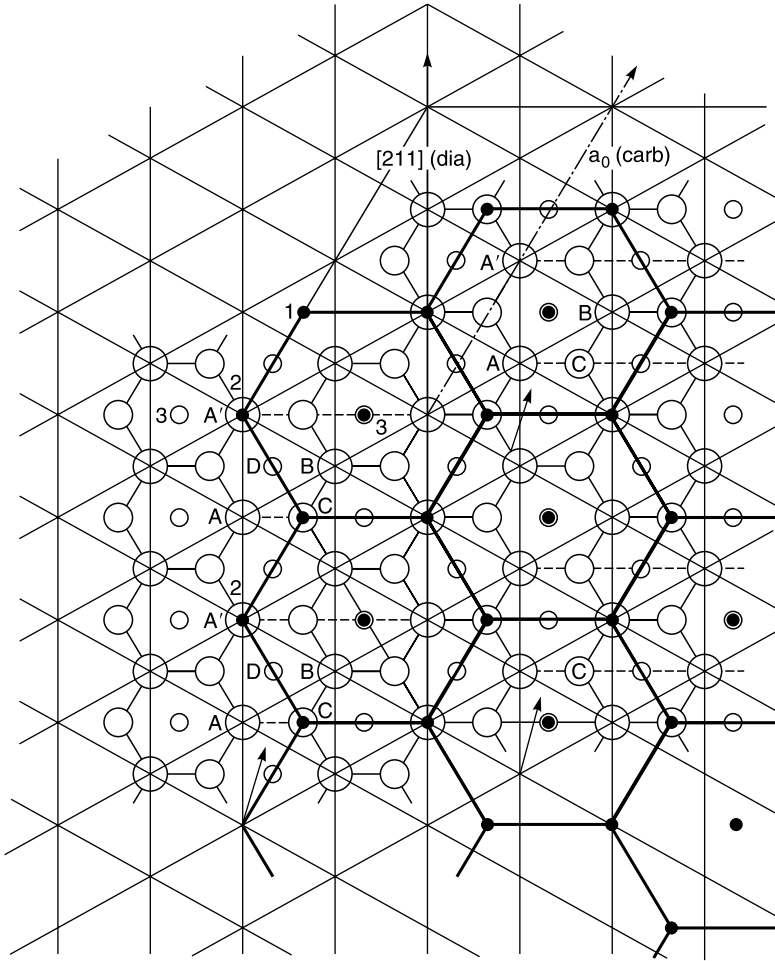


FIGURE 3.2 Proposed epitaxial relationship between an unreconstructed (1×1) diamond surface (thin triangular net), a buckled reconstructed $(111)-(2 \times 1)$ surface (open circles) and a 2-D hexagonal (00.1) surface of carbyne (solid circles, thick lines).

of the diamond lattice and positions C of the second atomic layer, respectively. The chains 3 coincide with position D that corresponds to the fourth atomic layer. Hence warped carbyne layers will be formed with a lattice mismatch of less than 1.5% from ideality. This close match may be even more improved assuming that at the (111) surface of diamond with increasing temperature a flat conformation is being formed before the (2×1) state will be reached [23]. This means that the surface warping decreases and hence the conditions for epitaxial growth will improve.

3.3 EQUIPMENT

3.3.1 CHEMICAL VAPOR DEPOSITION (CVD) REACTOR

The polycrystalline diamond template used as a substrate to deposit the carbyne films was produced by coating a semiconductor Si (100) wafer in a CVD reactor (Figure 3.3).

The CVD reactor consists of a vitreous silica tube of about 20 cm in diameter (8") and a height of 30.5 cm (1 ft). The filament was made from tantalum wire with 0.5 mm diameter and attached to water-cooled copper electrodes. Heat treatment in a methane atmosphere produces a thin layer of tantalum carbide that protects the sample from contamination with metallic tantalum. A gas-leaking unit allows the introduction of various gases and their mixtures into the reaction chamber under controlled pressure. Before introducing or changing the gas the unit's internal pressure was reduced by a mechanical pump to about 0.1 Pa.

Before CVD deposition of polycrystalline diamond the Si surface was scratched with diamond paste (0.5 μm) and then ultrasonically cleaned several times in deionized water and acetone. This treatment generates tiny surface defects that will become efficient nucleation sites for diamond. After mounting the Si substrate on the z-moveable and rotatable sample holder the reactor chamber was filled with a mixture of hydrogen (98%) and methane (2%). By varying the gas pressure, filament temperature, distance between filament and sample surface, partial pressure of methane, and

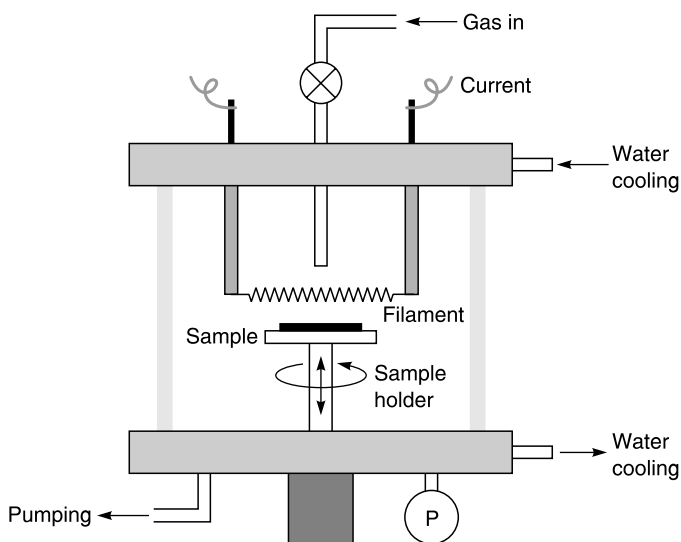


FIGURE 3.3 CVD reactor (Integrity Testing Laboratory Inc., Markham, ON, Canada).

deposition time, diamond crystals with a preset size and preferred orientation of growth, *i.e.* (111) can be deposited.

3.3.2 D.C. MAGNETRON

An existing D.c. magnetron sputtering system (series 2200, model 2305, Vacuum Industries Inc.) was completely redesigned to house a tungsten filament, an optical system for remote temperature measurement, a cassette-type moveable 6-position sample holder, a set of permanent magnets, an electron gun sample heating system, a sample temperature control system, a gas supply and distribution system as well as a pneumatic lift system for the heavy vacuum chamber top (Figure 3.4).

The magnetron sputtering device uses a magnetic field, created by permanent magnets behind the carbon target, that passes through the target and is traverse to the electric field generated by application of a D.c. potential to the target. This magnetic field traps electrons formed by ionization of the residual gas (argon) and emits them from the target surface (Figure 3.5). This greatly enhances the deposition rate by intensifying the plasma owing to the higher density of electrons and the resultant high ionization probability of the argon gas atoms. When an electron collides with an Ar atom the latter can be ionized, $e + \text{Ar} \rightarrow e + e + \text{Ar}^+$, and both residual electrons

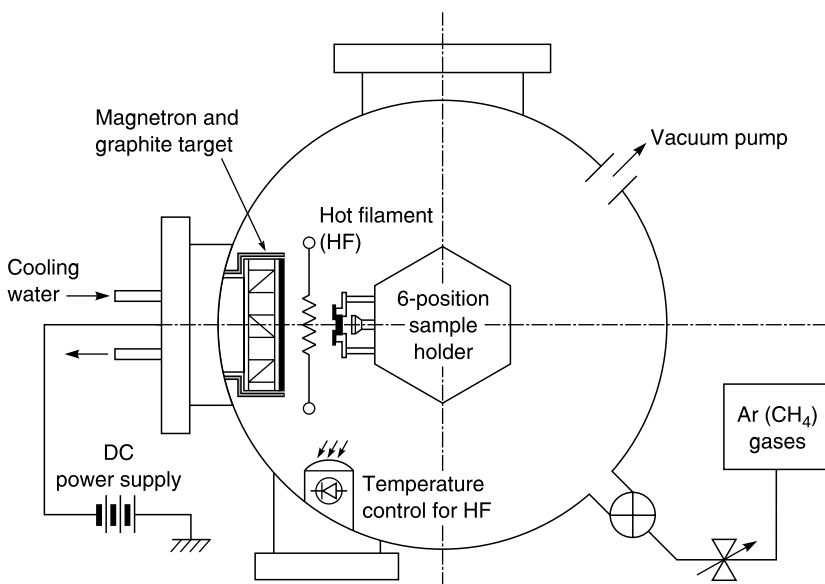


FIGURE 3.4 Schematic view of the dedicated D.c. magnetron sputter apparatus.

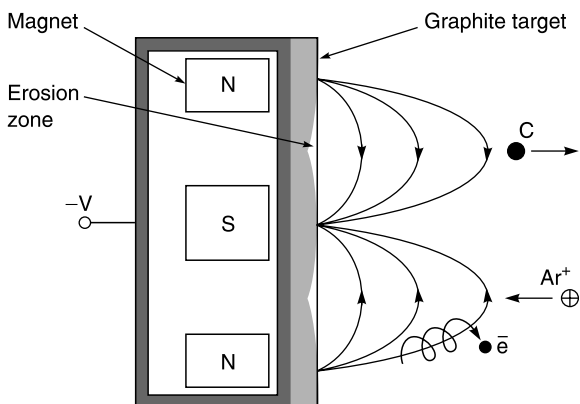


FIGURE 3.5 Schematic of the magnetron sputtering process.

are subject to excitation of Ar atoms. Relaxation of these atoms by photon emission is the main reason for the bright discharge visible in the reactor.

Sputtering occurs because impacting energetic ions at the surface of the target cause the ejection of target atoms by momentum transfer. The sputtering yield (ratio of sputtered species to incident ions) varies with the target voltage. For singly ionized argon ions incident on a carbon target the yield increases approximately linearly with voltage. Below a few keV the sputter yield is also highly dependent upon the surface morphology, *i.e.* the atomic surface roughness. Since the target heats up substantially during the sputter process it was essential to design an efficient water-cooling system (Figure 3.4).

To avoid the contamination of the samples with tungsten atoms emitted from the hot filament the latter was carbonized *in situ* in the vacuum chamber in a methane atmosphere for 20 min. The layer of tungsten carbide formed has a much lower vapour pressure compared to metallic tungsten within the temperature range of the filament chosen (1800–2500°C). Figure 3.6 shows an SEM micrograph of a carbonized filament.

The optical system for remote temperature control of the tungsten filament consisted of a water-cooled manganin (Mn–Ni–Cu alloy) calibration resistor wire, a tungsten filament, two voltmeters, a D.c. power supply and a photometer. From the voltage–current (V – I) characteristics of the tungsten filament the temperature dependence of its specific conductivity can be obtained. The filament temperature is dependent on the photometer reading L in lux, and can be expressed by polynomial approximation as $T(\text{K}) = 1325 + 385L - 76.46L^2 + 29.8L^3$. Highly oriented pyrolytic graphite (HOPG, courtesy: Dr. Yoshinori Koga, Research Center for Advanced Carbon Materials, AIST, Tsukuba, Japan) was used as a D.c.-sputtering target.

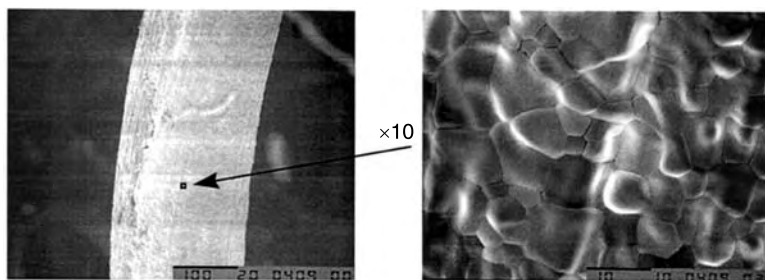


FIGURE 3.6 SEM micrograph of a tungsten filament after carbonization treatment.

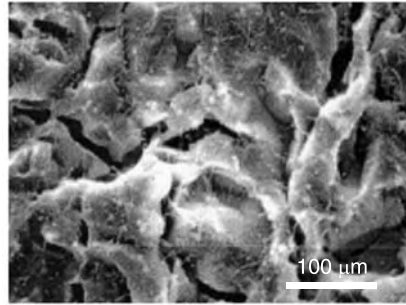
3.4 DEPOSITION AND CHARACTERIZATION OF CARBYNE

Carbyne layers were grown using the D.c. magnetron system described above. A tungsten filament of 0.2 mm in diameter was carbonized as shown above, placed between the HOPG target and the Si wafer CVD-coated with diamond, and heated to 2000–2400°C. The distance between the target and the filament, and the distance between the filament and the substrate were typically 50 mm and 20–30 mm, respectively. Sputtering was carried out under pure argon gas pressure of 13 to 20 Pa. The background pressure before sputtering was below 1.3×10^{-4} Pa. The temperature of the substrate varied between 200 and 400°C. The power supplied to the graphite target was between 450 and 600 W, and the deposition time varied between 1 and 6 h.

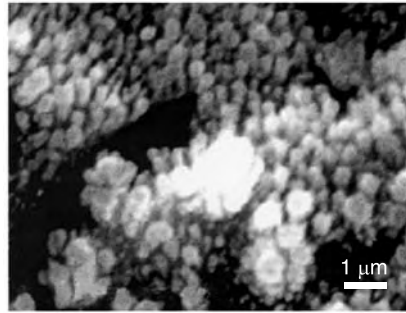
Figure 3.7 shows a typical carbyne deposit formed on a CVD diamond-coated Si(100) substrate with a power of 450 W, substrate temperature 200–400°C, filament temperature 2400°C, deposition time 5 h.

As shown in Figure 3.7b the carbyne layer deposited consists of small columnar crystallites about 1 μm long that are arranged more or less perpendicular to the substrate surface, *i.e.* (111) of diamond. These structures closely resemble those reported by Onuma et al. [17] and Kawai et al. [18], and attributed to chaoite, a carbyne polytype with an assumed chain length of $n = 11$ carbon atoms [12].

Grazing incidence x-ray diffraction (GIXD) measurements (Figure 3.8) showed conclusively that well-crystallized carbyne (chaoite) has been deposited. The interplanar spacings are listed in Table 3.1, together with interplanar spacings of chaoite taken from the literature [24,25]. As shown in Table 3.1, the (hk.l) indexing of the interplanar spacings of References 24 and 25 are quite different. We intuitively tend towards that of Reference 25 since the orientation of the crystals predominately perpendicular to the substrate surface suggests reflections with only $l = 0$. This is also in accord with the seminal paper by El Goresy and Donnay [20] on the “Ries Crater carbyne”. The intensity of the (111) diamond spacing at 206 pm shown



(a)



(b)

FIGURE 3.7 Carbyne deposited on a CVD diamond-coated Si(100) wafer (power 450 W, substrate temperature 200–400°C, filament temperature 2400°C, deposition time 5 h).

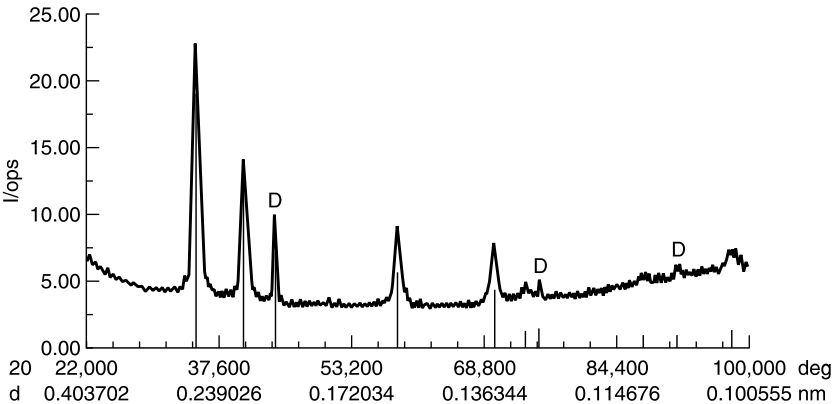


FIGURE 3.8 Grazing incidence x-ray diffraction (GIXD) pattern of a thin carbyne deposit. D = diamond substrate.

TABLE 3.1
Interplanar Spacings (in pm) (CuK α) of Chaoite Deposit and the Diamond Substrate

d_{obs}	(hk.l)* [24]	d	(hk.l)† [25]	d
–	10.1	440.3	11.0	446.5
256.8	11.0	257.5	30.0	257.7
222.2	20.2	221.1	22.0	223.2
205.6	111			
			14.0	168.8
157.3	21.5	160.6	33.0	148.8
128.4	22.0	129.2	60.0	128.8
125.9	220			
117.4	31.7	118.1		
114.2				
110.9	40.4	110.8	44.0	111.6
107.4	311			
102.1	32.1	103.0	17.0	102.4

*Based on a trigonal lattice with $a=516$ pm and $c=2653$ pm

†Based on a hexagonal lattice with $a=894.8$ pm ($= 516 \sqrt{3}$ pm)

in Figure 3.8 is much larger than those of the (220) spacing at 126 pm and (311) spacing at 107 pm. It indicates the dominant (111)-textured orientation of the CVD-deposited polycrystalline diamond film.

Raman scattering investigations (Micro-Raman Jobin-Yvon T 64000 system equipped with a liquid N₂ cooled CCD camera; CW-Ar⁺ ion laser, 514.5 nm) are routinely used to ascertain the nature of carbon films. However, there is a general problem with carbynes, in that they will be quickly converted to more or less amorphous structures with a high proportion of sp² bonds by interchain cross-linking owing to the laser energy deposited into the film; in particular, in the presence of oxygen and air [26]. Since the destruction proceeds from the outside layers of the deposit the top of it will undergo conversion first with the layers underneath trailing behind. Hence it is not surprising that GIXD, probing deeper regions of the carbyne deposit, still shows evidence of carbyne whereas Raman spectroscopy does not. This finding will also confirm our original contention that thin carbyne deposits may be structurally stabilized by a polycrystalline diamond (111) template.

From Figure 3.9a it is evident that there is a strong and sharp D-band at 1340 cm⁻¹ and an even sharper G-band at 1610 cm⁻¹ that is indicative of the sp²-hybridized graphene sheets produced from the carbyne by cross-linking. The intensity ratio of the D- and G-bands $I(\text{D})/I(\text{G})$ is 0.7, following the

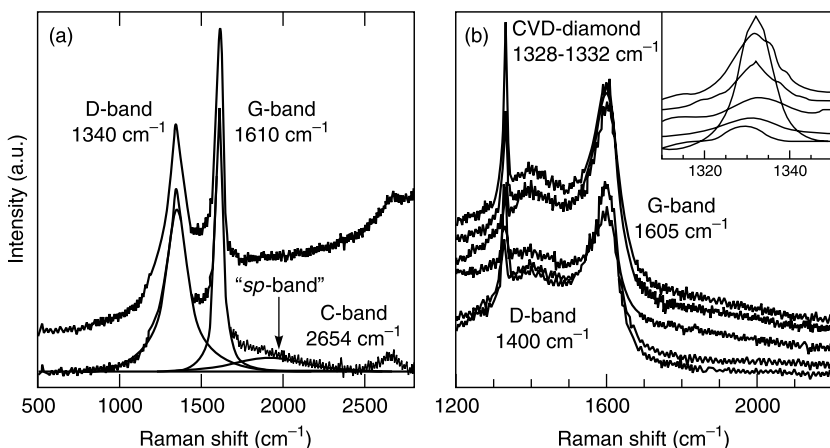


FIGURE 3.9 (a) Raman spectrum ($\lambda = 514.5$ nm) of the carbyne deposit shown in Figure 3.7. Top spectrum: as-measured, bottom spectrum: baseline subtracted and deconvoluted. (b) UV-Raman spectrum ($\lambda = 325$ nm) recorded at different surface points of the carbyne deposit shown in Figure 3.7. The inset shows the down-shifting of the diamond peak position from 1332 to 1328 cm^{-1} with decreasing crystallite size.

Tuinstra–Koenig relation $I(\text{D})/I(\text{G}) \sim 1/L_a$ where L_a is the in-plane correlation length corresponding to phonon confinement in graphitic domains [27]. The relation is often presented as $I(\text{D})/I(\text{G}) = 4.4 L_a$ [28], making the L_a parameter equal to 6.2 nm. The typical “sp-band” around 2000 cm^{-1} is consequently very weak and only discernible at the low frequency tail of the strong G-band. This will be aggravated by the strong photoluminescence emission of the film. The C-band centered around 2654 cm^{-1} can be explained as either the 2nd order vibration of the D-band or as vibrations assigned to the frequency of the Σ_g “k = 0” mode of linear oligoyne chains with 4 to 5 carbon atoms conjugation length as calculated by the Longuet–Higgins–Salem model, where $\nu(n) = 1750 + 3980/n$ ($\nu(4) = 2745$ cm^{-1} , $\nu(5) = 2546$ cm^{-1}) [29]. However, this assumption has to be confirmed by additional studies.

In the visible Raman spectra the cross section of the sp^2 phase is much higher (50–250 times for 514.5 nm) than that of the sp^3 phase. Hence UV Raman spectroscopy (Renishaw 2000 system) with a He–Cd laser (325 nm wavelength) was used for vibrational studies of the sp^3 -bonded carbon phase. The resulting spectra recorded at different points at the surface besides the D- and G-band demonstrated a new feature in the range 1328–1332 cm^{-1} , which corresponds to the CVD-deposited nanocrystalline-sized diamonds (Figure 3.9b). The curve shape analysis of this band, *i.e.* its peak position and width provides information about the size of the CVD-deposited diamond crystallites [30]. With diamond size decreasing from 1000 nm to

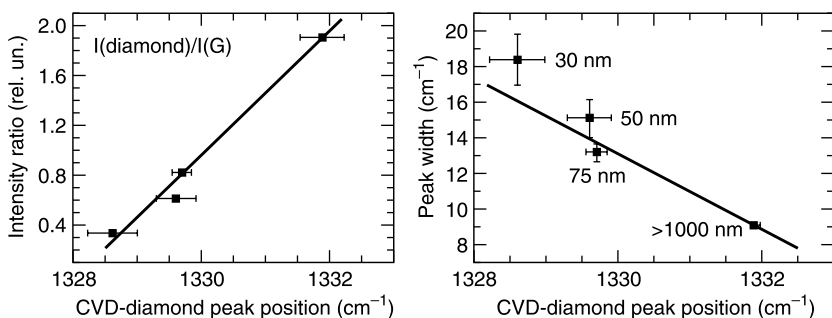


FIGURE 3.10 Dependency of the intensity ratio $I(\text{D})/I(\text{G})$ (left) and the diamond peak width (right) on the size of CVD-deposited nanocrystals of diamond (see Figure 3.9b and its inset).

30 nm, the diamond peak is blue-shifted from 1332 to 1328 cm^{-1} , the line width of the peak broadens (Figure 3.10, right panel), and the intensity ratio $I(\text{D})/I(\text{G})$ decreases accordingly (Figure 3.10, left panel). The down-shifting and broadening of the diamond peak depending on the particle size are consistent with the phonon confinement model.

3.5 CONCLUSIONS

D.c. magnetron sputtering of an HOPG target generated a cloud of carbon atoms that was made to condense at the surface of small (111)-oriented polycrystalline diamond crystals, previously deposited by CVD on (100) surfaces of semiconductor silicon wafers. The orientation relation is $(111)_{\text{dia}}// (100)_{\text{Si}}$. The introduction of a heated tungsten filament close to the substrate surface caused thermal “cracking” of large carbon chains and clusters, respectively. It is thought that such small clusters will rather easily reassemble into an sp-hybridized carbyne structure. This structure will be spatially stabilised by an epitaxial relationship between (00.1) of carbyne and (111) of diamond. The thin carbyne deposits consist of about $1\text{ }\mu\text{m}$ sized columnar crystallites arranged perpendicular to the (111) surface of diamond. The fact that Raman scattering experiments did not reveal sp-hybridized carbon structures may be related to the high thermal energy input by the laser that will effectively destroy the carbyne structure [31]. Only deeper regions of the deposit will retain their structure that could then be probed by GIXD.

Future experiments will include a strong magnetic field through which the sputtered carbon cloud passes. This magnetic field will be applied to maximize the proportion of medium-sized carbon chain clusters with $n = 11$ (chaoite [12]) by enhancing the ion-neutral reactions that will result in an

increase of ionic species produced by collisional ionisation of initially neutral species through a confinement of electrons [32].

ACKNOWLEDGMENTS

The authors are obliged to Gerhard Schreiber, Department of Metallurgy, Technische Universität Bergakademie Freiberg for performing the grazing incidence x-ray diffraction (GIXD) work. The German Research Association (DFG) is acknowledged for sponsoring the project under the contract number He 923/16-1.

REFERENCES

- [1] Heimann, R.B. The nature of carbyne – pros and cons. In: *Carbyne and Carbynoid Structures*, R.B. Heimann, S.E. Evsyukov, L. Kavan, Eds., Physics and Chemistry of Materials with Low-Dimensional Structures, Kluwer Academic Publishers: Dordrecht, Boston, London, **1999**, Vol. 21, pp. 7–15.
- [2] Whittaker, A. Personal written communication, January 20, 1996.
- [3] Rohlfing, E.A.; Cox, D.M.; Kaldor, A. Production and characterisation of supersonic carbon cluster beams. *J. Chem. Phys.* **1984**, *81*, 3322–3330.
- [4] Kudryavtsev, Yu.P.; Evsyukov, S.E.; Babaev, V.G.; Guseva, M.B.; Khvostov, V.V.; Krechko, L.M. Oriented carbyne layers. *Carbon* **1992**, *30*, 213–221.
- [5] Heimann, R.B.; Kleiman, J.; Salanski, N.M. Structural aspects and conformation of linear carbon polytypes. *Carbon* **1984**, *22*, 147–156.
- [6] Bartik, T.; Bartik, B.; Brady, M.; Dembinski, R.; Gladysz, J.A. Durch schrittweises Kettenwachstum zu eindimensionalen Kohlenstoffallotropen mit terminalen Metallkomplexfragmenten; Synthese von C12-, C16- und C20- μ -Polyindiyllkomplexen. *Angew. Chem.* **1996**, *108*(4), 467–469.
- [7] Lagow, R.J.; Kampa, J.J.; Wei, H.C.; Battle, S.L.; Genge, J.W.; Laude, D.A.; Harper, C.J.; Bau, R.; Stevens, R.C.; Haw, J.F.; Munson, E. Synthesis of linear acetylenic carbon; the sp carbon allotrope. *Science* **1995**, *267*, 362–367.
- [8] van Thiel, M.; Ree, F.H. Properties of carbon clusters in TNT detonation products: graphite–diamond transition. *J. Appl. Phys.* **1987**, *62*, 1761–1767.
- [9] Jansta, J.; Dousek, F.P. Some aspects of existence of elementary carbon with sp-hybridised bonds. *Carbon* **1980**, *18*, 433–437.
- [10] Kavan, L.; Kastner, J. Molecular and electron spectroscopy of carbyne structures. Raman and infrared spectroscopy. In: *Carbyne and Carbynoid Structures*, R.B. Heimann, S.E. Evsyukov, L. Kavan, Eds., Physics and Chemistry of Materials with Low-Dimensional Structures, Kluwer Academic Publishers: Dordrecht, Boston, London, **1999**, Vol. 21, pp. 343–356.
- [11] Zhao, X.; Ando, Y.; Liu, Y.; Jinno, M.; Suzuki, T. Carbon nanowire made of long linear carbon chain inserted inside a multiwalled carbon nanotube. *Phys. Rev. Lett.* **2003**, *90*(18), 187401-1 to -4.
- [12] Heimann, R.B.; Kleiman, J.; Salansky, N.M. A unified structural approach to linear carbon polytypes. *Nature* **1984**, *306*, 164–167.

- [13] Heimann, R.B. Should carbyne be described by paracrystal theory? *Carbon* **1997**, 35, 1669–1671.
- [14] Evsyukov, S.E. Chemical dehydrohalogenation of polymers. In: *Carbyne and Carbynyoid Structures*, R.B. Heimann, S.E. Evsyukov, L. Kavan, Eds., Physics and Chemistry of Materials with Low-Dimensional Structures, Kluwer Academic Publishers: Dordrecht, Boston, London, **1999**, Vol. 21, pp. 55–74.
- [15] Yabe, A. Photo- and laser-induced dehydrohalogenation of polymers. In: *Carbyne and Carbynyoid Structures*, R.B. Heimann, S.E. Evsyukov, L. Kavan, Eds., Physics and Chemistry of Materials with Low-Dimensional Structures, Kluwer Academic Publishers: Dordrecht, Boston, London, **1999**, Vol. 21, pp. 75–91.
- [16] Kasatochkin, V.I.; Kazakov, M.E.; Savranski, V.V.; Nabatnikov, A.P.; Radimov, N.P. Synthesis of new allotropic carbon forms from graphite. *Dokl. Acad. Nauk SSSR* **1971**, 201(5), 1104–1105 (in Russian).
- [17] Onuma, Y.; Kawai, Y.; Nakao, M.; Kamimura, K. Highly oriented crystalline carbon thin films obtained by d.c. magnetron sputtering with a hot filament. *Jpn. J. Appl. Phys.* **1996**, 35, L1354–L1356.
- [18] Kawai, Y.; Oo, M.T.; Nakao, M.; Kamimura, K.; Matsushima, H.; Onuma, Y. Highly preferred crystalline carbon thin films obtained by DC magnetron sputtering with a hot filament. *Appl. Surf. Sci.* **1997**, 121/122, 156–159.
- [19] Heimann, R.B. Epitaxie von kristallinem Carbin (Chaoit) auf (111)-Flächen von Diamant. Final report DFG project (He 923/16-1), 2001–2002.
- [20] El Goresy, A.; Donnay, G. A new allotropic form of carbon from the Ries crater. *Science* **1968**, 161, 363–364.
- [21] Sladkov, A.M.; Kasatochkin, V.I.; Kudryavtsev, Yu.P.; Usenbaev, K. Synthesis and properties of linear carbons. *Izv. Akad. Nauk SSSR, Ser. Khim.* **1961**, 12, 2697–2704 (in Russian).
- [22] Pate, B.B. The diamond surface: atomic and electronic structure. *Surf. Sci.* **1986**, 165, 83–142.
- [23] Jungnickel, G.; Porezag, D.; Frauenheim, Th.; Heggie, M.I.; Lambrecht, W.R.L.; Segall, B.; Angus, J.C. Graphitization effects on diamond surfaces and the diamond/graphite interface. *Phys. Stat. Sol. (A)* **1996**, 154, 109–125.
- [24] Udod, I.A. Carbyne intercalation compounds. In: *Carbyne and Carbynyoid Structures*, R.B. Heimann, S.E. Evsyukov, L. Kavan, Eds., Physics and Chemistry of Materials with Low-Dimensional Structures, Kluwer Academic Publishers: Dordrecht, Boston, London, **1999**, Vol. 21, pp. 269–294.
- [25] Whittaker, A.G.; Kintner, P.L. Carbon: Observation on the new allotropic form. *Science* **1969**, 165, 589–591.
- [26] Ravagnan, L.; Siviero, F.; Lenardi, C.; Barborini, E.; Milani, P.; Casari, C.; Li Bassi, A.; Bottani, C.E. Cluster beam deposition and in situ characterisation of carbyne-rich films. *Phys. Rev. Lett.* **2002**, 89, 285506-1 to -4.
- [27] Ferrari, A.C. Determination of bonding in diamond-like carbon by Raman spectroscopy. *Diamond Rel. Mater.* **2002**, 11, 1053–1061.
- [28] Kavan, L.; Kastner, J. Molecular and electron spectroscopy of carbyne structures: Raman and infrared spectroscopy. In: *Carbyne and Carbynyoid Structures*, R.B. Heimann, S.E. Evsyukov, L.Kavan, Eds., Physics and Chemistry of Materials with Low-Dimensional Structures, Kluwer Academic Publishers: Dordrecht, Boston, London, **1999**, Vol. 21, pp. 343–356.

- [29] Kastner, J.; Kuzmany, H.; Kavan, L.; Dousek, F.P.; Kürti, J. Reductive preparation of carbyne with high yield. An *in situ* Raman scattering study. *Macromolecules* **1995**, 28, 344–353.
- [30] Sun, Z.; Shi, J.R.; Tay, B.; Lau, S.P. UV Raman characteristics of nanocrystalline diamond films with different grain size. *Diamond Relat. Mater.* **2000**, 9, 1979–1983.
- [31] Casari, C.S.; Li Bassi, A.; Ravagnan, L.; Siviero, F.; Lenardi, C.; Piseri, P.; Bongiorno, G.; Bottani, C.E.; Milani, P. Chemical and thermal stability of carbyne-like structures in cluster-assembled carbon films. *Phys. Rev. B* **2004**, 69, 075422-1 to-7.
- [32] Kokai, F.; Koga, Y.; Heimann, R.B. Magnetic field enhanced growth of carbon clusters in the laser ablation plume of graphite. *Appl. Surf. Sci.* **1995**, 96/98, 261–266.

4 Electrochemical Synthesis of Carbyne-Like Materials and Other Nanocarbons

Ladislav Kavan

CONTENTS

4.1	Introduction	53
4.1.1	Electrochemical vs. Chemical Carbonization: Fundamentals	54
4.1.2	Electrochemical Carbonization: Refined Model	57
4.2	Electrochemical Routes to Carbyne-Like Chains	59
4.2.1	Carbyne-Like Materials Made by “Wet” Electrochemistry	62
	4.2.1.1 Low-Molecular Weight Precursors	62
	4.2.1.2 Polymeric Precursors	64
4.2.2	Carbyne-Like Materials Made by “Dry” Electrochemistry	66
4.3	Electrochemical Synthesis of Fullerenes and Carbon Onions	68
4.4	Electrochemical Synthesis of Carbon Nanotubes	69
	4.4.1 Indirect Synthesis of Nanotubes from Polyyne	70
	Acknowledgment	71
	References	71

4.1 INTRODUCTION

Carbon science and electrochemistry are interconnected since the early days of both disciplines [1]. Electrochemistry provides significant inputs for characterization and, eventually, practical applications of carbon materials, e.g. in Li-ion batteries and supercapacitors. The discovery of fullerenes and nanotubes promoted further electrochemical research on carbons in general

and on nanocarbons in particular [2]. A possibility to synthesize carbons electrochemically (the so-called “electrochemical carbons” [3]) was explored much less. In general, electrochemical preparations are restricted to energetically demanding syntheses of unstable and reactive products, which are hardly accessible by other reactions. The production of chlorine, aluminum, alkali metals, ozone etc. are examples of such syntheses, which have even been scaled up to an industrial level.

The electrochemical synthesis of carbon is still considered an academic curiosity. The reaction usually does not require high temperatures and/or pressures, as the traditional pyrolytic syntheses of elemental carbon. Exclusion of air oxygen and humidity is, however, needed, since the electrochemical potentials of carbonization are outside the electrochemical window of H_2O [3]. The electrochemical carbonization benefits from three specific features compared to traditional high-temperature syntheses: 1. the possibility of production of unstable carbon chains [3]; 2. easy templating of carbon nanostructures by the precursors, allowing tailored syntheses of fullerenes and nanotubes [4,5]; and 3. defined kinetics of certain reactions, yielding carbon films with precisely controlled thickness [4,5].

4.1.1 ELECTROCHEMICAL VS. CHEMICAL CARBONIZATION: FUNDAMENTALS

The generic process for electrochemical synthesis of sp-carbon chains was electrochemical reductive carbonization (corrosion) of poly(tetrafluoroethylene) (PTFE) by alkali metal amalgams, pioneered by Jansta and Dousek [6–9] (for review see [Reference 3](#)). The reaction occurs at the interface of a “dry contact” between PTFE and alkali metal amalgams, hence, it does not seem to recall an electrochemical synthesis in its classical sense. The “purely electrochemical” carbonization of PTFE on a Pt electrode in aprotic electrolyte solution is also possible [3], but the amalgam-driven process is superior, presenting a clean and well-defined alternative to classical (wet) electrochemistry.

In general, there is no sharp border between chemical and electrochemical processes for the reaction geometry shown schematically on [Figure 4.1](#). Here, a solid film of reaction products (carbon + byproducts of the reaction) is formed at the interface of reactant 1 (R_1) and reactant 2 (R_2). If the reactants R_1/R_2 are not soluble in the film and the film is non-porous, the reaction would have to stop after the formation of the primary single layer of products, because the film would prevent reactants R_1/R_2 from their direct chemical contact. However, Jansta and Dousek [6–9] have demonstrated that there is a pathway for overcoming this “chemical blockade”, assuming: 1. the film is formed by redox process; and 2. the film is electrically conducting both for electrons and ions. In this case the interface behaves as

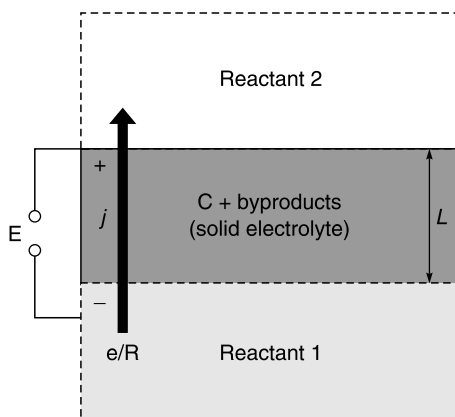


FIGURE 4.1 General scheme of electrochemical carbonization. Reactant 1 is capable of redox-reaction with Reactant 2 leading to carbon. A flat three-layer galvanic cell (voltage E) is formed at the interface. The cell is short-circuited through the formed film composed of carbon and the corresponding byproducts. The reaction propagates as the short-circuit current (j) flows through the carbonaceous film.

a short-circuited galvanic cell of a voltage E (Figure 4.1), which is defined by the faradaic processes occurring at the interfaces R_1/film and R_2/film . The reaction is driven by the corresponding change of the Gibbs free energy ΔG_0 , hence the cell voltage equals

$$E = -\frac{\Delta G_0}{nF}, \quad (4.1)$$

where F = Faraday constant and n is the number of electrons involved in the elementary reaction of R_1 and R_2 . The film growth is then controlled by the current flowing through the film. Assuming R_1 is the reducing agent and R_2 is a precursor molecule, which is reducible to carbon, the galvanic process requires transport of electrons and the corresponding cations (R_1^+) through the film (Figure 4.1). The current density (j), flowing through the (R_1/film) interface (Figure 4.1), can be expressed according to Faraday's law:

$$\int_0^t j dt = \frac{LnF\rho}{aM}, \quad (4.2)$$

where L is the thickness of carbonized layer, ρ is the density of the precursor R_2 , t is the time, M is the molar mass of R_2 and a is a dimensionless correction factor. This factor is a ratio of L to the thickness of the consumed

precursor R_2 (typical values are 1.1–2 [10]). Apparently, Eq. 4.2 is a more exact form of Faraday law for the corrosion process compared to that of Jansta and Dousek [7,8,10]. The current j also obeys Ohm's law, assuming a serial combination of ionic (σ_i) and electronic (σ_e) conductivities of the film (Figure 4.1):

$$j = \frac{E\sigma_e\sigma_i}{L(\sigma_e + \sigma_i)}. \quad (4.3)$$

Combining Eqs 4.2 and 4.3 and solving of the relevant integral equation leads to

$$L = \sqrt{\frac{2EaM\sigma_e\sigma_i t}{nF\rho(\sigma_e + \sigma_i)}} = K_0 \cdot t^{1/2}, \quad (4.4)$$

where K_0 is a rate constant. The exact value of K_0 , which considers explicitly the $j=j(t)$ dependence, differs from that derived by the approximate theory of Jansta and Dousek [7,8,10] just by a factor of $\sqrt{2}$. In actual systems, the ionic conductivity is usually much lower than the electronic conductivity, hence the total conductivity can be approximated:

$$\sigma = \frac{\sigma_e\sigma_i}{\sigma_e + \sigma_i} \cong \sigma_i; \quad (\sigma_e \gg \sigma_i). \quad (4.5)$$

Table 4.1 summarizes some experimental values of rate constants K_0 . The most precise data exist for the amalgam-driven carbonization of PTFE and various other fluoropolymers [3,10,11].

The theoretical treatment presented (Eqs 4.1–4.5) is applicable also for direct “wet” electrochemistry on Pt cathode in aprotic electrolyte solution [12,13] (Table 4.1) and for some other “chemical” reductants, R_1 , viz. benzoin dianion [14] and sodium dihydronaphthylide [15] (Table 4.1). Apparently, the decision between “chemical” and “electrochemical” carbonization may not be straightforward. The latter scenario requires a compact solid electrolyte with mixed electron/ion conductivity to be present at the interface. This occurs almost ideally in the reactions of solid fluoropolymers with diluted alkali metal amalgams [3]. If the interfacial layer is mechanically cracked, both electrochemical and chemical carbonization may take place, and the actual kinetics deviates from that predicted by Eq. 4.4 [10]. There is, however, another mechanism, leading to the perturbations of the Jansta and Dousek's electrochemical model (Eq. 4.4). This situation typically occurs if gaseous perfluorinated precursors react with Li-amalgam [4,5], and it will be theoretically treated in the next section.

TABLE 4.1
Carbonizations of perfluorinated precursors (R_2) with reductants (R_1), which follow the square-root kinetics. Rate constant, K_0 is quoted at 25°C. δ = doping level of carbon (calculated per carbon atom), g = gas, s = solid

	Precursor (R_2)	Reactant (R_1)	K_0 (nm/s ^{1/2})	δ	Reference
C ₄ F ₆	Perfluoro-2-butyne (g)	Li-amalgam	120	0.21	[5]
C ₄ F ₈	Perfluorocyclobutane (g)	Na-amalgam	2.9	0.12	[5]
C ₁₀ F ₁₈	Perfluorodecalin (g)	Na-amalgam	5	0.34	[4]
C ₅ F ₈	Perfluorocyclopentene (g)	Na-amalgam	9.5	0.18	[5]
C ₁₀ F ₈	Perfluoronaphthalene (g)	Na-amalgam	18 ^(a)	0.16	[4]
C ₄ F ₆	Perfluoro-2-butyne (g)	Na-amalgam	9	0.14	[5]
C ₅ F ₈	Perfluorocyclopentene (g)	K-amalgam	0.2	0.13	This work
C ₁₀ F ₈	Perfluoronaphthalene (g)	K-amalgam	0.3	0.14	This work
(-CF ₂) _n	PTFE (s)	Li-amalgam	47.5	0.21	[8,10]
(-CF ₂) _n	PTFE (s)	Na-amalgam	2.67	0.2	[8,10]
(-CF ₂) _n	PTFE (s)	K-amalgam	0.1	0.2	[10]
(-CF ₂) _n	PTFE (s)	Mg-amalgam	< 0.01	-	[31]
(-C ₂ ClF ₃) _n	PCTFE (s)	Li-amalgam	124	0.32	[10]
(-C ₂₀ F ₃₈ O ₅ S-) _n	NAFION 117 (s)	Li-amalgam	15.3	0.20	[11]
(-C ₁₁ F ₂₂ O-) _n	PTFE-PPVE (s)	Li-amalgam	38.3	0.21	[10]
(-CF ₂) _n	FEP (s)	Li-amalgam	47.0	0.2	[87]
(-CF ₂) _n	FEP (s)	Na-amalgam	2.7	0.2	[87]
(-CF ₂) _n	FEP (s)	K-amalgam	0.1	0.2	[87]
(-C ₃ F ₄ O-) _n	PPPO (s)	Li-amalgam	40	-	[10]
(-CF ₂) _n	PTFE (s)	Benzoin dianion	2 ^(b)	-	[14]
(-CF ₂) _n	PTFE (s)	Dihydronaphthylide	0.4 ^(b)	-	[15]
(-CF ₂) _n	PTFE (s)	e ⁻ /NEt ₄ ⁺ ^(c)	120 ^(b)	-	[12]
(-CF ₂) _n	PTFE (s)	e ⁻ /NBu ₄ ⁺ ^(c)	70 ^(b)	-	[12,13]
(-CF ₂) _n	PTFE (s)	e ⁻ /NOct ₄ ⁺ ^(c)	30 ^(b)	-	[12]

^(a) This value is valid only for larger film thicknesses. For thinner films (early stages of the reaction) see text and Table 4.2.

^(b) Estimated value from literature experimental data

^(c) Direct electrochemistry on Pt cathode in the presence of the given counterion (Et = ethyl, Bu = butyl, Oct = octyl) in dimethylformamide solution

PCTFE = poly(chlorotrifluoroethylene)

PTFE-PPVE = poly(tetrafluoroethylene-co-perfluoropropylvinylether)

FEP = poly(tetrafluoroethylene-co-hexafluoropropene)

PPPO = poly(perfluoropropenoxide)

4.1.2 ELECTROCHEMICAL CARBONIZATION: REFINED MODEL

Certain reactions of Li-amalgam with gaseous perfluorinated precursors do not follow Eq. 4.4 [4,5]. An example is the reaction of perfluorocyclopentene

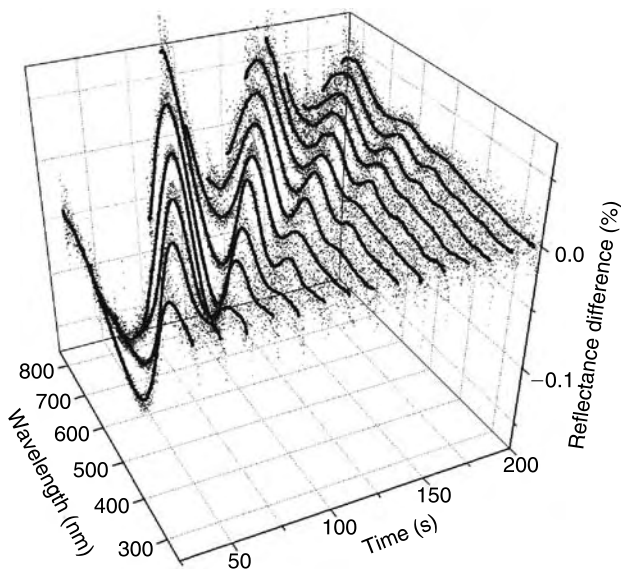


FIGURE 4.2 UV-vis reflectance spectra of liquid Li-amalgam, which was exposed at time $t=0$ to a saturated vapor of perfluorocyclopentene at 25°C. The growth of carbonaceous film manifests itself by interference peaks, which give rise to periodically changing interference colors at early stages of the film growth. After ca. 200 s the film becomes black, and visual monitoring of the colors is not possible.

with Li-amalgam. Figure 4.2 shows the reflectance UV-vis spectrum of the surface of liquid Li-amalgam, which was at the time $t=0$ contacted with saturated vapor of perfluorocyclopentene at 25°C. Early stages of the carbonization are accompanied by visual changes of interference colors. The corresponding interference fringes in the growing film (Figure 4.2) may subsequently serve for evaluation of the growth kinetics [4,5]. Analysis of the system in Figure 4.2 showed that the layer thickness, L , was proportional to the reaction time, t , and not to $t^{1/2}$ as predicted by Eq. 4.4.

To interpret this inconsistency, a refined model is outlined below for the cell shown in Figure 4.1. The current density, j , is still expressed by the Faraday law (Eq. 4.2) and Ohm's law (Eq. 4.3). However, Eq. 4.3 cannot apparently apply if L approaches zero. In such a case the current is controlled by the intrinsic rate of the faradaic process, and not by the conductivity of the solid electrolyte, σ . Hence, the cell voltage E consists of the ohmic, E_{ohm} , and activation, E_a , parts. The corresponding current density is then expressed as follows:

$$j = j_0 \exp\left(\frac{\alpha n F E_a}{RT}\right) \quad (4.6)$$

(α is the charge transfer coefficient) and

$$j = \frac{E_{\text{ohm}}\sigma}{aL}. \quad (4.7)$$

These two equations can be combined with regard to $E = E_a + E_{\text{ohm}}$ to obtain

$$E = \frac{RT}{\alpha y F} \ln \left(\frac{L \rho n F}{j_0 \text{Mat}} \right) + \frac{jL}{\sigma} \quad (4.8)$$

Eliminating j from Eqs. 4.6 and 4.7 leads to a transcendental equation for L :

$$E = \frac{RT}{\alpha y F} \ln \left(\frac{L \rho n F}{j_0 \text{Mat}} \right) + \frac{L^2 \rho n F}{\text{Mat} \sigma} \quad (4.9)$$

Unfortunately, it cannot be solved analytically, but for $E_a \rightarrow 0$ or $L \gg 0$, the first term can be neglected, which gives $L \sim K_0 \sqrt{t}$ (cf. Eq. 4.4). On the other hand, for large E_a or $L \rightarrow 0$ (short time) the second term can be neglected, and we obtain

$$L = \frac{j_0 t \text{Mat}}{\rho n F} \cdot \exp \left(\frac{\alpha n F E}{RT} \right) = K_1 \cdot t. \quad (4.10)$$

The reactions exhibiting linear film growth (Eq. 4.10) are listed in Table 4.2. Most of them comprise reactions of Li-amalgam with various fluorocarbons. Only the perfluoro-2-butyne reacts with Li-amalgam according to Eq. 4.4 with $K_0 = 120 \text{ nm/s}^{1/2}$ (Table 4.1). The interpretation is straightforward: the faradaic carbonization of perfluoro-2-butyne is so fast that the overall kinetics is controlled by E_{ohm} (Li^+ transport in the growing film) and not by E_a . While most tested reaction systems follow unique kinetics (either Eq. 4.4 or Eq. 4.10) at all practically accessible film thicknesses, the reaction of perfluoronaphthalene with Na-amalgam exhibits distinct linear kinetics (with $K_1 = 0.3 \text{ nm/s}$) at early stages, but it changes to square-root kinetics at later stages (with $K_0 = 18 \text{ nm/s}^{1/2}$). In other words, the Na^+ transport is rate determining only for thicker films, but not for thinner films in this particular case.

4.2 ELECTROCHEMICAL ROUTES TO CARBYNE-LIKE CHAINS

Carbyne is an ill-defined crystal containing sp-bonded all-carbon chains [16]. Species approaching this structure are carbon molecules in the carbon melt [17], vapor, or in inert matrices at low temperatures [18,19] and end-capped oligynes [20,21]. An “infinite” sp-bonded carbon chain has two possible

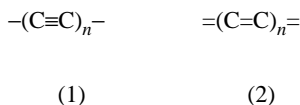
TABLE 4.2

Reactions of perfluorinated precursors with Li-amalgam, which follow linear kinetics. Rate constant, K_1 , is quoted at 25°C. δ = doping level of carbon (calculated per carbon atom)

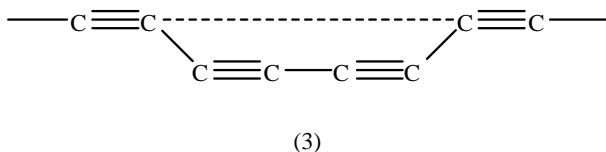
	Precursor (R_2)	Reactant (R_1)	K_1 (nm/s)	δ	Reference
C_6F_{14}	Perfluorohexane	Li-amalgam	0.03	0.23	[5]
C_4F_8	Perfluorocyclobutane	Li-amalgam	0.2	0.24	[5]
C_6F_{12}	Perfluorocyclohexane	Li-amalgam	0.002	0.18	[5]
$C_{10}F_{18}$	Perfluorodecalin	Li-amalgam	0.5	0.20	[4]
C_5F_8	Perfluorocyclopentene	Li-amalgam	7	0.21	[4]
C_6F_6	Perfluorobenzene	Li-amalgam	0.06	0.20	[5]
$C_{10}F_8$	Perfluoronaphthalene	Li-amalgam	0.15	0.19	[5]
$C_{10}F_8$	Perfluoronaphthalene	Li-amalgam	0.2	-	[4]
$C_{12}F_{10}$	Perfluorobiphenyl	Li-amalgam	0.01	0.17	This work
C_6F_5CN	Perfluorobenzonitrile	Li-amalgam	5	0.13	[5]
C_5F_5N	Perfluoropyridine	Li-amalgam	1	0.18	[5]
$C_3F_3N_3$	Cyanurfluoride	Li-amalgam	0.003	0.14	This work
$C_{10}F_8$	Perfluoronaphthalene	Na-amalgam	0.3 ^(a)	0.16	[4]

^(a) This value is valid only for thin film (early stages of the reaction). For thicker films see text and Table 4.1.

configurations: **(1)** polyethynylene (polyyne) and **(2)** polyethylene diylidene (polyvinylene diylidene, polycumulene):

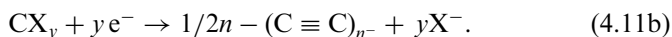
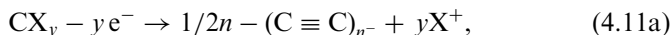


The first isomer (polyyne) is considered to be theoretically more stable [22–25]. Heimann et al. [16,26–28] have formulated a general idea that an sp-carbon chain can be further stabilized by kinks. For instance, the kinked polyyne can exist both in the *trans* configuration **(3)**:



or *cis* configuration, and the same applies for polycumulene [28]. These building blocks may then form a paracrystal [28] whose stabilizing defects

are introduced, e.g. by impurities. Stabilization of sp-carbon chain was also considered inside a carbon nanotube [29,30] or in siliceous molecular sieve MCM41 [31]. Baughman et al. [32] have calculated the heat of formation of polyynes $-(C\equiv C)_n-/2n$ to be 106 kJ/at. Such an energetically demanding process may, perhaps, well proceed electrochemically. Let us assume that “electrochemical carbyne” is produced from a molecular precursor CX_y (X is a general substituent(s)). Depending on the nature of X, the reaction is either oxidative (4.11a) or reductive (4.11b):

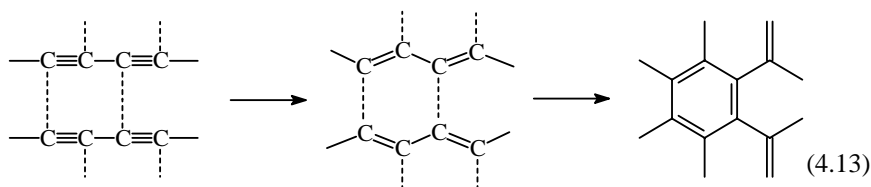


The assessment of the driving force follows from the reaction standard Gibbs free energies ΔG_0 , calculated by using the corresponding energies of formation of the reactant CX_y (ΔG_R) and the products (ΔG_P) in reactions (4.11a,b).

$$\Delta G_0 = y\Delta G_P - \Delta G_R. \quad (4.12)$$

The ΔG_0 values can be transformed into the corresponding standard electrochemical potentials, E_0 (Eq. 4.1). For instance, the conversion of PTFE ($\Delta G_R = -365$ kJ/mol CF_2) into polyynes and HF (reaction (4.11b) in a hypothetical cell with standard hydrogen electrode) would have $\Delta G_0 = -71$ kJ/mol. The corresponding standard redox potential PTFE/polyne is $E_0 = 0.74$ V, which is just 0.36 V smaller than the standard potential of PTFE/graphite ($E_0 = 1$ V) [3]. Apparently, in terms of the reaction thermodynamics, the “electrochemical carbyne” should be easily accessible via cathodic reduction of PTFE. Analogously, the oxidation of acetylene ($\Delta G_R = -209.9$ kJ/mol) to polyynes (Eq. 4.11a) corresponds to $\Delta G_0 = 2.1$ kJ/mol, $E_0 = -0.02$ V.

Unfortunately, reactions (4.11a and 4.11b) do not stop at the stage of pure polyynes, $-(C\equiv C)_n$, but there are two other pathways of product transformation. Polyynes are unstable against interchain crosslinking, which leads to sp^2 carbon structures [33]:



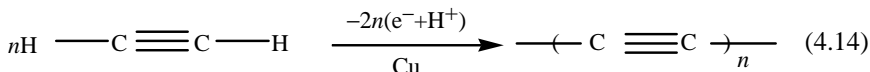
It occurs at sites where the chains get into the close distance, promoting covalent interactions. A second mechanism of polyynes transformation

is doping. This process was explored in detail for cathodic carbonizations (Eq. 4.11b), and it turned out that the *n*-doping (superstoichiometric over-reduction) generally accompanies reaction 4.11b (see Sections 4.2.1 and 4.2.2).

4.2.1 CARBYNE-LIKE MATERIALS MADE BY “WET” ELECTROCHEMISTRY

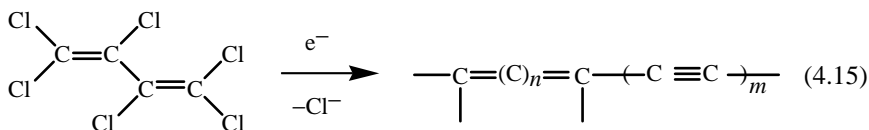
4.2.1.1 Low-Molecular Weight Precursors

There is only one example of the polyne formation by an anodic reaction. Ohmura et al. [34] oxidized acetylene in dimethylformamide electrolyte solution containing CuCl catalyst:

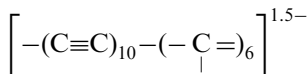


This reaction is an alternative of the Hay oxidative coupling, and it produces a carbonaceous material with some proportion of IR active sp-bonded carbon chains [34].

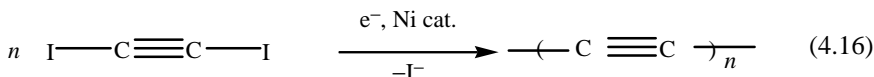
The cathodic production of carbyne was explored more extensively. Nishihara et al. [35–38] have carbonized hexachlorobuta-1,3-diene on Pt or glass-like carbon electrode in acetonitrile medium. Kijima et al. [39–41] have found that the product contained also considerable proportion of sp-bonded carbon atoms in addition to sp² carbon:



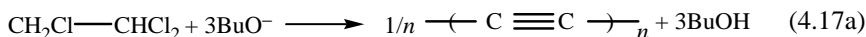
The product of reaction 4.14 was, actually, over-reduced (*n*-doped) to a formal composition:



(The *n*-doping of carbon during cathodic dehalogenation is a common side-reaction (see Tables 4.1, 4.2 and the text below). Kijima et al. [39,42,43] reduced diiodoacetylene to carbon at a platinum electrode in dimethylformamide media:



However, the actual product contained also sp^2 carbon and impurities (H, N, I and Ni) [42,43]. Along with direct electrochemical carbonization processes (Eqs 4.14–4.16) also indirect reactions were explored, in which the active species is electrochemically generated and consumed for the chemical carbonization in a regenerative loop. For instance, dehydrochlorination of 1,1,2-trichloroethylene proceeds with *t*-buthanolate (BuO^-), which is generated from *t*-butylalcohol ($BuOH$) on a Ni cathode in dimethylsulfoxide electrolyte solution [44].



Based on IR and Raman spectra, the product of reaction 4.17a was formulated as “carbyne-like” material. The band position (1960 cm^{-1}) supports the suggestion that the sp -bonded carbon chains in dehydrohalogenated $C_2H_3Cl_3$ have high conjugation lengths [44]. Wang et al. [44] claim that this material shows the most intense Raman signal of the $C \equiv C$ stretch of all previously reported “electrochemical carbynes”. (Note, however, Reference [45] for a colliding statement). Another example of indirect electrochemical process was demonstrated by Kyotani et al. [46]. They have cathodically reduced fluorinated naphthalene pitch in tetrahydrofuran. The product contained, according to Raman spectroscopy, some carbyne-like structures. The procedure employed electrochemistry with Mg as a sacrificial anode (see reaction 4.21 below).

Hexafluoro-2-butyne is smoothly carbonized by Li- and Na-amalgams [5], which is promising for polyynes production. Figure 4.3 shows a TEM image of carbon, obtained from C_4F_6 and Li-amalgam and washed with water in air. This procedure probably destroyed polyynes in the product [47,48], but we may note typical lamellar carbon having 4–8 graphene layers. Such ribbon-like graphite is reminiscent of the material grown from polyynes upon irradiation with electron beams at 800°C [46], despite the fact that, in this case (Figure 4.3), no heat treatment was applied.

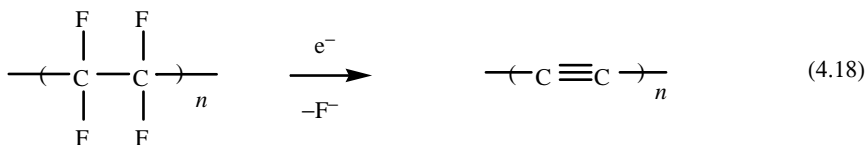
Demyashev et al. [49] have introduced a different approach to electrochemical carbyne. They have electropolished titanium carbide, TiC, in acid electrolyte containing acetic acid and $HClO_4$. At certain voltages, the Ti atoms were found to be removed preferentially from the TiC surface, which in turn became enriched with carbon. TEM and electron diffraction of the surface revealed a possible existence of carbyne in this layer, and it was predicted that such a production of carbyne might be generally adopted for some other carbides.



FIGURE 4.3 TEM image of pure carbon made from perfluoro-2-butyne and Li-amalgam at 25°C. The LiF byproduct was extracted from the raw material by water.

4.2.1.2 Polymeric Precursors

Poly(tetrafluoroethylene) (PTFE) is a promising precursor for carbyne. The linear polymeric chain of PTFE could be transferred into polyyne according to the ideal scheme:



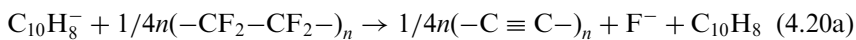
The carbonization of PTFE on a metal cathode in aprotic electrolyte solutions was pioneered by Brewis et al. [50], and further studied by this [12,13, 51–54] and other groups [55–63]. The charge consumed in reaction 4.17 slightly exceeds that for a total dehalogenation of PTFE [12,13,53]. This superstoichiometric reduction indicates n-doping of the formed carbon:



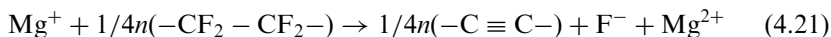
The doping level δ was about 0.05–0.45 [12,13,53]. Similar doping (Eq. 4.19) was later found in many other electrochemical carbonizations [3,10] (Tables 4.1 and 4.2).

The electrochemical carbonization of PTFE is anisotropic, propagating rapidly along the oriented macromolecule chains [12,54]. Although the aim of early studies [12,13,50–54] was just surface modification of PTFE for improving of its adhesion, the authors have intuitively suggested the formation of polyne (cf. Eq. 4.18) [52]. This prediction was later confirmed by IR spectroscopy [56,60,61]. The reactivity of *ex*-PTFE carbon was recently used for its subsequent functionalization with diazonium salts [62] and metallization [63].

Besides direct electroreduction of PTFE on metal cathode, the indirect dehalogenation was carried out by electrochemically generated reactants. A classical reaction employs naphthalene radical cation, which is generated electrochemically in a solution of naphthalene in dimethylformamide + NBu_4BF_4 or NBu_4ClO_4 [50,56] (Eq. 4.20). The radicals react with PTFE while the naphthalene is regenerated (4.20a) and the reaction propagates in a catalytic loop:



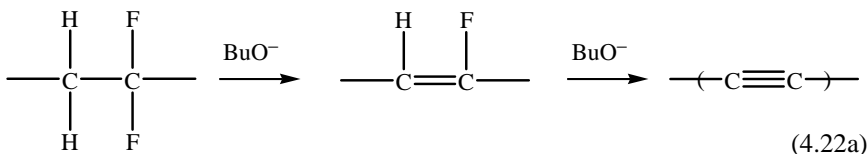
Amatore et al. [64] studied similar reactions mediated by phthalonitrile, 4-cyanopyridine, pyridazine, 4-phenylpyridine and benzonitrile. They aimed at detailed kinetic analysis, while the nucleophilic radical anion was generated at a gold-band ultramicroelectrode [64]. An alternative approach, employing inorganic reductant, instead of organic radical cation, was introduced by Yasuda et al. [65–71]. The electrochemical carbonization of PTFE proceeded in tetrahydrofuran electrolyte solution into which a sacrificial Mg anode dissolved galvanically. It was suggested that the active reactant for carbonization is the magnesium radical cation, Mg^+ , though this species is not well defined [70]:



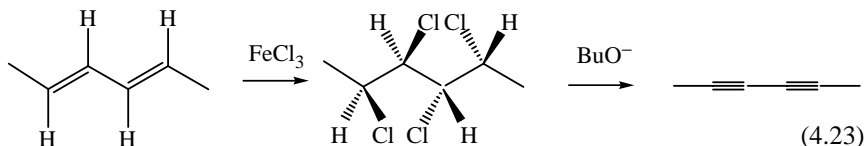
Poly(chlorotrifluoroethylene) (PCTFE) is also smoothly carbonizable by electrolysis in aprotic media [72–75]. The carbonization is slower for crystalline PCTFE as compared to amorphous polymer [76], and for a polymer pretreated with γ -photons [73]. The structure of carbonized PCTFE was investigated in less detail compared to that of *ex*-PTFE carbons.

The partially halogenated hydrocarbons, such as poly(vinylidene fluoride) (PVDF) and polyvinylchloride (PVC) are not carbonizable by direct reductive dehalogenation [59]. Nevertheless, PVDF carbonizes indirectly by

reactions similar to Eqs. (4.16 and 4.16a) [77]:



The product contains (besides some residual F and H) also inserted NBu_4^+ , *i.e.* it is naturally n-doped. Even in the absence of BuOH, reactive nucleophiles like $[(\text{CH}_3)_2\text{NCHO}]^-$ or $(\text{CH}_3)_2\text{N}^-$ can be generated by pre-electrolysis of dimethylformamide solutions [59]. Such a process allows electrochemical deposition of diamond-like carbon on an aluminum electrode [78] and it also produces polyynes from PVDF (cf. Eq. 4.22a). At similar conditions, PTFE shows no reactivity [59] and polyvinylchloride is dehydrohalogenated only to polyacetylene [79–82]. However, *trans*-polyacetylene, which was stereoregularly chlorinated by FeCl_3 , is carbonizable by electrochemically generated BuO^- (cf. reactions 4.22 and 4.22a) [83]:



The presence of carbynoid structures was confirmed by IR and Raman spectra [83].

4.2.2 CARBYNE-LIKE MATERIALS MADE BY “DRY” ELECTROCHEMISTRY

The principle of electrochemical carbonization at the “dry” interface of reactants was treated in Section 4.1.1 (cf. also Figure 4.1). The generic reaction is a carbonization of PTFE with diluted liquid amalgams of alkali metals (Li, Na, K). The dehalogenation is stoichiometrically quantitative with regular n-doping (see Table 4.1). The polyynes were monitored by Raman band of the $\text{C} \equiv \text{C}$ stretch at $\approx 2000 \text{ cm}^{-1}$ (cf. Figure 4.4) [47,48,84]. Screening of perfluoro-*n*-alkanes ($\text{C}_x\text{F}_{2x+2}$, $x = 1, 2, 6, 9, 20, 24, \approx \infty$) [48] pointed at PTFE giving optimum yields of polyynes. The yields further increased in the series of alkali metal amalgams: $\text{Li} < \text{Na} < \text{K}$ [47,48]. Further improvement was traced if highly oriented PTFE was used as

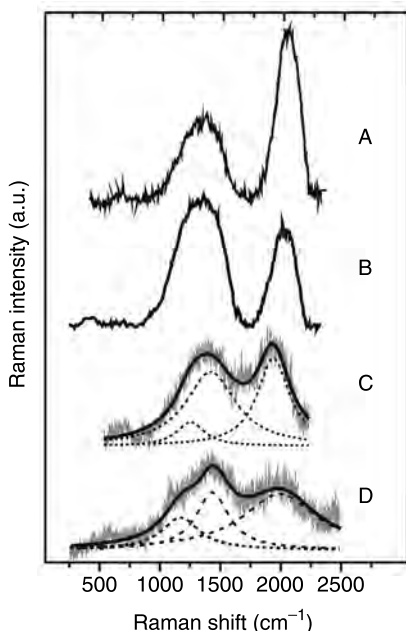


FIGURE 4.4 Raman spectra of the products of the amalgam-driven carbonization of PTFE at 25°C. The reactants were as follows (A) PTFE foil + Na-amalgam, (B) PTFE foil + Li-amalgam, (C) Highly oriented PTFE film + Na-amalgam, (D) Highly oriented PTFE film + Li-amalgam. Reprinted with permission from *Chemistry of Materials* **11**, 329 (1999). Copyright (1999) American Chemical Society.

precursor [84] (cf. Figure 4.4). In this case, the conjugation length was estimated to be nine triple bonds [84].

In principle, however, the yield of polyyne can hardly be determined from Raman spectroscopy, because of resonance enhancement. Independent methods are needed, such as x-ray diffraction or selective reactions with *in-situ* generated carbenes [85]. In actual samples, the yield of polyyne varied between 5 and 40% [85]. A detailed Raman study indicated a downshift of the intensity of the C≡C line and blue-shift of its frequency (*i.e.* decrease of the conjugation length) if a freshly prepared sample is stored in vacuum at room temperature [3,47,48]. The aging rate decreased in the series: Li > Na > K. It can be further monitored by long-time (years) decreases of electronic resistivity [3,86], photoluminescence intensity [3,47] and UV-vis absorption [3,87]. These changes are controlled by defined kinetics, and accelerate upon heating and especially after extraction of the reaction by-product (alkali metal fluoride) with water [3,48]. All these features lead to a self-consistent structural picture. Polyyne, formed by reaction 4.18, decomposes to graphene (reaction 4.13); the cross-linking rate being

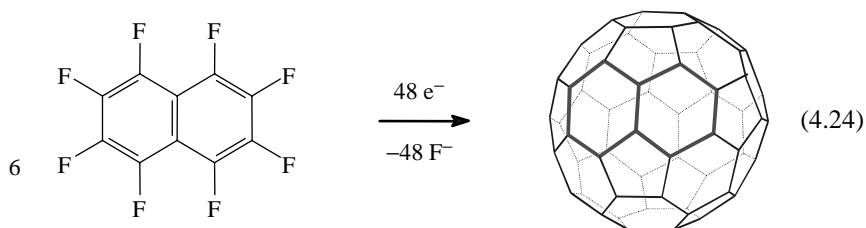
controlled by a spatial separation of polyyne chains with interspersed alkali metal fluoride.

PTFE does not react with Mg-amalgam, and only thin-layer chemical carbonization is observed without any electrochemical propagation [88]. Also, the electrochemical mechanism is perturbed by cracking of the carbon film if the reaction is carried out with concentrated amalgams [10], suspension of alkali metals [89], or gaseous alkali metals instead [90,91]. The reduction of PTFE with pure lithium {A943}, sodium [90] or potassium [90,91] was explored by Yamada et al. [90,91]. The best quality product was formed by gaseous potassium; it exhibited a strong Raman band of sp-bonded carbon at 1950 cm^{-1} , which dominated the spectrum. Thus, prepared carbon also gave interestingly high electrochemical capacitance (199 F/g) for the prospective application in double-layer supercapacitors {A943}.

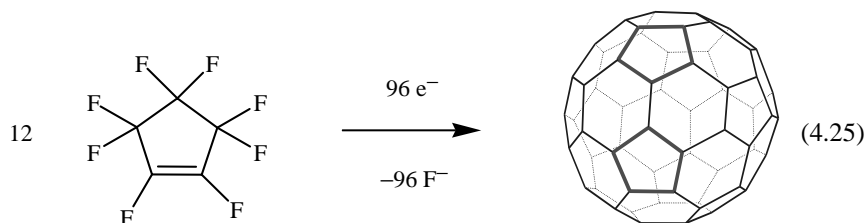
The amalgam carbonization of poly(chlorotrifluoroethylene) (PCTFE) is even more facile as compared to that of PTFE (Table 4.2) [10], which is due to the presence of a labile C–Cl bond. The yields and conjugation lengths of polyyne from PCTFE are significantly smaller [48].

4.3 ELECTROCHEMICAL SYNTHESIS OF FULLERENES AND CARBON ANIONS

Total electrochemical dehalogenation of perhalogenated hydrocarbons may present a template pattern for the synthesis of fullerenes. The idea of replicating of the precursor's structure was fruitful for the synthesis of C_{60} from perfluoronaphthalene:



and perfluorodecalin [4]. Alternatively, C_{60} condenses also from perfluorocyclopentene:



These precursors provided fullerene C_{60} in yields of ca. 0.1% [4]. Sometimes, small amounts of C_{70} and graphite onions of diameters 20–100 nm were also detected [4]. A variant of reaction 4.25 was reported by Lee et al. [93], who produced carbon onions from hexachlorocyclopentadiene and sodium. Interestingly, hexachlorobenzene gave only graphite in the same reaction [93]. This confirms that C_{60} can be constructed from sole pentagons C_5 as building blocks. Still another variant of reaction 4.25 was reported by Lu et al. [94]. They have produced C_{60} from hexachlorocyclopentadiene and potassium in the yield of ca. 3%. However, this reaction required the presence of Ni catalyst and temperatures 550–600°C. (The amalgam-driven dehalogenation of perfluorocyclopentene (reaction 4.25) amalgam proceeded at room temperature without a catalyst.)

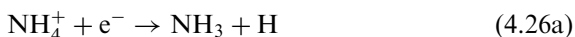
4.4 ELECTROCHEMICAL SYNTHESIS OF CARBON NANOTUBES

Kroto et al. [95–98] have reported on the synthesis of multiwalled carbon nanotubes and carbon onions during electrolysis on carbon electrodes in molten LiCl (at 600°C). The nanotubes were 2–10 nm in diameter and >500 nm long, and contained occasionally encapsulated lithium oxide, lithium chloride or lithium metal. The yield of nanotubes was 20–30% and, by tuning the electrolysis conditions, the morphology of nanotubes varied between straight, bent and spring-like ones [96–98]. The process was further optimized by Chen et al. [99], while nanotube yields up to 50% were reported during electrolysis on graphite electrodes in molten LiCl, NaCl and KCl. Further optimization by Bai et al. [100] even allowed demonstration of single walled carbon nanotubes in NaCl melt at 810°C.

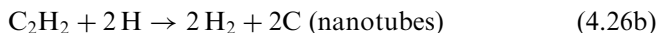
Nanotubes and onions were also prepared by electrolysis of acetylene at -40°C in liquid ammonia, without deliberately added supporting electrolyte [101]. This is the lowest temperature record for the production of nanotubes. In contrast to reaction 4.14, this carbonization was not aided by a catalyst. The mechanism started from dissociation of NH_3 :



followed by the formation of atomic hydrogen:



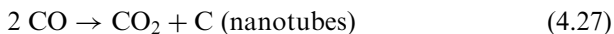
which finally carbonized acetylene:



Perfluorocyclopentene, perfluorodecalin and perfluoronaphthalene were carbonized by Li-amalgam and gave, besides small amounts of fullerenes and onions (Section 4.3), also carbon nanotubes in ca. 1–2% yield [4,5]. The tubes were capped and multiwalled, typically 15 nm in diameter and about 50–200 nm long. Whereas the tubes from C_5F_8 were straight, the tubes from $C_{10}F_{18}$ and $C_{10}F_8$ were curly and substantially longer [4,5].

Wang et al. [102] prepared carbon nanotubes through a reaction of tetrachloroethylene, C_2Cl_4 with potassium at 200°C in the presence of Au/Fe catalyst. Jiang et al. [103] have reported on the formation of multiwalled carbon nanotubes from hexachlorobenzene and potassium at 350°C in the presence of a Co/Ni catalyst. The authors claimed their reaction temperature to be the lowest record for nanotube production [103]. However, by cross-checking the older literature [4], this claim was, apparently, not correct. A similar reaction of hexachlorobenzene with sodium did not produce nanotubes, but graphite only [93].

Carbon nanotubes and nested fullerenes were also prepared by reductive carbonization of CO_2 with magnesium metal. Motiei et al. [104] reported on the production of nanotubes in ca. 0% yield and nested fullerenes in ca. 1–2% yield at 1000°C by the reaction of dry ice and magnesium. The reductive carbonization of CO_2 is reminiscent of the HiPco process [105, 106], based on disproportionation of carbon monoxide (the Boudouard reaction):



It occurs catalytically on the surface of Fe nanoparticles grown from $Fe(CO)_5$. Also, the conventional synthesis of nanotubes by catalytic CVD from acetylene or methane can be formally considered as redox reaction. Nevertheless, the electrochemical model of carbonization (Sections 4.1.1 and 4.1.2) is hardly applicable for CVD and HiPco, since the nanotubes grow on the catalyst particle by apposition from the gas phase, and not from the barrier film (Figure 4.1). The yield and quality of electrochemically made nanotubes are usually not competitive to those of catalytic processes in carbon arc, laser ablation, CVD and HiPco. However, this methodology demonstrated that nanotubes (and also fullerenes and onions (Section 4.3)) can be prepared by “soft chemistry” at room or sub-room temperatures [4,5,101]. Secondly, some electrochemical syntheses of nanotubes do not require a catalyst [4,5,95–98,100,101]. This might be attractive if high-purity, metal-free tubes are required.

4.4.1 INDIRECT SYNTHESIS OF NANOTUBES FROM POLYNE

Although the mechanism of gas phase growth of fullerenes and nanotubes is not clearly understood, the short-chain sp-bonded carbon molecules, formed for example during laser vaporization of graphite {A214}, surely

play a role. Lagow et al. [21] have even suggested that fullerenes grow from long chains in helical conformation via the spiral zipper mechanism. The gas-phase assembling of polyyynes into nanotubes is also possible, and it may even lead to encapsulation of polyyne inside the nanotube [29,30]. Polyyynes may trigger the formation of graphene-based sp^2 structures also in condensed phase at lower temperatures via cross-linking (Eq. 4.13). This process is undesired for the synthesis of carbyne, but the spontaneous conversion of sp -chains into graphene may lead to nanotubes and other interesting nanocarbons in the solid phase. This subject was pioneered in 1998 by Yasuda et al. [65–71]. They have generated polyyne from PTFE by electrochemical dehalogenation with Mg anode (reaction 4.21). The nanotube growth was promoted by irradiation with a 100 keV electron beam at 600–800°C. The nanotubes had diameters about 10–50 nm and lengths ca. 1 μ m [65,69]. Besides nanotubes, carbon nanocapsules and nanoparticles [70] were also detected by TEM.

A similar strategy was adopted by Hlavaty et al. [108–110], but the poorly defined *ex*-PTFE polyyne was replaced by pure low-molecular weight oligoynes [108,110]. Nanotubes were obtained by carbonization of 1,3,5-hexatriyne, 1-iodo-1,3,5-hexatriyne [108] and dialkali hexatriynides [110]. They were straight, multi-walled, with diameter of 10–20 nm, length of 100–200 nm, and end-capped [108]. Interestingly, the nanotubes grew exclusively from six-membered oligoynes. Higher or lower homologs of hexatriyne do not provide nanotubes [109], although they also polymerize spontaneously towards carbons [111,112].

ACKNOWLEDGMENT

This work was supported by the Academy of Sciences of the Czech Republic (contract No. A4040306) and by the Czech Ministry of Education (contract No. ME487).

REFERENCES

- [1] Besenhard, J.O.; Fritz, H.P. Elektrochemie schwarzer Kohlenstoffe. *Angew. Chem.* **1983**, *95*, 954–980.
- [2] Kavan, L.; Dunsch, L.; Kataura, H. Electrochemical tuning of electronic structure of carbon nanotubes and fullerene peapods. *Carbon* **2004**, *42*, 1011–1019.
- [3] Kavan, L. Electrochemical carbon. *Chem. Rev.* **1997**, *97*, 3061–3082.
- [4] Kavan, L.; Hlavaty, J. Carbon nanostructures from perfluorinated hydrocarbons. *Carbon* **1999**, *37*, 1863–1865.
- [5] Kavan, L. Nanocarbons made by soft chemistry. *Mol. Cryst. Liq. Cryst.* **2002**, *386*, 167–172.
- [6] Jansta, J.; Dousek, F.P. Electrochemical corrosion of PTFE contacting lithium amalgam. *Electrochim. Acta* **1973**, *18*, 673–674.

- [7] Dousek, F.P.; Janstá, J. Kinetics of electrochemical corrosion of PTFE by alkali metal amalgams. *Electrochim. Acta* **1975**, *20*, 1–6.
- [8] Jansta, J.; Dousek, F.P.; Riha, J. Quantitative explanation of the mechanism of corrosion of PTFE caused by active alkali metals. *J. Appl. Polym. Sci.* **1975**, *19*, 3201–3210.
- [9] Jansta, J.; Dousek, F.P.; Patzelová, V. Preparation of carbon from PTFE. *Carbon* **1975**, *13*, 377–380.
- [10] Kavan, L.; Dousek, F.P.; Micka, K. The role of ion transport in the electrochemical corrosion of fluoropolymers. Preparation and properties of n-doped polymeric carbon with mixed ion/electron conductivity. *Solid State Ionics* **1990**, *38*, 109–118.
- [11] Kavan, L.; Dousek, F.P.; Weber, J. Electrochemical reduction of NAFION 117. *J. Electroanal. Chem.* **1986**, *208*, 109–116.
- [12] Dahm, R.H.; Barker, D.J.; Brewis, D.M.; Hoy, L.R.J. Surface treatment of PTFE. In: *Adhesion 4*, Allen, K.W. (Editor), Applied Science Publ.: London, 1980, 215–232.
- [13] Barker, D.J.; Brewis, D.M.; Dahm, R.H.; Hoy, L.R.J. The electrochemical reduction of PTFE. *Electrochim. Acta* **1978**, *23*, 1107–1110.
- [14] Costello, C.A.; McCarthy, T.J. Surface selective introduction of specific functionalities onto PTFE. *Macromolecules* **1987**, *20*, 2819–2828.
- [15] Bening, R.C.; McCarthy, T.J. Surface treatment of poly(tetrafluoroethylene-co-hexafluoropropene), introduction of alcohol functionality. *Macromolecules* **1990**, *23*, 2648–2655.
- [16] Heimann, R.B.; Evsyukov S.E.; Kavan L. *Carbyne and Carbynoid Structures, Physics and Chemistry of Materials With Low-Dimensional Structures, Volume 21*, Kluwer Academic Publ.: Dordrecht, 1999.
- [17] Wang, C.Z.; Ho, K.M.; Chan, C.T. Structure and dynamics of liquid carbon. *Phys. Rev. B* **1993**, *47*, 14835–14841.
- [18] Maier, J.P. Electronic spectroscopy of carbon chains. *Chem. Soc. Rev.* **1997**, *26*, 21–28.
- [19] Orden, A.V.; Saykally, R.J. Small carbon clusters, spectroscopy, structure and energetics. *Chem. Rev.* **1998**, *98*, 2313–2357.
- [20] Gibtnier, T.; Hampel, F.; Gisselbrecht, J.P.; Hirsch, A. End-capped oligoynes: model compounds for carbyne. *Chem. Eur. J.* **2002**, *8*, 408–432.
- [21] Lagow, R.J.; Kampa, J.J.; Wei, H.C.; Battle, S.C.; Genge, J.W.; Laude, D.A.; Harper, C.J.; Bau, R.; Stevens, R.C.; Haw, J.F.; Munson, E. Synthesis of linear acetylenic carbon: The sp carbon allotrope. *Science* **1995**, *267*, 362–367.
- [22] Kertesz, M.; Koller, J.; Azman, A. Ab initio Hartree–Fock crystal orbital studies. *J. Chem. Phys.* **1978**, *68*, 2779–2782.
- [23] Phillpot, S.R.; Rice, M.J.; Bishop, A.R.; Campbell, D.K. Dynamics, photo-excitation, and coherent anharmonicity in polyyne. *Phys. Rev. B* **1987**, *36*, 1735–1744.
- [24] Rice, M.J.; Phillpot, S.R.; Bishop, A.R.; Campbell, D.K. Solitons, polarons, and phonons in the infinite polyyne chain. *Phys. Rev. B* **1986**, *34*, 4139–4149.
- [25] Springborg, M.; Drechsler, S.L.; Málek, J. Anharmonic model for polyyne. *Phys. Rev. B* **1990**, *41*, 11954–11966.
- [26] Heimann, R.B.; Kleiman, J.; Salansky, N.M. Structural aspects and conformation of linear carbon polytypes. *Carbon* **1984**, *22*, 147–156.

- [27] Heimann, R.B.; Kleiman, J.; Salansky, N.M. A unified structural approach to linear carbon polytypes. *Nature* **1983**, *306*, 164–167.
- [28] Heimann, R.B. Should carbyne be described by paracrystal theory? *Carbon* **1997**, *35*, 1669–1671.
- [29] Wang, Z.; Ke, X.; Zhu, Z.; Zhang, F.; Ruan, M.; Yang, J. Nanotube templating carbyne. *Phys. Rev. B* **2000**, *61*, R2472–R2474.
- [30] Zhao, X.; Ando, Y.; Liu, Y.; Jinno, M.; Suzuki, T. Carbon nanowire made of long linear carbon chain. *Phys. Rev. Lett.* **2003**, *90*, 187401-1 to -4.
- [31] Hlavaty, J.; Rathousky, J.; Zukal, A.; Kavan, L. Carbonization of 1,4-diiodo-1,3 butadiyne and 1-iodo-1,3,5-hexatriyne inside the siliceous molecular sieve MCM41. *Carbon* **2001**, *39*, 53–60.
- [32] Baughman, R.H.; Eckhardt, H.; Kertesz, M. Structure–property predictions for new planar forms of carbon. *J. Chem. Phys.* **1987**, *87*, 6687–6699.
- [33] Springborg, M.; Kavan, L. On the stability of polyyne. *Chem. Phys.* **1992**, *168*, 249–258.
- [34] Ohmura, K.; Kijima, M.; Shirakawa, H. Synthesis of conducting polymers with conjugated carbon–carbon triple bonds by electrochemical condensation of acetylene derivatives catalyzed by copper complex. *Synth. Metals* **1997**, *84*, 417–418.
- [35] Nishihara, H.; Harada, H.; Kaneko, S.; Tateishi, M.; Aramaki, K. Synthesis of graphite film by electrochemical reduction of hexachlorobuta-1,3-diene. *J. Chem. Soc. Chem. Commun.* **1990**, 26–27.
- [36] Nishihara, H.; Harada, H.; Tateishi, M.; Ohashi, K.; Aramaki, K. Graphite synthesis by electrochemical reduction of hexachlorobuta-1,3-diene. *J. Chem. Soc. Faraday Trans.* **1991**, *87*, 1187–1192.
- [37] Nishihara, H.; Harada, H.; Kaneko, S.; Tateishi, M.; Aramaki, K.; Murray, R.W. Electrochemical and electrical properties of poly(hexachlorobuta-1,3-diene), an electrochemically graphitized film. *J. Chem. Soc. Faraday Trans.* **1991**, *87*, 319–324.
- [38] Nishihara, H.; Ohashi, K.; Kaneko, S.; Tanaka, F.; Aramaki, K. Electrochemical and electrical properties of carbonaceous films formed by electro-reduction of perhalogenocarbons. *Synth. Metals* **1991**, *41–43*, 1495–1499.
- [39] Kijima, M. Electrochemical synthesis of linear carbons. *Recent Res. Devel. Pure Appl. Chem.* **1997**, *1*, 27–33.
- [40] Kijima, M.; Toyabe, T.; Shirakawa, H. Novel approach to synthesis of a carbyne film by electrochemical reduction of hexachlorobuta-1,3-diene. *Chem. Commun.* **1996**, 2273–2274.
- [41] Kijima, M.; Toyabe, T.; Shirakawa, H.; Kawata, S.; Kyotani, H.; Nakamura, Y.; Endo, M. Synthesis of carbyne by cathodic electrolysis of hexachlorobutadiene. *Synth. Metals* **1997**, *86*, 2279–2280.
- [42] Kijima, M.; Sakai, Y.; Shirakawa, H. A novel approach for synthesis of carbyne by electroreductive polymerization of diiodoacetylene catalyzed by Ni complex. *Chem. Lett.* **1994**, 2011–2014.
- [43] Kijima, M.; Sakai, Y.; Shirakawa, H. Electrochemical synthesis of carbyne catalyzed by nickel complex. *Synth. Metals* **1995**, *71*, 1837–1840.
- [44] Wang, X.; Shi, G.; Liang, Y. Synthesis of carbyne by electrochemical dehydrochlorination of 112 trichloroethane. *J. Electroanal. Chem.* **1999**, *470*, 95–97.

- [45] Shi, G. Synthesis of carbyne nanoparticles by dehydrochlorination. *Chem. Commun.* **1998**, 2271–2272.
- [46] Kyotani, M.; Yamaguchi, C.; Goto, A.; Sasaki, K.; Matsui, H.; Koga, Y. Nanoribbon graphite from carbyne like carbon. *Synth. Metals* **2001**, *121*, 1237–1238.
- [47] Kastner, J.; Kuzmany, H.; Kavan, L.; Dousek, F.P.; Kürti, J. Electrochemical preparation of carbyne with high yield. An in situ Raman scattering study. *Macromolecules* **1995**, *28*, 344–353.
- [48] Kavan, L.; Hlavaty, J.; Kastner, J.; Kuzmany, H. Electrochemical carbyne: synthesis and stability studied by Raman scattering. *Carbon* **1995**, *33*, 1321–1329.
- [49] Demyashev, G.M.; Taube, A.L.; Siores, E. Surface modification of titanium carbide with carbyne. *J. Nanosci. Nanotechnol.* **2002**, *2*, 133–137.
- [50] Brewis, D.M.; Dahm, R.H.; Konieczko, M.B. Reaction of PTFE with electrochemically generated intermediates. *Angew. Makrom. Chem.* **1975**, *43*, 191–194.
- [51] Dahm, R.H. Surface analysis and pretreatment of plastics. In: *Surface Analysis and Pretreatment of Plastics and Metals*, Brewis, D.M. (Editor), Applied Science Publ.: London, 1982, 227.
- [52] Barker, D.J.; Brewis, D.M.; Dahm, R.H.; Gribbin, J.; Hoy, L.R.J. Surface treatment of PTFE. *J. Adhesion* **1981**, *13*, 67–76.
- [53] Barker, D.J.; Brewis, D.M.; Dahm, R.H.; Hoy, L.R.J. Study of the intercalated carbon formed by electrochemical reduction of PTFE. *Polymer* **1978**, *19*, 856–858.
- [54] Barker, D.J.; Brewis, D.M.; Dahm, R.H.; Hoy, L.R.J. Anisotropic electrochemical reduction of PTFE. *J. Mater. Sci.* **1979**, *14*, 749–751.
- [55] Pud, A.A.; Shapoval, G.S.; Mikulina, O.E. Cells for the study of electrochemical properties and surface modification of polymers. *Pribory Tekh. Exp.* **1991**, 213–215.
- [56] Pud, A.A.; Shapoval, G.S. Cathodic transformation of PTFE in the presence of electron mediator. *Theor. Exp. Khim.* **1996**, *32*, 40–42.
- [57] Pud, A.A.; Mikulina, O.E.; Shapoval, G.S.; Tomilov, A.P. Cathodic decomposition of PTFE in galvanostatic regime. *Elektrokhimiya* **1996**, *32*, 1000–1003.
- [58] Shapoval, G.S.; Pud, A.A.; Tomilov, A.P. Electrochemical reductive decomposition of some polymer dielectrics. *Dokl. Akad. Nauk SSSR* **1985**, *283*, 434–438.
- [59] Pud, A.A.; Mikulina, O.E.; Shapoval, G.S. Electrochemically induced functionalization of fluorocontaining polyolefins. *Macrom. Reports* **1995**, *A32(Suppls. 5 & 6)*, 621–628.
- [60] Pud, A.A.; Shapoval, G.S. Electrochemistry as the way to transform polymers. *Macrom. Reports* **1995**, *A32(Suppls. 5 & 6)*, 629–638.
- [61] Pud, A.A.; Shapoval, G.S. Electrochemical decomposition of solid polymers on a cathode. *Elektrokhimiya* **1992**, *28*, 654–668.
- [62] Combellas, C.; Kanoufi, F.; Mazouzi, D.; Thiébault, A.; Bertrand, P.; Medard, N. Surface modification of PTFE. *Polymer* **2003**, *44*, 19–24.
- [63] Combellas, C.; Kanoufi, F.; Mazouzi, D.; Thiébault, A. Surface modification of halogenated polymers 5. *J. Electroanal. Chem.* **2003**, *556*, 43–52.
- [64] Amatore, C.; Combellas, C.; Kanoufi, F.; Sella, C.; Thiébault, A.; Thouin, L. Micrometrically controlled surface modification of teflon by redox catalysis. *Chem. Eur. J.* **2000**, *6*, 820–835.

- [65] Kawase, N.; Yasuda, A.; Matsui, T. In-situ formation of nanoscale carbon tubules. *Carbon* **1998**, *36*, 1864–1865.
- [66] Kawase, N.; Yasuda, A.; Matsui, T.; Yamaguchi, C.; Matsui, H. Transformation of polyyne to carbon nanotubes. *Carbon* **1999**, *37*, 522–524.
- [67] Yasuda, A.; Kawase, N.; Matsui, T.; Shimidzu, T.; Yamaguchi, C.; Matsui, H. Carbyne: electrochemical preparation and nanotube formation. *Reactive Funct. Polymers* **1999**, *41*, 13–19.
- [68] Yasuda, A.; Mizutani, W.; Shimizu, T.; Tokumoto, H. Nanotube from polyyne by electron beam. *Surf. Sci.* **2002**, *514*, 216–221.
- [69] Yasuda, A.; Kawase, N.; Mizutani, W. Nanotube formation from polyyne. *J. Phys. Chem. B* **2002**, *106*, 13924–13928.
- [70] Yasuda, A.; Kawase, N.; Banhart, F.; Mizutani, W.; Shimizu, T.; Tokumoto, H. Formation of nanotubes and onions from PTFE. *J. Phys. Chem. B* **2002**, *106*, 1247–1251.
- [71] Yasuda, A.; Kawase, N.; Banhart, F.; Mizutani, W.; Shimizu, T.; Tokumoto, H. Nanotube formation in-situ TEM. *J. Phys. Chem. B* **2002**, *106*, 1849–1852.
- [72] Kublanovskiy, V.S.; Litovcenko, K.I.; Stezeryanskiy, E.A.; Shpak, A.P. Mechanism of electrochemical reduction of poly(chlorotrifluoroethylene). *Dokl. Akad. Nauk Ukr. SSR Ser. B Geol. Khim. Biol. Nauki* **1989**, 36–39.
- [73] Kublanovskiy, V.S.; Litovcenko, K.I.; Zub, V.Y.; Stezeryanskiy, E.A. Effect of irradiation on electrochemical reduction of poly(chlorotrifluoroethylene). *Dokl. Akad. Nauk Ukr. SSR Ser. B Geol. Khim. Biol. Nauki* **1990**, 39–42.
- [74] Stezeryanskiy, E.A.; Litovcenko, K.I.; Kublanovskiy, V.S. Kinetics and mechanism of electrochemical reduction of poly(chlorotrifluoroethylene). *Ukr. Khim. Zhur.* **1990**, *56*, 487–492.
- [75] Stezeryanskiy, E.A.; Litovcenko, K.I.; Kublanovskiy, V.S. Effect of the electrolyte cation on electrochemical reduction of poly(chlorotrifluoroethylene). *Ukr. Khim. Zhur.* **1989**, *55*, 826–829.
- [76] Stezeryanskiy, E.A.; Litovcenko, K.I.; Kublanovskiy, V.S. Electrochemical reduction of a bonded PTFE. *Dokl. Akad. Nauk Ukr. SSR Ser. B Geol. Khim. Biol. Nauki* **1990**, 51–54.
- [77] Kijima, M.; Toyabe, T.; Shirakawa, H. Electrocatalytic dehydrofluorination of PVDF. *Chem. Lett.* **1995**, 553–554.
- [78] Cai, K.; Cao, C.; Zhu, H. Deposition of diamond like carbon by electrochemistry. *Carbon* **1999**, *37*, 1860–1862.
- [79] Shapoval, G.S.; Kontsur, Y.V.; Pud, A.A.; Tomilov, A.P. Indirect electrochemical triggering of dehydrohalogenation of polyvinylchloride in acetonitrile. *Elektrokhimiya* **1996**, *32*, 138–141.
- [80] Shapoval, G.S.; Kontsur, Y.V.; Pud, A.A. Electrochemical dehydrohalogenation of polyvinylchloride. *Elektrokhimiya* **1996**, *32*, 142–147.
- [81] Kontsur, Y.V.; Shapoval, G.S.; Pud, A.A. Indirect electrochemical dehydrochlorination of polyvinylchloride. *J. Macrom. Sci. Pure Appl. Chem.* **1995**, *A32*, 687–693.
- [82] Shapoval, G.S.; Kontsur, Y.V. Electrochemical initiation of surface dehydrohalogenation of polyvinylchloride films. *J. Macrom. Sci. Pure Appl. Chem.* **1995**, *A32*, 49–54.
- [83] Kijima, M.; Mukai, S.; Ohmura, K.; Shirakawa, H.; Kyotani, M. Synthesis of conjugated polymer with carbynoid structure by dehydrochlorination. *Synth. Metals* **1999**, *101*, 59–60.

- [84] Kavan, L.; Dousek, F.P.; Janda, P.; Weber, J. Carbonization of highly-oriented PTFE. *Chem. Mater.* **1999**, *11*, 329–335.
- [85] Hlavaty, J.; Kavan, L. Modification of electrochemical carbon by in-situ generated carbenes. *Carbon* **1997**, *35*, 127–131.
- [86] Kavan, L.; Dousek, F.P.; Micka, K. Time-dependent electrical resistivity of carbon. *J. Phys. Chem.* **1990**, *94*, 5127–5134.
- [87] Kavan, L.; Micka, K.; Kastner, J. UV-vis absorption of thin electrochemical carbon layers on poly(tetrafluoroethylene-co-hexafluoropropene). *Synth. Metals* **1994**, *63*, 147–152.
- [88] Kavan, L.; Janda, P.; Weber, J. Surface modification of PTFE by magnesium amalgam. *J. Mater. Sci.* **2001**, *36*, 879–885.
- [89] Hlavaty, J.; Kavan, L. The preparation of polymeric carbon from PTFE in the suspension of alkali metals. *Carbon* **1999**, *37*, 1029–1032.
- [90] Tanaike, O.; Yoshizawa, N.; Hatori, H.; Yamada, Y.; Shiraishi, S.; Oya, A. Mesoporous carbon from PTFE. *Carbon* **2002**, *40*, 445–467.
- [91] Liang, T.T.; Yamada, Y.; Yoshizawa, N.; Shiraishi, S.; Oya, A. Preparation of porous carbon by defluorination of PTFE. *Chem. Mater.* **2001**, *13*, 2933–2939.
- [92] Shiraishi, S.; Kurihara, H.; Tsubota, H.; Oya, A.; Soneda, Y.; Yamada, Y. Electric double layer capacitance of highly porous carbon derived from lithium metal and PTFE. *Electrochem. Solid-State Lett.* **2001**, *4*, A5–A8.
- [93] Lee, C.Y.; Chiu, H.T.; Peng, C.W.; Yen, M.Y.; Chang, Y.H.; Liu, C.S. Polygnon building route to sp² carbon based materials. *Adv. Mater.* **2001**, *13*, 1105–1107.
- [94] Lu, J.; Cong, D.F.; Li, Y.J.; Peng, R.F.; Wang, G.W.; Xie, Y. Highly efficient synthesis of C₆₀. *J. Am. Chem. Soc.* **2004**.
- [95] Hsu, W.K.; Hare, J.P.; Terrones, M.; Kroto, H.W.; Walton, D.R.M.; Harris, P.J.F. Condensed-phase nanotubes. *Nature* **1995**, *377*, 687.
- [96] Terrones, M.; Hsu, W.K.; Hare, J.P.; Kroto, H.W.; Terrones, H.; Walton, D.R.M. Graphitic structures: from planar to spheres, toroids and helices. *Phil. Trans. R. Soc. Lond. A* **1996**, *324*, 2025–2053.
- [97] Hsu, W.K.; Terrones, M.; Hare, J.P.; Terrones, H.; Kroto, H.W.; Walton, D.R.M. Electrochemical formation of carbon nanostructures. *Chem. Phys. Lett.* **1996**, *262*, 161–166.
- [98] Terrones, H.; Hsu, W.K.; Hare, J.P.; Kroto, H.W.; Walton, D.R.M. Synthetic routes to novel nanomaterials. *Fullerene Sci. Technol.* **1997**, *5*, 813–827.
- [99] Chen, G.Z.; Fan, X.; Luget, A.; Shaffer, M.S.P.; Fray, D.J.; Windle, A.H. Electrolytic conversion of graphite to carbon nanotubes in fused salts. *J. Electroanal. Chem.* **1998**, *446*, 1–6.
- [100] Bai, J.B.; Hamon, A.L.; Marraud, A.; Jouffrey, B.; Zymly, V. Synthesis of SWCNTs and MWCNTs by molten salt (NaCl) method. *Chem. Phys. Lett.* **2002**, *365*, 184–188.
- [101] Matveev, A.T.; Golberg, D.; Novikov, V.P.; Klimkovich, L.L.; Bando, Y. Synthesis of carbon nanotubes below room temperature. *Carbon* **2001**, *39*, 155–158.
- [102] Wang, X.; Lu, J.; Xie, Y.; Du, G.; Guo, Q.; Zhang, S. Nanotubes made from C₂Cl₄. *J. Phys. Chem. B* **2002**, *106*, 933–937.

- [103] Jiang, Y.; Wu, Y.; Zhang, S.; Xu, C.; Yu, W.; Xie, Y.; Qian, Y. Nanotubes from C₆Cl₆. *J. Am. Chem. Soc.* **2000**, *122*, 12383–12384.
- [104] Motiei, M.; Hacoheh, Y.R.; Calderon-Moreno, J.; Gedanken, A. Preparing carbon nanotubes and nested fullerenes from supercritical CO₂. *J. Am. Chem. Soc.* **2001**, *123*, 8624–8625.
- [105] Nikolaev, P.; Bronikowski, M.J.; Bradley, R.K.; Rohmund, F.; Colbert, D.T.; Smith, K.A.; Smalley, R.E. Gas phase growth of single-walled carbon nanotubes from CO. *Chem. Phys. Lett.* **1999**, *313*, 91–97.
- [106] Bronikowski, M.J.; Willis, P.A.; Colbert, D.T.; Smith, K.A.; Smalley, R.E. Gas-phase production of carbon single walled nanotubes from carbon monoxide via the HIPCO process a parametric study. *J. Vac. Sci. Technol. A* **2001**, *19*, 1800–1805.
- [107] Heath, J.R.; Zhang, Q.; Brien, S.C.O.; Curl, R.F.; Kroto, H.W.; Smalley, R.E. The formation of long carbon chain molecules during laser vaporization of graphite. *J. Am. Chem. Soc.* **1987**, *109*, 359–363.
- [108] Hlavaty, J.; Kavan, L.; Kasahara, N.; Oya, A. Polymerisation of 1-iodo-1,3,5-hexatriyne and 1,3,5-hexatriyne: a new synthesis of carbon nanotubes at room temperature. *Chem. Commun.* **2000**, 737–738.
- [109] Hlavaty, J.; Kavan, L.; Kubista, J. Carbonaceous polymers from end-capped alkynes. *Carbon* **2002**, *40*, 345–349.
- [110] Hlavaty, J.; Kavan, L.; Okabe, K.; Oya, A. Carbonaceous polymers and nanotubes from alpha-omega dialkali hexatriynides. *Carbon* **2002**, *40*, 1147–1150.
- [111] Hlavaty, J.; Kavan, L. Preparation of polymeric carbon from diiodoacetylene and tetraiodoethylene. *Angew. Makrom. Chem.* **1998**, *254*, 75–78.
- [112] Hlavaty, J.; Kavan, L. Derivatization of polymeric carbon isolated after polymerization of diiodoacetylene. *Angew. Makrom. Chem.* **1998**, *259*, 83–85.

5 Synthesis of Carbynoid Structures by the Combustion Flame Method

*Jean-Baptiste Donnet, Hanae Oulanti,
Raymond Wey, Thang Le Huu,
Wang Chuang Cun and Loïc Vidal*

CONTENTS

5.1	Introduction	79
5.2	Experimental Details	82
5.2.1	Deposition of Carbyne Films.....	82
5.2.2	Characterization	83
5.3	Results and Discussions	84
5.3.1	Scanning Electron Microscopy and Energy Dispersive X-Ray Analysis	84
5.3.1.1	Carbon Film Deposited at $\tau=1.15$	84
5.3.1.2	Carbon Film Deposited at $\tau=1.1$	85
5.3.1.3	Carbon Film Deposited at $\tau=1.05$	86
5.3.2	Raman Spectroscopy Analysis	86
5.3.2.1	Carbon Film Deposited at $\tau=1.15$	86
5.3.2.2	Carbon Film Deposited at $\tau=1.1$	87
5.3.3	Transmission Electron Microscopy Analysis	90
5.3.4	Atomic Force Microscopy Analysis	92
5.4	Conclusions.....	95
	References	95

5.1 INTRODUCTION

Carbon, a versatile element, can have many allotropic forms. The two pure forms known for centuries are diamond (sp^3 hybridization) and graphite (sp^2 hybridization). A linear carbon chain (one-dimensional)

with sp hybridization was discovered only in 1960 [1]. Carbyne is an ideal form of solid elemental carbon made by sp-hybridized carbon chains: polyethynylene ($-\text{C}\equiv\text{C}-$)_n, called polyyne, or isomeric polyethynylene diylidene ($=\text{C}=\text{C}=$)_n, called polycumulene ($n = 1, 2, 3 \dots \infty$). The interest in polyyne is constantly growing because they are considered to be the precursors of soot formation [2,3] and the intermediates for the synthesis of C₆₀ and carbon nanotubes. Because of the nature of the bonding, the thermodynamic stability of these allotropic systems differs. Theoretically, the transformation of one form to another more stable form can be obtained by an exothermic reaction. Boese et al. [4] reported that highly unsaturated dehydroannulene derivatives with sp-carbon skeletons exhibited explosive reactions when heated in a furnace under vacuum to form onion carbon and tube-like structures. Ajayan et al. [5] reported the transformation of single-walled nanotubes into open graphitic sheets upon exposure to the light of a photoflash. However, the existence of carbynes and their stability have been an issue of controversy [6]. Since its discovery, carbyne has been the subject of great interest for theoreticians and experimenters. A significant amount of work has been focused on the synthesis of carbynes and a variety of methods has been developed yielding mainly carbynoid structures, which are solid carbon materials where sp-hybridized carbon chains co-exist with other carbon nanostructures (disordered sp²-carbon, diamond-like sp³-carbon).

The synthetic methods for carbyne employed so far have involved the dehydrohalogenation of polyvinylidene halides [7], dehydrochlorination of chlorinated polyacetylene [8], defluorination of poly(tetrafluoroethylene) [9], and phase transition from carbon materials, such as graphite, under severe conditions.

A good approach for the synthesis of infinite polyyne or cumulene may be the polymerization of a monomeric compound. Hay [10] in 1969, Matsuda et al. [11] in 1984 and Kudryavtsev [12,13] have shown the possibility of synthesizing carbyne by oxidative dehydropolycondensation of acetylene. They found that carbyne powder was obtained by passing acetylene through an aqueous ammoniacal solution of a Cu(II) salt. The carbyne obtained by this method was nano-crystalline but it might be unstable under an oxygen atmosphere. Most recent re-investigation of this synthetic route by Cataldo and Capitani [14], who used solid state ¹³C-NMR, infrared and Raman spectroscopy and other analytical techniques, has revealed that the carbonaceous matter obtained is indeed rich in carbynoid structures but also consists of sp²- and sp³-carbon atoms.

By condensation of carbon vapor obtained by electrical arc discharge Tanuma [15] obtained a quasi one-dimensional carbon crystal, but the carbon chain only consisting of four atoms. The specific weight was 1.46 g/cm³. This value is smaller than the values of 2.68 g/cm³ of α-carbyne and 3.13 g/cm³ of β-carbyne. The crystals were metastable at temperature above 350 K. Tsuji et al. [16,17] have shown that polyyne in solution can be generated by laser

ablation of graphite or fullerene particles suspended in an organic solvent. Recently, Cataldo [18,19] reported the production of a mixture of polyynes having the general structure $\text{H}-(\text{C}\equiv\text{C})_n-\text{H}$, with $n=2, 3, 4, 5, 6, 7$, and 8, by using an electric arc between two graphite electrodes submerged in a solvent like decalin or acetonitrile. The interest in this technique lies in the fact that the polyynes absorption band can be detected in any solvent (Cataldo also used toluene, *n*-hexane, *n*-dodecane, acetonitrile, and a mixture of acetonitrile and water, 80:20). The formation of polyynes depends only on the graphite electrodes and not on the nature of the solvent. Particularly, the polyynes solution in decalin are stable in air for more than a week. This is in contrast to the usual situation, where high instability and reactivity of polyynes is encountered.

The synthesis of carbyne from graphite was first performed by Kasatochkin et al. [20], Whittaker et al. [21] since 1970, Lagow et al. [22] in 1995 and early in 2004 by Wakabayashi et al. [23]. In these techniques, carbon vapor was produced either by evaporation of resistively heated graphite rods or by laser ablation of graphite targets in a high vacuum (10^{-7} Torr). The vapor, which consisted of carbon atoms and molecules, was co-condensed with an excess of argon or neon gas on a substrate. The energy of the ions impinging on the substrate varies within the range of 1.5–2 keV. The rate of films growth is very slow, typically ~ 1 nm/min. Microcrystalline carbyne of 10–100 nm size were obtained by this method.

The first attempt to produce carbyne from carbon by dynamic pressure was by Litvinova et al. [24] in 1976, and then by Kleiman et al. [25] in 1984, and Yamada et al. [26] in 1991. The principle of this method was based on the pressure–temperature phase and transformation diagram of carbon. The critical point, which has been estimated for transformations from graphite to other solid phases (carbyne), is 0.2 GPa/6800 K [27]. Experiments were performed with a starting material of amorphous acetylene black (> 99% pure, 45 nm average particle size) packed into a sample chamber of a cylindrical container to form a cylinder 40 mm in height and 10 mm in diameter. Several carbyne polytypes with various carbon chain conjugation lengths and bonding type were obtained. The carbyne crystals were surrounded by tetragonal disordered diamond grains.

Kavan [28] and Kijima et al. [29] have used the electrochemical method to synthesize carbyne. This technique may be realized by “classical” electrochemistry whereby the charge transfer reaction occurs at interface of a metal electrode and liquid electrolyte solution. Electrons in reaction were supplied either through redox active molecules or through an electrode, which contacts an ionically conducting solid or liquid phase and the precursor. In general, the structure and properties of electrochemical carbon may differ considerably from those of usual pyrolytic carbons. The advantage of this technique is the synthesis of carbyne at low (room) temperature. It was shown that the best product was prepared by cathodic defluorination of poly(tetrafluoroethylene) and some other perhalo-*n*-alkanes. The carbyne

or carbynoid material resulting from the synthesis contained up to 30–300 carbon atoms [30]. This technique is a promising strategy towards molecular engineering of sp-carbon structures.

In this paper we present a new technique for the synthesis of carbon film with carbynoid structures. The basis of the method described here consists of a combustion reaction between oxygen and acetylene and particular parameters for flame conditions. The flame volume can be considered as the reaction chamber as in conventional chemical vapor deposition (CvD) or physical vapor deposition (PVD) methods. This technique provides a method of synthesizing carbyne at high growth rates and of obtaining better crystals.

5.2 EXPERIMENTAL DETAILS

5.2.1 DEPOSITION OF CARBYNE FILMS

The experimental set-up used to obtain the carbynes is shown in Figure 5.1. A commercial welding torch with a 1 mm tip orifice was used to generate the flame. The flow rates of oxygen and acetylene are controlled by mass

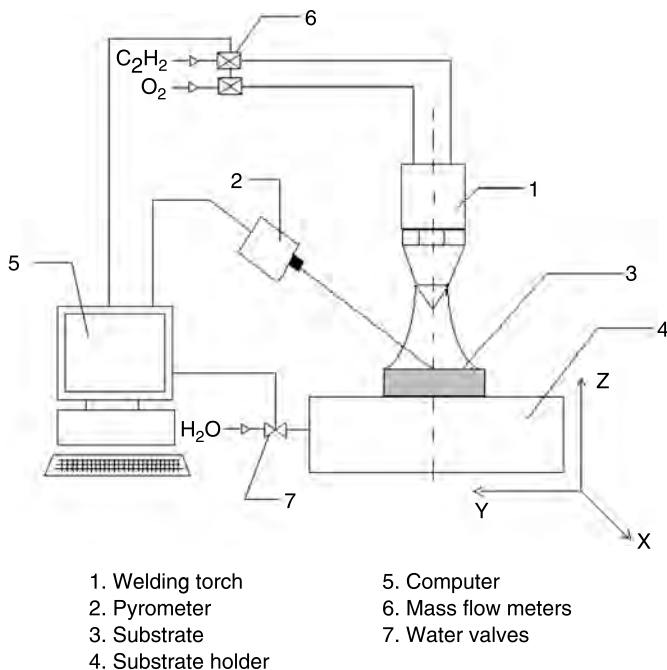


FIGURE 5.1 Diagram of the experimental setup for carbyne synthesis.

flow meters. The substrate temperature T_s is measured with a two-color pyrometer and is controlled by opening and closing a water valve, depending on the pyrometer signal.

Tungsten carbide is used as a substrate for the growth of carbon film. It is in contact with a water-cooled holder made of copper. The substrate holder is attached to an x - y - z translation system for positioning the substrate relatively to the welding torch.

This experimental setup was used to synthesize diamond and has been reported elsewhere [31]. The growth of diamond and carbyne crystals occurred by the simultaneous effect of many deposition parameters: substrate temperature, T_s , distance between the substrate and the inner flame cone, d , ratio in volume τ of acetylene to oxygen.

For the growth of diamond films the influence of the key parameters on the growth rate, quality, morphology, and orientation of diamond coatings has been studied and presented in previous papers [32,33]. Results can be summarized as follows.

At low substrate temperature, the diamond crystals present predominantly a cubic $\{111\}$ facet. These films are made of very small crystals. The increase of the growth temperature leads to an increase of the crystals size and an increase of the proportion of the $\{100\}$ relative to the $\{111\}$ orientation.

The polycrystalline diamond films change from $\{111\}$ orientation at low acetylene concentration to $\{100\}$ orientation if the acetylene concentration increases. In general, the diamond coatings are continuous and of high quality.

In our experiments, for the “carbyne” crystals growth, we have used deposition parameters as follows: substrate temperature, $T_s = 750^\circ\text{C}$; deposition times, $t = 10$ ms; distance between the substrate and the inner flame cone being 2 mm and with different ratio in volume τ of acetylene to oxygen.

5.2.2 CHARACTERIZATION

The surface morphology, thickness and quality of the deposited carbon films are analyzed by scanning electron microscopy (SEM), by energy dispersive x-ray (EDx) and by Raman spectroscopy (RS). The Raman spectrum was recorded using an argon ion laser Raman microprobe. The exciting laser wavelength is 632.81 nm with a laser power equal to 1.75 mW. The instrument was operated in the multi-channel mode with the beam focused to a spot diameter of approximately $2\text{ }\mu\text{m}$.

The atomic structure of the carbon deposited was studied by TEM using a JEM-100C electron microscope in the micro-diffraction mode. The structure of the “carbyne” crystals is analyzed by atomic force microscopy (AFM). The images are obtained by contact mode. The film thickness was determined from SEM observations of the film cross sections.

5.3 RESULTS AND DISCUSSIONS

5.3.1 SCANNING ELECTRON MICROSCOPY AND ENERGY DISPERSIVE X-RAY ANALYSIS

The morphology and the chemical composition of the deposited film were analyzed by SEM and EDX. Results showed that the ratio of acetylene to oxygen is an important parameter in determining the growth rate and the quality on the structure of carbon deposited films.

5.3.1.1 Carbon Film Deposited at $\tau = 1.15$

The film was made of small crystals of average size about $1\ \mu\text{m}$. Crystals with hexagonal and rhombohedral forms assigned to “carbyne” were observed.

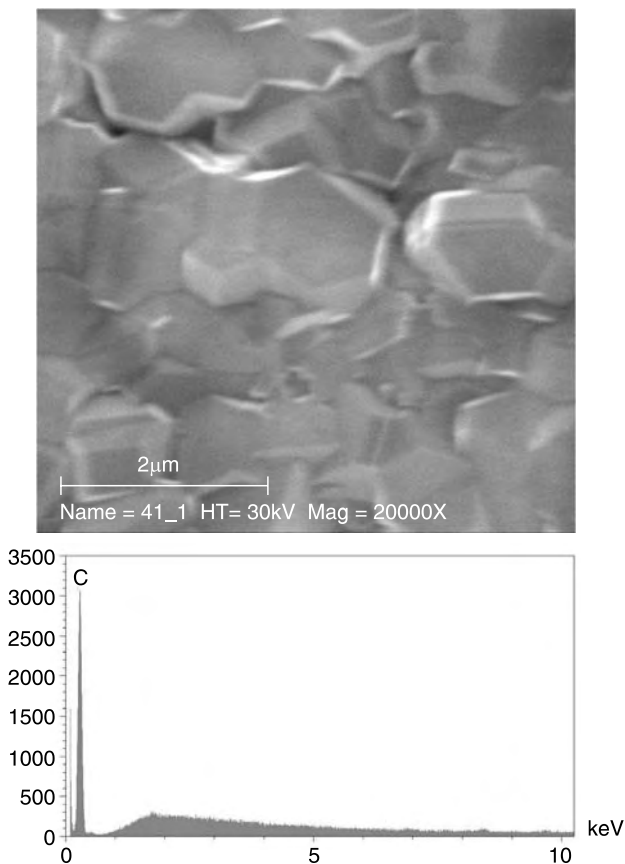


FIGURE 5.2 SEM image and EDX analysis of carbyne film obtained by the combustion flame method; $\tau = 1.15$.

These “carbyne” crystals were surrounded by disordered diamond crystals (Figure 5.2(a)). The film thickness was determined from SEM observation, and was about 15 μm . EDX analysis shows that the deposited films were constituted of pure carbon (Figure 5.2(b)).

5.3.1.2 Carbon Film Deposited at $\tau = 1.1$

Crystals with a hexagonal form assigned to “carbyne” or “tetragonal” crystallized diamond were observed (Figure 5.3(a)). The film’s texture was constituted of small crystals. The average crystal size is about 1–2 μm . These crystals were surrounded by diamond crystals. The film thickness was about 10 μm . EDX analysis shows that the deposited films were constituted of pure carbon (Figure 5.3(b)).

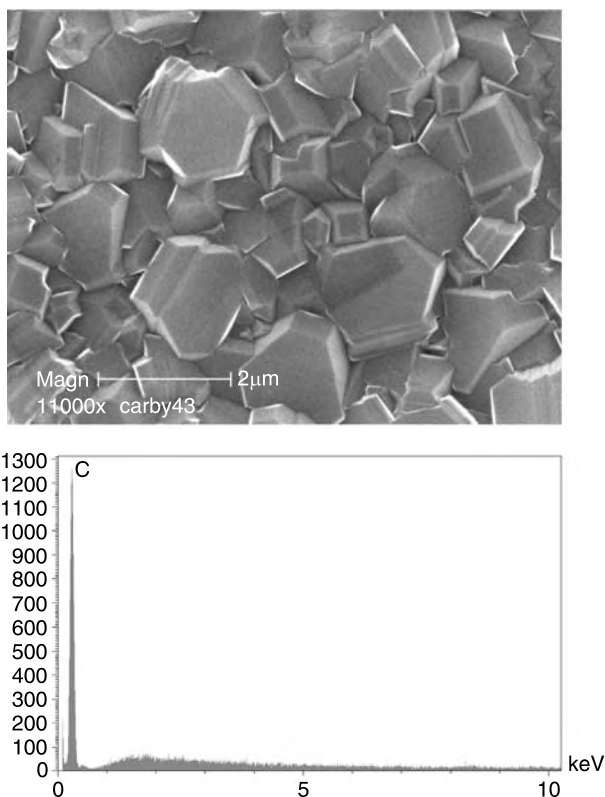


FIGURE 5.3 SEM image and EDX analysis of carbyne film obtained by the combustion flame method; $\tau = 1.1$.

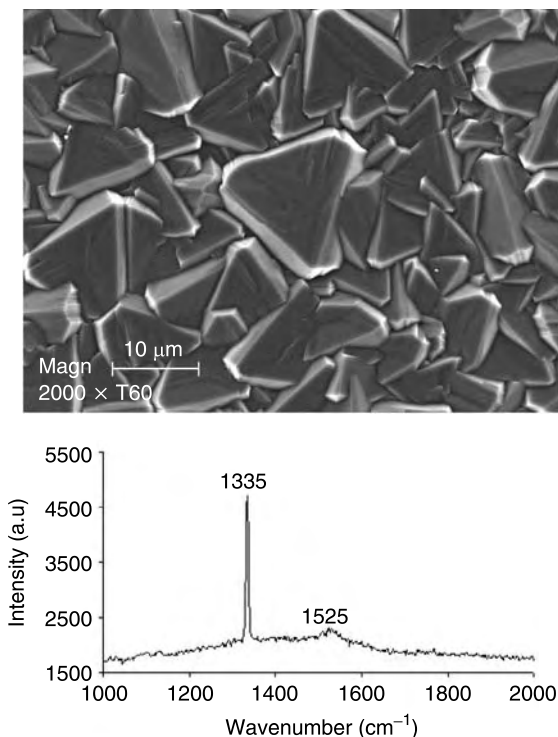


FIGURE 5.4 SEM image and Raman spectrum of diamond film obtained by the combustion flame method; $\tau = 1.05$.

5.3.1.3 Carbon Film Deposited at $\tau = 1.05$

The carbon films obtained were diamond crystals (Figure 5.4(a)). The diamond crystals present predominantly a (111) facet. Raman spectrum of the film is shown in Figure 5.4(b). The sharp peaks due to diamond detected at 1335 cm^{-1} showed the good quality of diamond. The average crystal size is about $10\text{ }\mu\text{m}$. The influence of the ratio of acetylene to oxygen and of substrate temperature on the qualities and orientation of diamond have been discussed in a previous paper [33].

5.3.2 RAMAN SPECTROSCOPY ANALYSIS

To confirm these observations, the carbon deposited films were analyzed by Raman spectroscopy.

5.3.2.1 Carbon Film Deposited at $\tau = 1.15$

The Raman spectrum of the carbon film shown in Figure 5.5(b) present a peak near 1445 cm^{-1} assigned to carbon-carbon double bonds and a broad

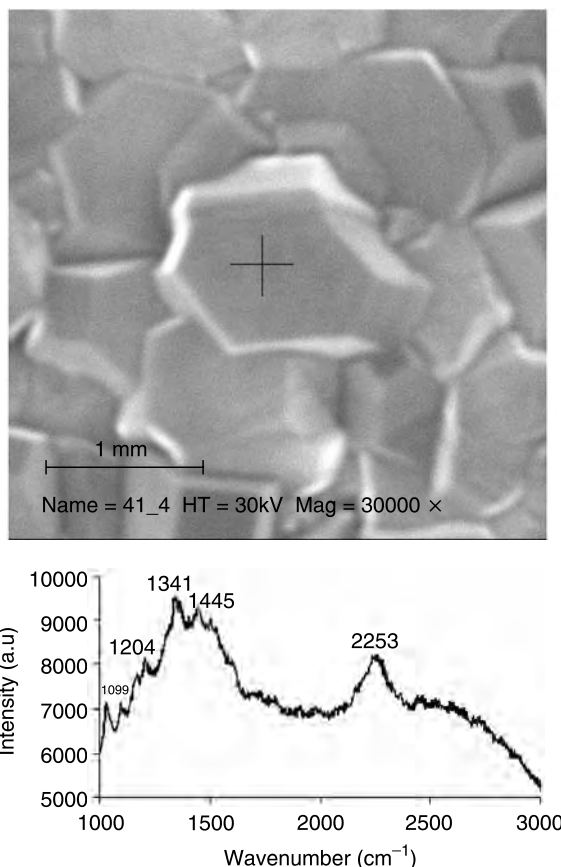


FIGURE 5.5 SEM image and Raman spectrum of carbyne film obtained at $\tau = 1.15$.

band between 2100 cm^{-1} and 2300 cm^{-1} assigned to $\text{C}\equiv\text{C}$ stretching mode of sp-bond carbon chains and particularly to carbon–carbon triple bonds. The characteristic $\text{C}\equiv\text{C}$ stretch “carbyne-band” in this sample was well developed in the Raman spectrum of a carbyne prepared by carbonization of poly(tetrafluoroethylene) with sodium amalgam [34]. The peak at 1341 cm^{-1} due to diamond was detected in the spectrum.

5.3.2.2 Carbon Film Deposited at $\tau = 1.1$

The Raman spectrum of the carbon film shown in [Figure 5.6\(b\)](#) presents one peak at 1460 cm^{-1} and two sharp peaks detected near 1864 cm^{-1} and 2248 cm^{-1} are assigned to allenic and acetylenic stretching mode of sp-bond carbon chains [35]. The frequency of the Raman peak in the spectra depends on the excitation wavelength and the length of carbon chains in the carbyne.

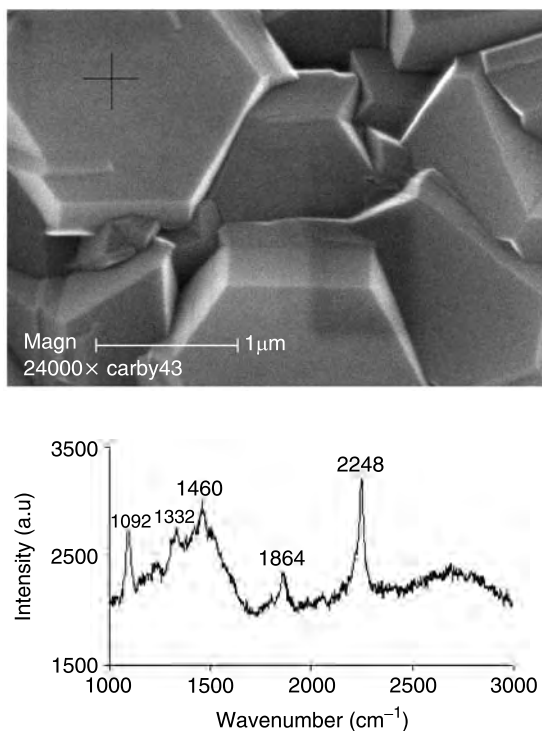


FIGURE 5.6 SEM image and Raman spectrum of carbyne film obtained at $\tau = 1.1$.

Generally, Raman spectra of carbyne-like materials show a characteristic band between 1750 cm^{-1} and 2300 cm^{-1} [9].

The peak assigned to $\text{C}\equiv\text{C}$ stretching mode appears in our sample at 2248 cm^{-1} (in contrast to the carbynoid peak at 2150 cm^{-1} as usually observed). This shift can be interpreted in terms of high residual stress of carbon films growing in these conditions, *i.e.* about 10 GPa. High residual stress was formed in the coating on cooling owing to the relatively high deposition temperature and the mismatch in coefficient of thermal expansion between coating and substrate.

In a study of the Raman spectra and pressure tuning Raman on the multinuclear metal carbyne complexes, Xu et al. [36] have shown that in $[\text{Cl}(\text{CO})_2(\text{TMEDA})\text{W}\equiv\text{CC}_6\text{H}_4\text{NC}]_2\text{ReCl}(\text{CO})_3$, the pressure sensitivities, $d\nu/dp$ of $\nu(\text{C}\equiv\text{O})$ Raman band (2039 cm^{-1}), are $0.46\text{ cm}^{-1}\text{ kbar}^{-1}$ in the low pressure phase area and very low $0.02\text{ cm}^{-1}\text{ kbar}^{-1}$ in the high pressure area. The $d\nu/dp$ of $\nu(\text{C}\equiv\text{O})$ Raman band (1923 cm^{-1}) are $0.9\text{ cm}^{-1}\text{ kbar}^{-1}$ in the low pressure phase area and $0.53\text{ cm}^{-1}\text{ kbar}^{-1}$ in the high pressure area.

The peak near 1099 cm^{-1} in the Raman spectra is due to the vibration density of states feature of the random sp^3 network [37]. The high excitation

energy allows sp^3 sites to be excited with a cross section comparable to sp^2 sites. In another study, Evsyukov [38] has shown that the peak in the Raman spectra near 1100 cm^{-1} is likely to result from C–O–C stretching vibrations. This structure can arise in the reaction products due to combustion of oxy-acetylene. The peak at 1332 cm^{-1} due to diamond was also detected in the spectrum.

It is not possible to assess the ratio of carbon–carbon double bonds (polycumulene)/triple bonds (polyne) in the film solely by Raman spectroscopy. Theoretically the quantum–chemical simulation shows that both isomers have very similar Raman spectra [39].

The equation given by Kastner et al. [40],

$$\nu_{\text{C}=\text{C}}(N) = 1750 + 3980/N,$$

allows the number of carbon atoms, N , in the chain to be calculated:

$$N = 3980/(\nu_{\text{C}=\text{C}} - 1750),$$

where $\nu_{\text{C}=\text{C}}$ is the wavenumber (cm^{-1}) that was obtained in the Raman spectra.

For the carbyne film obtained at $\tau=1.15$, a chain length of only 8 carbon atoms can be calculated (2253 cm^{-1}). For the carbyne film obtained at $\tau=1.1$ there are two types of chain: the acetylenic chains having 8 carbon atoms (2248 cm^{-1}) and allenic or, better, cumulenic chains of unknown length.

From the cross section of the SEM image, the growth rate of a carbon film could be calculated. It grows by increasing the ratio of acetylene to oxygen. The growth rate is about $100\text{ }\mu\text{m/h}$ at $\tau=1.15$ and decreased to $60\text{ }\mu\text{m/h}$ at $\tau=1.1$ but the quantity of the carbyne in the film was increased. The quantity of carbyne content present in the sample can be estimated by the intensity of the carbyne band relative to the lines of carbonaceous byproducts $I_{\text{c}}/I_{\text{bypr}}$ [41].

Raman spectra of the carbon sample obtained by combustion flame are in agreement with Raman spectra reported in literature [42]. The results were also in agreement with the results obtained by shock-quenched graphite of Heimann et al. [43]. The “carbyne” obtained by this method was also surrounded by tetragonal disordered diamond grains.

In 2000, Donnet et al. [44], during synthesis diamond by shock-wave compression, also found the crystalline carbyne in the sample. The crystalline structure of this film was examined by x-ray. The results obtained show that the film is composed of a mixture of diamond and carbyne.

5.3.3 TRANSMISSION ELECTRON MICROSCOPY ANALYSIS

After analysis by Raman spectroscopy and x-ray diffraction, these carbyne films were examined by TEM. The sample was prepared by dispersing the carbon powder (which deposited in the sample) in chloroform by using ultrasound. Some drops of the suspension were deposited on the surface of a grid for analysis. Many particles gave ring diffraction patterns corresponding to the natural carbyne observed in the Ries Crater and to the data values of α -carbyne obtained by other methods [45]. These were also particles giving diffraction patterns corresponding to crystalline diamond.

Figures 5.7, 5.8 and 5.9 show the diffraction pattern and transmission electron micrograph of the particles in the carbyne films produced by the combustion flame method. In Figures 5.7 and 5.8, the d-spacing of our particles is in good agreement with values of the α -modification of carbyne [47]. The evaluated lattice parameters were $a_0 = 0.892$ nm, $c_0 = 1.536$ nm. Figure 5.8 also shows that the interplanar spacing (21.0) and (30.0) of carbyne monocrystal obtained by combustion flame is coinciding with the value obtained by Heimann et al. [46]. The transmission electron micrograph shows the rhombohedral crystal flake of carbyne with a size of 230×274 nm.

In Figure 5.9, the electron diffraction data of our particles are in good agreement with the reported values of the carbyne monocrystal obtained by thermobaric treatment of a polyacetylene/sodium system [48]. The evaluated lattice parameters were $a_0 = 0.516$ nm, $c_0 = 2.563$ nm. The transmission electron micrograph shows that the hexagonal crystal flake of carbyne

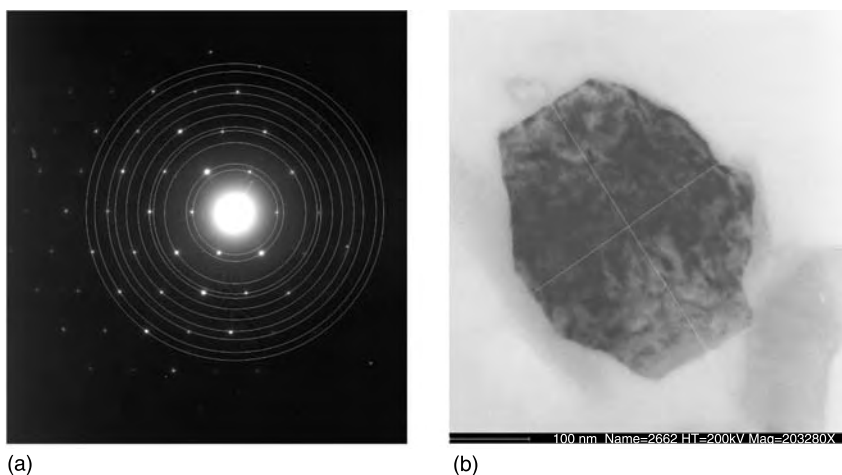


FIGURE 5.7 Typical electron pattern from a carbyne crystal flake with rhombohedral form: (a) diffraction pattern and (b) transmission electron micrograph.

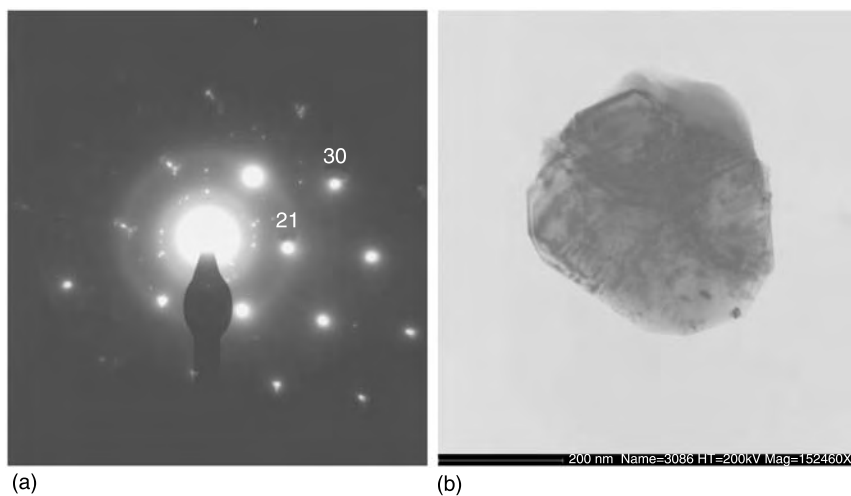


FIGURE 5.8 Typical electron pattern from a carbyne crystal flake with rhombohedral form: (a) diffraction pattern and (b) transmission electron micrograph.

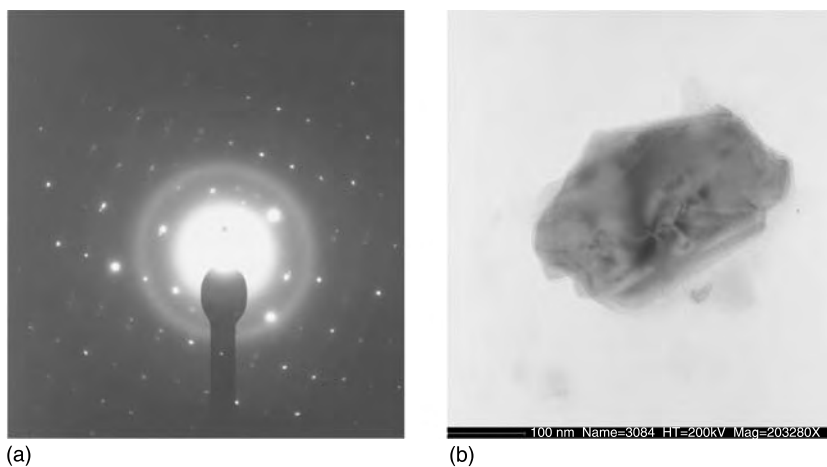


FIGURE 5.9 Typical electron pattern from a carbyne crystal flake with hexagonal form: (a) diffraction pattern and (b) transmission electron micrograph.

TABLE 5.1
Comparison of d-spacing measured for carbynes obtained by the combustion flame method with natural carbyne and published values for α -carbyne

Present Work (nm)	Present Work (nm)	Reference [45]	Present Work (nm)	References [25 and 39]
Figure 5.7	Figure 5.8		Figure 5.9	
0.372	–	0.372	0.212	0.211
0.318	–	0.322	0.175	0.168
0.217	0.212	0.213	0.162	0.163
0.191	0.194	0.194	0.141	0.141
0.180	–	–	0.130	0.129
0.161	0.171	0.166	0.110	0.110
0.145	–	0.150	0.106	–
0.130	–	0.137	0.101	0.102
0.122	0.122	0.122	0.096	0.096
0.110	0.110	0.112	0.090	0.090
0.105	0.101	0.106	0.084	0.086
–	0.090	0.086	0.079	0.081
–	0.078	–	0.075	0.075
–	0.073	–	0.070	0.072
–	0.070	–	0.068	0.068
–	0.060	–	0.066	–

corresponds to a size of 600 nm. The interplanar spacing values are given in Table 5.1.

5.3.4 ATOMIC FORCE MICROSCOPY ANALYSIS

The deposited carbon film (obtained by combustion flame method) was studied by using AFM. Figure 5.10 shows an image of the film surface in a height mode. The image clearly shows a hexagonal crystal with a size of about 0.75 μm (Figure 5.10(a)). Analysis of the lateral face of this crystal showed that the crystal was multilayered (Figure 5.10(b)). The thickness of the layer was about 8.411 nm. These results are in good agreement with a structural model of a multilayered tetracarbon film presented by Babaev and Guseva [47].

According to Heimann et al. [48], for a polyyne chain, the length of carbon chain is given by

$$C_O(\text{polyyne}) = \frac{n}{2} \cdot r(C\equiv C) + \frac{n}{2} - 1) \cdot r(C-C) + r_p^*,$$

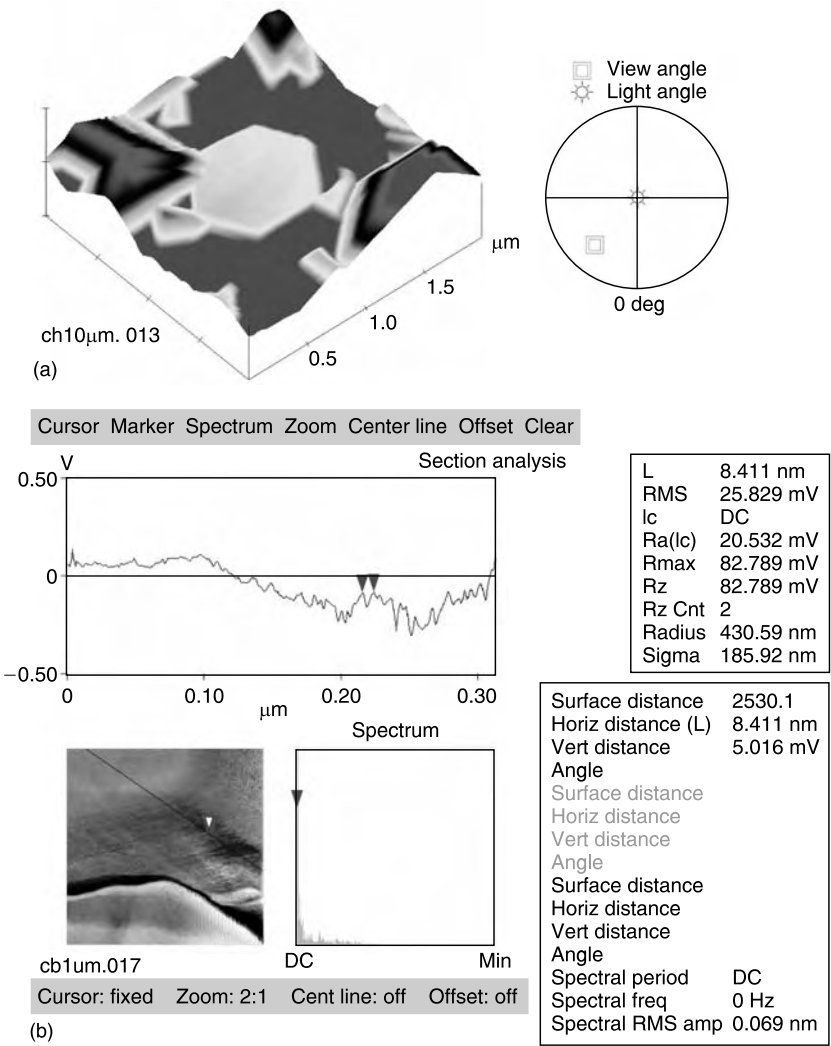


FIGURE 5.10 AFM analysis of a carbyne crystal. (a) On the surface; (b) analysis of a layered structure.

where n is number of carbon atoms,

$r_{(C\equiv C)} = 0.1207\text{nm}$, is the covalent radius for carbon triple bond,

$r_{(C-C)} = 0.1379\text{nm}$, is the covalent radius for carbon single bond,

$r^*p = r_{(C-C)} \cdot \cos 60^\circ = 0.0689 \text{ nm}$.

For $n = 35$, $C_O = 4.4565$ nm was calculated. It was suggested that each layer of carbyne was constituted from 2 to 4 carbon chains.

In order to understand the atomic nucleation processes, let us recall some theoretical concepts concerning the kinetic processes of film growth. The process can be understood as a competition between nucleation and step propagation; there are only three modes of crystals growth of material A on a substrate B (layer, island, island plus layer) depending on their relative surface energies γ_A and γ_B . A study by Bauer in 1958 and reviewed by Venables [49] shows that the initial growth of A on B is of island type if $\gamma_A > \gamma_B$ (if $\gamma_A < \gamma_B$ the initial growth is layer).

In the combustion flame method, the nucleation process leading to growth of carbon films (sp^1 , sp^2 or sp^3) results from a high gaseous flow at slightly higher than the atmospheric pressure which arrives on the substrate surface and which contains the combustion species including carbon atoms, hydrogen atoms, hydrocarbon free radicals and ionized particles. The carbon atoms from the vapor arriving on the substrate surface can either nucleate a new island on the terraces by meeting another free atom, or walk to the step edges causing a propagation of such steps. In the initial growth, these carbon atoms have low bonds on the surface and may evaporate, or may alternatively start the nucleation chain of small clusters. The high concentration of carbon atoms that arrive is due to the incident gaseous flow which decreases the re-evaporation rate. In that situation, many of carbon adatoms will bond together before they reach the step and create a nucleation site, which opens up another channel for the loss of adatoms.

The role of hydrogen atoms in chemical vapor deposition (CVD) carbon film growth has been studied by many authors [50,51]. It generally proceeds as follows: hydrogen atoms incident on the surface abstract hydrogen to produce vacant sites, where growth species can then stick to the carbon layer. Gas-phase hydrogen atoms may also produce condensable carbon radicals by reactions with hydrocarbons and, by impinging on the surface, they may create surface radicals and refill vacant sites by adsorption. Once adsorbed, atomic hydrogen may also stabilize the carbon chains. A study of Cataldo [52] has shown that carbon chains of any length must be terminated by end groups to ensure stability. The simplest end groups are hydrogen atoms. Some zigzag-like polycumulene carbon chains can be formed as a result of a simple poly-recombination reaction of short-chain clusters with an odd number of carbon atoms [45]. In the initial growth, the sp chains are short, metastable and have the tendency to undergo cross-linking reactions to form the sp^2 phase or onion carbon, tube-like structures [4] or sp^3 . Depending on the deposition conditions (surface temperature, condensation of carbon atoms on the substrate surface, incident angle etc.) the carbon chains can recombine by Baeyer's mechanism [53] to form a system of aromatic rings.

One drawback of the combustion flame method is the non-uniformity of the flame, with radical variations in velocity, temperature and, particularly,

in the incident angle at the intersection of the flame front and the substrate. By observing the flame during deposition, we found that in the central zone the incident flame jet is perpendicular to the surface. The incident angle decreases with increasing distance from the center, and the flame forms a toric swirling flow at the periphery. These parameters are an important factor affecting the crystallites carbyne growth. The non-uniformity of the flame can lead to the formation of different lengths of linear carbon chains and to different allotropic forms of carbon in the same film.

From the surface point of view and from experimental observation, the initial growth of carbyne on a carbide tungsten substrate is always an island growth. In this growth mode, the equilibrium state is obtained when all the deposited carbon atoms are in one large island. The driving force to approach this equilibrium is the reduction of the surface energy. Some carbyne crystallites of approximately equal size can be closely packed in a mosaic crystal, as seen in the figures. Comparable dimensions of crystallites can in turn be determined by similar growth conditions of the crystal nuclei [39].

5.4 CONCLUSIONS

In this paper we have presented the synthesis of carbynoid structures by the combustion flame method and investigated the influence of the ratio acetylene/oxygen on the morphology and quality of the carbon film deposited. Under our deposition conditions, the following conclusions can be drawn:

Linear carbon chains with variable crystal lattice parameters could be obtained. The carbon film is composed of a mixture of sp^3 - and sp -hybridized carbon atoms. Therefore we are dealing with carbynoid structures. Carbynoid crystals of $1\ \mu m$ size were obtained.

Decreasing the ratio acetylene/oxygen from $\tau = 1.15$ to $\tau = 1.1$ causes a decrease in the content of sp -carbon atoms in the films but increases the chain length of sp -hybridized carbon.

At a low ratio of acetylene/oxygen ($\tau = 1.05$) only crystalline diamond is obtained.

The structure of the carbyne deposited is multilayered.

REFERENCES

- [1] Kudryavtsev, Yu.P. The discovery of carbyne. In: *Carbyne and Carbynoid Structures*. Kluwer Academic Publishers: Dordrecht /Boston/London, 1999; 1–6.

- [2] Krestinin, A.V. Detailed modelling of soot formation in hydrocarbon pyrolysis. *Combustion Flame* **2000**, *121*, 513–524.
- [3] Richter, H; Howard, J.B. Formation of polycyclic aromatic hydrocarbons and their growth to soot — a review of chemical reaction pathways. *Prog. Energy. Comb. Sci.* **2000**, *26*, 565–608.
- [4] Boese, R; Matzger, A.J; Volhardt, K.P.C. Synthesis, crystal structure, and explosive decomposition of 1,2:5,6:11,12:15,16-tetrabenz-3,7,9,13,17,19-hexa-dehydro[20]annulene: formation of onion- and tube-like closed-shell carbon particles. *J. Am. Chem. Soc.* **1997**, *119*, 2052–2053.
- [5] Ajayan, P.M; Terrones, M; de la Guardia, A; Huc, V; Grobert, N; Wei, B.Q; Lezec, H; Ramanath, G; Ebbesen, T.W. Nanotubes in a flash-ignition and reconstruction. *Science* **2002**, *296*, 705.
- [6] Heimann, R.B. In: Heimann, R.B; S.E. Evsyukov, S.E; Kavan, L. (Editors), *Carbyne and Carbynoid Structures*. Kluwer Academic Publishers: Dordrecht/Boston/London, 1999.
- [7] Evsyukov, S.E.; Kudryavtsev, Yu.P.; Korshak, Yu.V.; Khvostov V.V; Babaev V.G., Guseva, M.B.; Korshak, V.V. Synthesis of carbyne on the basis of polyvinylidene halides. *Polymer Science USSR* **1989**, *31*, 29–37.
- [8] Akagi, K; Nishiguchi, M; Shirakawa, H; Furukawa, Y; Harada, I. One-dimensional conjugated carbyne — synthesis and properties. *Synth. Met.* **1987**, *17*, 557–562.
- [9] Kavan, L; Dousek, F.P. Carbynoid species in electrochemical polymeric carbon. *Synth Met.* **1993**, *58*, 63–72.
- [10] Hay, A.S. Oxidative polymerisation of diethynyl compounds. *J. Polym. Sci.* **1969**, *A17*, 1625–1634.
- [11] Matsuda, H.; Nakanishi, H.; Kato, M. Conducting polyyne and poly(metal-lyne) from butadiyne. *J. Polym. Lett. Ed.* **1984**, *22*, 107–111.
- [12] Kudryavtsev, Yu.P. Oxidative dehydropolycondensation — a new method to synthesize polymers with triple bonds. In: *Progress of Polymer Chemistry*. Nauka, 1969; 87–112.
- [13] Kudryavtsev, Yu.P. Syntheses of carbyne and carbynoid structure. In: *Carbyne and Carbynoid Structures*. Kluwer Academic Publishers: Dordrecht/Boston/London, 1999; 39–45.
- [14] Cataldo, F.; Capitani, D. Preparation and characterization of carbonaceous matter rich in diamond-like carbon and carbyne. *Materials Chem. Phys.* **1999**, *59*, 225–231.
- [15] Tanuma, S. Condensation of carbon vapor obtained by electrical arc discharge. In: *Carbyne and Carbynoid Structures*. Kluwer Academic Publishers: Dordrecht/Boston/London, 1999; 149–158.
- [16] Tsuji, M; Tsuji, T; Kuboyama, S; Yoon S.H; Korai, Y; Tsujimoto, T. Formation of hydrogen-capped polyyynes by laser ablation of graphite particles suspended in solution. *Chem Phys Lett.* **2002**, *355*, 101–108.
- [17] Tsuji, M; Kuboyama, S; Matsuzaki, T; Tsuji, T. Formation of hydrogen-capped polyyynes by laser ablation of C60 particles suspended in solution. *Carbon* **2003**, *41*, 2141–2148.
- [18] Cataldo, F. Simple generation and detection of polyyynes in an arc discharge between graphite electrodes submerged in various solvents. (Letters to the Editor) *Carbon* **2003**, *41*, 2653– 2689.

- [19] Cataldo, F. Synthesis of polyynes in a submerged electric arc in organic solvents. *Carbon* **2004**, 47, 129–142.
- [20] Kasatochkin, V.I.; Savranskii, V.V.; Simimov, V.N.; Mel'nichenko, V.M. A study of carbyne condensed from carbon vapor. *Dokl. Akad. Nauk SSSR* **1971**, 217, 796–799.
- [21] Whittaker, A.G.; Wolten, G.M. Carbon: a suggested new hexagonal crystal form. *Science* **1972**, 178, 54–56.
- [22] Lagow, R.J.; Kampa, J.J.; Wei, H.Ch.; Battle, S.L.; Genge, J.W.; Laude, D.A.; Harper, C.J.; Bau, R.; Steven, R.C.; Haw, J.F.; Munson, E. Synthesis of linear acetylenic carbon: the “sp” carbon allotrope. *Science* **1995**, 267, 362–367.
- [23] Wakabayashi, T.; Ong, A.L.; Strelnikov, D.; Kratschmer, W. Flashing carbon on cold surface. *J. Phys. Chem. B* **2004**, 108, 3686–3690.
- [24] Livinova, V.A.; Cherkinskaya, K.T. Phase transformations in pyrographite and glassy carbon on shock impact. *Khim. Tverd. Topliva*. **1976**, 159–164.
- [25] Kleiman, J.I.; Yamada, K.; Sawaoka, A.B.; Heimann, R.B. Dynamic pressure synthesis of carbyne. In: *Carbyne and Carbynoid Structures*. Kluwer Academic Publishers: Dordrecht/Boston/London, 1999; 173–187.
- [26] Yamada, K.; Kunishige, H.; Sawaoka, A.B. Formation process of carbyne produced by shock compression. *Naturwiss* **1991**, 78, 450–465.
- [27] Bundy, F.P.; Basset, W.A.; Weathers, M.S.; Hemlay, R.J.; Maoand, H.K.; Goncharov, A.F. The pressure–temperature phase and transformation diagram for carbon. *Carbon* **1996**, 34(2), 141–153.
- [28] Kavan, L. Electrochemical methods. In: *Carbyne and Carbynoid Structures*. Kluwer Academic Publishers: Dordrecht/Boston/London, 1999; 189–214.
- [29] Kijima, M.; Toyabe, T.; Shirakawa, H. Novel approach to synthesis of a carbyne film by electrochemical reduction of hexachlorobuta-1,3-diene. *Chem. Commun.* **1996**, 2273–2274.
- [30] Kavan, L. Electrochemical preparation of hydrogen free carbyne-like material. *Carbon* **1988**, 36, 801–808.
- [31] Le Huu, T.; Schmitt, M.; Paulmier, D.; Mamalis, A.G.; Grabchenko, A. Tribological properties of smooth diamond coatings for cutting tools. *Wear* **1999**, 843–847.
- [32] Paulmier, D.; Le Huu, T.; Zaidi, H. Growth and orientation of diamond crystal thin films obtained by the combustion flame method. *Surface Sci.* **1997**, 377–379, 866–870.
- [33] Le Huu, T.; Zaidi, H.; Paulmier, D. About the growth of diamond crystals obtained by the combustion flame method: used for coatings on large area substrates. *Thin Solid Films* **1997**, 308–309, 147–153.
- [34] Kavan, L.; Kastner, J. Carbyne form of carbon: continuation of the story. *Carbon* **1994**, 32, 1533–1536.
- [35] Nakamizo, M.; Kammereck, R.; Walker, P.L. Laser Raman studies on carbons. *Carbon* **1974**, 12, 259–267.
- [36] Xu, Z.; Butler, I.S.; Mayr, A. The pressure tuning Raman and IR spectral studies on the multinuclear metal carbyne complexes. *Spectrochimica. Acta. part A* **2004**, 995–1000.
- [37] Ferrari, A.C.; Robertson, J. Origin of the 1150 cm^{-1} Raman mode in nano-crystalline diamond. *Physical Rev. B* **2001**, 63, 121405-1–121405-4.

- [38] Evsyukov, S.E. Chemical dehydrohalogenation of polymers. In: *Carbyne and Carbynoid Structures*. Kluwer Academic Publishers: Dordrecht/Boston/London, 1999; 55–74.
- [39] Udod, I.A. Carbyne intercalation compounds. In: *Carbyne and Carbynoid Structures*. Kluwer Academic Publishers: Dordrecht/Boston/London, 1999; 269–294.
- [40] Kastner, J.; Kuzmany, H.; Kavan, L.; Dousek, F.P.; Kürti, J. Reductive preparation of carbyne with high yield. An in situ Raman scattering study. *J. Macromolecules* **1995**, 28, 344–353.
- [41] Hlavaty, J.; Kavan, L. Modification of electrochemical polymeric carbon by in-situ generated carbenes. *Carbon* **1997**, 35, 127–131.
- [42] Akagi, K.; Nishiguchi, C.; Shirakawa, H. One dimensional conjugated carbene — synthesis and properties. *Synth. Metals* **1987**, 17, 557–562.
- [43] Heimann, R.B.; Fujiwara, S.; Kakudate, Y.; Koga, Y.; Komatsu, T.; Nomura, M. A new carbon form obtained by wear shock compression of carbyne. *Carbon* **1995**, 33, 859–863.
- [44] Donnet, J.B.; Fousson, E.; Wang, T.K.; Samirant, M.; Baras, C.; Pontier Johnson, M. Dynamic synthesis of diamond. *Diamond and Related Materials* **2000**, 9, 887–892.
- [45] Kasatochkin, V.I.; Korshak, V.V.; Kudraytsev, Y.P.; Sladkov, A.M.; Sterenberg, I.E. On crystalline structure of carbyne. *Carbon* **1973**, 11, 70–72.
- [46] Babaev, V.G.; Guseva, M.B. Ion-assisted condensation of carbon. In: *Carbyne and Carbynoid Structures*. Kluwer Academic Publishers: Dordrecht/Boston/London, 1999; 159–171.
- [47] Heimann, R.B.; Kleiman, J.; Salansky, N.M. Structural aspects and conformation of linear carbon polytypes (carbynes). *Carbon* **1984**, 22, 147–156.
- [48] Heimann, R.B.; Fujiwara S.; Kakudate, Y.; Koga, Y.; Komatsu, T.; Nomura, M. A new carbon form obtained by weak shock compression of carbyne. *Carbon* **1995**, 33, 859–861.
- [49] Venables, J.A. Atomic processes in crystal growth. *Surface Sci.* **1994**, 299/300, 798–817.
- [50] Spear, K.E. Diamond–ceramic coating of the future. *J. Am. Ceram. Soc.* **1989**, 72, 171–175.
- [51] Klein-Douwel, R.J.H.; Ter Meulen, J.J. Spatial distributions of atomic hydrogen and C₂ in an oxyacetylene flame in relation to diamond growth. *J. Appl. Phys.* **1998**, 83, 4734–4745.
- [52] Cataldo, F. Polyyynes: a new class of carbon allotropes. About the formation of dicyanopolyyynes from an electric arc between graphite electrodes in liquid nitrogen. *Polyhedron* **2004**, 23, 1889–1896.
- [53] Baeyer, A. Ueber polyacetylenverbindungen. *Ber. Deuts. Chem. Ges.* **1885**, 18, 2269–2281.

6 Cyclic Polyynes: Generation, Characterization, and Reactions

Yoshito Tobe and Tomonari Wakabayashi

CONTENTS

6.1	Introduction	99
6.2	Monocyclic Carbon Rings.....	101
6.2.1	Theory and Detection: An Historical Overview	101
6.2.2	Generation from Structurally Well-Defined Organic Precursors	102
6.2.3	Cumulenic vs Acetylenic Forms	105
6.2.4	Photoelectron Spectroscopy	108
6.2.5	Towards the IR Detection of Cyclic C ₁₀	111
6.3	Multicyclic Polyynes	112
6.3.1	Class of Hybrid sp–sp ² Carbon Networks	112
6.3.2	Bicyclic and Tricyclic Polyynes.....	113
6.4	Three-Dimensional Polycyclic Polyynes	117
6.4.1	Macrocyclic Polyynes to Size-Selective Fullerene Formation	117
6.5	Conclusions.....	120
	Acknowledgment	120
	References	120

6.1 INTRODUCTION

Increasing interest has been focused on the acetylene-based polymer chemistry relevant to cyclic polyynes — the topic of this chapter [1]. Cyclic polyynes are unique members in the family of sp-carbon allotropes. Like linear polyynes, they are composed of unsaturated carbon atoms covalently

bonded with two neighboring atoms. That they have two-dimensional ring-type structures, thus having no terminable end, makes them constitute another class of molecular polyyne. The ring-shaped all-carbon molecules C_n are also referred to as cyclic carbon clusters or cyclo[n]carbons in relation to cluster science or organic chemistry [1–9]. Concerning the electronic structure of the polyyne ring, two orthogonal π -electron systems are not identical due to the strained bent arrangement of bonds. Incorporating trivalent sp^2 or tetravalent sp^3 carbons as atomic junctions, the polyyne chains can extend large branching structures forming two- or three-dimensional polygons. With such characteristic features in mind, researchers have thought that cyclic polyyne may serve as new building blocks of hybrid sp – sp^2 – sp^3 carbon networks or carbynoid structures, and in some cases such compounds have been successfully constructed and characterized in organic chemistry [1b–d]. More generally, one may realize that the strained bent carbon chains are found commonly within the polymeric systems that form during the aggregation of linear polyyne.

The formation of carbon molecules, including cyclic polyyne, has been performed so far by laser vaporization of graphite that was initiated with relevance to astrophysics [10] and finally leading to the discovery of fullerenes [11,12] and nanotubes [13]. For the cyclic polyyne, generation from organic precursors of well-defined structures having a dehydroannulene framework has been a topic in organic chemistry in recent years [1–9]. Also noted for cyclic polyyne is reactivity of their highly unsaturated bonds. The carbon-rich compounds are so reactive as to condense easily forming polymers. Similarly to the linear polyyne, the unsaturated carbon atoms form cross-linking bonds towards the other molecules upon collisions (see [Section 6.3.2](#)). To avoid the undesired reactions, characterization of such transient species has been performed in vacuum or in matrix-isolated states. For instance, under the collision-free conditions in vacuum, the organic precursors having carbon-ring structures of C_n ($n = 12$ – 30) that are stabilized by some protecting groups successfully liberate bare carbon molecules C_n through expulsion of the ligand molecules upon UV laser irradiation (Section 6.2.2) [2–5,9], and characterized by anion photoelectron spectroscopy (Sections 6.2.3 and 6.2.4) [6]. In solution, on the other hand, the product materials observed upon UV irradiation are uncharacterized polymers or ligand-substituted compounds [5c]. In order to trap the molecules containing highly strained polyyne units, the precursor molecules are co-condensed in an inert matrix at low temperatures, then irradiated with UV light to observe the IR absorption spectra in which the high frequency stretching vibrations characteristic of these polyyne chains are detected [2b].

The approach to form carbon ring molecules from organic precursors has been extended to produce three-dimensional macrocyclic polyyne of larger sizes (Section 6.4). Despite the fragility and explosive reactivity, the precursory molecules containing polyyne structures are successfully isolated and well characterized. The liberated pure carbon molecules have been

detected under vacuum by means of mass spectroscopy. Since the first report on the generation of cyclic C_{18} by Diederich and co-workers [2a], the activity in this area has continually grown to report various macrocyclic carbon molecules in a size-selective manner. The carbon clusters so far produced from the organic precursors are C_{12} , C_{15} , C_{16} , C_{18} , C_{20} , C_{24} , C_{30} , C_{36} , C_{60} , and C_{78} .

In this chapter, keeping in mind the generation, characterization, and reactions of the cyclic polyynes, the interplay of organic chemistry and carbon cluster science during the last decade is presented. First, following short historical remarks (Section 6.2.1), recent research activity on the production of cyclo[n]carbons from well-defined organic precursors is surveyed (Section 6.2.2). Second, major structural and electronic properties of monocyclic carbon clusters are presented in the context of theoretical considerations (Section 6.2.3), followed by observational results of photoelectron spectroscopy (Section 6.2.4). Third, considerations on the infrared activity of cyclic C_{10} will be presented (Section 6.2.5). Finally, this chapter ends with experimental as well as theoretical proposals for the structures of multicyclic polyynes (Section 6.3) and their relevance to the formation of fullerenes, in particular from polycyclic polyynes (Section 6.4).

6.2 MONOCYCLIC CARBON RINGS

6.2.1 THEORY AND DETECTION: AN HISTORICAL OVERVIEW

In 1959, during a theoretical study of the properties of thermodynamic equilibrium of carbon vapor molecules above high-temperature graphite, Pitzer and Clementi took cyclic molecules C_n as well as linear C_n into account [14]. Using the extended Hückel theory, Hoffmann predicted that cyclic carbon molecules having $4m + 2$ π electrons are stable in cumulenic forms, *i.e.* an electron-delocalized structure showing aromatic behavior [15]. Raghavachari and Binkley compared calculated stability of linear and cyclic clusters [16]. They found that for odd numbered clusters linear forms are the most stable up to $n = 9$, while for even numbered C_n of $n > 10$ monocyclic forms are more stable than linear forms. For even numbered small clusters of C_4 , C_6 , and C_8 , the linear and cyclic forms were found to be almost isoenergetic. Using ultraviolet photoelectron spectroscopy (UPS), Yang et al. found indications of monocyclicity for cluster anions C_n^- of $n \geq 10$ produced by laser vaporization of graphite in helium gas [17]. Ion chromatography experiments indicated that small carbon cluster ions exist in linear, monocyclic, bicyclic, and polycyclic ring structures [18–20]. The collision-induced annealing of mass selected cluster ions revealed transformation of the polycyclic rings into fullerene cages (see [Section 6.3.2](#) for details) [21–24]. Also, in the condensed solid rare-gas matrices at low temperatures, carbon molecules are studied extensively (see also [Chapter 1](#)). Concerning the cyclic

carbon molecules, Presilla-Marquez et al. recently suggested an assignment of the IR absorption line to cyclic C_6 on the basis of the frequency shifts by isotopic substitution [25]. Independently, Wang et al. found that the assignment is consistent with the calculated frequency obtained from the density functional theory (DFT) [26]. Grutter et al. reported UV absorption spectra of mass selected C_{10} as well as C_{12} and C_{14} clusters in neon matrices and discussed on their monocyclic nature based on the high-level configuration interaction (CI) method in molecular orbital calculations [27].

The above historical remarks might convey a subtle and scattered impression. It is true that any direct evidence has not yet been presented in the sense that monocyclic nature is proven by rotationally resolved spectroscopy, NMR spectroscopy, or high-resolution images by scanning tunneling microscopy (STM) or transmission electron microscopy (TEM).

6.2.2 GENERATION FROM STRUCTURALLY WELL-DEFINED ORGANIC PRECURSORS

In order to generate monocyclic carbon clusters, also called cyclo[n]carbons in the field of organic chemistry, of specific ring size selectively, fragmentation of structurally well-defined organic precursors has been extensively studied [1]. Figure 6.1 shows representative precursors developed by the group of Diederich and Rubin and that of Tobe. The precursor **1** possessing three dibenzobicyclo[2.2.2]octatriene units would generate C_{18} by expulsion of three molecules of anthracene in a retro-Diels–Alder sense [2]. Although the formation of C_{18}^+ was indeed observed in the laser-desorption time-of-flight (LD TOF) mass spectra of **1**, attempts to prepare macroscopic quantities of C_{18} were not successful. Similarly, attempted decomplexation of stable dinuclear cobalt complexes **2a** and **2b**, which can be regarded as transition metal complexes of C_{18} and C_{24} , respectively, was also unsuccessful [2b,3]. Multi-step decarbonylation of the precursors **3a–c** having cyclobutenedione units took place in the positive and negative modes of the laser-desorption Fourier transform (FT) mass spectra to form C_{18} , C_{24} , and C_{30} ions [2b,4]. Interestingly, C_{60}^+ was formed by coalescence between C_{30}^+ and C_{30} derived from the precursor **3c**, suggesting the key role of cyclic polyyne in the formation mechanism of fullerenes. Irradiation of **3a** dispersed in a low-temperature glass matrix resulted in the formation of ketene intermediates and subsequent loss of carbon monoxide. However, definite spectroscopic evidence for the formation of monocyclic C_{18} has not been obtained yet [2b].

Tobe and Wakabayashi utilized, on the other hand, [4.3.2]propella-1,3,11-triene units as the leaving group which would generate a carbon–carbon triple bond in a retro [2+2] sense ([2+2] cycloreversion), and prepared dehydroannulenes **4a–c** and **5a,b** as precursors of cyclo[n]carbons of $n = 12, 16, 20, 18$, and 24 , respectively [5]. In their negative mode LD TOF mass spectra, the formation of monocyclic C_n anions ($n = 12, 16, 18$,

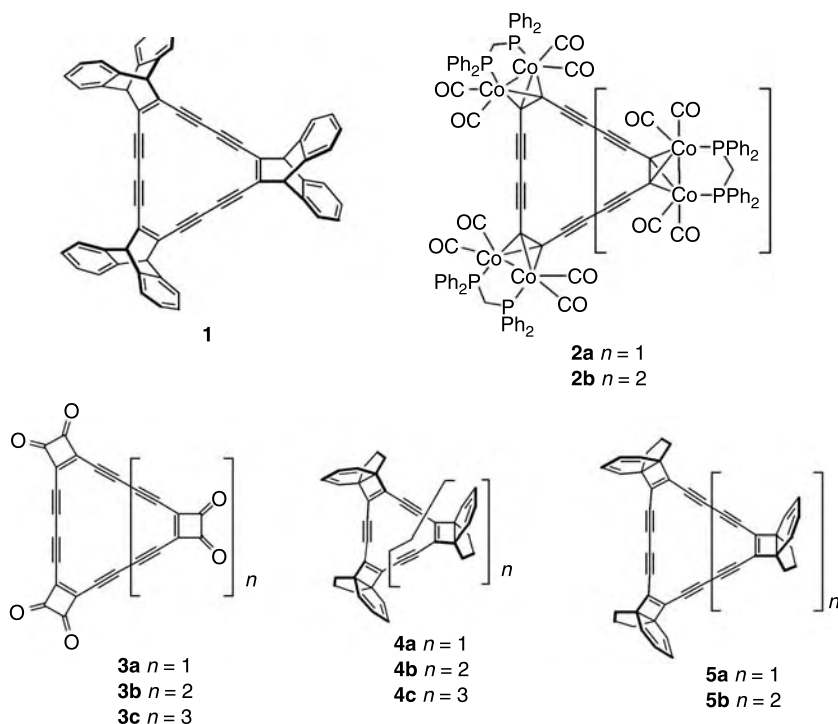


FIGURE 6.1 Organic precursors of monocyclic carbon clusters.

20, 24) resulting from the successive expulsion of the indane fragments was observed. The structures of the carbon cluster anions (C_{12}^- , C_{16}^- , C_{18}^- , C_{20}^- , and C_{24}^-) thus generated were investigated by UPS and were compared with those of the mass-selected anions generated by laser vaporization of graphite [6]. On the basis of the splitting frequencies due to vibrational excitation of the neutral cyclocarbons produced by detaching an electron from the corresponding anions, it was deduced that cyclo[n]carbons with $4m$ carbon atoms, i.e., C_{16} , C_{20} , and C_{24} , should possess a polyyne structure with alternating single and triple bonds, while cyclo[18]carbon bearing $4m + 2$ carbon atoms must have a cumulenic structure (see also Section 6.2.3).

The [2+1] fragmentation of the precursors shown in Figure 6.2 also provides a potential route to monocyclic carbon clusters. Thus cyclic dehydro oligomers of diethynyl[4.4.1]propellatetraenes **6a,b** incorporated in a fullerene structure have been prepared and their fragmentation was investigated by mass spectrometry [7]. MALDI TOF mass spectra of **6a,b** exhibited peaks due to the stepwise loss of the fullerene fragments, leading to the formation of mono-fullerene adducts of C_{15} and C_{20} . However, the

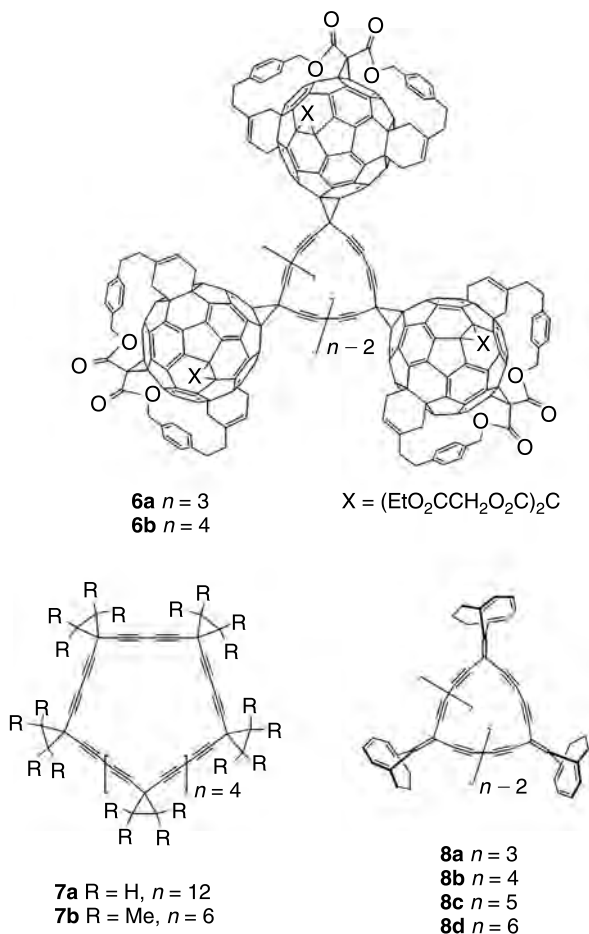


FIGURE 6.2 [2+1] type organic precursors of monocyclic carbon clusters.

observation of cyclocarbon was not achieved owing to the extensive fragmentation under strong laser power. Dehydro oligomers of 1,1-diethynylcyclopropane such as **7a,b** were also prepared by de Meijere et al., from which extrusion of tetramethylethylene or ethylene would form cyclo[5*m*]carbons [8]. However, it remains to be seen whether these form C_{30} and C_{60} , respectively, by fragmentation in the gas phase. Moreover, radialenes **8a–d** having bicyclo[4.3.1]deca-1,3,5-triene units were prepared which would produce cyclo[6*m*]carbons through the isomerization of the corresponding vinylidene intermediates generated by the loss of the indane fragments [9]. Indeed, the negative mode LD TOF mass spectra of **8a–d** exhibited the peaks due to the corresponding carbon anions (C_{18}^- , C_{24}^- , C_{30}^- , and C_{36}^-)

formed by the stepwise loss of the aromatic indane fragments. The carbon cluster anions were assumed to possess monocyclic structures in view of the results of the photolysis of acyclic model compounds.

6.2.3 CUMULENIC VS ACETYLENIC FORMS

Monocyclic carbon clusters are conceived as existing in various symmetrical forms. Concerning the lowest-energy structure, there has been a long-standing argument along with the theoretical calculations [16,28–35]. Also, in view of the spectroscopic characterization, considerations on the ground-state structure are crucial because the electronic and vibrational properties strongly depend on the molecular symmetry. Figure 6.3 shows possible structures of a planar monocycle in order to explain the symmetry lowering of the cluster by taking monocyclic C_{10} as an example. The totally symmetric structure with D_{10h} point-group symmetry (left) can be deformed into two possible D_{5h} structures; namely, cumulenenic (bottom) and acetylenic (top) forms. The angle alternation is introduced for the former while the bond-length alternation for the latter. A further lowering of symmetry leads to a structure with C_{5h} symmetry (right) when both the angle and bond-length alternations are adopted. To answer the question which structure is the lowest in energy is primarily the issue of its electronic configuration. The molecular orbital (MO) considerations provide basic ideas on the stability and structure of the monocycles.

The planer monocyclic carbon clusters have two distinct π -orbital systems as schematically shown in Figure 6.4; namely, in-plane π and out-of-plane π orbital systems. The former consists mostly of the carbon 2p orbitals within the plane of the ring and with substantial 2s characters that results in a bigger robe in the outer rim (see left panel in Figure 6.4), while the latter consists purely of the carbon 2p orbitals perpendicular to the plane of the ring (Figure 6.4, right). In the MO theory, the molecular orbitals are composed of linear combinations of these atomic orbitals (AOs) so as to minimize the total electronic energy of the molecule. Figure 6.5 depicts the

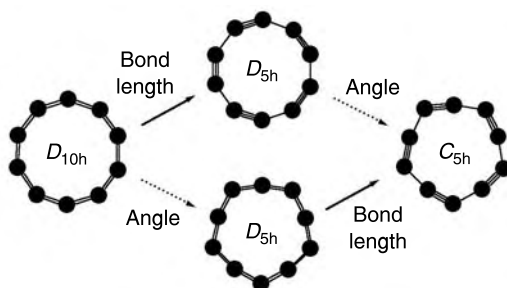


FIGURE 6.3 Symmetry lowering of the monocyclic carbon ring; C_{10} as an example.

patterns, that is, two non-degenerated levels at the bottom (A_1' in D_{5h} symmetry) and top (A_2') and four doubly degenerated levels (E_1' and E_2') in between. The left and right columns in Figure 6.5(a) represent the in-plane π and out-of-plane π orbital systems, respectively. Each of the π systems has similar level patterns to the occupied valence- σ system and 10 electrons are distributed for each. Note that in the cumulenic ground state the highest occupied out-of-plane π (E_2'') and in-plane π (E_2') levels are doubly degenerated.

For monocyclic C_{12} , the acetylenic structure with C_{6h} symmetry is turned out to be the lowest-energy form [33a]. In Figure 6.5(b), among the 48 valence electrons 24 electrons occupy the lowest 12 valence- σ orbitals. As a result of the bond-length alternation, *i.e.* the distortion into the acetylenic form, within the 12 σ -level patterns two levels in the middle split into two B_u levels and are no longer degenerated. The same splitting is seen for both the in-plane π and out-of-plane π orbital systems, giving split B_u levels for the former and split B_g levels for the latter. Owing to this relatively large splitting, the number of π electrons for the in-plane π and out-of-plane π systems are 12 for each and thus balanced. This energy-level splitting and the occupation with electrons of the split lower level render an additional stability that prefers the acetylenic form. Note that in the acetylenic ground state the highest occupied out-of-plane π (B_g) and in-plane π (B_u) levels are fully occupied but no longer degenerated.

The above MO considerations conclude that the monocyclic C_{10} prefers the cumulenic form while the monocyclic C_{12} the acetylenic form. This result can be basically extended to larger rings; namely, cumulenic forms for the series of C_{4m+2} rings and acetylenic forms for C_{4m} rings [32–34]. Concerning the latter series of C_{4m} rings, the tendency of the preferential bond-length alternation is associated with the splitting of energy levels in the middle of the σ - and π -electron systems. This is explained in terms of the first-order Jahn-Teller (FOJT) effect, where the system having half-filled degenerated energy levels is stabilized by the distortion to decouple the degeneracy [35a]. For monocyclic C_{20} as an example of the C_{4m} monocycles with C_{2mh} symmetry, the molecular orbital functions of the highest occupied MO (HOMO) and the lowest unoccupied MO (LUMO) for the in-plane π and out-of-plane π systems are representatively shown in Figure 6.6. Concomitantly with the introduction of the bond-length alternation, the amplitude of the wave function of the HOMO levels is localized on the triple bonds, whereas the LUMO has localized amplitudes on the single bonds.

As a result of the second-order effect, also large C_{4m+2} monocycles are expected to be acetylenic as is explained by the Peierls distortion that is seen in one-dimensional electronic systems with periodic potentials [35b–e]. This effect is associated with the distortion of the potential energy surface to lower the total energy of the system through electron–phonon coupling [35b]. For a molecular system, the same effect is also referred to as the second-order Jahn–Teller (SOJT) effect that leads to the vibrational-mode

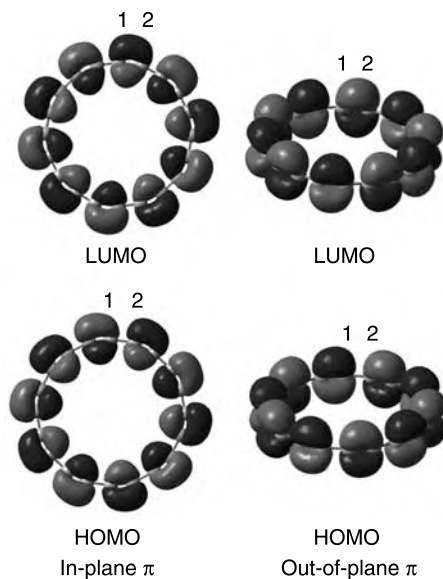


FIGURE 6.6 Molecular orbital (MO) functions of the highest-occupied MO (HOMO) and lowest-unoccupied MO (LUMO) levels in the in-plane π and out-of-plane π systems of monocyclic C_{20} , a member of the $4m$ carbon rings. In each panel, the bond between the atoms 1 and 2 corresponds to the single bond (longer bond) and the alternating bond lengths follow. The LUMO function has amplitudes on the single bonds while the HOMO function on the triple bonds.

softening towards the acetylenic structure [35c]. The schematic drawing in [Figure 6.7](#) represents the distortion of the potential energy surface of a monocyclic carbon ring along the normal coordinate that induces the acetylenic structure. Owing to the first- and second-order effects, the distortion is introduced to give the identical double minima corresponding to the acetylenic form. Depending on the degree of the electron correlation considered, the size of cyclic C_{4m+2} at which the cumulenic form changes into acetylenic one largely scatters from $m = 3$ to $m > 10$ [35].

6.2.4 PHOTOELECTRON SPECTROSCOPY

Ultraviolet photoelectron spectroscopy (UPS) of anionic C_n^- provides information on the electron affinity (EA), and electronic and vibrational structures of the corresponding neutral species. The size dependence of EAs and the vibrational fingerprints are useful to distinguish isomers when combined with mass spectrometry. In 1988 Yang et al. reported the first experimental indication of the presence of monocyclic carbon clusters C_n in laser vaporization of graphite in helium gas [17]. For clusters C_n

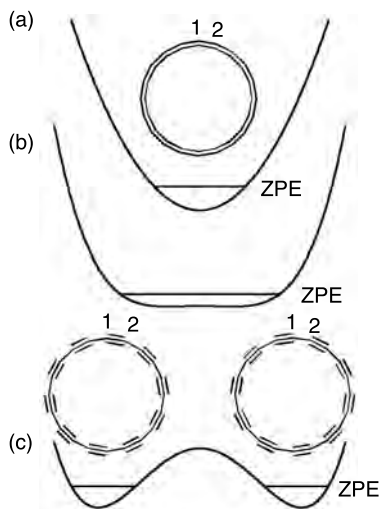


FIGURE 6.7 Schematic view of the potential energy surfaces showing the distortion from the single-well cumulenenic minimum (a), the wide minima of an averaged cumulenenic structure having a softened large-amplitude vibrational motion (b), to the double-well acetylenic minima (c). ZPE: the level of summed zero point energy of vibrational modes.

($10 \leq n \leq 29$), the authors found a series of EAs that is distinctly lower than the series for linear C_n ($n \leq 9$). They noticed also that there is a 4-fold resemblance in the spectral details for $n \geq 10$.

Handschuh et al. investigated the vibrational structures of carbon clusters C_n up to $n \sim 70$ by UPS and discussed the structural transition from linear, monocyclic, bicyclic, to fullerene-like cage structures as a function of the cluster size [36]. Using dehydroannulene derivatives having carbon ring size of $n = 12, 16, 18, 20$, and 24 , Wakabayashi and Tobe measured photoelectron spectra of C_n^- liberated from the precursors by laser ablation under vacuum [6]. In these experiments, the high-frequency vibrational progression ($> 2000 \text{ cm}^{-1}$) is observed for the clusters of $4m$ carbon atoms ($m = 5, 6$) as in the spectrum in Figure 6.8 [37].

For the assignment of the vibrational structure in the photoelectron spectrum of C_{20}^- in Figure 6.8, the electron distribution (square of the MO wave function) is considered for the LUMO level from which the electron is detached upon the UPS measurement. The LUMO of cyclic C_{20} (see the upper panels in Figure 6.6) has higher electron density on the single bonds that strengthens the single bonds to decrease the corresponding bond lengths in the anionic state. Upon the electron detachment, the single bonds are loosened to increase the bond lengths. This will induce the collective motions of the carbon nuclei that enhance the acetylenic form. Accordingly,

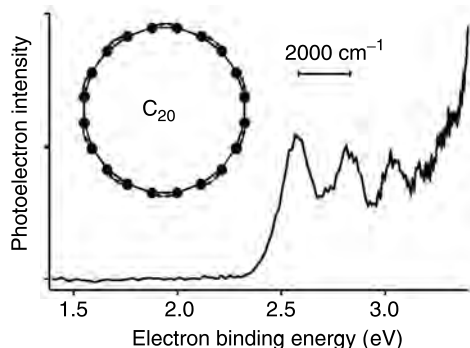


FIGURE 6.8 Photoelectron spectrum of C_{20}^- produced by laser vaporization of graphite in helium gas (spectrum reproduced from Reference 37). Inset: the totally symmetric tangential stretching mode of the acetylenic structure.

the vibration of the tangential stretching mode (see the inset in Figure 6.8) will be selectively excited. As a consequence, some vibrationally excited levels of the tangential stretching mode as well as the ground level must be populated as the final states of the electron detachment. Therefore, the assignment of the progression in the spectrum in Figure 6.8 to the tangential stretching mode of monocyclic C_{20} (the inset in Figure 6.8) is most likely. Furthermore, the calculated Franck–Condon factors with the excitation of the totally symmetric tangential stretching mode reproduce well the UPS spectra [38a]. In order to distinguish the isomers of C_{20} , Prinzbach et al. further examined several organic compounds having different carbon frameworks, including monocyclic, bowl-shaped, and cage isomers and clearly demonstrated that the fragmented anionic clusters C_n^- upon a discharge show distinct UPS spectra explainable by the simple liberation of the pure carbon skeleton [38b,39].

For the series of $4m+2$ carbon rings ($m=2-4$), the photoelectron spectra exhibit rather broad bands [6,36]. Since, in the anions, the occupation with an electron of the degenerated LUMO level may lead to the FOJT distortion to lower the molecular symmetry, the electron detachment process should accompany a deformation between the different symmetry structures leading to complex excitations of more than one vibrational mode. The anionic C_{10}^- is calculated to have C_{2v} symmetry while D_{5h} symmetry for the neutral, thereby “ $C_{2v} \rightarrow D_{5h}$ ” transition from the anion to the neutral species gives rise to a large Franck–Condon shift consistent with the observed UPS spectra [38c].

The anion photoelectron spectroscopy has demonstrated its advantageous features in many occasions of the first detection [17], the characterization of fragments [6,39], and the discussion on the structural evolution from monocyclic to polycyclic structures [36]. The detection efficiency of the

UPS measurements is so high that the spectrum is available for small amounts of the mass selected anions in the gas phase.

6.2.5 TOWARDS THE IR DETECTION OF CYCLIC C₁₀

There have appeared theoretical as well as experimental results suggestive of the stability and abundance of monocyclic C₁₀ in a molecular beam produced by laser vaporization of graphite [28–30,40,41]. A further experiment beyond mass spectroscopy and electronic spectroscopy will confirm the monocyclic nature and the bonding structure of C₁₀. Vibrational spectroscopy is useful for molecular structure determination if reliable theoretical prediction of the normal-mode frequencies and their intensities is available. Recent DFT methods have been recognized as such theoretical tools that provide harmonic frequencies comparable to the experimental data. Concerning the major stretching modes of linear carbon clusters of $n \leq 9$, agreement is found between the observed IR and calculated spectral patterns, although the discrepancy between the experimental and theoretical frequencies is not still satisfactorily small. For example, linear C₉ is detected by the fundamental transitions of the three IR-active stretching modes at 2080, 2014 [42] and 1601 cm⁻¹ [43], for which the DFT calculation provides harmonic frequencies at 2182, 2073, and 1624 cm⁻¹ [32], respectively (see Table 6.1).

TABLE 6.1

Comparison of selected IR-active stretching vibrational frequencies and intensities of linear C₉ and cyclic C₁₀

Molecule	Mode	DFT ^a		B3LYP / cc-pVDZ ^b		CCSD / 6-31G* ^c		Experiment	
		Freq. [†]	Int. [‡]	Freq. [†]	Int. [‡]	Freq. [†]	Int. [‡]	Freq. [†]	Int. [§]
Linear C ₉ (D _{8h})	$\nu_5\sigma_u$	2182	2324 (0.77)	2217	4077 (0.63)	2239	3675 (0.21)	2079.6736 ^d	0.108 ^d
	$\nu_6\sigma_u$	2073	3030 (1.0)	2132	6520 (1.0)	2132	17810 (1.0)	2014.2780 ^d	1.0 ^d
	$\nu_7\sigma_u$	1624	376.5 (0.12)	1670	394 (0.06)	1696	423 (0.02)	1601 ^e	—
Cyclic C ₁₀ (D _{5h})	e_1'	2024	332.1 (0.11)	2038	441 (0.07)	—	—	—	—
	e_1'	1045	105.4 (0.04)	1067	37 (<0.01)	—	—	—	—

[†]Frequency in cm⁻¹.

[‡]Calculated intensity in km/mol (relative intensity in parentheses).

[§]Experimental relative intensity.

BLYP density functional theory [32].

B3LYP/cc-pVDZ density functional theory [33a].

CCSD/6-31G* coupled-cluster method [33b].

Gas-phase high-resolution IR diode spectroscopy [42].

Matrix-isolation FTIR spectroscopy in solid Ar [43].

In order to pin down the frequency regions to be surveyed for the detection of unknown vibrational transitions of the cyclic species and to estimate the expected intensities, Table 6.1 compares the theoretical frequencies and intensities for linear C_9 and cyclic C_{10} and the experimental data for linear C_9 . Concerning the relative intensity of the two different IR-active modes of linear C_9 , the best agreement with the experimental data is seen for the coupled-cluster (CCSD) method [33b,42]. For cyclic C_{10} , calculated intensities are reported only at the DFT methods [32,33a]. Cyclic C_{10} is a rather compact molecule compared to linear C_9 , and thus generates relatively small variation of the electric dipole moment upon the vibrational excitation. Therefore, cyclic C_{10} may exhibit the IR absorption not as intensely as the linear C_9 does. If we compare the intensities from the DFT calculation in Table 6.1, the most intense IR mode of cyclic C_{10} shows the intensity only on the order of one tenth of the most intense IR mode of linear C_9 . This suggests that the detection of cyclic C_{10} requires ten times the amount of molecules than linear C_9 . In the matrix isolation experiment, many weak absorption lines remains unassigned and some of them may belong to the cyclic species (see also Chapter 1) [44]. The difficulty in the assignment of these peaks arises from the fact that the sample is a mixture of carbon clusters of various sizes. To avoid confusion in the assignment, a cluster source that generates a sufficient number of mass selected clusters is needed.

6.3 MULTICYCLIC POLYYNES

6.3.1 CLASS OF HYBRID sp - sp^2 CARBON NETWORKS

Besides linear and monocyclic carbon clusters, there exist increasing numbers of possible structures with increasing size of carbon clusters. These include multicyclic structures such as bicyclic, tricyclic polyyynes consisting of both sp and sp^2 carbons, graphitic and bowl-shaped structures consisting solely of sp^2 carbons, and cage-shaped clusters including fullerenes also constructed only by sp^2 carbons [17,19,20,22,34a]. In contrast to the extensive structural studies on linear carbon clusters and the steady progress for monocyclic carbon clusters, little has been done for the other structures except for the isolable fullerenes such as C_{60} and C_{70} . This is due to the limit of the spectroscopic methods to characterize the precise structures of relatively large but highly reactive species and the fact that several structurally and geometrically isomeric forms can coexist in most case. Therefore, the experimental characterizations of multicyclic polyyynes are limited to bi- and tricyclic polyyynes, which have been performed by means of the ion chromatography together with the theoretical ion mobility calculations. The structures of polyyynes with more than four macrocyclic polyyne units have not been characterized. In connection with the proposed mechanisms of fullerene

formation, however, some three-dimensional polycyclic polyynes were purposely generated from their respective organic precursors in the gas phase and were found to isomerize to the corresponding fullerenes with the same carbon numbers.

6.3.2 BICYCLIC AND TRICYCLIC POLYINES

Before discussing the structures of “bicyclic” and “tricyclic” polyynes, one trivial issue regarding the technical terms should be made clear in order not to mislead, because the usage of the terms in the literatures discussing these structures is different from the common organic nomenclature. For example, all of the structures **9–13** for C_{24} isomers shown in Figure 6.9 are named “bicyclic” in the literatures since they possess two macrocyclic rings [18]. However, **9** and **10** should be called “tricyclic” and **12** should be a “tetracyclic” structure by counting the number of the all rings present in the structures. Similarly, the “tricyclic” structures **14** and **15** (Figure 6.9) proposed for C_{36} isomers [19] should be regarded as “tetracyclic” and “pentacyclic”, respectively, according to the organic names. To avoid the confusion, however, this review adopts the literature definition: compounds **9–13** are all classified as “bicyclic” and **14** and **15** as “tricyclic”.

Bowers reported on the basis of the average arrival times of the mass-selected C_{20}^+ in the ion chromatography that the structure of the most abundant C_{20}^+ is monocyclic [18]. However, they observed a small amount of C_{20}^+ whose mobility matched those calculated for bicyclic structures such as **16** and **17** (Figure 6.9) incorporating both sp and sp^2 carbons. It should be pointed out that **16** possesses two ten-membered polyynic rings in accord

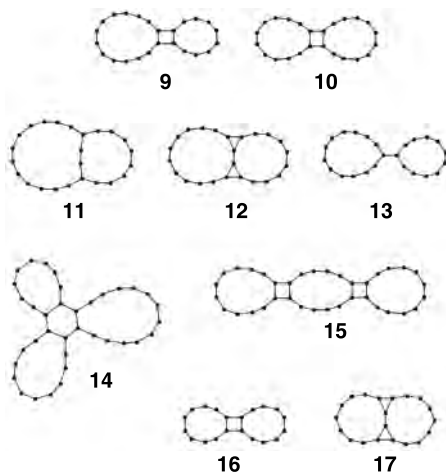


FIGURE 6.9 Bicyclic forms of C_{20} and C_{24} and tricyclic forms of C_{36} .

with the smallest carbon number of the monocyclic polyyynes. For C_{24}^+ , the amount of the bicyclic isomers relative to the monocyclic one increased substantially for which structures **9–13** with comparable energies were suggested. For negative ion C_{20}^- and C_{24}^- , negligible, or only a small distribution, of the bicyclic structures was detected due to the electron affinity difference for the different cluster isomers. No cup (bowl-shaped), cage (fullerene), or graphitic structures were observed for $C_{20}^{+/-}$ and $C_{24}^{+/-}$.

Bowers extended the ion chromatography experiments to unannealed carbon cluster cations up to 84 atoms and investigated the dependence of distribution of the isomeric structures on the number of carbon atoms [19,20]. The structures of the cluster cations were assigned on the basis of the comparison between the experimental and theoretical arrival time distributions (ATDs), the latter derived from the calculated mobilities of the individual isomers. It was found that the linear structures exist up to C_{10}^+ , while monocyclic rings begin to appear from C_7^+ and become dominant at C_{10}^+ . From C_{11}^+ to C_{20}^+ , the monocyclic forms exist as exclusive isomers. These structures then become less abundant as the number of carbon atoms increases, but they persist beyond C_{40}^+ . It is worth noting that C_{60}^+ having the monocyclic form does not exist at all [21]. Instead, bicyclic isomers like **9** and **10** (for C_{24}) begin to appear at C_{21}^+ and they become major component from C_{27}^+ up to around C_{35}^+ . From C_{30}^+ , tricyclic isomers like **14** and **15** (for C_{36}) begin to appear. At the same time, fullerene isomers with even number atoms also start to merge, which become the major component beyond C_{46}^+ . The population of odd numbered fullerenes, on the other hand, is small until C_{41}^+ , which increases rapidly at C_{47}^+ and C_{51}^+ and reaches 60–80% of the larger clusters. For cluster cations larger than C_{40}^+ , it was necessary to take tetracyclic isomers (structures not shown) into account in order to fit the theoretical ATDs of the multicyclic cluster cations to the experimental ones. Also, a fraction called “3D rings” starts to appear at C_{29}^+ and continues to be present in small abundance up to mid 40’s. The structures of the “3D rings” are tentatively assigned to propeller-shaped three-dimensional multicyclic isomers on the basis of the reasonable agreement of the ATDs. On the contrary, the possibility of cup or bowl-shaped isomers was excluded in view of the discrepancy of the ATDs. Also, planar graphitic isomers are excluded, mainly because no precursors of the graphitic structures were observed below C_{29}^+ and they do not account for the observed preference of odd numbered clusters of the “3D rings”. On the basis of the above data, coupled with the annealing studies, simple growth mechanism for carbon clusters was suggested. Thus, small linear clusters grow to form monocyclic rings starting from C_{10} . The reactions of monocyclic rings with linear clusters would result in larger monocyclic rings, while the reactions with other monocyclic rings would form multicyclic isomers such as bicyclic, tricyclic structures, and so on. Isomerization of multicyclic rings larger than C_{50} to fullerenes takes place readily, but to promote the

corresponding isomerization of smaller rings (around C_{36}) activation by collision to the buffer gas is necessary. Planar graphitic as well as bowl-shaped isomers are not observed, suggesting that these isomers are not involved in the carbon growth mechanism.

It was shown by collision-induced annealing experiments that relatively large, multicyclic carbon cluster cations with more than around 40 atoms were easily converted to fullerenes [21,22]. Annealing experiments were carried out by von Helden et al. for medium-sized cluster cations C_{30}^+ to C_{40}^+ , which were composed by a mixture of mono- and multicyclic isomers (bicyclic forms as the major component) [23]. It was revealed that, in contrast to the larger cluster cations, most of the multicyclic forms of C_{30}^+ to C_{34}^+ isomerized to the corresponding larger monocyclic forms of the same carbon numbers. However, the collision-induced fragmentation also took place by the loss of small fragments such as C_1 , C_2 or C_3 to form smaller cluster cations which were determined to possess fullerene structures on the basis of their ATDs. The ratio of fragmentation increases with increasing cluster size.

Shelimov et al. also performed detailed annealing study of medium-sized cluster cations, C_{24}^+ to C_{36}^+ , whose major components are bicyclic ring isomers, in order to investigate the rings-to-rings transformation [24]. These cations are also shown to isomerize to monocyclic forms with an activation energy of around 2.4 eV, which slightly decrease with increasing cluster size. With larger injection energies, fragmentation to small clusters took place as observed by von Helden et al. [23]. A model has been proposed based on the [2+2] and [4+2] cyclo-additions, as shown in Figure 6.10, which explains the formation of bicyclic isomers from two monocyclic forms (C_{20}) and its transformation into a larger monocyclic form (C_{40}). For the formation of bicyclic isomers, the [2+2] cycloaddition is assumed to be favorable because the positive charge would lower the inherently high activation energy of a symmetry-forbidden [2+2] cycloaddition. The [4+2] cycloaddition, on the

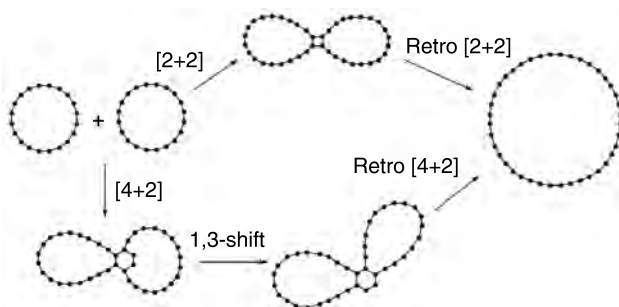


FIGURE 6.10 Possible [2+2] and [4+2] pathways for the transformation of monocyclic and bicyclic forms of carbon clusters (for C_{40}).

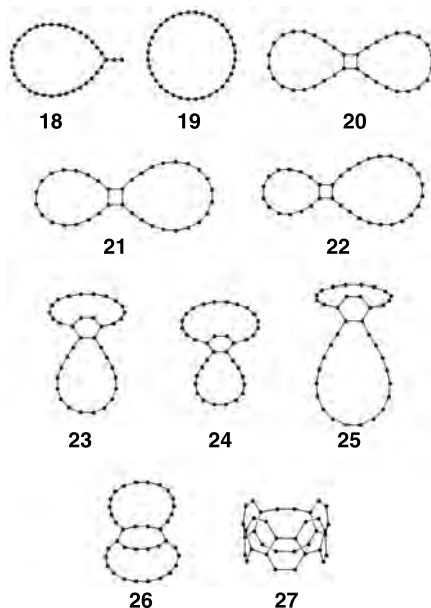


FIGURE 6.11 Monocyclic forms, planar bicyclic ([2+2]) forms, bent bicyclic ([4+2] and [6+4]) forms, and cylindrical carbon hoop of C_{36} .

other hand, would require substantial steric distortion in the transition state. Moreover, while the [2+2] dimer can undergo cycloreversion directly to form the corresponding larger monocyclic ring, conversion of the [4+2] dimer into the monocyclic ring would require two steps; a 1,3-shift followed by a [4+2] cyclo-reversion.

Strout et al. pointed out, on the basis of the theoretical calculations, that there exist other possible structures for the monocyclic as well as multicyclic ring isomers of carbon clusters [45]. For monocyclic isomers, those having a small branch such as **18** for C_{36} , would exhibit indistinguishable mobility and comparable energy with those of the monocyclic ring **19** without any branch (Figure 6.11). For [2+2] bicyclic isomers, unsymmetrical structures such as **21** ($C_{16}+C_{20}$) and **22** ($C_{14}+C_{22}$) would exhibit similar mobilities and energies with those of symmetrical isomer **20** ($C_{18}+C_{18}$). Most importantly, the authors suggested that the bent, three-dimensional structures such as **23** ($C_{18}+C_{18}$), **24** ($C_{16}+C_{20}$), and **25** ($C_{20}+C_{16}$) formed by [4+2] cycloaddition are more probable candidates for the tricyclic ring isomers rather than the planar structures such as **14** and **15** proposed by von Helden et al., because the [4+2] isomers are mechanistically more conceivable and energetically comparable to the planar isomers. They also considered the possibility of [6+4] cycloadducts such as **26** ($C_{18}+C_{18}$) for the candidates of tricyclic ring

isomers [46]. Because of the bent structures of the [4+2] and [6+4] adducts, it is suggested that sequential cycloaddition between the closely located polyyne rings would result in the formation of a cylindrical structure such as **27** called a carbon “hoop”. Possible pathways of bond reorganization from hoops to fullerene cages are also predicted.

The distributions of the carbon cluster anions are considerably different from those of the corresponding cations though the structure types of both ions are identical [47]. Namely, linear clusters persist up to C_{30}^- even though their abundance drops from C_{10}^- . More remarkably, planar ring isomers, including monocyclic and multicyclic ring isomers, become major components, starting from C_{10}^- and continue to present most abundantly even beyond C_{60}^- . The fullerene structures comprise only 20% of the isomers even around C_{60}^- . Among the planar rings, monocyclic rings are major components from C_{10}^- up to around C_{40}^- , where bicyclic rings start to take the first place. Tricyclic forms begin to appear at C_{30}^- and gradually increase up to C_{40}^- . The observed difference between the isomer distribution of cations and that of anions are attributed to the difference between the electron affinities of different isomeric cluster ions. Annealing the monocyclic anions of C_{10}^- to C_{13}^- by injecting them into the ion chromatography cell with a high voltage resulted in the exclusive transformation into the corresponding linear form. Above C_{15}^- , however, monocyclic forms start to predominate and annealing of C_{20}^- to C_{30}^- results in the complete conversion of bicyclic rings into monocyclic forms.

6.4 THREE-DIMENSIONAL POLYCYCLIC POLYYNES

6.4.1 MACROCYCLIC POLYYNES TO SIZE-SELECTIVE FULLERENE FORMATION

In contrast to the monocyclic, bicyclic, and tricyclic forms of carbon clusters, none of the structures of polycyclic polyynes has thus far been characterized. However, substantial interest has been focused on such species in connection with their relevance to the fullerene formation. Namely, in addition to the study by Strout and Scuseria described above [46], a number of formation mechanisms of fullerenes have been proposed which include cyclic polyynes as the key intermediates [48]. For example, in view of the abundance of monocyclic polyynes in the size regime of C_{10} – C_{20} , Wakabayashi and Achiba proposed the ring-stacking model assuming a sequential stacking of monocyclic polyyne rings of appropriate ring size [49]. Moreover, on the basis of the results of the collision-induced fragmentation of carbon cluster cations, using the ion chromatography as described in the previous section, Hunter et al. proposed a mechanism for C_{60} fullerene formation, which includes the ring formation by “zipping up” of the spiraling polyyne chains [22d]. It should be pointed out that they also predicted

that similar polyyne cyclization of appropriate precursors would form larger fullerenes such as C_{70} and C_{76} as well through similar pathways [22d]. Polycyclic polyynes may therefore be regarded as viable precursors for the size-selective and even geometry-selective construction of the desired fullerene structure. Besides the annealing experiments of carbon cluster ion generated by vaporization of graphite and their structural elucidation based on the ion chromatography, the crucial role of monocyclic carbon clusters in the formation mechanism of fullerenes has been supported experimentally by their selective formation from organic precursor molecules. Thus McElvany et al. first observed the size-selective formation of fullerene C_{60}^+ by the gas phase coalescence of the cyclic polyyne C_{30}^+ , which was produced size-selectively from its well-defined organic precursor [4c].

In view of this circumstantial evidence for the polyyne route to fullerenes, the groups led by Rubin and Tobe developed, independently, an approach to C_{60} from well-defined, three-dimensional (3D) polyyne precursors $C_{60}H_6$ and $C_{60}Cl_6$, which were generated from the corresponding organic precursors by expulsion of stable fragments such as carbon monoxide [50] or indane [51] by laser irradiation. As an initial step, Rubin prepared $C_{60}H_{18}$ (**28**) shown in Figure 6.12 which was composed of two benzene rings and three C_{16} enyne bridges [52]. In the MALDI mass spectrum (negative mode) of **28**, partial dehydrogenation down to $C_{60}H_{14}^-$ was observed, suggesting the possibility of complete dehydrogenation from more unsaturated precursors to C_{60} . The desired precursor $C_{60}H_6$ (**29a**) having three C_{16} polyyne chains was deemed too reactive for isolation in view of the previous studies on the synthesis of linear polyynes. Thus Rubin utilized the decarboxylation of cyclophane **30** possessing cyclobutenedione units to generate **29a** [50]. As expected, in the negative mode ICR LD mass spectrum of **30**, not only $C_{60}H_6^-$ but also a strong peak due to C_{60}^- was observed, suggesting that cyclization of the polyyne chain took place efficiently accompanied by dehydrogenation to form the fullerene cage. On the other hand, Tobe and Wakabayashi observed, in the positive mode LD TOF mass spectrum of [4.3.2]propellatriene-containing precursor **31a**, a peak due to C_{60}^+ formed by the loss of eight indane fragments and six hydrogen atoms from **31a** [51]. The negative mode LD TOF mass spectrum of **31a** showed, in contrast to the positive mode spectrum, the peak due to $C_{60}H_6^-$ formed by the loss of all indane units. The mass spectrum also showed the small peak due to C_{60} anion formed by spontaneous dehydrogenation of all hydrogen atoms from $C_{60}H_6^-$. Moreover, hexachloro derivative **31b** exhibited in the positive mode LD TOF mass spectrum a very strong peak of C_{60}^+ besides weak peaks, due to the C_2 loss and those up to C_{120}^+ which might be formed by an ion-molecule reaction of C_{60} and the subsequent fragmentation of the dimeric cluster ion. The formation of C_{60}^+ is facilitated by the electron capture by the chlorine atoms, as supported by the observation of a strong peak of Cl^- in the negative mode spectrum. The negative mode LD TOF mass spectrum of **31b** also exhibited the peak due to $C_{60}Cl_6^-$ (**29b** $^-$) from which stepwise

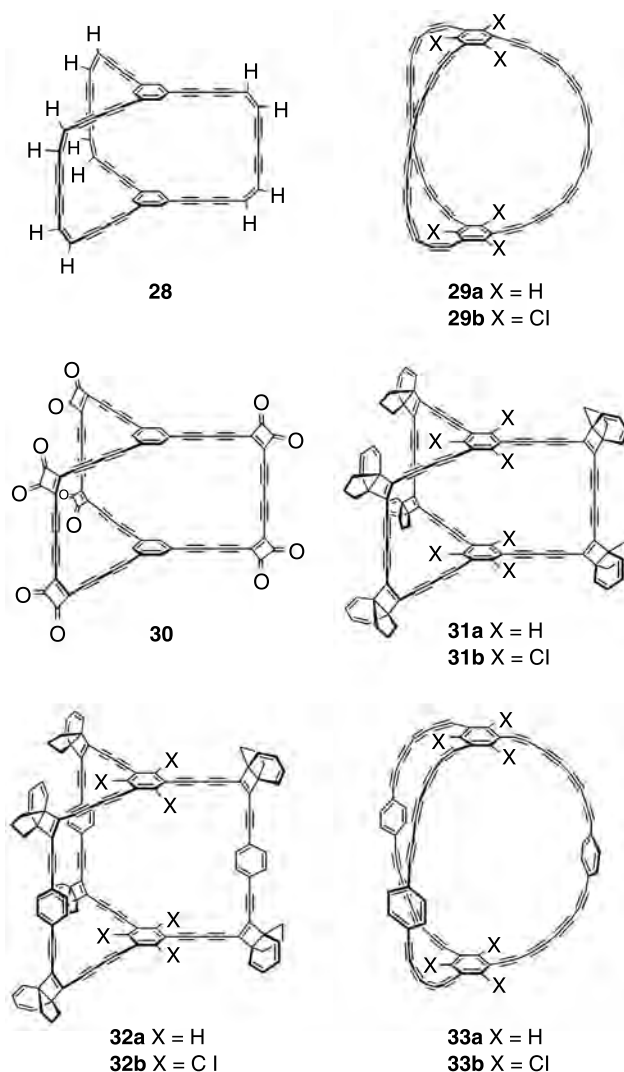


FIGURE 6.12 3D polyynes serving as organic precursors of C_{60} and C_{78} .

loss of chlorine atoms was observed, leading ultimately to C_{60}^- . The preparative scale synthesis of C_{60} has not been achieved yet by this route, although Scott et al. recently succeeded in the synthesis of C_{60} by high-temperature pyrolysis of a polycyclic aromatic chlorohydrocarbon [53].

However, Tobe has shown that the polyynes route can be extended to the size-selective formation of a large fullerene C_{78} [54]. Regarding large fullerenes, it has been well known that the number of possible geometrical isomers

increases dramatically with increasing number of the constituent carbon atoms [55]. Therefore, it would be extremely interesting to see if geometry-selective synthesis is possible under kinetically controlled conditions based on an organic synthesis method. As an initial step toward this goal, in order to produce C_{78} fullerene in a size-selective manner, three-dimensional cyclophanes **32a** and **32b** having the [4.3.2]propellane units were prepared as precursors of polyyynes **33a** and **33b**, respectively. In the negative mode LD TOF mass spectrum of **32a**, an intense peak due to $C_{78}H_{18}^-$ (**33a** $^-$) formed by expulsion of all indane units was observed. However, only partial dehydrogenation down to $C_{78}H_{14}^-$ took place, just as in the case of $C_{60}H_{18}$ (**28**). On the other hand, in the case of hexachloro derivative **32b**, fragmentation of $C_{78}H_{12}Cl_6^-$ (**33b** $^-$) formed by the loss of all indane fragments from **32b** took place to release hydrogen and chlorine atoms simultaneously, leading to the formation of C_{78}^- together with some $C_{78}H_2^-$ and $C_{78}H_4^-$, in which a few hydrogen atoms remained intact. Although the structure of the C_{78} ion remains to be established, the observed C_2 losses from C_{78}^- down to C_{70}^- are the strong indication of its fullerene structure.

6.5 CONCLUSIONS

A new class of strain and bent polyyynes has become accessible by the generation of molecular cyclic polyyynes through decomposition of structurally well-defined organic precursors, as well as by the laser vaporization of graphite. This has opened new aspects in relation to the hybrid $sp-sp^2-sp^3$ network systems or polymeric carbynoid structures. The molecules of interest spanning from two-dimensional monocyclic, bicyclic, tricyclic, polycyclic rings, to three-dimensional macrocyclic polyyynes, provide a chance of new challenges for further research on generation, characterization, and reactions of the relatively large polyyynes.

ACKNOWLEDGMENT

This work was supported by CREST, Japan Science and Technology Agency (JST).

REFERENCES

- [1] For reviews: (a) Diederich, F. Oligoacetylenes. In: *Modern Acetylene Chemistry*, Stang, P.J.; Diederich, F., Eds. VCH: Weinheim, 1995; 443–471. (b) Diederich, F.; Rubin, Y. Synthetic approaches toward molecular and polymeric carbon allotropes. *Angew. Chem., Int. Ed. Engl.* **1992**, 31(9), 1101–1123. (c) Diederich, F.; Gobbi, L. Cyclic and linear acetylenic molecular scaffolding.

- Top. Curr. Chem.* **1999**, 201, 43–79. (d) Bunz, U.H.F.; Rubin, Y.; Tobe Y. Polyethynylated cyclic π -systems: scaffolds for novel two and three-dimensional carbon networks. *Chem. Soc. Rev.* **1999**, 28(2), 107–119. (e) Tobe, Y. All-carbon molecules from small-ring propellanes. In: *Advances in Strained and Interesting Organic Molecules*. Halton, B., Ed., JAI Press: Stamford, 1999; Vol. 7, 153–184. (f) Tobe, Y.; Wakabayashi, T. Carbon-rich compounds: acetylene-based carbon allotropes. In: *Acetylene Chemistry: Chemistry, Biology and Material Science*. Stang, P.J.; Diederich, F.; Tykwinski, R., Eds. VCH: Weinheim, 2005; 387–426.
- [2] (a) Diederich, F.; Rubin, Y.; Knobler, C.B.; Whetten, R.L.; Schriver, K.; Houk, K.N.; Li, Y. All-carbon molecules: evidence for the generation of cyclo[18]carbon from a stable organic precursor. *Science* **1989**, 245, 1088–1090. (b) Diederich, F.; Rubin, Y.; Chapman, O.L.; Goroff, N.S. Synthetic routes to the cyclo[n]carbons. *Helv. Chim. Acta* **1994**, 77(5), 1441–1457.
- [3] Rubin, Y.; Knobler, C.B.; Diederich, F. Synthesis and crystal structure of a stable hexacobalt complex of cyclo[18]carbon. *J. Am. Chem. Soc.* **1990**, 112(12), 4966–4968.
- [4] (a) Rubin, Y.; Knobler, C.B.; Diederich, F. Precursors to the cyclo[n]carbons: from 3,4-dialkynyl-3-cyclobutene-1,2-diones and 3,4-dialkynyl-3-cyclobutene-1,2-diols to cyclobutenodehydroannulenes and higher oxides of carbon. *J. Am. Chem. Soc.* **1990**, 112(4), 1607–1617. (b) Rubin, Y.; Kahr, M.; Knobler, C.B.; Diederich, F.; Wilkins, C.L. The higher oxides of carbon $C_{8n}O_{2n}$ ($n=3-5$): synthesis, characterization, and x-ray crystal structure. Formation of cyclo[n]carbon ions C_n^+ ($n=18, 24$), C_n^- ($n=18, 24, 30$), and higher carbon ions including C_{60}^+ in laser desorption Fourier transform mass spectrometric experiments. *J. Am. Chem. Soc.* **1991**, 113(2), 495–500. (c) McElvany, S.W.; Ross, M.M.; Goroff, N.S.; Diederich, F. Cyclocarbon coalescence: mechanisms for tailor-made fullerene formation. *Science* **1993**, 259, 1594–1596.
- [5] (a) Tobe, Y.; Fujii, T.; Matsumoto, H.; Naemura, K.; Achiba, Y.; Wakabayashi, T. A new entry into cyclo[n]carbons: [2+2] cycloreversion of propellane-annelated dehydroannulenes. *J. Am. Chem. Soc.* **1996**, 118(11), 2758–2759. (b) Tobe, Y.; Matsumoto, H.; Naemura, K.; Achiba, Y.; Wakabayashi, T. Generation of cyclocarbons with $4n$ carbon atoms (C_{12} , C_{16} , and C_{20}) by [2+2] cycloreversion of propellane-annelated dehydroannulenes. *Angew. Chem., Int. Ed. Engl.* **1996**, 36(16), 1800–1802. (c) Tobe, Y.; Fujii, T.; Matsumoto, H.; Tsumuraya, K.; Noguchi, D.; Nakagawa, N.; Sonoda, M.; Naemura, K.; Achiba, Y.; Wakabayashi, T. [2+2] Cycloreversion of [4.3.2]propella-1,3,11-trienes: an approach to cyclo[n]carbons from propellane-annelated dehydro[n]annulenes. *J. Am. Chem. Soc.* **2000**, 122(8), 1762–1775.
- [6] Wakabayashi, T.; Kohno, M.; Achiba, Y.; Shiromaru, H.; Momose, T.; Shida, T.; Naemura, K.; Tobe, Y. Photoelectron spectroscopy of C_n^- produced from laser ablated dehydroannulene derivatives having carbon ring size of $n=12, 16, 18, 20$, and 24 . *J. Chem. Phys.* **1997**, 107(13), 4783–4787.
- [7] (a) Isaacs, L.; Seiler, P.; Diederich, F. Solubilized derivatives of C_{195} and C_{260} : the first members of a new class of carbon allotropes $C_{n(60+5)}$. *Angew. Chem., Int. Ed. Engl.* **1995**, 34(13/14), 1466–1469. (b) Isaacs, L.; Diederich, F.; Haldimann, R.F. Multiple adducts of C_{60} by tether-directed remote functionalization and synthesis of soluble derivatives of new carbon allotropes $C_{n(60+5)}$. *Helv. Chim. Acta* **1997**, 80(2), 317–342.

- [8] (a) de Meijere, A.; Kozhushkov, S.I. Macrocyclic structurally homoconjugated oligoacetylenes: acetylene- and diacetylene-expanded cycloalkanes and rotanes. *Top. Curr. Chem.* **1999**, *201*, 1–42. (b) de Meijere, A.; Kozhushkov, S.I. Completely spirocyclopropanated macrocyclic oligodiacetylenes and their permethylated analogues: preparation and properties. *Chem. Eur. J.* **2002**, *8*(14), 3195–3202.
- [9] (a) Tobe, Y.; Iwasa, N.; Umeda, R.; Sonoda, M. Vinylidene to alkyne rearrangement to form polyyne: synthesis and photolysis of dialkynylmethylene-bicyclo[4.3.1]deca-1,3,5-triene derivatives. *Tetrahedron Lett.* **2001**, *42*(31), 5485–5488. (b) Tobe, Y.; Umeda, R.; Iwasa, N.; Sonoda, M. Expanded radialenes with bicyclo[4.3.1]decatriene units: new precursors to cyclo[n]carbons. *Chem. Eur. J.* **2003**, *9*(22), 5549–5559.
- [10] Douglas, A.E. *Nature (London)* **1977**, *269*, 130–131.
- [11] Kroto H.W.; Heath, J.R.; O'Brien, S.C.; Curl, R.F.; Smalley, R.E. *Nature (London)* **1985**, *318*, 162–163.
- [12] Krätschmer, W.; Fostiropoulos, K.; Huffman, D. *Nature (London)* **1990**, *347*, 354–358.
- [13] Iijima, S. *Nature (London)* **1991**, *354*, 56–58.
- [14] Pitzer, K.S.; Clementi, E. Large molecules in carbon vapor. *J. Am. Chem. Soc.* **1959**, *81*(17), 4477–4485.
- [15] Hoffman, R. *Tetrahedron* **1966**, *22*(2), 521–538.
- [16] (a) Raghavachari, K.; Binkley, J.S. Structure, stability, and fragmentation of small carbon clusters. *J. Chem. Phys.* **1987**, *87*(4), 2191–2197. (b) Raghavachari, K. Theoretical studies on carbon and silicon clusters: comparison of the structures and stabilities of neutral and ionic forms. *Z. Phys. D* **1989**, *12*, 61–64.
- [17] Yang, S.; Taylor, K.J.; Craycraft, M.J.; Conceicao, J.; Pettiette, C.L.; Cheshnovski, O.; Smalley, R.E. UPS of 2–30-atom carbon clusters: chains and rings. *Chem. Phys. Lett.* **1988**, *144*(5,6), 431–436.
- [18] von Helden, G.; Hsu, M.T.; Gott, N.G.; Kemper, P.R.; Bowers, M.T. Do small fullerenes exist only on the computer? Experimental results on $C_{20}^{+/-}$ and $C_{24}^{+/-}$. *Chem. Phys. Lett.* **1993**, *204*(1–2), 15–22.
- [19] von Helden, G.; Hsu, M.T.; Gott, N.G.; Bowers, M.T. Carbon cluster cations with up to 84 atoms: structures, formation mechanism, and reactivity. *J. Phys. Chem.* **1993**, *97*(31), 8182–8192.
- [20] von Helden, G.; Hsu, M.T.; Kemper, P.R.; Bowers, M.T. Structures of carbon cluster ions from 3 to 60 atoms: linear to rings to fullerenes. *J. Chem. Phys.* **1991**, *95*(5), 3835–3837.
- [21] Hunter, J.; Fye, J.; Jarrold, M.F. Annealing C_{60}^{+} : synthesis of fullerenes and large carbon rings. *Science* **1993**, *260*, 784–786.
- [22] (a) von Helden, G.; Gotts, N.G.; Bowers, M.T. Experimental evidence for the formation of fullerenes by collisional heating of carbon rings in the gas phase. *Nature (London)* **1993**, *363*, 60–63. (b) Hunter, J.; Fye, J.; Jarrold, M.F. Carbon rings. *J. Phys. Chem.* **1993**, *97*(14), 3460–3462. (c) Hunter, J.; Fye, J.; Jarrold, M.F. Annealing and dissociation of carbon rings. *J. Chem. Phys.* **1993**, *99*(3), 1785–1795. (d) Hunter, J.; Fye, J.; Roskamp, E.J.; Jarrold, M.F. Annealing carbon cluster ions: a mechanism for fullerene synthesis. *J. Phys. Chem.* **1994**, *98*(7), 1810–1818.

- [23] von Helden, G.; Gotts, N.G.; Bowers, M.T. Annealing of carbon cluster cations: rings to rings and rings to fullerenes. *J. Am. Chem. Soc.* **1993**, *115*(10), 4363–4364.
- [24] Shelimov, K.B.; Hunter, J.M.; Jarrold, M.F. Small carbon rings: dissociation, isomerization, and a simple model based on strain. *Int. J. Mass Spectrom. Ion Processes* **1994**, *138*, 17–31.
- [25] (a) Presilla-Marquez, J.D.; Sheehy, J.A.; Mills, J.D.; Carrick, P.G.; Larson, C.W. Vibrational spectra of cyclic C_6 in solid argon. *Chem. Phys. Lett.* **1997**, *274*(5–6), 439–444. (b) Presilla-Marquez, J.D.; Harper, J.; Sheehy, J.A.; Carrick, P.G.; Larson, C.W. Vibrational spectra of cyclic C_8 in solid argon. *Chem. Phys. Lett.* **1999**, *300*(5–6), 719–726.
- [26] (a) Wang, S.L.; Rittby, C.M.L.; Graham, W.R.M. Detection of cyclic carbon clusters. I. isotopic study of the $\nu_4(e')$ mode of cyclic C_6 in solid Ar. *J. Chem. Phys.* **1997**, *107*(16), 6032–6037. (b) Wang, S.L.; Rittby, C.M.L.; Graham, W.R.M. Detection of cyclic carbon clusters. II. isotopic study of the $\nu_{12}(e_u)$ mode of cyclic C_8 in solid Ar. *J. Chem. Phys.* **1997**, *107*(18), 7025–7033. (c) Wang, S.L.; Rittby, C.M.L.; Graham, W.R.M. On the identification of the vibrational spectrum of cyclic C_8 in solid Ar. *J. Chem. Phys.* **2000**, *112*(3), 1457–1461.
- [27] Grutter, M.; Wyss, M.; Riaplov, E.; Maier, J.P.; Peyerimhoff, S.D.; Hanrath, M. Electronic absorption spectra of linear C_6 , C_8 and cyclic C_{10} and C_{12} in neon matrices. *J. Chem. Phys.* **1999**, *111*(16), 7397–7401.
- [28] Liang, C.; Schaefer, H.F., III. Carbon clusters: The structure of C_{10} studied with configuration interaction methods. *J. Chem. Phys.* **1990**, *93*(12), 8844–8849.
- [29] Andreoni, W.; Scharf, D.; Giannozzi, P. Low-temperature structures of C_4 and C_{10} from the Car-Parrinello method: singlet states. *Chem. Phys. Lett.* **1990**, *173*(5,6), 449–455.
- [30] Watts, J.D.; Bartlett, R.J. The nature of monocyclic C_{10} . A theoretical investigation using coupled-cluster methods. *Chem. Phys. Lett.* **1992**, *190*(1,2), 19–24.
- [31] Grossman, J.C.; Mitas, L.; Raghavachari, K. Structure and stability of molecular carbon: importance of electron correlation. *Phys. Rev. Lett.* **1995**, *75*(21), 3870–3873.
- [32] Hutter, J.; Lüthi, H.P.; Diederich, F. Structures and vibrational frequencies of the carbon molecules C_2 – C_{18} calculated by density functional theory. *J. Am. Chem. Soc.* **1994**, *116*(2), 750–756.
- [33] (a) Martin, J.M.L.; El-Yazal, J.; Francois, J.P. Structure and vibrational spectra of carbon clusters C_n ($n=2$ –10, 12, 14, 16, 18) using density functional theory including exact exchange contributions. *Chem. Phys. Lett.* **1995**, *242*(6), 570–579. (b) Martin, J.M.L.; Taylor, P.R. Structure and vibrations of small carbon clusters from coupled-cluster calculations. *J. Phys. Chem.* **1996**, *100*(15), 6047–6056.
- [34] (a) Jones, R.O.; Seifert, G. Structure and bonding in carbon clusters C_{14} to C_{24} : chains, rings, bowls, plates, and cages. *Phys. Rev. Lett.* **1997**, *79*(3), 443–446. (b) Jones, R.O. Density functional study of carbon clusters C_{2n} ($2 \leq n \leq 16$). I. Structure and bonding in the neutral clusters. *J. Chem. Phys.* **1999**, *110*(11), 5189–5200.

- [35] (a) Bylaska, E.J.; Weare, J.H.; Kawai, R. Development of bond-length alternation in very large carbon rings: LDA pseudopotential results. *Phys. Rev. B* **1998**, 58(12), R7488–R7491. (b) Bylaska, E.J.; Kawai, R.; Weare, J.H. From small to large behavior: The transition from the aromatic to the Peierls regime in carbon rings. *J. Chem. Phys.* **2000**, 113(15), 6096–6106. (c) Saito, M.; Okamoto, Y. Second-order Jahn–Teller effect on carbon $4N+2$ member ring clusters. *Phys. Rev. B* **1999**, 60(12), 8939–8942. (d) Torelli, T.; Mitas, L. Electron correlation in C_{4N+2} carbon rings: Aromatic versus dimerized structures. *Phys. Rev. Lett.* **2000**, 85(8), 1702–1705. (e) Livioti, E.; Ubertaini, F.; Erdős, P. Bond configuration in the Peierls–Hubberd model of small ring-shaped molecules. *J. Chem. Phys.* **2000**, 111(6), 2392–2400.
- [36] Handschuh, H.; Ganteför, G.; Kessler, B.; Bechthold, P.S.; Eberhardt, W. Stable configurations of carbon clusters: chains, rings, and fullerenes. *Phys. Rev. Lett.* **1995**, 74(7), 1095–1098.
- [37] Kohno, M. Photoelectron spectroscopy of carbon clusters and metal/carbon binary clusters. Dissertation for Dr. Sci. Tokyo Metropolitan University 1997, p. 108.
- [38] (a) Saito, M.; Sugino, O. Vibrational fine structures in photoelectron spectra of carbon ring clusters. *Phys. Rev. B* **2000**, 61(19), 12674–12677. (b) Saito, M.; Miyamoto, Y. Theoretical identification of the smallest fullerene, C_{20} . *Phys. Rev. Lett.* **2001**, 87(3), 035503-1-4. (c) Saito, M.; Sugino, O. Anomalous temperature effect on the broad asymmetric Franck–Condon photoelectron spectrum of the C_{10}^- monocyclic ring cluster. *Phys. Rev. A* **2001**, 63(5), 053201-1-5.
- [39] Prinzbach, H.; Weiler, A.; Landenberger, P.; Wahl, F.; Wörth, J.; Scott, L.T.; Gelmont, M.; Olevano, D.; V. Issendorf, B. Gas-phase production and photoelectron spectroscopy of the smallest fullerene, C_{20} . *Nature (London)* **2000**, 407, 60–63.
- [40] (a) Kaizu, K.; Kohno, M.; Suzuki, S.; Shiromaru, H.; Moriwaki, T.; Achiba, Y. Neutral carbon clusters distribution upon laser vaporization. *J. Chem. Phys.* **1997**, 106(23), 9954–9956. (b) Ohara, M.; Suwa, M.; Ishigaki, T.; Shiromaru, H.; Achiba, Y.; Krätschmer, W. Resonance-enhanced multiphoton electron detachment (REMPED) spectra of C_{10}^- and C_{11}^- . *J. Chem. Phys.* **1998**, 109(4), 1329–1333.
- [41] (a) Wakabayashi, T.; Momose, T.; Shida, T.; Shiromaru, H.; Ohara, M.; Achiba, Y. Preferential formation of C_{10}^- upon tandem irradiation of graphite with IR and UV laser pulses. *J. Chem. Phys.* **1997**, 107(4), 1152–1155. (b) Wakabayashi, T.; Momose, T.; Shida, T. Mass spectroscopic studies of laser ablated carbon clusters as studied by photoionization with 10.5 eV photons under vacuum. *J. Chem. Phys.* **1999**, 111(14), 6260–6263. (c) Kato, Y.; Wakabayashi, T.; Momose, T. Preferential formation of neutral C_{10} upon laser vaporized in He gas as studied by photoionization mass spectroscopy with 10.5 eV photons. *J. Chem. Phys.* **2003**, 118(12), 5390–5394. (d) Kato, Y.; Wakabayashi, T.; Momose, T. A mass spectroscopic study of laser vaporized graphite in H_2 and D_2 gases: the stability of $C_{2n}H_2$ ($n=2-5$) and C_{10} . *Chem. Phys. Lett.* **2004**, 386(4–6), 279–285.
- [42] Van Orden, A.; Provencal, R.A.; Keutsch, F.N.; Saykally, R.J. Infrared laser spectroscopy of jet-cooled carbon clusters: The ν_5 band of linear C_9 . *J. Chem. Phys.* **1996**, 105(15), 6111–6116.

- [43] Kranze, R.H.; Withey, P.A.; Rittby, C.M.L.; Graham, W.R.M. Fourier transform infrared observation of the ν_7 stretching mode of linear C_9 in Ar at 10 K. *J. Chem. Phys.* **1995**, *103*(16), 6841–6850.
- [44] Cermak, I.; Monninger, G.; Krätschmer, W. Absorption spectra of matrix-isolated small carbon molecules. *Advances in Molecular Structure Research* **1997**, *3*, 117–146.
- [45] Strout, D.L.; Book, L.D.; Millan, J.M.; Xy, C.; Scuseria, G.E. How unequivocally do ion chromatography experiments determine carbon cluster geometries? *J. Phys. Chem.* **1994**, *98*(35), 8622–8626.
- [46] Strout, D.L.; Scuseria, G.E. A cycloaddition model for fullerene formation. *J. Phys. Chem.* **1996**, *100*(16), 6492–6498.
- [47] (a) von Helden, G.; Kemper, P.R.; Gotts, N.G.; Bowers, M.T. Isomers of small carbon cluster anions: linear chains with up to 20 atoms. *Science* **1993**, *259*, 1300–1302. (b) Gotts, N.G.; von Helden, G.; Bowers, M.T. Carbon cluster anions: structure and growth from C_5^- to C_{62}^- . *Int. J. Mass Spectrom. Ion Processes* **1995**, *149/150*, 217–229.
- [48] (a) Schwarz, H. The mechanism of fullerene formation. *Angew. Chem. Int. Ed. Engl.* **1993**, *32*(10), 1412–1415. (b) Goroff, N.S. Mechanism of fullerene formation. *Acc. Chem. Res.* **1996**, *29*(2), 77–83.
- [49] Wakabayashi, T.; Achiba, Y. A model for the C_{60} and C_{70} growth mechanism. *Chem. Phys. Lett.* **1992**, *190*(5), 465–468.
- [50] Rubin, Y.; Parker, T.C.; Pastor, S.J.; Jalisiatgi, S.; Boule, C.; Wilkins, C.L. Acetylenic cyclophane as fullerene precursors: formation of $C_{60}H_6$ and C_{60} by laser desorption mass spectrometry of $C_{60}H_6(CO)_{12}$. *Angew. Chem. Int. Ed.* **1998**, *37*(9), 1226–1229.
- [51] (a) Tobe, Y.; Nakagawa, N.; Naemura, K.; Wakabayashi, T.; Shida, T.; Achiba, Y. [16.16.16](1,3,5)Cyclophanetetracosayne ($C_{60}H_6$): a precursor to C_{60} fullerene. *J. Am. Chem. Soc.* **1998**, *120*(18), 4544–4545. (b) Tobe Y.; Nakagawa, N.; Kishi, J.; Sonoda, M.; Naemura, K.; Wakabayashi, T.; Shida, T.; Achiba, Y. Polyyne cyclization to form carbon cage: [16.16.16](1,3,5)Cyclophanetetracosayne derivatives $C_{60}H_6$ and $C_{60}Cl_6$ as precursors to C_{60} fullerene. *Tetrahedron* **2001**, *57*(17), 3629–3636.
- [52] Rubin, Y.; Parker, T.C.; Kahn, S.I.; Holliman, C.L.; McElvany, S.W. Precursors to endohedral metal fullerene complexes: synthesis and x-ray structure of a flexible macrocyclic acetylenic cyclophane $C_{60}H_{18}$. *J. Am. Chem. Soc.* **1996**, *35*(22), 5308–5309.
- [53] Scott, L.T.; Boorum, M.M.; McMahon, B.J.; Hagen, S.; Mack, J.; Blank, J.; Wegner, H.; de Meijere, A. A rational chemical synthesis of C_{60} . *Science* **2002**, *295*, 1500–1503.
- [54] Tobe, Y.; Umeda, R.; Sonoda, M.; Wakabayashi, T. Size-selective formation of C_{78} fullerene from a three-dimensional polyyne precursor. *Chem. Eur. J.* **2005**, *11*(5), 1603–1609.
- [55] Fowler, P.W.; Manolopoulos, D.E. *Atlas of Fullerenes*. Oxford University Press, Oxford, 1995.

7 Formation of $C_{2n}H_2$ Polyynes by Laser Ablation of Graphite, Coal or C_{60} Particles Suspended in Selected Solvents

*Masaharu Tsuji, Shingo Kuboyama,
Takeshi Tsuji and Taro Hamagami*

CONTENTS

7.1	Introduction	127
7.2	Experimental	129
7.3	Results and Discussion	130
7.3.1	Polyynes from Graphite	130
7.3.2	Polyynes from Coals	139
7.3.3	Polyynes from C_{60}	140
7.4	Formation Mechanism of Polyynes from Three Carbon Sources in Solutions.....	146
7.5	Conclusions.....	151
	Acknowledgments	152
	References	152

7.1 INTRODUCTION

Compared with extensive studies on the formation of carbon clusters by laser ablation of graphite in the gas phase since the discovery of C_{60} [1], little work has been done on the laser ablation of graphite in the liquid phase, except for the following pioneering studies [2,3]. Fojtik and Henglein [2]

studied laser ablation of small graphite particles in solutions using a focused 694 nm ruby laser beam of 500 J/cm^2 with a long pulse period of about 1 ms. In the product analysis, using the high-performance liquid chromatography (HPLC), they obtained three peaks of C_{60} , C_{70} , and $\text{C}_{80}\text{--C}_{90}$ fullerenes in toluene solution. They found that the relative intensity of C_{70} peak was unusually stronger than that of more stable C_{60} peak. Gaumet et al. [3] studied laser ablation of a graphite cylinder in benzene using a focused 266, 532, and 1064 nm YAG laser (180 mJ/pulse) with a short pulse period of about ~ 10 ns. On the basis of a product analysis using gas chromatography/mass spectrometry (GC/MS), they obtained experimental evidence for the formation of small C_1 , C_2 , C_3 , and C_4 carbon clusters by laser vaporization of graphite in solution. Two types of laser reactions were observed: addition of carbon clusters to a phenyl radical and aggregation of carbon clusters resulting in hydrogen-capped C_{2n}H_2 ($n=4$ and 6) polyyynes.

Due to its unique geometrical structure, polyyynes are ranked on promising one-dimensional conducting materials, which can be used for “molecular wires” [4]. Unlike fullerenes and carbon nanotubes, however, the existence of polyyynes is still disputed. Therefore, studies on polyyynes are rather rare compared with those on fullerenes and carbon nanotubes. The synthesis of mixtures of polyyynes up to 32 carbon atoms was reported by Eastmond et al. in 1972 [5]. C_{2n}H_2 polyyynes were prepared using copper chloride (Hay coupling) and mixtures of acetylenic carbon compounds that contained 2 to 16 acetylene units $(\text{Et})_3\text{Si}-(\text{C}\equiv\text{C})_n-\text{Si}(\text{Et})_3$ (Et, ethyl). Synthesis of polyyynes via Hay coupling must be carried out at low temperature, because short-chain polyyynes are only stable at low temperatures. Since multisteps are required for the synthesis of long-chain polyyynes via Hay coupling, laser ablation in solutions at room temperature is a new promising technique for the one-pot synthesis of polyyynes.

We have recently studied laser ablation of graphite and C_{60} particles suspended in solutions [6,7]. It was found that hydrogen-capped polyyynes (C_{2n}H_2 ; $n=4\text{--}8$) were produced from graphite particles suspended in benzene, toluene, or hexane solution [6], while C_{2n}H_2 ($n=4\text{--}6$) polyyynes were formed from C_{60} in hexane or methanol solution [7]. Cataldo [8,9] has recently synthesized C_{2n}H_2 ($n=2\text{--}9$) polyyynes by a submerged electric arc discharge in organic solvents.

In this review, in addition to more detailed experimental data for the synthesis of polyyynes by laser ablation of graphite in solutions, new data for Indonesian and Australian coals are reported. In the experiments for graphite, besides benzene, toluene, and hexane used in our previous report [6], cyclohexane and methanol are used as solvents. It is known that long C_{2n}F_2 polyyynes are generated by laser ablation of graphite in an F-containing gas [10]. Therefore, such F-containing solvents as hexafluorobenzene, perfluorooctane, and perfluorodecaline are also used as new solvents. The absorbances of polyyynes in each solvent are measured not only at 355 nm laser irradiation reported previously [6] but also at 266, 532, and

1064 nm laser irradiation. In order to obtain more information on the formation mechanism of polyynes from suspension of graphite particles, absorbances of polyynes in toluene are measured as a function of the concentration of the graphite particles, the laser power, or the laser irradiation time at 355 nm laser irradiation. The relative abundance of polyynes from graphite, coal, and C_{60} particles is compared and their formation mechanism from each carbon source by laser ablation in solutions is discussed.

7.2 EXPERIMENTAL

Figure 7.1 shows a schematic view of laser ablation apparatus in solutions used for the formation of polyynes. Small particles of graphite (Kishida Chem. diameter 75 μm), coal (Indonesian Tanito Harum or Australian Workworth), or C_{60} (MER corporation) were suspended in a selected solvent. The amount of particles used was 0.05–0.1 g per 10 ml. Elemental analyses of Tanito Harum and Workworth coals showed the following C:H:N:O ratios: 71.2:4.4:1.6:21.7% and 79.9:5.6:1.6:12.8%, respectively. As solvents, benzene, toluene, hexane, cyclohexane, methanol, hexafluorobenzene, perfluorooctane, and perfluorodecaline (Kishida Chem Ind. Tokyo Kasei, or Azmax spectral grade) were used for graphite, hexane was used for coals, and hexane and methanol were employed for C_{60} .

The experiments were performed using fundamental (1064 nm) and frequency-multiplied outputs (532, 355, and 266 nm) of a Nd:YAG laser (Spectra Physics GCR-100 or Continuum Surelight I-10). The energy of the Nd:YAG laser was generally maintained at 40 mJ/pulse (200 mJ/cm²) in

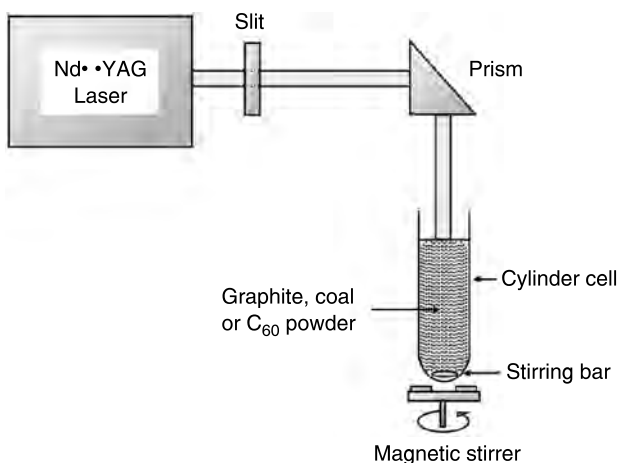


FIGURE 7.1 Laser ablation cell of various kinds of carbon particles suspended in solution.

order to prevent splashes of liquid from reaching the prism at higher energies. The laser was operated at 10 Hz, and the pulse duration was 5–9 ns for the Nd:YAG laser. The non-focused laser light was introduced into a suspended solution of graphite, coal, or C_{60} particles through the opening of a cylindrical cell. The suspension was stirred during the ablation using a magnetic stirrer. After laser irradiation for 60 min, residual reagent particles and insoluble products were removed by filtration. Then, soluble products were analyzed by using HPLC coupled with a multichannel UV and visible spectrometer (Hitachi 7000 system) and by GC/MS. The HPLC chromatograms, obtained using a Toso Tskgel CDS-120T column and hexane or 1:1 mixture of hexane/methanol solvent as mobile phase, were monitored at the highest absorption wavelength of each HPLC peak. They are called “the best HPLC chromatograms” in this work. UV and visible spectra of products were also measured in the 250–800 nm region by using a Shimadzu UV-2450 spectrometer. Hitachi G-5000M, with a fused silica column, and Hitachi M-7200 were used as GC and MS, respectively. The column conditions used were the same as those reported previously [6]. Insoluble products obtained from C_{60} were analyzed with a Raman Spectrometer (JASCO NRS-2100).

7.3 RESULTS AND DISCUSSION

7.3.1 POLYINES FROM GRAPHITE

Figure 7.2(a–f) shows “the best HPLC chromatograms of polyynes” obtained from benzene, toluene, hexafluorebenzene, hexane, cyclohexane, and methanol solutions, respectively, for irradiation with 355 nm laser light. The chromatogram of benzene solution in Figure 7.2(a) consists of a strong solvent peak of PhH at a retention time of ~ 2 min and four peaks, denoted as A–D, in the retention time range of 2.4–5.7 min. The chromatogram of toluene solution in Figure 7.2(b) is very similar to that for benzene except for the observation of a strong solvent peak of PhCH₃. Only a strong peak of C_6F_6 solvent is observed from C_6F_6 in Figure 7.2(c). The HPLC chromatograms of perfluorooctane and perfluorodecaline solutions were similar to that of C_6F_6 . The HPLC chromatograms of hexane, cyclohexane, and methanol solutions are similar, where a strong additional peak, denoted as E, is observed at a retention time of 2.1–2.3 min beside peaks A and B.

The UV absorption spectra of the HPLC peaks of the chromatograms in Figure 7.2 are shown in Figure 7.3. The UV and visible spectra of HPLC peaks E and A–D exhibit strong absorption below 330 nm and similar well-separated vibrational structures, having a vibrational spacing of $1800\text{--}2200\text{ cm}^{-1}$, corresponding to the characteristic vibrational structures of the $C\equiv C$ stretching mode. The observed wavelengths of these structured spectra agreed well with those of hydrogen-capped polyynes reported by

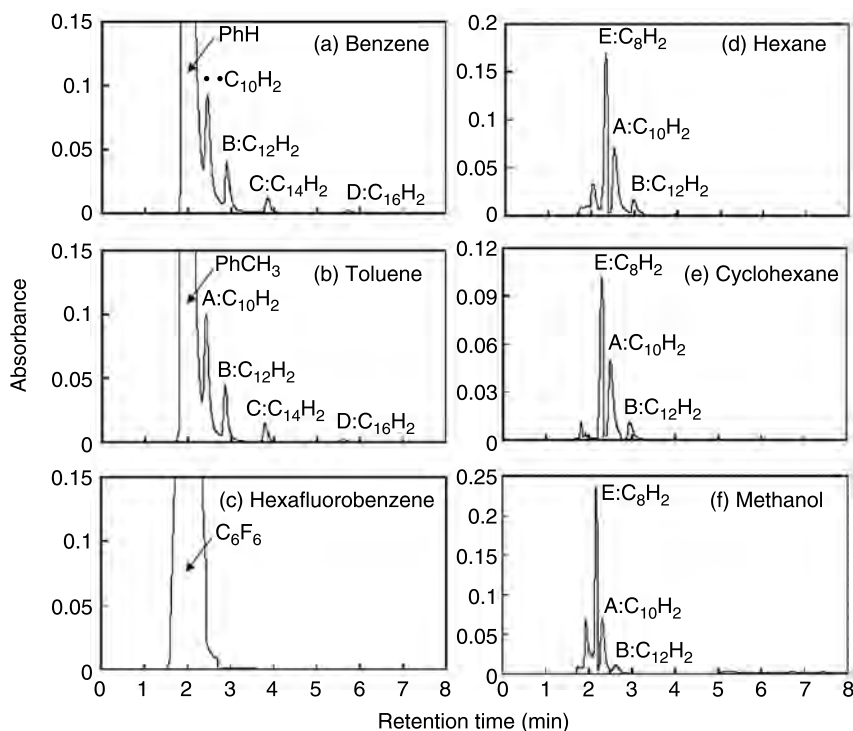


FIGURE 7.2 HPLC chromatograms of products resulting from unfocused 355 nm laser irradiation on graphite particles suspended in benzene, toluene, hexafluorebenzene, hexane, cyclohexane, and methanol solutions for 60 min. Hexane was used as an HPLC solvent.

Eastmond et al. [5] in hexane, as reported previously [6,7]. Therefore, peaks E and A–D are ascribed to hydrogen-capped $C_{2n}H_2$ ($n=4-8$) polyynes, respectively.

When HPLC chromatograms of products in benzene or toluene solution were measured using hexane as an HPLC solvent, no C_8H_2 peak could be detected due to its heavy overlapping with an intense benzene or toluene peak. In order to separate the C_8H_2 peak from the solvent benzene or toluene peak, 1:1 mixture of hexane/methanol solution was used as an HPLC solvent. Figure 7.4(a) shows a typical HPLC chromatogram in benzene solution, where two peaks, E and A, are observed at retention times of 1.37 and 1.43 min, respectively. Their UV spectra are shown in Figure 7.4(b and c). The observed wavelengths of vibrational structure coincide with those of C_8H_2 and $C_{10}H_2$, shown in Figure 7.3(a and b), respectively. In Figure 7.4(c), the $C_{10}H_2$ band in the 230–250 nm region and the C_8H_2 band in the 200–230 nm region appear overlapped due to

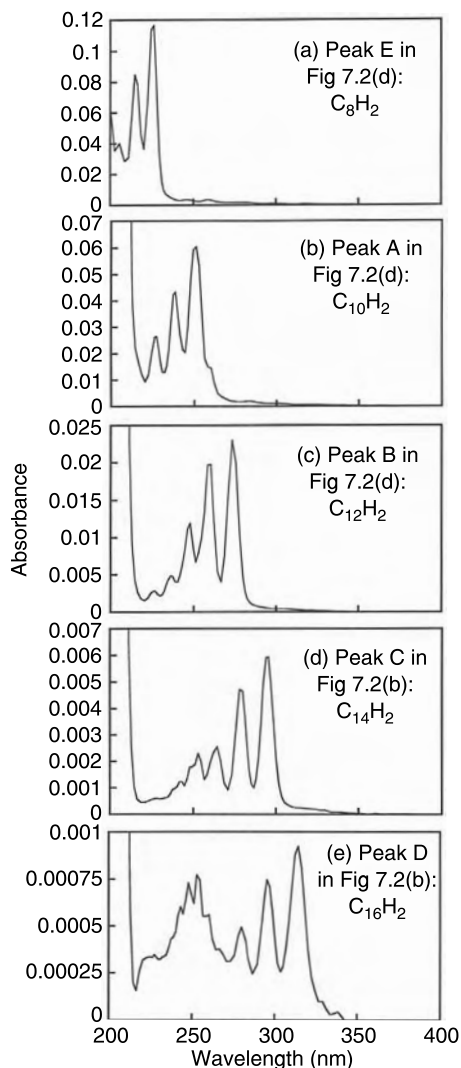


FIGURE 7.3 Absorption spectra of the HPLC peaks E, A, B, C, and D in Figure 7.2.

incomplete separation of the two HPLC peaks. A similar HPLC chromatogram was obtained in toluene solution. It is well known that hydrogen atoms of $C_{2n}H_2$ polyynes are easily substituted by Cu, leading to precipitation of $C_{2n}Cu_2$ by the addition of Cu_2Cl_2 . When Cu_2Cl_2 was added to the solution, HPLC peaks A–E greatly reduced their intensities. These findings give a further evidence that HPLC peaks A–E were associated with $C_{2n}H_2$ polyynes.

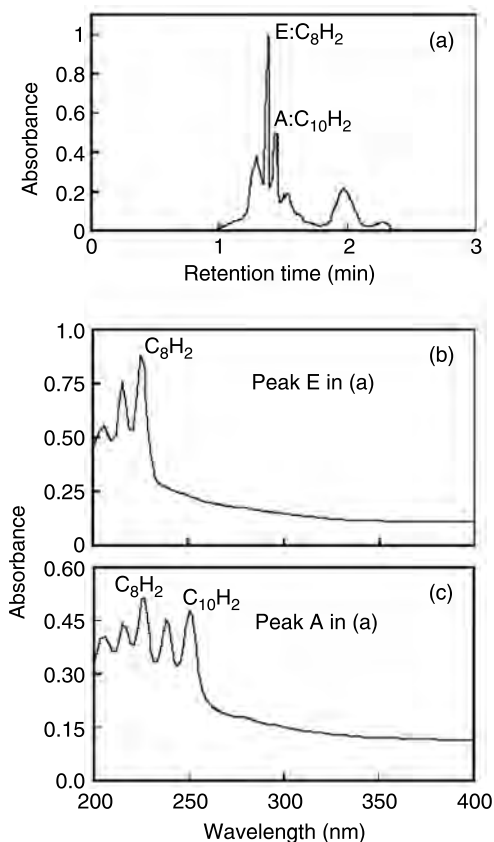


FIGURE 7.4 (a) HPLC chromatogram. (b) and (c) UV absorption spectra of HPLC peaks E and A in (a) resulting from unfocused 355 nm laser irradiation on graphite particles suspended in benzene for 60 min. 1:1 mixture of hexane/methanol solution was used as an HPLC solvent.

In order to further confirm the formation of polyynes, GC/MS spectra of products were measured. A weak GC peak with a parent ion of $m/z = 98$ was observed at a retention time of about 4.1 min in benzene, toluene, hexane, cyclohexane, and methanol. The mass spectrum of the GC peak at 4.1 min was composed of a strong peak at $m/z = 98$ and a weak peak at $m/z = 97$ with a relative intensity of 0.0093. These two peaks could be assigned to $C_8H_2^+$ and C_8H^+ , respectively. In addition, a GC peak with a parent ion of $m/z = 122$ was detected at a retention time of 12.7 min. The mass spectrum of the GC peak at 12.7 min consisted of a strong peak at $m/z = 122$ and weak peaks at $m/z = 121$, 120, 85, and 61, with relative intensities of 0.090, 0.032, 0.020, and 0.052, respectively. These five peaks were ascribable to $C_{10}H_2^+$, $C_{10}H^+$, C_{10}^+ , C_7H^+ , C_5H^+ , respectively.

The observation of $C_8H_2^+$ and $C_{10}H_2^+$ peaks in GC/MS spectra gives a definitive evidence for the production of polyyynes.

In our previous analysis by using GC/MS, no $C_8H_2^+$ peak was observed from products in benzene and toluene solutions [6]. In general, HPLC is more sensitive than GC/MS for the detection of C_nH_2 polyyynes due to their extremely large absorption coefficients ($\log \varepsilon = 5$). When GC/MS spectra were measured under higher sensitivity than that in the previous measurements [6], a weak peak of $C_8H_2^+$ was observed in benzene and toluene. The detection of C_8H_2 polyyne in benzene and toluene by HPLC and GC/MS measurements leads us to revise our previous conclusion that C_8H_2 polyyne is not formed in benzene and toluene solutions [6]. We found here that it is a major product as in the cases of other nonaromatic solvents.

Some soluble products may not be detected in HPLC chromatograms due to their heavy overlapping with strong solvent peaks. Total absorption spectra of products were measured using UV-visible spectrometer in order to examine the presence of such products. The product solutions were filtered before recording spectra. Figure 7.5(a–e) show absorption spectra of products in benzene, toluene, hexafluorobenzene, hexane, and methanol in the 250–600 nm region. Since there is strong absorption in the 250–270 nm region for benzene, toluene, and hexafluorobenzene, it was difficult to detect weak $C_{2n}H_2$ peaks in these aromatic solvents. In hexane and methanol solutions, some vibrational structures due to $C_{2n}H_2$ ($n=5$ and 6) are observed in the 250–300 nm region partially overlapping with a broad tail band in the 250–450 nm region. Similar broad tail bands degrading to red appear more strongly in aromatic solvents. Since these broad bands were absent from laser irradiation of solvents without adding graphite particles, graphite must be a dominant source of these continuous bands. The lack of these broad bands in the HPLC chromatograms is probably due to their overlapping with a strong HPLC peak of solvent. These bands may be due to Mie scattering bands of particles involving nanocarbons, as observed by laser ablation of carbon thin film in water [2]. When transmission electron micrograph (TEM) of products from C_6F_6 was observed, no particles were observed. This may be due to the fact that products particles were too small to be detected, as reported by Fojtik and Henglein [2] in the laser ablation of carbon thin film in water.

Although $C_{2n}H_2$ polyyynes can be detected by both HPLC and GC/MS measurements at 355 nm laser irradiation, as shown above, $C_{2n}H_2$ analyses at 266, 532, and 1064 nm laser irradiation were dominantly carried out by using more sensitive HPLC apparatus. In Figure 7.6(a–e) and Table 7.1 are summarized absorbance of each polyyne at 266, 355, 532, and 1064 nm laser irradiation in benzene, toluene, hexane, cyclohexane, or methanol solution. Laser ablation of graphite in benzene and toluene at 266 nm laser irradiation was difficult, because these aromatic molecules absorb 266 nm light. Under such a case, no laser ablation leading to polyyynes occurred. Thus, no data are given for products in benzene and toluene at 266 nm light. Since the $\log \varepsilon$

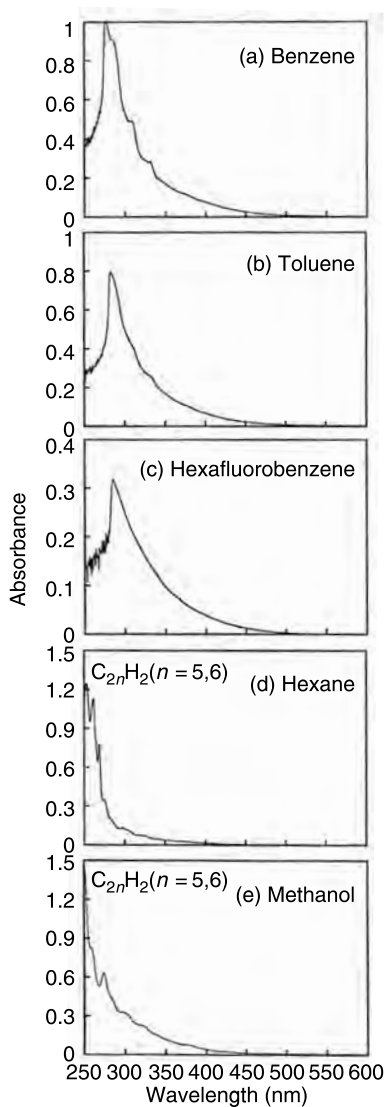


FIGURE 7.5 UV and visible absorption spectra of products resulting from unfocused 355 nm laser irradiation on graphite particles suspended in benzene, toluene, hexafluorobenzene, hexane, or methanol solution.

values of $C_{10}H_2$ and $C_{14}H_2$ have not been measured, the relative abundance of $C_{2n}H_2$ ($n = 5, 7$) was determined from the intensity ratio among $C_8H_2^+$, $C_{10}H_2^+$, and $C_{14}H_2^+$ in the GC/MS spectra. The following general aspects were found from Figure 7.6(a–e) and Table 7.1.

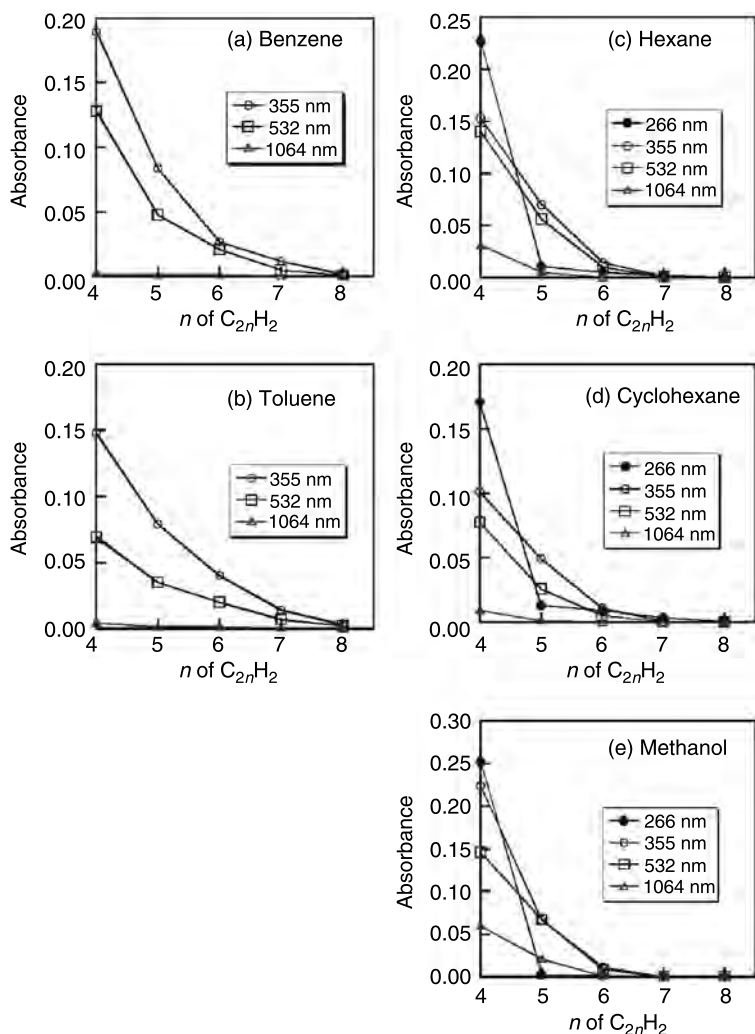


FIGURE 7.6 Absorbances of $C_{2n}H_2$ polyynes after 266, 355, 532, and 1064 nm laser irradiation on graphite particles in benzene, toluene, hexane, cyclohexane, or methanol solution for 60 min.

In all solvents, absorbances of $C_{2n}H_2$ polyynes from graphite are largest at $n = 4$ and decreased with increasing n from 4 to 8. There are no significant differences among the absorbances of $n = 4$ and 5 polyynes from aromatic and aliphatic hydrocarbons and methanol at 355 and 532 nm laser irradiation. However, absorbances of $n = 6$ –8 polyynes from aromatic hydrocarbons are larger than those from hexane, cyclohexane, and methanol.

TABLE 7.1

Measured absorbances of the highest peaks of $C_{2n}H_2$ in laser ablation of graphite, suspended in solutions. The relative abundance of $C_{2n}H_2$ obtained from known absolute absorption coefficients ($\log \varepsilon$) of the highest peaks in hexane and methanol [5] are also given

Target	Solvent	Laser Wavelength (nm)		C_8H_2	$C_{10}H_2$	$C_{12}H_2$	$C_{14}H_2$	$C_{16}H_2$
Graphite	Benzene	355	Absorbance	0.19	0.084	0.027	0.012	0.0019
		532		0.13	0.048	0.021	0.0050	0.00094
		1064		0.0025	0.0014	0.0015	0.00014	0
	Toluene	355	Absorbance	0.15	0.079	0.04	0.014	0.003
		532		0.069	0.035	0.02	0.007	0.002
		1064		0.0042	0.0013	0.0017	0.0005	0
	Hexane	266	Absorbance	0.23	0.011	0.0050	0.0019	0.00035
		355		0.15	0.070	0.014	0.0017	0
		532		0.14	0.056	0.010	0.00061	0
		1064		0.031	0.0053	0	0	0
			log ε in hexane	5.28		5.51		5.54
		266	Relative abundance	0.81	0.029	0.010	0.0040	0.00068
		355		0.55	0.19	0.030	0.0035	0
		532		0.50	0.15	0.021	0.0012	0
		1064		0.11	0.014	0	0	0
	Cyclohexane	266	Absorbance	0.17	0.013	0.0091	0.0034	0.00052
		355		0.10	0.049	0.011	0.00064	0
		532		0.078	0.026	0.0052	0.00037	0
		1064		0.0091	0.0012	0	0	0
	Methanol	266	Absorbance	0.25	0.0023	0.0013	0	0
		355		0.22	0.066	0.011	0	0
		532		0.15	0.067	0.0081	0	0
		1064		0.059	0.020	0.00089	0	0
			log ε in methanol	5.25		5.47		5.48
		266	Relative abundance	0.96	0.0069	0.0031	0	0
		355		0.86	0.20	0.025	0	0
		532		0.56	0.20	0.019	0	0
		1064		0.23	0.061	0.0021	0	0

These findings indicate that there is a solvent effect for the n -distribution of polyyynes between aromatic and non-aromatic solvents.

The absorbances of polyyynes generally decreased rapidly with increasing laser wavelength, so that little polyyne is observed at 1064 nm laser irradiation. This result indicates that the laser wavelength significantly affects the formation rates of polyyynes. The absorbances of C_8H_2 polyyne at 266 nm laser irradiation in hexane, cyclohexane, and methanol are larger than those at 355, 532, and 1064 nm laser irradiation. However, absorbances of $C_{2n}H_2$ ($n \geq 5$) polyyynes at 266 nm laser irradiation are smaller than those at 355, 532, and 1064 nm laser irradiation. This is explained by the photochemical decomposition of $C_{2n}H_2$ ($n \geq 5$) polyyynes under 266 nm laser irradiation because they have absorption at 266 nm laser irradiation (cf. Figure 7.3).

In order to obtain further information on the formation mechanism of polyyynes, the absorbances of polyyynes were measured as a function of the concentration of graphite particles, the laser power, or the laser irradiation time at 355 nm laser irradiation. The absorbances of $C_{2n}H_2$ ($n=4$ and 5) increased with increasing particle concentration from 0.5 to 4 mg/ml, and then decreased until 10 mg/ml [6]. The decrease beyond 4 mg/ml suggests that the laser light does not effectively ablate graphite particle at higher concentrations, probably due to scattering caused by particles. The observation of similar tendencies for $C_{12}H_2$ and $C_{14}H_2$ indicated that the degree of polymerization of polyyynes is independent of the particle concentration. When $\ln[C_8H_2]$ was plotted against $\ln(\text{laser fluence})$, $[C_8H_2]$ was proportional to 3.0 powers of the laser fluence. This implies that three photons participate in the formation of C_8H_2 under 355 nm laser irradiation. The absorbances of $C_{2n}H_2$ ($n=4$ and 5) increased with increasing laser irradiation time from 0 to about 60 min, and leveled off in the 60–120 min range. When a focused laser beam was used for the laser ablation of graphite in benzene, toluene, and hexane solutions, the observed HPLC and GC/MS spectra of $C_{2n}H_2$ were similar to those observed using unfocused laser beam. This indicates that the chain-length distribution of $C_{2n}H_2$ is essentially independent of the energy density of the laser radiation. When a focused laser was irradiated into a fixed graphite rod in toluene, polyyynes were also produced.

In all our laser ablation experiments of graphite suspension and rod in solutions using an unfocused or focused Nd:YAG laser, no evidence for the formation of C_{60} and C_{70} fullerenes was obtained from HPLC chromatograms, laser desorption time-of-flight mass spectra (TOFMS), and ^{13}C -NMR spectra. Our findings are strongly in contrast with the observation of Fojtik and Henglein [2], who obtained C_{60} and C_{70} fullerene by laser ablation in toluene solution. It is known that C_{60} and C_{70} are soluble not only in benzene and toluene but also in hexane [11,12]. Actually, strong HPLC peaks of C_{60} and C_{70} , having their characteristic electronic absorption spectra, were observed at retention times of 2.5 and 3.0 min, respectively, when standard C_{60} and C_{70} samples in benzene, toluene, or hexane

solution were injected into HPLC. Thus, the absence of C_{60} and C_{70} in the products of the present study is not attributable to their low solubility but to their low formation rates under our conditions. Kasuya et al. [13] have succeeded in producing C_{60} by 500 ms CO_2 laser ablation of graphite in the presence of a buffer gas (He, Ar or N_2) at room temperature. They report that the formation of C_{60} requires annealing above $1000^\circ C$ for more than $400\mu s$ and that such annealing could rearrange the structure of the C_{60} precursors that led to the formation of C_{60} . Thus, the lack of C_{60} and C_{70} in our experiments can be attributed to the much weaker laser intensity ($200 J/cm^2$) and the shorter pulse duration (5–9 ns) than those in the experiments of Fojtik and Henglein ($500 J/cm^2$ and 1 ms) [2].

7.3.2 POLYINES FROM COALS

The laser ablation of coals was examined for Tanito Harum and Workworth coals in hexane at 355, 532, and 1064 nm laser irradiation. Figure 7.7(a–d) shows HPLC chromatographs of Tanito Harum and Workworth coals after laser irradiation at 355 and 532 nm in hexane, respectively, where strong C_8H_2 peaks and weak $C_{10}H_2$ and $C_{12}H_2$ peaks are observed. Figure 7.8(a and b) and Table 7.2 show the absorbances and the relative abundance of $C_{2n}H_2$ ($n=4-6$) in hexane solution after 355, 532, and 1064 nm laser irradiation for 60 min.

Only short-chain $C_{2n}H_2$ ($n=4-6$) polyynes are produced from two coals. The n -distribution of $C_{2n}H_2$ has a peak at $n=4$ and rapidly decreases with

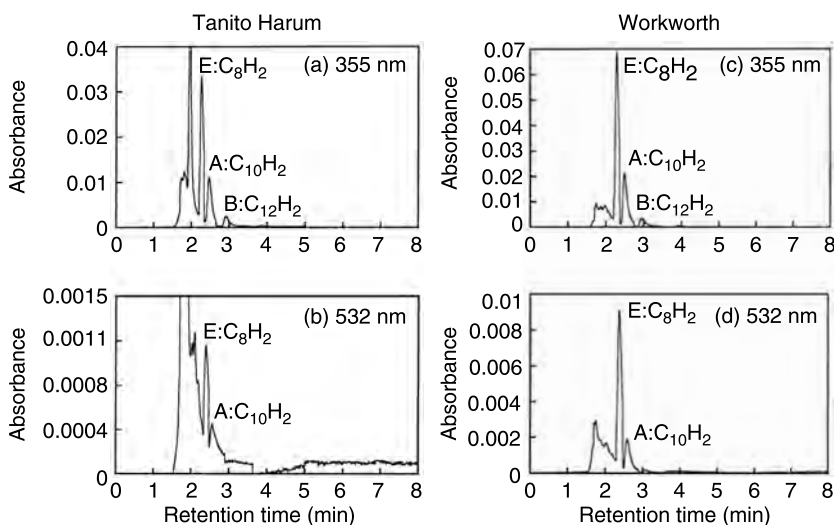


FIGURE 7.7 HPLC chromatograms of Tanito Harum and Workworth coals at 355 and 532 nm laser irradiation in hexane.

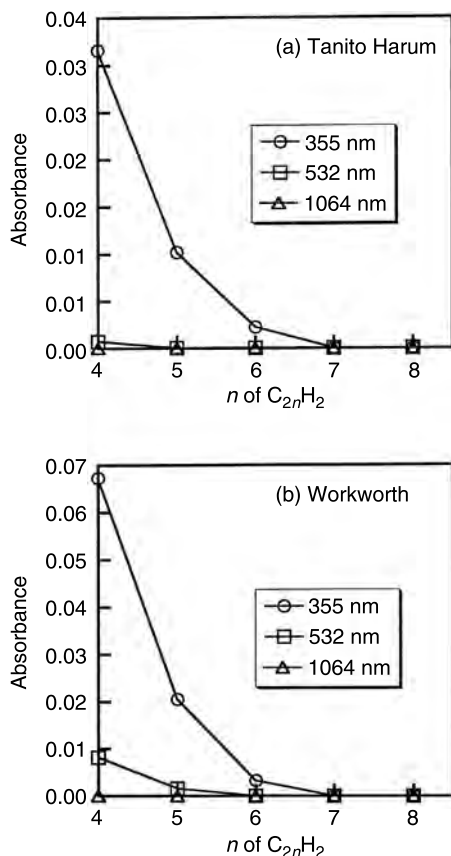


FIGURE 7.8 Absorbances of C_nH_2 polyynes in hexane solution after 355, 532, and 1064 nm laser irradiation on Tanito Harum and Workworth coals for 60 min.

increasing n . The relative abundance of $n=4$ and 5 polyynes from Workworth at 355 nm laser irradiation is larger than that from Tanito Harum by a factor of about 2. Combining this result with elementary analysis data for these two coals shows that the formation rate of polyynes from a coal with a larger C/O ratio is faster. The relative abundance of polyynes decreases significantly with increasing laser wavelength, and no polyynes were observed at 1064 nm laser irradiation from both coals.

7.3.3 POLYINES FROM C_{60}

Two kinds of experiments were carried out for C_{60} , because solubility of C_{60} depends strongly on the solvent. In the first experiment, C_{60} was

TABLE 7.2
Measured absorbances of the highest peaks of C_{2n}H₂ in laser ablation of coals and C₆₀ suspended in solutions, and the relative abundance of C_{2n}H₂

Target	Solvent	Laser Wavelength (nm)		C ₈ H ₂	C ₁₀ H ₂	C ₁₂ H ₂	C ₁₄ H ₂	C ₁₆ H ₂
Coal (Tanito Harum)	Hexane	355	Absorbance	0.032	0.010	0.0022	0	0
		532		0.00072	0	0	0	0
		1064		0	0	0	0	0
		355	Relative abundance	0.11	0.028	0.0046	0	0
		532		0.0026	0	0	0	0
		1064		0	0	0	0	0
		355	Absorbance	0.067	0.020	0.0032	0	0
		532		0.0081	0.0015	0	0	0
Coal (Workworth)	Hexane	1064		0	0	0	0	0
		355	Relative abundance	0.24	0.056	0.0068	0	0
		532		0.029	0.0042	0	0	0
		1064		0	0	0	0	0
		355	Absorbance	0.080	0	0	0	0
		355		0.28	0.017	0.0064	0	0
		532		0.20	0.0023	0	0	0
		1064		0.00089	0	0	0	0
C ₆₀	Hexane	266	Relative abundance	0.29	0	0	0	0
		355		1.0	0.047	0.013	0	0
		532		0.71	0.0063	0	0	0
		1064		0.0032	0	0	0	0
	Methanol	266	Absorbance	0.10	0	0	0	0
		355		0.098	0.017	0	0	0
		532		0	0	0	0	0
		1064		0	0	0	0	0
		266	Relative abundance	0.38	0	0	0	0
		355		0.38	0.051	0	0	0
		532		0	0	0	0	0
		1064		0	0	0	0	0

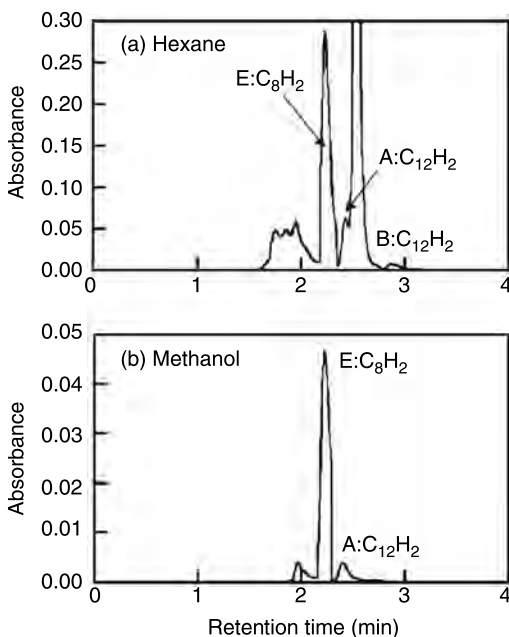


FIGURE 7.9 HPLC chromatograms of products resulting from unfocused 355 nm laser irradiation on C_{60} particles suspended in hexane or methanol solution for 60 min.

completely dissolved in toluene solution. When 355 nm Nd:YAG laser beam was directed into C_{60} solution in toluene, no appreciable color change in purple solution was observed. HPLC chromatograph of products consisted of only a strong peak due to reagent C_{60} . In the second experiment, C_{60} particles were suspended in hexane or methanol solution because of low solubility of C_{60} in these solvents. For example, Figure 7.9(a and b) shows typical HPLC chromatographs at 355 nm laser irradiation in hexane and methanol solutions, respectively. Three product peaks, which can be assigned to C_8H_2 , $C_{10}H_2$, and $C_{12}H_2$ polyynes by absorption spectra, are observed at retention times of 2.2, 2.4, and 2.9 min, respectively. In Figure 7.10(a and b) and Table 7.2 are summarized the absorbances and the relative abundance of $C_{2n}H_2$ ($n=4-6$) in hexane or methanol solution after 266, 355, 532, and 1064 nm laser irradiation for 60 min. The following general aspects were found from these data.

1. Although short-chain $C_{2n}H_2$ ($n=4-6$) polyynes are observed from C_{60} , long-chain $C_{2n}H_2$ ($n=7$ and 8) polyynes could not be detected. In general, the n -distribution of $C_{2n}H_2$ has a sharp peak at $n=4$ and rapidly decreases with increasing n .

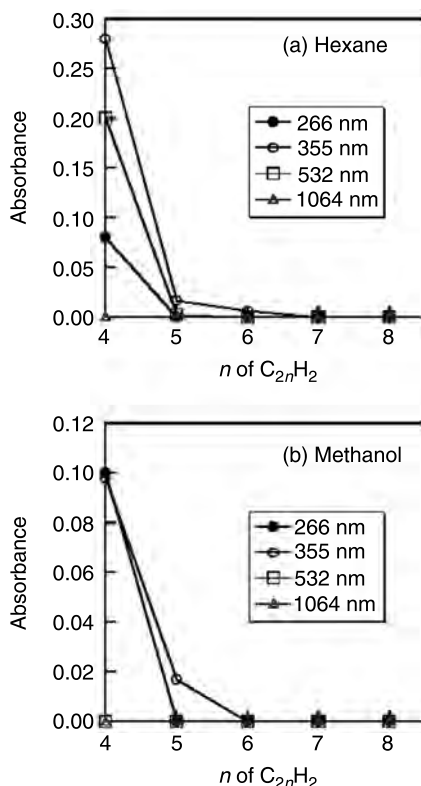


FIGURE 7.10 Absorbances of C_nH_2 polyynes in hexane or methanol solution after 266, 355, 532, and 1064 nm laser irradiation on C_{60} particles for 60 min.

2. There are solvent effects for the formation of polyynes in hexane and methanol. The relative abundance of polyynes in hexane is larger than that in methanol except for 266 nm laser irradiation. The largest relative abundance was obtained at 355 nm laser irradiation in hexane.
3. In general, the relative abundance of polyynes decreases with increasing laser wavelength except for the case of 266 nm laser irradiation in hexane, where it is smaller than that at 355 nm laser irradiation. Although the formation of small amounts of polyynes is observed in hexane at 532 and 1064 nm laser irradiation, no polyynes are detected in methanol.

The absorbance of C_8H_2 in hexane was measured as a function of the C_{60} particle concentration at 355 nm laser irradiation [7]. It increased with

increasing particle concentration from 0 to about 2 mg/ml, and then decreases until 6 mg/ml. When $\ln[\text{C}_8\text{H}_2]$ was plotted against $\ln(\text{laser fluence})$ at 355 nm laser irradiation, $[\text{C}_8\text{H}_2]$ was proportional to 1.7 (≈ 2) powers of the laser fluence. This implies that two photons participate in the formation of C_8H_2 under 355 nm laser irradiation. The absorbance of C_8H_2 rapidly increased with increasing laser irradiation time from 0 to about 60 min, and leveled off in the 60–120 min range [7].

A small amount of C_{60} is dissolved in hexane (solubility 0.040 mg/ml). Therefore, a characteristic purple solution was obtained when C_{60} particles were suspended in hexane. On the other hand, since C_{60} is insoluble in methanol, C_{60} particles were completely undissolved. In such a case, the suspended solution of C_{60} particles in methanol was nearly colorless. When 266, 355, 532, or 1064 nm Nd:YAG laser beam was directed into suspension of C_{60} particles, black particles appeared besides soluble products involving polyyne. Figure 7.11(a–c) shows Raman spectra of insoluble products in the 1000–1700 cm^{-1} obtained after 355 nm laser irradiation. For comparison, Figure 7.11(d and e) shows Raman spectra of standard samples of C_{60} and graphite, respectively. Raman spectrum of C_{60} consists of $\text{A}_g(2)$ mode at 1467 cm^{-1} , and two $\text{H}_g(7,8)$ modes at 1423 and 1572 cm^{-1} [14–16], while that of graphite is composed of E_{2g} mode at 1580 cm^{-1} (G band) and A_g mode at 1360 cm^{-1} (D band) [14–16]. The G band arises from pure stretching mode of C=C bond of polyaromatic ring, while the D band is due to breathing mode of ring. It is known that the latter D band becomes weak with increasing the degree of ring condensation [17]. The $\text{A}_g(2)$ and $\text{H}_g(7)$ modes of C_{60} peaks are observed in Figure 7.11(a–c). These peaks probably arise from intact C_{60} units or small islands interacting with the surrounding graphite-like carbon. In addition to these C_{60} peaks, a broad G band is observed at $\sim 1600 \text{ cm}^{-1}$ and a weaker broad D band is observed in the 1300–1400 cm^{-1} region. These bands are characteristic of graphite-like carbon, which is composed of three-coordinated and bound by sp^2 -type hybrid orbitals [14–16]. The bandwidth of the G band was essentially independent of the laser power and the laser irradiation time, indicating that the degree of graphitization does not change with laser power and irradiation time. On the other hand, the relative intensity of the D band to that of the G band became weak with increasing laser power and laser irradiation time. This suggests that larger aromatic rings are produced with increasing the power and laser irradiation time. These findings led us to conclude that C_{60} particles suspended in solution transform to disordered sp^2 carbon and change to graphite-like carbon under laser ablation. During laser irradiation, cage-opening reactions and coalescence of fullerene fragments occur to form disordered carbon network. The degree of condensation of aromatic ring increased with increasing laser power and irradiation time. When the polyyne structure is present in the insoluble product particle, a strong Raman band of the $\text{C}\equiv\text{C}$ stretch appears at 2000–2100 cm^{-1} [18,19]. Such a band could not be observed in this experiment in the longer wavenumbers.

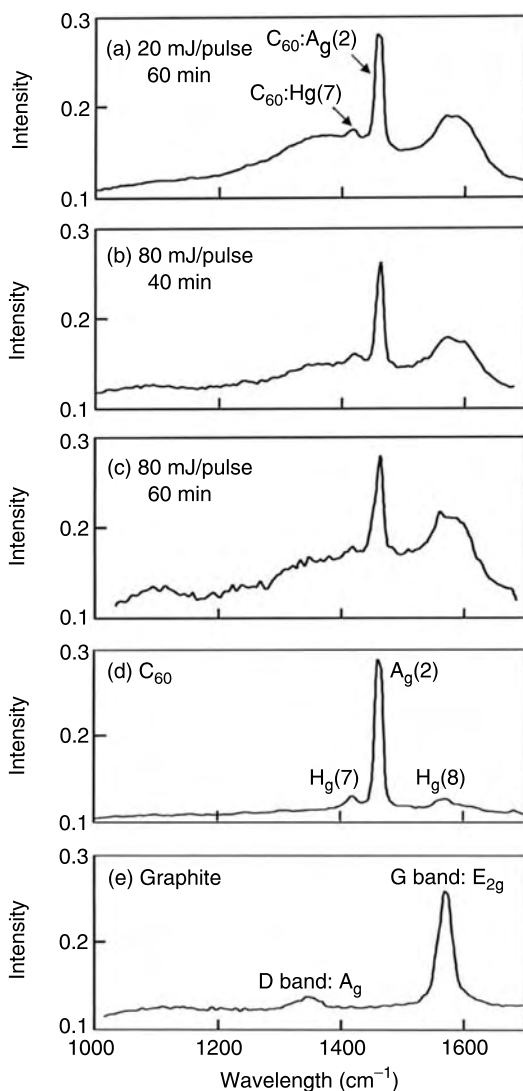


FIGURE 7.11 (a)–(c) Raman spectra of insoluble products from C_{60} after laser irradiation in hexane, (d) C_{60} and (e) graphite. Reprinted from ref. [7], copyright 2005, with permission from Elsevier.

It was therefore concluded that the polyyne structure is not involved in the black insoluble particles.

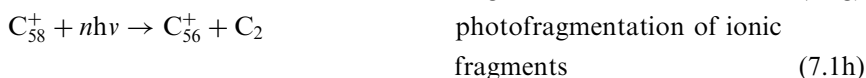
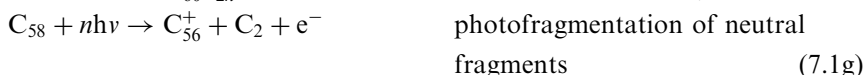
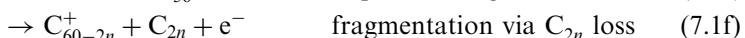
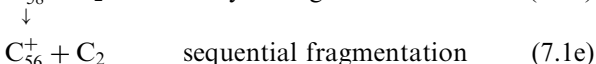
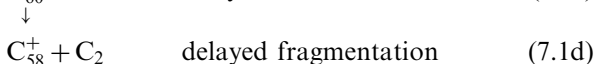
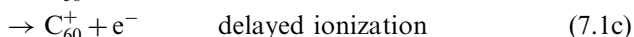
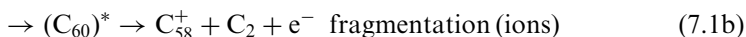
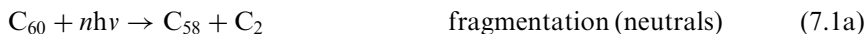
7.4 FORMATION MECHANISM OF POLYINES FROM THREE CARBON SOURCES IN SOLUTIONS

The laser ablation of graphite, coal, and C_{60} particles occurs by multiple absorption of laser photon energy. The conversion of multiphoton energy into thermal energy is significant for irradiation with visible 532 nm (2.33 eV) and IR 1064 nm (1.17 eV) laser lights, while photochemical excitation to states above their dissociation limit is important for irradiation with the UV 355 nm (3.50 eV) and 266 nm (4.66 eV) laser lights. It was found that the relative abundance of polyynes from the three carbon materials generally increased with increasing one-photon energy of laser. This indicates that conversion of multiphoton energy to photochemical reactions, such as excitation and dissociation of the C-C and C=C bond, play significant roles in the initial step of ablation of graphite, coals, and C_{60} particles suspended in solutions leading to polyynes.

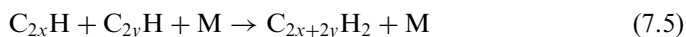
Although the relative abundance of polyynes from C_{60} generally increased with decreasing laser wavelength, that at 266 nm laser irradiation in hexane and methanol is either smaller than or comparable with those at 355 nm laser irradiation. On the basis of known UV and visible absorption spectrum of C_{60} [20], the absorbance of C_{60} generally increases with decreasing the wavelength. Although the absorbance of C_{60} at 266 nm was found to be larger than that at 355 nm by a factor of about 9 in our measurement of absorption spectrum of C_{60} in toluene, the relative abundance of polyynes at 266 nm laser irradiation was either similar to or smaller than that at 355 nm laser irradiation. C_{60} is rapidly transformed into black graphite-like carbon at 266 nm laser irradiation, for which relative formation rates of precursor C_m clusters are smaller and its scattering occurs more significantly at 266 nm laser irradiation than those at 355 nm laser irradiation. Therefore, the relative abundance of polyynes is suppressed at 266 nm laser irradiation, even though one-photon absorption coefficient of C_{60} at 266 nm is larger.

Since the decomposition process of C_{60} is well known and simple, it provides fundamental information on the formation of polyynes from carbon materials. We found that $C_{2n}H_2$ polyynes are produced under irradiation of pulse Nd:YAG laser into C_{60} particles suspended in hexane or methanol solution at room temperature. Laser photodissociation and photoionization of C_{60} in the gas phase leading to neutral and ionic carbon clusters has been studied by O'Brien et al. [21] and Lykke and Wurz [22,23]. According to their results C_2 -loss processes are major dissociation

pathways in both neutral and ionic dissociation processes of C_{60} under laser irradiation.



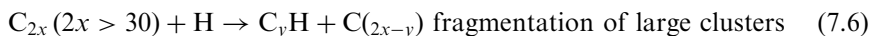
For the case of 355 nm laser irradiation, we found number n in process (7.1a) to be 2. Since the ionization potential of C_{60} (7.6 eV) is higher than two-photon excitation energy of 355 nm (6.98 eV), neutral processes (7.1a) will be more significant than ionization processes (7.1b–f) at 355 nm laser irradiation. After above C_2 -loss processes, $C_{2n}H_2$ polyynes are formed via following polymerization and hydrogenation of C_{2x} and $C_{2x}H$ radicals in hexane or methanol solution.



Here, M represents a third body solvent molecule, which is an acceptor of an excess energy released in each three-body recombination reaction. Hydrogen atoms in reactions (7.3) and (7.4) must be supplied from either photodissociation of solvent or H-atom abstraction reaction from solvent.

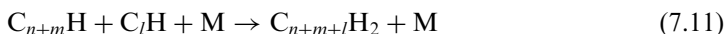
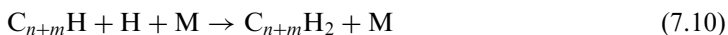
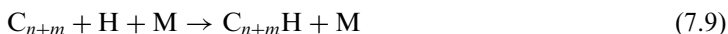
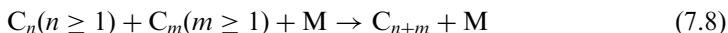
Kato et al. [24] have recently made a mass spectroscopic study on the formation of $C_{2n}H_2$ and $C_{2n}D_2$ ($n=2-5$) polyynes from graphite under the presence of H_2 and D_2 in the gas phase. When the delay time of the ionization pulse relative to the vaporization pulse was changed, two distinctly different mass patterns were found: rather non-selective signals of C_n ($n=6-20$) and C_nH_m ($n=3-20$ and $m=1-4$) at shorter delay times, while

selective signals of $C_{2n}H_2$ ($n=2-5$) and C_{10} at longer delay times. On the basis of laser power and delay time dependence between vaporization pulse and ionization pulse, the selective formation of $C_{2n}D_2$ ($n=2-5$) polyyynes at long delay time was attributed to the fragmentation of larger carbon clusters C_m ($m > 30$) by collisions with thermally decomposed hydrogen atoms produced by intense vaporization pulses, and to survival from heavy collisions due to the chemically inert nature of polyyynes. In our experiments for the laser ablation of C_{60} , besides C_{2x} carbon clusters, large C_{60-2x} clusters must be produced after C_2 -loss processes. Thus, similar fragmentation reactions between large carbon clusters C_m ($m > 30$) and H, as proposed for the formation of $C_{2n}D_2$ polyyynes from graphite in the gas phase [24], may also contribute to the formation of $C_{2n}H_2$ ($n=4-8$) polyyynes from C_{60} in solutions.



The relative abundance of $C_{2n}H_2$ polyyynes from C_{60} in hexane is larger than that in methanol at 355 and 532 nm laser irradiation. Bond dissociation energies of C-H in hexane and C-H and O-H bond in methanol are ~ 4.2 , 4.5 , and 4.1 eV, respectively [25]. The dissociation energy of C-H bond in hexane is smaller than that in methanol. Number ratios of H atom in hexane and methanol in the same volume were calculated to be 1.1:1.0, respectively, using their known densities, molecular weights, and numbers of hydrogen atoms in molecules [25]. Thus, the number ratio of hydrogen atom in hexane is slightly larger than that in methanol. Based upon the above facts, one possible reason for larger relative abundance of $C_{2n}H_2$ from C_{60} in hexane is larger H concentration in hexane than that in methanol. Another reason is slower H-abstraction reactions of C_{2n} radicals with methanol than those with hexane. Therefore, C_{2n} radicals polymerize to form large carbon ring clusters, and they finally grow to graphite-like carbon.

It is known that laser ablation of graphite in the gas phase give C atoms and C_m ($m \geq 2$) clusters with a wide m distribution [26,27]. This is strongly contrasted with the case of C_{60} , where simple C_2 -loss processes are dominated. $C_{2n}H_2$ polyyynes from graphite are expected to be formed via following polymerization and recombination reactions.



In addition to the above polymerization and recombination reactions, fragmentation of large carbon clusters C_m ($m > 30$) due to collisions with H atoms and recombination of $C_{2n}H$ clusters with H atoms, reactions 7.6 and 7.7, may also be responsible for the production of $C_{2n}H_2$ ($n=4-8$) polyynes.

The branching ratios of long chain $C_{2n}H_2$ ($n \geq 5$) polyynes from graphite are larger than those from C_{60} . Although the formation of small C_2 radicals is major laser decomposition processes of C_{60} , not only small C_2 radicals but also larger clusters are produced directly from the laser ablation of graphite [26,27]. This will be one reason for the large formation rates of $C_{2n}H_2$ ($n \geq 5$) polyynes from graphite. The other possible reason is that fragmentation reactions of large clusters C_m ($m > 30$) from graphite by collisions with H atoms give C_{2n} ($n \geq 5$) clusters more efficiently than those from C_{60} .

In our experimental conditions, $C_{2n}H_2$ ($n=4-8$) polyynes were selectively produced from laser ablation of graphite particles suspended in aromatic and aliphatic hydrocarbons and methanol solutions. Although C_8H_2 is dominant in all cases, the relative formation rates of $C_{2n}H_2$ ($n=6-8$) polyynes in aromatic solvents are larger than aliphatic hydrocarbons and methanol. This indicates there are some solvent effects for the formation of $C_{2n}H_2$ ($n=4-8$) polyynes. When polyynes are formed by polymerization of C_{2n} clusters, polymerization of C_8 to C_{10} competes with hydrogenation leading to $C_{10}H$ and $C_{10}H_2$. The higher formation rates of $C_{2n}H_2$ ($n=6-8$) in aromatic solvents suggest that polymerization rates of C_8 leading to longer polyynes in aromatic solvents are faster than those in aliphatic hydrocarbons and methanol. These facts can be explained by the fact that H concentrations in the aliphatic hydrocarbons and methanol are larger than those in aromatic hydrocarbons and/or that H-abstraction reactions of C_8 clusters with the former solvents are faster than those with the latter solvents.

No fluorine-capped polyynes were obtained from laser ablation of graphite particles suspended F-containing solvents. When hexafluorobenzene was used as a solvent, $C_6F_5-C_6F_5$ was found as a main product in the GC/MS spectrum. This indicates that C_6F_5-F bond scission occurs under laser irradiation. Thus, the lack of $C_{2n}F_2$ polyynes in C_6F_6 is not due to the fact that F atoms are not generated from F-containing solvents. One possible reason is that precursor C_m radicals are polymerized and grown to form small carbon particles, which give a broad band in UV spectrum (cf. Figure 7.5).

We found also that $C_{2n}H_2$ ($n=4-6$) polyynes are produced from coals. Since coals consist of polycondensed aromatic rings with various substituents involving H, N, and O atoms, their decomposition mechanism under laser ablation in solution will be more complicated than that of graphite and C_{60} . However, the formation mechanism of polyynes from coals will be similar to that from graphite, because there are small sizes of graphene sheets in coals.

When the relative abundance of major C_8H_2 polyyne in hexane at 355 nm laser irradiation is compared among the three carbon sources, that from C_{60} is largest. It is larger than that from graphite and coals by factors of about 2 and 4–9, respectively. In coals, a large amount of O-containing substituents such as OH, CO, and COOH are involved. One reason for the low formation rates of polyyne from coals will be suppression of formation reactions of polyyne due to various side reactions of precursor carbon clusters with O-containing substituents.

Heath et al. [28] have studied the clustering reactions of carbons ablated from a graphite disk by a focused Nd:YAG 532 nm (30–40 mJ/pulse) laser. Graphite was laser ablated into a He carrier gas containing simple molecules such as H_2 , H_2O , NH_3 , and CH_3CN , supersonically expanded, and skimmed into a molecular beam, and the beam was interrogated by photoionization TOF spectrometry. Without added reactants in the He carrier gas, C_n clusters up to $n=130$ were readily observed. In the presence of added gases (H_2 and H_2O), $C_{2n}H_2$ polyyne were formed. They explained the production of these carbon-chain molecules on the basis that a significant proportion of the C_{2n} species initially formed is reactive radicals with linear carbon-chain structures, which can readily add H at the ends to form relatively stable polyyne. On the other hand, Kato et al. proposed that $C_{2n}D_2$ ($n=2-5$) polyyne from graphite in H_2 or D_2 gas are dominantly produced by fragmentation reactions of large clusters of C_m ($m > 30$) by the thermally decomposed hydrogen atoms produced under intense vaporization field. We found that $C_{2n}H_2$ ($n=4-8$) polyyne were produced by laser ablation of graphite, coals, and C_{60} particles suspended in solutions. Although reaction conditions in this study (liquid phase) are different from those employed by Heath et al. [28] and Kato et al. [24] (gas phase), the present observation for three carbon materials is consistent with previous findings for graphite. Thus, solvents play a similar role to added gases (H_2 , H_2O) in the gas phase.

Heath et al. [28] measured the dependence of n -distribution of polyyne on the pressure of added gases. They found that the C_8H_2 peak was dominant at high added gas pressures of H_2 as this species did not undergo any further reaction. A similar inertness of C_8H_2 was found for H_2O , CH_3CN , and NH_3 , though its tendency was not so severe as that for H_2 . In all our experiments using graphite, coals, and C_{60} in solutions, C_8H_2 was a dominant polyyne and small amounts of longer polyyne $C_{2n}H_2$ ($n=5-8$) were observed. These findings led us to conclude that the inertness of C_8H_2 is also kept for clustering reactions in solutions and the reactivity of ablated species in solutions is similar to that in the gas phase under the presence of added gases (H_2 , H_2O , CH_3CN , NH_3).

We found that major products of C_{60} suspended in hexane and methanol under laser ablation are graphite-like carbon. It probably arises from photo-decomposition of fullerene network and photochemical and/or thermal isomerization from fullerene structure to graphite-like one. Another formation route of graphite-like carbon is clustering of small carbon clusters.

The relative abundance of polyynes increased with increasing the laser irradiation time and leveled off at longer irradiation time above 60 min. This may be due to the fact that the relative formation rates of precursor C_{2n} clusters from graphite-like carbon are smaller than those from C_{60} . Black graphite-like carbon absorbs more laser light than nearly colorless C_{60} particle does. Thus, the decrease in the relative abundance of polyyne at high C_{60} particle concentration can be attributed to the scattering of laser light by graphite-like carbon. We found a similar peak in the dependence of the relative abundance of polyyne on the graphite concentration. The decrease in the relative abundance of polyyne at high particle concentration of graphite is also attributable to the scattering of laser light by graphite particles. On the other hand, a major reason for the decrease in the formation rates of polyynes from graphite at long irradiation time may be due to a change in graphite structure to other amorphous carbon structures for which the formation rates of precursor C_{2n} clusters are small.

7.5 CONCLUSIONS

$C_{2n}H_2$ ($n=4-8$) polyynes are produced by laser ablation of graphite, coal, and C_{60} particles suspended in solutions. relative abundance of polyynes rapidly increased with decreasing laser wavelength due to an increase in the photochemical effects. All substrates favor C_8H_2 formation, which was consistent with reported gas phase reactions of carbon clusters with added gases. Thus, it was concluded that solvents play the same role as that of foreign added gases for the polymerization and hydrogenation of carbon clusters. The relative abundance of C_8H_2 polyyne from graphite, coals, and C_{60} in hexane at 355 nm laser irradiation was 0.55:0.11 or 0.24:1.0, respectively. The small relative abundance of polyynes from coals was attributed to the existence of OH, CO, and COOH chemical groups in coals. The n -distribution of polyynes depended on the solvent. The larger distributions of long-chain polyynes from graphite in aromatic hydrocarbons than those in aliphatic hydrocarbons and methanol were explained by the fact that H concentrations in the latter solvents are larger than those in aromatic hydrocarbons, and/or that H-abstraction reactions of C_{2n} radicals with the latter solvents are faster than those with the former solvents.

We reported here that $C_{2n}H_2$ ($n=4-8$) polyynes could be synthesized by laser ablation of various carbon materials in one pot, though their relative abundance depended strongly on the experimental parameters. The present technique will contribute to the development of an efficient method for one-pot synthesis of polyynes, one of the materials for potential use in molecular electronics.

ACKNOWLEDGMENTS

The authors acknowledge financial support from a Grant-in-Aid for Scientific Research Number 15651046 from the Japanese Ministry of Education, Science, Sports, and Culture, and Professors I. Mochida and Y. Korai for supplying sample coals and for the use of a Raman spectrometer. We thank the Research Laboratory for High Voltage Electron Microscopy, Kyushu University, for the use of TEM.

REFERENCES

- [1] Kroto, H.W.; Heath, J.R.; O'Brien, S.C.; Curl, R.F.; Smalley, R.E. C₆₀: Buckminsterfullerene. *Nature (London)*, **1985**, 318, 162–163.
- [2] Fojtik, A.; Henglein, A. Laser ablation of films and suspended particles in a solvent: Formation of cluster and colloid solution. *Ber. Bunsenges. Phys. Chem.* **1993**, 97(2), 252–254.
- [3] Gaumet, J.J.; Ouachini, A.E.; Peter, S.; Millon, E.; Muller, J.F. Formation of carbon clusters C_n (1 ≤ n ≤ 4) by laser vaporization of graphite and a study of their chemical reactivity by gas chromatography–mass spectrometry. *J. Chem. Soc. Faraday Trans.* **1996**, 92(11), 1831–1834.
- [4] Beck, W.; Niemer, B.; Wieser, M. Methods for the synthesis of μ-hydrocarbon transition metal complexes without metal–metal bonds. *Angew. Chem. Int. Ed. Engl.* **1993**, 32(7), 923–949.
- [5] Eastmond, R.; Johnson, T.R.; Walton, D.R.M. Silylation as a protective method for terminal alkynes in oxidative couplings: A general synthesis of the parent polyynes H(C≡C)_nH (n = 4–10, 12). *Tetrahedron* **1972**, 28(17), 4601–4616.
- [6] Tsuji, M.; Tsuji, T.; Kuboyama, S.; Yoon, S.-H.; Korai, Y.; Tsujimoto, T.; Kubo, K.; Mori, A.; Mochida, I. Formation of hydrogen-capped polyynes by laser ablation of graphite particles suspended in solution. *Chem. Phys. Lett.* **2002**, 355(1,2), 101–108.
- [7] Tsuji, M.; Kuboyama, S.; Matsuzaki, T.; Tsuji, T. Formation of hydrogen-capped polyynes by laser ablation of C₆₀ particles suspended in solution. *Carbon* **2003**, 41(11), 2141–2148.
- [8] Cataldo, F. Polyynes and cyanopolyynes synthesis from the submerged electric arc: about the role played by the electrodes and solvents in polyynes formation. *Tetrahedron* **2004**, 60(19), 4265–4274.
- [9] Cataldo, F. Synthesis of polyynes in a submerged electric arc in organic solvents. *Carbon* **2004**, 42(1), 129–142.
- [10] Lagow, R.J.; Kampa, J.J.; Wei, H.C.; Battle, S.L.; Genge, J.W.; Laude, G.A.; Harper, C.J.; Bau, R.; Stevens, R.C.; Haw, J.F.; Munson, E. Synthesis of linear acetylenic carbon: The “sp” carbon allotrope. *Science* **1995**, 267, 362–367.
- [11] Sivaraman, N.; Dharamodaran, R.; Kaliappan, I.; Srinivasan, T.G.; Vasudeva, Rao P.R.; Mathews, C.K. Solubility of C₆₀ in organic solvents. *J. Org. Chem.* **1992**, 57(22), 6077–6079.
- [12] Ruoff, R.S.; Tse, D.S.; Malhotra, R.; Lorents, D.C. Solubility of fullerene (C₆₀) in a variety of solvents. *J. Phys. Chem.* **1993**, 97(13), 3379–3383.

- [13] Kasuya, D.; Kokai, F.; Takahashi, K.; Yudasaka, M.; Iijima, S. Formation of C_{60} using CO_2 laser vaporization of graphite at room temperature. *Chem. Phys. Lett.* **2001**, 337(1–3), 25–30.
- [14] Nakamizo, M.; Honda, H.; Inagaki, M. Raman spectra of ground natural graphite. *Carbon* **1978**, 16(4), 281–283.
- [15] Milani, P.; Manfredini, M.; Bottani, C.E. Fullerenes as precursors of carbon-based materials. *Syn. Metals* **1996**, 77(1–3), 81–83.
- [16] Matsuishi, K.; Ohno, T.; Yasuda, N.; Nakanishi, T.; Onari, S.; Arai, T. Photo-induced transformation of C-60 films and single crystals by laser irradiation. *J. Phys. Chem. Solid.* **1997**, 58(11), 1747–1752.
- [17] Terai, T. (editor). Recent experimental techniques of carbon materials (in Japanese). *Japanese Society of Carbon Materials*, Sipek, Tokyo, **2001**, 89–99.
- [18] Kavan, L.; Hlavatý, J.; Kastner, J.; Kuzmany K.H. Electrochemical carbyne from perfluorinated hydrocarbons: synthesis and stability studied by Raman scattering. *Carbon* **1995**, 33(9), 1321–1329.
- [19] Kastner, J.; Kuzmany, H.; Kavan, L.; Dousek, F.P.; Kürti, J. Reductive preparation of carbyne with high yield. An *in situ* Raman scattering study. *Macromolecules* **1995**, 28(1), 344–353.
- [20] Hare, J.P.; Kroto, H.W.; Taylor, R. Preparation and UV/visible spectra of fullerenes C_{60} and C_{70} . *Chem. Phys. Lett.* **1991**, 177(4,5), 394–398.
- [21] O'Brien, S.C.; Heath, J.R.; Curl, R.F.; Smalley, R.E. Photophysics of buckminsterfullerene and other cluster ions. *J. Chem. Phys.* **1988**, 88(1), 220–230.
- [22] Lykke, K.R.; Wurz, P. Direct detection of neutral products from photo-dissociated C_{60} . *J. Phys. Chem.* **1992**, 96(8), 3191–3193.
- [23] Wurz, P.; Lykke, K.R. Multiphoton excitation, dissociation, and ionization of C_{60} . *J. Phys. Chem.* **1992**, 96(25), 10129–10139.
- [24] Kato, Y.; Wakabayashi, T.; Momose, T. A mass spectroscopic study of laser vaporized graphite in H_2 and D_2 gases: the stability of $C_{2n}H_2$ ($n=2-5$) and C_{10} . *Chem. Phys. Lett.* **2004**, 386(4–6), 279–285.
- [25] *Kagaku binran* (in Japanese), 4th Ed. Japanese Chem. Soc., Maruzen, Tokyo, **1993**, II-322-3.
- [26] Gaumet, J.J.; Wakisaka, A.; Shimizu, Y.; Tamori, Y. Energetics for carbon clusters produced directly by laser vaporization of graphite: dependence on laser power and wavelength. *J. Chem. Soc. Faraday Trans.* **1993**, 89(11), 1667–1670.
- [27] Kaizu, K.; Kohno, M.; Suzuki, S.; Shiromaru, H.; Moriwaki, T.; Achiba, Y. Neutral carbon cluster distribution upon laser vaporization. *J. Chem. Phys.* **1997**, 106(23), 9954–9956.
- [28] Heath, J.R.; Zhang, Q.; O'Brien, S.C.; Curl, R.F.; Kroto, H.W.; Smalley, R.E. The formation of long carbon chain molecules during laser vaporization of graphite. *J. Am. Chem. Soc.* **1987**, 109(2), 359–363.

8 Polyynes: Synthesis with the Submerged Electric Arc

Franco Cataldo

CONTENTS

8.1	Introduction	156
8.2	Experimental Aspects on the Synthesis and Analysis of Polyynes with the Electric Arc.....	157
8.2.1	Synthesis of Polyynes in a Submerged Electric Arc	157
8.2.2	HPLC Analysis of the Polyynes	159
8.2.3	Study of the End-Capping of the Polyynes Chains.....	159
8.2.4	The Electric Arc Between Graphite Electrodes in <i>n</i> -Hexane	159
8.2.5	The Electric Arc Between Graphite Electrodes at Very High Current Density	160
8.2.6	Electric Arc Between Titanium Electrodes in <i>n</i> -Hexane ..	160
8.2.7	The Electric Arc Between Titanium Electrodes in Methanol: A Comparison with Carbon Arc	161
8.3	Results and Discussion	161
8.3.1	Some Kinetic Aspects on the Formation of Polyynes	161
8.3.2	Detection and Identification of Polyynes by HPLC–DAD and Other Analytical Techniques	164
8.3.3	PAHs as Byproducts Formed with the Polyynes During Arcing	169
8.3.4	The Role Played by the Nature of the Electrodes in the Polyynes Formation	174
8.3.5	Formation of Carbon Coke or Pyrocarbon: A Comparison with a Series of Halogenated Solvents....	176
8.4	Conclusions.....	177
	Acknowledgments	178
	References	178

8.1 INTRODUCTION

Polyyynes are a fascinating class of molecules because they are involved in many processes and in many different fields of science. For instance, it has been demonstrated that they are the precursors in fullerene synthesis [1–7]. Since nanotubes and nanohorns are obtained under electric arc conditions similar to those adopted for polyyne production [8–11], it may be supposed that they may also play a role in nanotube formation. Furthermore, polyyynes are also considered the key intermediates in the mechanism of soot formation in flames or in thermal decomposition processes of hydrocarbons [12]. Polyyynes also represent a very wide class of naturally occurring organic molecules synthesized by plants, microorganisms, and fungi; about 1000 of naturally occurring polyyynes are known [13]. They display biological activity, including antibiotic and anticancer activity [13] and may find application in the treatment of certain diseases. Carbon chains are also produced from carbon-rich late-type stars and are released in the interstellar medium. It is quite possible that in this medium the carbon chains are the precursors of several exotic molecules and also of interstellar carbon dust. Polyyne derivatives known as cyanopolyyynes have been identified by radioastronomy in the molecular clouds of the interstellar medium [14]. It is quite astonishing that the largest molecule identified till now in molecular clouds of the interstellar space is just a cyanopolyyne: $C_{11}N$. Polyyynes are thought to also play a major role in the interstellar medium and have been advocated as a source of the diffuse interstellar bands (DIBs), although this has not been definitively proven [15–17], and they may play a role in the formation mechanism of interstellar carbon dust. Polyyynes and cyanopolyyynes are present in the atmosphere of Titan, the giant moon of Saturn, and are thought to be involved in the haze formation in this satellite [18–20]. Furthermore, the formation of polyyynes and derivatives is expected also in the atmospheres of the giant gaseous planets such as Jupiter and Saturn and have been found in cometary dust [21]. Polyyne chains are also considered as models of molecular wires and in the synthesis of push–pull chemical structures [22].

The polyyynes are described by the general formula $R-(C\equiv C)_n-R'$ where R and R' are the end groups which can be any chemical group in general or metal atom and n an integer 1,2,3,... In the present chapter we will limit our discussion to the hydrogen-terminated polyyynes where $R = R' = H$. Polyyynes with other end groups are treated in other chapters of this book.

Polyyynes are made by a sequence of sp-hybridized carbon atoms. For an extremely long carbon chain ($n \rightarrow \infty$) the resulting high polymer is called carbyne. Thus, by using the language of polymer chemistry, it is possible to affirm that the polyyynes are oligomers of acetylene while carbyne is the resulting high polymer.

The first systematic synthesis of polyyynes was achieved in 1972 [23] with an elegant multi-step synthetic approach. Polyyne synthesis by coupling

reactions remained almost the only approach for the production of these molecules and was adopted recently [24–27]. However, the formation of polyynes chains has been detected by mass spectrometry both in the evaporation of elemental carbon in vacuum [28] and more recently by laser ablation of graphite [29]. The latest two mentioned approaches for the production of polyynes are not useful for preparative purposes since the amount of these molecules obtained is so low that it is sufficient only to feed a mass spectrometer. Very recently it has been found that polyynes in solution can be produced by laser ablation of graphite particles or even from fullerenes and other carbonaceous materials suspended in organic solvents [30,31]. Alternatively, and more easily, polyyne solutions can be prepared by an electric arc between graphite electrodes submerged in an organic solvent [32–39]. The extremely easy access to polyynes will have an enormous impact in the possibility of studying the chemical and physical properties of these molecules and in using them as intermediates for organic synthesis.

8.2 EXPERIMENTAL ASPECTS ON THE SYNTHESIS AND ANALYSIS OF POLYYNES WITH THE ELECTRIC ARC

8.2.1 SYNTHESIS OF POLYYNES IN A SUBMERGED ELECTRIC ARC

The synthesis of polyynes from a submerged electric arc is a simple and easy technique, not expensive and accessible to everybody. It requires only two graphite electrodes having 99.999% purity (but this high purity is not strictly required) which can be acquired from Aldrich. The graphite electrodes used in our study were graphite rods having a diameter of 0.6 cm and length of 15 cm.

The graphite electrodes were mounted inside to rubber stopcocks and inserted into a 100 ml three-necked round-bottomed flask as illustrated in [Figure 8.1](#). The two electrodes were put in contact each other with a “V” geometry and connected to a d.c. power supply using commercial copper wires. The contacts between the graphite electrodes and the wires were ensured by an insulating tape band (see [Figure 8.1](#)). The third neck of the flask was fitted with a valve. A solvent (usually 50 ml) was poured inside the flask so that the ends of the electrodes are fully submerged into the solvent. Typical solvents that can be used are hydrocarbons and alcohols. With hydrocarbons we have obtained very good synthetic results by using decahydronaphthalene (decalin). Additionally *n*-alkanes, especially those having relatively high boiling points, give good results. Thus, dodecane, decane, octane, heptane and even hexanes are all satisfactory. Among the alcohols, methanol, ethanol, and *n*-propanol or *i*-propanol give satisfactory results.

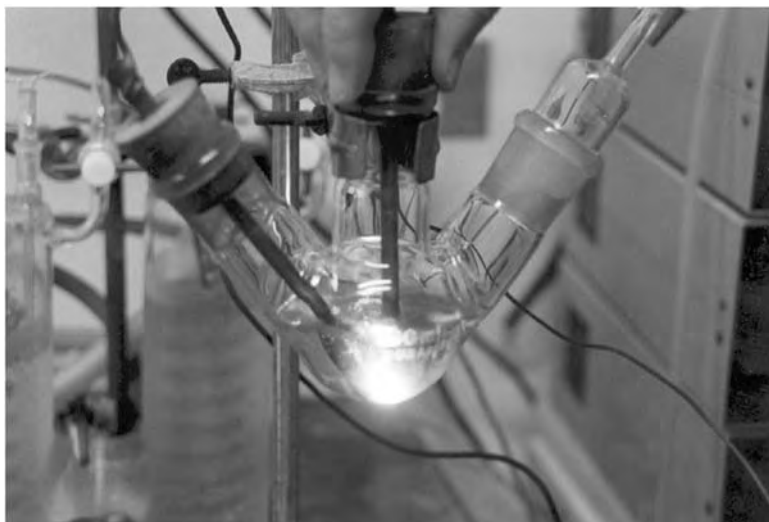


FIGURE 8.1 Submerged electric arc between graphite electrodes at 10 A.

The d.c. power supply we used in our study was the model Cosmo 3000 from KERT srl, Via P. Viganò 21, 31031 Caerano di S. Marco (TV), Italy. E-mail: sales@kert.it. Web site: www.kert.it

In our standard conditions we have arced the graphite electrodes by setting the current at 10 A and moving slightly up and down by hand one of the two electrodes in contact with the other, leaving the tension to change freely in the range of 15–30 V (**WARNING! Always wear suitable insulating gloves! Avoid touching the electrodes directly!**). The electrodes were inserted into insulating rubber supports. It is also possible to deliver into the solution more than 10 A, for instance 20 A, by connecting in parallel two or more d.c. power supply, but the volume of the solvent must be increased adequately otherwise the enormous amount of energy delivered into the solvent causes its vaporization and decomposition [33]. By working with 10 A, it is sufficient to externally cool the flask with a bath of cold water and ice, avoiding extensive vaporization. The arc is ignited immediately after the power is switched on and is sustained by the small movement of one electrode over the other. A bright white light is emitted in the contact area (see Figure 8.1) between the two graphite electrodes. The anode is consumed and this can be observed by extensive cratering of its surface in the contact area. Also, the cathode undergoes changes with the deposition of macroscopic carbon bulges. Periodically, arcing can be interrupted for sampling the solution. Polyynes accumulate in the solution and can be easily detected by electronic absorption spectroscopy [32–34,40]. A UV spectrometer (Shimadzu model 160 A) was used in our laboratory.

For the registration of the spectra or for the HPLC analysis (see next section) it is essential to filter the solution because arcing causes the formation of very small carbon particles which remain in suspension. The crude reaction mixtures were always filtered prior to analysis with a syringe fitted with PVDF filtering membrane having a pore size of 0.45×10^{-6} m. By using different current intensities and different solvents the growth of certain absorption bands of the electronic absorption spectra was studied as function of the arcing time.

8.2.2 HPLC ANALYSIS OF THE POLYINES

The high-performance liquid chromatographic analysis (HPLC) was performed on an Agilent Technologies model 1100, equipped with a diode-array detector that was set at wavelengths of 225, 250, 274, 295, and 350 nm. The solution containing the crude mixture of products, after filtration, was injected into a 4.6×150 mm HPLC column (Zorbax Eclipse XDB-C8). A mobile phase of $\text{CH}_3\text{CN}/\text{H}_2\text{O}$ 80/20 (v/v) was used under isocratic conditions at a flow rate of 1.5 ml/min and 151 bar. The polyynes eluted from the column were identified by a diode-array detector through their typical spectra, which are given in the literature [23,24,41].

8.2.3 STUDY OF THE END-CAPPING OF THE POLYINE CHAINS

The crude polyyne mixture obtained by the submerged electric arc between graphite electrodes in *n*-hexane or *n*-dodecane or decahydronaphthalene were treated with an excess of Ilosvay's reagent. The reagent was prepared by dissolving 1.5 g of CuI and 1.3 g of $\text{NH}_2\text{OH}\cdot\text{HCl}$ (hydroxylamine hydrochloride) in 55 ml of distilled water together with 33 ml of 33% aqueous NH_3 . It was sufficient to shake the organic solution with the aqueous reagent and immediately a brown precipitate is obtained due to the formation of the copper acetylide derivatives. The formation of the copper acetylides was abundant in solutions prepared by prolonged arcing and the acetylides can be even collected by filtration (**WARNING! Acetylides are all explosive when they are dry. Always keep them humid and destroy them by treatment with conc. HCl**).

The detection of the polyynes end groups can be done by FT-IR spectroscopy on concentrated solutions of polyynes using an FT-IR model IR300 from Thermo-Optek and an IR cell for liquids. The concentrated solution of polyynes can be prepared by prolonged arcing in dodecane or in decahydronaphthalene.

8.2.4 THE ELECTRIC ARC BETWEEN GRAPHITE ELECTRODES IN *n*-HEXANE

This section describes the search for products other than polyynes and presents the evidence for the formation of polycyclic aromatic hydrocarbons

(PAHs). The polyyne solution in hexane obtained after 15 min arcing was filtered, poured into 100 ml of an aqueous solution of ammonia (26%), Cu(I)Cl (2.5 g) and hydroxylamine hydrochloride (1.5 g). The organic solution was vigorously shaken with the aqueous solution for a long time and then left to settle. All polyyne were precipitated as copper salts (acetylides) and could be observed as copper-colored precipitates. The hexane solution still showed absorption bands in the UV spectrum. It is clear that the polyyne are accompanied by other molecules not precipitable with Ilosvay's reagent. HPLC analysis of the solution revealed the presence of polycyclic aromatic hydrocarbons (PAHs). About 15 components were separated by the C8 column. One third of them show electronic spectra of ene-ynes or cyclic polyyne. The remaining two thirds of the components eluted were identified as PAHs on the basis of their UV spectra. Among the PAHs, naphthalene, acenaphthalene, benzo[b]fluoranthene, pyrene, and crysene were unequivocally identified.

8.2.5 THE ELECTRIC ARC BETWEEN GRAPHITE ELECTRODES AT VERY HIGH CURRENT DENSITY

The electric arc between graphite electrodes in hexane was repeated as detailed in Section 8.2.1. Instead of using 10 A, by connecting two power supplies in parallel, it was possible to work with 20 A at about 32 V. Enhanced formation of carbon black was observed. The filtered hexane solution was analyzed by HPLC with a diode array detector (DAD). The polyyne C_6H_2 , C_8H_2 , $C_{10}H_2$, and $C_{12}H_2$ were clearly identified. Possibly $C_{14}H_2$ was also present. C_8H_2 was no more dominant, as in the usual conditions of arcing at 10 A. In fact, at 20 A both C_6H_2 and $C_{10}H_2$ appear to have a concentration comparable to that of C_8H_2 . The concentrations of the PAHs now appear dominant in comparison to the polyyne concentration; exactly the opposite conditions occurred at low current density where the polyyne are the dominant species. About 17 PAHs and other components were eluted by the C8 column. Among them naphthalene, acenaphthalene, and pyrene have been firmly identified.

8.2.6 ELECTRIC ARC BETWEEN TITANIUM ELECTRODES IN *n*-HEXANE

The electric arc between two titanium electrodes submerged in *n*-hexane was conducted in the usual manner (as described in Section 8.2.1 but by replacing the graphite electrodes with titanium electrodes from Aldrich). The electric arc in this specific case appeared much less intense and less bright than in the case of a carbon arc made with graphite electrodes under similar conditions. A gradual darkening of the solvent was noticed, progressing with the arcing time. The titanium electrodes were slightly consumed and a deposit of carbon black can be observed at the bottom of the flask; the amount increased as arcing progressed. The analysis of the filtered

solution was made as usual by HPLC–DAD. The following polyyne were clearly identified as C_6H_2 , C_8H_2 , $C_{10}H_2$ with the second being largely dominant. The polyyne are accompanied by PAHs and other byproducts. Indene, naphthalene, and acenaphthylene were identified among the PAHs.

8.2.7 THE ELECTRIC ARC BETWEEN TITANIUM ELECTRODES IN METHANOL: A COMPARISON WITH THE CARBON ARC

The electric arc between titanium electrodes submerged in methanol was conducted according to the standard method given in Section 8.2.1. After 10 min arcing the polyyne solution obtained was filtered and injected into the HPLC–DAD column for analysis. The formation of carbon derived from the carbonization of the solvent was much less significant than in the previous experiment carried out in *n*-hexane. In this case, no polyyne were detected even in trace amounts by HPLC analysis. Only a mixture of about 12 PAHs was obtained. Among them biphenyl, naphthalene, acenaphthalene, phenanthrene, anthracene, perylene, and fluoranthene were identified.

For comparison the titanium electrodes were replaced with graphite electrodes and the above experiment repeated under the same conditions with fresh and pure methanol in the three-necked flask. After arcing for 10 min and after filtration the solution obtained was analyzed by HPLC–DAD. The polyyne C_8H_2 was by far the most abundant molecular species detected followed by $C_{10}H_2$ and C_6H_2 . The polyyne $C_{12}H_2$ was present in detectable amounts. The other byproducts, essentially PAHs, were present in trace amounts relative to C_8H_2 . Naphthalene and acenaphthalene were identified.

8.3 RESULTS AND DISCUSSION

8.3.1 SOME KINETIC ASPECTS OF THE FORMATION OF POLYINES

The electric arc between graphite electrodes can be considered to arise as a result of the passage of electrons from the cathode to the anode in a small electrode area. Due to the very high electric fields involved in the small area of contact between the two electrodes ($< 1 \text{ mm}^2$), the electrons undergo very strong acceleration and bombard the anode surface, depositing their energy, which is liberated in the form of broad range, emitted electromagnetic radiation and with the formation elemental carbon vapor such as the C_2 and other species. In fact, the carbon arc is known to emit radiation in the UV and the visible, mimicking that emitted by the sun [42]. Furthermore, the carbon arc is also known to be a source of electromagnetic radiation in the infrared and radio frequency ranges [42].

The basic mechanism for polyyne formation involves carbon vaporization from the graphite electrodes under the extremely high temperature

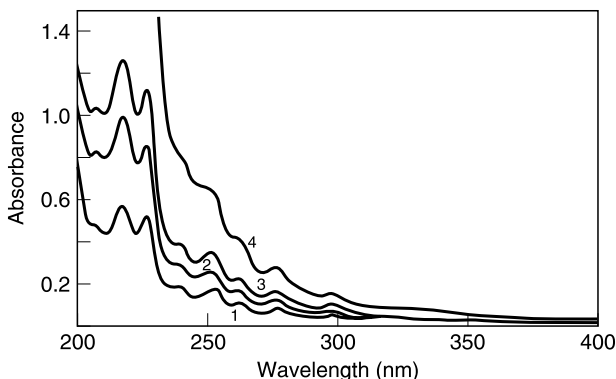


FIGURE 8.2 Electronic adsorption spectra of the polyynes produced from a submerged electric arc between graphite electrodes in *n*-hexane. Spectrum 1 was recorded after 40 s arcing; spectrum 2 after 90 s arcing; spectrum 3 after 90 s arcing; and spectrum 4 after 150 s arcing. The figure shows the growth in absorbance as a function of arcing time.

produced by the electric arc (estimated to be above 4000°C), above the vaporization point of elemental carbon. Elemental carbon is vaporized from the electrodes and oligomerizes to form polyyne chains and then is quenched into the cold solvent surrounding the plasma ball of the arc. The same mechanism was proposed by Tsuji and co-workers for polyyne formation under laser ablation of graphite particles suspended in a hydrocarbon solvent [30,31].

Arcing graphite electrodes in hexane or in other solvents mentioned in the experimental section causes the formation and the accumulation of the polyynes in solution. This can be seen in Figure 8.2 where there is a growth in the absorption spectra of the hexane solution as a function of arcing time. This demonstrates that new molecules are formed during arcing and accumulate into the solution. All the polyynes are produced in the mixture and display the unique spectrum of Figure 8.2 resulting from the overlap of each polyyne individual spectrum [32–34].

By plotting selected absorption bands of the spectra of Figure 8.2 as function of the arcing time it is possible to study the kinetics of the formation of the polyynes in solution. The behavior is linear for all solvents studied, *i.e.* the formation of polyynes at 10 A and 55 ml volume of solvent is linear with the arcing time. This is illustrated in Figure 8.3 where the growth of the absorption at 277 nm is plotted against the arcing time. The differences seen in Figure 8.3 are only due to the different slopes in the kinetics which have all the form of

$$A = kt$$

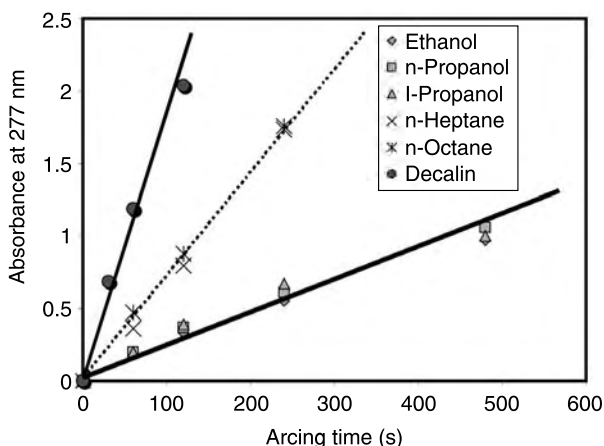


FIGURE 8.3 Kinetics of polyyne formation during graphite arcing in selected solvents. The solvent volume is 55 ml and the current is 10 A.

where A is the absorbance (a.u.) at about 280 nm and t is the arcing time in seconds and k the slope.

In decahydronaphthalene (decalin) the formation of polyynes is largely favored and $k = 0.0178$ a.u./s, while the rate of polyyne formation in other hydrocarbons, like *n*-heptane or *n*-octane, is intermediate, with $k = 0.0072$ a.u./s and, finally, in all alcohols tested (methanol, *n*-propanol and *i*-propanol) is three times lower, with $k = 0.0022$ a.u./s.

It appears that the chemical nature of the solvent affects the formation rate of the polyynes. More precisely, it appears that the solvent molecules acting as hydrogen donors are the solvent favoring polyyne formation. This is the case of decalin which is a well-known hydrogen donor at high temperature [43], followed by the alkanes and then by the alcohols.

Another interesting linear response in the formation of polyynes can be obtained by plotting the absorbance at about 280 nm against the arcing time produced at 3, 5, and 10 A (see Figure 8.4, solvent heptane). The slope increases almost linearly by increasing the current and hence the energy power. In fact $k = 0.0072$ a.u./s at 10 A and passes 0.0037 a.u./s at 5 A. Finally, at 3 A, $k = 0.0025$ a.u./s.

Figure 8.5 shows that the rate of formation of polyynes is not affected by the volume of the solvent. By using 50 ml of methanol, $k_{50} = 0.0025$ a.u./s, but by doubling the solvent volume to 100 ml, the formation rate drops to a half: $k_{100} = 0.0014$ a.u./s. Therefore, the formation rate is constant at a given current (10 A in this case) and only a dilution factor gives an apparent change in the rate.

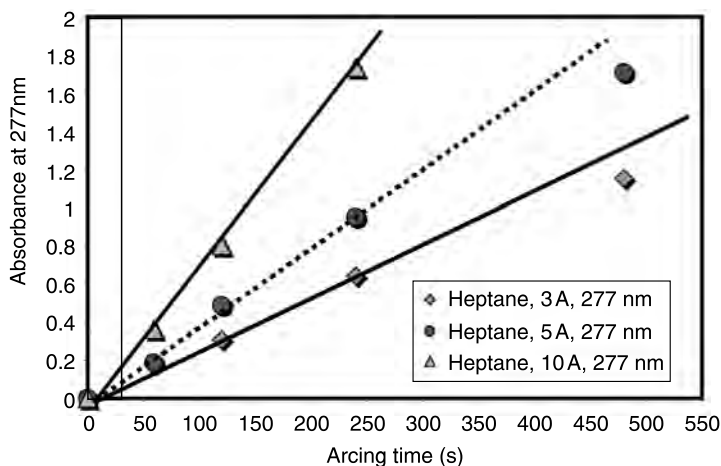


FIGURE 8.4 Formation of polyynes in *n*-heptane (55 ml) at different currents.

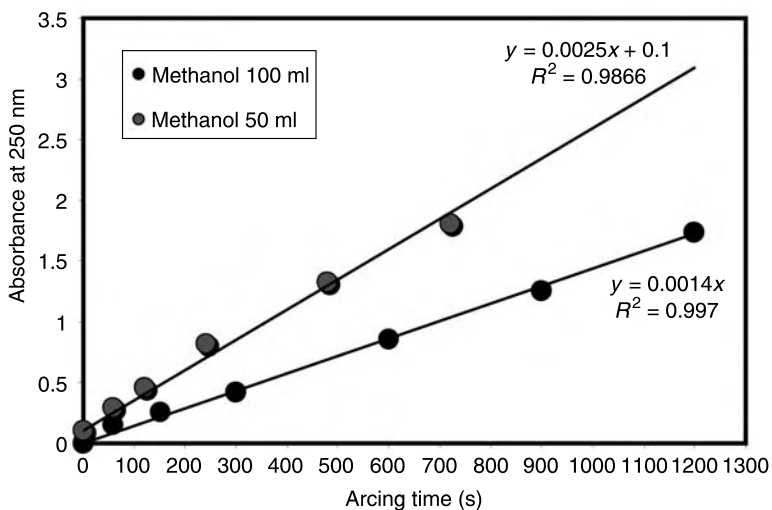


FIGURE 8.5 Formation of polyynes by arcing graphite at 10 A in different volumes of methanol. Growth of the band at 250 nm as a function of arcing time.

8.3.2 DETECTION AND IDENTIFICATION OF POLYNES BY HPLC–DAD AND OTHER ANALYTICAL TECHNIQUES

Polyynes display a very peculiar set of electronic absorption spectra with very high molar extinction coefficients, permitting an easy and certain

identification of the species formed in the submerged electric carbon arc. Liquid chromatographic analysis implies the separation of each individual polyyne molecular species from the others and the registration of the relative electronic absorption spectrum.

A typical liquid chromatogram of the products formed from the submerged electric arc between graphite electrodes in hexane is shown in Figure 8.6(A). The separation achieved between the components having a retention time larger than 1 min is satisfactory and the detection of the peaks of the

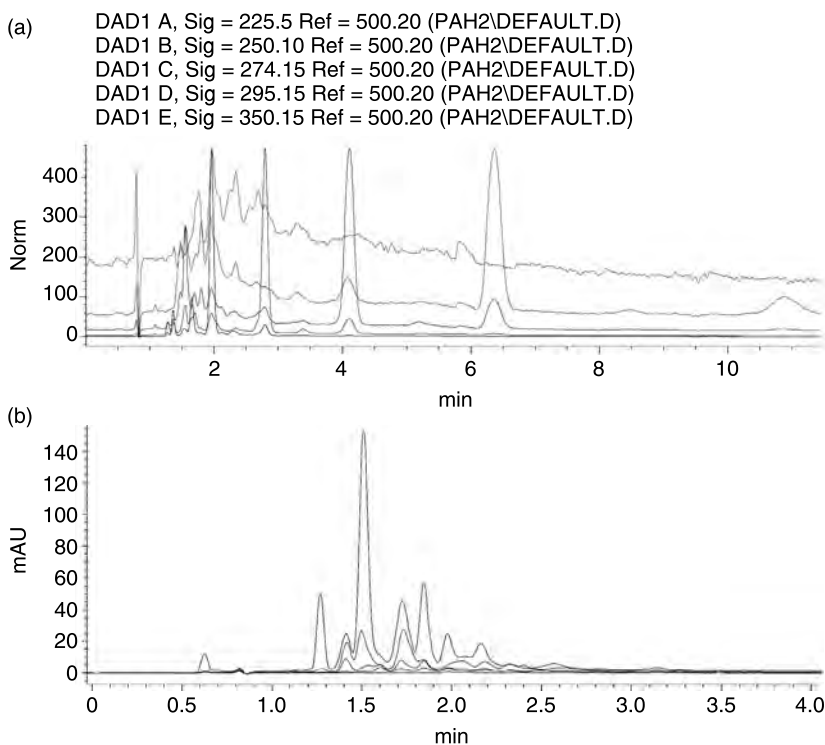


FIGURE 8.6 (A) Normalized HPCL chromatogram showing the polyynes formed in *n*-hexane in standard conditions at 10 A. Each sharp peak is a polyyne. The polyynes detected are C_8H_2 , $C_{10}H_2$, $C_{12}H_2$, $C_{14}H_2$, and even $C_{16}H_2$, as a broad peak at a retention time of 10 min. The abscissa is the elution time (in minutes) and the ordinate is the DAD response (in normalized milli-absorption units). The colored lines show the detection of compounds at the following wavelengths (in nanometers): blue, 225; red, 250; green, 274; pink, 295; and gray, 350. (B) HPLC chromatogram of molecular species non-precipitable as acetylides, identified as PAHs on the basis of their electronic spectra. Note the absence of the C_8H_2 , $C_{10}H_2$, and $C_{12}H_2$ polyynes which appear at about 2, 2.7, and 4 min in panel A. The abscissa and ordinate, as well as the blue and red lines, are as given in panel A.

eluates was satisfactorily achieved by an adequate setting of the detector at pre-fixed wavelengths (see the [experimental](#) section). The electronic absorption spectra of each chromatographic peak was stored by the DAD device permitting the identification of each molecular species associated with a certain peak. As a reference, the literature data were used on polyyne spectra.

A homologous series of spectra were, in fact, obtained among the molecular species separated by the column and are shown in [Figure 8.7](#) together with the retention times in the column. It can be observed that the homologous series of spectra are essentially characterized by about four intense absorption bands with the band at the longest wavelength having the maximum intensity. Furthermore, the position of the bands shifts systematically at longer wavelengths by increasing the retention time and hence the molecular weight of the molecular species eluted. This is well illustrated in [Figure 8.7](#). The spectrum at the top of the figure has a retention time of 1.69 min and the longest wavelength band lies at 227 nm, the following spectrum (from top to bottom of [Figure 8.7](#)) has a retention time of 2.21 min and the longest wavelength absorption band at 250 nm followed by the compounds having, respectively, retention times at 3.01 min, 4.25 min, 6.38 min, and longest wavelength bands at 275, 297, and 316 nm. By comparing the band position of the spectra in [Figure 8.7](#) with the published spectra of polyyne [33–36], it can easily be concluded both from the band pattern, but also by the band position, that we are dealing with a series of polyyne having $n=4$, 5, 6, 7, and 8 respectively. The polyyne having $n=8$ is an acetylenic carbon chain having 16 carbon atoms whose spectrum is at the bottom of [Figure 8.7](#).

HPLC analysis also reveals additional molecular species which can hardly be discovered on the basis of the crude electronic spectrum of mixture of polyyne. As discussed previously [33–36], we have also identified polyyne with $n=2$ and 3, again on the basis of comparison with literature data. The detection of members of the polyyne series with $n=1$ and 2 is not very easy with HPLC analysis using the wavelengths selected and the spectral window available from our instrument (see [Section 18.2.2](#)). In fact, acetylene has its maximum absorption at 152 nm followed by a moderate transition at 182 nm and by a very weak absorption at 220 nm. The first two bands are beyond the detection limits of our DAD, while the transition at 220 nm can be detected only if considerable concentrations of acetylene are present in solution, which is not the case. In the gas phase diacetylene also has its strongest absorption band at 165 nm, again beyond the detection limits of our instrument. We have used other weaker bands for identification of this molecule.

To further confirm that the polyyne detected by HPLC have hydrogen end groups and not other end groups, we performed a series of experiments which demonstrate, in a complementary way to the electronic spectroscopy, the presence of H end groups in the polyyne produced in a submerged

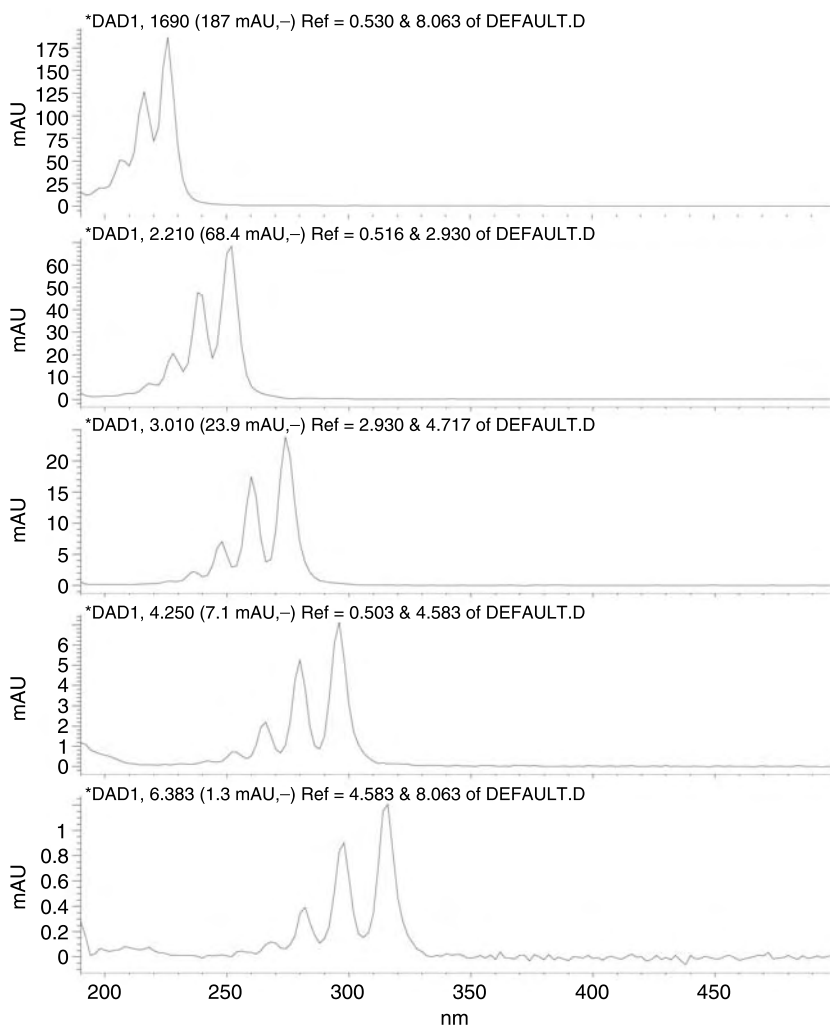


FIGURE 8.7 From top to bottom: the electronic absorption spectra of polyynes with $n=4, 5, 6, 7,$ and 8 . The assignment is unequivocal (see [Table 8.1](#)). These spectra were recorded by the diode-array detector of the HPLC system on each peak shown in [Figure 8.6\(A\)](#).

electric arc between graphite electrodes. As reported in the experimental section, we have used Ilosvay's reagent to make this assay. Ilosvay's reagent is simply a solution of CuI in aqueous ammonia in the presence of hydroxylamine. This reagent is of great importance both for the preparation of copper acetylides from terminal acetylenes ($\text{R} = \text{R}' = \text{Cu}$) and also to test the presence of $-\text{C}\equiv\text{C}-\text{H}$ group in a given molecule. When polyynes solutions in

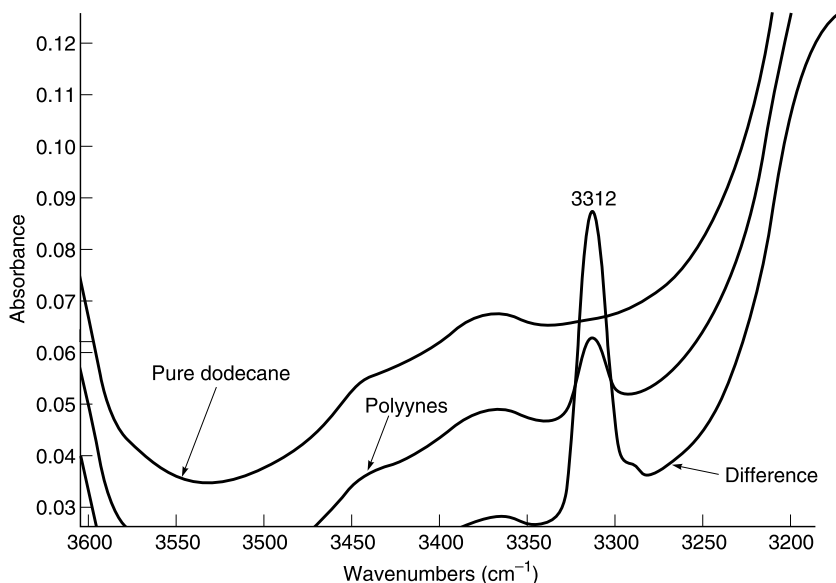


FIGURE 8.8 FT-IR spectra (recorded in an IR cell for liquids) of pure dodecane (blank) and polyynes dissolved in dodecane after arcing of graphite electrodes submerged in dodecane. The polyne solution shows the peak at 3312 cm^{-1} which is due to the stretching of the $\text{-C}\equiv\text{C-H}$ group. This adsorption band is enhanced by the subtraction of the blank. The $\text{-C}\equiv\text{C-H}$ stretching demonstrates that the polyynes are hydrogen capped.

acetonitrile or other solvents (*n*-hexane, *n*-dodecane, and decalin) are treated with Ilosvay's reagent invariably they produce a brown precipitate of copper acetylides, which can be formed only when we are dealing with molecules with $\text{-C}\equiv\text{C-H}$ groups. Thus, it is demonstrated that the polyynes formed are truly polyynes and not cyclopolyyynes, alkyl-terminated polyynes or cyanopolyyynes. However, HPLC analysis has shown that, together with the H-capped polyynes, other products are formed. These will be discussed in the next section.

The evidence concerning hydrogen-terminated polyynes is not limited to the electronic absorption spectra and the reactivity with Ilosvay's reagent. In fact, in Figure 8.8 we present direct evidence of the presence of acetylenic end groups, $\text{-C}\equiv\text{C-H}$, in a solution of polyynes in dodecane. The spectrum of pure dodecane is exempt from any specific absorption band in the specific absorption region of acetylenic end groups at 3312 cm^{-1} ; this can be seen in Figure 8.8. Prolonged arcing of graphite electrodes in dodecane causes the development of a new absorption band at 3312 cm^{-1} which can be enhanced and clarified by subtracting the spectrum of pure dodecane from the spectrum of the polyne solution in dodecane (see Figure 8.8). The spectra of

Figure 8.8 were recorded directly on the crude solution of polyynes in dodecane and on pure dodecane (blank) using an IR cell for liquids with CaF_2 windows and a cell thickness of 0.05 cm. It can be concluded that the infrared stretching of the $-\text{C}\equiv\text{C}-\text{H}$ groups provide direct and definitive evidence of the formation of hydrogen-terminated polyynes. Since the molar extinction coefficient ε of the band at 3312 cm^{-1} associated with the $-\text{C}\equiv\text{C}-\text{H}$ group is about $100\text{ mol}^{-1}\text{ cm}^{-1}$ [35], and since the absorption A of the peak in Figure 8.6 is 0.09 with a cell pathlength b of 0.05 cm, using the Lambert–Beer law ($A = \varepsilon bc$), we can estimate that the concentration, c , of the hydrogen terminated polyynes in the solution of Figure 8.6 was $9 \times 10^{-3}\text{ mol/l}$.

8.3.3 PAHS AS BYPRODUCTS FORMED WITH THE POLYINES DURING ARCING

When the graphite electrodes are arced into a hydrocarbon solvent like *n*-hexane, as described in the experimental section, although the main reaction product consists predominantly of a mixture of polyynes, it is possible to detect other byproducts by HPLC–DAD analysis. These byproducts are not found when graphite electrodes are arced in liquid nitrogen or are present in extremely small trace amounts when the arc is made in certain solvents like methanol, ethanol or water (see Table 8.1).

To elucidate the nature of these byproducts, as described in the experimental section, we precipitated all the hydrogen-terminated polyynes present in an *n*-hexane solution as acetylides by treatment with a Cu(I) reagent. After this treatment, it was possible to observe a profound alteration of the electronic absorption spectrum of the hexane solution (see Figure 8.9). Before the precipitation, the electronic absorption spectrum of the graphite arced hexane solution (Figure 8.9(A)) was dominated by the absorption bands due to the polyynes, but after their precipitation as Cu(I) acetylides it was possible to observe the spectrum (Figure 8.9(B)) of the non-precipitable byproducts. Of course, if the unique result of arcing between graphite electrodes in hexane would have been the polyynes, after their precipitation the hexane solution should have appeared completely clean and free from absorption bands. This is not the case, because the HPLC–DAD analysis of such a solution freed from polyynes reveals a plethora of products but no trace of the polyynes. This is illustrated in Figure 8.6(A and B). In Figure 8.6(A) the polyynes are clearly distinguishable as a sharp and intense peak in the chromatogram but they are completely absent from Figure 8.6(B) after their complete separation as acetylides. The molecular species of Figure 8.6(B) are a mixture of PAHs. This has been established on the basis of their retention time in the chromatogram and on the basis of their electronic absorption spectra compared with the spectra of our standards or of Agilent PAHs library spectra. For instance, we unequivocally identified the presence of naphthalene, acenaphthalene, benzo[b]fluoranthene, pyrene, and crysene

TABLE 8.1
Synopsis of Products Formed by Arcing Graphite or Titanium in Selected Solvents

	Hexane		Benzene		Methanol		Ethanol	
	Graphite (% mol)	Titanium (% mol)	Graphite (% mol)	Titanium (% mol)	Graphite (% mol)	Titanium (% mol)	Graphite (% mol)	Titanium (% mol)
Polyynes C ₆	20.3	23.9	13.8	detected	7.2	n.d.	8.9	n.d.
Polyynes C ₈	61.2	72.7	68.3	83	77.8	n.d.	73.5	n.d.
Polyynes C ₁₀	14.8	3.4	12.6	17	12.8	n.d.	12.3	n.d.
Polyynes C ₁₂	2.9	n.d.	3.2	traces	2.2	n.d.	3.7	n.d.
Polyynes C ₁₄	0.63	n.d.	2.1	traces	detected	n.d.	1.5	n.d.
Polyynes C ₁₆	0.17	n.d.	traces	n.d.	n.d.	n.d.	0.1	n.d.
Polyynes C ₁₈	n.d.	n.d.	n.d.	n.d.	n.d.	n.d.	n.d.	n.d.
Benzene	n.d.	traces ?			n.d.	traces	n.d.	traces
Indene	n.d.	traces	n.d.	n.d.	n.d.	n.d.	n.d.	n.d.
Naphthalene	traces	traces	detected	detected	traces	traces	traces	traces
Acenaphthene	traces	n.d.	detected	n.d.	n.d.	traces	n.d.	traces

Acenaphtylene	traces	traces	detected	detected	n.d.	n.d.	n.d.	n.d.
Biphenyl	n.d.	n.d.	detected	detected	n.d.	traces	n.d.	n.d.
Phenanthrene	n.d.	n.d.	detected	detected	n.d.	traces	n.d.	n.d.
Anthracene	n.d.	n.d.	detected	detected	n.d.	traces	n.d.	n.d.
Perylene	n.d.	n.d.	detected	detected	traces	traces	n.d.	n.d.
Pyrene	traces	n.d.	detected	n.d.	n.d.	n.d.	n.d.	n.d.
Crysene	traces	n.d.	detected	n.d.	n.d.	n.d.	n.d.	n.d.
Fluoranthene	n.d.	n.d.	detected	detected	n.d.	traces	n.d.	n.d.
Benzo[b]fluoranthene	traces	traces ?	detected	detected	traces	n.d.	n.d.	n.d.
Benzo[b]naphto[2,1-cd]thiophene	n.d.	n.d.	traces	traces	n.d.	n.d.	n.d.	n.d.
Total polyynes conc. mol/l	4×10^{-4}	2×10^{-6}	5×10^{-4}	2×10^{-5}	5×10^{-4}	none	3×10^{-4}	none
Carbon black formation	Yes	Yes	Abundant	Abundant	Small	Small	Small	Small

Note: n.d. = not detected.

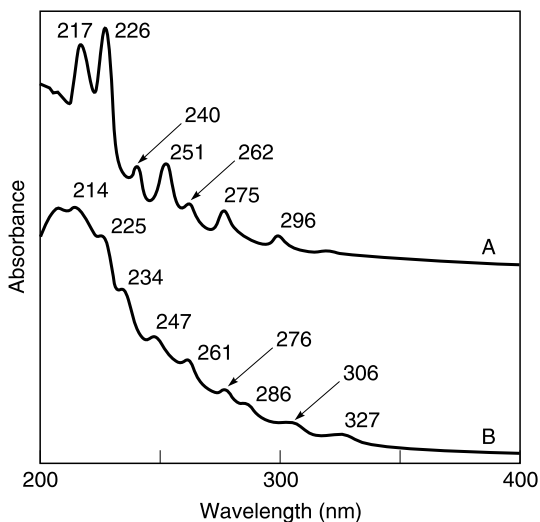


FIGURE 8.9 (A) Electronic absorption spectrum of polyynes obtained in *n*-hexane after arcing with graphite electrodes. (B) Spectrum after polyyne precipitation from solution as acetylides. The residual absorption bands are due to PAHs formed as secondary products during arcing. The two spectra have been shifted for clarity. The absorbance units on the ordinate are a binary scale.

(see Table 8.1) from a total of 17 different compounds eluted, all with spectra suggesting a PAH nature, although in some cases some cyclic polyynes and ene-yne cannot be excluded. Because of the lack of standard and reference spectra, no other assignments were made other than those reported.

The presence of PAHs in solvents subjected to the electric arc is not a complete surprise. For instance, Beck and colleagues [44–46] investigated the effect of electric discharges in toluene with the aim of producing C_{60} fullerene. Instead, in all cases, they found the formation of mixtures of PAHs, and in some cases fullerenes were present but only in trace amounts. The same authors [44–46] explored different conditions of electric discharges in hydrocarbon solvents ranging from an arc between graphite electrodes to scintillysis, from radio frequency plasma to silent electric discharges, conditions which are completely different from those used in our previous works [32–39] and in the present study. Only in one case have Beck et al. used an electric arc in conditions that are very close to ours [44]. They used an electric arc at 10–15 A, but also failed to detect polyynes and, instead, obtained a complex mixture of PAHs. The reason for this failure may be attributed to the workup used for product isolation and analysis: the toluene solution after 2-h arcing was distilled under reduced pressure to dryness after the addition of dichloromethane. The residue after solvent evaporation

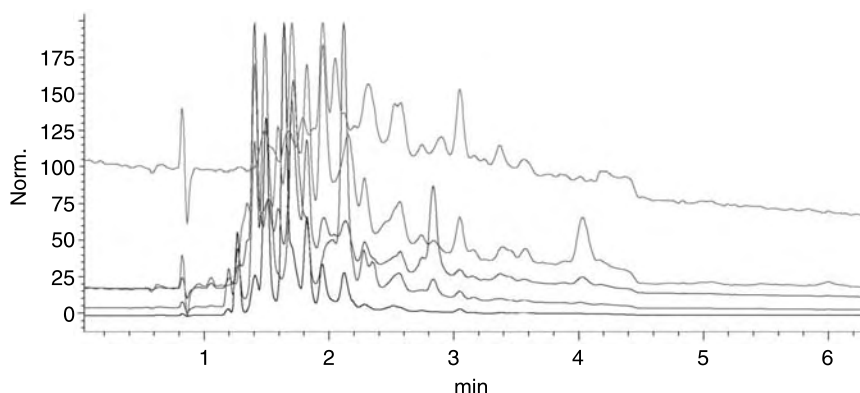


FIGURE 8.10 HPLC chromatogram obtained by arcing at 20 A instead of the usual 10 A in *n*-hexane. The polyyne is still produced but the PAHs are largely prevailing under these conditions. Compare this figure with Figure 8.6(A). The abscissa, ordinate, and the colored lines are as given in the legend to Figure 8.6(A).

was used for the GC–MS analysis [44]. However, we know from our studies [32–39] that polyyne is only stable in solution. When solvent is distilled off the polyyne decomposes into other products. This explains the failure of Beck et al. to detect linear polyyne.

Since we used HPLC techniques coupled with a diode array detector for the analysis of the products of the arcing, we have not caused any alteration of the components of the crude mixture of products which was injected as it was produced after simple filtration. Furthermore, as shown in Figure 8.10, when arcing in hexane is conducted at 20 A, the polyyne is still present and detectable but the fraction of other products (PAHs) increases significantly. Under these conditions PAHs may become the dominant products.

Beck and co-workers [46] also made an interesting comparative study between the products formed by solvent thermal pyrolysis above 1000°C and the products formed by electric discharges in organic solvents like scintillysis, radio frequency plasma treatment and silent electric discharges. In all cases examined, more or less the same PAH mixtures are produced, together with the formation of thermal carbon black or, which is the same, pyrocarbon. Thus, it appears clear that electric discharge in solvents causes their carbonization. The PAHs detected are the byproducts and the intermediates leading to the formation of carbon black [38], but polyyne is also considered the key intermediates leading both to PAHs and soot formation [5].

Based on the preceding discussion, it appears clear that the PAHs observed by arcing graphite electrodes in hexane are derived from solvent pyrolysis in the plasma ball of the arc while the polyyne is released by the graphite electrodes. Since polyyne is also considered the precursors of

PAHs and soot formation it cannot be excluded that a fraction of them, once formed, are converted into PAHs and soot during the arcing operation.

8.3.4 THE ROLE PLAYED BY THE NATURE OF THE ELECTRODES IN POLYYNES FORMATION

Once the role of the graphite electrodes in the production of the polyyynes had been clarified, two crucial tests were carried out by replacing the graphite electrodes with titanium electrodes. The first study was conducted in *n*-hexane by arcing with titanium electrodes. Surprisingly, and in contrast to all the partial conclusions of the preceding sections, C_6H_2 , C_8H_2 , and $C_{10}H_2$ polyyynes were found in the hexane solution arced between titanium electrodes [38]. Five other products were found in comparable concentrations to the two polyyynes mentioned. All were PAHs and three were identified as naphthalene, acenaphthalene, and indene while the remaining two presumed PAHs remained unidentified. The formation of polyyynes observed by arcing hexane with titanium electrodes seems to contradict many conclusions of the preceding sections. However, it must be noticed that arcing in hexane produced a significant amount of carbon black or pyrocarbon. Since no carbon electrodes were used, it appears clear that all the carbon black was derived from the pyrolysis and carbonization of *n*-hexane. To explain the polyyne formation, it is possible to consider that the pyrocarbon particles formed from hexane plasmalysis entered into the plasma ball of the arc or coated the surface of the titanium electrodes as a thin layer. Under these conditions the pyrocarbon acted as a source of carbon vapor in the plasma phase for the production of the polyyynes.

As shown in Table 8.1, although the relative concentration of the polyyynes detected in *n*-hexane arced with Ti electrodes appears comparable to the distribution of polyyynes in *n*-hexane prepared with graphite electrodes, the overall polyyne concentration in the solution prepared with graphite electrodes exceeds by two order of magnitudes the total concentration of the polyyynes in *n*-hexane prepared with Ti electrodes under similar conditions (same current intensity and arcing time). Thus, the fundamental contribution from the graphite electrodes in supplying elemental carbon for the polyyne production is clear. Furthermore, it is remarkable that with graphite electrodes long-chain polyyynes, $C_{12}H_2$, $C_{14}H_2$, and $C_{16}H_2$, were also formed and detected in appreciable amounts, while with Ti electrodes the longest detectable chain was $C_{10}H_2$ (see Table 8.1).

Approximately similar results were observed when *n*-hexane was replaced with benzene (Table 8.1): graphite electrodes produced a higher concentration of polyyynes with a wider distribution of detectable chains in comparison to titanium electrodes. A striking peculiarity of benzene is the formation of a plethora of HPLC–DAD detectable PAHs as reported in Table 8.1 (plus others separated by HPLC but not identified on the basis of the electronic absorption spectra), the distribution of the PAHs was richer and

more complete with graphite electrodes than with Ti electrodes. In this case, the contribution of the solvent to PAHs and pyrocarbon formation appears quite clear.

Completely opposite results to those discussed in the case of *n*-hexane and benzene have been observed in the case of alcohols like methanol and ethanol (Table 8.1). When methanol or ethanol were used as the solvent for arcing with Ti electrodes, the formation of carbon black derived from solvent carbonization was reduced to a minimum. Simultaneously, the HPLC–DAD analysis revealed the complete absence of any polyyne in these oxygenated solvents. Instead, only PAHs were detected, but in trace amounts (Table 8.1). Among the PAHs detected in methanol, biphenyl, naphthalene, acenaphthalene, phenanthrene, and anthracene were easily identified, based both on their retention times and on their peculiar UV spectral pattern in comparison with the spectral pattern of authentic reference compounds. Perylene and fluoranthene were also reasonably identified, based on the retention times and the reasonable matches of reference UV spectra. In any case, the PAHs formed under these conditions were present in at least two orders of magnitude lower concentration than the polyyne formed by arcing the graphite electrodes in methanol. Moreover, PAH formation in methanol was considerably lower than the trace amounts produced in *n*-hexane.

Arcing of graphite electrodes in methanol or, even better, in ethanol, produces the cleanest polyyne solution with extremely small to negligible amounts of PAHs (Table 8.1). Thus, to date, these alcohols appear the best solvents for the cleanest synthesis of polyyne with the electric arc technique. As already reported for other solvents, in methanol and ethanol the dominant polyyne is also C_8H_2 , accounting for more than 70% mole percent of the total polyyne mixture. The yield of longer polyyne decreases as the chain length increases (Table 8.1). Polyyne $C_{10}H_2$ and $C_{12}H_2$ were formed in appreciable amounts together with C_6H_2 . The polyyne $C_{14}H_2$ and $C_{16}H_2$ were also detected in ethanol.

To explain the various results in different solvents, as reported in Table 8.1, it is useful to recall a petrochemical process known as “coking” which involves the thermal carbonization of a hydrocarbon (or hydrocarbon mixture) [43,47]. The coke produced can be considered equivalent to the pyrocarbon mentioned above. The coking tendency of a hydrocarbon under pyrolytic conditions depends on its C/H ratio and the presence of oxygen in the molecule but essentially it depends from its free energy of formation [43,47]. Thus, the energy necessary to produce 1 kg of carbon is +2325 kJ/kg in the case of *n*-hexane and becomes +9787 kJ/kg in the case of ethanol but reaches the very high value of +16770 kJ/kg in the case of methanol. In the case of aromatic hydrocarbons, coking is an exothermic process and occurs with the evolution of considerable amount of heat. For instance, in the case of benzene, the heat evolved in the process is –1150 kJ/kg, and for naphthalene –1270 kJ/kg. The maximum value of heat emission in the coking

process is offered by acetylene: -9450 kJ/kg [47]. In these last two cases the coking process is spontaneous due to the exothermicity of the process. Therefore, when arcing is conducted with aromatic hydrocarbons like benzene (or toluene) [44–46], because of their spontaneous tendency to carbonization, the formation of PAH mixtures in relatively large quantity can be observed together with pyrocarbon or coke. Instead, the amount of PAHs and coke decreases significantly when *n*-hexane is arced and decreases further when methanol is used in place of *n*-hexane for arcing. This is because of the unfavorable thermodynamics in the carbonization process. As shown above, the carbonization thermodynamics of alcohols are extremely unfavorable because these molecules contain oxygen. Thus, in the case of alcohols, PAH formation is extremely low to negligible and a similar conclusion can be reached for pyrocarbon formation in these media.

8.3.5 FORMATION OF CARBON COKE OR PYROCARBON: A COMPARISON WITH A SERIES OF HALOGENATED SOLVENTS [48]

In Section 8.3.4 we have shown that the formation of pyrocarbon during arcing is very low in alcohols, increases in aliphatic solvents and reaches its maximum in aromatic solvents. In this section we report the measured amount of pyrocarbon formed in a series of selected solvents, including halogenated solvents. Table 8.2 gives the amounts of pyrocarbon formed by arcing with graphite electrodes and using 50 ml of each selected solvent under our standard arcing conditions at 10 A for 6 min. The anomaly is the high formation rate of pyrocarbon when any halogenated solvents are arced.

TABLE 8.2
Coke Formation Rate in the Electric Carbon Arc

Solvent	Coke Formation Rate (mg/h at 10 A ARC)
CCl_4	636
CHCl_3	735
CH_2Cl_2	347
CH_2I_2	319
CH_3I	not determined
Methanol	7
Ethanol	10
<i>n</i> -propanol	14
<i>n</i> -heptane	43
<i>n</i> -octane	47
Decahydronaphthalene	62

In CCl_4 and CHCl_3 the high formation rate of pyrocarbon is accompanied by the complete absence of polyne formation in the respective solutions checked by the HPLC–DAD. No PAHs were found: only a mixture of halogenated derivatives. Evidently, the large amount of Cl radicals produced by the plasmalysis of these solvents is sufficient to easily chlorinate the polyne chains or to cause their cyclization into other products. The results of these experiments are discussed in more detail in Reference 48.

8.4 CONCLUSIONS

The synthesis of polyynes with the submerged electric arc has been described, with the emphasis on the experimental approach. The synthesis is relatively simple, economic, and promising for further developments.

The kinetics of polyynes production with the submerged carbon arc appears linear with the arcing time and the amount of current or energy (power) supplied to the reaction system.

The best analytical technique for detecting polyynes is HPLC coupled with a diode array detector (DAD). The polyynes are easily and effectively separated on a C8 column with a mobile phase of acetonitrile/water, 80/20, vol/vol. The effectiveness of this technique is due to the peculiarity of the polyynes electronic absorption spectra coupled with very high molar extinction coefficients. HPLC–DAD analysis has revealed that, in all cases, the polyne C_8H_2 is dominant (Table 8.1) and this is in agreement with the results of Tsuji and colleagues (see Chapter 7) who have found the same results on the production of polyynes by laser. The reason why C_8H_2 is produced in larger amounts in comparison to its lower homologs is unclear at present but the fact that the higher homologs of C_8H_2 are gradually less abundant as the chain length increases is quite expected.

The polyynes produced by arcing graphite electrodes in hydrocarbons or alcohols are all hydrogen terminated. This has been demonstrated by the reactivity of the polyynes with a specific reagent, with the consequent formation of the respective copper acetylides, with FT–IR spectroscopy, which has shown the presence of the $-\text{C}\equiv\text{C}-\text{H}$ stretching band at 3312 cm^{-1} and by the band pattern of the electronic absorption spectra of the individual polyynes species, which match the published data.

The graphite electrodes play a key role in the generation of polyynes. Elemental carbon is released from the electrode surface during arcing due to the electrons bombarding the graphite surface and the very high temperature reached (about 4000°). Simultaneously, the hydrogen is supplied by the plasmalysis of the solvent. The production rate of polyynes is enhanced significantly when hydrogen-donor solvents are used, such as decahydronaphthalene. Secondary products of the submerged electric arc are represented by the formation of PAHs (polycyclic aromatic hydrocarbons) and by the formation of pyrocarbon or coke. Based on the data available, it

appears that both PAHs and pyrocarbon are essentially formed from the plasmalysis of the solvent. When halogenated solvents are employed in the carbon arc in place of hydrocarbons or alcohols no polyyynes and PAHs are formed but only halogenated products. The formation rate of pyrocarbon becomes extremely high in comparison to other solvents (see Table 8.2).

Arcing titanium electrodes in alcohols in place of graphite electrodes causes complete suppression in the formation of any polyyne. Only PAHs produced from the pyrolysis of the solvents are obtained. This fact demonstrates the key role played by the graphite electrodes in supplying the elemental carbon for the formation of the polyyynes.

ACKNOWLEDGMENTS

ASI, the Italian Space Agency, is gratefully acknowledged for financial support of this work under grant I/R/070/02. Discussions with W. Kraetschmer, L. Kavan, and P. Milani are gratefully acknowledged.

REFERENCES

- [1] Heat JR. In: *Fullerenes. Synthesis, Properties and Chemistry of Large Carbon Clusters*. Edited by Hammond GS and Kuck VJ. ACS Symposium Series 481, American Chemical Society, Washington DC, 1992, Chapter 1.
- [2] Kroto HW, Walton DRM. Polyyynes and the formation of fullerenes. *Phil. Trans. R. Soc. Lond. A* **1993**, 343, 103.
- [3] Rubin Y, Parker TC, Salvador JP, Jalisatgi S, Boulle C, Wilkins CL. Acetylenic cyclophanes as fullerene precursors: formation of $C_{60}H_6$ and C_{60} by laser desorption mass spectrometry of $C_{60}H_6(CO)_{12}$. *Angew. Chem. Int. Ed. Engl.* **1998**, 37, 1126.
- [4] Goroff NS. Mechanism of fullerene formation. *Acc. Chem. Res.* **1996**, 29, 77.
- [5] Krestinin AV, Moravsky AP. Mechanism of fullerene synthesis in the arc reactor. *Chem. Phys. Lett.* **1998**, 286, 479.
- [6] Churilov GN, Novikov PV, Tarabanko VE, Lopatin VA, Vnukova NG, Bulina NV. On the mechanism of fullerene formation in a carbon plasma. *Carbon* **2002**, 40, 891.
- [7] Alekseev NI, Dyuzhev GA. Evolution of carbon from atomic clusters to fullerenes. *Technical Physics* **2002**, 47, 634 and 637.
- [8] Zhu HW, Li XS, Jiang B, Xu CL, Zhu YF, Wu DH, Chen XH. Formation of carbon nanotubes in water by the electric arc technique. *Chem. Phys. Lett.* **2002**, 366, 664–669.
- [9] Lange H, Sioda M, Huczko A, Zhu YQ, Kroto HW, Walton DRM. Nanocarbon production by arc discharge in water. *Carbon* **2003**, 41, 1617.
- [10] Murakami Y, Miyauchi Y, Shoei C, Maruyama S. Characterization of single-walled carbon nanotubes catalytically synthesized from alcohol. *Chem. Phys. Lett.* **2003**, 34, 53.
- [11] Wang H, Chhowalla M, Sano N, Jia S, Amaratunga GAJ. Large-scale synthesis of single-walled carbon nanohorns by submerged electric arc. *Nanotechnology* **2004**, 15, 546.

- [12] Krestinin AV. Detailed modelling of soot formation in hydrocarbon pyrolysis. *Combustion & Flame* **2000**, 121, 513.
- [13] Steglich W, Fugmann B, Lang-Fugmann S. *Rompp Encyclopedia of Natural Products*. Georg Thieme Verlag, Stuttgart, 2000.
- [14] Kroto HW. C₆₀ buckminsterfullerene, the celestial sphere that fell to Earth. *Angew. Chem. Int. Ed. Engl.* **1992**, 31, 111.
- [15] Maier JP, Walker GAH, Bohlender DA. On the possible role of carbon chains as carriers of diffuse interstellar bands. *Astrophys. J.* **2004**, 602, 286.
- [16] Fulara J, Krelowski J. Origin of diffuse interstellar bands: spectroscopic studies of their possible carriers. *New Astron. Rev.* **2000**, 44, 581.
- [17] Duley WW, Williams DA. Interstellar polyyne from the disruption of carbon grains. *Mon. Not. R. Astr. Soc.* **1984**, 211, 97.
- [18] Raulin F, Coll P, Smith N, Benilan Y, Bruston P, Gazeau MC. New insights into Titan's organic chemistry in the gas and aerosol phases. *Adv. Space Res.* **1999**, 24, 453.
- [19] Wilson EH, Atreya SK. Chemical sources of haze formation in Titan's atmosphere. *Planetary and Space Sci.* **2003**, 51, 1017.
- [20] Vuitton V, Scemama A, Gazeau MC, Chaquin P, Benilan Y. IR and UV spectroscopic data for polyyne: prediction for long carbon chain compounds in Titan's atmosphere. *Adv. Space Res.* **2001**, 27, 283.
- [21] Formenkova MN. On the refractory components of cometary dust. *Space Sci. Rev.* **1999**, 90, 109.
- [22] Schwab PHF, Levin MD, Michl J. Molecular rods. 1. Simple axial rods. *Chem. Rev.* **1999**, 99, 1863.
- [23] Eastmond R, Johnson TR, Walton DRM. Silylation as a protective method for terminal alkynes in oxidative couplings. A general synthesis of the parent polyyne H(C≡C)_nH (*n* = 4–10,12). *Tetrahedron* **1972**, 28, 4601.
- [24] Gibtner Th, Hampel F, Gisselbrecht JP, Hirsch A. End-cap stabilized oligoynes: model compounds for the linear sp carbon allotrope carbyne. *Chem. Eur. J.* **2002**, 8, 408 (and ref. cited therein).
- [25] Hlavaty J, Kavan L, Kubista J. Carbonaceous materials from end-capped carbynes. *Carbon* **2002**, 40, 345.
- [26] Hlavaty J, Kavan L, Okabe K, Oya A. Carbonaceous polymers and nanotubes from α - ω hexatriynides. *Carbon* **2002**, 40, 1131.
- [27] Bartik T, Bartik B, Brady M, Dembinski R, Gladysz JA. A step-growth approach to metal-capped one-dimensional carbon allotropes: Synthese of C₁₂, C₁₆ and C₂₀ μ -polyynediyl complexes. *Angew. Chem. Int. Ed. Engl.* **1996**, 35, 414.
- [28] Hintenberger H, von Franzen J, Schuy KD. Die periodizitäten in den häufigkeitsverteilungen der positiv und negativ geladenen vielatomigen kohlenstoffmolekulonen C_n⁺ und C_n⁻ im hochfrequenzfunken zwischen graphitelektroden. *Zeitschrift für Naturforschung* **1963**, A18, 1236.
- [29] Heath JR, Zhang Q, O'Brien SC, Curl RF, Kroto HW, Smalley RE. The formation of long carbon chain molecules during laser vaporization of graphite. *J. Am. Chem. Soc.*, **1987**, 109, 359.
- [30] Tsuji M, Tsuji T, Kuboyama S, Yoon SH, Korai Y, Tsujimoto T, Kubo K, Mori A, Mochida I. Formation of hydrogen-capped polyyne by laser ablation of graphite particles suspended in solution. *Chem. Phys. Lett.* **2002**, 355, 101.

- [31] Tsuji M, Kuboyama S, Matsuzaki T, Tsuji T. Formation of hydrogen-capped polyyynes by laser ablation of C₆₀ particles suspended in solution. *Carbon* **2003**, *41*, 2141.
- [32] Cataldo F. Simple generation and detection of polyyynes in an arc discharge between graphite electrodes submerged in various solvents. *Carbon* **2003**, *41*, 2671.
- [33] Cataldo F. Synthesis of polyyynes in a submerged electric arc in organic solvents. *Carbon* **2004**, *42*, 129.
- [34] Cataldo F. Polyyynes production in a solvent-submerged electric arc between graphite electrodes. 1. Synthesis and Spectroscopy. *Fullerenes, Nanotubes and Carbon Nanostructures* **2004**, *12*, 603.
- [35] Cataldo F. Polyyynes production in a solvent-submerged electric arc between graphite electrodes. 2. Analysis by liquid chromatography. *Fullerenes, Nanotubes and Carbon Nanostructures* **2004**, *12*, 619.
- [36] Cataldo F. Polyyynes production in a solvent-submerged electric arc between graphite electrodes. 3. Chemical reactivity and stability toward air, ozone and light. *Fullerenes, Nanotubes and Carbon Nanostructures* **2004**, *12*, 633.
- [37] Cataldo F. Submerged electric arc between graphite electrodes: a one-pot tool for the synthesis of long chain polyyynes in solution. *Tetrahedron Lett.* **2004**, *45*, 141.
- [38] Cataldo F. Polyyynes and cyanopolyyynes synthesis from the submerged electric arc: about the role played by the electrodes and solvents in polyyynes formation. *Tetrahedron* **2004**, *60*, 4265.
- [39] Cataldo F. Polyyynes: a new class of carbon allotropes. About the formation of dicyanopolyyynes from an electric arc between graphite electrodes in liquid nitrogen. *Polyhedron* **2004**, *23*, 1889.
- [40] Gillam AE, Stern ES, Jones ERH. *An Introduction to Electronic Absorption Spectroscopy in Organic Chemistry*. Edward Arnold Publishers Ltd, London, 1954, pp. 78–79.
- [41] Perkampus HH. *UV–VIS Atlas of Organic Compounds*. 2nd edition, VCH-Weinheim, 1992, Table A12T1.
- [42] Kalachnikov S. *Electricité*. Mir Editions, Moscow, 1983.
- [43] Cataldo, F. Ultrasound-induced cracking and pyrolysis of some aromatic and naphthenic hydrocarbons. *Ultrasonics Sonochemistry* **2000**, *7*, 35.
- [44] Beck MT, Dinya Z, Keki S. Formation of polycyclic aromatic compounds upon electric discharges in liquid toluene. *Tetrahedron* **1992**, *48*, 4919.
- [45] Beck MT, Dinya Z, Keki S, Papp L. Formation of C₆₀ and polycyclic aromatic hydrocarbons upon electric discharges in liquid toluene. *Tetrahedron* **1993**, *49*, 285.
- [46] Beck MT, Dinya Z, Dombi A, Fetzer JC, Keki S, Papp L, Szabò P, Szepevolgy J, Zsuga M. *Proceedings of the Symposium Recent Advances in the Chemistry and Physics of Fullerenes and Related Materials*. Edited by Kadish KM and Ruoff RS. The Electrochemical Society Inc., Pennington, NJ, USA, 1994.
- [47] Zhorov Yu. M. Thermodynamics of Chemical Processes. In: *Petrochemical Synthesis, Processing of Petroleum, Coal and Natural Gas*. Mir Editions, Moscow, 1987, p. 166 and 243.
- [48] Cataldo, F. Soot and other products formation from the submerged electric arc in halogenated solvents. *Fullerenes, Nanotubes and Carbon Nanostructures* **2005**, *13*(4) (in press).

9 Polyynes ($C_{2n}H_2$, $n=2-5$) and Other Products from Laser-Ablated Graphite: A Time-of-Flight Mass Spectroscopic Study in Combination with One-Photon Ionization

*Tomonari Wakabayashi, Yoshiyasu Kato,
Takamasa Momose and Tadamasa Shida*

CONTENTS

9.1	Introductory Remarks.....	182
9.2	Outline of the Study	182
9.3	Experimental	183
9.4	Results	185
9.4.1	Comparison of One-Photon and Multi-Photon Ionization in the He Buffer Gas	185
9.4.2	One-Photon Ionization in the H_2 Buffer Gas	187
9.4.3	Effect of Ablation Laser Power on the Mass Spectral Pattern	191
9.4.4	Structure and Formation Mechanism of the Ablated Products	193
9.5	Concluding Remarks	193
	Acknowledgment	194
	References	194

9.1 INTRODUCTORY REMARKS

Polyynes and other novel carbonaceous molecules are worthy of thorough studies from the viewpoint of both pure and applied sciences. Thus, they are investigated in various fields such as molecular spectroscopy, combustion chemistry, material sciences, and interstellar chemistry. They are produced under various conditions as described in other chapters of this book. In this chapter we will present the results of our study by time-of-flight mass spectroscopy of the title molecules to obtain insights into some aspects of their formation and stability in the gas phase.

9.2 OUTLINE OF THE STUDY

Laser ablation of graphite in buffer gases as well as in a vacuum has been employed to study carbon clusters and their derivatives. To mention a few examples, ablated emissive products are studied by emission spectroscopy [1,2] and by fast ICCD photography [2]. Also, ions directly produced by ablation are studied by mass spectroscopy [3–6]. All these techniques, however, are insensitive to neutral species in the ground electronic state, which are supposedly the most abundant products of ablation. For the study of these non-emissive neutral species, time-of-flight (TOF) mass spectroscopy is combined with photoionization techniques. Most of these studies employed the multi-photon ionization (MPI) technique with intense lasers of a photon energy lower than the ionization energy of ablated products [7–11]. The MPI technique is powerful for ionization but is plagued by extensive fragmentation of nascent neutral products due to the strong electric field of multiple photons. To get information on the ablated products as intact as possible, one-photon ionization is preferable to MPI, provided that the photon energy of the former is high enough to ionize ablated products by one-photon absorption with the intensity being moderate enough to prevent the extensive fragmentation [12–18].

Such a one-photon ionization was performed with the use of photons of 10.5 eV/photon (= 118 nm), that is, the ninth harmonics of the fundamental radiation of a Nd:YAG laser [14]. At this photon energy a considerable number of ablated products can be one-photon ionized.

Using the same technique we have been studying TOF mass spectra of neutral products which are laser-ablated from graphite [15–18]. In our studies we mainly monitored the change of TOF mass spectra as a function of the time interval between the ablation laser pulse and the one-photon ionizing laser pulse. This time interval will be called, synonymously, “delay time”, for convenience. The observed dependence of the mass spectra on the delay time has provided us with information on the formation and stability of some products.

To be specific, we have detected mass peaks corresponding to the chemical formula of C_n with $n \geq 6$ in the He buffer gas, whereas, in the H_2 gas, hydrocarbons of C_nH_m with $n \geq 4$ and $m = 1-4$ were detected in addition to the bare carbon clusters. All these products were observed when the delay time was shorter than, say, about a few tens of microseconds in the present work. At longer delay times, on the other hand, only a few specific products were detected, namely, $C_{2n}H_2$ with $n = 2-5$ and C_{10} . The detection of these products, long after the ablation pulse was over, means that they somehow continued to reach the ionization region.

Moreover, these long-lived products arrived at the ionization region with three different velocities, that is, with fast (I), intermediate (II), and slow (III) components. From these findings we have concluded that $C_{2n}H_2$ and C_{10} were formed by a time-taking process and/or survive due to chemical inertness and to robustness against destructive collisions as compared with other products.

Such a chemical and physical robustness suggests a polyynic form, $H-(C \equiv C)_n-H$, in the case of $C_{2n}H_2$ and a monocyclic form in the case of C_{10} . The separation into three components with different velocities will be considered in terms of their behavior during the period between the ablation and the ionization in the buffer gas.

Besides the dihydrides stated above there was another type of hydrocarbons disappearing as fast as component I of the dihydrides. These hydrocarbons have a common chemical formula of $C_{2n+1}H_m$ with $m = 1-4$, which are plausibly associated with cumulenes of a form of $:C=C=(C=C)_{n-1}C:$, the four electrons to be attacked one by one by incoming hydrogen atoms.

In order to find a clue to the mechanism of the formation of the hydrocarbons stated above, we have studied the dependence of the TOF mass spectral pattern upon the power of the ablation laser. As a result, it will be proposed that the hydrocarbons are formed by reactions between large carbon clusters C_n ($n \gg 10$) and hydrogen atoms which are produced from the buffer hydrogen gas thermally dissociated in the intense field of the ablation laser.

9.3 EXPERIMENTAL

The apparatus for the TOF mass spectroscopic measurement is shown schematically in Figure 9.1. A rotating graphite rod (1 cm in diameter, $^{12}C: ^{13}C = 98.9\%:1.1\%$) was ablated in a vacuum chamber by the second harmonics of a Q-switched Nd:YAG laser (Spectra-Physics DCR-11, 532 nm, 7 ns duration, 7.1 mJ/pulse). The ablation laser pulse was loosely focused with a lens of a focal length of 25 cm. The ablated products were introduced into the ionization region by a pulsed buffer gas flow of H_2/He . The back-pressure of the buffer gases was set at 15 atm (1.52×10^6 Pa) to

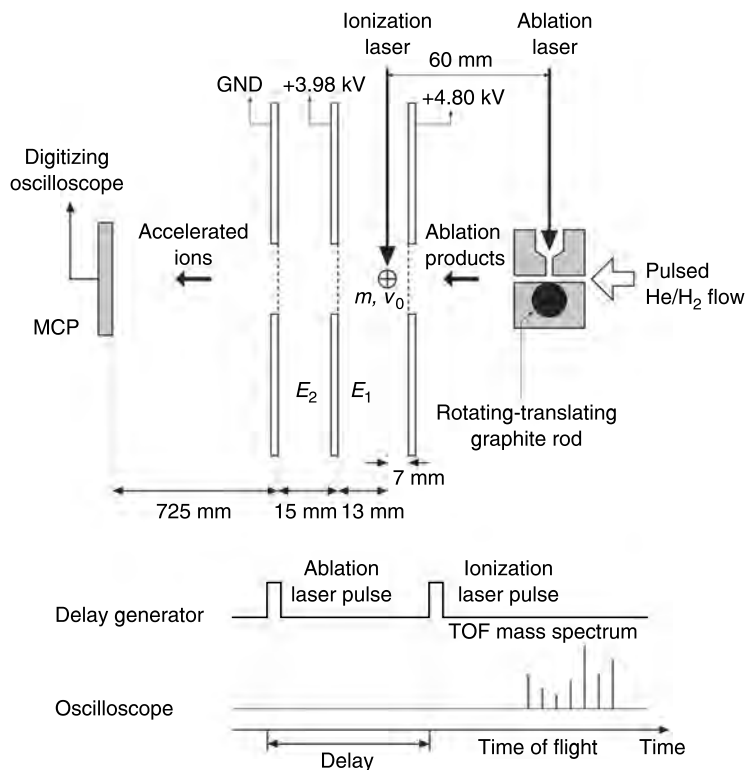


FIGURE 9.1 Upper: A schematic set-up of the TOF mass experiment. Lower: Time sequence of measurements.

maximize the intensity of mass signal. The pressures of the vacuum chamber without and with the buffer gas were about 1×10^{-7} Torr (1.3×10^{-5} Pa) and about 1×10^{-6} Torr (1.3×10^{-4} Pa), respectively.

The ablated products were ionized by pulsed photons of 10.5 eV/photon (=118 nm) 60 mm downstream from the ablation spot. The 10.5 eV photon was generated as the third harmonics of 355 nm radiation in a Xe gas cell [19,20]. The cell was made of stainless steel (2 cm in diameter, 20 cm in length). The third harmonics of a Q-switched Nd:YAG laser (Continuum Powerlite 8010, 5 ns pulse width, 150 mJ/pulse) was tightly focused into the cell filled with 16 Torr of Xe gas by a CaF₂ lens ($f=10$ cm at 355 nm) to generate the 10.5 eV photons. The photons thus generated were paralleled by an LiF lens ($f=10$ cm at 118 nm), and then separated from the 355 nm radiation by an LiF prism before being introduced into the ionization region through an 8 mm diameter aperture. The power of the 10.5 eV photons was weak enough so that only single photonic ionization occurred in the ionization region.

Products ionized by the 10.5 eV photons were accelerated with static electric fields created by three plates whose voltages were kept at +4.80 kV, +3.98 kV, and 0 V, respectively, as shown in Figure 9.1. The distances between the first and second electrodes and the second and third electrodes were 2 cm and 1.5 cm, respectively. The accelerated ions were detected by MCPs (multi-channel plates, Galileo 6205) placed at 75.3 cm downstream from the ionization point. The signals detected by the MCPs were recorded with a digitizing oscilloscope (Tektronix TDS544A) and plotted as a function of time to obtain TOF mass spectra. All the measurements were carried out at a repetition rate of 10 Hz.

The time sequence of the ablation pulse, the ionization pulse, and the recording of TOF signals by the detector is shown in the lower part of Figure 9.1. Spectra were recorded for various time intervals between the ablation and ionization pulses. These time intervals are called delay times as stated in Section 9.2 (see Figure 9.1). The timings of all the instruments were controlled by delay generators (Stanford Research Systems DG535).

9.4 RESULTS

9.4.1 COMPARISON OF ONE-PHOTON AND MULTI-PHOTON IONIZATION IN THE He BUFFER GAS

In order to investigate intact neutral ablated products one has to ionize the molecules as gently as possible to avoid secondary decomposition by laser. In this sense, often used MPI techniques are not suited, as mentioned briefly in Section 9.2; intense electric fields of MPI pulses tend to cause extensive fragmentation of the ablated products. Moreover, accidental resonance enhancement of some specific mass peaks may distort the true mass distribution pattern.

An example of the difference in the effect of one-photon ionization (1PI) and MPI can be seen from the two mass spectra in Figure 9.2, which were obtained by using the ninth harmonics of a Nd:YAG laser ($118\text{ nm} = 10.5\text{ eV/photon}$) for 1PI and by using the third harmonics of a Nd:YAG laser ($355\text{ nm} = 3.5\text{ eV/photon}$) for MPI in the He buffer gas.

The energy of 10.5 eV/photon can ionize all the carbon clusters C_n with $n \geq 6$ by a single photon, as is shown in Figure 9.3 (see also Figure 9.2 of Reference 17). The TOF mass pattern obtained by 1PI showed an intensity distribution of products peaking at about the cluster size n of C_n equal 10. Larger clusters up to C_{80} were detected, but the signal intensities of the larger carbon clusters were 100 times smaller than the signal of C_{10} . It is noted that both even-numbered clusters and odd-numbered clusters were detected as the products of larger n values, as is seen in the inset of the right

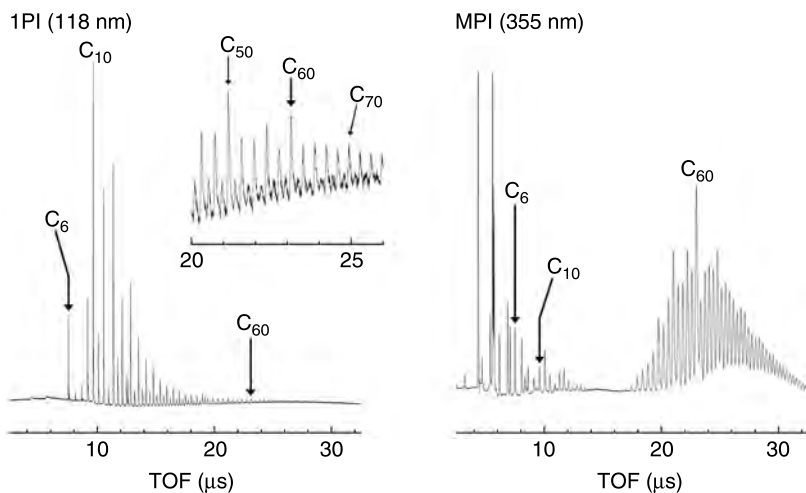


FIGURE 9.2 Comparison of TOF mass spectra obtained by one-photon ionization (1PI) and multi-photon ionization (MPI) of laser ablated graphite in the He buffer gas.

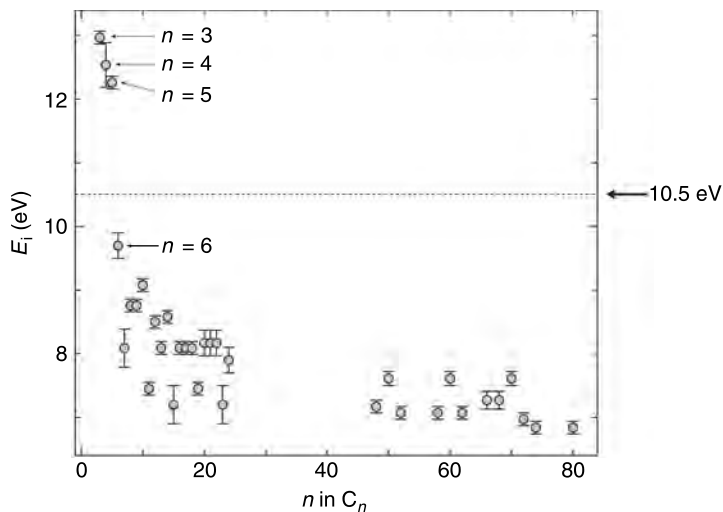


FIGURE 9.3 Ionization energies (E_i) of carbon clusters plotted as a function of the carbon number (n). The horizontal line indicates the energy of the ninth harmonics of a Nd:YAG laser.

panel of Figure 9.2, although the intensity of the odd-numbered clusters were weak compared with those of the even-numbered clusters.

In contrast, the TOF mass pattern obtained by MPI with the use of the third harmonics of a Nd:YAG laser ($355\text{ nm} = 3.5\text{ eV/photon}$) showed a bimodal distribution of products separated at about the cluster size n of C_n equal 30. Products of larger n values are known to have only even numbers of the carbon atom. This clear difference between the right and left panels of Figure 9.2 indicates that the mass spectral pattern obtained by MPI, especially clusters larger than C_{30} , must be attributed to fragmentation of precursory larger clusters ($n \gg 100$) due to intense ionization laser fields.

9.4.2 ONE-PHOTON IONIZATION IN THE H_2 BUFFER GAS

Since we are interested in possible formation of hydrogenated carbons in the present work, we now switch the buffer gas from He to H_2 expecting formation of polyynes and other novel hydrocarbons. The mass spectrum at the bottom of Figure 9.4 was obtained in the H_2 buffer gas for a delay time of $35\text{ }\mu\text{s}$. There are several points to note in this spectrum, which are as follows.

Most peaks disappeared quickly as the delay time was changed from $35\text{ }\mu\text{s}$ to $55\text{ }\mu\text{s}$ (note the amplification factor of 20 and 40 for the delay times of $55\text{ }\mu\text{s}$ and on).

As the bottom spectrum shows, two types of species, *i.e.* C_n ($n \geq 6$) and C_nH_m ($n \geq 4$, $m = 1-4$) were observed whose ionization energies are lower than the photon energy of 10.5 eV . The absence of C_4 , C_5 , and C_4H , whose ionization energies exceed the photon energy of 10.5 eV , supports the presumption that in the present work only one-photon ionization, but not MPI, took place which is favorable for the study of ablated neutral products.

As is seen from the bottom spectrum, hydrocarbon peaks corresponding to C_nH_m ($n \geq 4$) were absent for $m \geq 5$. In addition, the relative intensity of four to five peaks belonging to the family containing the same number of carbon atoms did not vary drastically for odd numbers ($n = 5-15$), whereas species containing carbon atoms of even numbers showed a prominent intensity for $C_{2n}H_2$ ($2n = 4-14$). These results will be consistently accounted for in terms of favored formation of polyynic and cumulenic species.

As the three spectra for the delay times between $65\text{ }\mu\text{s}$ and $8000\text{ }\mu\text{s}$ in Figure 9.4 show, only the peaks of C_4H_2 , C_6H_2 , C_8H_2 , $C_{10}H_2$, and C_{10} were discernible. They reveal a splitting into two as indicated by vertical dotted lines in Figure 9.4. However, as shown in Figure 9.5, closer examination revealed that the splitting was actually into three components for one and the same mass, which can be rephrased that there were a fast (I), an intermediate (II), and a slow (III) component. This splitting will be further examined in Figure 9.5.

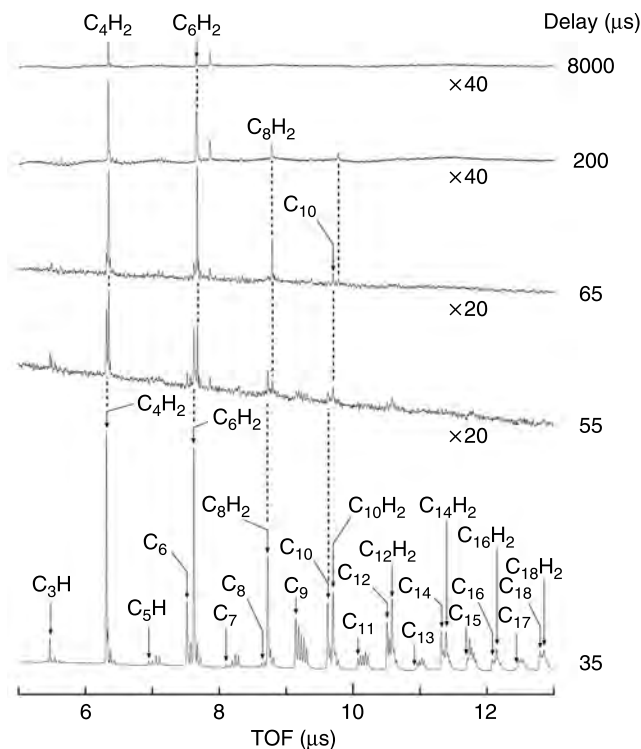


FIGURE 9.4 Mass spectra of laser ablated graphite in the H_2 buffer gas. One-photon ionization with 10.5 eV/photon. Delay times (μs) are shown to the right. Spectra observed at 55 and 65 μs are expanded by a factor of 20 and those at 200 and 8000 μs by 40. TOF mass peak assignment is given in the bottom spectrum. Vertical dotted lines are to assist reading the subtle but significant shift of the peaks.

Notice that the upper four spectra of Figure 9.4 show a quick disappearance of most of the TOF mass peaks as the delay time was increased from the shortest of 35 μs . The rapid disappearance at longer delay times implies that the neutral products giving the disappearing TOF mass peaks passed the ionization region before the ionizing laser was fired, which, in turn, implies a faster initial velocity of the products when they entered the ionization region.

The relationship between the initial velocity of the incoming neutral species and the TOF for the ionized species to reach the MCP detector is well known for the set-up shown in Figure 9.1, which is known as the Wiley–McLaren-type TOF mass spectrometer [21]. The right and left ordinates of the lower panel of Figure 9.6 show the relationship between the initial velocity and the flight time under our experimental set-up. Detailed discussion on the relation will be made elsewhere [18]. Instead, we will focus on

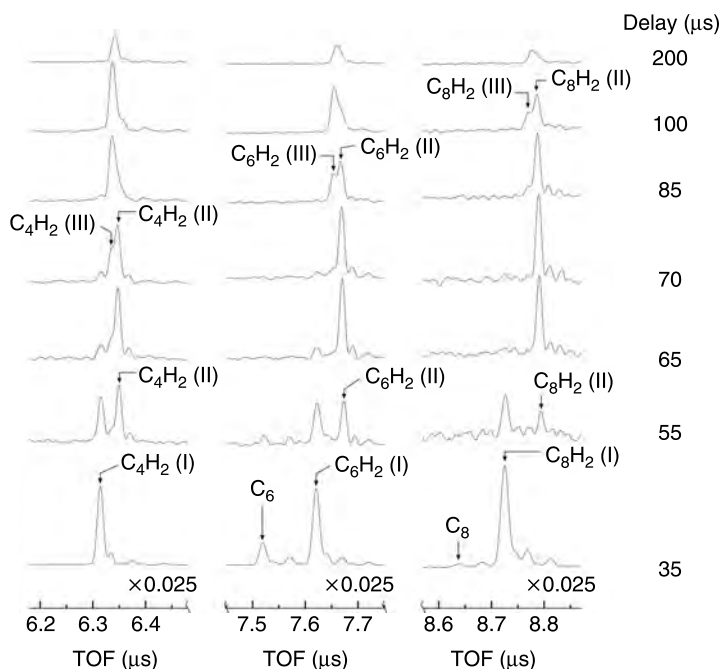


FIGURE 9.5 Expansion of Figure 9.4 for C_4H_2 (left), C_6 and C_6H_2 (middle), and C_8 and C_8H_2 (right). Delay times (μs) are shown to the right. Spectra at delay time of $35 \mu s$ are reduced by a factor of 0.025. Symbols (I, II, and III) correspond to the fast, intermediate, and slow components, respectively.

the long-lived species seen in the mass spectra obtained for the delay times of $55-8000 \mu s$ (see Figure 9.4).

Figure 9.5 shows the spectral region of our interest which is an expansion of Figure 9.4. Note that the strong signal observed for the delay time of $35 \mu s$ is greatly reduced in Figure 9.5 for the convenience of comparison with the other spectra (note the multiplication factor of $\times 0.025$ in the bottom spectra).

As designated in Figure 9.5, the apparently complicated spectra are attributed to the three dihydrides C_4H_2 , C_6H_2 , and C_8H_2 having different velocity component: I–III. That the observed spectra can be associated with the same dihydrides has been examined preliminarily by comparison of the result of using D_2 gas instead of H_2 as the buffer gas, because mass peaks of monodeuterated $^{12}C_nD$ could be clearly distinguished from the peak of the isotopomer $^{13}C^{12}C_{n-1}$ [17].

Here, all three components are interpreted as follows: the laser-ablated plume containing $C_{2n}H_2$ expands adiabatically immediately after the ablation. Most of them are first brought into the ionization region without

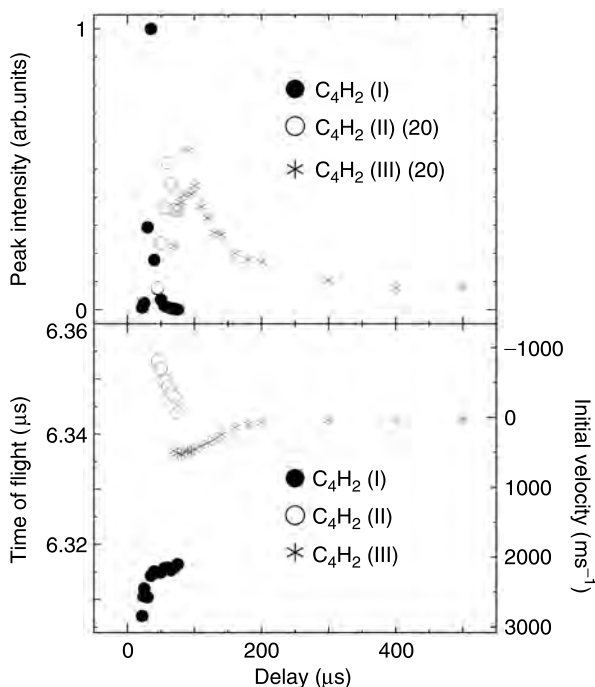


FIGURE 9.6 Changes of the TOF mass peak intensity (top) and shifts of TOF (bottom) of C_4H_2 as a function of the delay time. The products were ionized by one-photon in the H_2 buffer gas. The three components (I, II, and III) are differentiated by closed circles, open circles, and asterisks, respectively. Peak intensities of II and III are multiplied by a factor of 20 for legibility.

significant perturbation by the flowing H_2 buffer gas. Thus, they are attributed to the fast component (I) of the smallest TOF among the three. The closed circles in Figure 9.6 correspond to this component.

Some of the expanding $C_{2n}H_2$ molecules, however, may be scattered backward or retarded as a result of the turbulence during the expansion of the buffer gas. They are attributed to the intermediate component (II) having a negative velocity component. The open circles in Figure 9.6 correspond to this component.

As the slow component (III) appears last, it is considered to be the neutral species that lingers on the graphite surface and leaves the surface only after repeated collisions with the pushing H_2 gas flow. The existence of this last component has been studied in detail as the product of laser ablation [22].

In the intermediate component (II) and the slow component (III), ablated products are subjected to heavy collisions with the buffer gas and/or

other products. Thus, the species in components II and III must be robust and/or chemically inactive.

9.4.3 EFFECT OF ABLATION LASER POWER ON THE MASS SPECTRAL PATTERN

In an attempt to identify these long-lived species we examined the effect of varying ablation laser power on the mass spectral pattern. Figures 9.7 and 9.8 demonstrate the result of experiments using laser powers of 4.0 mJ/pulse and 7.1 mJ/pulse. Figure 9.8 is essentially the same as Figure 9.4, but is reproduced for ease of comparison with Figure 9.7, which shows the result for the laser power reduced from 7.1 mJ/pulse to 4.0 mJ/pulse. The comparison reveals the following features. First, at a delay time of 35 μ s the reduction of the power suppressed all the peaks, but the suppression of the bared carbon clusters was relatively small. Second, the persistence of the dihydrides and C_{10} was observed for the run of the reduced power, as in the case of the power at 7.1 mJ/pulse.

If the observed dihydrides ($C_{2n}H_2$) were formed by reactions of the observed C_{2n} with the buffer gas, the peaks of C_{2n} for the run of the power at 7.1 mJ/pulse would be noticeably increased in conformity with the observed enhancement of $C_{2n}H_2$. Since there seems no such correlation, the carbon atoms constituting the dihydrides have to originate from carbon clusters larger than those recorded in the spectra.

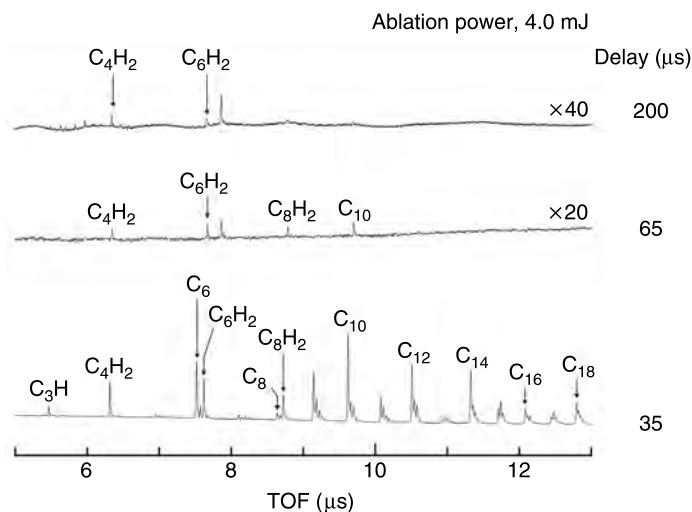


FIGURE 9.7 TOF mass spectra observed similarly to those in Figures 9.4 and 9.8 but with a reduced ablation laser power.

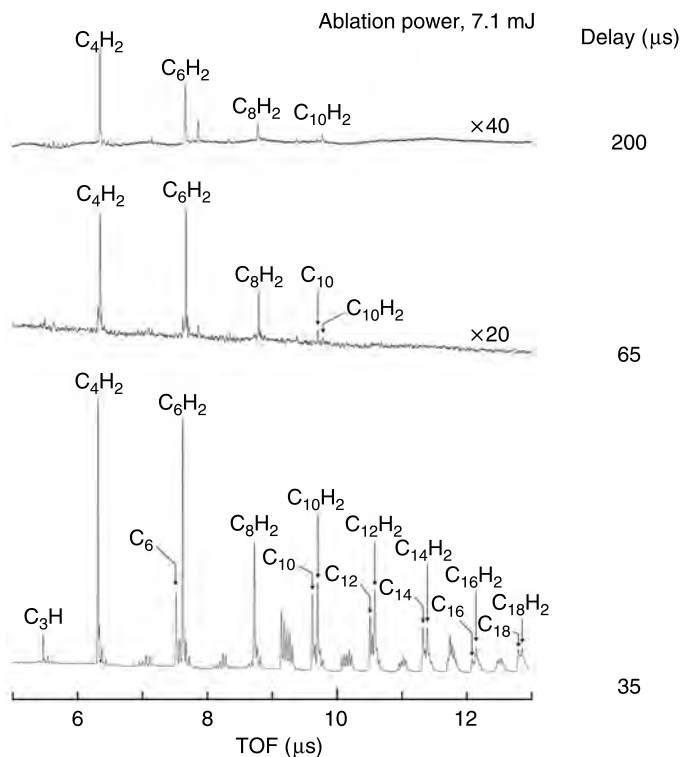


FIGURE 9.8 Reproduction of [Figure 9.4](#) with a slight change for the convenience with [Figure 9.7](#).

It is known that hydrogen molecules are decomposed thermally into hydrogen atoms under intense pulses of ablation laser. In addition, it is known that the formation of larger clusters, say, C_n ($n > 30$), is favored with the increase in the ablation laser power. Therefore, it is concluded that the hydrocarbons were formed by reactions between the larger carbon clusters and the hydrogen atoms which were produced from the buffer hydrogen gas thermally dissociated in the intense field of the ablation laser. On the other hand, the drastic increase in the production of the dihydrides at higher laser power indicates that hydrogen molecules are regarded as less effective in the production of the hydrocarbons than the hydrogen atoms.

Figure 9.8 (bottom spectrum) shows clearly that the hydrocarbons of the type of $C_{2n+1}H_m$ were limited only to those with $m = 1-4$. The step-wise addition of four hydrogen atoms indicates that the hydrocarbons were formed by reactions with hydrogen atoms thermally dissociated in the stronger field of ablation laser.

9.4.4 STRUCTURE AND FORMATION MECHANISM OF THE ABLATED PRODUCTS

The fact that no hydrogen adducts with $m \geq 5$ were observed suggests strongly a cumulenic carbon skeleton of $:C=C=(C=C=)_{n-1}C$: as stated in Section 9.2. Furthermore, the absence of the adducts with $m \geq 5$ implies that the hydrogen atoms attack selectively the two terminal carbon atoms only; that is to say, the cumulenic double bond refuses the addition of hydrogen atom to yield hydrocarbons with more than four hydrogen atoms.

Figure 9.8 (bottom spectrum) shows that the hydrocarbons of the type of $C_{2n}H_m$ were also limited only to those with $m=1-4$ with a definite abundance of $C_{2n}H_2$. The fact is most naturally explained by assuming that the carbon skeleton in $C_{2n}H_2$ is polyynic as stated briefly in Section 9.2. The absence of $C_{2n}H_m$ with $m \geq 5$ suggests that the third and fourth hydrogen atoms in $C_{2n}H_m$ attached only to the two terminal carbon atoms as in the case of the cumulenic system considered above.

Such a terminal addition to a polyynic should yield the ethylenic end, $=CH_2$. In between the two ends, highly conjugative carbon chains of C_{2n-2} with $n=1, 2, 3, \dots$ should result. Like in the case of the cumulenic system, the absence of $C_{2n}H_m$ with $m \geq 5$ suggests that the above-stated conjugative carbon chains appear to refuse the addition of further hydrogen atoms to yield hydrocarbons with more than four hydrogen atoms. Also, as in the case of the cumulenic system, it is obvious that hydrogen atoms, but not hydrogen molecules, participate in the formation of $C_{2n}H_m$.

The remarkable longevity of the dihydrides $C_{2n}H_2$ and C_{10} is most noteworthy. Radi et al. discussed the possibility of a preferential ejection of C_{10} from large clusters [23]. This is consistent with the above-stated conjecture that the dihydrides in the present study originate from the fragmentation of large carbon clusters. Since both the assumed polyynic dihydrides and C_{10} must be subjected to collisions with the buffer gas molecules, hydrogen atoms, and other products during the period between the ablation and the ionization, both the dihydrides and C_{10} must be physically and/or chemically robust.

The stability of C_{10} suggests a monocyclic form because linear C_{10} , whether cumulenic or polyynic, must be subjected to the attack by hydrogen atoms according to the discussion stated above. More convincing evidence for the cyclic form is desired, however.

9.5 CONCLUDING REMARKS

This treatise presents a new approach for the study of $C_{2n}H_2$ which are most plausibly polyynic in view of their relative stability against chemical reactions and collisions. Although the details of the formation mechanism of the dihydrides and the structural information of the proposed monocyclic

C₁₀ are yet to be studied, the result presented in this work clearly shows the remarkable stability of the two types of neutral products from the laser ablated graphite in the hydrogen buffer gas.

ACKNOWLEDGMENT

This work was supported by Grants in Aid from the Ministry of Education, Sports, Culture, Science and Technology of Japan, and by a project in CREST of the Japan Science and Technology Agency (JST).

REFERENCES

- [1] E.A. Rohlfing, Optical emission studies of atomic, molecular, and particulate carbon produced from a laser vaporization cluster source, *J. Chem. Phys.* 1988, **89**, 6103–6112.
- [2] A.A. Poretzky, D.B. Geohegan, R.E. Haufler, R.L. Hettich, X.-Y. Zheng, and R.N. Compton, Laser ablation of graphite in different buffer gases, *AIP Conference Proceedings*, 1993, **288**, 365–374.
- [3] A. Kasuya and Y. Nishina, Transient chemical forms of molecular ions emitted from a graphite surface by N₂ laser excitation, *Phys. Rev. B*, 1983, **28**, 6571–6574.
- [4] L.A. Bloomfield, M.E. Geusic, R.R. Freeman, and W.L. Brown, Negative and positive cluster ions of carbon and silicon, *Chem. Phys. Lett.* 1985, **121**, 33–37.
- [5] P. Pradel, P. Monchicourt, J.J. Laucagne, M. Perdrix, and G. Watel, Carbon cluster ion formation in a direct laser vaporization source, *Chem. Phys. Lett.* 1989, **158**, 412–416.
- [6] Y.A. Yang, P. Xia, A.L. Junkin, and L.A. Bloomfield, Direct ejection of clusters from nonmetallic solids during laser vaporization, *Phys. Rev. Lett.* 1991, **66**, 1205–1208.
- [7] E.A. Rohlfing, D.M. Cox, and A. Kaldor, Production and characterization of supersonic carbon cluster beams, *J. Chem. Phys.* 1984, **81**, 3322–3330.
- [8] H.W. Kroto, J.R. Heath, S.C. O'Brien, R.F. Curl, and R.E. Smalley, C₆₀: Buckminsterfullerene, *Nature* 1985, **318**, 162–163.
- [9] J.R. Heath, Q. Zhang, S.C. O'Brien, R.F. Curl, H.W. Kroto, and R.E. Smalley, The formation of long carbon chain molecules during laser vaporization of graphite, *J. Am. Chem. Soc.* 1987, **109**, 359–363.
- [10] H.W. Kroto, J.R. Heath, S.C. O'Brien, R.F. Curl, and R.E. Smalley, Long carbon chain molecules in circumstellar shells, *Astrophys. J.* 1987, **314**, 352–355.
- [11] M. Doverstål, B. Lindgren, U. Sassenberg, and H. Yu, Reaction of small carbon clusters with hydrogen during laser vaporization of graphite, *Z. Phys. D*, 1991, **19**, 447–449.
- [12] Q.L. Zhang, S.C. O'Brien, J.R. Heath, R.F. Curl, H.W. Kroto, and R.E. Smalley, Reactivity of large carbon clusters: spheroidal carbon shells and their possible relevance to the formation and morphology of soot, *J. Phys. Chem.* 1986, **90**, 525–528.

- [13] E.A. Rohlfing, High resolution time-of-flight mass spectrometry of carbon and carbonaceous clusters, *J. Chem. Phys.* 1990, **93**, 7851–7862.
- [14] K. Kaizu, K. Kohno, S. Suzuki, H. Shiromaru, T. Moriwaki, and Y. Achiba, Neutral carbon cluster distribution upon laser vaporization, *J. Chem. Phys.* 1997, **106**, 9954–9956.
- [15] T. Wakabayashi, T. Momose, and T. Shida, Mass spectroscopic studies of laser ablated carbon clusters as studied by photoionization with 10.5 eV photons under high vacuum, *J. Chem. Phys.* 1999, **111**, 6260–6263.
- [16] Y. Kato, T. Wakabayashi, and T. Momose, Preferential formation of neutral C_{10} upon laser vaporized graphite in He gas as studied by photoionization mass spectroscopy with 10.5 eV photons, *J. Chem. Phys.* 2003, **118**, 5390–5394.
- [17] Y. Kato, T. Wakabayashi, and T. Momose, A mass spectroscopic study of laser vaporized graphite in H_2 and D_2 gases: the stability of $C_{2n}H_2$ ($n=2-5$) and C_{10} , *Chem. Phys. Lett.* 2004, **386**, 279–285.
- [18] Y. Kato, T. Wakabayashi, T. Momose, and T. Shida, to be submitted.
- [19] J.F. Ward and G.H.C. New, Optical third harmonic generation in gases by a focused laser beam, *Phys. Rev.* 1969, **185**, 57–72.
- [20] A.H. Kung, J.F. Young, and S.E. Harris, Generation of 1182-Å radiation in phase-matched mixtures of inert gases, *Appl. Phys. Lett.* 1973, **22**, 301–302.
- [21] W.C. Wiley and I.H. McLaren, Time-of-flight mass spectrometer with improved resolution, *Rev. Sci. Instr.* 1955, **26**, 1150–1157.
- [22] R. Kelly and R.W. Dreyfus, On the effect of Knudsen-layer formation on studies of vaporization, sputtering, and desorption, *Surf. Sci.* 1988, **198**, 263–276.
- [23] P.P. Radi, T.L. Bunn, P.R. Kemper, M.E. Molchan, M.T. Bowers, A new method for studying carbon clusters in the gas phase: Observation of size specific neutral fragment loss from metastable reactions of mass selected C_n^+ , $n \leq 60$, *J. Chem. Phys.* 1988, **88**, 2809–2814.

10 Polyynes-Type Materials

Masashi Kijima

CONTENTS

10.1	Introduction	197
10.2	End-Capped Polyynes	198
10.3	Polyynes-Type Polymers	202
10.3.1	Poly(<i>p</i> -phenylene-alt-oligoethynylene)s	203
10.3.2	Poly(aryleneethynylene)s	206
10.3.3	Poly(arylenebutadiynylene)s and Other Analogs	209
10.4	Summary and Conclusions	213
	References	214

10.1 INTRODUCTION

Huge polyyne-type compounds are now known. The definitive polyyne must be poly(ethynylene), with an infinite conjugation length, but the term “polyyne” is conventionally used for compounds or materials having poly (or oligo)ethynylene structures with a finite conjugation length. Naturally occurring polyynes [1] are described in [Chapter 19](#), various polyyne-type synthetic intermediates and compounds [2] and cyclic polyynes [3] in [Chapter 7](#), and carbynoid materials in [Chapters 4](#) and [12](#). Finding carbyne (chaoite), an allotrope of carbon consisting only of sp hybrid carbons, has accelerated investigations into the synthesis and properties of polyyne since the 1960s [4–6]. Some physical methods have successfully synthesized some crystalline forms of carbyne on a micron scale [6], although this was not enough to elucidate the exact structure and general properties of carbyne. On the other hand, various carbynoid materials have been synthesized in forms such as powder, film, and pellet by chemical polymerization of acetylenic monomers, reductive polycondensation of organic halides, and polymer modifications by chemical and electrochemical methods [6–8]. The most carbynoid materials have been ill-characterized insoluble materials with semiconducting properties. In spite of much effort, there is still no convincing evidence that carbyne is a unique material with good stability shown by

graphite and diamond. The discovery that polyyne compounds with long π -conjugation and amorphous carbynoid materials are quite unstable has caused the development of newly devised synthetic methods for polyynes. The instability is mainly due to the high reactivity of linear carbon-chain species with oxygen and radical reactions between the carbon chains, including Diels–Alder-type addition. In order to overcome the difficult handling of the polyyne materials caused by the instability, stabilization of the polyyne chains by end capping with steric and electronic effects is frequently attempted, affording some stable end-capped polyynes. Such methods are quite effective for obtaining stable polyyne-type materials. The synthesis of Si-capped, long, conjugated oligoynes [9], the detection of end-capped linear carbons consisting of more than a hundred sp-carbons [10], and the isolation of long polyynes with end-capped metal complexes [11] are impressive and successful cases.

In this chapter, stable polyyne-type compounds and materials are surveyed with regard to their synthesis, properties, and possible applications. They are classified into end-capped polyynes with or without metals and alternating co-polymers having a polyyne unit with or without metals. In order to determine the possible application of polyynes, the detailed chemical and physical properties in solution, and in the liquid, and solid states, must be known.

10.2 END-CAPPED POLYYNES

Various end-capped polyynes have been synthesized in a stepwise manner by classical methods using Glaser, Hay, Eglinton, or Cadiot–Chodkiewicz couplings with appropriate modifications. The most convenient method of characterizing polyynes is absorption spectroscopy. Oligoyne usually shows a well separated comb-like absorption spectrum due to vibronic effect. HOMO–LUMO energy gaps (E_g) of these compounds can be estimated from the longest absorption maximum (λ_{\max}) in solution. As the polyyne conjugation becomes longer, the energy gap becomes the narrower. A proportional relation between λ_{\max}^2 values and the numbers of triple bonds (n) has been observed in several oligoynes ($R-(C\equiv C)_n-R$) [9,12]. However, the Lewis–Calvin plot (λ_{\max}^2 vs n) frequently did not fit well into the large n region. Here I show better fitting of the optical results [9,12] with power function ($\ln \lambda = a + b \ln n$) as shown in Figure 10.1, but $\lambda(n=8)$ should approach to a limit value.

Crystallographic characterizations of the polyynes provide significant information with respect to crystalline carbyne structure. Crystallographic results of a number of end-capped tetraynes and octaynes are reviewed by Szafert and Gładysz [13], where bond lengths and angles, the space group, the volume of the unit cell, the number of molecules in the unit cell (Z), and

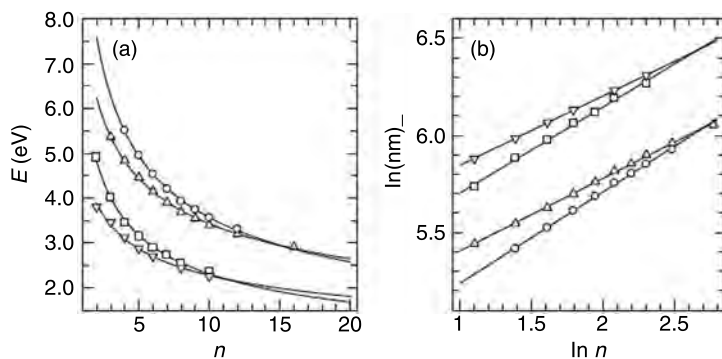


FIGURE 10.1 Power function fitting of E_g (eV) vs number of acetylene n (a) and $\ln \lambda$ (nm) vs $\ln n$ plot (b) of end-capped oligoynes. ○: $H-(C\equiv C)_n-H$; Δ: $Et_3Si-(C\equiv C)_n-SiEt_3$; □: $tBu-(C\equiv C)_n-tBu$; ∇: $Ph-(C\equiv C)_n-Ph$.

the density for each compound are summarized. Typical compounds are shown in Chart 10.1.

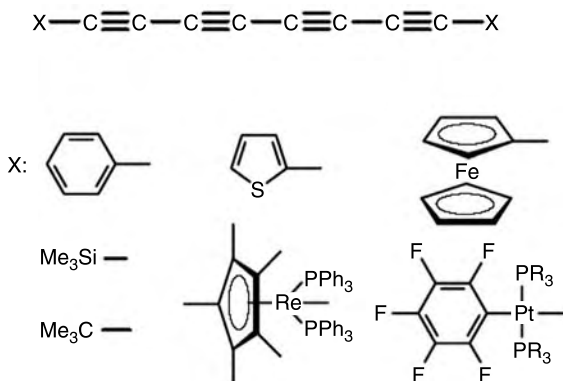


CHART 10.1 Typical samples of crystallographically characterized 1,3,5,7-tetraynes.

From bond length analysis of 32 samples of 1,3,5,7-tetraynes, apparent differences between aromatic or aliphatic non-metal tetraynes and metal-containing tetraynes were not observed. Average $C\equiv C$ and $C-C$ bond lengths were calculated from 28 tetraynes, two hexaynes, and six octaynes, respectively, as shown in Figure 10.2. The average $C\equiv C$ bond lengths are almost identical to non-conjugated acetylenes (1.198–1.2135 Å) and butadiyne (1.218 Å), whereas the average $C-C$ bond lengths between two $C\equiv C$ bonds are shorter than that of butadiyne (1.384 Å). However, as the results

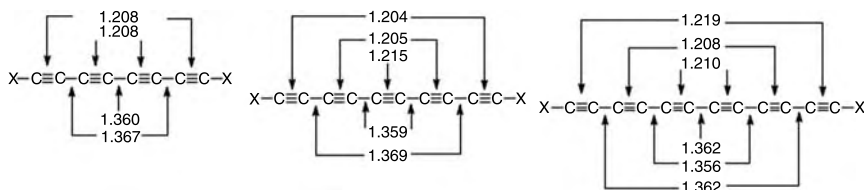


FIGURE 10.2 Average carbon-carbon bond lengths (Å) in oligoynes [13].

of bond length analysis of the oligoynes, the average of all $C\equiv C$ bond lengths in the octayne (1.216 Å) was greater than the corresponding averages for all hexaynes (1.212 Å), pentaynes (1.207 Å), and tetraynes (1.208 Å). The average of all $C-C$ bond lengths in the octaynes (1.351 Å) was shorter than the corresponding averages for all hexaynes (1.360 Å), pentaynes (1.364 Å), and tetraynes (1.365 Å). Thus, the $C\equiv C$ bonds appear to become longer, and the $C-C$ bonds shorter, as the chain lengthen. Although $C\equiv C$ bonds lengthened and $C-C$ bonds contracted as the carbon chains were extended to the macromolecular limit of one-dimensional carbon, different asymptotic limits were proposed as 1.25 Å for $C\equiv C$ and 1.32–1.33 Å for $C-C$, respectively.

Another interesting examination of the crystallographically characterized oligoynes was the carbon chain conformations. Polyyne and oligoynes must be regarded as “essentially linear”, but it is suggested that types of carbon chain conformations are classified into (A) linear, (B) symmetric bow, (C) unsymmetrical bow, (D) kinked, (E) S-shaped, and (F) random from the crystallographical analyses. There was no example classified into strictly linear (A), while bow-shaped and S-shaped conformations (B and E) were quite common.

Furthermore, the tetraynes and higher homologs crystallize in a number of space groups. In order to compare the crystalline oligoynes, key packing parameters (angle φ and offset distances) were defined as shown in the brick wall-like packing by analogy to the 1,3-butadiyne analyses (Figure 10.3), since parallel chains were always evident. In a few molecules, closest parallel chains are very close to the sum of the sp carbon van der Waals radii (3.56 Å). The offset distance (or angle φ) and chain-chain distance (d) are quite important to predict reactivity of polyyne analogs. Some polyyne with small end groups such as hydrogen, halogen, or methyl are known to be explosive, but polyyne with larger endgroups or bulkier transition metal endgroups that enforce greater chain-chain separations give more stable compounds. For topochemical polymerizations such as crystalline 1,3-butadiynes ($n=0$) to crystalline polydiacetylenes in Figure 10.4, an appropriate φ (ca. 45°) and a small chain-chain separation (d =ca. 3.5 Å) must be required [14].

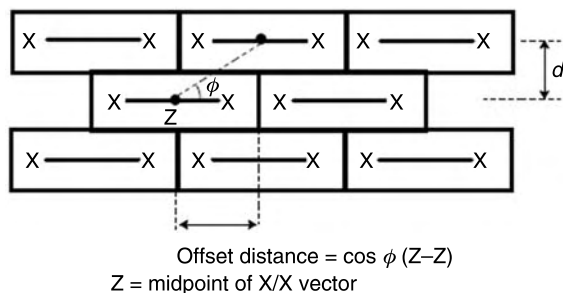


FIGURE 10.3 Brick wall packing and definition of parameters.

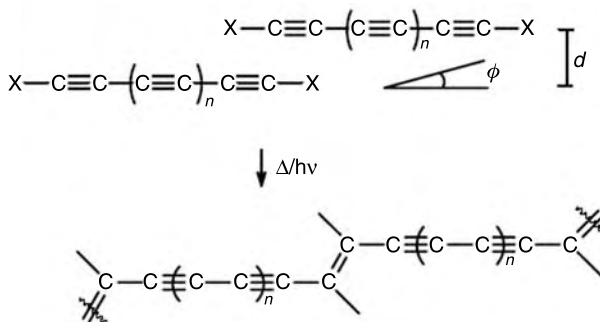


FIGURE 10.4 Topochemical polymerization of α,ω -oligoynes.

Huge molecular rods have been synthesized, so far primarily driven by interest in two areas: 1. long-distance interaction phenomena such as electron and energy transfer, magnetic coupling, etc., and 2. use of molecular rods and connectors for the construction of supramolecular assemblies and giant molecules. From the view point of “molecular rods”, related molecules and materials are reviewed by Michl et al. in 1999 [15]. The stable end-capped oligoynes, one of the categories of “molecular rods”, are not only a model for carbyne but also potential functional molecules. The oligoynes are essentially “molecular wire” that can consist of the rigid rod-like π -conjugated carbon chain with functional molecular moieties in both sides of the wire end, where the carbon chain plays a role of reliable separation of the end functions. The end functions might be photosensitivity, luminescence, redox ability, chromism, and so on. An interesting oxidation–reduction relation has been observed between the oligoynes when the terminal substituents are metals [11,16]. Synthesis of anthracene–polyyne–porphyrins, a photosynthetic model (Chart 10.2) [17,18], might be one of the potential approaches of the functional oligoynes. Since recent

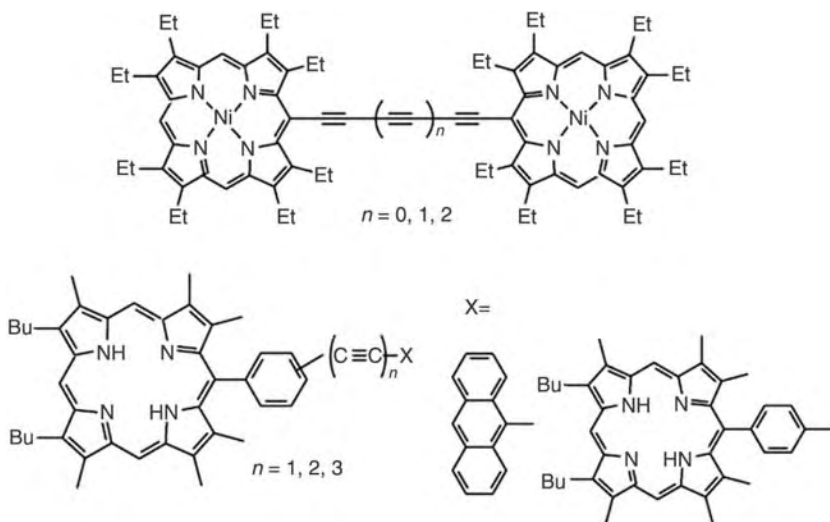


CHART 10.2 Chemical structure of some photosynthetic models [17,18].

vigorous development of nanotechnology enables various molecular devices to be made, the functional oligoyynes should be one of those candidates.

10.3 POLYKYNE-TYPE POLYMERS

Instability of polyyynes in solution or solid is mainly due to reactions between close π -conjugated polyyne chains in a radical or Diels–Alder mechanism and due to vigorous reactions with oxygen, which is usually suppressed by introducing appropriate end-capping groups. Even if oligoyynes are stable enough to be handled at room temperature in air, the oligoyynes having a short parallel chain distance (d) with an appropriate offset angle (φ) in the crystalline state, easily give rise to topochemical polymerization as described in the foregoing chapter (Figure 10.4). Polymeric materials having long conjugated polyyne structures prepared from polytetrafluoroethylene (PTFE) [19], diiodoacetylene [20], or hexachlorobutadiene [21] showed a characteristic Raman signal due to polyyynyl $C\equiv C$ stretching vibration in relatively very low frequency region at about 2000 cm^{-1} . The lower shift of the Raman peak in wavenumber is important evidence that long conjugated polyyynyl $C\equiv C$ bonds are present in the material, which is consistent with crystallographic results of a lengthened $C\equiv C$ bond in the longer oligoyynes. However, the signal disappeared soon by heat treatment or exposure to air, which suggested the polyyne structure in solid materials was quite unstable. A major reason for the instability is heterogeneity of materials in terms of structure and crystallinity. In order to

investigate properties of polyyne-type materials, crystalline polyyne materials such as crystalline carbyne (chaoite) or polydiacetylene analogs must be synthesized in quantity, otherwise polyyne chains in the materials must be stabilized by regular chemical structures. Poly(*p*-phenylenebutadiynylene) PpPB had been considered as a π -conjugated polymeric model for carbyne [6], because it is an alternate copolymer of phenylene and butadiynylene that is adequately stable under atmospheric conditions at room temperature. The butadiyne moiety in the polymer is always stabilized by the adjacent phenylene moieties in both sides. Thus this section is focused on synthesis, properties, and possible applications of this type of polymer, poly(phenylene-alt-oligoethynylene) analogs including metal complexes in the polymer structure.

10.3.1 POLY(*p*-PHENYLENE-ALT-OLIGOETHYNYLENE)S

Poly(*p*-phenylene-alt-oligoethynylene)s are alternate copolymers of 1,4-phenylene and α,ω -oligoethynylene (oligoynes) whose chemical structure is summarized in Chart 10.3. Among the series of the linear conjugated polymers, PpPB (Chart 10.3, $m=2$) was first synthesized by a Russian group from 1,4-diethynylbenzene with the Glaser method [6], which was alternatively prepared in the presence of a Cu^+ catalyst under aerobic conditions (the Hay method) [22] (Scheme 10.1(A)). Poly(*p*-phenyleneethynylene) PpPE ($m=1$) was prepared from 1,4-diethynylbenzene and dibromobenzene (or diiodobenzene) in the presence of a Pd complex–CuI catalyst under inert atmospheric conditions [23] by Sonogashira–Hagihara coupling (Scheme 10.1(B)). Poly(*p*-phenyleneoctatetraynylene) PpPO ($m=4$) was prepared from 1,4-bis(triethylsilylbutadiynyl)benzene by a modified Hay coupling according to the reported method [24]. Triyne polymer ($m=3$) and the longer analogs ($m > 4$) have not been synthesized so far. Three kinds of polymers obtained as a yellowish white powder were ill-characterized materials with semi-conducting properties and almost insoluble in any solvents.

The stability of the polyyne-type polymers can be examined by thermogravimetry and differential thermal analysis (TG/DTA). From the DTA curves in Figure 10.5, an exothermic peak is observed in all cases. The very broad peak for PpPE is observed around at 350°C, while the sharp peak is observed at 207°C for PpPB and at 138°C for PpPO, respectively. The exothermic peak temperature should be related with thermal stability of the polyyne-type polymers, thus it is concluded that the most stable is PpPE

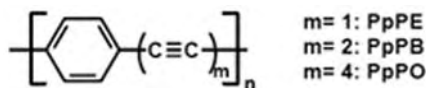
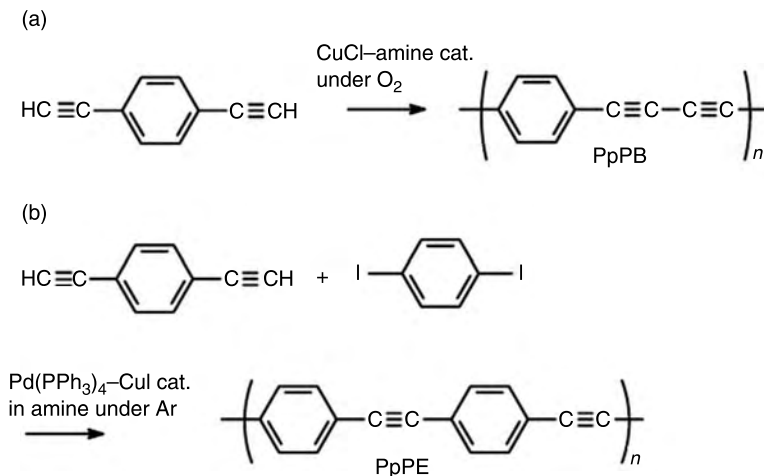


CHART 10.3 Chemical structure of poly(*p*-phenylene-alt oligoethynylene)s.



SCHEME 10.1 General synthetic route of PpPB and PpPE.

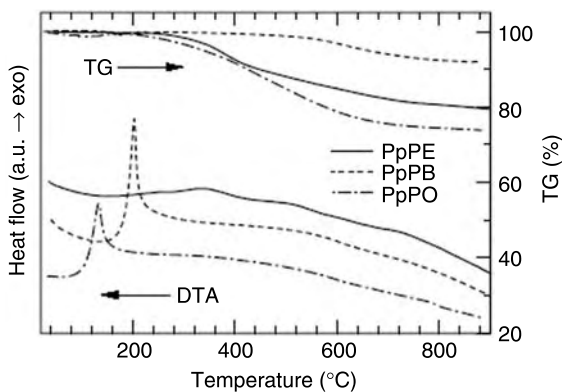
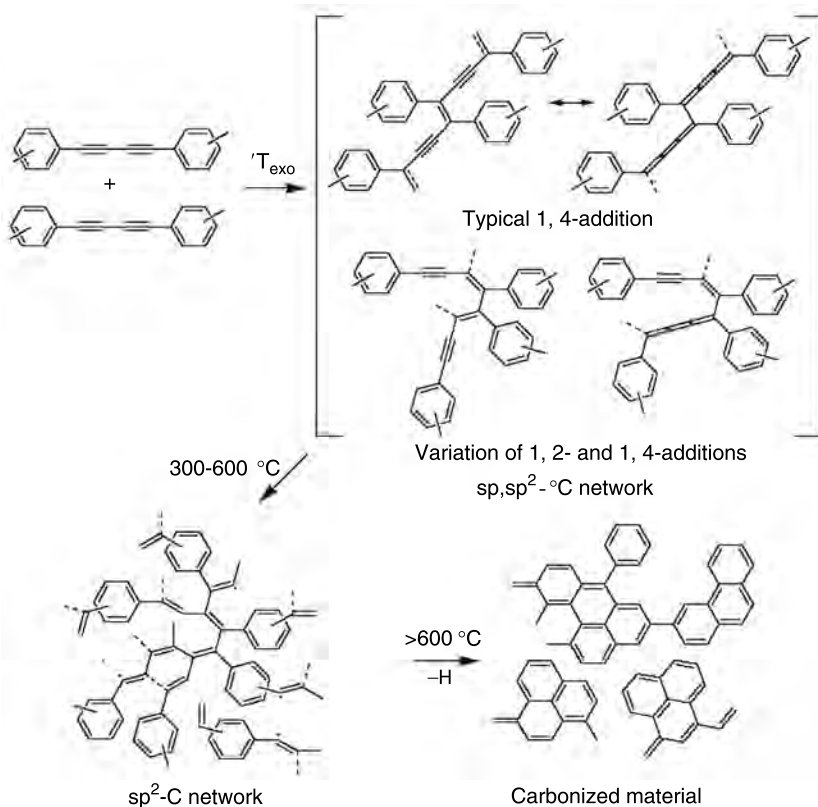


FIGURE 10.5 TG/DTA results of PpPE, PpPB, and PpPO under an argon atmosphere.

having the shortest polyne unit ($m=1$). From the peak area, the heat of reaction (ΔH) (in/kJ g⁻¹) is estimated to be in the order PpPE < PpPB < PpPO, but the ΔH (kJ (mol acetylene)⁻¹) values are almost constant at about 40 kJ (mol acetylene)⁻¹. Since the exothermic reaction is due to cross-linking reactions between the polyne chains, the total amount of heat is approximately estimated by subtracting the bond dissociation energy of a conjugated C≡C bond to a C=C bond from the sum of the bonding energies of C–C newly formed by the cross-linking reaction. However, for example, the experimental value of ΔH for PpPB (86 kJ (mol

butadiyne)⁻¹) is much smaller than the estimated value, if all butadiyne moiety is perfectly converted to 1,2- or 1,4-type adducts, which suggests partial reactions between polymer chains and incomplete cross-linking.

High carbonization behavior is observed especially for PpPB (92%) in TG curves (Figure 10.5) and suggests that the polyyne-type conjugated polymers are good precursory materials for carbons [25]. Conventional polymers usually degrade over 200°C yielding carbonaceous materials in very low yields with elimination of many volatile ingredients, whereas some thermosetting polymers, such as phenolic resins and polyimide resins, can carbonize relatively good yields of about 60%. In the case of PpPB, random and incomplete cross-linking reactions, including 1,2- and 1,4-additions, occurred at the butadiynylene moiety forming a thermal stable mixed sp- and sp²-C polymer network at exothermic temperatures, which successively carbonizes to microcrystalline graphitic carbon with elimination of hydrogen through a sp²-C network precursor, as shown in Scheme 10.2. The formation of thermal stable C-network intermediates during the carbonization process seems to result in the high-yield carbonization.



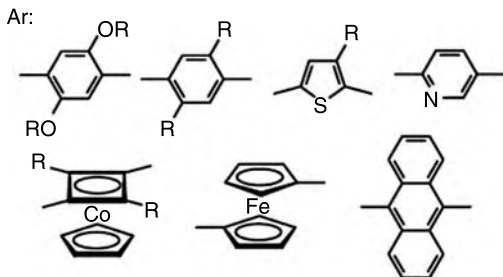
SCHEME 10.2 Carbonization process of poly(phenylenebutadiynylene)s.

Another notable feature is that the carbonized material derived from PpPB was highly porous with specific surface area (S_{BET}) of about $1000 \text{ m}^2/\text{g}$ [25]. The porous carbon was obtained by the only heating process under an argon atmosphere, although usual manufacturing of porous carbons inevitably includes an activation process of precarbons or carbonized materials. Porosity of the carbonaceous material derived from PpPB is mainly due to micropore (diameter $< 2 \text{ nm}$) formation. The rigid character of the polymer backbones and the intermediate C-network seems to cause an ångström-level separation between entangled graphitic microcrystallites in the contracting carbonization process. It has been also reported that different type of porous carbon can be obtained from carbynoid materials derived from poly(tetrafluoroethylene) PTFE [26].

In conclusion of this section, because of instability and inhomogeneity it is difficult to answer how we directly utilize the carbynoid materials in applications. Recently, Yasuda et al. have demonstrated the possibility that carbynoid materials derived from PTFE are useful as precursory materials for nano-carbons [27]. In this sense, the above-mentioned nano-structured porous carbon formation from PTFE [26] belongs to the same category. In the present case of poly(phenylene-alt-oligoethynylene)s having regular alternating phenylene and linear carbons structure, they have strongly linked rigid chains and the reactive $\text{C}\equiv\text{C}$ moiety, thus it is thought that the polymers are potential precursors for nano-structured graphitic carbons; namely, size-controlled nano-porous carbons, nano-sized graphite, and nano-functionalized graphite. Because the above-described carbonization reaction is carried out within thermodynamically favored conditions of graphitic carbon materials, it is mentioned last: types of carbon other than graphite could possibly be synthesized from the polymers under unusual carbonization conditions such as under high pressure or low pressure. Attempts to synthesize carbon from polymers with a regular structure might be a promising method of finding or developing new types of carbon materials.

10.3.2 POLY(ARYLENEETHYNYLE)S

Poly(*p*-phenylene-alt-oligoethynylene)s without substituents were insoluble and infusible materials that are difficult to characterize. Introduction of appropriate substituents at the phenylene moiety or substitution of the phenylene to arylene has greatly improved the solubility of some conducting polymers such as polyacetylene and poly(phenylenevinylene) PPV. Such modifications brought about a new interest in the semiconducting properties of conducting polymers. Similarly, PPE has been modified and characterized, as it is recognized to be as important a semiconducting polymer as PPV. A review by Bunz in 2000 summarized recent researches on the syntheses, properties, structures, and applications of various poly(aryleneethynylene)s, PAEs [28].

$$\xrightarrow{\text{Pd-Cu cat.}} \left(\text{Ar}^1 - \text{C} \equiv \text{C} - \text{Ar}^2 - \text{C} \equiv \text{C} \right)_n$$


$$\text{CH}_3-\text{C}\equiv\text{C}-\text{C}_6\text{H}_2(\text{R})_2-\text{C}\equiv\text{C}-\text{CH}_3 \xrightarrow{\text{W or Mo cat.}} \text{CH}_3-(\text{C}\equiv\text{C}-\text{C}_6\text{H}_2(\text{R})_2-\text{C}\equiv\text{C})_n-\text{CH}_3$$

The method for the synthesis of PAEs commonly uses a Pd-catalyzed Sonogashira–Hagihara coupling of terminal alkynes with aromatic bromides or iodides in amine solvents, and another is metathesis by using W or Mo complexes (Scheme 10.3). The former is suitable for synthesizing various types of alternate co-polymers by combination of Ar¹ and Ar², and the latter has the advantage of preparing high molecular weight PAEs.

The main interest in soluble PAEs has historically been their electronic properties as conjugated polymers. The longest absorption band is due to a π - π^* transition that corresponds to a HOMO-LUMO energy gap of the polymer. The λ_{\max} values of PAEs change from about 300 to 500 nm by combination of substituents (alkyl, alkoxyl, ester etc.) and arylene (*p*-phenylene, *m*-phenylene, thienylene, etc.) of PAEs. Further degrees of polymerization and the solvent used frequently influence the λ_{\max} value. In a filmy solid state, the absorption λ_{\max} observed in solution bathochromically shifts to longer wavelengths, which largely depend on the morphology of polymer in the solid state.

Early on, an attractive feature of PAEs was a marked fluorescence in dilute solution. Emission λ_{\max} and the fluorescence quantum yield depend upon the substituent and the arylene moiety of PAEs. Later, the fluorescence quantum yield of PAEs in solution can reach unity. The rigid character of PAEs seems to make intramolecular dissipation difficult, and insofar fluorescence is efficient. Some PAEs can exhibit strong fluorescence even in the filmy solid state, which opens a way to applications in polymeric light-emitting diodes (PLED) as well as PPV.

There also has been some interest in PAEs as nonlinear optical materials, and several groups have determined χ^3 values. Susceptibilities in the order of 10^{-11} esu are reported by some research groups.

From the point of view of the structure, PpPE analogs are one of the ideally conjugated linear macromolecules. In the solid-state ordering of rigid-rod polymers, they generally take in three structural types depending upon the concentration of solubilizing side chains per repeating unit. If the side-chain concentration is very high, such as in 2,5-disubstituted poly(*p*-phenylene), cylindrical shape polymers assemble each other with no close contacts between the polymer backbones. If the concentration of the side chain is decreased, a lamellar morphology results in which the structure of polymer is almost dominated by side-chain packing (Figure 10.6(a)). In the case of further lower concentration of side chains, an interdigitated phase will result in interaction between the side chains of the different polymers (Figure 10.6(b)). Both lamellar and interdigitated phases have been observed in 2,5-disubstituted PpPEs [29,30].

The fact that the substituted PpPEs aggregate to crystalline materials suggests the presence of strong interactions between macromolecules. A point to note is that such aggregations affect largely electronic and photonic properties of the polymer in the solid state. If the strong interaction can be eased by an appropriate method such as solvation or heating, a mesophase will appear between the solid crystal and isotropic liquid phases. Although lyotropic liquid crystalline (LC) and thermotropic LC behaviors have been observed in some PpPEs, two main obstacles always remained which lead to conclusive results: it was not possible to obtain isotropic melts

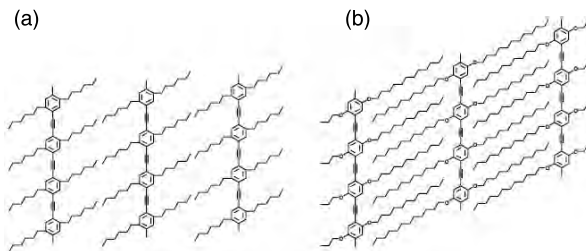


FIGURE 10.6 Lamellar structure (a) and interdigitated structure (b) of PpPEs.

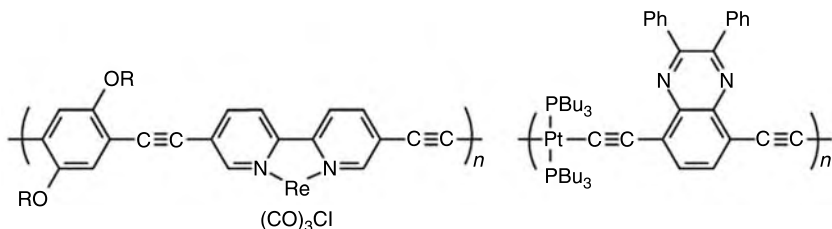


CHART 10.4 Typical examples of metal containing PAEs with photophysical function.

for relatively high-molecular weight materials, and clear-cut LC textures had never been observed by polarizing microscopy.

The end of this section refers to possible applications of PAEs. The concept of the molecular wire approach to sensing has been pioneered by Swager [31]. A principle of “PAEs sensor” is fluorescence quenching of emissive PAEs by analyte (quencher) accessing to binding sites of PAEs. Fabrication of light-emitting diodes has also been reported by several groups [32,33]. The band diagram of PAEs suggests a low-lying LUMO, which means electron injection from the cathode is superior to PPV analogs but hole injection from ITO is more difficult. For the sake of linear structure of macromolecules and the liquid crystalline properties, it is possible to manufacture some oriented PAE materials that might be applied to plastic sheet polarizers and energy-transfer materials. Additionally, the effect of metals in PAEs should be noted. Metals can be introduced into a PAE as an organo-metallic or metal complex moiety. Specific functions of metals such as various oxidation states, metal-to-ligand energy transfer, stable phosphorescence emission, and so on, can collaborate with typical organic PAE functions. Some photophysical aspects of metal–organic π -conjugated polymers have been reviewed [34], and high-efficient electroluminescence from singlet-states in Pt-containing PAEs has been reported [35] (Chart 10.4).

10.3.3 POLY(ARYLENBUTADIYNYLE)S AND OTHER ANALOGS

Development of soluble PpPEs has spread over the research field of PAEs. To begin with, fundamental properties of soluble poly(*p*-phenylene-alt-oligoethynylene)s, of which various structures are shown in Chart 10.5, are compared with each other [36,37]. In the UV–Vis spectrum, the longer oligoethynylene $-(C\equiv C)_m-$ unit of the polymer has the longer the absorption maximum (λ_{\max}) of the polymer shifts. Each λ_{\max} value of the polymers in solution or thin solid state satisfies the relation, λ_{\max}^2 vs number of ethynylene noieties (m) in the unit as well as phenyl-terminated oligoynes (Figure 10.7). The fact of fitting in the Lewis–Calvin plot (λ_{\max}^2 vs m)

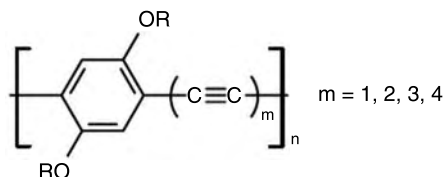


CHART 10.5 Soluble poly(2,5-dialkoxy-*p*-phenylene-alt-oligoethynylene)s.

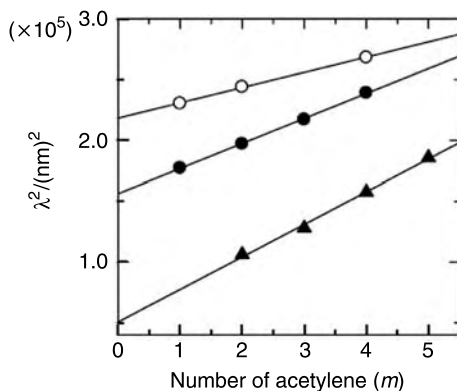


FIGURE 10.7 Lewis-Calvin plot of poly(2,5-dialkoxy-*p*-phenylene-alt-oligoethynylene)s in CHCl_3 (•), in thin solid film state (o), and α,ω -diphenyloligoethynylenes (▲) in CHCl_3 .

suggests that π -conjugation of the polymer chain is essentially equivalent to π -conjugation of oligoynes; in other words, the electronic properties of the polymers are dominated by electronic characters of the repeating oligoyne moieties in the polymer. Likewise the absorption λ_{max} , fluorescence emission maximum (Em_{max}) shifts to longer wavelengths as m increases. Although they all have very small Stokes shift ($\Delta\lambda = Em_{\text{max}} - \lambda_{\text{max}}$), the relative intensity of emission is variable and in the order 1.00 ($m=2$) > 0.25 ($m=1$) > 0.12 ($m=3$) > 0.051 ($m=4$). The highest fluorescence quantum efficiency ($\phi=0.64$) is observed for the butadiynylene polymer ($m=2$). From the preliminary analysis of poly(arylene-alt-oligoethynylene)s, the butadiynylene analog ($m=2$) shows superior properties compared to the ethynylene analog ($m=1$). Thus, in this section, the focus is on poly(arylenebutadiynylene)s ($m=2$), PABs.

A distinctive feature of PABs is that synthesis can easily be carried out from diethynylarenes as the monomer by the Hay method (Scheme 10.1(A)) affording acetylene-terminated PABs in high yield without defects. For synthesis of an air-sensitive PAB, or for use as an air-sensitive monomer, a modified or alternative method can be applied to the reaction [24,38,39].

Poly(phenylenebutadiynylene)s, PPBs, having small substituents at the phenylene moiety, are almost insoluble in most organic solvents. Substitution of the phenylene to another unsubstituted aromatic moiety such as pyrrole, pyridine or thiophene is not effective in solubilizing the polymer. These insoluble PABs are difficult to use in optoelectronic applications because of poor processability, but they can be used as precursor polymers for carbon [40].

Soluble and fusible PpPB is achieved by introduction of a long alkoxy substituent (octyloxy, decyloxy or dodecyloxy) at the 2,5-positions of the 1,4-phenylene moiety [36,37,41,42]. The degree of polymerization of the polymers is in the range of about 10 to 20. They have a characteristic Raman signal at 2110 cm^{-1} due to $\nu_{\text{C}\equiv\text{C}}$. Typical results of UV-Vis absorption maximum (λ_{max}) is about 424 nm. The HOMO–LUMO energy gap is about 2.6 eV and the HOMO level is -6.20 eV . They have an intense fluorescence both in solution ($Em_{\text{max}} = 475\text{ nm}$, $\varphi \sim 0.64$) and in the solid state ($Em_{\text{max}} = 503\text{ nm}$, $\varphi \sim 0.3$).

Differential scanning calorimetry (DSC) of poly(2,5-didecyloxy-1,4-phenylenebutadiynylene) in Figure 10.8 shows two endothermic peaks in the heating process and two exothermic peaks in the cooling process, which suggests presence of an enantiotropic liquid crystalline (LC) phase. In the cooling process of phase transitions, heat flow amount of isotropic to LC (about -75 J/g) is larger than that of LC to crystalline (about -15 J/g), which suggests the former follows larger change of structural state than the latter. From consideration of XRD analysis of LC and crystalline phase, the polymer takes nematic orientation with chain separation of about 4 \AA in the LC state and the interdigitated orientation characterized with side-chain separation (4.3 \AA) and planar sheet distance (3.7 \AA) in the crystalline state, respectively. Since the distance between phenylene moieties on the polymer main chain of PpPB is longer than that of PpPE, the side-chain concentration of PpPB is lower than PpPE, thus PpPB takes the interdigitated

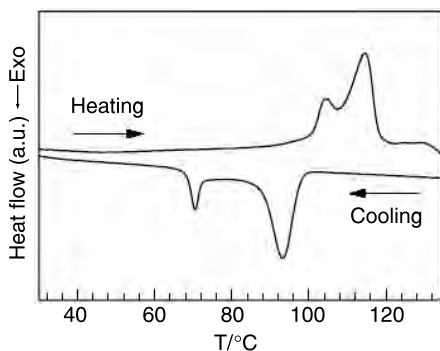


FIGURE 10.8 DSC thermogram of poly(2,5-didecyloxy-1,4-phenylenebutadiynylene).

orientation in the crystalline state rather than the lamellar orientation. Further, the longer separation between phenylene moieties results in much weakening interaction between side chains, which causes considerable lowering of phase transition temperatures; e.g. observation of the clear phase transition from LC to isotropic liquid around 120°C. Some other PpPB derivatives and LC-PABs have been synthesized [43,44]. In addition, it is noteworthy that a high quality uniform molecular alignment of poly(2,5-dialkoxy-*p*-phenylenebutadiynylene) has been achieved by a conventional simple rubbing procedure [45].

Since PPBs show good fluorescence emission, as do PPEs, some attempts have been made to prepare polymeric LEDs. The first electroluminescence (EL) of PABs was achieved by Yoshino et al. from a single layer device (ITO/polymer/Mg-In) using poly(2,5-dialkoxy-*p*-phenylenebutadiynylene) as the emissive layer [46]. For the sake of efficient EL emissions, the polymer must be improved in terms of good contact with the electrodes. Problems included the high crystallinity in the solid state, low solubility in solvents, and low molecular weight of the PpPB, which might result in low efficiency of the LED devices. Most problems were dramatically solved by simple modification by co-polymerization with a *m*-phenylene monomer. Furthermore, multi-color emissions covering blue to orange-red are also achieved by the co-polymerization (Chart 10.6) [37,47,48]. Nonetheless, the

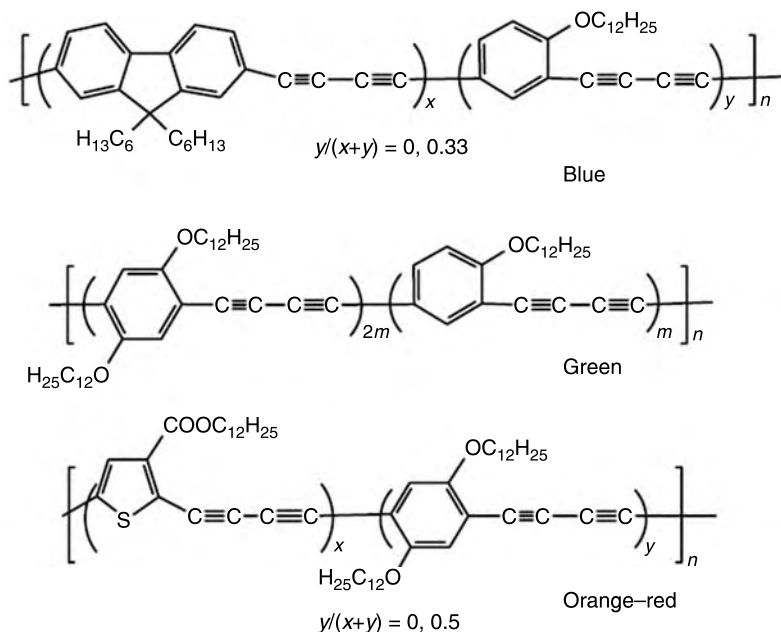


CHART 10.6 PAB co-polymers for polymeric LED.

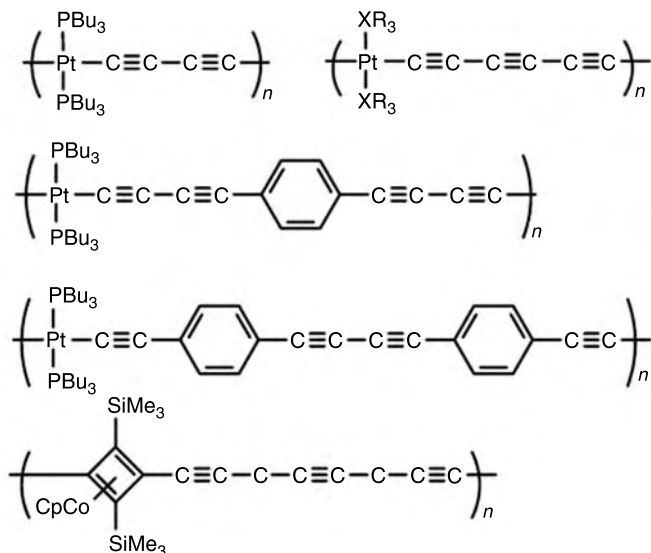


CHART 10.7 Typical structures of stable organometallic polyynes.

instability of the butadiynylene moiety in the device under a high applied voltage remains an unsolved problem.

Some metal-containing polymers in the category of PABs and the longer analogs have been synthesized and investigated. In early synthetic approaches for carbyne by polymerization of acetylenes, some poly(metal-yne) analogs were synthesized from butadiyne by the Hay method [49]. The poly(metal-yne) is randomly or alternatively constituted of butadiyne and Cu. The interesting feature was that I_2 -doped polymers behaved like a metal. Although it is indicated that the poly(metal-yne)s gradually degrade under an air atmosphere at room temperature, it is necessary to be careful when handling metal acetylides. A few years ago Takahashi et al. reported the preparation of poly(Pt-butadiyne)s, stable organometallic polyynes that showed a lyotropic liquid crystalline behavior [50]. Similar kinds of Pt-polymers have been reported which show interesting optical properties of absorption and emission [51]. Lastly, another type of metal-containing polyynes has been synthesized by Bunz [52,53]. The chemical structure of metal-polyynes described above is summarized in Chart 10.7.

10.4 SUMMARY AND CONCLUSIONS

In this chapter, I have attempted to give an overview of the field of polyynes-type materials. End-capped oligoynes supply fundamental properties about polyynes chains; e.g. chemical reactivity, electronic properties, structural information, and so on. Certain characteristics of each oligoyne lead to

particular applications, such as molecular wire sensors and nano-sized molecular devices. Macromolecules with the cumulative structure of α,ω -diaryl-capped oligoynes, named poly(arylene-alt-oligoethynylene)s, show unique properties of photophysics, polymer liquid crystals, and carbonization, although the electronic properties are almost identical to the corresponding low molecular weight oligoynes. The soluble polymers have the necessary processability for making materials in appropriate forms, e.g. spin-cast thin films, fibers, and plastic sheets, so various applications are possible. The intense and efficient fluorescent properties of the polymers in the solid state indicate their use in photovoltaic devices. Achieving electroluminescence in some polymers has given impetus to making some polymeric LED devices.

The appearance of a liquid crystalline phase makes trials of photoelectronic devices with anisotropy. On the other hand, insoluble polymers show notable carbonization behavior. The high-yield carbonization reaction is useful for making nano-structured carbon materials. In addition to these, the metal-polyyynes, although they are still not fully understood, must attain unique multi-functions. Although it is apparent that the polyyne-type materials are not identical to carbyne or polyyne, some polyyne-type materials mentioned in this chapter certainly perform as models for carbyne or polyyne with regard to property and structure. Nevertheless, more important is that they are being recognized as novel functional materials.

REFERENCES

- [1] Jones, E.R.H. Sir; Thaller, V. Natural acetylenes. In *The Chemistry of the Carbon–Carbon Triple Bond*; Patai, S., Ed: John Wiley & Sons: New York, **1978**, 621–633.
- [2] Huntsman, W.D. Synthetic acyclic polyacetylenes. In *The Chemistry of the Carbon–Carbon Triple Bond*; Patai, S., Ed: John Wiley & Sons: New York, **1978**, 553–620.
- [3] Nakagawa, M. Cyclic acetylenes. In *The Chemistry of the Carbon–Carbon Triple Bond*; Patai, S., Ed: John Wiley & Sons: New York, **1978**, 635–712.
- [4] Sladkov, A.M. Carbyne — a new allotropic form of carbon. *Sov. Sci. Rev. B.* **1981**, 3, 75–110.
- [5] Kudryavtsev, Y.P.; Heimann, R.B.; Evsyukov, S.E. Carbynes: Advances in the field of linear carbon chain compounds. *J. Mater. Sci.* **1996**, 31, 5557–5571.
- [6] Kudryavtsev, Y.P.; Kijima, M.; Shirakawa,.; Evsyukov, S.E.; Yabe, A.; Udod, I.A.; Sokolowska, A.; Olszyna, A. H.; Heimann, R.B.; Tanuma, S.; Babaev, V.G.; Guseva, M.B.; Kleiman, J.I.; Yamada, K.; Sawaoka, A.B. Syntheses of carbyne and carbynoid structures. In *Carbyne and Carbynoid Structures*; Heimann, R.B.; Evsyukov, S.E.; Kavan, L., Eds.: Kluwer Academic: Dordrecht, **1999**, 139–187.
- [7] Kijima, M. Recent approaches for chemical and electrochemical synthesis of linear carbons, *Recent Res. Develop. Pure Appl. Chem*; Pandalai, S.G., Ed.: Transworld, India, **1997**, Vol. 1, 27–33.

- [8] Kavan, L. Electrochemical carbon. *Chem. Rev.* **1997**, 97, 3061–3082.
- [9] Eastmond, R.; Johnson, T.R.; Walton, D.R.M. Silylation as a protective method for terminal alkynes in oxidative couplings. *Tetrahedron* **1972**, 28, 4601–4616.
- [10] Lagow, R.J.; Kampa, J.J.; Wei, H.-C.; Battle, S.L.; Genge, J.W.; Laude, D.A.; Harper, C.J.; Bau, R.; Stevens, R.C.; Haw, J.F.; Munson, E. Synthesis of linear acetylenic carbon: The “sp” carbon allotrope. *Science* **1995**, 267, 362–367.
- [11] Bartik, T.; Bartik, B.; Brady, M.; Dembinski, R.; Gladysz, J.A. A step-growth approach to metal-capped one-dimensional carbon allotropes: Syntheses of C₁₂, C₁₆, and C₂₀ μ -polyynediyl complexes. *Angew. Chem. Int. Ed. Engl.* **1996**, 35(4), 414–417.
- [12] Johnson, T.R.; Walton, D.R.M. Silylation as a protective method in acetylene chemistry. *Tetrahedron* **1972**, 28, 5221–5236.
- [13] Szafert, S.; Gladysz, J.A. Carbon in one dimension: structural analysis of higher conjugated polyynes. *Chem. Rev.* **2003**, 103(11), 4175–4205.
- [14] Shirakawa, H.; Masuda, T.; Takeda, K. Synthesis and properties of acetylenic polymers. In *The Chemistry of Triple-Bonded Functional Groups: Supplement C2*; Patai, S., Ed.: John Wiley & Sons: New York, **1994**, Chapter 17, 945–1016.
- [15] Schwab, P.F.H.; Levin, M.D.; Michl, J. Molecular rods. 1. Simple axial rods. *Chem. Rev.* **1999**, 99, 1863–1933.
- [16] Coat, F.; Lapinte, C. Molecular wire consisting of a C₈ chain of elemental carbon bridging two metal centers: synthesis and characterization of [Fe(η^5 -C₅Me₅)(dppe)]₂(m-C₈)]. *Organometallics* **1996**, 15(2), 477–479.
- [17] Kawabata, S.; Yamazaki, I.; Nishimura, Y. Synthesis and photochemical properties of anthracene–polyyne–porphyrin assemblies. *Bull. Chem. Soc. Jpn.* **1997**, 70, 1125–1133; Kawabata, S.; Tanabe, N.; Osuka, A. A convenient synthesis of polyyne-bridged porphyrin dimmers. *Chem. Lett.* **1994**, (10), 1797–1800.
- [18] Arnold, D.P.; James, D.A. Dimers and model monomers of nickel(II) octaethylporphyrin substituted by conjugated groups comprising combinations of triple bonds with double bonds and arenes. *I. J. Org. Chem.* **1997**, 62(11), 3460–3469.
- [19] Kastner, J.; Kuzmany, H.; Kavan, L.; Dousek, F.P.; Kürti, J. Reductive preparation of carbene with high yield. An *in situ* Raman scattering study. *Macromolecules* **1995**, 28, 344–345.
- [20] Kijima, M.; Sakai, Y.; Shirakawa, H. A novel approach for synthesis of carbyne by electroreductive polymerization of diiodoacetylene. *Chem. Lett.* **1994**, (11), 2011–2014.
- [21] Kijima, M.; Toyabe, T.; Shirakawa, H. Novel approach for synthesis of carbyne film by electrochemical reduction of hexachloro-1,3-butadiene, *Chem. Commun.* **1996**, 2273–2274.
- [22] Hay, A.S. Oxidative polymerization of diethynyl compounds. *J. Polym. Sci. Part A-1* **1969**, 7, 1625–1634.
- [23] Sanechika, K.; Yamamoto, T.; Yamamoto, A. Palladium catalyzed C–C coupling for synthesis of π -conjugated polymers composed of arylene and ethynylene units. *Bull. Chem. Soc. Jpn.* **1984**, 57(3), 752–755.
- [24] Kijima, M.; Kinoshita, I.; Shirakawa, H. Synthesis and characterization of a novel linear conjugated polymer, poly(2,5-didodecyloxy-1,4-phenyleneocta-tetraynylene) *Chem. Lett.* **1999**, (6), 531–532.

- [25] Kijima, M.; Tanimoto, H.; Shirakawa, H.; Oya, A.; Liang, T.-T.; Yamada, Y. Poly(phenylenebutadiynylene)s as an efficient carbonizing precursor. *Carbon* **2001**, 39(2), 297–300.
- [26] Liang, T.-T.; Yamada, Y.; Yoshizawa, N.; Shiraishi, S.; Oya, A. Preparation of porous carbon by defluorination of poly(tetrafluoroethylene) and the effect of γ -irradiation on the polymer. *Chem. Mater.* **2001**, 13(9), 2933–2939.
- [27] Yasuda, A.; Mizutani, W. Carbon nanostructure formation by a reduction of PTFE. *Thin Solid Films* **2003**, 438, 313–316.
- [28] Bunz, U.H.F. Poly(aryleneethynylene)s: syntheses, properties, structures, and applications. *Chem. Rev.* **2000**, 100, 1605–1644.
- [29] Moroni, M.; Le Moigne, J.; Luzzati, S. Rigid rod conjugated polymers for nonlinear optics. 1. Characterization and linear optical properties of poly(aryleneethynylene) derivatives. *Macromolecules* **1994**, 27, 562–571.
- [30] Li, H.; Powell, D.R.; Hayashi, R.K.; West, R. Poly((2,5-dialkoxy-*p*-phenylene)ethynylene-*p*-phenyleneethynylene)s and their model compounds. *Macromolecules* **1998**, 120(1) 52–58.
- [31] Swager, T.M. The molecular wire approach to sensory signal amplification. *Acc. Chem. Res.* **1998**, 31, 201.
- [32] Swanson, L.S.; Shinar, J.; Ding, Y.W.; Barton, T.J. Photoluminescence, electroluminescence, and optically detected magnetic resonance study of 2,5-dialkoxy derivatives of poly(*p*-phenyleneacetylene)(PPA) and PPA-based light-emitting diodes. *Synth. Met.* **1993**, 55(1), 1–6.
- [33] Hirohata, M.; Kawai, T.; Tada, K.; Yoshino, K.; Onoda, M. Electroluminescence in conducting polymers based on poly(phenyleneethynylene). *Synth. Met.* **1997**, 85(1–3), 1273–1274.
- [34] Ley, K.D.; Schanze, K.S. Photophysics of metal–organic *p*-conjugated polymers. *Coord. Chem. Rev.* **1998**, 171, 287–307.
- [35] Wilson, J.S.; Dhoot, A.S.; Seeley, A.J.A.B.; Khan, M.S.; Köhler, A.; Friend, R.H. Spin-dependent exciton formation in *p*-conjugated compounds. *Nature* **2001**, 413, 828–831.
- [36] Kijima, M.; Kinoshita, I.; Shirakawa, H. Spectroscopic study of soluble poly(2,5-dialkoxy-1,4-phenylene-alt-oligoethynylene)s. *J. Mol. Struct.* **2000**, 521, 279–283.
- [37] Kijima, M.; Kinoshita, I.; Hiroki, K.; Shirakawa, H.; Yoshikawa, K.; Mishima, Y.; Sasaki, N. Optical properties of conjugated polymers having linear carbon moieties. *Curr. Appl. Phys.* **2002**, 2, 289–294.
- [38] Hattori, T.; Kijima, M.; Shirakawa, H. Oxidative polycondensation of acetylene by iodine in the presence of palladium–copper catalyst. *Synth. Met.* **1997**, 84, 357–358.
- [39] Ohmura, K.; Kijima, M.; Shirakawa, H. Synthesis of conducting polymer with conjugated carbon–carbon triple bond by electrochemical condensation of acetylene derivatives by copper complex. *Synth. Met.* **1997**, 84, 417–418.
- [40] Kijima, M.; Tanimoto, H.; Shirakawa, H. Poly(arylenebutadiynylene)s as high yield carbonaceous precursory polymers. *Synth. Met.* **2001**, 119 (1–3), 353–354.
- [41] Kijima, M.; Kinoshita, I.; Hattori, T.; Shirakawa, H. Synthesis of a novel liquid crystalline polymer, poly(2,5-didecyloxy-1,4-phenylenebutadiynylene). *J. Mater. Chem.* **1998**, 8(10), 2165–2166.

- [42] Kijima, M.; Kinoshita, I.; Hattori, T.; Shirakawa, H. Poly(2,5-dialkoxy-*p*-phenylenebutadiynylene)s. Novel rigid conjugated polymers with liquid crystalline property. *Synth. Met.* **1999**, 100(1), 61–69.
- [43] Kinoshita, I.; Kijima, M.; Shirakawa, H. Liquid crystalline behavior of poly(*m*-phenylenebutadiynylene)s having a mesogenic substituent. *Mol. Cryst. Liq. Cryst.* **2001**, 365, 1193–1202.
- [44] Kijima, M.; Matsumoto, S.; Kinoshita, I. Synthesis and optical properties of disubstituted poly(*p*-phenylenebutadiynylene)s. *Synth. Met.* **2003**, 135–136, 391–392.
- [45] Ozaki, M.; Fujisawa, T.; Fujii, A.; Tong, L.; Yoshino, K.; Kijima, M.; Kinoshita, I.; Shirakawa, H. *Adv. Mater.* **2000**, 12(8), 587–589.
- [46] Fujii, A.; Fujisawa, T.; Yoshino, K.; Kijima, M.; Kinoshita, I.; Shirakawa, H. Optical properties of poly(2,5-dialkoxy-*p*-phenylenebutadiynylene). *Jpn. J. Appl. Phys. Part 2* **1999**, 38(4A), L406–409.
- [47] Kinoshita, I.; Kijima, M.; Shirakawa, H. Syntheses and properties of copoly(2,5-dialkoxy-*p*-phenylenebutadiynylene/arylenebutadiynylene). *Synth. Met.* **2001**, 119(1–3), 187–188.
- [48] Kinoshita, I.; Kijima, M.; Yoshikawa, K.; Mishima, Y.; Sasaki, N. Syntheses of copoly(arylenebutadiynylene)s for polymeric light emitting diodes. *Synth. Met.* **2003**, 137(1–3), 1059–1060.
- [49] Matsuda, H.; Nakanishi, H.; Kato, M. Conducting poly-yne and poly(metal-yne) from butadiyne. *J. Polym. Sci. Polym. Lett. Ed.* **1984**, 22, 107–111.
- [50] Takahashi, S.; Murata, E.; Kariya, M.; Sonogashira, K.; Hagihara, N. A new liquid-crystalline material. Transition metal–poly(yne) polymers. *Macromolecules* **1979**, 12(5), 1016–1018.
- [51] Lewis, J.; Khan, M.S.; Kakkar, A.K.; Johnson, B.F.G.; Marder, T.B.; Fyfe, H.B.; Wittmann, F.; Friend, R.H.; Dray, A.E. Di-, tri-, pseudo-di- and pseudo-tetra-acetylenic polymers of platinum: synthesis, characterization and optical spectra. *J. Organomet. Chem.* **1992**, 425, 165–176.
- [52] Altmann, M.; Bunz, U.H.F. Synthesis and characterization of a poly[(para-cyclobutadienylencyclopentadienylcobalt)butadiynylene], a butadiyne–cyclobutadiene copolymer. *Macromol. Rapid Commun.* **1994**, 15, 785–789.
- [53] Altmann, M.; Enkelmann, V.; Bunz, U.H.F. Synthesis and characterization of a novel cyclobutadiene–octatetrayne polymer. *Chem. Ber.* **1996**, 129, 269–273.

11 Carbon Material with a Highly Ordered Linear-Chain Structure

*V.G. Babaev, M.B. Guseva, N.D. Novikov,
V.V. Khvostov and P. Flood*

CONTENTS

11.1	Introduction	219
11.2	Experimental Set-Up	224
11.3	Methods of Characterization	225
11.4	Results and Discussion	225
11.4.1	Electron Band Structure	225
11.4.2	EELS Measurements	229
11.4.3	Raman Spectroscopy	231
11.4.4	Atomic Force Microscopy	234
11.4.5	Scanning Tunneling Microscopy	235
11.4.6	Electric Conductivity	236
11.4.7	Optical Properties	238
11.4.8	Field Effect Measurements	238
11.4.9	Al/sp ¹ -C/p-Si Heterojunction	240
11.4.10	Cold Electron Emission	241
11.4.11	Injection of Electrons in Dielectrics	242
11.4.12	The Dependence of Atomic Structure of sp ¹ -Hybridized Carbon Films on their Thickness	243
11.4.13	Carbon Electronics	246
11.5	The New Carbon Material Tetracarbon TM	247
11.6	Conclusions	250
	Acknowledgments	250
	References	251

11.1 INTRODUCTION

The problem of obtaining linear-chain carbon has been of great interest in the past few decades [1,2]. Experimental and theoretical investigations of carbon vapor at high temperatures ($T > 2000$ K) have shown that carbon clusters C_n with the sp^1 -type hybridization becomes the most stable at temperatures up to 4000 K [3–5]. However, these clusters are very reactive and begin to interact with each other and with oxygen at very low temperatures (below 12 K) [6,7]. Thus, despite the great interest in and intensive research activity on chain-like carbon, this subject still needs to be investigated further. The most chemically active parts of the carbon chains are their end groups, which can react with end groups of other chains, resulting in cross-linking or formation of chemical bonds with molecules of the gas atmosphere.

Basically, the problem of instability of chain-like carbon is related to low stability of the free ensemble of the free linear-chain carbon clusters with sp^1 -type a electron hybridization. The stability of linear-chain carbon can be improved if the chains grow on the surface of a substrate, as one end of the carbon chain becomes fixed on the substrate surface. The stability of chain-like carbon can also be enhanced as a result of the parallel growth of carbon chains in the perpendicular direction to the substrate surface [9].

In 1990 we established the experimental conditions suitable for the formation of carbon films of highly oriented carbon chains by means of ion-assisted condensation of carbon on the surface of NaCl [9]. Later we proposed a new pulsed-plasma condensation method [10], which allowed us to deposit such films on large surfaces and at high growth rate. The films deposited in such a way were designated with registered trade name TetracarbonTM. At present a number of interesting applications are found for TetracarbonTM because of its unique properties. In medicine it can be used as a biocompatible coating, in industry as a protective coating and as a cold welding sub-layer, etc. In spite of that, the hypothesis concerning the linear-chain structure of TetracarbonTM still needs to be confirmed. The present work provides clear evidence for the presence of kinks in the linear-chain structure in TetracarbonTM.

The films of TetracarbonTM were found to be characterized by unique electron diffraction, as shown in Figure 11.1. The electron diffraction pattern consists of only one bright narrow diffraction ring (Figure 11.1(c)) or six point reflections equally spaced in this ring (Figure 11.1(a)). According to the electron diffraction pattern the inter-plane distance $d_{10,0}$ lies between 0.415 and 0.439 nm for samples obtained at various deposition parameters. If the electron beam was tilted with respect to normal to the film surface two arcs can be seen instead of the ring in the diffraction pattern (Figure 11.1(b)). These arcs are situated symmetrically with respect to the ring center providing evidence for the presence of an axis texture in the film.

The electron diffraction pattern shown in Figure 11.1(a) corresponds to the hexagonal crystal lattice with the lattice parameter varying from 0.490

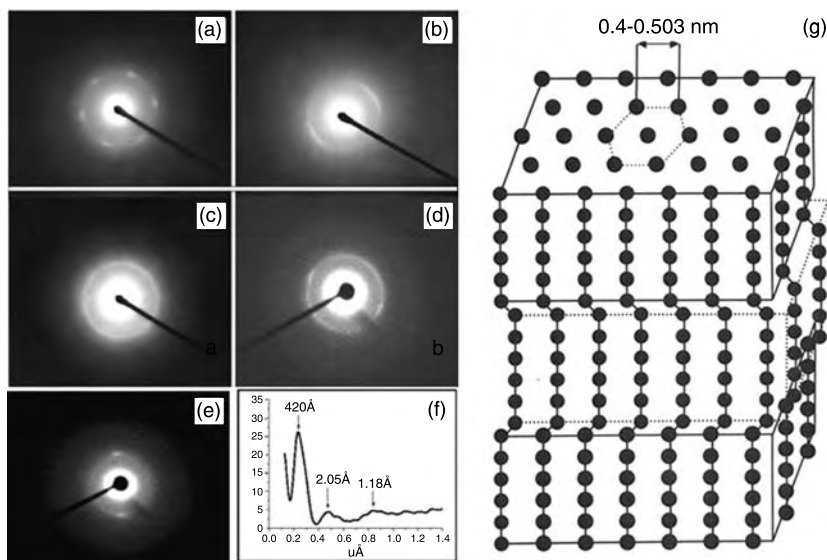


FIGURE 11.1 Electron diffraction patterns of the linear chain carbon films (a–c), the distribution of electron diffraction intensity, its atomic arrangement (g), the Langmuir–Blodgett multi-layered film diffraction patterns (d,e).

to 0.507 nm and indicates a high degree of ordering in the film. The distribution of electron diffraction intensity shown in Figure 11.1(f) reveals the specific features of the diffraction patterns obtained. There is strong attenuation of higher-order reflections, so that the intensity of the second-order reflections is decreased by an order of magnitude compared to the first-order reflections. This can be attributed to the layered structure of the film with small (~ 0.09 nm) random displacements between the layers that the film consists of [9]. Similar diffraction patterns and inter-plane spacing in the range of 0.4–0.5 nm can be observed in a multi-layered film prepared by the Langmuir–Blodgett (LB) method (Figure 11.1(d)). The LB film consists of chain-like organic molecules $\text{C}_{15}\text{H}_{32}\text{O}_2$ oriented normally with respect to film surface. These layers are assembled into hexagonally ordered layers by the weak van der Waals forces. As a result, one-axis texture in the diffraction pattern similar to that mentioned above is observed (Figure 11.1(e)). It should be noted that inter-plane spacing in the range between 0.412 and 0.456 nm is a characteristic feature of only one known carbon form, that is carbyne with the sp^1 type of electron hybridization of carbon atoms. Thus, the atomic structure of TetracarbonTM is thought to be similar to the LB films with the two-dimensional ordered layered chain structure.

Highly oriented carbon films of high quality were also deposited by the ion-assisted condensation method in nitrogen-containing glow discharge at

confirmed by electron spectroscopy including electron energy loss spectroscopy (EELS) and atomic emission spectroscopy (AES) with x-ray excitation (see [Section 11.4.1](#)). The spectroscopic results provide clear evidence that the TetracarbonTM films were composed of carbon chains with sp^1 hybridization.

The data obtained permitted us to propose the model of atomic arrangement of the film structure, which is similar to that published before [2]. The structure shown in [Figure 11.1\(g\)](#) is multi-layered with each layer consisting of carbon atom chains in the sp^1 -hybridization state. These chains are densely packed into a hexagonal lattice. According to the diffraction pattern and atomic force microscopy (AFM) images the distance between the chains is in the range of 0.490 to 0.503 nm.

According to the results on attenuation of the higher-order electron diffraction reflections, the layers are randomly shifted with respect to each other. In other words, the film structure is composed of identical kinked chains with the kinks randomly oriented with respect to the chain axis. The presence of the kinks is well correlated with the Raman peak at $1552\text{--}1583\text{ cm}^{-1}$ in the Raman spectrum shown in [Figure 11.2](#) and [Figure 11.11](#). The kinks of the neighboring chains are presumably correlated and positioned in the same plane and at the same direction. When taking into account the length of sp^1 hybridized carbon bounds (0.128 nm in cumulene) and the possible inter-chain distances of 0.480 to 5.00 nm, the density of TetracarbonTM having a hexagonal crystal lattice is calculated to lie between 1.54 and 1.18 g/cm^3 . This is in good agreement with the density value determined from the EELS measurement (1.35 g/cm^3) described below (see [Section 11.4.2](#)). By means of the linear combination of atomic orbitals (LCAO) method the density of valence electron states (DOVS) of infinite sp^1 carbon chains with periodic kinks as a function of the kink angle α was also calculated. The possibility of decreasing the total energy of the chains is found to have a maximum at $\alpha = 55^\circ$. The phonon spectrum of infinite sp^1 carbon chain with periodic kinks was also calculated.

The anisotropic structure of the films obtained on the basis of the proposed model of its crystal and atomic structure is in agreement with the anisotropy of its physical properties described below.

The new results on experimental and theoretical investigations of the linear chain-like structure presented below confirm the proposed model of its atomic and crystal structure. The major question still remains: is sp^1 -hybridized chain-like carbon stable or unstable with respect to the formation of cross-linkages among carbon chains? The viewpoint that sp^1 -hybridized chain-like carbon is unstable is based on studies of free, randomly oriented sp^1 carbon chains, which can simply be cross-linked. In the case when the chain ends are strongly fixed on the surface of substrate, the substrate plays an important role of a “command” surface [8]. This means that the surface controls the orientation of the chains and keeps them at a distance apart from cross-linking. However, the substrate can

presumably have an impact on the film structure only at a limited distance from the surface-film interface. Therefore, the dependence of the atomic structure of the film was studied as a function of film thickness below (Section 11.4.12). The results presented below indicate that the certain orientation of carbon chains was kept at a film thickness of up to roughly 100 nm. If the film thickness exceeds this value, the carbon films start losing their chain-like structure, transforming finally into diamond-like films when the thickness reaches 200 nm. In spite of this limit, such relatively thin films can be successfully used in many applications such as protective coatings, microelectronics, medicine, *etc.* Some applications of such carbon films in practice are described below.

11.2 EXPERIMENTAL SET-UP

The two-dimensional ordered layered linear chain carbon films were produced using a pulsed plasma ion-assisted technology [10]. The films were obtained at a rate of 100 nm/min on various substrates (metals, ceramics, polymers, *etc.*) with good adhesion and homogeneity of the films on the areas of $150 \times 150 \text{ mm}^2$.

The experimental set-up is a vacuum unit for pulsed deposition of carbon film from carbon-based plasmas at a plasma density of 10^{13} to 10^{14} cm^{-3} , ionization rate of about 95% and pulse frequency varied from 1 to 30 Hz. The pulse duration was 100 μs . Figure 11.3 schematically illustrates the plasma deposition system [10]. The system consists of a high purity graphite cathode (1), anode (2), ignition electrodes (3,4) with dielectric separator (5), second anode of auxiliary discharge (6) and substrate holder (7). The capacitors C_1 and C_2 are connected to a power supply unit with

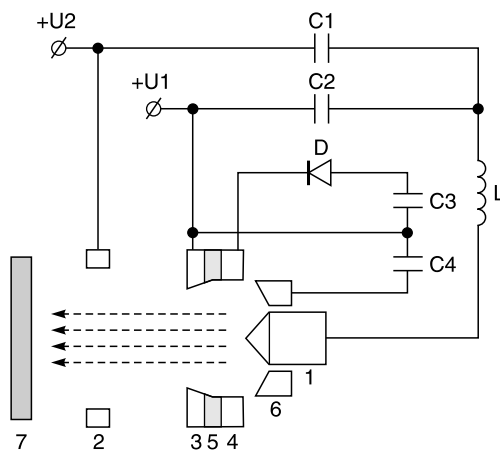


FIGURE 11.3 Schematic representation of experimental installation.

varied voltage (100–300 V). The ignition electrodes are supplied by pulsed voltage with an amplitude of 800 V. The inductance L reduces the current growth rate to a required value.

The growth of sp^1 carbon is enhanced by irradiation with Ar ions during the film growth. The flux of Ar ions is formed by a low-pressure ion source, installed in a separate section of the vacuum chamber. The energy of ions bombarding the substrate surface depends on the substrate bias voltage, being varied in the range 0–300 eV by both the carbon plasma parameters and the ion source extractor voltage, depending on the parameters of the plasma assisted deposition. The films were deposited onto Si wafer, metals, and NaCl single crystals at an ion energy of 150 eV. The operating pressure during the deposition was 10^{-4} Pa.

11.3 METHODS OF CHARACTERIZATION

The atomic structure of the films was studied by transmission electron microscopy (TEM) using a JEM 100C electron microscope in the micro-diffraction mode. The diffraction patterns were obtained at a low electron beam intensity using the CCD high-sensitive registration system to prevent the films from radiation damage by the electron beam.

X-ray photoelectron spectroscopy (XPS) and AES data were obtained using an MK II VG Scientific spectrometer with x-ray excitation (Al anode, $h\nu = 1486.6$ eV) and a “Riber” Auger spectrometer with electron excitation. The residual pressure during the measurements was 1×10^{-9} to 5×10^{-10} Torr. The spectra were recorded in a constant energy mode with transmission energy of 20 eV for x-ray photoemission spectra and 50 eV for Auger spectroscopic measurements. The structure of sp^1 carbon films was also studied by Raman spectroscopy by using a Jobin Yvon spectrometer with the aid of an argon laser ($\lambda = 488.0$ nm).

11.4 RESULTS AND DISCUSSION

11.4.1 ELECTRON BAND STRUCTURE

Figure 11.4 shows the ESCA spectrum of the carbon film having a thickness of 50 nm. The spectrum indicates that the film consists of carbon with purity higher than 99%.

Figure 11.5 shows the KVV carbon Auger line of the film (solid line) in comparison with that of other forms of carbon, namely, diamond (dot-dashed line), graphite (dashed line) and turbostratic carbon (dotted line). The energy calibration of the Auger spectrum was performed using the 1s line of carbon $E = 284.7$ eV, the energy position of which was accepted to be equal to the constant value at energy of 284.7 eV for all carbon samples to

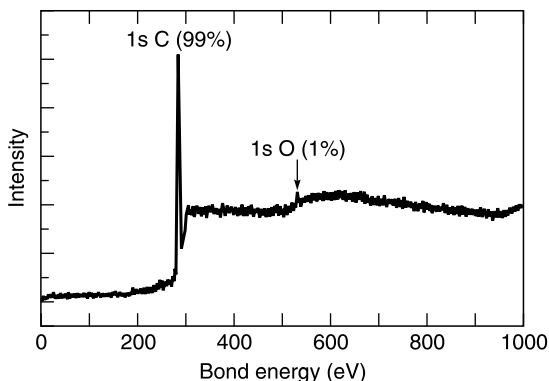


FIGURE 11.4 ESCA spectrum of linear chain carbon film.

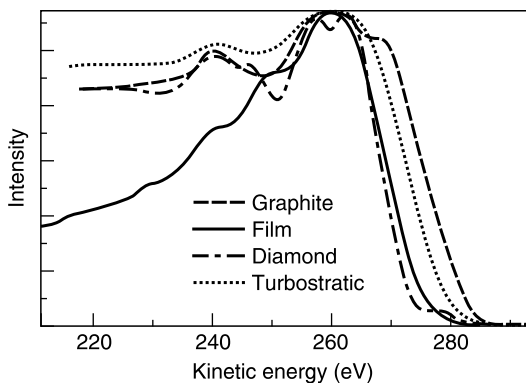


FIGURE 11.5 CKVV Auger line shape of linear chain carbon film.

exclude the effect of surface charging. The positions of higher energy edges of these CKVV lines are especially interesting. The high-energy edge of graphite is strongly shifted towards the high-energy region. The turbostratic carbon is close to graphite; its energy edge is shifted towards the low energy region by 3 eV compared to that of graphite.

The KVV high-energy edges of both the films of sp^1 -hybridized carbon and diamond are shifted toward the lower energies by nearly 5 eV compared to graphite. This means that the Fermi level of films is close to that of diamond but its electron structure is completely different to that of diamond. More detailed information about the electron structure can be obtained from the density of valence band states (DOVS).

Figure 11.6(a) represents the DOVS (solid line) of carbon chain without kinks ($\alpha=0$) calculated by the LCAO method. The occupied states are

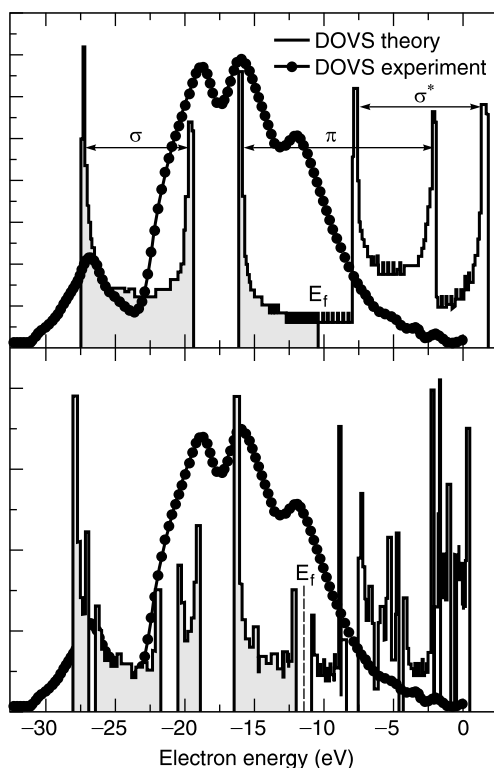


FIGURE 11.6 Calculated DOVS of cumulene chain without kinks (a) and with periodical kinks (55°), dotted symbol experiment.

marked by the gray color below the Fermi level. The experimental curves of DOVS are shown in the same figure by the pointed line. As can be seen from the figure, the calculated position of the σ -bond sub-band lies at exactly the same position as the experimental DOVS in the region of 19 eV to 27 eV. The calculated low energy edge of the π -band at -16 eV lies also at a similar energy value as that obtained experimentally. The σ^* anti-bonding band is found to be empty. The cumulene chain should be a metal as the Fermi level E_f falls into the π -band. The maximum on the experimental curve at 12 eV is located close to the calculate Fermi level but does not fit well with the calculated DOVS. The presence of this peak can be explained by the appearance of the forbidden gap due to metal–dielectric transition, which is a characteristic property of one-dimensional systems with the half-filled valence band. This result is in good agreement with the theory of one-dimensional transition in carbon chains (Peierls transition or dimerization [12], charge density and spin density waves without dimerization [13,14]). According to these theories, carbon chains with equally spaced carbon

atoms are a metal and intrinsically unstable. The stabilization occurs through charge density or spin density waves or by means of periodic alternation of bond lengths in the chain. The latter is equivalent to breaking up the chains into periodic linear fragments. The forbidden gap in a π -band forms as a result of this type of stabilization. In the half-filled band only its lower part below the gap is filled and, as a result of that, the total energy of the system decreases. In this respect periodic kinks in the carbon chains are one possible way to decrease the total energy of the system by kink waves. Accordingly, the linear fragments with purely sp^1 bonds can be separated by periodic kinks with sp^2 bonds.

To prove the hypothesis described above we have calculated the DOVS of an infinite carbon chain with regular kinks separating carbon chain into C_4 linear fragments. The simulation was performed using the following model of kinked carbon chain shown in Figure 11.7. The distance between the atoms was chosen to be equal to 0.13 nm, which corresponds to the sp^1 -hybridization type of chemical bonding. The α angle was varied between zero and 90° . The kink angle α was varied from zero (for cumulene) to 90° . The calculation results show that the minimum of the total energy is achieved at $\alpha = 55^\circ$ which corresponds to the energy per atom of 0.25 eV (Figure 11.8). Besides the forbidden gap of 1.5 eV width appears in the π

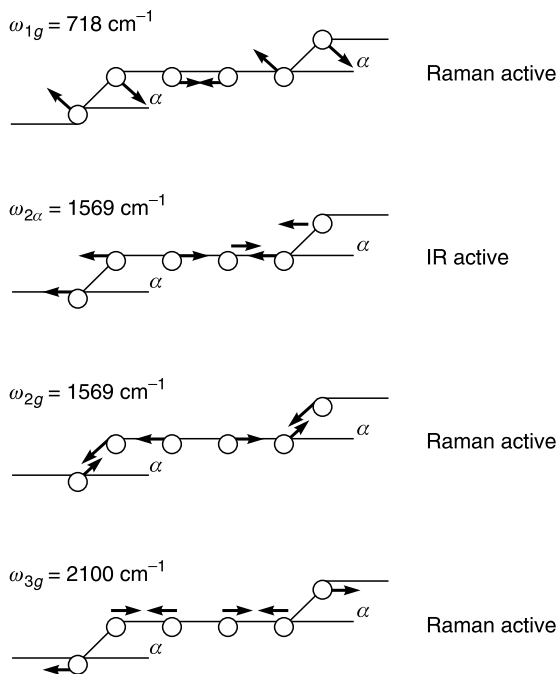


FIGURE 11.7 Calculated vibration modes of carbon chain with kinks.

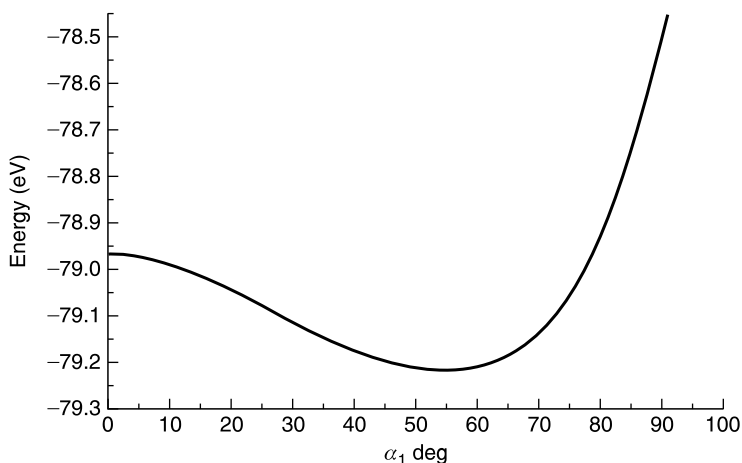


FIGURE 11.8 Calculated total electron energy of the chain as a function of kink angle.

band and the maximum found experimentally at 12 eV now corresponds to the bottom of the forbidden gap (Figure 11.6(b)). Thus, the periodic kinks in a carbon chain are an example of a deformation wave decreasing the total energy of the chain where the linear sp^1 carbon chains are regularly separated by carbon atoms in p^2 states. The kink angle α was varied from zero (for cumulene) to 90° .

11.4.2 EELS MEASUREMENTS

The EELS results provide reliable information about the density of electrons in the valence band of solids, electron excitations in solids, and volume density of the material. The EELS spectrum was obtained from the spectrum of the 1s carbon photoemission line corresponding to the electron energy of about 1 keV. We have followed the procedure described in ref. [15] and removed the elastic 1s line to obtain the loss function in order to evaluate the energy losses as shown in Figures 11.9 and 11.10(a).

Figure 11.9 shows the EELS spectrum of diamond (dash dotted line) [16], graphite (dashed line) [17], polyacetylene (dotted line) [15] and oriented carbon film (solid line). Energy losses were recorded in a low energy region from zero to 40 eV, which corresponds to both one-particle excitation and collective excitation modes (plasmons). The loss function is $S(E) = -Im(1/\epsilon(E))$ where $\epsilon(E) = \epsilon_1(E) + i\epsilon_2(E)$ is a complex dielectric function. The maximum of $S(E)$ at the energy $E = 3.7$ eV corresponds to one particle interband excitation enhanced by the π -plasmon in carbon films. The broad maximum at energy of 21.8 eV is the $\sigma + \pi$ -plasmon excitation energy.

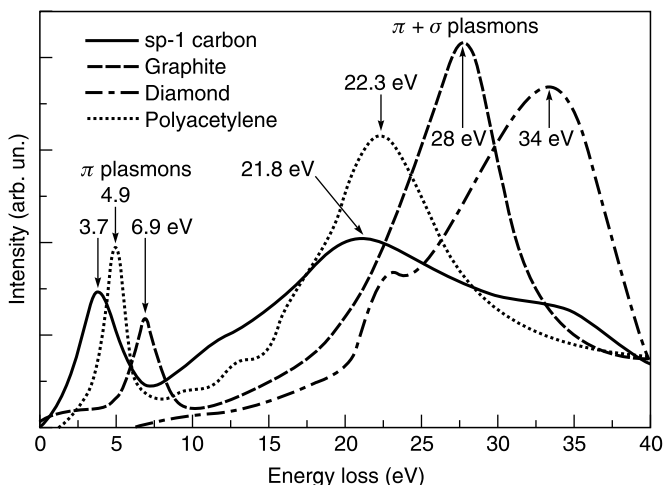


FIGURE 11.9 EELS spectra of carbon films with sp^1 -type hybridization, graphite, diamond, polyacetylene.

The plasmon energy is given by the expression $E_p = \hbar\omega_p$ and the density N_e of electrons in the valence band is given in Reference 18 as follows:

$$\omega_p = \sqrt{(4\pi N_e e^2 / m)^{1/2}},$$

where ω_p is $\sigma + \pi$ -plasmon frequency. The density of the sp^1 -hybridized carbon film is found to be equal to 1.35 g/cm^3 as the volume density of the material is proportional to N_e . This is much smaller than that for diamond (3.54 g/cm^3 , $E_p = 35 \text{ eV}$) and graphite (2.26 g/cm^3 , $E_p = 28 \text{ eV}$). It is important that the electron mean free path corresponding to the electron energy of 1 keV is equal to about 1 nm . This is the distance that is approximately equal to the dimension of atomic layers, therefore, the depth of the EELS examinations of the order of several atomic layers. In this respect, the influence of pores becomes negligible which is confirmed by the similarity of EELS of graphite and fullerenes, which are extremely porous (see, for example, Reference 19).

The calculated real part $\varepsilon_1(E)$ and imaginary part $\varepsilon_2(E)$ of the dielectric function are presented in Figure 11.10(b) $\varepsilon_1(E)$ by dotted line and $\varepsilon_2(E)$ by solid line. The $\varepsilon_1(E)$ value corresponding to energy of roughly 2 eV corresponds to the optical refraction index of the film $n = 3.32$ which was obtained by optical ellipsometry of the sample ($\lambda = 632.8 \text{ nm}$, $\hbar\omega = 1.96 \text{ eV}$). As can be seen from Figure 11.10(b) $\varepsilon_2(E)$ reveals a narrow peak at energy of 1.6 eV and a maximum at 2 V . The latter can be explained by electron transition from the top of the valence band to the bottom of the conduction

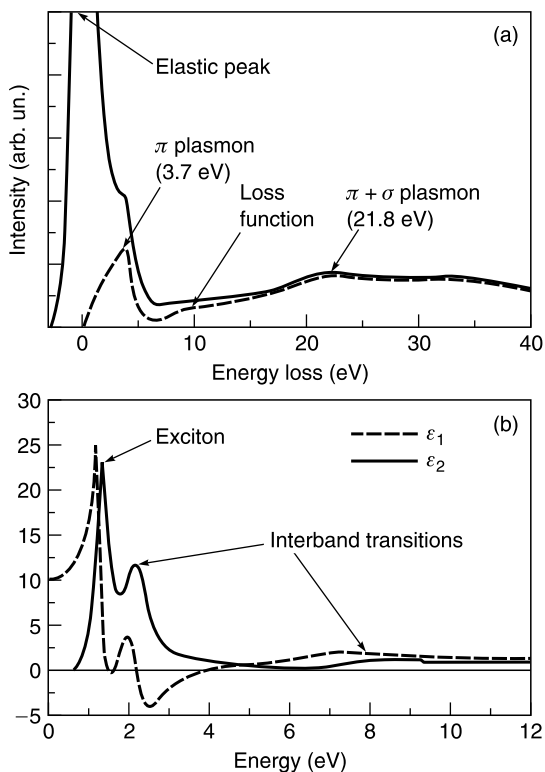


FIGURE 11.10 EELS spectrum taken from sp^1 oriented carbon films (a), real and imaginary part of dielectric function (b).

band. The very narrow peak at 1.6 eV corresponds to exciton. The π -plasmon excitation occurs at the energy where $\epsilon_1(E)=0$, *i.e.* at $E_p=3.7$ eV and is smaller than in graphite ($E_p=6$ eV). It should be noted that similar features in the EELS spectra are observed in polyacetylene [15], which also comprises sp^1 -hybridized triple $-C\equiv C-$ bonds in the carbon skeleton. In spite of that, the π -plasmon energy of polyacetylene is higher than that obtained in the present study (4.9 eV).

As was shown for polydiacetylene [15] the presence of the exciton peak at the energy of 1.6 eV provides evidence for the high degree of ordering of carbon chains in the film. Therefore we can conclude that the sp^1 -hybridized carbon films also consist of a very highly ordered material.

11.4.3 RAMAN SPECTROSCOPY

The Raman spectrum of an sp^1 -hybridized carbon-chain film with thickness of 50 nm shown in Figure 11.11(a) consists of two broad maximums at

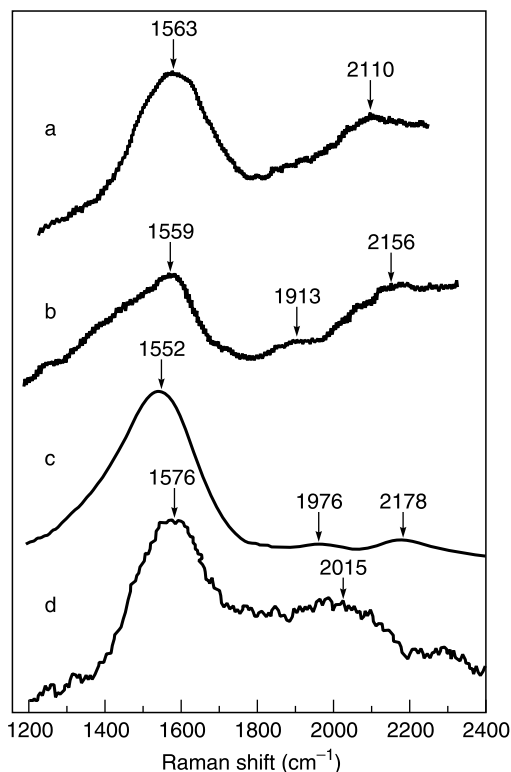


FIGURE 11.11 Raman spectrum of thin sp^1 carbon films $h = 50$ nm (a), after heating at 150°C in vacuum (b) and $h = 150$ nm (c) and doped with sulfur.

1563 and 2110 cm^{-1} , the position of which corresponds well to that already published [11,20–25]. Figure 11.11(b) shows the Raman spectrum of thin sp^1 -hybridized carbon film ($h = 500\text{ Å}$) after heating at 150°C in vacuum. The heating at 150°C slightly changes the positions of the maximums in its Raman spectrum, shown in Figure 11.11(b); an additional maximum at 1913 cm^{-1} appears in Raman spectrum of the annealed film (a splitting of the band).

An increase of the thickness of the carbon film results in decreasing the intensity of the high frequency maximum compared to that of the maximum at 1552 cm^{-1} (Figure 11.11(c)). Doping the carbon films with sulfur results in some changes in the shape of the Raman spectrum shown in Figure 11.11(d) and the enhancement of the high-frequency peak at 2015 cm^{-1} .

For the interpretation of the results of the IR and Raman spectroscopy one can use phonon frequencies calculated by using the so-called harmonic approximation widely used in solid-state physics [26]. The selection rules for

the IR and Raman examination for the correct assignment of the calculated vibration modes should also be taken into account.

The high-frequency band in the region of 2000 cm^{-1} is commonly attributed to stretching vibrations frequency, ω of long sp^1 -hybridized carbon chains, which can be approximately calculated from the following equation:

$$\omega = (4k/m)^{1/2}$$

where k is an elastic constant, m is mass of the carbon atom. The other peak at $1550\text{--}1580\text{ cm}^{-1}$ corresponds to the position of the sp^2 -carbon bond vibration frequency and, therefore, it is conventionally considered to be a feature of sp^2 -carbon phase. However, this peak can alternatively be explained by the presence of regular kinks in the polycumulene carbon chains [2]. Figure 11.12 shows a calculated density of phonon states in the polycumulene carbon chain where elastic constants were chosen to be equal to k_1 in linear fragments of the chain and to k_2 in the region of the kink; the k_2/k_1 value is varied from 1 (Figure 11.12(a)) to zero (Figure 11.12(e)). In these calculations only one component of the atomic coordinates was taken into account (*i.e.* along the chain axis). As can be seen from Figure 11.12, the phonon band of cumulene (a) transforms to discrete frequencies of the butatriene molecule when $k_2 = 0$ (e) due to the alternation of the k constant. Besides that, every sub-band has two maximums at the threshold values, which are a specific feature of the one-dimensional system. This may be

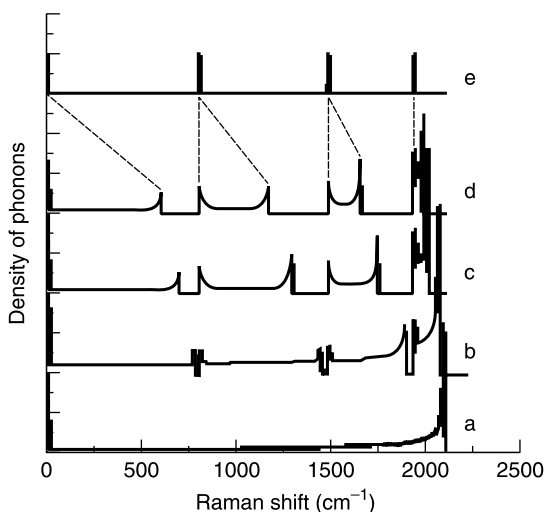


FIGURE 11.12 Calculated carbon chain phonon density of states for $k_2/k_1 = 1.0$ (a), 0.9 (b), 0.6 (c), 0.4 (d), 0 (e).

a reason for splitting the high-frequency Raman band (Figure 11.12(c)) into two maximums at 1976 and 2178 cm^{-1} .

The calculation results also indicate that the bands that lie in the region from 750 to 1200 and from 1500 to 1700 cm^{-1} are Raman inactive, which is shown in Figure 11.12(d), while bands that are Raman active are 0–700 and 1900–2000 cm^{-1} . The more accurate calculations, however, should also take into account both the transversal and longitudinal components of atomic vibrations in kinked carbon chains. When the *trans*-polycumulene infinite chain with regular kinks is taken into consideration, the following vibration modes and frequencies can be obtained (Figure 11.7) where $\omega_0 = (k/m)^{1/2} = 1132 \text{ cm}^{-1}$ and $\alpha = 60^\circ$. The Raman active modes are the only ones that have a center of symmetry (symmetric vibrations) in Figure 11.7. In the case of anti-symmetric modes they are IR active.

The calculations show that there are two modes with the same frequency of 1569 cm^{-1} , one of which is Raman active and the other one is IR active. The IR active mode corresponds to longitudinal vibrations. The Raman active 1569 cm^{-1} mode was not obtained in our simplified calculations. This mode corresponds to a vibration of the kinks, which are directed along the chemical bonds on the ends of linear fragments. The 2100 cm^{-1} mode is directed along the chain axis.

Thus, it can be concluded that the Raman peak at 1569 cm^{-1} is sensitive to both the transverse and longitudinal components of the electric field, while the mode at 2100 cm^{-1} is sensitive only to the longitudinal component and therefore can be screened by the electrons in the conduction band of the carbon chain. This screening can influence both the intensity and the position of this peak.

One well-known example confirming our calculations is the vibration mode of polydiacetylene, which demonstrates three strong maximums in the Raman spectrum at $\omega_1 = 2116 \text{ cm}^{-1}$ (along the chain axis) and $\omega_2 = 1517 \text{ cm}^{-1}$ (along the kinks) and at $\omega_3 = 1072 \text{ cm}^{-1}$ [25]. The deviation of ω_3 from the experimental value can be explained by the influence of side groups in the polydiacetylene polymer chain on the ω_3 frequency.

11.4.4 ATOMIC FORCE MICROSCOPY

The oriented linear sp^1 -hybridized carbon-chain film with the thickness of 4 nm was deposited epitaxially on the surface of a single mica crystal ($a = 0.515 \text{ nm}$); the film was studied by atomic force microscopy (AFM). Figure 11.13(a) shows the AFM image of the film surface in the height mode.

The image provides evidence for the hexagonal crystal lattice of carbon atoms, which are seen on the tops of carbon chains. The crystal lattice parameter a was found to be equal to 0.486 nm. The result is in good agreement with the parameter of the hexagonal crystal lattice obtained by AFM and TEM ($0.490 \pm 0.002 \text{ nm}$).

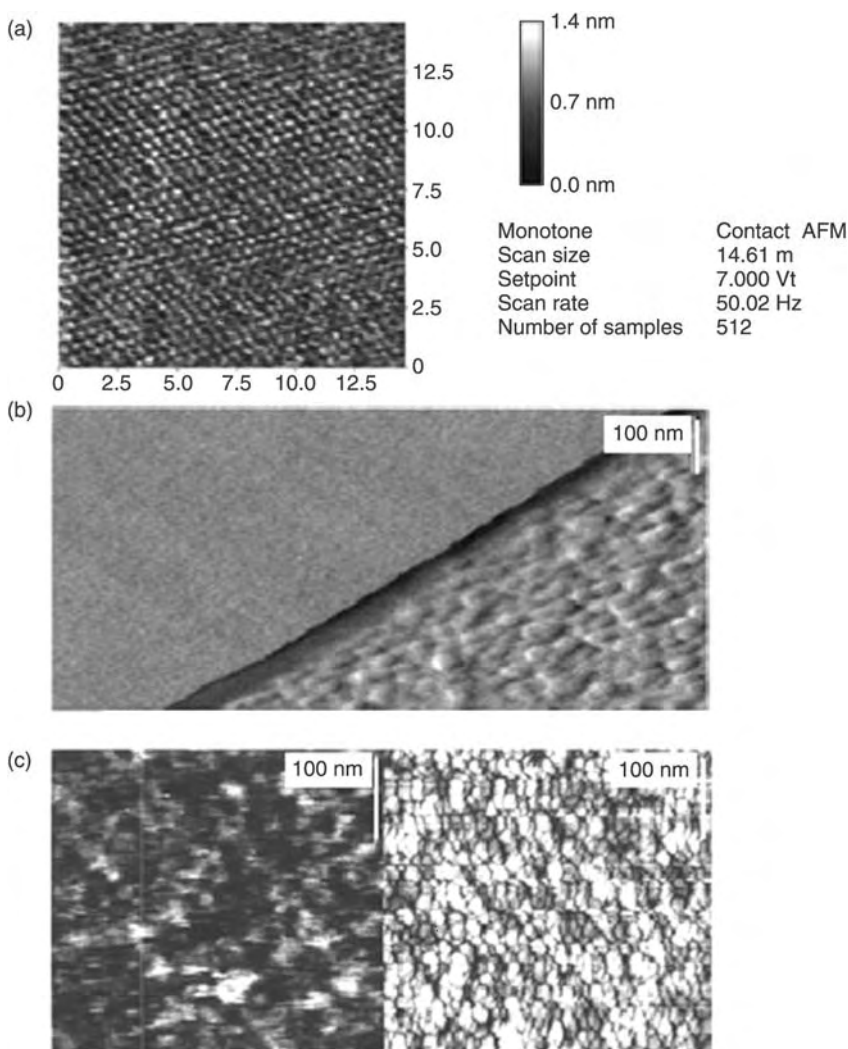


FIGURE 11.13 AFM image of epitaxially oriented carbon film (a), AFM image of carbon film edge on the surface of gold particles (b), STM image of the same region (c). (Carbon film on the left; underlying gold particles on the right).

11.4.5 SCANNING TUNNELING MICROSCOPY

A free-standing film consisting of sp^1 -hybridized carbon was placed on a gold film and the film thickness was determined by AFM measurement of the step height on the edge of the carbon film. Figure 11.13(b) shows the AFM image of the carbon film edge placed on the substrate with gold particles on

it (below). The STM image of the film was obtained by a Nanoscope-3 microscope and is shown in Figure 11.13(c). For comparison The STM image of the golden supporting layer is also shown in Figure 11.13(c) for comparison. According to AFM studies the surface of the film is extremely smooth in contrast to that obtained by STM. The STM image reveals the features, which are relevant to the underlying gold substrate with gold particles on it. This means that the STM image is explained by tunneling transparency of the sp^1 -hybridized carbon film but not by the surface corrugation. This effect presumably has the same origin as the tunneling conductivity of long-chain hydrocarbon films deposited on conductive substrates.

11.4.6 ELECTRIC CONDUCTIVITY

According to the proposed model of atomic structure of the chain carbon films the conductivity of the films should be high in the direction of carbon chains and low in the direction perpendicular to the chain axis, because the distance between the chains is much higher than that between the carbon atoms in the chain. Therefore, electron hopping among the chains is quite small.

The value of electric conductivity of the film was measured using a four-point system of gold contacts. The film thickness was 80 nm. The room temperature electric conductivity in the vertical direction was found to be $17.7 \Omega \cdot m$ while that in the horizontal direction was $3.2 \times 10^6 \Omega \cdot m$. The ratio between the electric conductivity in the vertical and horizontal directions is equal to 2×10^5 . This means that the oriented sp^1 -hybridized carbon films indeed belong to anisotropic conductors.

The dark d.c. electric conductivity $\sigma(T)$ of the films (Figure 11.14) in the direction parallel to the film surface depends on both the temperature and film thickness. There are two different regions in the $\sigma(T)$ curves plotted in the activation coordinates $\log(\sigma) - 1/T$. The first one at temperatures of $150 K < T < 300 K$ is linear and is characterized by a slope, which depends on the film thickness. The mechanism of conductivity changes at lower temperatures in the range of $70 K < T < 140 K$ and the $\sigma(T)$ dependence becomes nonlinear in this temperature region. The most appropriate mechanism of conductivity of the carbon films at high temperatures is their thermal activation from gap state into the states above mobility edge. The activation energy decreases from 0.16 eV to 0.06 eV when the thickness of the films increases from 20 nm to 100 nm.

The temperature behavior of conductivity follows the variable length hopping conductivity via electron states localized near the Fermi level and is described by the expression

$$\sigma(T) = \sigma \exp(-(T_o/T)^n),$$

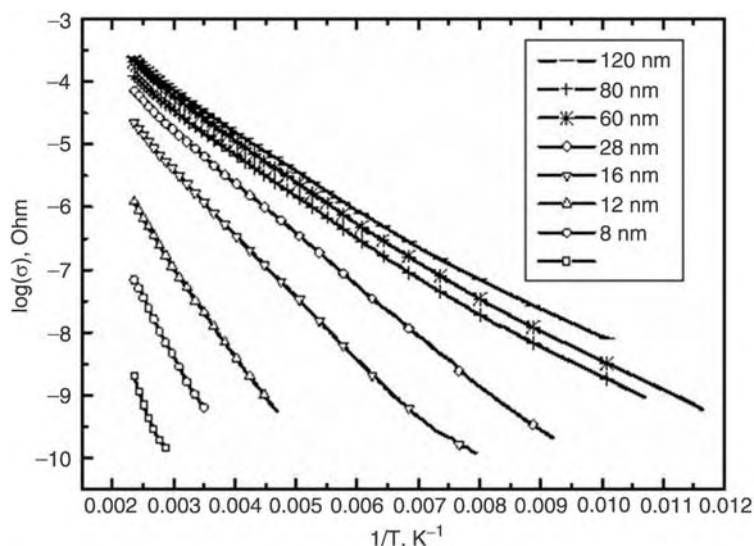


FIGURE 11.14 Temperature dependence of conductivity of oriented carbon films of different thickness.

where n is determined by the dimension of the sample and is equal to $1/4$ for three-dimensional and $1/3$ for two-dimensional samples. If $n = 1/2$, the Coulomb repulsion of electrons becomes important. It is thought that the electron states localized near the Fermi level can be formed as a result of the state of the chain kink (Figure 11.1(g)).

The temperature dependence of the d.c. electric conductivity of the sp^1 films in the direction parallel to the chain axis shows that it is characterized by the thermally activated behavior and the activation energy is equal to 0.02 eV in the temperature interval 160–300 K. This is in good agreement with the activation energy of solitons in polyyne chains.

As a result of doping the sp^1 -hybridized carbon films with H, N, Se, Te, and S, a decrease of electrical resistivity in the direction parallel to the film surface and an increase in the direction normal to the film surface by the factor of 100 is observed. At the same time the optical measurements show that the effective optical gap of the films increases up to 3 eV (see Section 11.4.7).

It was found by ESCA and TEM studies that some doping atoms (H and N) create strong chemical bonds with carbon chains during doping, whereas other atoms, for example S, do not form chemical bonds and are situated among the carbon chains.

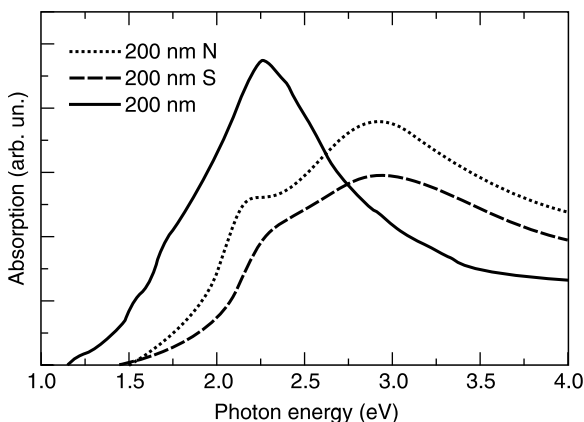


FIGURE 11.15 UV and visible light adsorption of sp^1 carbon films.

11.4.7 OPTICAL PROPERTIES

The UV and visible light adsorption of the linear-chain carbon films was measured by a Perkin Elmer spectrometer in reflection mode. The light adsorption coefficient, A , was recorded in the region of 250–1100 nm. In this region the A value is directly proportional to the optical joint density of states (OJDSs) of the material investigated [15–17]. Figure 11.15 illustrates the light adsorption results by use of the linear-chain carbon film with thickness of 200 nm. The maximum at 550 nm (2.26 eV) corresponds to the film composed of pure linear-chain carbon and at 425 nm (2.92 eV) to the film of S-doped linear-chain carbon. It can be seen from the figure that the OJDS of the S-doped film changes compared to the pure sp^1 -carbon film. The maximum on the dependencies shown in Figure 11.15 corresponds to the electron $\pi \rightarrow \pi^*$ transitions in the valence band. It can be seen that, as a result of doping, the maximum of adsorption shifts from 2.26 eV to 2.92 eV, so that the “effective” optical gap increases. This is in good agreement with the fact that the electric resistivity of the films increases after doping.

11.4.8 FIELD EFFECT MEASUREMENTS

Field effect measurements were performed on the sp^1 -hybridized carbon films doped with S. Figure 11.16(a) shows schematically the cross section of the sp^1 film deposited on a dielectric substrate, where $2a$ is the film width and h is its thickness. If $h \ll 2a$, the normal component of electric field created on the surface of the film can be calculated by the equation

$$E_n = \frac{1}{\sqrt{a^2 - x^2}}$$

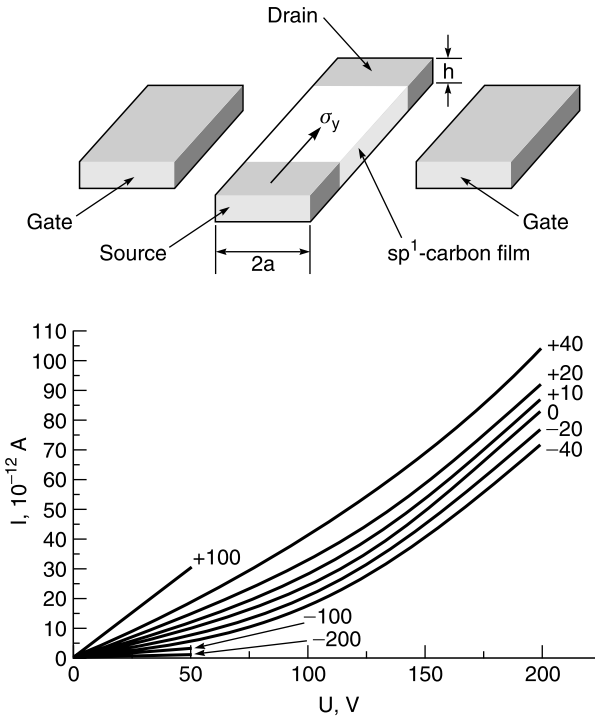


FIGURE 11.16 Field effect measurements.

for $|x| < a$ where x is the coordinate in the horizontal direction. The E_n becomes infinite on the edges of the film at $x = \pm a$. This makes the field effect simply observed on the edges of the film if the current flow is situated in the horizontal direction.

An alternative approach to horizontal current flow is the field effect measurement when the current flows in vertical direction (with respect to the film surface). In this case, the following equation describes the horizontal component of the field:

$$E_h = \frac{1}{\sqrt{x^2 - a^2}}$$

for $|x| > a$ and E_h is zero for $|x| < a$. This case is the most interesting because the electron mobility in this direction is expected to be very high. However, this requires preparing a very small source and draining contacts in a narrow area near the edges of the sp^1 -carbon film where the horizontal electric field becomes infinite.

The field effect measurements were performed using horizontal channel current. The S-doped sp^1 -carbon film on the surface of a single Al_2O_3 crystal with thickness of about 20 nm was used to prepare a conducting channel. The sulfur content in the sp^1 film measured by Auger spectroscopy was found to be 6%. The source and drain contacts were made from Al. The gate electrodes were deposited on both sides of the sp^1 -carbon channel and were separated from it by dielectric gaps.

As can be seen in Figure 11.16(b), the electric resistance of the film depends on the applied gate voltage and, therefore, its “in-plane” conductivity becomes a function of the applied electric field. On that basis we can conclude that the sp^1 film clearly demonstrates the field effect.

11.4.9 Al/ sp^1 -C/p-Si HETEROJUNCTION

The heterojunction of the p-type Si wafer was used as a substrate. Ohmic contacts were obtained by deposition of Al contacts on the p-type Si surface. Figure 11.17(a) shows the I - V characteristics of this device. For zero thickness of the carbon film the linear I - V characteristics were observed while for non-zero thickness they were nonlinear and can be described by the equation

$$I = I_0(e^{-eV/kT} - 1)$$

under forward biased conditions. In contrast, reverse bias I - V characteristic can be described by the Fowler–Nordheim field emission equation:

$$I = AV^2 \exp(c/V).$$

These features indicate that the Al/ sp^1 -C/p-Si heterojunction was obtained. The energy band diagram of this junction is schematically shown in Figure 11.17(b), where the band gap $E_g = 1.8$ eV of the sp^1 -carbon film was taken from the light adsorption measurements and the position of the top of sp^1 -carbon valence band $E_v = -4$ eV was determined from the photoelectron spectroscopy measurements in ultra-high vacuum. In the absence of a carbon film the Fermi level appears in the valence band of the p-type Si and the ohmic conductivity was observed while in the presence of the carbon film the Schottky-like barrier with the height of $\Delta\phi$ which depends on both the applied voltage and thickness of the sp^1 -carbon film. These result in the Schottky-like I - V characteristic. In the opposite direction, tunneling across the carbon film into the conduction band of Si from the Al contact may occur in strong electric fields, when the Fermi level of the Al contact is shifted above the bottom of the conduction band.

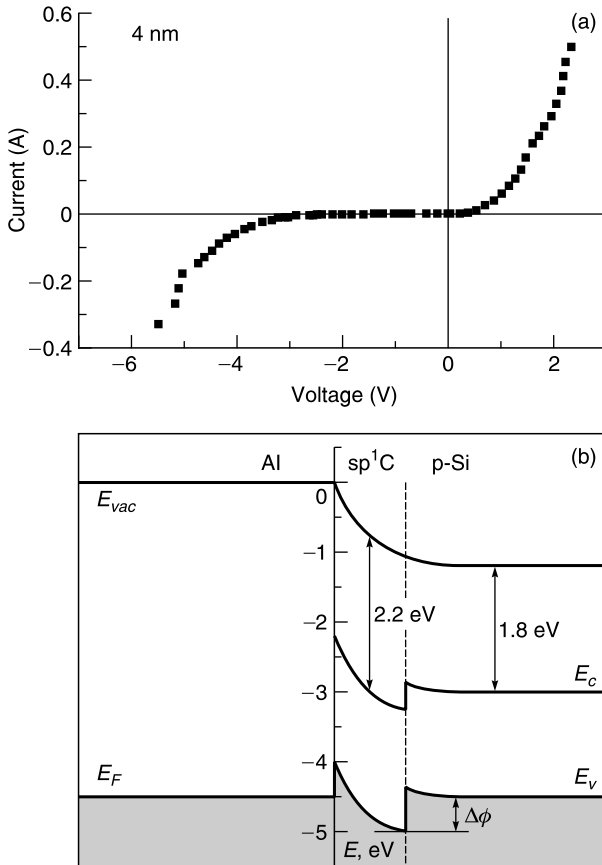


FIGURE 11.17 Volt–current characteristics of Al/sp¹-C/p-Si heterojunction (a) and schematic representation of energy band diagram (b).

11.4.10 COLD ELECTRON EMISSION

The surface of the sp¹-carbon film was examined as a cold emitter of electrons in a normal applied electric field. Figure 11.18 shows the volt–current characteristic of a vacuum diode with a flat sp¹-carbon cathode at room temperature. The figure is plotted in the Schottky coordinates $\log(I) - U^{1/2}$ where U is the applied voltage. The distance between the anode and cathode was about 0.3 mm. As can be seen in Figure 11.18, the electron emission from the cathode can be described by the Schottky law:

$$\log(I) = e^{3/2} U^{1/2} / kT,$$

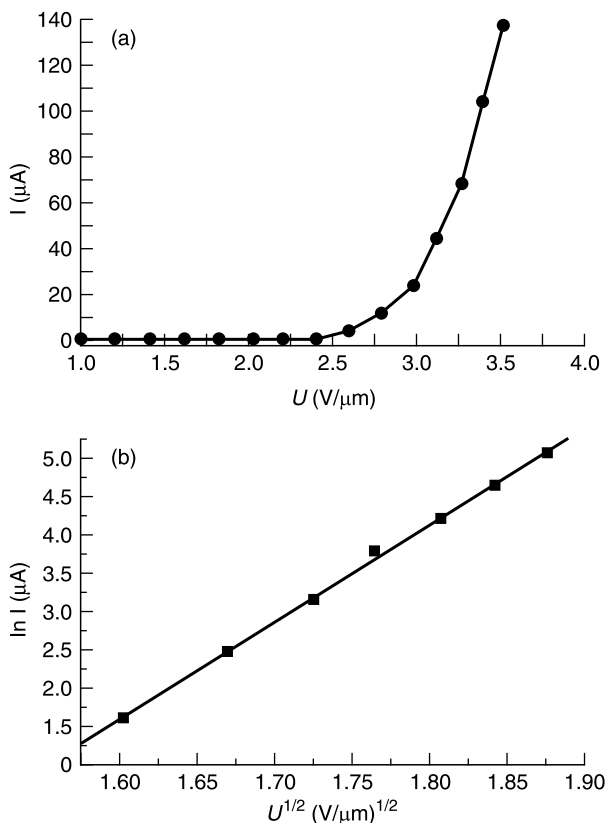


FIGURE 11.18 Volt–current characteristic of vacuum diode with flat sp^1 carbon cathode at room temperature (a), the same in Schottky coordinates (b).

which corresponds to the thermally activated electron current emitted above the potential barrier due to lowering the Schottky barrier by the applied electric voltage U . This result clearly shows that the sp^1 -carbon films are good electron emitters at very small applied electric fields (between 10^4 and $10^5 V/cm$) on the surface of the cathode. It should be mentioned that, in contrast to that, the cold emission from a film made of carbon nano-tubes is commonly described by the Fowler–Nordheim mechanism, which implies quantum tunneling through potential barriers in strong electric fields and requires a much stronger electric field (about $10^7 V/cm$).

11.4.11 INJECTION OF ELECTRONS IN DIELECTRICS

The sp^1 -hybridized carbon films can be used as injector electrodes to provide the injection of electron current into dielectrics such as SiO_2 and other

materials [27], as the work function of the films appears to be relatively small (see [Section 11.4.10](#)). This is important for the fabrication of electroluminescent devices, which require electric currents of both electrons and holes, recombination of which results in light emission. One of the interesting aspects of this issue is the possibility of obtaining oriented sp^1 -carbon films, which can be used as a command surface for deposition of different organic molecules on the surface of a substrate [8]. This property permits luminescent layers consisting of organic molecules of different types to be obtained. At the same time the electron injector serves as a supporting command surface.

11.4.12 THE DEPENDENCE OF ATOMIC STRUCTURE OF sp^1 -HYBRIDIZED CARBON FILMS ON THEIR THICKNESS

It is well known that the ensemble of sp^1 -carbon chains is unstable and used to form cross-bonds between the neighboring chains. This results in the formation of sp^2 and sp^3 chemical bonds between carbon atoms. However, on the substrate surface the situation is radically changed due to the interaction of carbon chains with the surface. In this case the growth of well-oriented carbon chains was observed in [9]. The film orientation is found to be strongly dependent both on the film thickness and deposition conditions. For thicker films the influence of the substrate surface becomes negligible and the films are not purely sp^1 .

The mean size of the crystallites of linear-chain carbon films calculated from the width of their electron diffraction maximums depends on the film thickness (Table 11.1). As can be seen from Table 11.1 the mean crystal size of the films is comparable with the film thickness if that thickness is about 4.0 nm. In this case, the films become highly oriented and there are sharp reflections in their diffraction pattern ([Figure 11.1\(a\)](#)). If the thickness of the films increases to 16.0 nm, the orientation still takes place. In films with a thickness greater than 60 nm amorphization is observed, with the formation of inter-chain bounds. This is clearly seen by increasing the intensity of diffraction maximums corresponding to the three-dimensional amorphous carbon phase and finally by the complete disappearance of diffraction maximums corresponding to the sp^1 phase.

TABLE 11.1
The Dependence of Crystal Mean Size on Film Thickness

Thickness (nm)	4.0	6.0	8.0	16.0	32.0	>64
Crystal mean size (nm)	3.5	2.5	2.3	2.0	1.7	<1.0

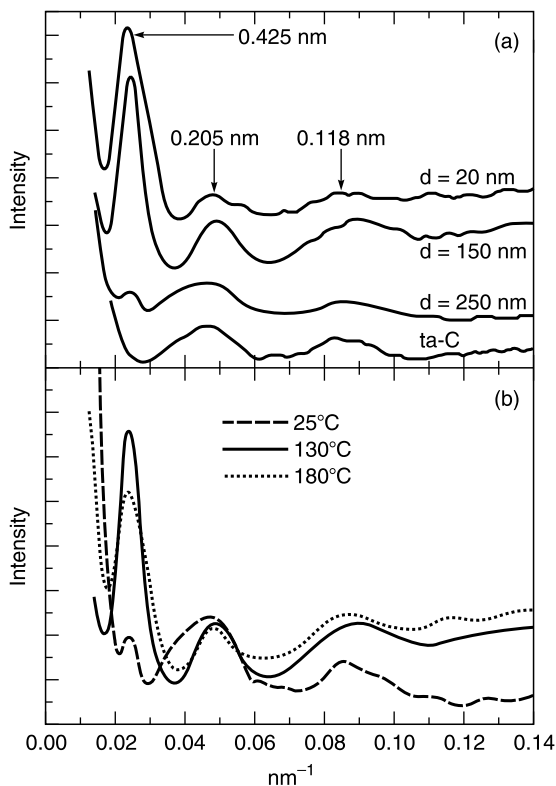


FIGURE 11.19 Distribution of the intensity of electron diffraction of two-dimensional ordered linear chain carbon films. (a) For different thickness, deposition temperature $T = 130^\circ\text{C}$, (b) for different deposition temperatures and the thickness 200 nm.

Figure 11.19(a) shows the distribution of the intensity of electron diffraction of the carbon films with the two-dimensional ordered linear carbon chains as a function of their thickness. As can be seen in Figure 11.19 the strongest reflections correspond to the inter-plane spacing of 0.425 nm and relate to the well-ordered carbon chain structure. In the case of thinner films, the intensities of higher orders are much weaker than those of the first one. An increase in the film thickness results in decreasing the intensity of the strongest maximum and increasing that of the maximums at $d = 0.205$ nm and $d = 0.118$ nm which are conventionally observed in diamond films. The peak in the region of 0.430–0.435 nm almost completely disappears at a thickness of 250 nm and the film transforms into that with a pure tetrahedral amorphous diamond-like structure (ta-C). Therefore, the influence of the surface on carbon film structure is observed until a thickness of

about 200 nm. This effect is also influenced by deposition temperature, electron irradiation, gas environment, *etc.*

Figure 11.19(b) illustrates the dependence of film structure on the deposition temperature. As can be seen the diffraction pattern corresponds to the structure of poorly ordered carbon at low temperatures with a small maximum in the region of the strongest reflection (0.430–0.435 nm). When the temperature increases to 130°C, the intensity of the strongest reflection dramatically increases. Further elevation of the temperature results in decreasing the amount of sp^1 fraction in the film and consequently the intensity of the strongest reflection.

The data obtained show that both the temperature and film thickness influence the film structure. We can conclude that it gradually decreases when the film thickness increases, as the first maximum characterizes the degree of atomic ordering in the films. This is in good agreement with the important role that the substrate surface plays in stabilization of carbon chains. On the other hand, the dependence of ordering on the deposition temperature clearly shows that the oriented growth of carbon chains is an energy-activated process requiring elevated temperature. The oriented growth can also be obtained during irradiation of the growing film with low energy ions [9,11].

Figure 11.20 shows the influence of electron beam irradiation with $E=100$ keV in a transmission electron microscope on thin film structure during 2 s of deposition. As can be seen in Figure 11.20 the electron irradiation of the film results in its amorphization, as the main maximum at $d=0.435$ nm attributing to the linear chain structure disappears; the film structure transforms into diamond-like carbon. This means that the electron beam excitation of carbon atoms leads to cross-linkages among carbon chains and, as a result, the transformation of sp^1 bonds into sp^2 and sp^3 bonds takes place.

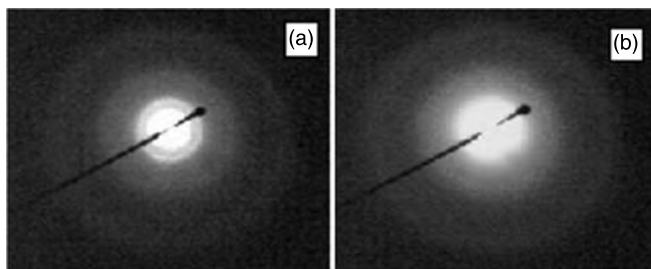


FIGURE 11.20 The influence of electron irradiation on the structure of the linear chain carbon films.

11.4.13 CARBON ELECTRONICS

Carbon electronics started from the investigation of diamond single crystals (sp^3 -type hybridization) because the diamond crystal structure is similar to that of Si and Ge. It was expected that both p- and n-type doping could be achieved in diamond to obtain the basic element of solid-state electronics: that is, the p-n junction. However, the conductivity of only the p-type was realized in diamond and it was the main obstacle to the creation of carbon electronics. Nevertheless, there is an alternative route to the creation of hetero-junctions by use of the highly oriented sp^1 -hybridized carbon films doped by different elements.

Figure 11.21(a) schematically shows a structure composed of a two-layered carbon film deposited on an Al surface by the pulsed-evaporation vacuum technique. The structure consists of a diamond-like film (ta-C) with tetrahedral sp^3 bonds between carbon atoms and an S-doped highly oriented sp^1 -hybridized carbon film. Figure 11.21(b) represents the I - V characteristics of such a structure, which is a Al/ sp^1 carbon- sp^3 carbon/Al junction.

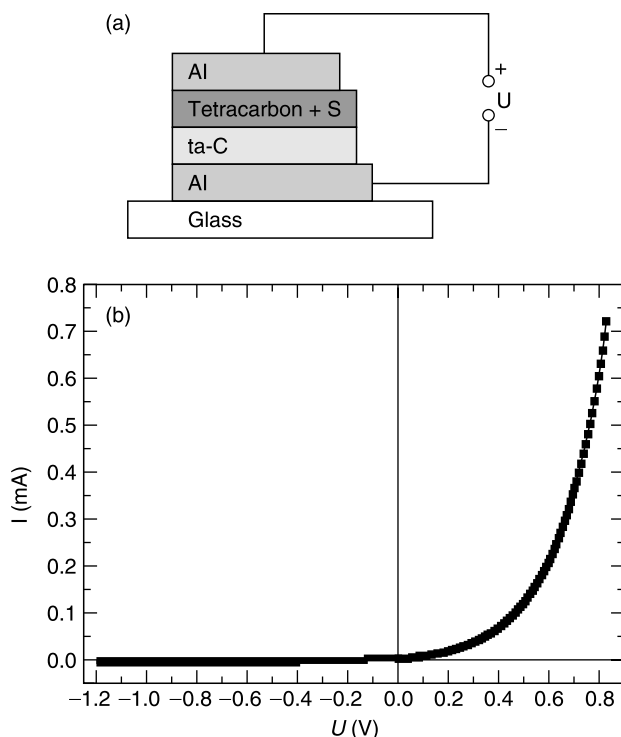


FIGURE 11.21 (a) Schematic representation of Al/ sp^1 carbon- sp^3 carbon/Al junction, (b) I - V characteristics of Al/ sp^1 carbon- sp^3 carbon/Al.

The I - V curve is found to have Schottky-type dependence under forward biased conditions. This means that a semiconducting diode can be successfully fabricated using the sp^1/sp^3 junction in the carbon-based structure. This result opens up a promising route to the creation of carbon electronics on the basis of using junctions consisting of carbon films with various types of electron hybridization with the aid of different dopants.

11.5 THE NEW CARBON MATERIAL TETRACARBONTM

A new carbon material, TetracarbonTM, was developed on the basis of sp^1 -hybridized highly oriented carbon films. Figure 11.1(g) indicates that TetracarbonTM consists of densely packed linear chains of sp^1 -hybridized carbon, oriented perpendicularly to the substrate surface. An analogy could be velvet, where linear carbon chains project perpendicularly to the substrate surface.

Thus, inter-atomic distances and the atomic state in TetracarbonTM are fundamentally different from all the known forms of carbon. The differences between clear and hard diamond on the one hand, and soft and black graphite on the other hand, illustrate the differences among TetracarbonTM and other forms of carbon. The distance between the neighboring sp^1 -carbon atoms within the TetracarbonTM chain is about 1.3 Å, whereas the distance between the carbon chains is 4.80–5.03 Å. It is interesting to note that in some respects TetracarbonTM is similar to tubulenes, as it can be considered as tubulene in the limit when the diameter of the tube approaches the diameter of carbon atom. Nevertheless, in TetracarbonTM the hybridization state of carbon atoms changes from sp^2 to sp^1 . It is basically a new purely one-dimensional sp^1 -carbon modification with one-dimensional electron band structure, whereas tubulene is a quasi-one-dimensional material in which the number of one-dimensional electron bands increases with increasing tubulene diameter. TetracarbonTM and tubulene are also similar in that the carbon chains in TetracarbonTM are oriented normally to the surface of the film, similar to the orientation in tubulene.

The sp^1 modification carbyne briefly described below is characterized by a different intrinsic structure and can be obtained only in the form of very small particles. Another analogous example is the sp^1 molecular crystals which are composed of short sp^1 -carbon chains with organic caps on the ends of the chains, which prevents them from collapsing into the amorphous state [28]. These crystals are not composed of pure sp^1 -hybridized carbon and are stacked into a cross-linked crystal structure, which is easily dissolved in many organic solvents and is completely different from TetracarbonTM.

Numerous tests of TetracarbonTM have shown a number of its valuable features. The TetracarbonTM coating process is performed at low temperature (20–200°C), so it can be used for coating polymers (polyethylene,

polyurethane), elastomeric materials (like silicone rubber), semiconductors, metals, ceramics, glass, and other materials. The adhesion of the TetracarbonTM coating is so high that it can be removed from the substrate together with substrate material. Thus, its adhesion to many substrates is higher than the substrate material strength. Samples of silicone rubber coated with TetracarbonTM were mechanically tested, including elongation by 300% and multiple deformations; the coating withstood these tests without visible damage, as no cracks or coating exfoliation were observed. The high flexibility and elasticity are unique features of TetracarbonTM. The low friction coefficient (0.1–0.2) against metals, smooth and uniform surfaces, and excellent adhesion allow TetracarbonTM to be employed in numerous applications. The unique characteristics of TetracarbonTM can be controlled and varied during its deposition, which allows customizing the TetracarbonTM coating for different applications.

In experiments on biomedical examination of TetracarbonTM, the absence of protein denaturation was found on its surface. It is also characterized by exceptionally low blood coagulation potential, thus having perfect blood compatibility. Figure 11.22 shows the rate of the clot growth on the surface of different materials in comparison with the TetracarbonTM films. As can be seen in Figure 11.22 the TetracarbonTM coating possesses a record thrombus resistance and allows improving biocompatibility of medical implants and devices, thus preventing thrombus formation and reducing the risk of implant rejection or inflammation. TetracarbonTM can

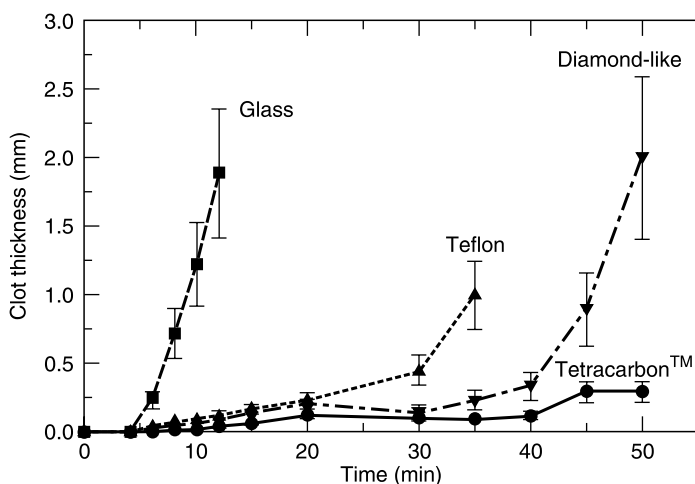


FIGURE 11.22 The rate of clot growth on the surfaces of different materials in comparison with Tetracarbon film.

be employed in cardiovascular devices, orthopedic and dental implants, contact lenses, artificial crystals, soft tissue implants, surgical needles and sutures.

The strong anisotropy of electrical conductivity is another attractive feature of TetracarbonTM, which can be explained by its regular structure consisting of densely packed linear chains of carbon atoms. The electrical conductivity along the chain direction is several orders of magnitude higher than that in other directions. In examinations by tunnel microscopy gold particles were clearly visible through 27.0 nm thick TetracarbonTM film. This occurs due to tunneling of electrons along the vertically situated carbon chains. The TetracarbonTM film deposited on a copper plate has an electric resistance of about 1 Ω , almost independently on the coating thickness varied from 16 nm up to 200 nm.

TetracarbonTM opens up great opportunities for electronics especially when taking into account the possibility of its doping to change the electrical, mechanical and optical properties, creating semiconducting junctions.

The problem of welding Cu with Al, or Ni with Al, which is of great importance in microelectronics, can be simply solved with the help of TetracarbonTM. In both cases welding cannot be carried out at any temperature and pressure. The deposition of the thin TetracarbonTM films of

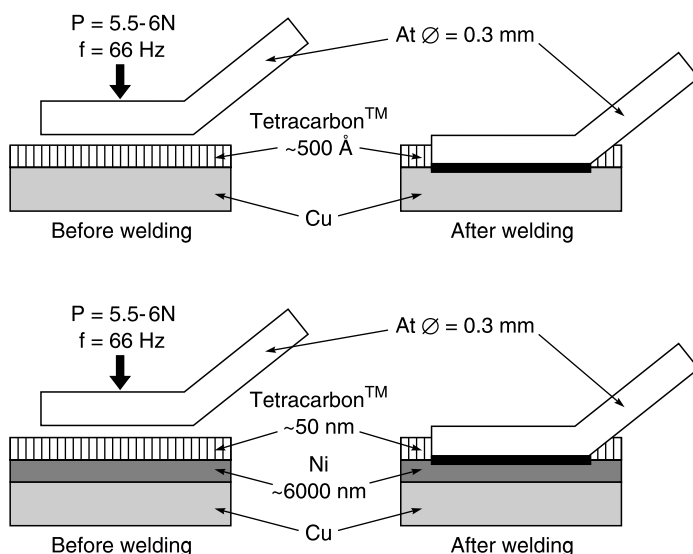


FIGURE 11.23 Scheme of cold welding between Al–Cu and Al–Ni metal pairs by means of an interface from a Tetracarbon layer.

less than 50 nm in thickness between these metal pairs can dramatically improve the ability of the metal pair to be welded; very good junctions in these systems can be obtained by cold ultrasonic welding (Figure 11.23). In both cases, the adhesion of junctions between Ni and Al, and Cu and Al was found to be equal to 6 N instead of 0.3 N required in electronic devices. It is interesting to note that no such an effect was observed for diamond-like and ta-C films. Thus, TetracarbonTM is a promising material for active and passive electronic components like transistors.

Some variants of TetracarbonTM are clear and can be employed in optics as protective coatings. The TetracarbonTM coating process and the deposition unit suitable for mass production have been developed and are being manufactured. TetracarbonTM, its coating process, the unit for its deposition and most prospective applications are patented [10].

11.6 CONCLUSIONS

A new material consisting of sp^1 -carbon which is characterized by a special electron diffraction pattern and DOVS distribution has been developed. This material is obtained by ion-assisted deposition from pulsed carbon plasmas.

On the basis of the TEM, AFM, STM, and Raman spectroscopy results the atomic structure of the new carbon material is found to correspond to two-dimensional ordered linear sp^1 -hybridized carbon.

According to the proposed model the new carbon material has a multi-layered structure consisting of densely packed linear carbon chains. The chains are connected with each other by correlated chain bends.

The results on examination of the electric conductivity and cold emission, as well as the mechanical and biological properties of the new carbon material, clearly show it can be employed in a broad field of applications, such as microelectronics, machine-building, *etc.* The excellent biological properties of TetracarbonTM make it the best material for many applications in medicine.

Table 11.2 presents some key characteristics of TetracarbonTM, based on the results of its tests performed at FORBAIRT (Dublin), Cork Technical College, and Lomonosov Moscow State University.

ACKNOWLEDGMENTS

We would like to thank Professor I. Yaminsky for preparing AFM and STM pictures of TetracarbonTM and Doctor A.P. Dementyev for XPS measurements. Financial support from the Copernicus Program (Contract ICA2-CT-2001-10008) is gratefully acknowledged.

TABLE 11.2
The Properties of Tetracarbon™ Films

Parameter	Value
Hardness	Variable from 4000 HV up to 9000 HV
Adhesion	On most substrates including stainless steel, glass, polymers, silicon rubber adhesion is higher then substrate strength itself
Coating thickness	Up to 10 μm (on hard substrates). Recommended thickness for most applications is 100–290 nm
Coating deposition rate	100 nm/min
Coating area	150 mm \times 150 mm. Larger items can be coated by item rotation
Wear resistance	Extremely high. At a low load, Tetracarbon™ wear performance is superior to diamond-like coatings
Coating texture	Very smooth and uniform coating
Thermal stability	Stable up to 300°C
Friction coefficient	0.1–0.2

REFERENCES

- [1] Kudryavtsev, Yu.; Evsyukov, S.; Guseva, M.; Babaev, V.; Khvostov, V. Carbyne — a linear chainlike carbon allotrope. In *Chemistry and Physics of Carbon, A Series of Advances*, Thrower P.A., Ed., Marcel Dekker Inc: New York, 1997, pp. 1–69.
- [2] Babaev, V.; Guseva, M. Ion assisted deposition. In *Carbyne and Carbonyl Structures*, Evsyukov S. and Kavan L., Eds., Kluwer Academic Publishers, 2000.
- [3] Chupka, W.; Inghram, M. *J. Chem. Phys.* **1954**, 22, 1472.
- [4] Brewer, L.; Engelke, J. *J. Chem. Phys.* **1962**, 36, 992.
- [5] Pitzer, K.; Clementi, E. Large molecules in carbon vapor. *J. Am. Chem. Soc.* **1959**, 81(17), 4477–4485.
- [6] Weltner, W.; Van Zec, J. Carbon molecules, ions and clusters. *Chem. Rev.* **1989**, 89, 1713–1747.
- [7] Ravaghnan, L.; Siviero, F.; Lenardi, C.; Milani, P. Cluster-beam deposition and *in situ* characterization of carbyn-rich carbon films. *Phys. Rev. Lett.* **2002**, 89, 285506.
- [8] Shibaev, P.; Guseva, M. Molecular orientation propyl- and hexyloxy-cyano-biphenyl vacuum deposited thin films. *J. Crystal Growth* **1992**, 119, 399–402.
- [9] Kudryavtsev, Yu.; Evsyukov, S.; Guseva, M.; Babaev, V.; Khvostov, V. Oriented carbon layers. *Carbon* **1992**, 30, 213–221.
- [10] Guseva, M.; Babaev, V.; Novikov, N. Tetracarbon. PCT Patent, International Application Number PCT/IB96/01487 from December 18 (1996); WO 97/25078, July 17 (1997); Guseva, M.; Babaev, V.; Novikov, N., Tetracarbon. US Patent 6,355,350 B1; Guseva, M.; Babaev, V.; Novikov, N., Tetracarbon. US Patent 6,454,797 B2.

- [11] Guseva, M.; Babaev, V.; Babaina, V.; Khvostov, V. Formation of oriented nitrogen doped carbon films. *JEPT Lett.* **1995**, 69(9), 715.
- [12] Rice, M.; Phillpot, S.; Bishop, A. Solitons, polarons and phonons in the finite polyyne chain. *Phys. Rev. B* **1986**, 34, 4139–4149.
- [13] Kertesz, M.; Koller, J.; Azman, A. Ab-initio Hartree–Fock crystal orbital studies energy bands of an infinite carbon chain. *J. Chem. Phys* **1978**, 68, 2779–2785.
- [14] Chugreev, A.; Misurkin, I. Electron structure of carbene in infinite Hartree–Fock approximation; *J. Structural Chem.* **1989**, 30, 24 (in Russian).
- [15] Fink, J.; Leisling, G. Momentum-dependent dielectric function of oriented *trans*-polyacetylene. *Phys. Rev. B* **1986**, 34(8), 5320–5328; Miyano, K.; Maeda, T. Photoluminescence, absorption and Raman spectra of a polydiacetylene. *Phys. Rev. B*, **1986**, 33(6), 4386–4388.
- [16] Daniels, J. In *Optical Constants of solids by Electron Spectroscopy*, Hohler, G., Ed., Springer Tracts in Modern Physics. Berlin: Springer-Verlag, 1970.
- [17] Daniels, J. In *Optical Constants of solids by Electron Spectroscopy*, Hohler, G., Ed., Springer Tracts in Modern Physics. Berlin: Springer-Verlag, 1970, p. 127.
- [18] Pines, D. *Elementary Excitations in Solids*. New York, Amsterdam: W.A. Benjamin Inc., 1963.
- [19] Kuzuo, R.; Terauchi, M.; Tanaka, M.; Saito, Y.; Shinohara H. High resolution electron energy loss spectra of solid C₆₀. **1991**, 30, no. 10a, p. L1817
- [20] Berdyugin, V.; Kudryavtsev, Yu.; Evsyukov, C. Raman spectroscopy of carbyne. *Dokladi AN USSR*, **1989**, 305, 3624.
- [21] Kavan, L.; Kastner, J. Carbyne forms of carbon: Continuation of the story. *Carbon* **1994**, 32, 1533.
- [22] Kijima, M.; Omura, K.; Shirakawa, H. Synthesis of conducting polymers with conjugated carbon–carbon triple bonds by electrochemical condensation of acetylene derivatives catalyzed by cooper complex. *Synth. Metals* **1997**, 84, 417.
- [23] Kijima, M.; Sakai, Y.; Shirakawa, H. Electrochemical synthesis of carbene catalyzed by nickel complex. *Synth. Metals* **1995**, 71, 1837.
- [24] Casari, C.; Bassi, A.; Ravagnan, L.; Siviero, F.; Bongiorno, G.; Bottani, C.; Milani, P. *Phys. Rev. B* **2004**, 17, 075422-7.
- [25] Miyano, K.; Maeda, T. Photoluminescence, adsorption and Raman spectra of a polydiacetylene monolayer. *Phys. Rev. B* **1986**, 33, 4386.
- [26] Lannoo, M.; Friedel, P. *Atomic and Electronic Structure of Surfaces*. Volume 16 in Springer Series in Surface Sciences. Berlin, Heidelberg: Springer-Verlag, 1991.
- [27] To be published.
- [28] Lagow, R.; Kampa, J. Synthesis of linear acetylenic. *Science* **1995**, 267, 362.

12 Synthesis of Carbynoid Materials by Chemical Dehydrohalogenation of Halogen-Containing Polymers

Sergey E. Evsyukov

CONTENTS

12.1	Introduction	253
12.2	Original Polymers	254
12.3	Dehydrohalogenating Agents	257
12.4	Characterization of the Dehydrohalogenation Products	259
12.4.1	Vibrational Spectroscopy	259
12.4.1.1	Infrared Spectroscopy	259
12.4.1.2	Raman Spectroscopy	259
12.4.2	UV–VIS Absorption Spectroscopy	261
12.4.3	Electron Spectroscopy	261
12.4.4	¹³ C Nuclear Magnetic Resonance Spectroscopy	262
12.5	Conclusions	264
	References	267

12.1 INTRODUCTION

Chemical dehydrohalogenation of some halogen-containing polymers [1] is known to be one of the most convenient and accessible methods for synthesizing carbynoid structures. The latter are generally defined as carbon-rich chain-like poly(or oligo)mers with both polyynes- and cumulene-type moieties, extended interchain cross-linking as well as end-capping and/or pendant side groups [2].

The main distinction between the dehydrohalogenation approach and polycondensation processes is that in the former case the carbon backbone is formed first by polymerizing relevant monomers, and the task for synthesizing polyyne and/or polycumulene is reduced to the complete elimination of hydrogen halide with the retention of one-dimensional structure.

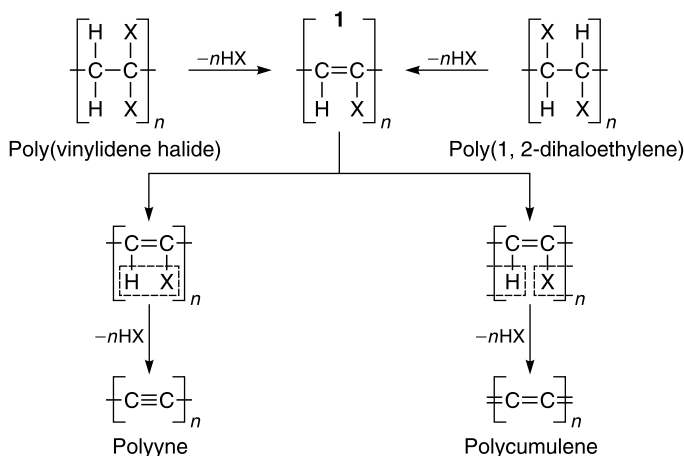
The vast majority of studies published in this field through 1997 have been extensively reviewed in 1999 [3]. Since then several studies exploring new possibilities have been published, and in the present review I will concentrate on those new accomplishments, although some issues of general importance from that review will be mentioned or briefly discussed as well. In addition, some relevant studies, which, for whatever reason, were not included in the 1999 review, will also be covered here.

12.2 ORIGINAL POLYMERS

The formation of carbyne by means of dehydrohalogenation is possible only if equal numbers of the halogen and hydrogen atoms are attached to neighboring carbon atoms in the original polymer chain. Theoretically, this allows complete elimination of side substituents in two steps to leave a 'naked' carbon chain, *i.e.* chemical carbonization of the original polymer. This requirement is satisfied in poly(vinylidene halides) (PVDHs) [4–8], poly(1,2-dihaloethylenes) [9–11], as well as in poly(1,1,2-trichlorobutadiene) and poly(1,2,3-trichlorobutadiene) [12,13]. All these types of polymers were used as original materials in numerous attempts to synthesize carbyne by the dehydrohalogenation reaction [3].

The dehydrohalogenation of halogen-containing polymers is generally held to proceed in two stages. In the first stage, the one molecule of hydrogen halide (HX) is eliminated from each repeating link of the polymer backbone to afford a halogen-substituted polyene structure **1** (Scheme 12.1, X = F, Cl, Br).

As it is seen from Scheme 12.1, the dehydrohalogenation of both poly(vinylidene halide)s and poly(1,2-dihaloethylene)s at the first stage results in the formation of the same (or very similar) polyhalovinylene, **1**. However, comparing these two types of polymers as starting materials, one should keep in mind that poly(vinylidene halide)s are produced by polymerization of corresponding 1,1-dihaloethylenes, whereas poly(1,2-dihaloethylenes), $(-\text{CHX}-\text{CHX}-)_n$, where X = Cl or Br, cannot be synthesized directly by radical polymerization of corresponding 1,2-dichloro-(or dibromo)ethylene because of steric hindrances [14]. Therefore, such polymers were prepared by halogenation of polyacetylene (polyvinylene), which can be synthesized either by polymerization of acetylene [9,10] or by dehydrohalogenation of poly(vinyl chloride) [11]. It should be noted here that each polymer-analogous transformation introduces additional chemical

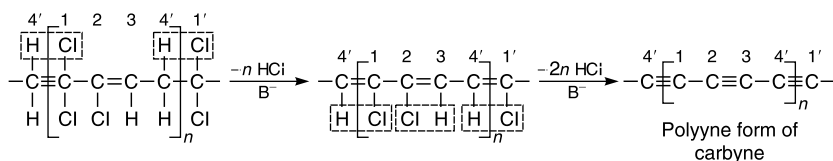


SCHEME 12.1

defects into the polymer chain, thus making complete elimination difficult and deteriorating the structure of ultimate products.

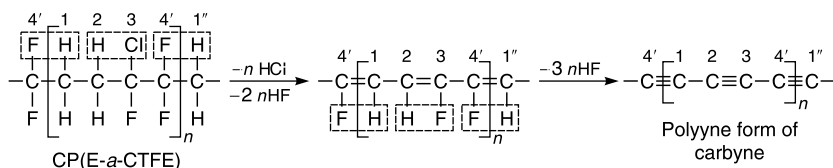
The complete dehydrohalogenation at the second stage can be expected to yield carbon chains of both polyyne and cumulene type, depending on the elimination course. The latter, in turn, is governed by the structure of original polymer (the type and amount of intrinsic defects), by the contribution of side reactions (substitution, oxidation, and cross-linking), and by the length of the sp-carbon chain being formed (long polyynes were reported to be more stable compared to cumulenes). Thermodynamic calculations by Cataldo showed that the formation of the polyyne structure during dehydrohalogenation is more favorable [15]. However, the contribution of defects (side groups), the length of carbynoid moieties being formed, and the reaction temperature, which can all affect the structure of products, were not taken into account.

Theoretically, the chemical structure of original polymers can affect the structure of the dehydrohalogenation products. Indeed, complete dehydrochlorination of poly(1,1,2-trichlorobutadiene) could be expected to result in the formation of the polyyne form of carbyne because there seemingly is no other way of elimination except that shown in Scheme 12.2 ($\text{B}^- = \text{base}$).



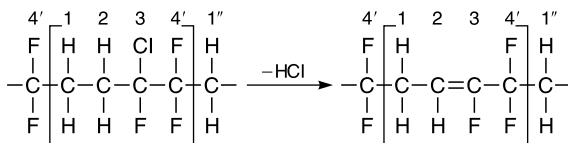
SCHEME 12.2

In a search for new starting materials for synthesizing carbynoid structures, Evsyukov et al. studied dehydrohalogenation of poly(ethylene-*alt*-chlorotrifluoroethylene) [18]. The starting polymer currently supplied by Aldrich is claimed to be an alternating co-polymer of ethylene and chlorotrifluoroethylene. Considering theoretically possible pathways of the dehydrohalogenation reaction of poly(ethylene-*alt*-chlorotrifluoroethylene) [PE-*a*-CTFE], one can conclude that the latter might be used as a precursor for synthesizing the polyynene form of carbyne. The first stage of dehydrohalogenation should bring about the formation of a fluorine-substituted polyene structure of poly(3,4-difluoro-2-butene-1,4-diylidene), regardless of the initiation site (Scheme 12.5).



SCHEME 12.5

Here it is pertinent to note that elimination of HCl from PE-*a*-CTFE should create an intermediate structure identical to that of poly(1,1,2-trihalobutadiene) (*cf.* Scheme 12.2) in the case of 1,4-polymers (Scheme 12.6).



SCHEME 12.6

Therefore, it is evident that further elimination of HF should give rise to the formation of analogous head-to-head polyhalovinylene, and complete dehydrohalogenation must yield the polyynene structure (Scheme 12.5).

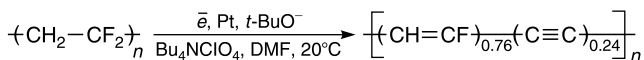
12.3 DEHYDROHALOGENATING AGENTS

Generally, basic reagents intended to be used for synthesizing carbynoid structures by a dehydrohalogenation reaction should meet three requirements. First, they should be strong enough to effect exhaustive elimination of hydrogen halides, particularly at the second stage of the reaction (*i.e.* the dehydrohalogenation of halogen-substituted polyenes, *cf.* Schemes 12.1 to 12.3, and 12.5). Secondly, their nucleophilicity must be low to avoid side

nucleophilic substitution reactions of halogen atoms. Finally, these reagents should be easily diffusible, *i.e.* capable of penetrating into a polymer substrate (particle or film). The diffusibility of reagents basically is governed by the nature of organic solvents (or co-solvents) used as a reaction medium. The role of the solvents can involve their catalytic action on the dehydrohalogenation reaction (*i.e.* solvation of the alkali metal cation can increase the activity of the hydroxide ion [7,8]) as well as the alteration of the interaction conditions in the polymer+reacting medium system (e.g. swelling of the polymer facilitates diffusion of the reactants in it). In each specific case the efficiency of the dehydrohalogenating system (base+solvent) depends on the relation between the solubility parameters (surface energies) of the system and the polymer being treated. Adding various polar co-solvents (like THF or acetone) or phase-transfer catalysts allows one to adjust the solubility parameters of the reacting medium and the polymeric substrate, thereby making it possible to perform the reaction efficiently [1].

Strong bases like alkali hydroxides [7,8,11–13,15,16,19], alkoxides [9,15,18], amides, and 1,8-diazabicyclo[5.4.0]-undec-7-ene (DBU) [4,5,9, 10,18] in various solvents are traditionally used as dehydrohalogenating agents. Most of these agents and systems that were reported to effect elimination of hydrogen halides yielding carbynoid structures (or their fragments) have been reviewed previously [3].

Here I would like to mention attempts of synthesizing carbynoid structures by Kijima et al. [6,9] using electrochemical approach. Cathodic electrolysis of a solution of poly(vinylidene fluoride) (PVDF) in DMF containing tetrabutylammonium perchlorate, and *tert*-butyl alcohol as a mediator was found to produce *n*-doped conjugated polymers consisting of 76% of poly(fluoro-acetylene) and 24% of carbynoid moieties [6] (Scheme 12.7):



SCHEME 12.7

In fact, the mediator, *i.e.* *t*-BuOH, is electrochemically reduced to the *t*-BuO[−] anion that nucleophilically attacks PVDF, in much the same way as potassium *tert*-butylate, to yield elimination products. The authors also studied electrochemical dehydrochlorination of oriented poly(1,2-dichloroethylene) films under heterogeneous conditions [9]. The starting polymer was produced by chlorination of polyacetylene [10,20]. The elimination product, however, was found to be predominantly polychlorovinylene with a small proportion of carbynoid moieties. The authors came to that conclusion because of very low intensity of the IR absorption peak attributable to triple C≡C-bonds. On the other hand, its low frequency at 2145 cm^{−1} could point to rather longer polyyne fragments.

12.4 CHARACTERIZATION OF THE DEHYDROHALOGENATION PRODUCTS

Numerous studies dealing with structural investigations of carbynoid materials with the use of various spectroscopic methods have been reviewed in details elsewhere [3]. Here I would like to briefly describe the most important findings, while focusing on recent studies published since 1998.

12.4.1 VIBRATIONAL SPECTROSCOPY

12.4.1.1 Infrared Spectroscopy

As the dehydrohalogenation of halogen-containing polymers proceeds, the absorption bands, typical of C–Hal vibrations (mostly in the 400–750 cm^{-1} frequency region), disappear from the IR spectra of the reaction products. New absorption bands appear therewith near 1600 (strong), 1720 (often appears as a shoulder), and 2100–2200 (medium to weak) cm^{-1} , being attributable to stretching vibrations of double C=C-bonds, carbonyl groups, and triple C \equiv C-bonds, respectively [4,6–13,15–19]. Noteworthy is the observation by Danno et al. of the peak at 2040 cm^{-1} , which is a surprisingly low frequency as compared with all other spectra of dehydrohalogenated polymers published to date [4]. Additional absorption bands (weak to medium) corresponding to C–H stretching vibrations in aliphatic groups appear in the 2850–3000 cm^{-1} frequency range, along with a strong broad band near 3400 cm^{-1} that can be assigned to both free (H_2O) and bonded hydroxy groups [7–13,15–19]. The peaks near 870 and 750 cm^{-1} are attributable to out-of-plane bending of aromatic protons [19], and the band at 1100–1110 cm^{-1} [19] is likely to result from C–O–C stretching vibrations in ether groups. Aromatic structures can arise in the reaction products due to dehydrohalogenation of six-membered rings formed via the Diels–Alder type cyclization, whereas the ether linkages are produced as a consequence of the alkoxylation side reactions through the nucleophilic substitution of chlorine atoms by ethoxide species or polymeric alkoxide ions [19].

Finally, it is worthy of particular note that the IR spectra of profoundly dehydrohalogenated polymers are amazingly similar (Figure 12.1), even if the structure of these polymers allows one to expect the formation of different isomers of carbyne (polyyne and cumulene) by exhaustive elimination of hydrogen halide (*cf.* Figure 12.1, spectra 6 and 7).

12.4.1.2 Raman Spectroscopy

Typically, Raman spectra of profoundly dehydrohalogenated polymers reveal two well-resolved lines around 1550 and 2150 cm^{-1} generally assigned to stretching modes of C=C and C \equiv C-bonds, respectively [5,10,17]. The line at 1540 cm^{-1} is common in all forms of polycrystalline graphite or amorphous carbons with predominantly sp^2 -type bonding. On the other hand,

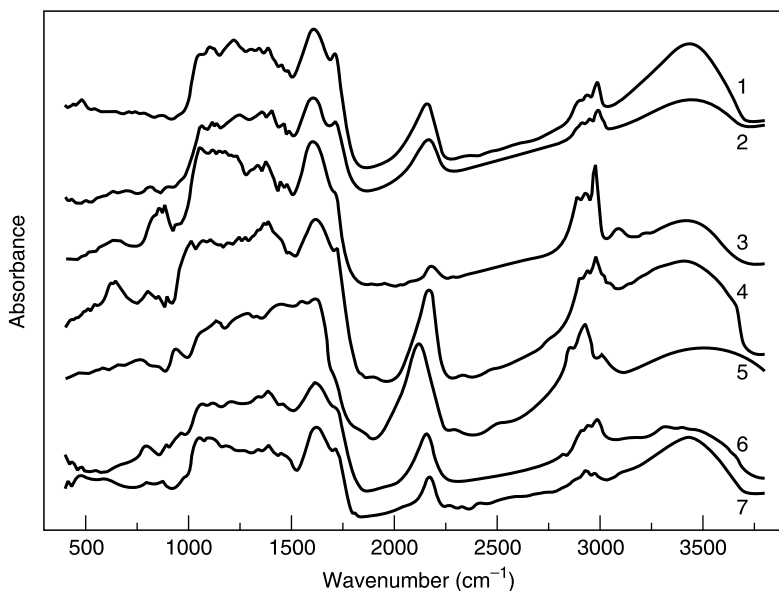


FIGURE 12.1 IR spectra of carbynoid materials produced by dehydrohalogenation of poly(vinylidene bromide) [7,8] (1); poly(vinylidene chloride) [7,8] (2); poly(vinylidene fluoride) [7,8] (3); poly(1,2-dibromoethylene) [11] (4); poly(1,2-dichloroethylene) [10] (5); poly(1,1,2-trichlorobutadiene) [12,13] (6); and poly(1,2,3-trichlorobutadiene) [12,13] (7).

the Raman spectrum of dehydrochlorinated poly(vinylidene chloride) showing virtually the same features, *viz.*, two marked peaks at 1550 and 2150 cm^{-1} , was interpreted by Berdyugin et al. in terms of kinked polycumulene model [21].

Sometimes, additional weak features in the 1100–1200 cm^{-1} region and near 1300 cm^{-1} were observed [5,17], whose interpretation is still somewhat controversial. Danno et al. assigned these two lines to stretching modes of C=C and C–C-bonds, correspondingly.

The first principles calculations performed by Kürti et al. have shown Raman bands of both polyyne and cumulene carbon chains to occur at around 2000 cm^{-1} [22]. The authors emphasized that distinguishing on the basis of Raman spectra between the polyyne and cumulene structures appears to be unlikely.

The frequency of the Raman bands in the spectra of dehydrohalogenated poly(vinylidene halides) [21] and poly(1,2-dichloroethylene) [10] was reported to depend on the excitation wavelength. This suggests a wide length-distribution of the carbyne fragments formed by dehydrohalogenation. Based on empirical relation, Akagi et al. [10] have calculated the length

of the carbyne (polyyne) fragments to be 12 (2157 cm^{-1}) to 65 (2113 cm^{-1}) conjugated triple bonds. However, considering quantum chemical calculations of the dependence of Raman frequency on the conjugation length accomplished by Kastner et al. [23], these lengths seem to be overestimated. Based on that relationship, Danno et al. calculated the average number of triple $\text{C}\equiv\text{C}$ -bonds in polyyne moieties produced by dehydrochlorination of poly(vinylidene chloride) to be 5 [5].

The Raman spectra of the dehydrochlorination products of chlorinated paraffin wax were studied by Cataldo [17]. The spectra were reported to show four clear lines at 1188, 1295, 1500, and 2170 cm^{-1} . Those peaks were assigned, correspondingly, to $\equiv\text{C}-\text{C}$ stretching overlapped with other types of $\text{C}-\text{C}$ stretching vibrations, double $\text{C}=\text{C}$ -bond bendings, stretching vibrations of conjugated double bonds, and stretchings of triple $\text{C}\equiv\text{C}$ -bonds. The latter peak in the spectrum of the most profoundly dehydrochlorinated sample was reported to appear at 2095 cm^{-1} . Based on empirical equations, the length of the polyyne sequences in that case was evaluated to be about 10 units.

Finally, it should be noted that Raman spectra of profoundly dehydrohalogenated poly(vinylidene chloride) or poly(vinylidene bromide) reveal striking similarity to the spectra of carbyne-rich nanostructured carbon films produced by supersonic cluster beam deposition [24–26].

12.4.2 UV–VIS ABSORPTION SPECTROSCOPY

Cataldo studied electronic absorption spectra of both soluble and insoluble dehydrochlorination products of chlorinated paraffins [15,16]. The author reported on a broad absorption band near 425 nm in the products of profound elimination. With the use of the Lewis–Calvin equation, the length of polynes produced was estimated to be 15 conjugated triple bonds. However, taking into account the length of starting paraffins (22–30 carbon atoms), their structure (the presence of tertiary carbon atoms at branching sites in iso-paraffins), and the structure of the reaction products (the presence of residual chlorine, carbonyl and hydroxyl groups, as well as cross-links surmised from IR spectra), one can conclude that this evaluation is rather exaggerated.

12.4.3 ELECTRON SPECTROSCOPY

Electronic structure of carbonaceous materials produced by chemical dehydrohalogenation of some halogen-containing polymers was studied by various methods of electron spectroscopy, including Auger electron spectroscopy (AES) [7,8,12,27,28], electron energy loss spectroscopy (EELS) [7,8,27,28], x-ray photoelectron spectroscopy (XPS) [12,13,29], and x-ray emission ($\text{C } K_{\alpha}$) spectroscopy [29] in order to corroborate the one-dimensional

structure of these materials as well as determine the nature of carbon–carbon bonds in them. All those studies have been reviewed in detail elsewhere [3].

The AES and EELS studies have corroborated the predominantly linear chain structure of the dehydrohalogenation products. Such features of the electronic structure as the continuity of the energy spectrum within the band, which attests to a large chain length, on the one hand, and a band width corresponding to short chains, on the other hand, suggest that the dehydrohalogenated chains consist of short, periodically repeated linear carbyne fragments [3,28]. In addition, the EELS data substantiated the splitting of the π sub-band and the metal–dielectric transition characteristic of one-dimensional systems with an energy spectrum of metallic type.

The XPS and C K_{α} studies provided additional data supporting the existence of conformation features and the limited length of linear carbyne fragments incorporated in the chain of the dehydrohalogenation products [3,29].

12.4.4 ^{13}C NUCLEAR MAGNETIC RESONANCE SPECTROSCOPY

One of the most promising characterization methods providing a deeper understanding of molecular structure of the dehydrohalogenation products is ^{13}C solid-state nuclear magnetic resonance (NMR) spectroscopy. Chemical shifts of linear carbynoid fragments occur in a range not occupied and, therefore, influenced by other resonances. Since the lengths of the fragments also affect the chemical shift, the NMR spectra yield additional information on the conformation of carbyne and carbynoid structures. Moreover, NMR spectroscopy seems to be the only method so far capable of distinguishing between two structural isomers of carbyne, *viz.* polyyne and polycumulene.

Evsyukov et al. studied ^{13}C solid-state NMR spectra of dehydrochlorinated poly(vinylidene chloride) [19]. The spectrum of the final product exhibits conspicuous features at 13.9 (strong, sharp), 28.8 (weak), 66.8 (strong, broad), 79.5 (weak), 133.9 (strong, very broad), 164.0 (shoulder), and 194.9 ppm (medium, broad) (Figure 12.2). The features at 66.8 and 164.0 ppm were assigned to, respectively, polyyne and cumulene carbynoid fragments. The peak at 13.9 ppm is attributable to methyl carbons in ethoxy groups that arise in macromolecules of the polymer due to a side reaction of nucleophilic substitution of chlorine atoms by ethoxide species under alkaline conditions (Williamson-type reaction). Nucleophilic addition to the multiple carbon–carbon bonds is also possible during later stages of dehydrochlorination. It should be noted that oxymethylene moieties, $-\text{O}-\text{CH}_2-$, of the ethoxy groups may also contribute to the broad peak at 66.8 ppm. The broad peak at 194.9 ppm is due to carbonyl $\text{C}=\text{O}$ groups arising in the reaction products through various mechanisms. For example, hydroxylated units formed via nucleophilic substitution of the chlorine

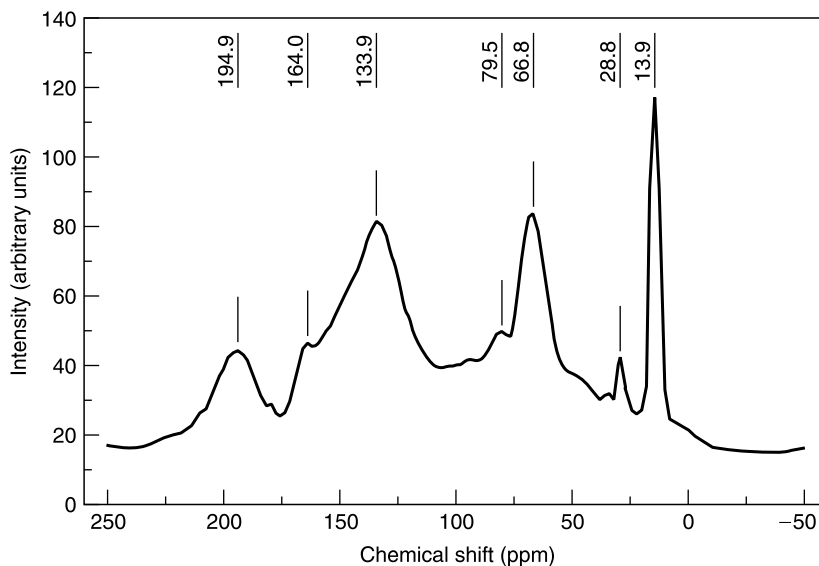


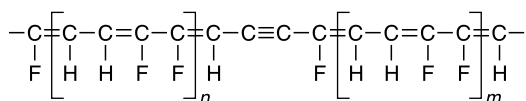
FIGURE 12.2 ^{13}C solid-state NMR spectrum of dehydrochlorinated poly(vinylidene chloride).

atoms by hydroxyl groups can undergo further reactions of elimination and tautomeric transformation [19]. Oxidation of multiple bonds in polyene, polyyne or cumulene fragments is also feasible during synthesis or work-up procedures. The low-intensity peak at 28.8 ppm can be assigned to methylene groups in the polymer chains as well as to methyl carbons in terminal ketomethyl (acetyl) groups, whereas the weak feature at 79.5 ppm could not be unambiguously interpreted and has yet to be dealt with. Finally, the broad asymmetric peak at 133.9 ppm is attributable to various sp^2 -carbon atoms in double bonds formed in the reaction products, mainly because of the dehydrochlorination of defect structures arising in the macromolecules of the original poly(vinylidene chloride) due to side reactions of nucleophilic substitution as well as cross-linking. The cross-linking is supposed to involve a Diels–Alder mechanism in polyene sequences formed during the first stage of dehydrochlorination, although other mechanisms can also be expected to occur through breaking of multiple bonds in the reaction products (in particular, addition reactions of α,β -unsaturated ketones). It should be noted that signals from the carbon atoms in the cumulene fragments can also contribute to the peak at 133.9 ppm.

The dehydrohalogenation products of poly(ethylene-*alt*-chlorotrifluoroethylene) were also studied using ^{13}C solid-state NMR spectroscopy and the cross-polarization magic angle spinning (CP MAS) technique [18]. The elimination reaction induced by potassium *tert*-butoxide (*t*-BuOK) in tetrahydrofuran (THF) was found to proceed slowly: only 50% of hydrogen

halide was removed from the polymer within 12 h of reaction. Subsequently, the reaction slows down further, and even within 4 days the conversion still did not exceed 60%. When the original polymer powder was refluxed in a 10% *t*-BuOK solution in THF at 65°C for 4 h, the degree of dehydrohalogenation was found to be 68%. However, higher temperatures are known to cause extended cross-linking and the formation of graphite-like structures during the dehydrohalogenation process [7,8]. The spectrum of the final product exhibits conspicuous features at 27.5 (strong, sharp), 45.9 (shoulder), 81.5 (weak), 111.8 (medium), 121.4 (shoulder), 149.4 (weak), 178.3 (weak), and 188.7 ppm (weak, shoulder). While the peaks at 27.5, 45.9, 111.8, 121.4, and 178.3 ppm are associated with the starting material, the other features appear in the spectra due to chemical transformations occurring in the polymer. The feature at 81.5 ppm is attributable to isolated triple C≡C-bonds inasmuch as conjugated polyynes are known to resonate in a 60–70 ppm region [18]. The peak at 149.4 ppm can be assigned to fluoromethine =CF-carbons in conjugated double C=C-bonds. Finally, the shoulder at 188.7 ppm is attributable to carbonyl C=O groups formed by oxidation of multiple bonds in the reaction products during synthesis or work-up procedures.

The ^{13}C NMR results along with the IR spectroscopic data have shown that chemical dehydrohalogenation of poly(ethylene-*alt*-chlorotrifluoroethylene), by treating with potassium *tert*-butoxide in THF, mainly yields halogen-substituted polyenyne structures containing randomly distributed isolated triple $\text{C}\equiv\text{C}$ -bonds. Based on the predominant structure of the original polymer, the polyene fragments can be described as head-to-head polyfluorovinylenes (Scheme 12.8).



SCHEME 12.8

Recently, Cataldo reported on ^{13}C NMR spectra of the dehydrochlorination products of chlorinated docosane, which were measured in solution [16]. The spectra show four broad but clear signals at 40, 45–70 (centered at 60), 85–95, and 125–135 ppm attributable to saturated (sp^3) carbon atoms bearing residual chlorine, polyyne sequences, isolated or carbonyl-conjugated triple bonds, and polyene structures, respectively.

12.5 CONCLUSIONS

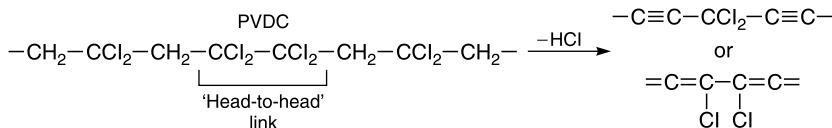
Modern spectroscopic techniques have allowed one to conclude that seemingly simple and straightforward reaction of chemical dehydrohalogenation

of halogen-containing polymers, induced by basic reagents, is in fact a complex process involving elimination of hydrogen halides as a target reaction and numerous side reactions of nucleophilic substitution and cross-linking, as well as some secondary transformations of both intermediate and final products. The target reaction of dehydrohalogenation brings about the formation of carbyne fragments — both polyynes and polycumulenes, whereas the side reactions produce various defect structures, *i.e.* alkoxy and hydroxy groups, carbonyl species, and cross-links randomly distributed along the polymer chains.

Based on the above considerations, it should be admitted that the ultimate dehydrohalogenation products cannot be regarded as carbyne *sensu strictu* but rather as carbyne-containing or carbynoid polymeric materials. Taking into account the fact that the contribution of side reactions to the dehydrohalogenation process is quite noticeable, it can be concluded that carbynoid fragments in these materials are rather short. This is in accord with evaluation of the length of linear carbyne fragments (*ca.* 8 carbon atoms) by Auger electron spectroscopy [27,28] and by Raman spectroscopy [5]. Since all basic compounds used to date as dehydrohalogenating agents always possess some (often significant) nucleophilic reactivity, the complete suppression of the substitution side reactions seems to be rather unlikely. Therefore, a search for new dehydrohalogenating systems possessing high basicity but low nucleophilicity still remains a pressing problem.

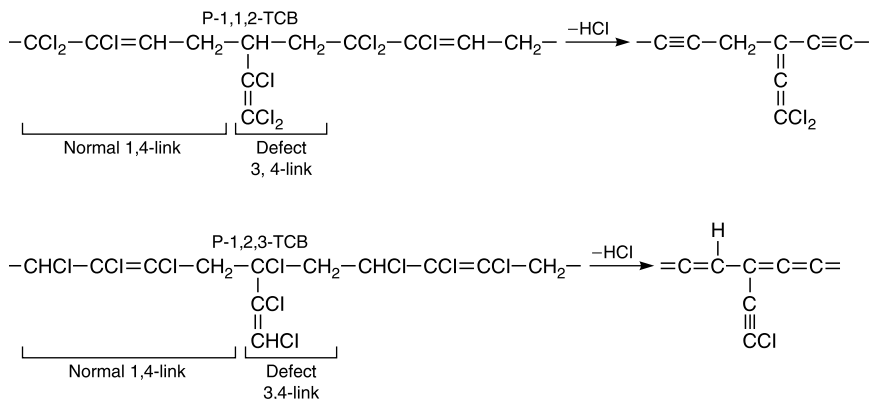
One promising way in this connection might be the use of new sterically hindered phosphazene and proazaphosphotriane [30] bases that have recently been made commercially available [31]. These reagents were reported to be orders of magnitude more basic than DBU and, at the same time, to be less nucleophilic. One can certainly expect some difficulties with the diffusibility of these bulky substances into a polymer substrate, but it is worth giving them a try anyway.

Yet another serious problem that makes the preparation of perfect carbyne structures (long-chain polyynes or cumulenes) an almost hopeless endeavor is the presence of intrinsic defects in the original halogen-containing polymers. The polymers produced by common polymerization technologies always contain some defect structures such as “head-to-head” and “tail-to-tail” links [32–34] as well as branching sites [35,36]. For instance, poly(vinylidene fluoride) was shown to contain up to 6 mol.% [32,33] and poly(vinylidene chloride) even 12.5% of abnormal links [34], which hamper exhaustive dehydrohalogenation (Scheme 12.9).



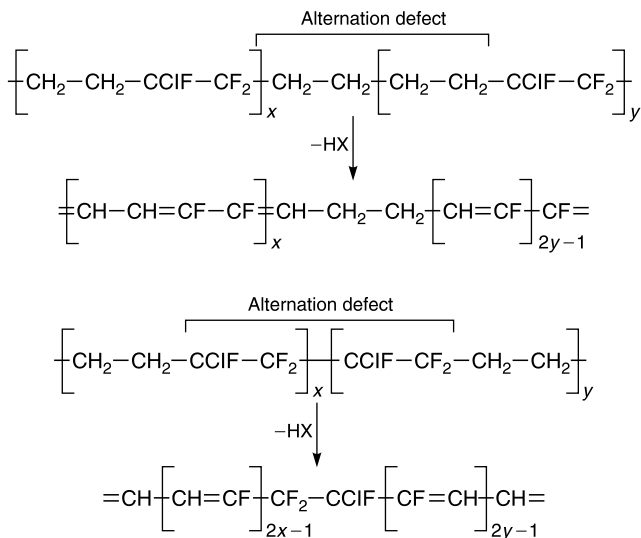
SCHEME 12.9

Similarly, poly(trichlorobutadiene)s contain 3,4-connected links, along with predominating 1,4-links [37], that will afford allenic or acetylenic pendants during dehydrohalogenation (Scheme 12.10).



SCHEME 12.10

Moreover, poly(trichlorobutadiene)s are known to undergo allylic rearrangements with migration of allylic chlorine (1–4%) and hydrogen (3–10%) atoms under the action of solvents [38]. This accounts for remarkable similarity of the IR spectra of dehydrochlorinated poly(1,1,2-trichlorobutadiene) and poly(1,2,3-trichlorobutadiene) (Figure 12.1).



SCHEME 12.11

Finally, poly(ethylene-*alt*-chlorotrifluoroethylene) was found to have an appreciable proportion of the alternation defects, which makes complete elimination of hydrogen halides impossible regardless of the nature of the dehydrohalogenating agent (Scheme 12.11) [18].

A possible way to overcome the hurdle of intrinsic defects could be synthesizing strictly linear, defect-free polymers with the use of modern, precisely controlled polymerization techniques and utilizing them as starting materials for dehydrohalogenation.

REFERENCES

- [1] Evsyukov, S.E.; Kudryavtsev, Yu.P.; Korshak, Yu.V. Chemical dehydrohalogenation of halogen-containing polymers. *Uspekhi Khimii* **1991**, 60(4), 764–798 (in Russian) [*Russ. Chem. Rev.* **1991**, 60 (4), 373–390 (Engl. Transl.)].
- [2] *Carbyne and Carbynoid Structures*. Heimann, R.B., Evsyukov, S.E., Kavan, L., Eds. Kluwer Academic Publishers: Dordrecht, The Netherlands, 1999.
- [3] Evsyukov, S.E. Chemical dehydrohalogenation of polymers. In *Carbyne and Carbynoid Structures*. Heimann, R.B., Evsyukov, S.E., Kavan, L., Eds. Kluwer Academic Publishers: Dordrecht, The Netherlands, 1999; 55–74.
- [4] Danno, T.; Murakami, K.; Ishikawa R. Preparation of carbyne-like films by dehydrochlorination of poly(vinylidene chloride). In *Electronic Properties of Novel Materials — Science and Technology of Molecular Nanostructures: XIII International Winterschool*. Kuzmany, H., Fink, J., Mehring, M., Roth, S., Eds. AIP Conf. Proc. 1999, Vol. 486, 213–216.
- [5] Danno, T.; Murakami, K.; Krause, M.; Kuzmany, H. Resonance Raman scattering from carbyne materials. In *Electronic Properties of Novel Materials — Molecular Nanostructures: XIV International Winterschool/Euroconference*. Kuzmany, H., Fink, J., Mehring, M., Roth, S., Eds. AIP Conf. Proc. 2000, Vol. 544, 473–476.
- [6] Kijima, M.; Toyabe, T.; Shirakawa, H. Electrocatalytic dehydrofluorination of poly(vinylidene fluoride). *Chem. Lett.* **1995**, 24(7), 553–554.
- [7] Korshak, V.V.; Kudryavtsev, Yu.P.; Korshak, Yu.V.; Evsyukov, S.E.; Khvostov, V.V.; Babaev, V.G.; Guseva, M.B. Formation of β -carbyne by dehydrohalogenation. *Makromol. Chem. Rapid Commun.* **1988**, 9(3), 135–140.
- [8] Evsyukov, S.E.; Kudryavtsev, Yu.P.; Korshak, Yu.V.; Khvostov, V.V.; Babaev, V.G.; Guseva, M.B.; Korshak, V.V. Synthesis of carbyne on the basis of poly(vinylidene halides). *Vysokomolek. Soedin., Ser. A* **1989**, 31(1), 27–33 (in Russian) [*Polym. Sci. USSR* **1989**, 31(1), 29–37 (Engl. Transl.)].
- [9] Kijima, M.; Mukai, S.; Ohmura, K.; Shirakawa, H.; Kyotani, M. Synthesis of conjugated polymer with carbynoid structure by dehydrochlorination of chlorinated polyacetylene film. *Synth. Met.* **1999**, 101(1–3), 59–60.
- [10] Akagi, K.; Nishiguchi, M.; Shirakawa, H.; Furukawa, Y.; Harada, I. One-dimensional conjugated carbyne — Synthesis and properties. *Synth. Met.* **1987**, 17 (1–3), 557–562.
- [11] Korshak, V.V.; Kudryavtsev, Yu.P.; Evsyukov, S.E.; Korshak, Yu.V.; Khvostov, V.V.; Babaev, V.G.; Guseva, M.B. Synthesis of carbyne on the basis of poly(vinyl chloride). *Doklady Akad. Nauk SSSR* **1988**, 300(4), 889–892 (in Russian) [*Dokl. Phys. Chem.* **1988**, 300(4), 510–512 (Engl. Transl.)].

- [12] Vointseva, I.I.; Gilman, L.M.; Kudryavtsev, Yu.P.; Evsyukov, S.E.; Pesin, L.A.; Gribov, I.V.; Moskvina, N.A.; Khvostov, V.V. Chemical dehydrochlorination of polytrichlorobutadienes — A new route to carbynes. *Eur. Polym. J.* **1996**, 32(1), 61–68; 403.
- [13] Vointseva, I.I.; Gilman, L.M.; Kudryavtsev, Yu.P.; Evsyukov, S.E.; Valetsky, P.M. Synthesis of polymorphous modifications of carbyne by chemical dehydrochlorination of polytrichlorobutadiene isomers. *Vysokomolek. Soedin., Ser. A* **1996**, 38(7), 1116–1121 (in Russian) [*Polym. Sci., Ser. A* **1996**, 38(7), 707–711 (Engl. Transl.)].
- [14] Korshak, V.V.; Matveeva, N.G. Macromolecular compounds. Report 56. Concerning the influence of stereochemical factors on the ability of halogen-substituted ethylenes to polymerize. *Izv. Akad. Nauk SSSR, Otdel. Khim. Nauk* **1953**, (2), 344–350 (in Russian).
- [15] Cataldo, F. Synthesis of polyyynes by dehydrohalogenation of chlorinated paraffins. *Angew. Makromol. Chem.* **1999**, 264, 65–72.
- [16] Cataldo, F. Synthesis of polyyynes (and ene-yne)s segments by dechlorination reactions of chlorinated polyethylene wax and chlorinated docosane. *J. Mater. Sci.* **2000**, 35(10), 2413–2419.
- [17] Cataldo, F. Raman spectra and thermal analysis on polyyne and polyene-yne chain segments. *J. Macromol. Sci., Pure Appl. Chem.* **2000**, A37(8), 881–892.
- [18] Evsyukov, S.E.; Thomas, B.; Heimann R.B. Chemical dehydrohalogenation of poly(ethylene-alt-chlorotrifluoroethylene). *Mater. Chem. Phys.* **2000**, 66(1), 34–40.
- [19] Evsyukov, S.E.; Paasch, S.; Thomas, B.; Heimann, R.B. Formation of carbynoid structures by chemical dehydrochlorination of poly(vinylidene chloride). A ^{13}C solid-state NMR study. *Ber. Bunsen-Ges. Phys. Chem.* **1997**, 101(5), 837–841.
- [20] Akagi, K.; Kadokura, T.; Shirakawa, H. Stereospecific chlorination of polyacetylene by chemical doping. *Polymer* **1992**, 33(19), 4058–4065.
- [21] Berdyugin, V.V.; Kudryavtsev, Yu.P.; Evsyukov, S.E.; Korshak, Yu.V.; Shorygin, P.P.; Korshak, V.V. Resonance Raman scattering spectra of β -carbyne. *Doklady Akad. Nauk SSSR* **1989**, 305(2), 362–365 (in Russian) [*Dokl. Phys. Chem.* **1989**, 305(1–3), 217–219 (Engl. Transl.)].
- [22] Kürti, J.; Magyar, C.; Balázs, A.; Rajczy, P. Vibrational analysis for short carbon chains with alternating and cumulenic structure. *Synth. Met.* **1995**, 71(1–3), 1865–1866.
- [23] Kastner, J.; Kuzmany, H.; Kavan, L.; Dousek, F.P.; Kürti, J. Reductive preparation of carbyne with high yield. An *in situ* Raman scattering study. *Macromolecules* **1995**, 28(1), 344–353.
- [24] Ravagnan, L.; Siviero, F.; Lenardi, C.; Piseri, P.; Barborini, E.; Milani, P.; Casari, C.; Li Bassi, A.; Bottani C.E. Cluster beam deposition and *in situ* characterization of carbyne-rich carbon films. *Phys. Rev. Lett.* **2002**, 89 (28, Pt.1), 285506/1–285506/4.
- [25] Casari, C.S.; Li Bassi, A.; Ravagnan, L.; Siviero, F.; Lenardi, C.; Piseri, P.; Bongiorno, G.; Bottani, C.E.; Milani P. Chemical and thermal stability of carbyne-like structures in cluster-assembled carbon films. *Phys. Rev. B* **2004**, 69(7), 75422/1–75422/7.
- [26] Casari, C.S.; Li Bassi, A.; Ravagnan, L.; Siviero, F.; Lenardi, C.; Barborini, E.; Piseri, P.; Milani, P.; Bottani C.E. Gas exposure and thermal stability of linear

- carbon chains in nanostructured carbon films investigated by *in situ* Raman spectroscopy. *Carbon* **2004**, 42(5–6), 1103–1106.
- [27] Korshak, V.V.; Kudryavtsev, Yu.P.; Khvostov, V.V.; Guseva, M.B.; Babaev, V.G.; Rylova, O.Yu. Electronic structure of carbynes studied by Auger and electron energy loss spectroscopy. *Carbon* **1987**, 25(6), 735–738.
- [28] Kudryavtsev, Yu.P.; Evsyukov, S.E.; Guseva, M.B.; Babaev, V.G.; Khvostov, V.V. Carbyne — the third allotropic form of carbon. *Izv. Akad. Nauk, Ser. Khim.* **1993**, (3), 450–463 (in Russian) [*Russ. Chem. Bull.* **1993**, 42(3), 399–413 (Engl. Transl.)].
- [29] Kudryavtsev, Yu.P.; Baytinger, E.M.; Kugeev, F.F.; Korshak, Yu.V.; Evsyukov, S.E. Electronic structure of carbyne studied by x-ray photoelectron spectroscopy and x-ray emission spectroscopy. *J. Electron Spectrosc. Relat. Phenom.* **1990**, 50(4), 295–307.
- [30] Strong and Hindered Bases in Organic Synthesis. *ChemFiles* **2003**, 3(1).
- [31] Verkade, J.G. P(RNCH₂CH₂)₃N: Very strong non-ionic bases useful in organic synthesis. *Topics Curr. Chem.* **2002**, 223, 1–44.
- [32] Görnitz, M.; Minke, R.; Trautvetter, W.; Weisberger, G. Struktur und Eigenschaften von Polyvinylfluorid (PVF) und polyvinylidenfluorid (PVF₂). *Angew. Makromol. Chem.* **1973**, 29/30(371), 137–162.
- [33] Cais, R.E.; Sloane N.J.A. A statistical theory of directional isomerism in polymer chains and its application to polyvinylidene fluoride. *Polymer* **1983**, 24(2), 179–187.
- [34] Semin, G.K.; Robas, V.I.; Babushkina, T.A. NQR in polymers, In *Solid-State Radiospectroscopy*, Atomizdat, Moscow, 1967, 218–220 (in Russian).
- [35] Russo, S.; Behari, K.; Chengji, S.; Pianca, M.; Barchiesi, E.; Moggi, G. Synthesis and microstructural characterization of low-molar-mass poly(vinylidene fluoride). *Polymer* **1993**, 34(22), 4777–4781.
- [36] Pianca, M.; Barchiesi, E.; Esposto, G.; Radice, S. End groups in fluoropolymers. *J. Fluorine Chem.* **1999**, 95(1–2), 71–84.
- [37] Vointseva, I.I.; Klimentova, N.V.; Niazashvili, G.A. Poly(1,1,2-trichlorobutadiene-1,3) and its compositions: Part I — Synthesis, structure and reactivity. *Int. J. Polym. Mater.* **1995**, 29, 69–96.
- [38] Lebedeva, T.L.; Vointseva, I.I.; Gil'man, L.M.; Petrovskii, P.V.; Larina, T.A. Solvent-induced allylic rearrangements in poly(trichlorobutadiene) chains. *Izv. Akad. Nauk, Ser. Khim.* **1997**, 763–768 [*Russ. Chem. Bull.* **1997**, 46, 732–738 (Engl. Transl.)].

13 Ion Irradiation of Solid Carbons

*G. Strazzulla, G.A. Baratta, S. Battiato and
G. Compagnini*

CONTENTS

13.1	Introduction	271
13.2	Synthesis and Characterization of Carbynoid-Rich Thin Films	273
13.3	Ion Irradiation of Carbyne-Rich Thin Films	276
13.4	Ion Irradiation of Related Materials	277
13.4.1	Asphaltite	278
13.4.2	Frozen Benzene	280
13.5	Conclusions	282
	Acknowledgments	282
	References	282

13.1 INTRODUCTION

The study of the effects induced by ion irradiation of solid materials, in particular solid carbons, is relevant in many fields of science and technology. Here we focus on its relevance in astrophysics. Solid carbon-bearing species are extremely abundant in space both in the gas and in the solid phases. A wide variety of solid carbons are observed in the interstellar and circumstellar medium as well as in many objects of the Solar System including those collected at or nearby Earth (interplanetary dust particles and meteorites). Observed and/or predicted carbon-bearing solids (or large molecules) include species with different hybridizations (sp , sp^2 , sp^3) such as amorphous carbons, polycyclic aromatic hydrocarbons, fullerenes, nano-diamonds, graphite, and carbon chain molecules. The literature in the field is enormous; interesting reviews can be found in a recent special volume of *Spectrochimica Acta* [1].

Linear carbon chains with sp hybridization have been proposed to be present in the interstellar medium [2–4]. These chains can be constituted by alternate single (C–C) and triple ($C\equiv C$) bonds (polyyynes) or double ($C=C$) bonds (poly-cumulenes) and have been proposed as building blocks for carbynes, a carbon allotrope [5].

In the laboratory, the study of the properties of pure polyyynes and poly-cumulenes is inhibited because of their extreme reactivity with oxygen and the formation of cross linked chains. In space, refractory dust made of silicates or carbonaceous material are formed in the atmosphere of evolved stars and released into the interstellar medium (ISM). In dense molecular clouds ($n_{\text{Hydrogen}} \geq 10^4 \text{ cm}^{-3}$, $T \approx 10\text{--}20 \text{ K}$) atoms and molecules that impinge on the grains stick on them and may react to form ice mantles.

Dense molecular clouds, after further contraction, are the places where stars are born. The observation of protostars, stars still embedded in their placental cloud, is a probe of the presence of ices in the clouds: the almost black-body continuum emitted from the young object is absorbed by grains whose temperature changes as a function of the distance from the object. These observations, which are mainly obtained by IR spectroscopy, may reveal the evolution of ices due to thermal and/or energetic (e.g. interaction with UV photons and/or stellar particle winds and cosmic rays) processing (e.g. Cox and Kessler [6]).

Carbon-based materials and C-rich ices are also present on many objects in the Solar System, such as the satellites of the external planets (Jupiter and beyond), the planet Pluto, the so called trans-Neptunian objects (a class of numerous small objects not yet well investigated), and comets [7]. Energetic (keV to MeV) particles impinging on solid surfaces made of refractory (carbonaceous and/or silicates) materials and/or ices are present in a variety of environments in space. These include the interstellar medium and the planetary system. Ion irradiation produces several effects, whose study has been based on laboratory simulations of relevant targets bombarded with fast charged particles under physical conditions as similar as possible to the astrophysical ones. Fast ions penetrating solids deposit energy in the target by elastic interactions with target nuclei and by inelastic collisions causing ionizations and excitations. Thus, bonds are broken along the path of the incoming ion and physico-chemical modifications occur, including the formation of molecules originally not present in the target which can be both more volatile or less volatile than the irradiated ones. When carbon is an important constituent of the irradiated target it gives rise to a refractory residue which is left over after warming up. That residue has a complex structure, which after prolonged irradiation evolves to form a hydrogenated amorphous carbon that we call IPHAC (ion produced hydrogenated amorphous carbon). IPHAC formation has been observed in several kinds of carbon-containing targets (polystyrene, polypropylene, graphite, diamond, *etc.*) and even in frozen gases (C_6H_6 , CH_4 , C_4H_{10} , *etc.*). This occurs for a combination of bombarding ions (H, He, Ar, Kr, *etc.*) and ion energies

(ranging between a few keV and MeV). We have shown that IPHAC has already been formed at low temperature during ion irradiation; this is a crucial point for the ion produced cometary crust theory [8].

Here we present some results concerning the role that ion irradiation has in 1. modifying cluster assembled carbon thin films obtained by low energy cluster beam deposition (LECBD) and containing a cabynoid component; and 2. producing carbynoid-like materials after irradiation of solid frozen benzene and of asphaltite, a natural bitumen.

13.2 SYNTHESIS AND CHARACTERIZATION OF CARBYNOID-RICH THIN FILMS

Cluster-assembled carbon thin films (100 nm thick) have been deposited at the Dipartimento di Scienze Chimiche Università di Catania, by LECBD on silicon single crystalline surfaces using a laser vaporization source similar to those reported by Perez et al. [9]. In the source, a plasma created by the impact of a 5 ns Nd:YAG pulsed laser beam (second harmonic at 532 nm) onto a graphite rod is generated in a small chamber and is thermalized by the injection of a pulsed helium stream at high pressure (4–8 bar) which permits the cluster growth. The mixture is then expanded in vacuum and forms a supersonic beam with cluster speeds around 1000 m/s. Several factors govern the cluster formation such as the amount of ablated material, the cluster residence time prior to the expansion and the plasma–carrier gas interaction. These factors are controlled through a number of experimental parameters like the helium pressure, the laser delay with respect to the pulsed helium injection, the helium pulse width (250 μ s), the laser fluence (10^3 J/cm²) and the geometrical shape of the nozzle.

The ionized part of the resulting cluster beam can be analyzed by a time of-flight mass spectrometer (TOFMS) which has been built up at 90° with respect to the beam direction. At the end the produced clusters land onto a substrate (generally a silicon single crystalline one) in a 10^{-8} mbar vacuum chamber. The substrate holder can be cooled down to 77 K. Several samples have been deposited at temperatures between 77 and 300 K.

A typical mass distribution of the obtained beam is reported in [Figure 13.1](#). Such a distribution is representative of a large variety of sizes and bonding behaviour. In particular it has been observed that small carbon clusters (below 40 atoms) have chains or ring structures [10] whereas larger clusters have the tendency to form three-dimensional cage-like structures characterized by sp² coordination [11]. The resulting deposited samples should then be a mixture of all these components. Figure 13.1 also shows transmission electron microscopy (TEM) results of a deposited sample, showing the porous structure consisting of closed graphite particles and graphene foils embedded in an amorphous matrix that is not well resolved.

One of the most powerful techniques for studying amorphous and crystalline carbon phases is Raman spectroscopy. For this reason, a series of

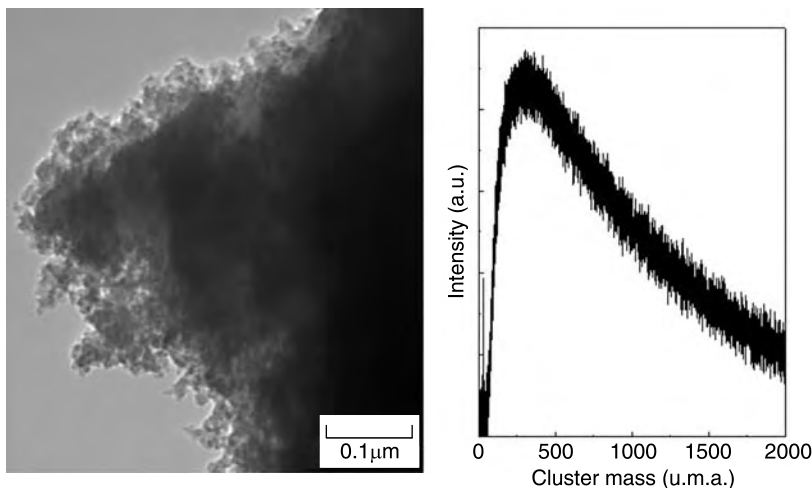


FIGURE 13.1 (left panel) Transmission electron microscopy (TEM) of a cluster of assembled carbon thin films deposited by low energy cluster beam deposition (LECBD). The image shows the porous structure consisting of closed graphite particles and graphene foils embedded in a not well resolved amorphous matrix; (right panel) Typical mass distribution of the cluster beam— it is representative of a large variety of sizes and bonding.

Raman spectra have been obtained with a Jobin Yvon single monochromator equipped with a notch filter and a CCD detector cooled at liquid nitrogen temperature. Raman scattering has been excited through a He–Ne laser (632.8 nm) at low power (6 mW) to avoid heating effects. Spectra have been taken both *in situ*, that is during and after the deposition in an ultra high vacuum (UHV) chamber, and *ex situ* after the exposition of the deposited film to atmosphere.

Figure 13.2 shows some Raman spectra taken under different experimental conditions. According to several pieces of literature data, it is possible to assign the Raman features observed in all of the reported spectra to different bonding configurations. Features located between 1000 and 2000 cm^{-1} are due to the presence of sp^2 components in the film. In many cases, this is the most relevant part of the spectrum and a huge amount of literature has been published to account for the correlation between these features and the atomic and electronic structure of the investigated samples (see e.g. Ferrari and Robertson [12]). In that spectral region two structures appear around 1330–1380 cm^{-1} (D line) and 1550–1500 cm^{-1} (G line). The position, width and intensity of the two lines are strongly dependent on the structure of the obtained carbon particles. However, it was clearly pointed out by a series of experiments (e.g. Ferrari and Robertson [13]) that the

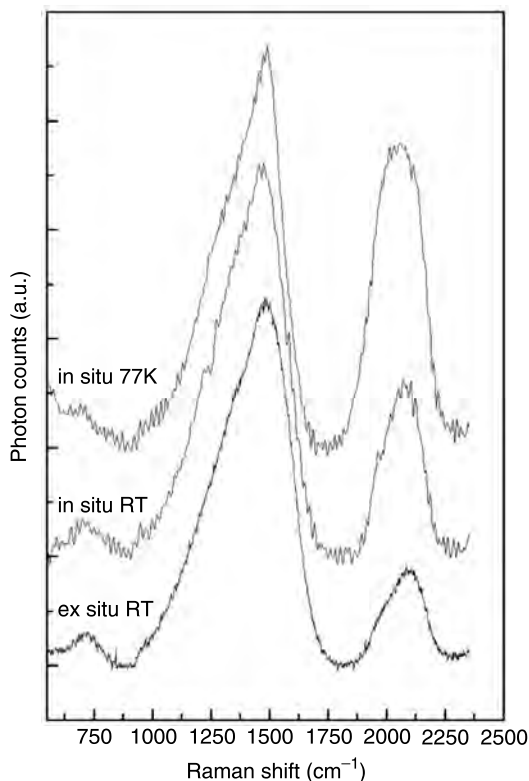


FIGURE 13.2 Raman spectra of a cluster assembled carbon thin film obtained *in situ* (i.e. with the sample obtained still within the vacuum chamber) at 77 K and at room temperature, and that taken after exposure to air (about 15 min). Spectra have been vertically shifted for clarity.

1000–2000 cm^{-1} region of the Raman spectrum of a carbon system is dramatically dependent on the exciting wavelength. This has ruled out all the speculations on the possibility of obtaining information on the sp^2/sp^3 bonding ratio from a single spectrum obtained with a single excitation wavelength. Indeed, a visible excitation wavelength definitely gives signals prevalently due to the graphitic component of the investigated system. The situation changes if ultraviolet excitation is employed, because cross section considerations give the possibility to observe a typical sp^3 signal (T line) located at around 1050–1100 cm^{-1} , although a resonance study is desirable even in these cases.

Signals considered to be representative of linear carbons (sp hybridization) are located at about 2000–2100 cm^{-1} . In this case the broad band found in our samples can be composed by a convolution of cumulene and polyene-like structures [14].

As a matter of fact, carbon samples obtained by LECBD are found to contain both of the above-mentioned carbon clusters and, indeed, this technique is considered the best one to obtain carbon nanostructures rich in carbynoid species.

It is evident that different experimental conditions lead to large difference in the relative amount of the produced sp and sp^2 components. Deposition at temperatures as low as 77 K gives the highest amount of sp component if compared with the result obtained for the sample deposited at room temperature and measured in the same experimental condition (*in situ* Raman spectra). A careful comparison between Raman spectra relative to these two thin films reveals that the shape of the overall carbyne vibrational feature is different. In fact, although a deconvolution into two components is not straight, room temperature samples appear to be less rich in the low frequency component (cumulene-like at about 1980 cm^{-1}) with respect to the high frequency one (polyyne-like at about 2100 cm^{-1}).

Moreover, although carbyne species are extremely reactive if exposed at the atmosphere, the third spectrum reported in Figure 13.2 and recorded after about 15 min from the sample removal from the vacuum chamber, reveals an appreciable amount of carbyne species evaluated as 1/2 with respect to the sample as deposited at room temperature. It was already observed that, in this situation, the carbyne signal continues to decrease with an exponential law and reaches a saturation after 10 h whose value depends on a number of experimental parameters (thickness of the sample, effective ambient temperature and ambient humidity).

13.3 ION IRRADIATION OF CARBYNE-RICH THIN FILMS

Some of the above-described cluster assembled carbon thin films have been extracted from the deposition chamber and brought to the laboratory for experimental astrophysics of the INAF-Osservatorio Astrofisico di Catania where they have been put inside a stainless steel vacuum chamber, in which pressure is kept below 10^{-7} mbar. The exposure of the samples to air was of about 20 min. Just after their insertion in the vacuum chamber Raman spectra have been taken and it has been verified they are very similar to those shown in Figure 13.2 (bottom curve). A continuous Ar ion laser beam (1 mm in diameter, 514.5 nm) was used as exciting radiation, with laser power of about 15 mW on the sample. The laser beam enters a confocal illuminator orthogonal to its optical axis, into which it is deflected by a micro-prism. In this confocal optical system any parallel beam incident along the optical axis in the opposite direction of the laser is focused onto the entrance slit of the spectrometer (a modified Triplemate SPEX). Two flat mirrors are used to reflect the laser beam toward the vacuum chamber, where it is focused, through a KBr window, on a $50\text{ }\mu\text{m}$ wide spot on the sample, using an achromatic optics. Since the laser beam is parallel, the Raman scattered light arising from the illuminated spot is collected by

the same optics and it is collimated into a parallel beam that is reflected back along the same path of the laser, in the optical axis of the confocal illuminator. A small fraction of this beam is intercepted by the micro-prism, while the rest is focused on the entrance slit of the spectrometer. A CCD camera is used as detector in the range 400–1000 nm. The spectral resolution is about 3 cm^{-1} and the positioning reproducibility is about 1 cm^{-1} .

The carbon thin films have been irradiated with 200 keV Ar^+ ions and their IR spectrum obtained *in situ* before, during and after irradiation, by an FTIR spectrometer (Bruker Equinox 55).

The vacuum chamber is interfaced to an ion implanter (200 kV) from which ions with energy up to 200 keV (400 keV for double ionizations) can be obtained. The IR spectrometer is positioned (by a moveable optical bench) in a way such that the IR beam is transmitted, through a hole of the sample holder, by the substrate. The sample holder is mounted at an angle of 45° both with the ion beam and with the incoming IR beam and spectra can be acquired *in situ* without tilting the sample. Samples can also be put in thermal contact with a closed-cycle helium cryostat whose temperature can be varied between 10 and 300 K. The spectra shown in this work have been taken with a resolution of 2 cm^{-1} and a sampling of 0.5 cm^{-1} .

The ion beam produces a spot larger than the hole in the sample holder and currents in the range of 100 nA cm^{-2} to tens of $\mu\text{A cm}^{-2}$. The integrated ion flux (fluence in ions cm^{-2}) is measured, by a charge integrator, from the ion current monitored during irradiation. For further details on the experimental apparatus see [15].

The results are shown in Figure 13.3. The as prepared cluster assembled carbon film exhibits the typical band of carbynoid materials at 2097 cm^{-1} [16] that appears quite broad, perhaps due to the superposition with cumulene bands. In addition, the films exhibit C–H stretching bands, in particular in the aliphatic region ($3000\text{--}2800\text{ cm}^{-1}$), and also an aromatic feature at 3071 cm^{-1} . These features have to come from contaminations, either in the vacuum chamber during the preparation of the samples, or most likely after their exposure to air. In any case, before irradiation, there are clear evidences both from Raman and IR spectroscopy of the survival of carbynoid structures along with a component of hydrogenated amorphous carbon. After irradiation (Figure 13.3 spectra b and c) the intensity of the $\text{C}\equiv\text{C}$ band at 2097 cm^{-1} increases, the intensity C–H stretching bands progressively decreases due to an hydrogen loss and a carbonization of the sample. A new band at about 3300 cm^{-1} appears, as indicated by an arrow, that is easily attributed to C–H stretching in $\text{R}-(\text{C}\equiv\text{C})-\text{H}$.

13.4 ION IRRADIATION OF RELATED MATERIALS

In this paragraph we report some results obtained after ion irradiation of asphaltite, a natural bitumen, and benzene frozen at low T (16 K).

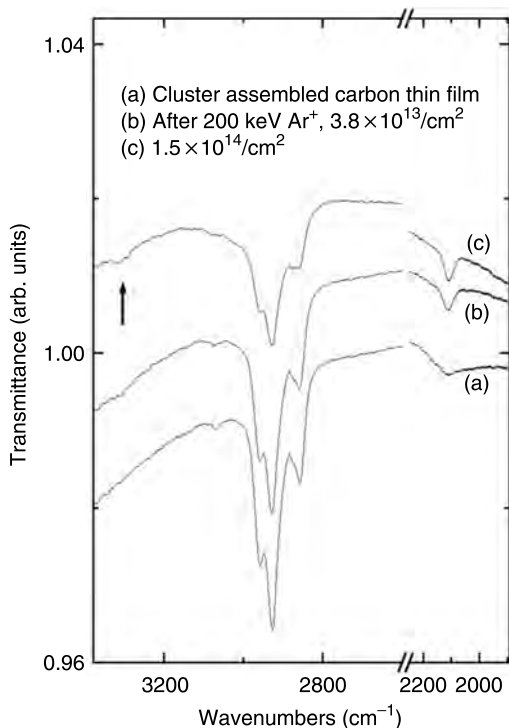


FIGURE 13.3 Transmittance IR spectra at room temperature of: (a) a cluster assembled carbon thin film after exposure to air (about 20 min); (b) after ion irradiation (3.8×10^{13} 200 keV Ar⁺ cm⁻²); and (c) after ion irradiation (1.5×10^{14} 200 keV Ar⁺ cm⁻²). Spectra have been vertically shifted for clarity.

13.4.1 ASPHALTITE

Asphaltite samples used in this work are from Izhem, Timano-Pechora Basin, Russia and have been analyzed by Moroz et al. [17]. Compared to most other solid oil bitumens, asphaltite is rich in H and has a relatively disordered structure. Its polycyclic aromatic structural units are relatively small. It is rather bright and transparent in the infrared due to a large optical gap (the energy gap between valence and conduction bands) [18]. Moreover, asphaltite is very dark in the visible range due to a broad complex electronic absorption feature typical of PAHs [18–21]. To obtain asphaltite samples suitable for ion irradiation and contemporary transmittance IR spectroscopy, we deposited some drops of asphaltite diluted in chloroform on a IR-transparent Si substrate. We allowed the mixture to evaporate and leave uniform asphaltite layers whose thickness was of the order of 1 μm , as evaluated by an optical microscope.

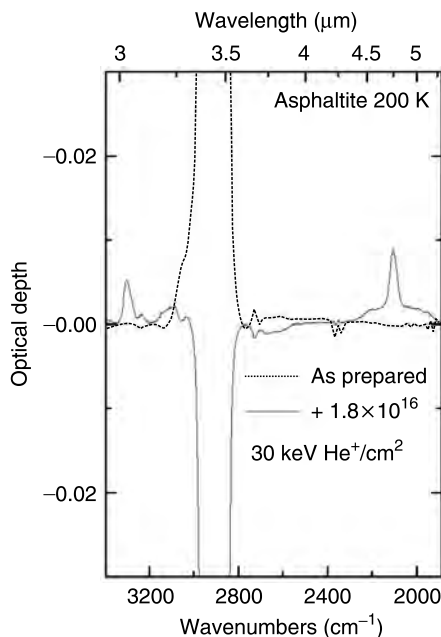


FIGURE 13.4 IR spectra (in optical depth units) of asphaltite ($3400\text{--}1900\text{ cm}^{-1}$) taken at 200 K before (dotted line) and after (solid line) ion irradiation (1.8×10^{16} $30\text{ keV He}^+ \text{ cm}^{-2}$). After the collection of the spectrum of the as prepared sample (dotted line) a new background has been taken that includes the sample itself. Thus newly formed bands are seen as having positive optical depths; bands with negative optical depths are those of asphaltite that is progressively destroyed.

Asphaltite exhibits several vibrational absorption bands mostly due to aliphatic and aromatic functional groups. The spectral range investigated here is $3700\text{--}1900\text{ cm}^{-1}$. In such a range, the most prominent bands are those due to the aliphatic and aromatic C–H stretchings.

Figure 13.4 shows two spectra of asphaltite taken at 200 K before (dotted line) and after (solid line) ion irradiation (1.8×10^{16} $30\text{ keV He}^+ \text{ cm}^{-2}$). After the collection of the spectrum of the as prepared sample (dotted line in Figure 13.4) a new background has been taken that includes the sample itself. In this way, after irradiation, newly formed bands are seen as having positive optical depths. Bands with negative optical depths are those of asphaltite that is progressively destroyed by ion irradiation. We can see the appearance of newly synthesized bands. The most intense are those at 3301 cm^{-1} and 2106 cm^{-1} that are attributed to C–H and $\text{C}\equiv\text{C}$ stretchings in $\text{R}-(\text{C}\equiv\text{C})-\text{H}$ systems. The appearance of these bands testifies for the ion-induced synthesis of carbynyoid structures.

13.4.2 FROZEN BENZENE

One of the main effects of ion irradiation of frozen gases is the formation of molecular species not present in the original sample as indicated by the appearance of new absorption features in the IR spectra. As stated above, after irradiation of carbon bearing refractory species, complex residues are formed (IPHAC). These have been suggested to be analog materials to that of some planetary surfaces [22].

Thin films of frozen (16 K) benzene have been obtained by vapor deposition on a cold silicon substrate. After deposition icy samples have been irradiated with different ions and different energies. In Figure 13.5 we show the IR spectrum of the original frozen benzene (dotted line) whose main bands (in the range $3100\text{--}3000\text{ cm}^{-1}$) are due to symmetric and anti-symmetric aromatic C–H stretching. In Figure 13.5 the spectrum obtained after irradiation with 400 keV Ar^{++} ions ($4 \times 10^{14}\text{ cm}^{-2}$) is shown (dashed line). The changes are dramatic: benzene is destroyed and new bands appear. The most intense are those at 3301 cm^{-1} (C–H stretching in $\text{R}-(\text{C}\equiv\text{C})-\text{H}$) and at 3236 cm^{-1} due to C–H stretching in acetylenes $\text{H}-\text{C}\equiv\text{C}-\text{H}$. The spectrum obtained after sample warming up to 200 K is also shown in Figure 13.5: volatile species have been lost and the residue includes species with different hybridizations (sp , sp^2 , sp^3).

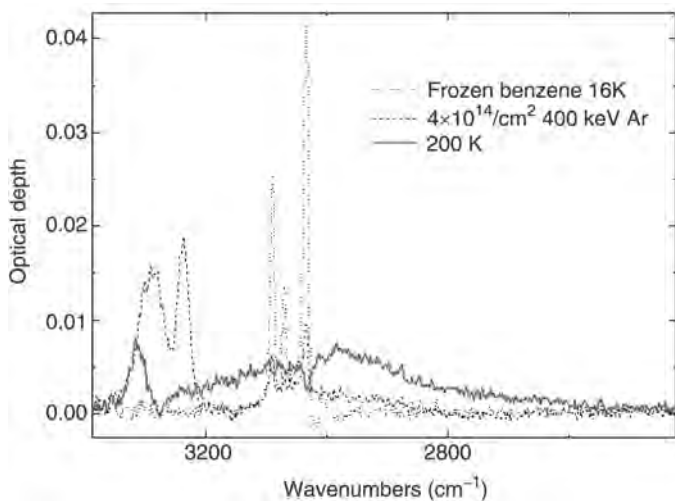


FIGURE 13.5 IR spectra (in optical depth units) of frozen (16 K) benzene ($3400\text{--}2600\text{ cm}^{-1}$) before (dotted line), after (dashed line) ion irradiation (4×10^{14} 400 keV $\text{Ar}^{++}\text{ cm}^{-2}$) and after warming up to 200 K (solid line).

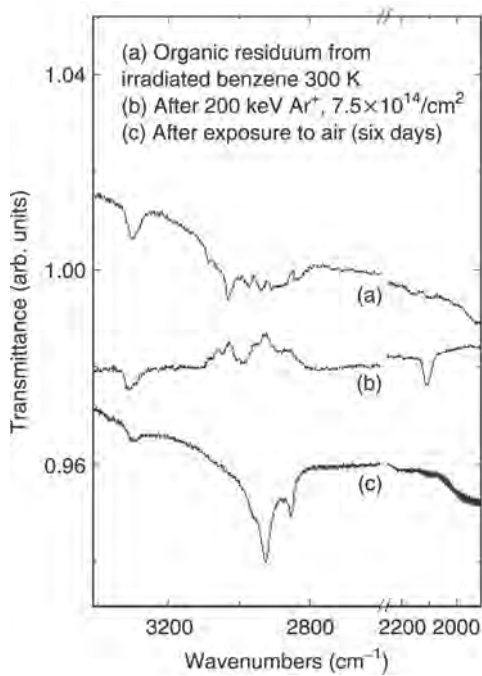


FIGURE 13.6 Transmittance IR spectra at room temperature of: (a) an organic residue left over after ion irradiation of frozen benzene; (b) after ion irradiation (7.5×10^{14} 200 keV Ar^+ cm^{-2}); and (c) after exposure to air (6 days). Spectra have been vertically shifted for clarity. After the collection of the spectrum (a) a new background has been taken that includes the sample itself. Thus newly formed bands are seen as “absorptions”; bands seen as “emissions” are those progressively destroyed.

The spectrum of another residue (at 300 K) is shown in Figure 13.6(a) from which it is possible to see again the appearance of C–H stretching bands of the three hybridizations. The sample has been further irradiated and the spectrum obtained is shown in Figure 13.6. As in the case of asphaltite, after the collection of spectrum (a) a new background has been taken that includes the sample itself. Thus newly formed bands are seen, in the transmittance scale, as “absorptions”; bands seen as “emissions” are those progressively destroyed. The appearance of the 3301 cm^{-1} and 2106 cm^{-1} bands testifies for the ion-induced synthesis of carbynoid structures. According to the literature data [14], carbynoid species are extremely reactive if exposed to air. In fact the $\text{C}\equiv\text{C}$ band completely disappears (see Figure 13.6c) if the sample is exposed to atmospheres for some days. At the same time new and different C–H bands are detected due to alterations as observed in the same spectrum.

13.5 CONCLUSIONS

We have presented some results that indicate the synthesis of sp hybridized carbons by ion irradiation of different carbon based materials (asphaltite, organic residues from frozen benzene, cluster assembled carbon films). Most likely these synthesized materials contain carbynoid structures.

Chemical alteration and the production of different molecular species by ion irradiation of carbon-based solid materials is relevant for application to several objects in space. As an example, it is widely accepted that ion irradiation might have produced dark planetary surfaces by converting carbon containing ices into refractory materials [23].

The experimental results have, however, to be applied with caution to the different astrophysical environments: in laboratory simulations some parameters are reproduced very well (e.g. the kind of ion) but others cannot be reproduced at all (e.g. the energy spectrum) [23].

A detailed application of the results presented here is not yet possible, but we like to outline that ion fluxes have been or are being measured (e.g. by Voyagers, Pioneers, *Galileo*, and *Cassini* spacecraft) to be high enough to be extremely relevant in many objects of the Solar System including planetary magnetospheres. Also, solid materials in the interstellar medium suffer energetic ion irradiation. As an example, Moore [24] has found that, in cold dense clouds, ions deposit about 300 eV/molecule (in 10^9 years) comparable with that deposited by photons (400 eV/molecule).

Thus, based on the results presented here, the presence of carbons that are irradiated by energetic ions in space very likely produces carbynoid structures. These could play a role in explaining one of the oldest mysteries in the study of the interstellar medium, namely the identifications of species responsible for the so-called diffuse interstellar bands, a forest of absorption lines seen in many directions of the sky. In fact, among the many suggested materials, linear carbon chains seem to be among the most promising (see e.g. References 2–4.)

ACKNOWLEDGMENTS

This research has been supported by the Italian Ministero dell'Università e della Ricerca Scientifica e Tecnologica (MURST).

REFERENCES

- [1] Salama, F.; Bauschlicher, C.W. (Guest Editors). *Molecular Spectroscopy in Astrophysics. Spectrochimica Acta* **57**, 2001.
- [2] Thaddeus, P.; McCarthy, M.C. Carbon chains and rings in the laboratory and in space. *Spectrochimica Acta* **2001**, *57*, 757–774.

- [3] Duley, W.W. Chemical evolution of carbonaceous material in interstellar clouds. *Astrophys. J.* **2000**, 528, 841–848.
- [4] Kroto, H.W.; Heath, J.R.; O'Brien, S.C.; Curl, R.F.; Smalley, R.E. Long carbon chain molecules in circumstellar shells. *Astrophys. J.* **1987**, 314, 352–355.
- [5] Heimann, R.B.; Evsyukov, S.E.; Kavan, L. *Carbyne and Carbynoid Structures*. Kluwer Academic Publishers, Dordrecht, 1999.
- [6] Cox, P.; Kessler, M.F. (Eds.). *The Universe as seen by ISO*, ESA-SP 427, 1999.
- [7] Pendleton, Y.J.; Tielens, A.G.G.M. (Eds.). *From Stardust to Planetesimals*, Astron. Soc. Pacific Conf. Series, 122, 1997.
- [8] Strazzulla, G.; Baratta, G.A. Carbonaceous material by ion irradiation in space. *Astron Astrophys*, **1992**, 266, 434–438.
- [9] Perez, A.; Melinon, P.; Dupuis, V.; Jensen, P.; Prevel, B.; Tuaillon, J.; Bardotti, L.; Martet, C.; Treilleux, M.; Broyer, M.; Pellarin, M.; Vaille, J. L.; Palpant, B.; Lerme, J. Cluster assembled materials: a novel class of nano-structured solids with original structures and properties. *J. Phys. D* **1997**, 30, 709–721.
- [10] Yang, S.; Taylor, K.J.; Craycraft, M.J.; Conceicao, J.; Pettiette, C.L.; Cheshnovsky, O.; Smalley, R.E. UPS of 2–30-atom carbon clusters: Chains and rings. *Chem. Phys. Lett.* **1988**, 144, 431–436.
- [11] Dugourd, Ph.; Hudgins, R.R.; Tenenbaum, J.M.; Jarrold, M.F. Observation of new ring isomers for carbon cluster anions. *Phys. Rev. Lett.* **1998**, 80, 4197–4200.
- [12] Ferrari, A.C.; Robertson, J. Resonant Raman spectroscopy of disordered, amorphous, and diamondlike carbon. *Phys. Rev. B* **2001**, 64, 075414.
- [13] Ferrari, A.C.; Robertson, J. Interpretation of Raman spectra of disordered and amorphous carbon. *Phys. Rev. B* **2000**, 61, 14095.
- [14] Ravagnan, L.; Siviero, F.; Lenardi, C.; Piseri, P.; Barborini, E.; Milani, P.; Casari, C.S.; Li Bassi, A.; Bottani, C.E. Cluster-beam deposition and in situ characterization of carbyne-rich carbon films *Phys. Rev. Lett.* **2002**, 89, 285506.
- [15] Strazzulla, G.; Baratta, G.A.; Palumbo, M.E. Vibrational spectroscopy of ion-irradiated ices. *Spectrochimica Acta* **2001**, 57, 825–842.
- [16] Kavan, L.; Kastner, J. Raman and infrared spectroscopy. In: *Carbyne and Carbynoid Structures*. Kluwer Academic Publishers, Dordrecht, 1999, 343–356.
- [17] Moroz, L.V.; Arnold, G.; Korochantsev, A.V.; Wäsch, R. Natural solid bitumens as possible analogs for cometary and asteroid organics: 1. Reflectance spectroscopy of pure bitumens. *Icarus* **1998**, 134, 253–268.
- [18] McMichael, B.D.; Kmetko, E.A.; Mrozowski S. An aromatic detector for the infrared. *J. Opt. Soc. Amer.* **1954**, 44, 26–30.
- [19] Brown, J.K. Infrared spectra of coals. *J. Chem. Soc.*, **March 1955**, 744–752.
- [20] Painter, P.; Starsinic, M.; Coleman, M. Determination of functional groups in coal by fourier transform interferometry. In: *Fourier Transform Infrared Spectroscopy: Application to Chemical Systems* (J.R. Ferraro and L.J. Basile, Eds.), v. 4, Acad. Press, London, **1985**, 169–241.
- [21] Ito, O.; Seki, H.; Iino, M. Diffuse reflectance spectra in near-i.r. region of coals; a new index for degrees of coalification and carbonization. *Fuel* **1988**, 67, 573–578.

- [22] Strazzulla, G.; Cooper, J.F.; Christian, E.R.; Johnson, R.E. Ion irradiation of TNOs: from the fluxes measured in space to the laboratory experiments. *Comptes Rendus Physique, Academie des Sciences, Paris* **2003**, *4*, 791–801.
- [23] Strazzulla, G.; Johnson, R.E. Irradiation effects on comets and cometary debris. In: “*Comets in the post-Halley Era*” (R.L. Newburn Jr., M. Neugebauer, J. Rahe, Eds.) Kluwer Publ. Co., London, **1991**, 243–275.
- [24] Moore, M.H. The physics and chemistry of ice in the interstellar medium. In: *Solid Interstellar Matter: the ISO Revolution* (L. d’Hendecourt, C. Joblin and A. Jones, Eds.), Springer-Verlag, Berlin, **1999**, 199–218.

14 Cyanoalkynes and Cyanopolyynes: From Crossed Beam Experiments to Astrochemistry

Nadia Balucani and Ralf I. Kaiser

CONTENTS

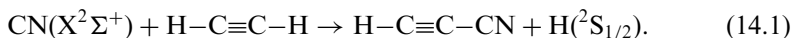
14.1	Introduction	285
14.2	The Crossed Molecular Beam Method	290
14.3	Data Analysis	293
14.4	Results on the Reaction of the CN Radicals with Simple Alkynes	298
14.4.1	The Reaction $\text{CN} + \text{C}_2\text{H}_2$	298
14.4.2	The Reaction $\text{CN} + \text{CH}_3\text{CCH}$	303
14.4.3	The Reaction $\text{CN} + \text{CH}_3\text{CCCH}_3$	309
14.5	Conclusions and Outlook	313
	Acknowledgments	314
	References	315

14.1 INTRODUCTION

In the last decades there has been much interest in the reaction of the cyano radicals, $\text{CN}(X^2\Sigma^+)$, with a variety of molecules, mainly because of their implication in combustion chemistry [1]. For this reason extensive studies of CN reactions with simple molecules of relevance in combustion, amongst which are simple unsaturated hydrocarbons, were performed [2–5]. More recently, a renewed interest in the reactions of CN radicals with simple unsaturated hydrocarbons has arisen because of their alleged role in some

extraterrestrial environments, namely the atmosphere of Saturn's moon Titan and in cold molecular clouds in the interstellar medium (ISM).

The atmosphere of Titan, a massive satellite with an atmosphere denser than that of Earth, has been investigated [6–27] with great effort because its composition and chemical evolution are supposed to help the understanding of the prebiotic chemistry of our planet. Earth and Titan are believed to be formed, indeed, with similar atmospheres from the solar nebulae [8]. In one thing the difference between the two is remarkable, though: the surface temperature of Titan is very cold, ~ 94 K, and even in the upper stratosphere the temperature does not exceed 170 K. In these conditions water is mainly in the solid state and the absence of liquid water certainly prevents the evolution of biochemistry as we know it. Paradoxically, however, exactly because such a low temperature has kept the chemical evolution frozen to an early stage, the study of the chemistry of Titan's atmosphere offers the possibility to reconstruct the scene of the primordial terrestrial atmosphere [22]. According to the data collected in the *Voyager* missions, molecular nitrogen (N_2) and methane (CH_4) are the main constituents of Titan's atmosphere followed by molecular hydrogen (H_2), the nitrogen-bearing molecules hydrogen cyanide (HCN), dicyan (C_2N_2), and cyanoacetylene (HCCCN), as well as the hydrocarbons acetylene (C_2H_2), ethylene (C_2H_4), ethane (C_2H_6), methylacetylene (CH_3CCH), propane (C_3H_8), and diacetylene (C_4H_2) [10,13–16]. The observation of simple nitriles, which occur only in trace amounts of a few parts per billion, has posed the question of how they are formed at those low temperatures. The initiation certainly originates from the phenomena occurring in the upper part of the atmosphere of Titan which is constantly bombarded by high-energy photons, cosmic ray particles, strongly ionizing high-energy electrons from Saturn's magnetosphere, and short wavelength solar ultraviolet photons ($\lambda < 155$ nm). In that environment, chemistry is mainly due to ion–molecule reactions [23,24]. However, longer wavelength photons are able to penetrate down to the stratosphere where they induce the dissociation of HCN into $CN(X^2\Sigma^+)$. Interestingly, the concentration of the cyano radical as a function of the altitude varies in such a way that its maximum overlaps with that of the profiles of some unsaturated hydrocarbons, such as acetylene; if they collide, a reaction might occur, possibly producing unsaturated nitriles such as cyanoacetylene via neutral–neutral reactions according to the reaction

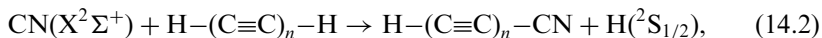


Cyanoacetylene and higher cyanopolyynes ($H-(C\equiv C)_n-C\equiv N$) are alleged to be possible intermediates towards the formation of simple amino acids and this motivates detailed studies focused on confirming the speculated formation routes [11,25]. The idea behind it is that the study of the chemical evolution of Titan's atmosphere will help us understand how biologically

active molecules and their nitrile precursors have been synthesized in reducing atmospheres. To account for the chemical composition and evolution of the atmosphere of Titan, complex photochemical models have been developed [13–16]. They consist of networks of elementary reactions, many of which are bimolecular collisions between a radical/atomic/ionic species and a closed shell molecule. In addition to these chemical models, some help comes from a series of laboratory experiments which mimic Titan's atmospheric chemistry. In different research groups N_2/CH_4 gas mixtures have been irradiated with various energy sources and the gas and solid phase products analyzed (for recent work see [References 26 and 27](#)). Several limitations of these methods, such as the wall effects, affect their validity and it has been recently suggested to reduce the complexity of the problem by carrying out laboratory experiments that mimic only a part of the chemical scheme of the model [26]. In other words, a detailed experimental knowledge of the involved elementary processes is required to understand better the global formation reactions.

Cyanopolyynes have been extensively identified in cold molecular clouds and outflow of late type AGB carbon stars and their production routes have been widely investigated [28–36]. All hydrogen-deficient nitriles observed so far in the interstellar medium can be arranged in four groups: cyanopolyynes of the general chemical formula $H-(C\equiv C)_n-CN$, methyl substituted cyanopolyynes ($CH_3-(C\equiv C)_n-CN$, cyanopolyynes radicals ($(C\equiv C)_n-CN$), and olefinic nitriles containing a double C–C bond and a CN group. Cyanopolyynes are ubiquitous in the ISM and hold high fractional abundances of up to 6×10^{-9} [37]; the simplest one, cyanoacetylene $HCCCN(X^1\Sigma^+)$, was identified in dark molecular clouds TMC-1 and OMC-1 as well as the carbon star IRC+10216 (CW Leo) [38]. Towards high intensity IR sources like IRC+10216 [39] and massive O-B stars within dense molecular clouds rotational transitions inside vibrationally excited states were observed as well [40]. Since $HCCCN$ is produced in the early stage of the cyanopolyynes chain growth, it is thought to be the key molecule in the cyanopolyynes formation. More complex cyanopolyynes $H-(C\equiv C)_2-CN$, $H-(C\equiv C)_3-CN$, $H-(C\equiv C)_4-CN$, and $H-(C\equiv C)_5-CN$ have been assigned in TMC-1 [41]. Based on chemical models on the synthesis of polycyanoacetylenes in IRC+10216 and TMC-1 and a decreasing fractional abundance of these nitriles with increasing molecular weight down to 10^{-10} , the more complex cyanopolyynes were classified as late time chemistry indicators [31,37,42]. The only methyl substituted cyanopolyynes observed so far is methylcyanoacetylene, $CH_3CCCNCN$ [28,43]. The radicals C_3N and C_5N were identified in TMC-1 and IRC+10216 with fractional abundances two orders of magnitude lower than their molecular HC_3N and HC_5N counterpart [44]. Vinylcyanide, C_2H_3CN , is the only olefinic nitrile identified so far towards TMC-1 [28], SgrB2(N) [45] and towards the star forming region Orion KL [46]. Despite the impressive astronomical assignments and line surveys, the question “How are nitriles synthesized in the interstellar medium?” is not resolved yet.

Since the average kinetic energy is typically confined to 0.8 kJ/mol in diffuse clouds and 0.08 kJ/mol in dark molecular clouds, the formation of cyanopolynes, as well as that of other molecular species, via gas phase reactions must involve reactions with no barriers and only binary collisions. Ternary encounters occur only once in a few 10^9 years and can be neglected considering mean interstellar cloud lifetimes of 10^6 years. That is why ion–molecule reactions are postulated to play a central role in interstellar reaction networks [47,48]. In particular, early models of interstellar cloud chemistry suggest that the HCCCNH^+ ion is the key intermediate in the formation of HCCCN and its isomer HCCNC, via the dissociative recombination of HCCCNH^+ with an electron of the cosmic radiation field. The ion HCCCNH^+ is thought to be formed via ion–molecule reactions. However, if this sequence of reactions is the real route of formation, the relative abundances of HCCCN and HCCNC should be about the same — in strong disagreement with astronomical observations which report a ratio of 160:1 [49]. In addition, the HCCCN fractional abundance predicted by the model are orders of magnitude lower than that observed [49]. A second shortcoming is the observation of ^{13}C isotopic enrichments in HCCCN isotopomers towards TMC-1 [50]. A detailed mapping indicates that H^{13}CCCN and HC^{13}CCN have similar intensity, but that H^{13}CCCN versus $\text{HCCC}^{13}\text{CN}$ shows a ratio of 1.4. If ion–molecule reactions are responsible for HCCCN formation, all three isotopomers should be formed with the same yield since the carbon atoms of $\text{c-C}_3\text{H}_3^+$ are indistinguishable. Finally, a recent theoretical investigation of the reaction $\text{N}(^4\text{S}) + \text{C}_3\text{H}_3^+$ (the most important step in this ion–molecule reaction network) showed that this reaction is not feasible in molecular clouds [51]. In conclusion, ion–molecule reactions are not able to explain the formation of HCCCN in the ISM. New formation mechanisms, based on the generalization of reaction 14.1a,



are being considered [33,52–54].

To verify if reactions 14.1 and 14.2 are responsible for the formation of cyanoacetylene/cyanopolynes in the low temperature environments of Titan and ISM, a confirmation from laboratory experiments is required. Provided that the elementary reactions of interest are thermodynamically feasible, it is necessary to reach the knowledge of at least two other factors: the relevant rate constants and the yield of the possible reaction products. Particularly this last piece of information will allow us to draw the sequence of elementary steps which account for the global reaction.

Certainly the perspective from which neutral–neutral reactions were considered changed significantly after a series of sophisticated experiments on the rate constants for CN reactions with acetylene, methylacetylene, and ethylene [55,56]. From these studies experimental evidence was given that

these reactions are very fast, with rate constants in the gas kinetics range, also at very low temperature (as low as 15 K). In other words, these experiments provided evidence that cyano radicals easily react also at the temperatures of Titan and ISM. At that point only one parameter remained to be checked: the nature and the yield of the reaction products. In fact, those kinetic investigations could only follow the decay rate of the CN concentration and the nature of products was only speculated [55,56].

A complementary approach is needed, namely the experimental investigation of the relevant elementary processes at the microscopic level. Such a strategy can be of considerable help, since the investigation at the microscopic level provides us with the most detailed knowledge of gas-phase reactions. This is the realm of reaction dynamics, a young branch of chemical physics. The main advantage of the reaction dynamics experiments is that the reactive events are investigated under single collision conditions, that is, secondary and wall collisions are avoided. The experimental techniques usually employed for gas-phase reaction dynamics studies fall essentially into two categories: crossed molecular beam (CMB) methods and laser-based spectroscopic methods [57].

The spectroscopic methods are based on time-resolved pump-probe schemes where the collision-free regime is usually attained by using low pressure conditions. Application of various linear and non-linear laser techniques, such as LIF (laser-induced fluorescence), REMPI (resonant-enhanced multiphoton ionization) and CARS (coherent antistokes Raman spectroscopy) have provided detailed information on the internal states of nascent reaction products [58]. Obviously, an essential prerequisite for the application of these techniques is the knowledge of the spectroscopic properties of the products.

The crossed beam technique with mass spectrometric detection was first developed in the 1970s and used to address fundamental aspects on the reaction mechanisms at the microscopic level [59]. Only recently, however, the improvements in the production of unstable species beams and vacuum technology have allowed us to study elementary reactions of practical interest [60–63]. The main advantage of the CMB experiments is that the reactants are confined into distinct supersonic beams which cross each other at a specific angle; the species of each beam are characterized by a well defined (both in magnitude and direction) velocity and are made to collide only with the molecules of the other beam, allowing us to observe the consequences of well-defined molecular collisions. Differently from the pump-probe experiments, therefore, the collision energy is very well defined. In CMB experiments the product detection can also be done by means of LIF or REMPI techniques [64,65], but it is the coupling with mass spectrometric detection to make the method “universal” that is applicable to the study of (at least in principle) any reaction. Every species can be ionized at the typical electron energy used in the ionizer (60–200 eV) which precedes the mass filter. Therefore, it is possible to determine the mass and the gross formula

of all the possible species produced from the reactions by ionizing the product and selecting different mass-to-charge ratio (m/e) in the mass selector. Even though some problems (as, for instance, dissociative ionization and background noise) limit the method, the advantages with respect to spectroscopic techniques are obvious, since the applicability of the latter needs the knowledge of the optical properties of the products, while, in most cases, their nature itself is not known.

The advantages of the CMB technique strongly motivate its extension to the study of reactions of interest in astrochemistry. In the last few years the CMB method with mass spectrometric detection has indeed been applied to the study of astronomically relevant reactions in different laboratories. In this way some reactions of the OH radicals [66], carbon atoms [67–69], nitrogen atoms [70], C_2H and C_6H_5 radicals [71,72], and C_2/C_3 [73,74] have been characterized.

In this chapter, the information available from crossed beam experiments on the reactions of CN radicals with simple unsaturated hydrocarbons leading to the formation of unsaturated nitriles will be reviewed after a brief introduction on the crossed molecular beam method. The results presented here are part of a systematic study which has been undertaken to characterize the reactions of CN radicals with small unsaturated organic molecules at the microscopic level [60,75–84].

14.2 THE CROSSED MOLECULAR BEAM METHOD

In a typical CMB experiment, beams of atoms and molecules with narrow angular and velocity spread are crossed in a vacuum chamber and the angular and time-of-flight (TOF) distributions of the products are recorded after well defined collisional events take place. The detector is an electron-impact ionizer followed by a quadrupole mass spectrometer (QMS) filter; the whole detector unit can be rotated in the collision plane around the axis passing through the collision center (Figure 14.1). The crossed beam machine used in the present experiments has been described in detail elsewhere [67, 79,80]. Briefly, it consists of two source chambers (10^{-4} mbar), a stainless-steel scattering chamber (10^{-7} mbar), and a rotatable, differentially pumped quadrupole mass spectrometric detector ($< 8 \times 10^{-13}$ mbar).

In reactive scattering experiments the production of supersonic beams of stable gases or vapors is trivial, while the production of suitable beams of unstable atomic or radical species presents some difficulties. In the experiments described here a pulsed supersonic cyano $CN(X^2\Sigma^+)$ radical beam was generated *in situ* via laser ablation of a graphite rod and subsequent reaction of the ablated species with molecular nitrogen [85]. The graphite rod is located 0.05 mm inside the extension channel of a Proch–Trickl pulsed valve (1.0 mm nozzle) which intersects the laser beam at 90° . The graphite rod is attached to a motor which is kept in a helical motion during the

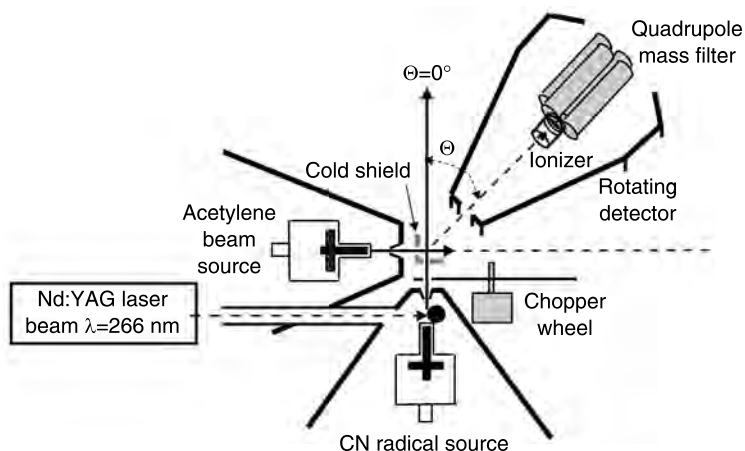
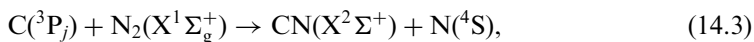


FIGURE 14.1 Schematic top view of the crossed molecular beam apparatus. The two pulsed beam source chambers and the detector (electron impact + quadrupole mass filter) rotating chamber are visible. In the case of the CN radical beam source, the carbon rod holder and the incident laser beam are also sketched. The chopper wheel and the cold shield are also shown.

laser irradiation. The rotational direction of the carbon rod is reversed by changing the polarities of the motor via a voltage switcher box. This has revealed to be essential for an homogeneous consumption of the carbon rod which guarantees the long term stability and reproducibility of the source. To produce a suitable $\text{CN}(X^2\Sigma^+)$ beam, the 266 nm and 30 Hz output of a Spectra Physics GCR-270-30 Nd:YAG laser was focused with 30 mJ per pulse on the carbon rod to a spot less than 0.4 mm in diameter. The supersonic expansion relaxes the diatomic radicals in their ground vibrational level and lowest rotational levels. When more than 30 mJ per pulse were used, some vibrationally excited states of CN radicals were seen to survive the supersonic expansion [85]. The laser beam entrance channel is completely isolated from the second source region to avoid reaction of CN radicals in the first source with background reactant molecules. The pulsed valve operates at 60 Hz, 80 ms pulses, and 4 atm backing pressure of neat nitrogen. The laser-ablated species react with the nitrogen in the laser-ablation zone, and, hence, form the cyano radicals *in situ*. The nitrogen reactant acts as a seeding gas as well. The mechanism of formation of CN radicals has not been well established. The possible reactions between molecular nitrogen and the ablated atomic carbon and C_2 ,



are both strongly endothermic [86]. Therefore, CN formation probably proceeds at the ablation center where the excess energy compensates for the reaction endothermicity. We characterized the beams on-axis and found that they contain a very small amount of CN_2 ($m/e=40$), while no other carbon–nitrogen species (such as C_2N , C_2N_2 , *etc.*) could be detected within the sensitivity of our system. Besides CN and CN_2 , $\text{C}(^3\text{P}_j)$, C_2 , and C_3 are formed as well. The presence of C_3 does not interfere in the present experiments, since C_3 was found to react with unsaturated hydrocarbons in CMB experiments only at very high collision energies [74]. Atomic carbon and C_2 are instead reactive with unsaturated hydrocarbons, as testified by a series of CMB experiments on these reactions [67,68,73]. The reactions of atomic carbon with unsaturated hydrocarbons, though, produce molecular/radical products with a quite different m/e [67,68]. As far as possible interferences from C_2 reactions are concerned, when using N_2 as seeding gas, the concentration of CN is an order of magnitude larger than that of C_2 . In addition to that, the reaction rate constants are also about one order of magnitude lower for the C_2 reactions with respect to those of CN and the mass of the product parent ions and their daughter fragments differ by 2 a.m.u. In conclusion, no interference is expected by the presence of other species in the beams [73].

The CN beam generated by high energy laser ablation has a quite broad profile, thus it is not well defined in velocity. For this reason a four-slot chopper wheel spinning at 240 Hz was placed between the skimmer and the interaction region. The 960 Hz output of an infrared diode mounted at the top of the motor frame defines precisely the time zero of the experiment. By choosing different delay times between the initial photodiode pulse and the pulsed valve, the chopper wheel operates in such a way to select distinct 9 μs slices of the pulsed CN beam. In other words, the use of the four-slot chopper wheel transformed a shortcoming of the source — that is, the production of a broad beam — into a resource because we could select different beam slices characterized by a different velocity by simply delaying the opening of the pulsed valve. That allowed us to perform experiments at different collision energies without changing the beam set-up (in this way the CN beam velocity could be varied between 900 and 1900 m/s). The number density at the interaction region of the CN radicals was estimated to be about $2\text{--}3 \times 10^{11}$ particles/ cm^3 , that is three orders of magnitude more intense than previous supersonic CN sources, based on photodissociation of C_2N_2 at 193 nm [85].

After entering the collision chamber, the cyano radical beam collides with the molecules of the second pulsed beam with a collision angle of 90° . The unsaturated hydrocarbon beams were produced by expanding the pure gas or vapor at room temperature through a pulsed valve. For the experiments described here the typical collision energies are in the range 13.0–35.0 kJ/mol. The reaction products are detected at different laboratory angles by the QMS which is preceded by an electron impact ionizer; the velocity distributions

for the different ionized species are obtained by recording the TOF distributions at each selected m/e . Since the electron impact ionizer and the QMS compactly reside in the rotating detector chamber, this setup allows recording the intensity of distinct m/e as a function of the flight-time at different laboratory angles in the scattering plane defined by the two crossing beams (the detector can span the angular range from $\Theta_{\min} = -25.0^\circ$ to $\Theta_{\max} = 72.0^\circ$, where $\Theta = 0^\circ$ represents the direction of the CN beam and $\Theta = 90^\circ$ represents the direction of the hydrocarbon beam). The detector chambers are separated and differentially pumped (regions I and II) to reduce the gas load from the main chamber; the innermost III region contains the Brink-type electron impact ionizer (surrounded by a liquid-nitrogen cold shield), the quadrupole mass filter, and the Daly-type scintillation particle detector. Despite the differential pumping setup, molecules desorbed from wall surfaces lying on a straight line with the electron impact ionizer (straight-through-molecules) cannot be avoided, since the mean free path of these species is of the order of 10^3 m compared to maximum detector dimensions of a few meters. To reduce these straight-through-molecules, a copper plate is attached to a two-stage closed cycle helium refrigerator and cooled to ~ 10 K. Since the copper shield is located between the two skimmers and the scattering region, the ionizer “views” a cooled surface from which only H_2 and He desorb at 10 K.

14.3 DATA ANALYSIS

The quantity which is measured in a CMB experiment with mass spectrometric and time-of-flight detection is the product intensity as a function of the scattering angle and arrival time; what we call the time-of-flight spectra. By integrating the TOF spectra with respect to time, we also obtain the intensity as a function of the scattering angle, the so-called laboratory (LAB) angular distribution. The measurements are carried out in the laboratory system of coordinates, but for the physical interpretation of the scattering data it is necessary to operate a coordinate transformation and move to the center-of-mass (CM) reference frame. The velocity vector or Newton diagram shown in Figure 14.2 graphically represents the relation between the LAB and CM quantities for an experiment where a typical CN beam crosses at 90° an unsaturated hydrocarbon (RH) beam and reacts according to $\text{CN} + \text{R-H} \rightarrow \text{R-CN} + \text{H}$. An observer in the LAB frame sees the CM moving with the CM velocity vector, \mathbf{v}_{CM} , and the particle beams approaching each other with \mathbf{v}_{CN} and \mathbf{v}_{RH} . An observer sitting on the CM would see the CM at rest and the particles approaching along the relative velocity vector, $\mathbf{v}_{\text{r}} = \mathbf{v}_{\text{CN}} - \mathbf{v}_{\text{RH}}$, with the CM velocities \mathbf{u}_{CN} and \mathbf{u}_{RH} . After the reactive collision takes place, the newly formed product R-CN and H are scattered with a LAB velocity \mathbf{v}_{RCN} and \mathbf{v}_{H} corresponding to the CM velocities \mathbf{u}_{RCN} and \mathbf{u}_{H} (in the Newton diagram of Figure 14.2 only \mathbf{v}_{RCN} and

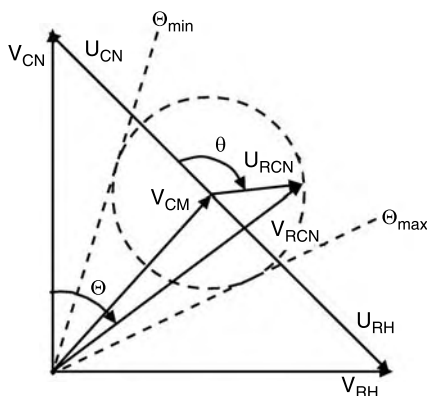


FIGURE 14.2 Velocity vector or Newton diagram showing the relation between the center-of-mass product scattering angle, θ , and velocity, \mathbf{u}_{RCN} , and the laboratory equivalent, Θ and \mathbf{v}_{RCN} . The reactant velocities and the maximum angular range within which the products can be scattered in the laboratory reference frame, $\Theta_{min} - \Theta_{max}$, are also shown.

\mathbf{u}_{RCN} are shown). By taking into account the reactant and product masses and the laws of conservation of the linear momentum and total energy, it is possible to calculate the maximum CM speed that the products can reach and therefore to draw the limiting circles in the Newton diagram which define the maximum LAB angular ranges (from Θ_{min} to Θ_{max}) within which the products can be scattered.

It can be easily demonstrated that the relation between LAB and CM product flux is given by [57,59]

$$I_{LAB}(\Theta, v) = \frac{I_{CM}(\theta, u)v^2}{u^2}, \quad (14.5)$$

where Θ and v are the LAB scattering angle and speed, respectively, while θ and u are the corresponding CM quantities. Since the electron impact–mass spectrometric detector measures the number density of products, $N(\Theta)$, rather than the flux, the actual relation between the LAB density and the CM flux is given by [59]

$$N_{LAB}(\Theta, v) = \frac{I_{CM}(\theta, u)v}{u^2}. \quad (14.6)$$

Nevertheless, because of the finite resolution of experimental conditions (angular and velocity spread of the reactant beams and angular resolution of the detector), the LAB to CM transformation is not single valued and,

therefore, analysis of the laboratory data is usually performed by forward convoluting tentative CM distributions over the experimental conditions. In other words the CM angular and velocity distributions are assumed, averaged and transformed to the LAB frame for comparison with the experimental distributions and the procedure is repeated until a satisfactory fit of the experimental distributions is obtained. The final outcome of a reactive scattering experiment is the generation of a velocity flux contour map of the reaction products, i.e., the plot of intensity as a function of angle and velocity in the CM system, $I_{\text{CM}}(\theta, u)$. The $I_{\text{CM}}(\theta, u)$ is called differential cross section and is commonly factorized into the product of the velocity (or translational energy) distribution, $P(u)$ (or $P(E'_T)$), and the angular distribution, $T(\theta)$.

The measurable quantities by this technique contain basic information. The main advantage with respect to common flow reactors coupled with a mass spectrometer is the possibility to measure product angular and velocity distributions, which allows one to directly derive the amount of the total energy available to the products and, therefore, the energetics of the reaction. This is crucial when more isomers with the same gross formula, but different enthalpy of formation, can be produced, as exemplified in [Figure 14.3](#) for an ideal experiment relative to a reaction involving CN radicals and a generic hydrocarbon RH. If two product isomers with the same gross formula RCN are formed and if the energetics of the two channels is significantly different, the two product isomers will be scattered within different angular ranges. In the example of [Figure 14.3](#) the enthalpy of reaction for the channels leading to the two isomers (RCN)' and (RCN)'' is very different and so is the total energy available to product translational motion. Recall that, because of the energy conservation rule, the total energy, E_{TOT} , is given by the sum of the initial collision energy, E_c , and the heat of reaction, $E_{\text{TOT}} = E_c - \Delta H^0$; in CMB experiments the internal energy of the reactants is negligible because of the cooling during the supersonic expansion. Since the energy available to the two isomers is very different, the maximum speed in the centre-of-mass frame that they can reach is different and the limiting circles in the Newton diagram will define laboratory angular ranges of different extent. When the difference is pronounced, the distinct contributions to the observed signal will be easily separated during the data analysis; when the difference is not sharp, accurate measurements of product velocity distributions as a function of scattering angle usually allow us to discriminate amongst different contributions.

Apart from what we learn from the energy release, the shape of the CM angular distribution, $T(\theta)$, can give us some information on the reactive event as well [57,59]. Several shapes of the flux distributions are possible corresponding to two different kinds of mechanism.

First, the $T(\theta)$ and corresponding flux contour map $I_{\text{CM}}(\theta, u)$ are symmetric with respect $\theta = 90^\circ$; in this case the flux intensity is the same for each θ and $180^\circ - \theta$ pair. The “forward–backward” symmetric shape is

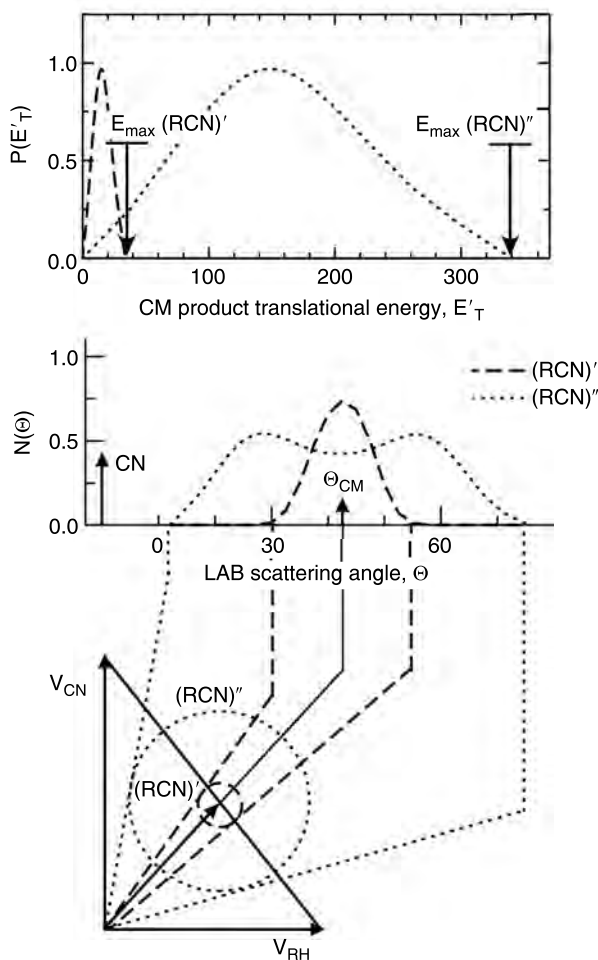


FIGURE 14.3 Bottom panel: laboratory angular distributions for the $(RCN)'$ and $(RCN)''$ isomeric products from a generic $CN + RH$ reaction together with the relative Newton diagram. The circles delimit the maximum speeds that the two isomeric products can achieve and the corresponding ranges of scattering angles. Top panel: product $(RCN)'$ and $(RCN)''$ translational energy distributions reflecting the large difference in exothermicity between the two isomer channels.

characteristic of a bimolecular reaction proceeding through the formation of a bound intermediate with a lifetime larger than its rotational period. In fact, a reaction intermediate which lives long enough to rotate several times will lose memory of the initial directions of the incoming collision partners and will fragment isotropically in the scattering plane. After averaging over

all collisions with all the possible orientations of the angular momentum, the resulting $T(\theta)$ peaks symmetrically in the forward and backward directions. These reactions are defined as proceeding through the formation of a long-lived complex or “indirect” mechanism. The interpretation of $T(\theta)$ can also be more complex. While the symmetry is an essential requirement, the detailed shape of $T(\theta)$ is determined by the disposal of the total angular momentum and a variety of shapes are indeed possible, depending on the correlation between initial and final angular momentum [57]. As a matter of fact, a symmetric distribution around 90° can be observed also when there is not a bound intermediate between reagents and products. In this case, the forward–backward symmetry originates from a decomposing transition state with a rotation axis which interconverts the leaving moiety. On this basis, the leaving moiety can be released into θ and $180^\circ - \theta$ with equal probability, thus producing a forward–backward symmetric flux distribution.

Second, the angular flux distribution can also be strongly asymmetric around 90° ; two distinct cases are possible: the angular flux distribution is peaked in the forward direction ($\theta = 0^\circ$) and is zero in the proximity of the other pole (“stripping dynamics”) or it is peaked in the backward direction ($\theta = 180^\circ$) and approaches zero at small angles (“rebound dynamics”). In both cases, the reaction is “direct” and usually proceeds through a transition state without involving an intermediate. Direct reactions are associated with repulsive potential energy surfaces, whereas a long-lived intermediate experiences the deep potential energy well of a bound species.

In real experiments, a combination of both mechanisms can be observed. That happens when multiple microscopic reaction mechanisms occur. Also, in certain cases where a bound intermediate does exist, its lifetime can be relatively short and insufficient to lose the memory of the initial directions of the reagents (“osculating complex”) [57].

In conclusion, by measuring angular and velocity distributions of the possible products from a bimolecular reaction, the CMB technique allows one to determine: 1. the primary reaction products, 2. the branching ratios of competing reaction channels, 3. the microscopic reaction mechanisms, 4. the product energy partitioning, and hence 5. the underlying potential energy surfaces governing the transformation from reactants to products. This last point deserves special attention. One objection which is often made to the CMB experiments is that they are performed at collision energies rather larger than those of interest in astrochemistry. In some laboratories the strategy of changing the beam crossing angle has been implemented to reach very low collision energies [65,69]. However, even when the experiments are performed with a fixed crossing angle, which limits the range of collision energies that can be explored as in the present case, the information is still valuable. In this case, it is the interplay with the theoretical calculations of the relevant potential energy surface which plays an important role. The CMB experiments corroborate or dispute the results of the calculations.

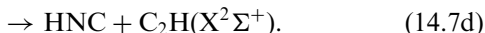
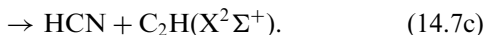
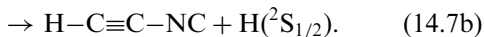
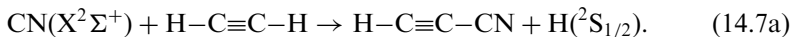
Once the validity of a computed PES is experimentally confirmed, then its predictions at very small collision energies can be regarded with more confidence.

14.4 RESULTS ON THE REACTIONS OF CN RADICALS WITH SIMPLE ALKYNES

In this section we report our experimental findings relatively to three different reactions of CN radicals with simple alkynes, namely acetylene, methylacetylene and dimethylacetylene. We have selected these reactive systems for different reasons: the reactions with C_2H_2 is the prototype for the class of reactions $CN + \text{alkynes/polyynes}$, thus is expected to reveal key concepts for reactions with the higher members of the same series; the reactions with methylacetylene and dimethylacetylene were selected to observe the effect of the H substitution with one or two alkyl groups. In all cases, the experimental results are discussed in the light of the *ab initio* electronic structure calculations for the stationary points of the relevant potential energy surfaces.

14.4.1 THE REACTION $CN + C_2H_2$

As already discussed in Section 14.1, the $CN + C_2H_2$ reaction is alleged to be the most important step in the formation of cyanopolyynes in different environments, such as planetary atmospheres and the interstellar medium. Its potential importance has been confirmed by kinetic studies which have found this reaction to be very fast in a large range of temperatures [2–5]. The possible reaction channels include:



Until very recently [5], the nature of the reaction products could not be determined in the kinetic studies and a tentative assignment was done by comparing the rate constants for the reactions $CN + C_2H_2$, $CN + C_2H_4$, and $CN + CH_2=CH-C\equiv CH$ [2]. In this way, it was speculated that all these reactions proceed through the addition of CN to the π bond(s) leading to the formation of nitriles and atomic hydrogen rather than through H-atom abstraction leading to the formation of HCN and alkenyl/alkynyl radicals. Two possible isomers of gross formula C_2HN can be formed by the H-atom displacement in the reaction $CN + C_2H_2$, namely cyanoacetylene, HCCCN (route 14.7a), and isocyanoacetylene, HCCNC (route 14.7b); between the

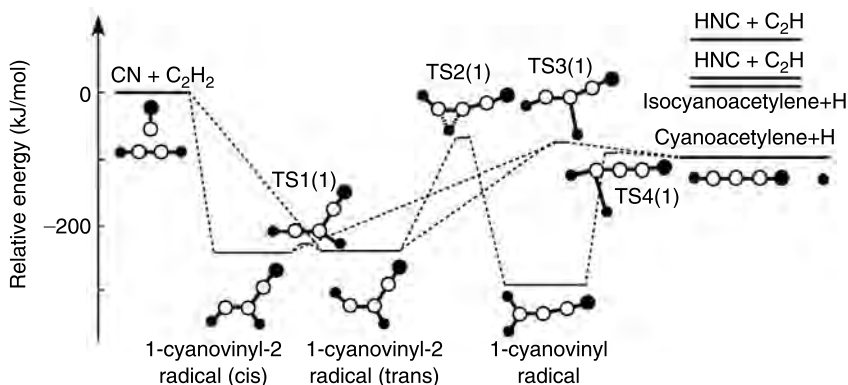


FIGURE 14.4 Schematic potential energy surface for the CN/C₂H₂ system (adapted from References 75 and 82).

two, cyanoacetylene is the one favored by thermochemical considerations (see Figure 14.4).

To establish whether the product thermodynamically favored is the one really formed, we carried scattering experiments at two different collision energies of 21.1 kJ/mol and 27.0 kJ/mol [75,82]. We were able to observe scattered products at two different mass-to-charge ratios, 51 and 50, which correspond to the ions C₂HN⁺ and C₂N⁺, respectively. However, the LAB distributions recorded at the two m/e values revealed identical patterns and could be fit with the same CM functions. This unambiguously indicates that the only product really formed under our experimental conditions has gross formula C₂HN and that it partly fragments to C₂N⁺ in the electron impact ionizer because of dissociative ionization. A signal at $m/e = 52$ corresponding to a possible stable reaction adduct of formula C₂H₂N was not observed. The lack of signal observation at $m/e = 52$ means that if a bound reaction intermediate exists, it fragments before reaching the detection region because of its high energy content. The complete set of final measurements were carried out at $m/e = 50$, since we had the best signal-to-noise ratio at this mass. In Figure 14.5 the LAB product angular distribution at $E_c = 21.1$ kJ/mol together with the TOF spectrum recorded at $\theta = 32^\circ$ are shown. The solid lines superimposed on the experimental results are the calculated curves when using the CM best-fit functions reported in the Figure 14.6. Another full set of data was recorded at a slightly higher collision energy (27.0 kJ/mol) [82]. The laboratory angular distributions recorded at both collision energies have a peak close to center-of-mass position angle, θ_{CM} , and show about the same intensity in the backward and forward directions (with respect to the CN radical beam direction). Also, they are quite wide, with scattered products extending for about 35° . The limiting circle shown in the Newton diagram of Figure 14.4 has been

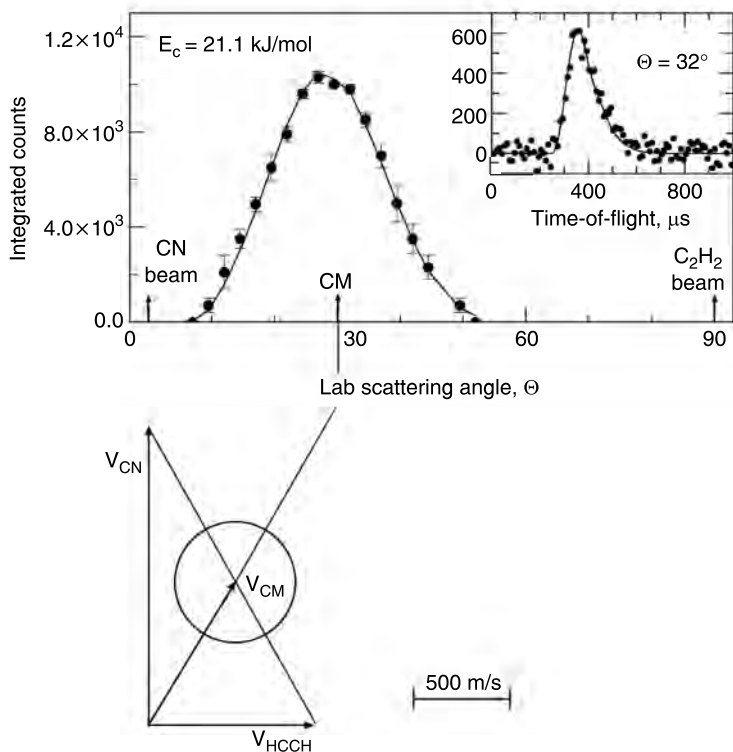


FIGURE 14.5 Laboratory angular distribution of the $m/e = 50$ ion (C_3N^+) at the collision energies of 21.1 kJ/mol together with the corresponding Newton diagram. The circle in the Newton diagram delimits the maximum velocity that the HCCCN product can attain on the basis of energy conservation if all the available energy for the corresponding channels goes into product translational energy. The TOF spectrum of the $m/e = 50$ ion at the center-of-mass angles of 32° is also shown. The solid lines superimposed to the experimental points are the calculated curves when using the best-fit center-of-mass functions of Figure 14.6 (adapted from References 75 and 82).

drawn assuming that all the available energy is released as product translational energy in the case that cyanoacetylene is the formed product. If we compare this limit with the experimentally determined maximum speed of the C_2HN product(s), the substantial coincidence indicates that HCCCN must be significantly formed. The two best fit values of $P(E'_T)$ are characterized by a maximum value of translational energy, E_{TOT} , of about 100–130 kJ/mol (note that by extending or cutting the high energy tails of the best fit values of $P(E'_T)$ by 10 kJ mol^{-1} the quality of the fit does not change significantly). Since the energy conservation rule states that $E_{TOT} = E_c - \Delta H^0$; once we account for the relative collision energies, the CN/H

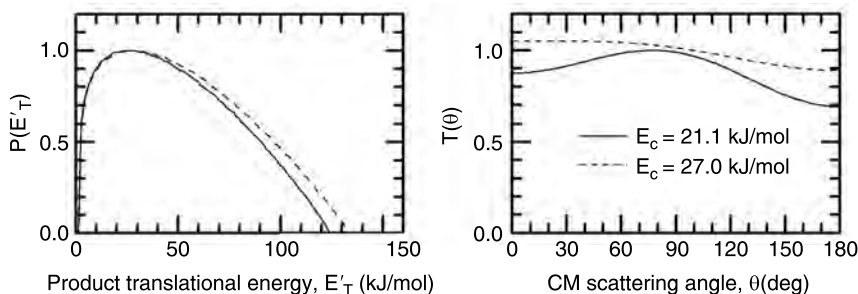


FIGURE 14.6 Best-fit CM product angular (right) and translational energy (left) distributions at the two collision energies investigated (adapted from Reference 82).

exchange reaction turns out to be exothermic by about 90 ± 10 kJ/mol. The thermochemistry of the channels leading to the two possible C_2HN isomers and atomic hydrogen is very different as recently derived by electronic structure *ab initio* calculations [82]. The exothermicity of the reaction channel leading to cyanoacetylene, $HCCCN$, and $H(^2S)$ was found to be -94.0 kJ/mol in contrast to the values $+13.0$ kJ/mol calculated for the reaction channel leading to the isomer, isocyanoacetylene; see Figure 14.4 [75,82]. In conclusion, from the energy cut-off of the product translational distributions we can establish that the thermodynamically more stable cyanoacetylene isomer is also the one dynamically favored.

Other important suggestions can be derived from the angular part of the differential cross section. At both collision energies, the values of $T(\theta)$ show more intensity in the forward direction ($\theta = 0^\circ$) as clearly shown in Figure 14.6. The product intensity observed in the whole angular range suggests that the reaction follows indirect scattering dynamics via a C_3H_2N complex formation; the scattering preference for the forward hemisphere implies that the complex lifetime is comparable to its rotational period according to the “osculating complex” model [57].

After the first experimental results at the microscopic level became available [75], *ab initio* calculations of the electronic structures of the stationary points along the C_3H_2N potential energy surface (PES) were also performed for the first time [82]. The statistical Rice–Ramsberg–Kassel–Marcus (RRKM) theory was also applied using the *ab initio* PES to predict the product branching ratio [82]. By comparing our experimental results, *ab initio* calculations and RRKM predictions we can now claim to have a complete picture of the reaction mechanism, the basic characteristics of which can be extended to the general case of $CN + H-(C\equiv C)_n-H$ reactions. The unpaired electron of the CN radical is mostly localized in the σ -symmetric $^2\Sigma^+$ -orbital of the carbon atom and therefore CN attacks the π_s/π_y -orbital of the acetylene molecule on the C-side. The approach leads to

a loose transition state with no entrance barrier and produces a strongly bound (242 kJ/mol) intermediate, the *cis/trans*-1-cyanovinyl-2 radical intermediate, HCCHCN, with a C_s symmetry on a $^2A'$ PES, cf. Figure 14.4. Both the *cis* and *trans* forms can isomerize easily via TS1(1) located only 14 kJ/mol above the initial collision complexes; since the isomerization barrier lies well below the total available energy, the *cis* and *trans* forms are expected to be present in equal amounts. The CN radical can attack the acetylene molecule also with its N-side without an entrance barrier. This approach, however, was not found to be efficient at leading to the isocyanoacetylene product because of significant barriers (~ 30 kJ/mol) along that reaction pathway. The *cis/trans* 1-cyanovinyl-2 radical intermediates can undergo either an H atom elimination to form cyanoacetylene through the transition state TS3(1) (-72 kJ/mol) or a 1,2-H atom shift through the transition state TS2(1) (-65 kJ/mol) leading to the 1-cyanovinyl radical which is the absolute minimum of the potential energy surface. This intermediate can also decompose to cyanoacetylene + H through the transition state TS4(1) (-87 kJ/mol). Two high-energy singlet cyanovinylidene ($+115$ kJ/mol) and singlet isocyanovinylidene ($+227$ kJ/mol) isomers also exist (not shown here). Since our maximum collision energy is limited to 27 kJ/mol, none of the vinylidenes is relevant to our experiments.

We have already commented on the fact that our experimental data are consistent with the formation of the most stable isomer cyanoacetylene, but by using the experimental results only we cannot exclude a small contribution from the HCCNC formation channel; we have employed RRKM calculations to tackle this problem. This procedure shows that HCCCN is the only reaction product and that only about 15% of it is formed after the rearrangement of *cis/trans* 1-cyanovinyl-2 radical intermediates into 1-cyanovinyl radical.

A last comment on the H atom abstraction channels leading to HCN (or HNC) and C_2H is due. These reaction channels could not be experimentally investigated because of the presence of a strong signal at the m/e of the reactant CN and the very unfavorable kinematics associated with the product masses. However, according to the *ab initio* calculations, the two H-abstraction channels are endothermic by 23 kJ/mol ($HCN + C_2H$) and 83 kJ/mol ($HNC + C_2H$), respectively, and involve transition states located at 41 kJ/mol and 96 kJ/mol above the reactants. In other words, they can occur neither under the present experimental conditions nor under the conditions of the ISM and Titan's atmosphere. Very recently, a room temperature kinetic study in which the H atoms could be monitored by VUV-LIF on the Lyman α transition confirmed that the H-displacement channels are the only active pathways [5].

Interestingly, in this specific case the reaction dynamics study confirms that the HCCCN + H channel is the main one, as could be simplistically predicted by mere thermochemistry. This conclusion should not be generalized; in many well-known cases the main reaction channel is not the one

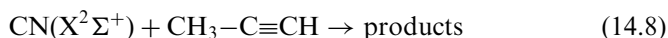
thermodynamically favored [70,73]. For instance, it was observed that the bonds newly formed by the reactant interactions fragment much more easily than the pre-existing ones, irrespectively of their absolute strength. The dynamic study of a reaction has exactly the aim of verifying whether a reaction pathway exists and whether it is easily accessible by the system.

In conclusion, the reaction mechanism for the $\text{CN} + \text{C}_2\text{H}_2$ reaction — the prototype of the class of reactions $\text{CN} + \text{H}-(\text{C}\equiv\text{C})_n-\text{H}$ — is relatively simple: amongst the possible approaches, the addition of the CN radical to the triple bond on the C side is the favored one; the dissociation of the *cis/trans* forms of the addition intermediates leads to the cyanoacetylene product and atomic hydrogen.

Probably, the most important conclusion of the present study is that the triple acetylenic bond is preserved in the reaction products and this in spite of the fact that the initial attack by the unpaired electron of the CN radical destroys it. The three possible reaction intermediates have, in fact, lost the triple bond, but when, because of the high internal energy with which they are formed, they dissociate to products, the triple bond is retrieved in the new molecular products. This observation can be generalized to the case of the reactions of CN with polyynes and is quite important for the speculated routes of formation of cyanopolynes in various environments.

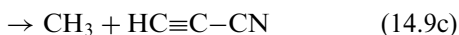
14.4.2 THE REACTION $\text{CN} + \text{CH}_3\text{CCH}$

As already mentioned in Section 14.1, methylcyanoacetylene, CH_3CCCN , has been identified in the ISM [43]. In addition, since both CN radicals and methylacetylene have appreciable concentrations in the 100–300 km region of Titan's atmosphere [16], CH_3CCCN could be formed in that environment as well, provided that the characteristics of the reaction



resemble those of reaction 14.7a. Similarly to the case of reaction 14.7, the total removal rate constant of $\text{CN} + \text{CH}_3\text{CCH}$ was found to be on the order of the gas kinetics value also at very low temperature (15 K) [4]. In this case, however, because of the presence of the methyl group, the reacting alkyne is not symmetric and the CN radical can attack either the α carbon atom (the one to which the CH_3 group is attached) or the β one.

Because of the higher complexity of the reacting molecule several reactive channels are possible (see Figure 14.7)



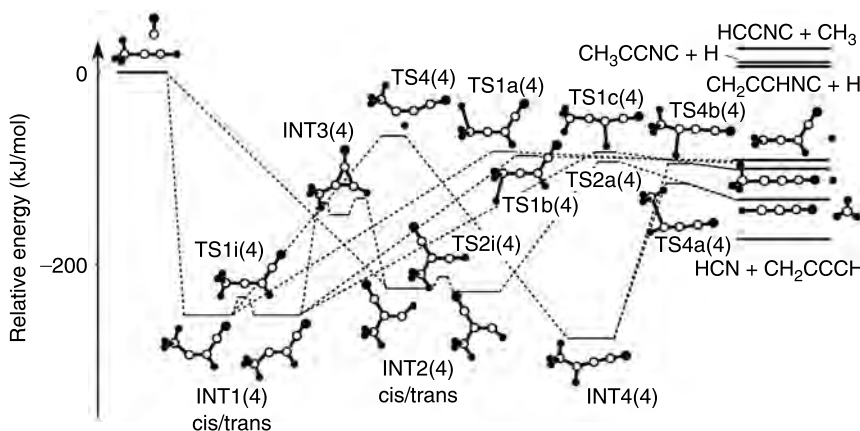
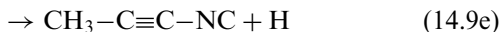


FIGURE 14.7 Schematic potential energy surface for the CN/CH₃CCH system (adapted from References 76 and 84).



Route 14.9b is also a CN/H exchange reaction, but in this case it is one of the H atoms of the methyl group to be eliminated, rather than the acetylenic one of route 14.9a. Route 14.9c corresponds, instead, to a CN/CH₃ exchange reaction. Routes 14.9f and 14.9g are exothermic (see Figure 14.7) as opposed to the case of reaction 14.7 because H abstraction from the methyl group is much easier than acetylenic-H abstraction.

We have investigated reaction 14.9 at three different collision energies of 13.4, 24.7 and 34.9 kJ/mol [76,84]. A reactive scattering signal was observed at $m/e = 65$ (corresponding to the ion C₄NH₃⁺), 64 (C₄NH₂⁺), 63 (C₄NH⁺), and 62 (C₄N⁺). In all cases, however, the TOF spectra at all mass-to-charge ratios revealed identical patterns, which means that a product with gross formula C₄NH₃ is the one formed in this range of masses and that the signal at lower m/e was originated from dissociative ionization. No signal at $m/e = 66$ corresponding to a possible stable reaction adduct of formula C₄H₄N was observed. All the final measurements were performed at $m/e = 62$ because of the best signal-to-noise ratio. In Figure 14.8 the LAB angular distribution at $E_c = 24.7$ kJ/mol is reported together with the TOF spectrum recorded at the CM angle. At all the collision energies investigated the LAB angular distributions were found to peak at the CM position angles and show about the same intensity in the backward and forward directions.

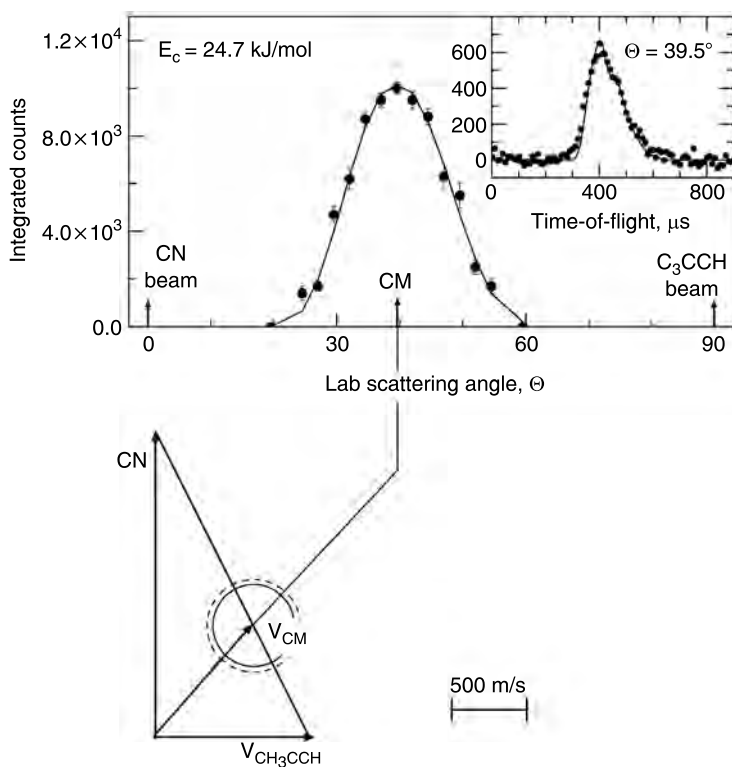


FIGURE 14.8 Laboratory angular distribution of the $m/e=62$ ion (C_4N^+) at the collision energies of 24.7 kJ/mol together with the corresponding Newton diagram. The circles in the Newton diagram delimit the maximum velocity that the two isomeric products, methylcyanoacetylene (dashed line) and cyanoallene (solid line), can attain on the basis of energy conservation if all the available energy for the corresponding channels goes into product translational energy. The TOF spectrum of the $m/e=62$ ion at the center-of-mass angles of 39.5° is also shown. The solid lines superimposed to the experimental points are the calculated curves when using the best-fit center-of-mass functions of Figure 14.9 (adapted from Reference 76).

All of them are quite broad, extending for $\sim 40^\circ$ in the scattering plane. The limiting circles reported in the Newton diagram of Figure 14.8 have been drawn assuming that all the available energy is channeled into the product translational energy, in the case that the two C_4H_3N isomer are formed, that is methylcyanoacetylene (dashed line) and cyanoallene (solid line). If these limits are compared with the experimentally determined scattering ranges, it is obvious that both product isomers methylcyanoacetylene and cyanoallene are consistent with the angular range of scattered products.

At each collision energy, our experimental data were fit using a single CM angular distribution and a single CM translational energy distribution,

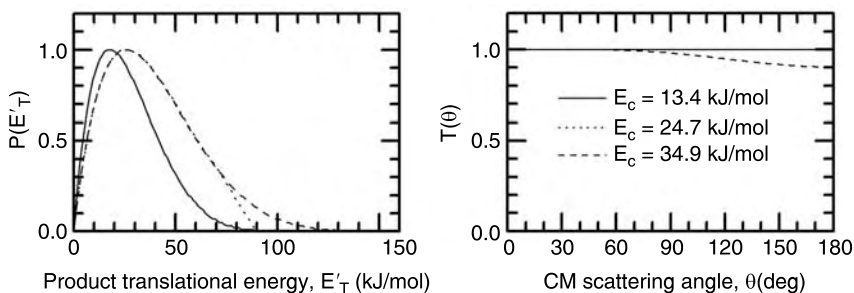


FIGURE 14.9 Best-fit CM product angular (right) and translational energy (left) distributions at the three collision energies investigated (adapted from References 76 and 84).

which are shown in Figure 14.9. In all cases, the values of $P(E'_T)$ peak away from zero translational energy and have a maximum located between 15 and 30 kJ/mol. The maximum reached by the $P(E'_T)$ values was found to be amongst 80–130 kJ/mol, 90–135 kJ/mol, and 90–140 kJ/mol, from the lowest to the highest collision energy. If we subtract the relative collision energies, the CN/H exchange reactions turn out to be exothermic by about 65–115 kJ/mol. This finding concords with the reaction enthalpies derived from electronic structure calculations relatively to the formation of both cyanomethylacetylene (calculated to be exothermic by 106 kJ/mol) and cyanoallene (exothermic by 94 kJ/mol) [83,84]. In other words, since the molecular products of routes 14.9a and 14.9b have the same gross formula and similar enthalpy of formation, it is not possible to discriminate which of the two is the one formed with the present experimental resolution. To establish whether the H atom is released from the methyl or acetylenic group of the methylacetylene molecule, we resorted to a trick commonly used in these cases: the use of an isotopically labelled reactant, namely the d_3 -methylacetylene CD_3CCH . The resolution of the quadrupole mass spectrometer was selected so that one mass unit could be separated and no mass leaking occurs. TOF spectra were recorded at the center of mass angle for $m/e = 68$, corresponding to the product $C_4D_3N^+$ (acetylenic H loss) and 67, corresponding to $C_4D_2NH^+$ (D atom loss from the CD_3 group). Then the TOF spectra were integrated upon time and corrected for the distinct mass combination of the products; the result for the D atom vs H atom loss channel branching ratio was about 1 [76].

The CM angular distribution, $T(\theta)$, is isotropic at the lowest collision energy investigated (see Figure 14.9). An isotropic distribution is backward–forward symmetric and, therefore, implies either a lifetime of the decomposing complex(es) longer than its rotational period or a symmetric exit transition state. Since the electronic structure calculations depict no symmetric exit transition state(s) [84], we conclude that the lifetime of the

intermediate(s) is longer than its (their) rotational periods. At the higher collision energies of 24.7 and 34.9 kJ/mol of the $\text{CN} + \text{CH}_3\text{CCH}$ reaction, best fits of our data were achieved with slightly forward-biased values of $T(\theta)$ with an intensity ratios of $I(180^\circ)/I(0^\circ) \sim 0.9$). In all cases, the values of $T(\theta)$ show intensity in the whole angular range between 0° and 180° demonstrating again that the reactions follow indirect scattering dynamics via $\text{C}_4\text{H}_4\text{N}$ complex(es). The absence of polarization in the values of $T(\theta)$ might result from a poor coupling between the initial, \mathbf{L} , and final orbital angular momentum, \mathbf{L}' , indicating that most of the total angular momentum channels into rotational excitation of the heavy product(s).

Also for this system, as the first experimental results at the microscopic level became available, *ab initio* calculations of the electronic structures of the stationary points along the $^2\text{A}'$ $\text{C}_4\text{H}_4\text{N}$ potential energy surface were performed [83,84]. According to the *ab initio* calculations, the CN attacks the π system of the methylacetylene molecule with the radical center located on the $^2\Sigma^+$ orbital of the carbon atom. The consequent addition to the β carbon atom is a barrier-less pathway which leads to the deeply bound (~ -250 kJ/mol) *cis/trans*-1-cyano-2-methyl-vinyl-2 radical intermediate, INT1a/b(4). The INT1(4) *trans* and *cis* structures easily interconvert through the transition state TS1i(4). The CN radical can also add to the α carbon of the methylacetylene, thus forming the *trans/cis* 1-cyano-1methyl-vinyl-2 radical intermediate, INT2a/b(4), which is slightly less stable (~ -225 kJ/mol) than the previous couple. The destabilization is due to the unfavorable repulsion of the cyano and methyl groups of INT2a/b(4). The intermediates INT1b(4) and INT2b(4) can also isomerizes to each other through a three-member cyclic intermediate, INT3(4). The addition to the α carbon atom of the methylacetylene is not favored. The electrophilic radical attack on unsaturated hydrocarbon molecules [87] takes place towards the carbon center which holds the highest electron density. Since the partial delocalization of the methyl π -group orbital increases the spin density of the β carbon atom with respect to that of the α one, the cyano radical will preferentially attack the terminal carbon atom. Also, the steric hindrance of the bulky methyl group reduces the cone of acceptance of α -C and hence the range of reactive impact parameters. Both effects direct the addition towards β -C. In other words, while large impact parameters can only correspond to the addition on the β -C, small impact parameters can bring also to the α -addition. Small impact parameters, however, cannot account for the rotational excitation of the reaction products, as experimentally evidenced by the isotropy of the angular distributions. In conclusion, all considerations suggest a predominant initial attack to the β -C of the methylacetylene molecule and only minor contributions from small impact parameters contributed to form INT2a/b(4).

The possible destinies of the initial addition intermediates INT1a/b(4) and INT2a/b(4) are: 1. H atom elimination, 2. methyl group loss, and 3. hydrogen atom migration. H atom elimination can occur in different ways.

If we consider the intermediates INT1a/b(4), a hydrogen atom can be ejected from the β carbon atom (through the transition state TS1c(4)) or from the methyl group adjacent to the α carbon (through the transition states TS1a/b(4)); in the first case, the molecular product is cyanomethylacetylene, in the second case the molecular product is cyanoallene. All transition states are characterized by about the same energy content. The overall reactions to form cyanomethylacetylene and cyanoallene were calculated to be exothermic by 106 and 94 kJ/mol, respectively. The H atom elimination from the intermediates INT2a/b(4) at the β position forms a singlet carbene-type isomer $\text{CC}(\text{CN})(\text{CH}_3)$, but this pathway is strongly endothermic and cannot occur under the condition of the experiments. Based on our isotopic substitution experiments, the addition intermediates decay via two pathways. The emission of the acetylenic hydrogen atom with the maintenance of the methyl group and formation of cyanomethylacetylene or the carbon–hydrogen (deuterium in the CD_3CCH experiment) bond rupture of one aliphatic bond of the methyl group with the formation of cyanoallene. This indicates that the lifetime of the intermediates is long enough to allow the energy to flow from the activated carbon–carbon σ bond to the breaking carbon–hydrogen bond of the methyl group.

As far as the methyl group loss pathway is concerned, a CH_3 -ejection from INT1a/b(4) would bring to a carbene, $\text{CC}(\text{CN})\text{H}$, but this pathway is strongly endothermic (+77.0 kJ/mol) and, therefore, plays no role under the present experimental conditions. A CH_3 group loss leading to cyanoacetylene is instead feasible from the intermediate INT2a(4) via TS2a(4), which is, as already commented, less favored than intermediate INT1a/b(4). This reaction pathway was not observed experimentally, but we cannot exclude the possibility that it partially contributes to the reaction because the unfavorable kinematics could have prevented us from detecting cyanoacetylene (see below the case of the reaction with dimethylacetylene).

The 1,2 hydrogen migration from the intermediate INT1a(4) brings to the isomer 1-cyano-2-methyl-vinyl-1 radical intermediate, INT4(4), which is the one energetically more stable. INT4(4) can either eject a methyl group via TS4a(4) and form cyanoacetylene or a hydrogen atom, thus forming 1-cyanomethylacetylene via TS4b(4). Both INT4(4) and INT2a(4) can undergo further hydrogen atom migrations from the methyl group leading to a cyanoallyl radical, which is the absolute minimum (~ -350 kJ/mol) of the PES (not shown in the figure). The cyanoallyl radical can only decompose to cyclic reaction products, 1-cyanocyclopropene (channel endothermic by 11 kJ/mol) and 2-cyanocyclopropene (+12 kJ/mol). These pathways, therefore, cannot account for the experimental observation of strongly exothermic reaction channels.

The formation of the related isonitriles (CH_3CCNC and $\text{H}_2\text{CCCH}(\text{NC})$) can only give a minor contribution (if any) to the reaction, since their formation reactions are endothermic by 8 and 6 kJ/mol, respectively. The formation of isocyanoacetylene plus CH_3 is also significantly endothermic

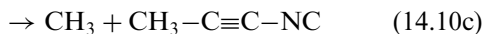
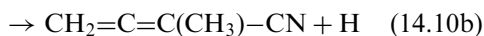
(+25 kJ/mol). The CN radical can also abstract one of the hydrogen atoms of the methyl group, since this pathway is attractive at the B3LYP level of theory. The formation of $\text{HCN} + \text{CH}_2\text{CCH}$ is strongly exothermic, -170 kJ/mol, and also the formation of $\text{HNC} + \text{CH}_2\text{CCH}$ is exothermic by 110 kJ/mol. However, the related reaction $\text{CN} + \text{CH}_4 \rightarrow \text{HCN/HNC} + \text{CH}_3$ is known to be characterized by an entrance barrier and a room temperature rate constant of $\sim 6 \times 10^{-13}$ [2,3], so we do not expect this channel to significantly contribute.

In conclusion, the crossed molecular beam study of the $\text{CN} + \text{CH}_3\text{CCH}$ reaction clearly demonstrated the occurrence of a CN versus H atom exchange channel. The investigation of isotopic variant $\text{CN} + \text{CD}_3\text{CCH}$ suggested the existence of two distinct reaction products, cyanomethylacetylene and cyanoallene. The yield of the two products is about the same at the collision energies investigated. The addition to the β position at the expense of the α C atom, based on the enhanced spin density of the α C and a simultaneous steric hindrance of the methyl group to attack the β position, appears to favor the H-loss over the CH_3 -loss channel.

Interestingly, the presence of the methyl group of methylacetylene strongly increases the complexity of the reaction if compared to that of the unsubstituted acetylene. In particular, amongst the possible products only cyanomethylacetylene and cyanoacetylene (routes 14.9a and 14.9c) preserve the triple acetylenic bond in the nitrile products, while the formation of cyanoallene (routes 14.9b) or allene (route 14.9d and 14.9e) can also occur. This observation implies two consequences relevant to observations and astrochemical models: on one side, it should be possible to observe cyanoallene in the same extraterrestrial environments where cyanomethylacetylene was observed, if reaction 14.9a is the real formation route of cyanomethylacetylene; on the other side, the models should take into account that the reactions of CN radical with short methyl-substituted polyynes do not necessarily form cyanopolynes.

14.4.3 THE REACTION $\text{CN} + \text{CH}_3\text{CCCH}_3$

In the previous section, we have seen how the presence of a $-\text{CH}_3$ group has a strong influence on the chemistry of CN addition to a triple acetylenic bond. In this section we further explore such an effect by moving to the fully CH_3 -substituted species, dimethylacetylene. Also, in this case, we expect a similar reactive approach with the cyano radical attacking the Π -orbital of the dimethylacetylene molecule. The possible reaction routes are (Figure 14.10)



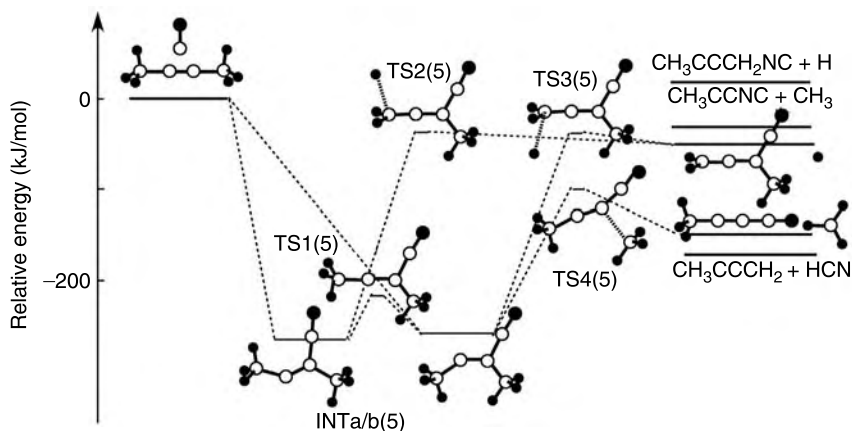
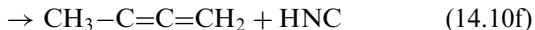
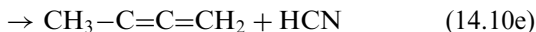


FIGURE 14.10 Schematic potential energy surface for the CN/CH₃CCCH₃ system (adapted from Reference 78).



We have carried out a CMB experiment at a collision energy of 20.8 kJ/mol [78]. We observed reactive scattering signal at $m/e = 79$, corresponding to the ion $\text{C}_5\text{H}_5\text{N}^+$. A reactive signal was observed at lower m/e values between 78 and 74 as well, but the TOF spectra recorded at those values showed identical patterns to the one at $m/e = 79$, thus implying that they derive from dissociative ionization of the same species. Also, in this case, the adduct $\text{C}_5\text{H}_6\text{N}$ could not be observed. We also put a lot of effort into an attempt to search for the methyl loss channel and checked for $m/e = 65$ ($\text{C}_4\text{H}_3\text{N}^+$). Unfortunately, this channel could not be detected experimentally. Based on the weak reactive scattering signal for the H-loss channel, the unfavourable kinematics of the CH_3 -loss channel, and their predicted branching ratio (see below), we estimate that data accumulation times of at least 50 h at the CM angle is necessary to obtain a signal-to-noise ratio comparable to that of the H-atom loss channel. Such a long accumulation time for a single TOF spectrum makes the measurements of the LAB distributions at $m/e = 65$ not feasible.

In Figure 14.11 the LAB product angular distribution recorded at $m/e = 78$ is shown together with the TOF spectrum recorded at $\Theta = 50^\circ$. The solid lines superimposed on the experimental results are the calculated curves when using the CM best-fit functions of Figure 14.12. The LAB angular distribution of the heavy $\text{C}_5\text{H}_5\text{N}$ fragment is relatively narrow. If we

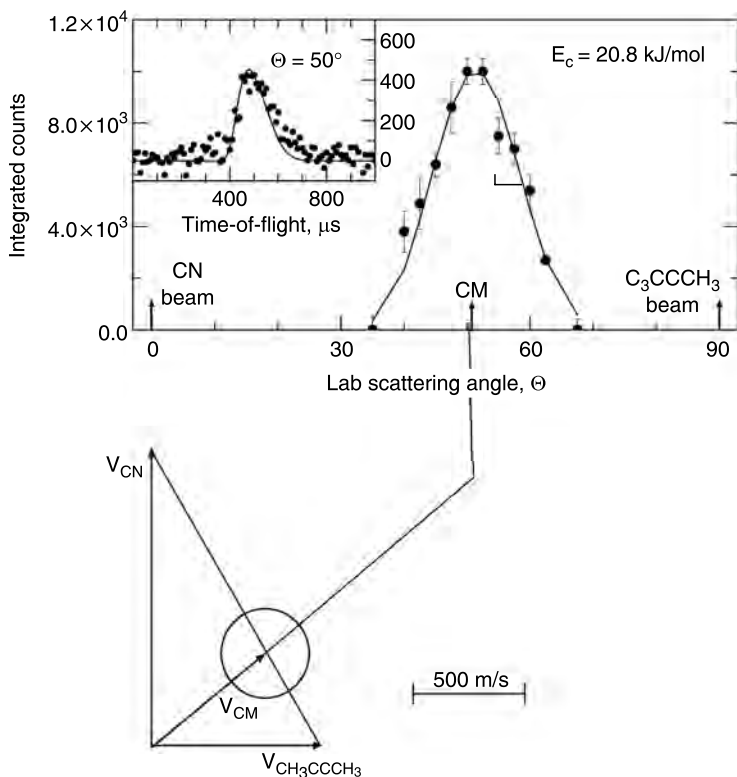


FIGURE 14.11 Laboratory angular distribution of the $m/e = 78$ ion ($C_5H_4N^+$) at the collision energies of 20.8 kJ/mol together with the corresponding Newton diagram. The circle in the Newton diagram delimits the maximum velocity that the $CH_2=C(CH_3)-CN$ product can attain on the basis of energy conservation if all the available energy for the corresponding channels goes into product translational energy. The TOF spectrum of the $m/e = 78$ ion at the center-of-mass angles of 50° is also shown. The solid lines superimposed to the experimental points are the calculated curves when using the best-fit center-of-mass functions of Figure 14.12 (adapted from Reference 78).

compare our observed scattering range with the one derived by the Newton circle constructed using the *ab initio* exothermicity for the $CH_2=C(CH_3)-CN + H$ channel, we find good agreement with the theory predicting no signal at angles less than 33.0° and larger than 70.0° . The best fit translational energy distribution $P(E'_T)$ extends to about 110 kJ/mol. The fit of the laboratory data does not change significantly if we extend or shorten the $P(E'_T)$ by about 20 kJ/mol. Correcting for the collision energy, the title reaction is exothermic by 90 ± 20 kJ/mol. Finally, the experimentally determined fraction of total available energy released into translational energy of

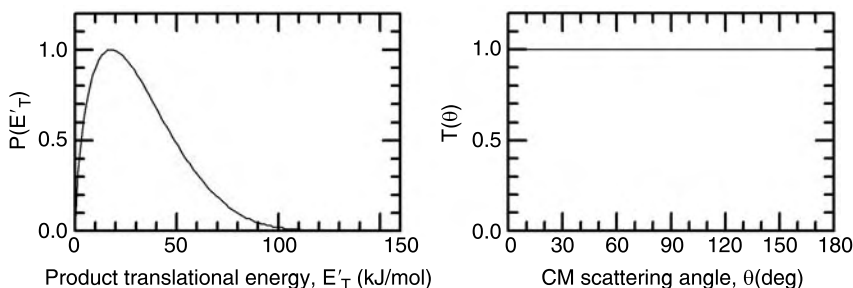


FIGURE 14.12 Best-fit CM product angular (right) and translational energy (left) distributions at the collision energy investigated (adapted from Reference 78).

the product is 30–35%. The $T(\theta)$ is forward–backward symmetric, implying that the reaction follows indirect scattering dynamics since no intermediate complex exists in which a rotation can interconvert the leaving hydrogen atom in the decomposing complex.

According to the *ab initio* calculations [78,83], the CN radical attacks the π orbital of dimethylacetylene along a $^2A'$ PES forming a new carbon–carbon σ bond in the *cis* and *trans*-1-cyano-2-buten-3-yl radical (CN)CH₃CCCH₃, INTa/b(5), stabilized by 236 and 241 kJ/mol with respect to the reactants. The fast RRKM rate constant of $k = 2.86 \times 10^{13} \text{ s}^{-1}$ of the *cis*–*trans* isomerization of both 1-cyano-2-buten-3-yl radicals strongly suggests that the chemical reaction dynamics are invariant on the initial concentration of the *cis* versus *trans* intermediates. The transition states TS2(5)/TS3(5) for the H-atom loss channel are located ~ -70 kJ/mol with respect to the reactants, that is only ~ 6 kJ/mol above the products. The methyl group elimination channel is also possible through the transition state TS4(5) located at -105 kJ/mol. The RRKM branching ratios show that this channel is largely dominant, with a branching ratio of the CH₃ versus H loss of about 360 at the collision energy investigated. If we go to 0 kJ/mol collision energy, approaching the very cold regions of the interstellar medium, this ratio increases to about 650. For this system, the reaction to the isonitrile isomer CH₃CCNC + CH₃ is exothermic by 36 kJ/mol, while formation of CH₃CCCH₂(NC) is endothermic by 14 kJ/mol. The H-atom abstraction channels leading to both HCN/HNC and CH₃CCCH₂ are exothermic (-176 and -118 kJ/mol, respectively), but are not expected to significantly contribute as discussed for the case of the reaction with methylacetylene.

A comparison with the CN reactions with acetylene and methylacetylene is in order. In all cases, the CN radical attacks a π orbital of the alkyne on the carbon side and the *cis/trans* doublet radical intermediates are formed. Whereas the acetylenic carbon atoms in acetylene and dimethylacetylene are chemically equivalent, methylacetylene is asymmetric and is characterized

by two distinct acetylenic carbon atoms. After the CN addition, in the case of the CN/HCCCH system only the HCCCN + H channel is active, while in the case of methyl and dimethyl-acetylene the addition intermediates can undergo more processes with the subsequent formation of methyl substituted cyanoacetylene or substituted allene isomer. The experimental observation of the substituted allene isomers suggests that the energy randomization is likely to be complete for the two reactions, since the C–H bond rupture does not take place at the carbon atom originally attacked.

14.5 CONCLUSIONS AND OUTLOOK

In this chapter, we have shown how the recent advances in the crossed molecular beam technique allow us to study complex polyatomic reactions of relevance in astrochemistry. The focus was on the CN radical reactions with simple alkynes, but the same approach has been also applied to the study of other CN radical reactions with unsaturated small organic molecules, such as ethylene, benzene, and allene, which are of relevance in astrochemistry as well [77,81,84].

The examples we have given here show how the method can unravel the dynamics of the reactions of interest, providing information also on the reaction intermediates and product isomers. By combining the experimental study with *ab initio* electronic structure calculations of the relevant potential energy surfaces, we have inferred useful information on the feasibility of the reactions of the cyano radical with acetylene and methyl-substituted acetylene in extraterrestrial environments. The reactions have no entrance barriers and are all exothermic. Since the transition states involved range well below the energy of the separated reactants, these reactive collisions can occur even in low temperature environments such as in cold molecular clouds and in the atmospheres of planets and their moons. Furthermore, we have identified the underlying reaction mechanism. All reactions proceed via an initial addition of the radical to the acetylenic triple bond. This is followed either by a hydrogen emission or by an additional hydrogen migration prior to an H-atom loss. The sequence of the CN radical addition followed by an H-atom loss is expected to be generalized and can be extended to predict the reactivity of hitherto not investigated reactions of cyano radicals. We gave experimental confirmation that cyanoacetylene is the sole product of the fast CN + acetylene reaction and that methylcyanoacetylene can be formed by the reaction CN + methylacetylene. The explicit assignment of the reaction pathways is unique to crossed beam experiments. Since the product radicals are extremely reactive, bulk experiments subjecting gas mixtures to discharges and coupling this setup to a gas chromatography–mass spectrometer (GC–MS) cannot identify open shell reaction products. Since important information can be lost in bulk experiments, detailed crossed beam experiments are clearly desirable to shed light on gas phase reactions.

The results of the present investigation can also guide future observations. The experimental results show that distinct structural isomers can be formed in the reaction with methylacetylene. These isomers have different spectroscopic properties, photochemical activities, and distinct chemical reactivity. Among them, CH_3CCCN has been detected in cold molecular clouds, but not yet in the atmosphere of Titan. Therefore, methylcyanoacetylene and cyanoallene deserve a special position in the list of the targets for the NASA–ESA *Cassini–Huygens* mission to Titan. The spacecraft *Huygens* will carry an IR mapping spectrometer as well as a quadrupole mass spectrometer capable of identifying closed shell isomers in Titan's atmosphere.

In addition to product isomers, the crossed beam technique also provides information on the highly unstable reaction intermediates. The identified intermediates have been characterized by resorting to *ab initio* electronic structure calculations: all the reaction intermediates are doublet radicals, internally excited, and hence highly reactive in planetary atmospheres. Although under the experimental single collision conditions the gas is too rarefied to allow three-body collisions, the collision induced stabilization of the intermediates is possible in Titan's dense atmosphere. Notably, these free radicals have unknown spectroscopic properties which could make them responsible for the orange color of the upper atmospheric layers.

The present work is only the very first step towards a comprehensive and systematic understanding of the fundamental elementary processes involved in the chemistry of hydrocarbon-rich planetary atmospheres and interstellar medium. Our experiments explicitly identified synthetic routes to nitriles — the alleged precursor molecules to amino acids. The experimental data can be employed to set up a systematic database of reaction products and can predict the formation of hitherto unobserved gas phase molecules. The applications of the crossed beam method to astrochemical problems have just begun. Many interesting problems remain to be studied. In the coming century, laboratory experiments of the kind we have presented here combined with observations and planetary-space missions will undoubtedly unravel the complex chemical processes which extend from atoms and simple molecules to large molecules and aggregates.

ACKNOWLEDGMENTS

R.I.K. is indebted to the Deutsche Forschungsgemeinschaft (DFG) for a Habilitation fellowship (IIC1-Ka1081/3-1) and D. Gerlich (University Chemnitz, Germany) for support; N.B. thanks the Institute of Atomic and Molecular Sciences (IAMS), Taiwan, for a visiting fellowship (January–March-1999) and the Italian Space Agency (ASI) for partial support. The experimental work of the cyano radical reactions was further supported by Academia Sinica (November 1998 to July 1999). Both authors thank

Y.T. Lee (IAMS) for providing the experimental setup for these experiments, and O. Asvany and L.C.L. Huang for experimental assistance. Special thanks to Y. Osamura, P.v.R. Schleyer, H.F. Schaefer, H.F. Bettinger, and F. Stahl for performing electronic structure calculations on these reactions. We are also indebted to Prof. A.H.H. Chang (Department of Chemistry, National Dong Hua University, Hualien, ROC) for carrying out RRKM calculations.

REFERENCES

- [1] See, for instance: Tsang, W. Chemical kinetic data for propellant combustion II: reactions involving CN, NCO, and HNCO. *J. Phys. Chem. Ref. Data* **1991**, *4*, 753–791. Schulz, C.; Volpp, H.-R.; Wolfrum, J. From elementary reactions to complex combustion systems. In: *Chemical Dynamics in Extreme Environments*. R.A. Dressler, Ed. World Scientific Publishing, Singapore 2001, 206–267. Shin, D.I.; Peiter, G.; Dreier, T.; Volpp, H.-R.; Wolfrum, J. Spatially resolved measurements of CN, CH, NH and H₂CO concentration profiles in a domestic gas boiler. 28th Symp. (Int.) on Combustion, The Combustion Institute, 2000, pp. 319–325. Ebert, V.; Schulz, C.; Volpp, H.-R.; Wolfrum, J.; Monkhouse, P. Laser diagnostics of combustion processes: From chemical dynamics to technical devices. *Israel J. Chem.* **1999**, *39*, 1–24.
- [2] Yang, D.L.; Lin, M.C. The reactions of the CN radical with molecules relevant to combustion and atmospheric chemistry. In: *The Chemical Dynamics and Kinetics of Small Radicals — Advanced Series in Physical Chemistry — Vol. 6*. Liu, K.; Wagner, A., Eds. World Scientific, Singapore, 1998, 164–213.
- [3] Yang, D.L.; Yu, T.; Wang, N.S.; Lin, M.C. CN radical reactions with selected olefins in the temperature-range 174 K–740 K. *Chem. Phys.* **1992**, *160*, 317–325. Herbert, L.; Smith, I.W.M.; Spencer-Smith, R.D. Rate constants for the elementary reactions between CN radicals and CH₄, C₂H₆, C₂H₄, C₃H₆, and C₂H₂ in the range $295 \leq T \leq 700$ K. *Int. J. Chem. Kinet.* **1992**, *24*, 791–802. North, S.W.; Rei, F.; Sears, T.J.; Hall, G.E. CN radical reaction rate measurements by time-resolved FM spectroscopy. *Int. J. Chem. Kinet.* **1997**, *29*, 127–129.
- [4] Sims, I.R.; Queffelec, J.-L.; Travers, D.; Rowe, B.R.; Herbert, L.B.; Karthausier, J.; Smith, I.W.M. Rate constants for the reactions of CN with hydrocarbons at low and ultra-low temperatures. *Chem. Phys. Lett.* **1993**, *211*, 461–468.
- [5] Choi, N.; Blitz, M.A.; McKee, K.; Pilling, M.J.; Seakins, P.W. H atom branching ratios from the reaction of CN radicals with C₂H₂ and C₂H₄. *Chem. Phys. Lett.* **2004**, *384*, 68–72.
- [6] Lunine, J.I.; Lorenz, R.D.; Hartmann, W.K. Some speculations on Titan's past, present and future. *Planet. Space Sci.* **1998**, *46*, 1099–1107.
- [7] Atreya, S.K.; Pollack, J.B.; Matthews, M.S. *Origin and Evolution of Planetary and Satellite Atmospheres*. The University of Arizona Press, Tucson, 1989.
- [8] Coustenis, A.; Taylor, F. *Titan — The Earth-Like Moon*. World Scientific, Singapore, 1999.
- [9] Owen, T. The composition and origin of Titan's atmosphere. *Planet. Space Sci.* **1982**, *30*, 833–838.

- [10] Letourneur, B.; Coustenis, A. Titan's atmospheric structure from Voyager 2 infrared spectra. *Planet. Space Sci.* **1993**, *41*, 593–602. Coustenis, A.; Bézard, B. Titan's atmosphere from Voyager infrared observations: IV. Latitudinal variations of temperature and composition. *Icarus* **1995**, *115*, 126–140. Maguire, W.C.; Hanel, R.A.; Jennings, D.E.; Kunde, V.G.; Samuelson, R.E. C_3H_8 and C_3H_4 in Titan's atmosphere. *Nature* **1981**, *292*, 683–686. Kunde, V.G.; Aikin, A.C.; Hand, R.A.; Jennings, D.E.; Maguire, W.C.; Samuelson, R.E. C_4H_2 , HC_3N , and C_2N_2 in Titan's atmosphere. *Nature* **1981**, *292*, 686–688. Samuelson, R.E.; Hanel, R.A.; Kunde, V.G.; Maguire, W.C. The mean molecular weight and hydrogen abundance of Titan's atmosphere. *Nature* **1981**, *292*, 688–693. Hanel, R.; Conrath, B.; Flasar, F.M.; Kunde, V.G.; Maguire, W.C.; Pearl, J.C.; Pirraglia, J.C.; Samuelson, R.E.; Herath, L.M.; Allison, M.; Cruikshank, D.; Gautier, D.; Gierasch, P.; Horn, L.; Koppany, R.; Ponnampuruma, C. Infrared observations of the Saturnian system from Voyager 1. *Science* **1981**, *212*, 192–200. Smith, G.R.; Strobel, D.F.; Broadfoot, A.L.; Sandel, B.R.; Shemansky, D.E.; Holberg, J.B. Titan's upper atmosphere: composition and temperature from the EUV solar occultation results. *J. Geophys. Res.* **1982**, *87*, 1351–1359.
- [11] Raulin, F.; Coll, P.; Gazeau, M.C.; Sternberg, R.; Bruston, P.; Israel, G.; Gautier, D. An exobiological view of Titan and the Cassini–Huygens mission. *Adv. Space Res.* **1998**, *22*, 353–362.
- [12] Griffith, C.A.; Owen, T.; Miller, G.A.; Geballe, T. Transient clouds in Titan's lower atmosphere. *Nature* **1998**, *395*, 575–578.
- [13] Yung, Y.L.; Allen, M.; Pinto, J.P. Photochemistry of the atmosphere of Titan — comparison between model and observations. *Astrophys. J. Suppl. Ser.*, **1984**, *55*, 465–506.
- [14] Lellouch, E. Atmospheric models of Titan and Triton. *Ann. Geophys.* **1990**, *8*, 653–660.
- [15] Toubanc, D.; Parisot, J.P.; Brillet, J.; Gautier, D.; Raulin, F.; McKay, C.P. Photochemical modeling of Titan's atmosphere. *Icarus* **1995**, *113*, 2–26.
- [16] Lara, L.M.; Lellouch, E.; Lopez-Moreno, J.J.; Rodrigo, R. Vertical distribution of Titan's atmospheric neutral constituents. *J. Geophys. Res.* **1996**, *101(E10)*, 12151–12172.
- [17] Raulin, F.; Accaoui, B.; Razaghi, A.; Dang-Nhu, M.; Coustenis, A.; Gautier, D. Infrared spectra of gaseous organics: application to the atmosphere of Titan-II. Infrared intensities and frequencies of C_4 alkanenitriles and benzene. *Spectrochimica Acta* **1990**, *46A*, 671–683.
- [18] Hidayat, T.; Marten, A.; Bézard, B.; Owen, T.; Matthews, H. E.; Paubert, G. Millimeter and submillimeter heterodyne observations of Titan: retrieval of the vertical profile of HCN and the $^{12}C/^{13}C$ ratio. *Icarus* **1997**, *126*, 170–182.
- [19] Tanguy, L.; Bézard, B.; Marten, A.; Gautier, D.; Gerard, E.; Paubert, G.; Lecacheux, A. Stratospheric profile of HCN on Titan from millimeter observations. *Icarus* **1990**, *85*, 43–57.
- [20] Clarke, D.W.; Ferris, J.P. Photodissociation of cyanoacetylene: Application to the atmospheric chemistry of Titan. *Icarus* **1995**, *115*, 119–125.
- [21] Clarke, D.W.; Ferris, J.P. Titan haze: Structure and properties of cyanoacetylene and cyanoacetylene–acetylene photopolymers. *Icarus* **1997**, *127*, 158–172.

- [22] Kaiser, R.I.; Balucani, N. Astrobiology — the final frontier in chemical reaction dynamics. *Int. J. Astrobiology* **2002**, *1*, 15.
- [23] Wilson, E.H.; Areya, S.K. Current state of modelling the photochemistry of Titan's mutually dependent atmosphere and ionosphere. *J. Geophys. Res.* **2004**, *109*, Art. No. E06002. Lara, L.M.; Rodrigo, R.; Coustenis, A.; Lopez-Moreno, J.J.; Chassefiere, E. Neutral composition of Titan's atmosphere. A theoretical model of Titan's ionosphere with detailed hydrocarbon ion. *Proc. Symp. Titan* **1991**, 338, 137–146.
- [24] Fox, J.L.; Yelle, R.V. Hydrocarbon ions in the ionosphere of Titan. *Geophys. Res. Lett.* **1997**, *24*, 2179–2182. Ewan, M.J.; Scott, G.B.I.; Anicich, V.G. Ion-molecule reactions relevant to Titan's ionosphere. *Int. J. Mass Spectr. Ion Processes* **1998**, *172*, 209–219. Nagy, A.F.; Cravens, T.E. Titan's ionosphere: a review. *Planet. Space Sci.* **1998**, *46*, 1149–1155.
- [25] Brack, A. *The Molecular Origins of Life — Assembling Pieces of the Puzzle*. Cambridge University Press, Cambridge, 1998.
- [26] Coll, P.; Coscia, D.; Smith, N.; Gazeau, M.-C.; Ramirez, S.I.; Cernogora, G.; Israel, G.; Raulin, F. Experimental laboratory simulation of Titan's atmosphere: aerosols and gas phase. *Planet. Space Sci.* **1999**, *47*, 1331–1339. Coll, P.; Coscia, D.; Gazeau, M.-C.; de Vanssay, E.; Guillemin, J.C.; Raulin, F. Organic chemistry in Titan's atmosphere: New data from laboratory simulations at low temperature. *Adv. Space Res.* **1995**, *16*, 93–103.
- [27] Gazeau, M.-C.; Cottin, H.; Vuitton, V.; Smith, N.; Raulin, F. Experimental and theoretical photochemistry: application to the cometary environment and Titan's atmosphere. *Planet. Space Sci.* **2000**, *48*, 437–444.
- [28] Ohishi, M.; Kaifu, N. Chemical and physical evolution of dark clouds — Molecular spectral line survey toward TMC-1. *Faraday Discuss.* **1998**, *109*, 205–216.
- [29] Millar, T.J.; Herbst, E. A new chemical-model of the circumstellar envelope surrounding IRC+10216. *Astron. Astrophys.* **1994**, *288*, 561–571.
- [30] Doty, S.D.; Leung, C.M. Detailed chemical modeling of the circumstellar envelopes of carbon stars: Application to IRC+10216. *Astrophys. J.* **1998**, *502*, 898–908.
- [31] Cherchneff, I.; Glassgold, A.E.; Mamon, G.A. The formation of cyanopolyne molecules in IRC+10216. *Astrophys. J.* **1993**, *410*, 188–201.
- [32] Millar, T.J.; Macdonald, G.H.; Gibbs, A.G. A 330–360 GHz spectral survey of G34.3+0.15. 2. Chemical modelling. *Astron. Astrophys.* **1997**, *325*, 1163–1173.
- [33] de Forets, P.; Flower, D.R.; Herbst, E. Thermal and chemical evolution of interstellar clouds — complex molecule formation. *Mon. Not. R. Astron. Soc.* **1991**, *253*, 359–363.
- [34] Fukuzawa, K.; Osamura, Y. Molecular orbital study of neutral–neutral reactions concerning HC₃N formation in interstellar space. *Astrophys. J.* **1997**, *489*, 113–121, and references therein.
- [35] Herbst, E.; Lee, H.H.; Howe, D.A.; Millar, T.J. The effect of rapid neutral–neutral reactions on chemical-models of dense interstellar clouds. *Mon. Not. R. Astron. Soc.* **1994**, *268*, 335–344.
- [36] Suzuki, H.; Yamamoto, S.; Ohishi, M.; Kaifu, N.; Ishikawa, S.; Hirahara, Y.; Takano, S. A survey of CCS, HC₃N, HC₅N, and NH₃ toward dark cloud cores and their production chemistry. *Astrophys. J.* **1992**, *392*, 551–570.

- [37] Bettens, R.P.A.; Lee, H.H.; Herbst, E. The importance of classes of neutral-neutral reactions in the production of complex interstellar-molecules. *Astrophys. J.* **1995**, *443*, 664–674.
- [38] Turner, B.E. Detection of interstellar cyanoacetylene. *Astrophys. J.* **1971**, *163*, L35–L41. Morris, M.; Gilmore, W.; Palmer, P.; Turner, B.E.; Zuckerman, B. Detection of interstellar SiS and a study of the IRC+10216 molecular envelope. *Astrophys. J.* **1975**, *199*, L47–L51. Broten, N.W.; Oka, T.; Avery, L.W.; MacLeod, J.M.; Kroto, H.W. The detection of HC₉N in interstellar space. *Astrophys. J.* **1978**, *223*, L105–L107. Cernicharo, J.; Guelin, M.; Kahane, X. A lambda 2 mm molecular line survey of the C-star envelope IRC+10216. *Astronom. Astrophys. Suppl. Series* **2000**, *142*, 181–215.
- [39] Turner, B.E. Detection of vibrationally excited SiS in IRC+10216. *Astronom. Astrophys.* **1987**, *183*, L23–L26.
- [40] Wyrowski, F.; Schilke, P.; Walmsley, C.M. Vibrationally excited HC₃N toward hot cores. *Astronom. Astrophys.* **1999**, *341*, 882–895.
- [41] Bell, M.B.; Feldman, P.A.; Travers, M.J.; McCarthy, M.C.; Gottlieb C.A.; Thaddeus, P. Detection of HC₁₁N in the Cold Dust Cloud TMC-1. *Astrophys. J.* **1997**, *483*, L61–L64. Bell, M.B.; Watson, J.K.G.; Feldman, P.A.; Travers, M.J. The excitation temperatures of HC₉N and other long cyanopolyyne in TMC-1. *Astrophys. J.* **1998**, *508*, 286–290.
- [42] Ruffle, D.P.; Hartquist, T.W.; Taylor, S.D.; Williams, D.A. Cyanopolyyne as indicators of late-time chemistry and depletion in star-forming regions. *Mon. Not. R. Astronom. Soc.* **1997**, *294*, 235–240.
- [43] Broten, N.W.; MacLeod, J.M.; Avery, L.W.; Friberg, P.; Hjalmarsen, A.; Hoglund, B.; Irvine, W. M. The detection of interstellar methylocyanoacetylene. *Astrophys. J.* **1984**, *276*, L25–L29.
- [44] Guelin, M.; Neininger, N.; Cernicharo, J. Astronomical detection of the cyanobutadiynyl radical C₅N. *Astron. Astrophys.* **1998**, *335*, L1–L4. Guelin, M.; Mezaoui, A.; Friberg, P. Astronomical study of the C₃N and C₄H radicals — Hyperfine interactions and Rho-type doubling. *Astron. Astrophys.* **1982**, *109*, 23–31.
- [45] Nummelin, A.; Bergman, P. Vibrationally excited vinyl cyanide in Sgr B2(N). *Astron. Astrophys.* **1999**, *341*, L59–L62.
- [46] Schilke, P.; Groesbeck, T.D.; Blake, G.A.; Phillips, T.G. A line survey of Orion KL from 325 to 360 GHz. *Astrophys. J. Suppl. S.* **1997**, *108*, 301–337.
- [47] Bohme, D.K. In: *Rate Coefficients in Astrochemistry*. Millar, T.J., Williams, D.A., Eds., Dordrecht: Kluwer, 1987, 117–122. Herbst, E.; Leung, C.M. Gas-phase production of complex hydrocarbons, cyanopolyyne, and related compounds in dense interstellar clouds. *Astrophys. J. Suppl. S.* **1989**, *69*, 271–300. Howe, D.A.; Millar, T.J. The formation of carbon chain molecules in IRC+10216. *Mon. Not. R. Astronom. Soc.* **1990**, *244*, 444–449. Knight, J.S.; Freeman, C.G.; McEwan, M.J.; Smith, S.C.; Adams, N.G.; Smith, D. Production and loss of HC₃N in interstellar clouds — Some relevant laboratory measurements. *Mon. Not. R. Astronom. Soc.* **1986**, *219*, 89–94.
- [48] Kawaguchi, K.; Kasai, Y.; Ishikawa, S.; Ohishi, M.; Kaifu, N.; Amano, T. Detection of a new molecular ion HC₃NH⁺ in TMC-1. *Astrophys. J.* **1994**, *420*, L95–L97.
- [49] Herbst, E.; Millar, T.J. In: *Molecular Clouds*. James R.A., Millar, T.J., Eds., Cambridge: Cambridge University Press, 1991, 209.

- [50] Takano, S.; Masuda, A.; Hirahara, Y.; Suzuki, H.; Ohishi, M.; Ishikawa, S.; Kaifu, N.; Kasai, Y.; Kawaguchi, K.; Wilson, T.L. Observations of C-13 isotopomers of HC_3N and HC_5N in TMC-1: evidence for isotopic fractionation. *Astron. Astrophys.* **1998**, 329, 1156–1169.
- [51] Takagi, N.; Fukuzawa, K.; Osamura, Y.; Schaefer III, H.F. Ion-molecule reactions producing HC_3NH^+ in interstellar space: forbiddenness the reaction between cyclic C_3H_3^+ and the N atom. *Astrophys. J.* **1999**, 525, 791–798.
- [52] Fukuzawa, K.; Osamura, Y.; Schaefer III, H.F. Are neutral–neutral reactions effective for the carbon-chain growth of cyanopolynes and polyacetylenes in interstellar space? *Astrophys. J.* **1998**, 505, 278–285.
- [53] Smith, I.W.M.; Herbst, E.; Chang, Q. Rapid neutral–neutral reactions at low temperature: a new network and first results for TMC-1. *Mon. Not. R. Astronom. Soc.* **2004**, 350, 232–330.
- [54] Winstanley, N.; Nejad, L.A.M. Cyanopolyyne chemistry in TMC-1. *Astrophys. Space Sci.* **1996**, 240, 13–37.
- [55] Smith, I.W.M. The Liversidge Lecture 2001–02. Chemistry amongst the stars: reaction kinetics at a new frontier. *Chem. Soc. Rev.* **2002**, 31, 137–146.
- [56] Smith, I.W.M.; Rowe, B.R. Reaction kinetics at very low temperatures: Laboratory studies and interstellar chemistry. *Acc. Chem. Res.* **2000**, 33, 261–268.
- [57] Levine, R.D.; Bernstein, R.B. *Molecular Reaction Dynamics and Chemical Reactivity*. Oxford University Press, New York, 1987. Smith, I.W.M. *Kinetics and Dynamics of Elementary Gas Reactions*, Butterworths, London, 1980.
- [58] See, for instance: Dagdijan, P.J. Reactive scattering II: Optical methods. In: *Atomic and Molecular Beam Methods*. Scoles, G., Ed., Oxford University Press, New York, 1987, Vol. 1, pp. 596–630. Hefter, U.; Bergmann, K. Spectroscopic detection methods. In: *Atomic and Molecular Beam Methods*. Scoles, G., Ed., Oxford University Press, New York, 1987, Vol. 1, 193–253. Parker, D.H. In: *Ultrasensitive Laser Techniques*. Klieger, D.S., Ed., Academic Press, New York, 1983.
- [59] Lee, Y.T. Reactive scattering I: Nonoptical methods. In: *Atomic and Molecular Beam Methods*. Scoles, G., Ed., Oxford University Press, New York, 1987, Vol. 1, 553–568. Lee, Y.T. Molecular beam studies of elementary chemical processes. In: *Nobel Lectures in Chemistry 1981–1990*. Fraegsmyr, T., Malstrom, B.G., Eds., World Scientific, Singapore, 1992, 320–357.
- [60] Kaiser R.I., Balucani N. The formation of nitriles in hydrocarbon-rich atmospheres of planets and their satellites: Laboratory investigations by the crossed molecular beam technique. *Acc. Chem. Res.* **2001**, 34, 699–706.
- [61] Kaiser R.I. Experimental investigation on the formation of carbon-bearing molecules in the interstellar medium via neutral–neutral reactions. *Chem. Rev.* **2002**, 102, 1309–1358.
- [62] Casavecchia P. Chemical reaction dynamics with molecular beams. *Rep. Prog. Phys.* **2000**, 63, 355–414. Casavecchia P.; Balucani N.; Volpi G.G. Crossed-beam studies of reaction dynamics. *Annu. Rev. Phys. Chem.* **1999**, 50, 347–376. Alagia, M.; Balucani, N.; Casavecchia, P.; Stranges, D.; Volpi, G.G. Reactive scattering of atoms and radicals. *J. Chem. Soc. Faraday Trans.* **1995**, 91, 575–596.
- [63] Casavecchia, P.; Balucani, N.; Alagia, M.; Cartechini, L.; Volpi, G.G. Reactive scattering of oxygen and nitrogen atoms. *Acc. Chem. Res.* **1999**, 32, 503–510.

- [64] Liu, K. Excitation functions of elementary chemical reactions: a direct link from crossed-beam dynamics to thermal kinetics? *Int. Rev. Phys. Chem.* **2001**, 20, 189–217. Liu K. Crossed-beam studies of neutral reactions: state-specific differential cross sections. *Annu. Rev. Phys. Chem.* **2001**, 52, 139–159.
- [65] Naulin, C.; Costes, M. Crossed-beam study of the $\text{Al}(\text{}^2\text{P}_{1/2,3/2}) + \text{O}_2(\text{X}^3\Sigma^-_g) \rightarrow \text{AlO}(\text{X}^2\Sigma^+) + \text{O}(\text{}^3\text{P}_j)$ reaction at low and very low kinetic energies. *Chem. Phys. Lett.* **1999**, 310, 231–239. Geppert, W.D.; Naulin, C.; Costes, M. Integral cross-section of the $\text{C}(\text{}^3\text{P}_j) + \text{O}_2(\text{X}^3\Sigma^-_g) \rightarrow \text{CO}(\text{X}^1\Sigma^+) + \text{O}(\text{}^1\text{D}_2)$ reaction between 0.41 and 12.0 kJ/mol. *Chem. Phys. Lett.* **2002**, 364, 121–126.
- [66] Alagia, M.; Balucani, N.; Cartechini, L.; Casavecchia, P.; Volpi, G.G. Dynamics of chemical reactions of astrophysical interest. In: *Molecules in Astrophysics: Probes and Processes, IAU Symposium 178*. van Dishoek, E.F., Ed., Kluwer Academic Publishers, Dordrecht, 1996, 271–280. Alagia, M.; Balucani, N.; Casavecchia, P.; Stranges, D.; Volpi, G.G. Crossed beam studies of four-atom reactions: the dynamics of $\text{OH} + \text{CO}$. *J. Chem. Phys.* **1993**, 98, 8341–8344. Alagia, M.; Balucani, N.; Casavecchia, P.; Stranges, D.; Volpi, G.G. Crossed beam studies of four-atom reactions: the dynamics of $\text{OH} + \text{D}_2$. *J. Chem. Phys.* **1993**, 98, 2459–2462.
- [67] Kaiser, R.I.; Ochsenfeld, C.; Stranges, D.; Head-Gordon, H.; Lee, Y.T. Combined cross molecular beams and ab initio investigation of the formation of carbon-bearing molecules in the interstellar medium via neutral–neutral reactions. *Faraday Discuss.* **1998**, 109, 183–204.
- [68] Kaiser, R.I.; Ochsenfeld, C.; Head-Gordon, M.; Lee, Y.T.; Suits, A.G. A combined experimental and theoretical study on the formation of interstellar C_3H isomers. *Science* **1996**, 274, 1508–1511. Kaiser, R.I.; Ochsenfeld, C.; Head-Gordon, M.; Lee, Y.T. Neutral–neutral reactions in the interstellar medium. II. Isotope effects in the formation of linear and cyclic C_3H and C_3D radicals in interstellar environments. *Astrophys. J.* **1999**, 510, 784–788. Kaiser, R.I.; Ochsenfeld, C.; Head-Gordon, M.; Lee, Y.T. The formation of HCS and HCSH molecules and their role in the collision of comet Shoemaker–Levy 9 with Jupiter. *Science* **1998**, 279, 1181–1184. Kaiser R.I.; Stranges D.; Lee Y.T.; Suits A.G. Neutral–neutral reactions in the interstellar medium. I. Formation of carbon hydride radicals via reaction of carbon atoms with unsaturated hydrocarbons. *Astrophys. J.* **1997**, 477, 982–989.
- [69] Clary, D.C.; Buonomo, E.; Sims, I.R.; Smith, I.W.M.; Geppert, W.D.; Naulin, C.; Costes, M.; Cartechini, L.; Casavecchia, P. $\text{C} + \text{C}_2\text{H}_2$: A key reaction in interstellar chemistry. *J. Phys. Chem. A* **2002**, 106, 5541–5552. Cartechini, L.; Bergeat, A.; Capozza, G.; Casavecchia, P.; Volpi, G.G.; Geppert, W.D.; Naulin, C.; Costes, M. Dynamics of the $\text{C} + \text{C}_2\text{H}_2$ reaction from differential and integral cross-section measurements in crossed-beam experiments. *J. Chem. Phys.* **2002**, 116, 5603–5611.
- [70] Balucani, N.; Alagia, M.; Cartechini, L.; Casavecchia, P.; Volpi, G.G.; Sato, K.; Takayanagi, T.; Kurosaki, Y. Cyanomethylene formation from the reaction of excited nitrogen atoms with acetylene: a crossed beam and ab initio study. *J. Am. Chem. Soc.* **2000**, 122, 4443–4450. Balucani, N.; Cartechini, L.; Alagia, M.; Casavecchia, P.; Volpi, G.G. Observation of nitrogen-bearing organic molecules from reactions of nitrogen atoms with hydrocarbons: a crossed beam study of $\text{N}(\text{}^2\text{D}) + \text{ethylene}$. *J. Phys. Chem. A*, **2000**, 104, 5655–5659. Casavecchia, P.; Balucani, N.; Cartechini, L.; Capozza, G.;

- Bergeat, A.; Volpi, G.G. Crossed beam studies of elementary reactions of N and C atoms and CN radicals of importance in combustion. *Faraday Discuss.* **2001**, *119*, 27–49.
- [71] Kaiser, R.I.; Chiong, C.C.; Asvany, O.; Lee, Y.T.; Stahl, F.; Schleyer, P.v.R.; Schaefer, H.F. Chemical dynamics of d1-methyldiacetylene (CH_3CCCCD ; X^1A_1) and d1-ethynylallene ($\text{H}_2\text{CCCH}(\text{C}_2\text{D})$; X^1A') formation from reaction of $\text{C}_2\text{D}(X^2\Sigma^+)$ with methylacetylene, CH_3CCH (X^1A_1), *J. Chem. Phys.* **2001**, *114*, 3488–3496. Stahl, F.; Schleyer, P.v.R.; Kaiser, R.I.; Lee, Y.T.; Schaefer, H.F. Reaction of the ethynyl radical, C_2H , with methylacetylene, CH_3CCH , under single collision conditions: Implications for astrochemistry. *J. Chem. Phys.* **2001**, *114*, 3476–3487.
- [72] Vereecken, L.; Peeters, J.; Bettinger, H.F.; Kaiser, R.I.; Schleyer, P.v.; Schaefer, H.F. Reaction of phenyl radicals with propyne. *J. Am. Chem. Soc.* **2002**, *124*, 2781–2789. Kaiser, R.I.; Vereecken, L.; Peeters, J.; Bettinger, H.F.; Schleyer, P.v.; Schaefer, H.F. Elementary reactions of the phenyl radical, C_6H_5 , with C_3H_4 isomers, and of benzene, C_6H_6 , with atomic carbon in extraterrestrial environments. *Astron. Astrophys.* **2003**, *406*, 385–391.
- [73] Kaiser, R.I.; Balucani, N.; Charkin, D.O.; Mebel, A.M. A crossed beam and ab initio study of the $\text{C}_2(X^1\Sigma^+_g, a^3\Pi_u) + \text{C}_2\text{H}_2(X^1\Sigma^+_g)$ reactions. *Chem. Phys. Lett.* **2003**, *382*, 112–119. Balucani, N.; Mebel, A.M.; Lee, Y.T.; Kaiser, R.I. A combined crossed molecular beam and ab initio study of the reactions $\text{C}_2(X^1\Sigma^+_g, a^3\Pi_u) + \text{C}_2\text{H}_4 \rightarrow \text{n-C}_4\text{H}_3(X^2A') + \text{H}(^2S_{1/2})$. *J. Phys. Chem. A* **2001**, *105*, 9813–9818.
- [74] Kaiser, R.I.; Le, T.N.; Nguyen, T.L.; Mebel, A.; Balucani, N.; Lee, Y.T.; Stahl, F.; Schleyer, P.v.R.; Schaefer III, H.F. A combined crossed molecular beam and ab initio investigation of C_2 and C_3 elementary reactions with unsaturated hydrocarbons — pathways to hydrogen deficient radicals in combustion flames. *Faraday Discuss.* **2001**, *119*, 51–66.
- [75] Huang, L.C.L.; Lee, Y.T.; Kaiser, R.I. Crossed beam reaction of the cyanogen radical, $\text{CN}(X^2\Sigma^+)$, with acetylene, $\text{C}_2\text{H}_2(X^1\Sigma^+_g)$: observation of cyanoacetylene, $\text{HCCCN}(X^1\Sigma^+)$. *J. Chem. Phys.* **1999**, *110*, 7119–7122.
- [76] Huang L.C.L.; Balucani, N.; Lee, Y.T.; Kaiser, R.I.; Osamura, Y. Crossed beam reaction of the cyano radical, $\text{CN}(X^2\Sigma^+)$, with methylacetylene: Observation of cyanopropyne and cyanoallene. *J. Chem. Phys.* **1999**, *111*, 2857–2860.
- [77] Balucani, N.; Asvany, O.; Chang, A.H.H.; Lin, S.H.; Lee, Y.T.; Kaiser, R.I.; Bettinger, H.F.; Schleyer, P.v.R.; Schaefer III, H.F. Crossed beam reaction of cyano radicals with hydrocarbon molecules I: chemical dynamics of cyano-benzene ($\text{C}_6\text{H}_5\text{CN}$; X^1A_1) and perdeutero cyanobenzene ($\text{C}_6\text{D}_5\text{CN}$; X^1A_1) formation from reaction of $\text{CN}(X^2S^+)$ with benzene, C_6H_6 (X^1A_{1g}) and d_6 -benzene, C_6D_6 (X^1A_{1g}). *J. Chem. Phys.* **1999**, *111*, 7457–7471.
- [78] Balucani, N.; Asvany, O.; Chang, A.H.H.; Lin, S.H.; Lee, Y.T.; Kaiser, R.I.; Bettinger, H.F.; Schleyer, P.v.R.; Schaefer III, H.F. Crossed beam reaction of cyano radicals with hydrocarbon molecules II: chemical dynamics of 1,1-cyanomethylallene ($\text{CNCH}_3\text{CCCCH}_2$; X^1A_1) formation from reaction of $\text{CN}(X^2S^+)$ with dimethylacetylene, CH_3CCCH_3 (X^1A_{1g}). *J. Chem. Phys.* **1999**, *111*, 7472–7479.
- [79] Balucani, N.; Asvany, O.; Huang, L.C.L.; Lee, Y.T.; Kaiser, R.I.; Osamura, Y. Laboratory investigation on the formation of unsaturated nitriles in Titan's atmosphere. *Planet. Space Science* **2000**, *48*, 447–462.

- [80] Kaiser, R.I.; Balucani, N.; Asvany, O.; Lee, Y.T. Crossed molecular beam experiments of radical-neutral reactions relevant to the formation of hydrogen deficient molecules in extraterrestrial environments. In: *Astrochemistry: from Molecular Clouds to Planetary Systems*. Mihn, Y.C., van Dishoek, E.F., Eds., Astronomical Society of the Pacific - IAU Series, Volume 197, 2000, 251–264.
- [81] Balucani, N.; Asvany, O.; Chang, A.H.H.; Lin, S.H.; Lee, Y.T.; Kaiser, R.I.; Osamura, Y. Crossed beam reaction of cyano radical with hydrocarbon molecules III: chemical dynamics of vinylcyanide (C_2H_3CN ; X^1A') formation from reaction of $CN(X^2S^+)$ with ethylene, C_2H_4 (X^1A_g) *J. Chem. Phys.* **2000**, *113*, 8643–8655.
- [82] Huang, L.C.L.; Chang, A.H.H.; Asvany, O.; Balucani, N.; Lin, S.H.; Lee, Y.T.; Kaiser, R.I.; Osamura, Y. Crossed beam reaction of cyano radicals with hydrocarbon molecules IV: Chemical dynamics of cyanoacetylene formation from reaction of $CN(X^2\Sigma^+)$ with acetylene. *J. Chem. Phys.* **2000**, *113*, 8656–8666.
- [83] Balucani, N.; Asvany, O.; Huang, L.C.L.; Lee, Y.T.; Kaiser, R.I.; Osamura, Y.; Bettinger, H.F. Neutral–neutral reactions in the interstellar medium III: formation of nitriles via reaction of cyano radicals, $CN(X^2S^+)$, with unsaturated hydrocarbons. *Astrophys. J.* **2000**, *545*, 892–906.
- [84] Balucani, N.; Asvany, O.; Kaiser, R.I.; Osamura Y. Crossed beam reaction of cyano radicals with hydrocarbon molecules V: formation of three C_4H_3N isomers from reaction of $CN(X^2S^+)$ with allene, H_2CCCH_2 (X^1A_1), and methylacetylene, CH_3CCH (X^1A_1). *J. Phys. Chem. A*, **2002**, *106*, 4301–4311.
- [85] Kaiser, R.I.; Ting, J.; Huang, L.C.L.; Balucani, N.; Asvany, O.; Lee, Y.T.; Chan, O.; Stranges, D.; Gee, D. A versatile source to produce high intensity, pulsed supersonic radical beams for crossed beam experiments — the cyano radical $CN(X^2S^+)$, as a case study. *Rev. Sci. Instrum.* **1999**, *70*, 4185–4184.
- [86] Baulch, D.L.; Cobos, C.J.; Cox, R.A.; Frank, P.; Hayman, G.; Just, Th.; Kerr, J.A.; Murrells, T.; Pilling, M.J.; Troe, J.; Walker, R.W.; Warnatz, J. Evaluated kinetic data for combustion modeling. Supplement I. *J. Phys. Chem. Ref. Data* **1994**, *23*, 847–1033.
- [87] Shaik, S.S.; Canadell, E. Regioselectivity of radical attacks on substituted olefins — application of the SCD model. *J. Am. Chem. Soc.* **1990**, *112*, 1446–1452.

15 Synthesis of Monocyanopolyynes and Dicyanopolyynes with the Submerged Electric Arc

Franco Cataldo

CONTENTS

15.1	Introduction	324
15.2	Experimental	324
15.2.1	Synthesis of Monocyanopolyynes by the Submerged Electric Carbon Arc in Acetonitrile	325
15.2.2	Synthesis of Dicyanopolyynes by the Submerged Electric Carbon Arc in Liquid Nitrogen	325
15.2.3	Electric Arc Between Graphite Electrodes Submerged in <i>n</i> -Octane	326
15.2.4	The Electric Arc Between Graphite Electrodes Submerged in Water	326
15.3	Results and Discussion	326
15.3.1	Monocyanopolyynes Produced in Acetonitrile	326
15.3.2	Formation of Polyynes from Electric Arc in Liquid Nitrogen Between Graphite Electrodes	330
15.3.3	Polyynes from the Electric Arc from Graphite Electrodes in Water	336
15.4	Conclusions	336
	Acknowledgments	337
	References	337

15.1 INTRODUCTION

The bulk synthesis of cyanopolyyne (called also cyano- and dicyanoacetylenes) is quite a complicated task. Hopf and Witulski have reviewed the organic synthesis of these molecules proposing the best synthetic route [1]. However, monocyanopolyyne and dicyanopolyyne can be easily produced in very small quantities by laser ablation of graphite targets in a He carrier gas in the presence of certain reactants [2,3]. For instance, when acetonitrile was added to the system, monocyanopolyyne was detected, but when N_2 was used as reagent dicyanopolyyne was formed [2,3]. With an excess of H_2 instead the exclusive products were hydrogen-terminated polyyne [2,3]. The synthesis of polyyne with laser ablation is an approach sufficient to feed a mass spectrometer to identify the products but is not useful for bulk synthesis. Cyanopolyyne was obtained in larger quantities when cyanogen gas at low pressure was admitted to the chamber confining the carbon arc working under the Kratschmer–Huffman conditions [4,5]. In the present chapter the production of monocyanopolyyne and dicyanopolyyne produced with the submerged electric arc technique is reported. Thus, data will be presented concerning the formation of polyyne $R-(C\equiv C)_n-R'$ with $R = H$ and $R' = CN$ (monocyanopolyyne) and with $R = R' = CN$ (dicyanopolyyne) in the electric arc under special conditions.

As reported in [Chapter 8](#), the importance of the cyanopolyyne resides in their easy formation in cold molecular clouds [6,7], their presence in the interstellar medium and around carbon-rich stars [8] as well as in the atmosphere chemistry of certain bodies of the Solar System [9]. They are objects of intense research efforts [10–15]. Furthermore, unsaturated polyyne is of paramount importance in the theories of the origin of life. For instance, one of the key components of nucleic acids, the pyrimidines, are thought to have been synthesized under prebiotic conditions from cyanoacetylene [16]. Surprisingly, cyanopolyyne is also produced by microorganisms in the earth. The molecule known under the trivial name diatreyne II, which is 7-cyano-2-heptene-4,6-diynoic acid, is an antibiotic substance produced by the basidiomycete *Tricholoma nudum* and by the fungus *Clitocybe diatreta* [17]. It has antibiotic properties but is unstable under the action of light.

15.2 EXPERIMENTAL

The same experimental setup detailed in Chapter 8 was adopted in the present study. Graphite rods 6 mm diam. and 150 mm length (99.999% purity) used as electrodes were obtained from Aldrich. All solvents used were analytical or HPLC grades from Fluka. Liquid nitrogen was supplied by SIAD gas tecnici (Italy). The electric arc was conducted using d.c. current set at 10 A. The electronic absorption spectra were recorded on a Shimadzu UV160A spectrophotometer on filtered solutions.

15.2.1 SYNTHESIS OF MONOCYANOPOLYYNES BY THE SUBMERGED ELECTRIC CARBON ARC IN ACETONITRILE

Two graphite electrodes were connected at the poles of the d.c. power supply and submerged in a Pyrex three-necked round-bottomed flask filled with 50 ml of acetonitrile. The two electrodes were arranged in a “V” geometry as shown in Chapter 8. The flask was immersed in a cooling bath. In normal conditions (“room temperature”) the cooling bath was made with tap water. In the experiment where acetonitrile was arced at -40°C , the flask was suspended (not immersed) into a large Dewar flask half-filled with acetone/dry ice mixture.

To ignite the arc the two electrodes were put in touch with each other under the solvent and then moved continuously up and down to produce an arc emitting bright white light. The best condition to ensure polyynes formation is to have the brightest light in the arc.

The solution containing the crude mixture of polyynes in acetonitrile was filtered with a syringe fitted with a PVDF Acrodisc[®] membrane having pore size of $0.45\text{ }\mu\text{m}$ to remove carbon particles suspended in the solvent. From 5 to $10\text{ }\mu\text{l}$ per run of the filtered solution were injected into a $4.6 \times 150\text{ mm}$ column (Zorbax Eclipse XDB-C8) of an HPLC from Agilent Technologies model 1100. A mobile phase of $\text{CH}_3\text{CN}/\text{H}_2\text{O}$ 80/20 (v/v) was used under isocratic conditions at a flow rate of 1.5 ml/min and 151 bar. The polyynes eluted from the column were identified by a diode-array detector through their typical spectra. The diode-array detector was set at 225, 250, 274, 295, and 350 nm. All the analyses were made by keeping the HPLC column at room temperature.

15.2.2 SYNTHESIS OF DICYANOPOLYYNES BY THE SUBMERGED ELECTRIC CARBON ARC IN LIQUID NITROGEN

A three-necked round bottomed Duran flask of 100 ml equipped with two graphite electrodes arranged in a “V” geometry was filled with liquid nitrogen and immersed in liquid nitrogen contained in a Dewar flask. The third neck of the flask was fitted with a valve connected with a Drechsel tube (a gas washing bottle) of 250 ml filled with 100 ml of *n*-octane.

The electric arc was ignited and sustained at 10 A (d.c.) by putting in contact and by moving slightly up and down the two graphite electrodes submerged in liquid nitrogen into the three-necked flask. The bright light of the arc was easily observed. The heat generated by the arc caused partial vaporization of the liquid nitrogen which was forced to bubble into the gas washing bottle attached to the reaction flask. The products formed in the electric arc were hence forced to pass into the octane solvent outside the reactor and hence were trapped in the solvent. Periodically, samples of the *n*-octane solution were collected and analyzed by electronic absorption spectroscopy and by HPLC–DAD analysis by injecting up to $20\text{ }\mu\text{l}$ of the

octane solution into the HPLC column, employing the usual mobile phase acetonitrile/water 80/20. The following polyyynes were identified based on the retention time and the electronic spectra: C_6N_2 , C_8H_2 , C_8N_2 , $C_{10}H_2$, $C_{10}N_2$. Similar results were obtained by filling the Drechsel tube of the trap with ethanol or with acetonitrile and by suspending (but not immersing) the tube into a Dewar pot containing a small quantity of liquid nitrogen in the bottom.

15.2.3 ELECTRIC ARC BETWEEN GRAPHITE ELECTRODES SUBMERGED IN *n*-OCTANE

To create a “blank” or a reference to the products formed by the carbon arc in liquid nitrogen, we have arced also graphite electrodes directly into *n*-octane at 10 A under the same conditions described previously ([Chapter 8](#)) for *n*-hexane. Indeed the products were practically the same as detected and reported in Chapter 8 for *n*-hexane. As usual, the polyyne C_8H_2 was the most abundant component in the polyyynes mixture consisting exclusively in hydrogen-terminated polyyynes.

15.2.4 THE ELECTRIC ARC BETWEEN GRAPHITE ELECTRODES SUBMERGED IN WATER

The arc was conducted between graphite electrodes submerged in distilled water at 10 A. The electronic absorption spectrum of the crude aqueous solution of polyyynes and other products showed the following absorption bands: 200, 215, and 226 nm as the most intense. Other weaker bands were observed at 238, 246, 250, 259, 274, 284, 300, and 323 nm.

The HPLC–DAD analysis revealed the presence of the following polyyynes: C_4H_2 , C_6H_2 , C_8H_2 , and $C_{10}H_2$. Polyyne C_8H_2 was by far the most abundant product.

15.3 RESULTS AND DISCUSSION

15.3.1 MONOCYANOPOLYYNES PRODUCED IN ACETONITRILE

Arcing graphite electrodes in any hydrocarbon solvent or in any alcohol invariably produces a mixture of polyyynes, with the molecular species C_8H_2 as the dominant component in all cases. These results have been presented and discussed in Chapter 8.

When acetonitrile is used as solvent for the arcing experiment, then a very peculiar liquid chromatogram is obtained as shown in [Figure 15.1](#). The chromatogram appears unusually richer in molecular species if compared with that obtainable in hydrocarbons and in alcohols.

The chromatogram at the top of Figure 15.1 is normalized and provides evidence that, between each two consecutive intense peaks, it is possible to

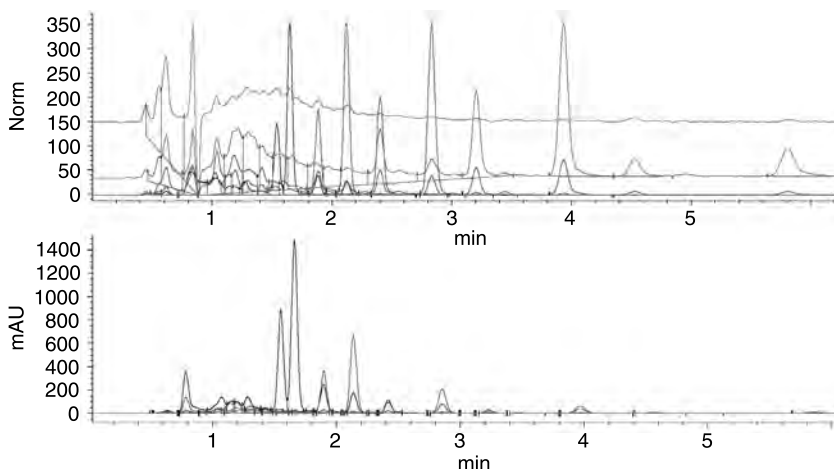


FIGURE 15.1 HPLC chromatogram of the polyynes and monocyanopolynes produced by the carbon arc in acetonitrile at -40°C . The chromatogram at the top of the figure has been normalized in order to show all the relevant peaks associated to the molecular species present in the mixture. The most intense peaks are hydrogen-capped polyynes the others are monocyanopolynes other than the peak with $R_t = 5.86$ min. The peak due to $\text{H}-(\text{C}\equiv\text{C})_9-\text{H}$ is not shown in the figure since it appears at $R_t = 9.67$ min and is weak. The chromatogram at the bottom of the figure shows the relative intensity and hence the relative abundance of the various molecular species. The most abundant species is $\text{H}-(\text{C}\equiv\text{C})_4-\text{H}$ with retention time $R_t = 1.65$ min, followed by $\text{H}-(\text{C}\equiv\text{C})_3-\text{CN}$ followed by $\text{H}-(\text{C}\equiv\text{C})_5-\text{H}$ and then by $\text{H}-(\text{C}\equiv\text{C})_4-\text{CN}$ and $\text{H}-(\text{C}\equiv\text{C})_6-\text{H}$ (see also Table 15.1).

observe a series of less intense peaks having approximately one third the intensity of the strong peaks. The analysis of the band pattern of the electronic absorption spectra of each individual strong peak of the chromatogram reveals that we are dealing with a series of hydrogen-capped polyynes $\text{R} = \text{R}' = \text{H}$ having the general formula $\text{H}-(\text{C}\equiv\text{C})_n-\text{H}$ already detected and discussed in Chapter 8 of this book. The assignment is also confirmed by comparing the retention times as discussed in previous studies [18,19].

Instead, the other series of molecules eluted between the polyynes series show another set of homologous spectra systematically red-shifted (see Figure 15.2) and with a different band pattern in comparison to the normal hydrogen-capped polyynes as clearly illustrated in Table 15.1. Based on the regular red shift of the most intense absorption band observed in these polyynes series, based on the fact that this series was observed exclusively in acetonitrile solvent and based on the intermediate retention time in the HPLC column between two “ordinary” hydrogen-capped polyynes, we reached the conclusion [18] that we were dealing with a series of

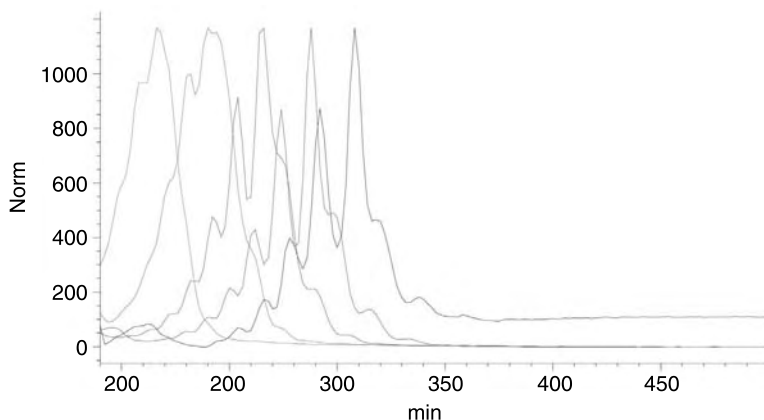


FIGURE 15.2 Overlapped electronic absorption spectra of monocyanopolyyne $\text{H}-(\text{C}\equiv\text{C})_n\text{-CN}$ produced by arcing graphite electrodes in an acetonitrile solution at -40°C (see Table 15.1). The spectra of monocyanopolyyne with 7, 9, 11, 13, 15 carbon atoms are shown in the respective order.

monocyanopolyyne with $\text{R} = \text{H}$ and $\text{R}' = \text{CN}$, hence with molecules having the general formula $\text{H}-(\text{C}\equiv\text{C})_n\text{-C}\equiv\text{N}$.

This conclusion is in perfect agreement with the work by Kroto and colleagues who have detected the formation of monocyanopolyyne when they added acetonitrile to their carbon cluster generator employing the laser ablation technique [2,3].

The chromatogram at the bottom of the Figure 15.1 shows the relative intensity and hence the relative abundance of the various molecular species. The most abundant species detected is, as usual, $\text{H}-(\text{C}\equiv\text{C})_4\text{-H}$ with retention time $R_t = 1.65$ min, followed by $\text{H}-(\text{C}\equiv\text{C})_3\text{-CN}$, which is followed by $\text{H}-(\text{C}\equiv\text{C})_5\text{-H}$ and then by $\text{H}-(\text{C}\equiv\text{C})_4\text{-CN}$ and $\text{H}-(\text{C}\equiv\text{C})_6\text{-H}$ (see also Table 15.1).

It is worth reporting here that arcing at -40°C led us to also detect the hydrogen-capped polyyne having 18 carbon atoms, the longest polyyne chain we have detected so far [18,19]: $\text{H}-(\text{C}\equiv\text{C})_9\text{-H}$.

The polyyne C_{18}H_2 was not detected in the acetonitrile solution arced at room temperature and was not found also in the methanol or hexane solutions arced at room and at low temperature. In these other cases the longest polyyne chain had only 16 carbon atoms.

The filtered polyyne and monocyanopolyyne solution prepared in acetonitrile at -40°C is not stable if stored at room temperature for 5 days in a closed flask. In fact, on standing, the solution becomes deep yellow. HPLC analysis of the aged solution produces the chromatogram shown in Figure 15.3 where it is possible to observe that the ordinary hydrogen-terminated polyyne survived unchanged while the monocyanopolyyne

TABLE 15.1
HPLC Analysis of the Polyynes Formed from Graphite Arcing in Acetonitrile at -40°C

Number of Carbon Atoms		Retention Time (min)	Wavelengths (nm)														
4	Found, this work	1.034	180	215		234	242	275		290							
4	Literature					224	234	246									
6	Found, this work	1.421	198	208		228	235	247	260	275	290	295					
6	Literature			207				242	255	268	284	300					
7	Monocyanopolyynes	1.541	200	208	218	225											
8	Found, this work	1.647		200	218	227											
8	Literature				215	226											
9	Monocyanopolyynes	1.887			214	222	232	240	263	275							
10	Found, this work	2.127			218	227	239	251									
10	Literature					227	239	251									
11	Monocyanopolyynes	2.407				223	233	243	255	268	277	290	308				
12	Found, this work	2.834					237		248	260	273						
12	Literature et al. [23]					225	236		247	260	275						
13	Monocyanopolyynes	3.234					230	245	250	261	275	288	300	315	334		
14	Found, this work	3.954					237		253	268		280	297				
14	Literature et al. [23]						237		253	266		281	297				
15	Monocyanopolyynes	4.554							254	268	277		290	308	320	338	368
16	Found, this work	5.861							255	268		281	298	318			
16	Literature et al. [23]								255	268		281	298	318			
18	Found, this work	9.674								268		282	296	316		333	
18	Literature et al. [23]									267		287	296	313		332	

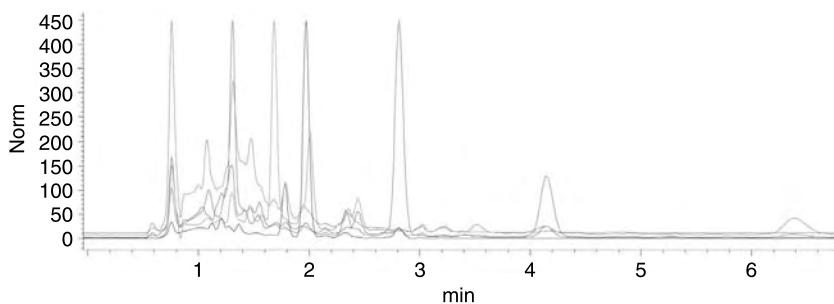


FIGURE 15.3 HPLC chromatogram of the polyynes and monocyanopolyynes solution prepared by arcing graphite at -40°C , after 5 days storage at room temperature. The monocyanopolyynes disappeared completely while the hydrogen-capped polyynes are still there.

disappeared completely. In their place it is possible to record unusual spectra of unknown molecules. Some of these spectra are shown in [Figure 15.4](#). These spectra are characterized by absorption bands at $\lambda \geq 350\text{ nm}$ which account for the yellow color of the solution. The long-term stability of the hydrogen-terminated polyynes in diluted solutions is well known as we have already reported this property [20–22]. The rather high instability of monocyanopolyynes in the same solution is quite unexpected. At present we do not know what kind of rearrangement takes place on these molecules. In any case, the knowledge that the hydrogen-terminated polyynes are much more stable than the monocyanopolyynes may have astrochemical implications. In fact, the latter are easily detected by radioastronomy because they possess a dipole moment but the ordinary polyynes are not detectable because they do not have a permanent dipole moment [11,12]. It is reasonable to propose that the ordinary polyynes may be as abundant, or even more abundant, than the monocyanopolyynes because of their higher stability and thanks to the great abundance of hydrogen in the interstellar medium.

15.3.2 FORMATION OF POLYINES FROM ELECTRIC ARC IN LIQUID NITROGEN BETWEEN GRAPHITE ELECTRODES

When the graphite electrodes are arced in liquid nitrogen the polyynes formed in the arc are quenched into the very cold reservoir of the liquid nitrogen surrounding the plasma ball. During arcing, part of the liquid nitrogen vaporizes to dissipate the heat generated by the electric arc. When liquid nitrogen vaporizes, a continuous stream of gaseous nitrogen drags the polyynes outside the reactor (see [experimental](#) section) into the gas washing bottle connected to the reactor and filled with a solvent (*n*-octane). When nitrogen bubbles into the bottle, it releases the polyynes into the *n*-octane

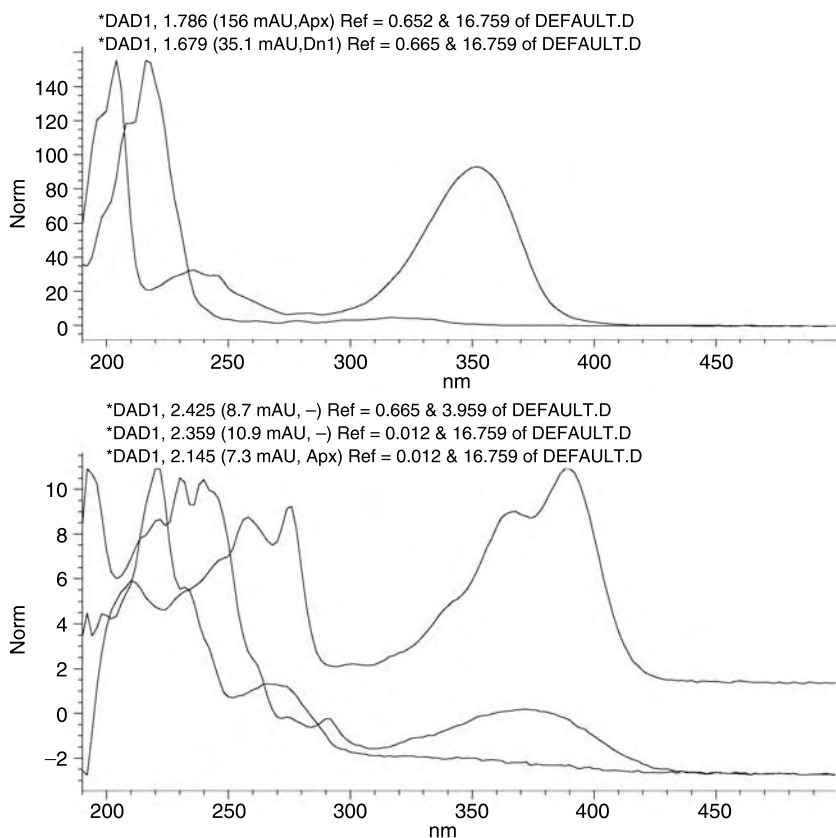


FIGURE 15.4 Electronic absorption spectra of unknown products derived from the decomposition or rearrangement of monocyanopolynes.

solvent, which acts as a trap. In fact, in [Figure 15.5](#) it is possible to see the typical polyynes spectrum from the octane solution used as a trap of these molecules.

Figure 15.5(B) shows the initial spectrum of the polyynes mixtures produced from the graphite arc in liquid nitrogen at the beginning of the experiment. In these conditions, the initial polyne concentration was estimated from their optical density in the spectrum to be around 10^{-7} M in the *n*-octane trap. Furthermore, the spectrum in Figure 15.5(B) of the polyynes produced from the arc in liquid nitrogen shows a different band pattern than the mixture of polyynes produced by arcing graphite electrodes directly into *n*-octane (compare Figure 15.5(B) with Figure 15.5(A)). In particular, in Figure 15.5(B) we can observe two main bands at 261 and 283 nm while the most intense bands in Figure 15.5(A) are located at 226, 239, and 251 nm.

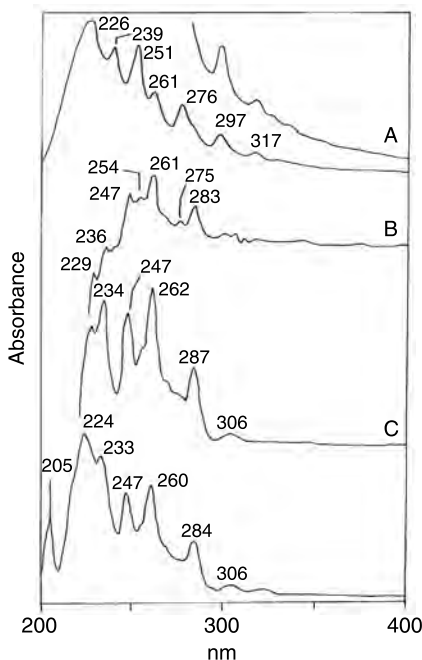


FIGURE 15.5 Electronic absorption spectra of polyynes mixture. 5A — Polyynes obtained by arcing graphite directly into *n*-octane (the top curve of 5A is an expansion of the spectrum above 280 nm to show finer details). 5B — Initial spectrum of the polyynes mixtures produced from the graphite arc in liquid nitrogen and trapped in *n*-octane at the beginning of the experiment. 5C — Same as 5B but after prolonged arcing in liquid nitrogen. 5D — Same as 5C at the end of the experiment; a final total concentration of polyynes estimated at about 8×10^{-6} M was achieved.

Since the end groups of polyyne chains are affected by the nature of the solvent where the graphite arc is struck, and since we know that usually the polyynes are hydrogen terminated when the arc is made in hydrocarbon solvents like *n*-hexane or *n*-octane while they are also cyano terminated when the arc is made in acetonitrile, these spectral differences can be taken as a first hint that the polyynes formed in liquid nitrogen are nitrogen and hence cyano terminated.

From Section 15.3.1, we know the electronic absorption spectra of a series of monocyanopolyyynes and from literature [4] we know the spectrum of the dicyanopolyyne C_8N_2 whose maximum wavelength absorption band lies just at 261 nm. In principle, it is quite obvious to expect to produce nitrogen-terminated polyynes by arcing graphite in liquid nitrogen since the high temperatures of the electric arc may cause the plasmalysis of molecular nitrogen into atomic nitrogen which, in turn, can easily form cyano

groups with carbon vapor and hence can terminate the polyyne chains into dicyanopolyynes: $\text{N}\equiv\text{C}-(\text{C}\equiv\text{C})_n-\text{C}\equiv\text{N}$. It is fascinating to think that similar synthetic processes leading to these or similar molecules are known to occur in the outflow of certain carbon-rich giant stars in the space [6,7].

By continuing arcing in liquid nitrogen with graphite electrodes, it is possible to accumulate the reaction products into the octane trap. This is illustrated in Figure 15.5(C) where the bands become more intense and better defined as function of the arcing time. In particular, in Figure 15.5(C) the concentration of the polyynes can be estimated at about 2.5×10^{-6} M. Arcing was stopped when all liquid nitrogen in the reaction flask was consumed, *i.e.* disappeared by vaporization. The final spectrum of the products collected in is shown in Figure 15.5(D) with a final total concentration of polyynes estimated at about 8×10^{-6} M.

The crude *n*-octane solution, after filtration, was chromatographed in the HPLC apparatus (see Section 15.2). The complex polyyne mixture formed by arcing graphite directly into liquid nitrogen was resolved into six main components whose electronic absorption spectra are shown all together in Figure 15.6. The three main components are easily and definitively identified from their electronic absorption spectra and are respectively C_6N_2 , C_8N_2 , and C_{10}N_2 (see below for further details). The former are

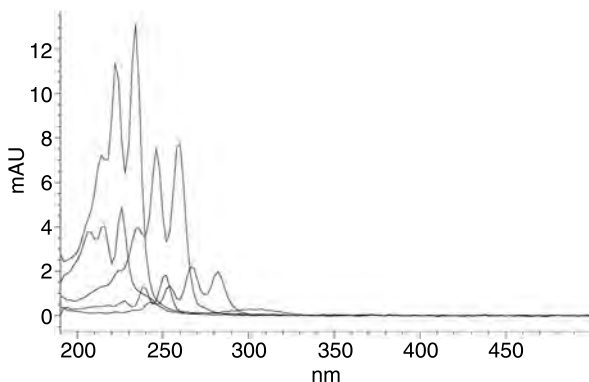


FIGURE 15.6 Electronic absorption spectra of the polyyne formed from graphite arcing in liquid nitrogen. The liquid chromatographic analysis (HPLC) was able to separate the mixture into its components. The electronic spectrum of each component eluted was recorded by the diode-array detector (DAD). The three main components are easily and definitively identified from their electronic absorption spectra and are respectively C_6N_2 , C_8N_2 , and C_{10}N_2 . The spectra of these three dicyanopolyyne in the figure are easily identifiable from the longest wavelength absorption band lying at 233, 260 and 283 nm respectively. There are also other two minor components in the figure: the hydrogen-terminated polyyne C_8H_2 , C_{10}H_2 . Furthermore, also C_{12}H_2 has been identified although at very low concentration (not shown in the figure).

the most abundant followed by the other two in respective lower concentration. Other minor components detected were hydrogen-terminated polyynes C_8H_2 , $C_{10}H_2$, and $C_{12}H_2$ in decreasing concentration and in general at much lower concentration than the corresponding dicyano-polyynes ($C_{12}H_2$ is not shown in Figure 15.6).

The individual spectra of the molecular species separated by the liquid chromatographic analysis are shown in Figure 15.7 following their retention time (R_t) from bottom to top of Figure 15.7. The first molecular species eluted with a $R_t = 1.55$ min was identified as C_6N_2 from its absorption spectrum ($\lambda_m = 235, 222, 213$, and 205 nm) in comparison to the well known [4] spectrum of C_8H_2 which eluted immediately after that species with a $R_t = 1.64$ min ($\lambda_m = 227, 218$, and 208 nm). It can be observed that both C_6N_2 and C_8H_2 have similar molecular weight (about 100 Da versus 98 Da, respectively), but from our previous study on polyynes and cyanopolyynes [18,19] we know that at more or less equal molecular weight the nitrogen-capped polyynes have shorter retention time than the hydrogen-capped polyynes on our HPLC column. Thus, the assignment appears correct. The next compound eluted with a $R_t = 1.87$ min is C_8N_2 which has been recognized from the band pattern of its spectrum which matches that reported in literature for this compound [4] (λ_m (found) = 260, 247, 233, 223 and 214 nm; λ_m (lit. [4]) = 261, 248, 236, 225, and 215 nm). After C_8N_2 with a

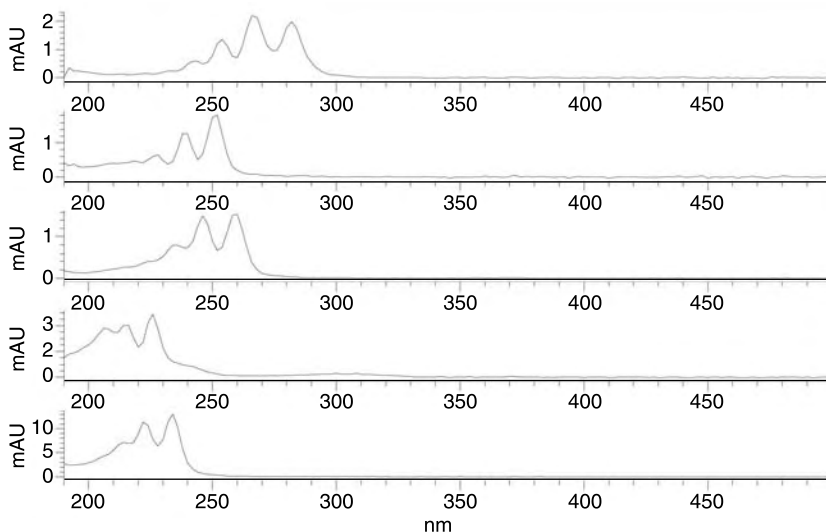


FIGURE 15.7 Individual spectra of each molecular species separated by the liquid chromatographic analysis. From bottom to top of Figure 15.4 it is possible to distinguish the spectrum of C_6N_2 with $R_t = 1.55$, then C_8H_2 with $R_t = 1.64$ followed by C_8N_2 ($R_t = 1.87$), $C_{10}H_2$ ($R_t = 2.11$) and $C_{10}N_2$ ($R_t = 2.39$).

molecular weight of about 124 Da, the hydrogen-capped polyyn C_{10}H_2 elutes. This has a molecular weight of 122 Da and a $R_t = 2.11$ min. Its spectrum completely matches the known [18,19] band pattern of this compound ($\lambda_m = \mathbf{251}$, 239, 227, and 218 nm). Finally, the detection of C_{10}N_2 occurs at a $R_t = 2.39$ min and the spectrum is characterized by $\lambda_m = 303$, **283**, **268**, 253, 243, and 232 nm. In all the spectral wavelengths reported, the most intense band is written in bold. It is also important to underline that in the assignments reported here we have also been guided by the typical retention times we have measured in earlier work for hydrogen-capped polyynes of monocyanopolynes as follows:

$R_t = 1.55$ for C_6N_2 in comparison to $R_t = 1.547$ for HC_7N [18,19].

$R_t = 1.64$ for C_8H_2 as already found [18,19].

$R_t = 1.87$ for C_8N_2 in comparison to $R_t = 1.89$ for HC_9N [18,19].

$R_t = 2.11$ for C_{10}H_2 as already found [18,19].

$R_t = 2.39$ for C_{10}N_2 in comparison to $R_t = 2.41$ for HC_{11}N [18,19].

The formation of polyynes in the electric arc in liquid nitrogen represents a clear indication that the elemental carbon for the polyynes chains is supplied essentially from the graphite electrodes and not from the solvent. This result is quite expected since we know that the electric arc in vacuum conditions between graphite electrodes produces polyynes ions. Furthermore, Grosser and Hirsch [4] have shown that the electric arc between graphite electrodes under Kratschmer–Huffman conditions in a reduced pressure of cyanogen (C_2N_2) produces a mixture of dicyanopolynes whose main components are C_8N_2 and C_{10}N_2 (respectively, 55% and 35%). Also, C_{12}N_2 , C_{14}N_2 and C_{16}N_2 were detected [4,5].

In the products of the electric arc in liquid nitrogen (Figure 15.6), we can estimate from the chromatographic analysis that C_6N_2 represents approximately 50% (by mol.) of the mixture, followed by C_8N_2 with about 25%, and by C_{10}N_2 with about 5%. The remaining products are essentially C_8H_2 , C_{10}H_2 , and C_{12}H_2 .

The hydrogen-terminated polyynes formed in minor quantities in our synthesis derive their hydrogen end-groups from the plasmalysis of the humidity present in the reactor and in the liquid nitrogen. Therefore, they must be regarded merely as secondary products. In the next section, we demonstrate experimentally that the hydrogen-terminated polyynes are formed from the plasmalysis of water. In fact, in our electric arc in liquid nitrogen we have excluded the presence of any organic solvent but not the presence of humidity. Therefore, the arc between graphite electrodes in liquid nitrogen necessarily also involves the plasmalysis of small amounts of water which supplies the hydrogen necessary for end capping the polyyn chains.

In Section 15.3.1 it has been reported that the monocyanopolynes are considerably less stable than “ordinary” polyynes. In fact, the former

disappear from solution after some days storage at room temperature while the latter remain unchanged. The same study was conducted on an acetonitrile solution of dicyanopolyyne and hydrogen-terminated polyyne prepared by arcing graphite electrodes in liquid nitrogen and trapping the products in a CH_3CN solution. HPLC–DAD analysis after only 1 day storage of the solution at room temperature showed the complete disappearance of all the dicyanopolyyne while the hydrogen-terminated polyyne were still present at the same concentration as on the previous day. New spectra of unknown products were detected. It appears that the dicyanopolyyne, as the monocyanopolyyne, rearrange into other products.

15.3.3 POLYINES FROM THE ELECTRIC ARC FROM GRAPHITE ELECTRODES IN WATER

In Section 15.3.2, the electric arc in liquid nitrogen produces cyanopolyyne as expected but also produces hydrogen-terminated polyyne, which are rather unexpected, unless we admit that traces of water play a role as a supplier of hydrogen atoms during the plasmalysis caused by the electric arc. In Section 15.2.3, we have clearly demonstrated that when the submerged electric arc between graphite electrodes is struck under distilled water, it is possible to observe the typical electronic spectrum of a mixture of polyyne in water. Furthermore, liquid chromatographic analysis permits the separation and identification of all the hydrogen-terminated polyyne series normally observed in organic solvents like methanol and *n*-hexane. Thus, it is demonstrated that the hydrogen atoms in a system of graphite electrodes and water are supplied by plasmalysis of water molecules. Consequently, it is now clear that the hydrogen-terminated polyyne observed as secondary products in the arcing experiment in liquid nitrogen derive from the humidity and traces of water present in the liquid nitrogen itself and in the reactor.

15.4 CONCLUSIONS

Arcing graphite electrodes in acetonitrile produces simultaneously two series of polyyne: the “ordinary” hydrogen-terminated polyyne and a series of monocyanopolyyne. Thus, acetonitrile is a solvent able to supply both H and CN radicals which attach to the growing carbon chains. In our earlier work (see also [Chapter 8](#)) [18–22] we have found that all the other solvents tested, either hydrocarbons or alcohols, invariably were able to supply hydrogen atoms as end capping and stabilizing moieties of the carbon chains. This approach may lead to an easier route to monocyanopolyyne.

In acetonitrile solution the monocyanopolyyne are unstable and disappear completely in some days if stored at room temperature. The hydrogen-terminated polyyne present in the same solution appear much more stable

and remain unchanged for much longer time in comparison to monocyanopolynes.

Dicyanopolynes series can be easily produced by arcing graphite electrodes into liquid nitrogen. C_6N_2 , C_8N_2 , and $C_{10}N_2$ have been easily trapped into solvents where the vaporized liquid nitrogen is bubbled and detected by liquid chromatography. This approach may lead to an easier route to almost pure dicyanopolynes.

The formation of dicyanopolynes is accompanied by the formation of small amounts of hydrogen-terminated polyynes whose formation is due to the presence of water humidity in the experimental system adopted.

Also, the dicyanopolynes are unstable in an acetonitrile solution at room temperature and after 1 day storage they disappear completely.

ACKNOWLEDGMENTS

ASI, the Italian Space Agency, is gratefully acknowledged for the financial support of this work under the grant I/R/070/02.

REFERENCES

- [1] Hopf H, Witulski B. In *Modern Acetylene Chemistry*, edited by P.J. Stang and F. Diederich, VCH, Weinheim, 1995.
- [2] Heath JR, Zhang Q, O'Brien SC, Curl RF, Kroto HW, Smalley RE. The formation of long carbon chain molecules during laser vaporization of graphite. *J. Am. Chem. Soc.*, **1987**, 109, 359.
- [3] Kroto HW, Heath JR, O'Brien SC, Curl RF, Smalley RE. Long carbon chain molecules in circumstellar shells. *Astrophys. J.* **1987**, 314, 352.
- [4] Grosser T, Hirsch A. Synthesis of cyanopolynes. *Angew. Chem. Int. Ed. Engl.* **1993**, 32, 1340.
- [5] Gibtner Th, Hampel F, Gisselbrecht JP, Hirsch A. End-cap stabilized oligoynes: model compounds for the linear sp carbon allotrope carbyne. *Chem. Eur. J.* **2002**, 8, 408 (and ref. cited therein).
- [6] Smith IWM. Chemistry amongst the stars: reaction kinetics at a new frontier. *Chem. Soc. Rev.* **2002**, 31, 137.
- [7] Herbst E. Ion-molecule chemistry in interstellar medium. *Adv. Gas-Phase Ion Chem.* **1998**, 3, 1.
- [8] Kroto HW. C_{60} buckminsterfullerene, the celestial sphere that fell to Earth. *Angew. Chem. Int. Ed. Engl.* **1992**, 31, 111.
- [9] Kaiser RI, Balucani N. The formation of nitriles in hydrocarbon-rich atmospheres of planets and their satellites: laboratory investigations by the crossed molecular beam technique. *Acc. Chem. Res.* **2001**, 34, 699.
- [10] Balucani N, Asvany O, Osamura Y, Huang LCL, Lee YT, Kaiser RI. Laboratory investigation on the formation of unsaturated nitriles in Titan's atmosphere. *Planet. Space Sci.* **2000**, 48, 447.

- [11] McCarthy M, Thaddeus P. Microwave and laser spectroscopy of carbon chains and rings. *Chem. Soc. Rev.* **2001**, 30, 177.
- [12] Thaddeus P, McCarthy M. Carbon chains and rings in the laboratory and in space. *Spectrochim. Acta* **2001**, 57, 757.
- [13] Houdson RL, Moore MH. Reaction of nitriles in ices relevant to Titan, comets and interstellar medium: formation of cyanate ion, ketenimines and isonitriles. *Icarus* **2004**, in press.
- [14] Maier JP, Walker GAH, Bohlender DA. On the possible role of carbon chains as carriers of diffuse interstellar bands. *Astrophys. J.* **2004**, 602, 286.
- [15] Fulara J, Krelowski J. Origin of diffuse interstellar bands: spectroscopic studies of their possible carriers. *New Astron. Rev.* **2000**, 44, 581.
- [16] Miller SL. The endogenous synthesis of organic compounds. Chapter 3 in *The Molecular Origin of Life*, edited by André Brack. Cambridge University Press, Cambridge, 2000.
- [17] Budavari S, editor. *The Merck Index*, 12th edition. Merck Research Labs, Whitehouse Station, NJ, 1996, 3041.
- [18] Cataldo F. Synthesis of polyynes in a submerged electric arc in organic solvents. *Carbon* **2004**, 42, 129.
- [19] Cataldo F. Submerged electric arc between graphite electrodes: a one-pot tool for the synthesis of long chain polyynes in solution. *Tetrahedron Lett.* **2004**, 45, 141.
- [20] Cataldo F. Polyynes production in a solvent-submerged electric arc between graphite electrodes. 1. Synthesis and Spectroscopy. *Fullerenes, Nanotubes and Carbon Nanostructures* **2004**, 12, 603.
- [21] Cataldo F. Polyynes production in a solvent-submerged electric arc between graphite electrodes. 2. Analysis by liquid chromatography. *Fullerenes, Nanotubes and Carbon Nanostructures* **2004**, 12, 619.
- [22] Cataldo F. Polyynes production in a solvent-submerged electric arc between graphite electrodes. 3. Chemical reactivity and stability toward air, ozone and light. *Fullerenes, Nanotubes and Carbon Nanostructures* **2004**, 12, 633.
- [23] Eastmond R, Johnson TR, Walton DRM. Silylation as a protective method for terminal alkynes in oxidative couplings. A general synthesis of the parent polyynes $H(C\equiv C)_nH$ ($n = 4-10, 12$). *Tetrahedron* **1972**, 28, 4601.

16 Natural Carbynes, Including Chaoite, on Earth, in Meteorites, Comets, Circumstellar and Interstellar Dust

Frans J.M. Rietmeijer and Alessandra Rotundi

CONTENTS

16.1	Introduction	339
16.2	Metastable Carbynes: Are They Minerals?	340
16.3	The Carbon Phase Diagram Revisited: Carbon “Melting”	342
16.4	Terrestrial Chaoite: A Special Case.....	346
16.5	Carbyne Identification	348
16.6	Carbynes in Meteorites	352
16.7	Comets	354
16.8	Carbyne Crystals: What Link to Cumulene and Polyynes Gas Molecules?	356
16.9	Laboratory Carbon Condensation Experiments.....	357
16.10	A New Carbyne Structure	358
16.11	Circumstellar Dust.....	360
16.12	Interstellar Dust	362
16.13	Conclusions	363
	Acknowledgments	364
	References	364

16.1 INTRODUCTION

This paper on natural carbynes adopts a strictly mineralogical approach that will be necessary to appreciate the information available on these

peculiar carbons. Ternary classification of elemental carbons using the sp-hybridized carbon bond character, sp^3 (cubic diamond), sp^2 (hexagonal graphite) and sp^1 (linear carbynes), creates “chemical” order [1] to focus discussions. It presumes equality among elemental carbon solids in a mineralogical sense when, for example, considering carbon allotropy rather than polymorphy that is, strictly speaking, incorrect. Mineralogists accept only two carbon allotropes (hexagonal graphite and cubic diamond) each with a thermodynamic pressure–temperature (P – T) stability field that could “trespass” on each other’s stability field for kinetic factors delaying an equilibrium transformation. Hence, orthorhombic graphite, cubic graphite (cliftonite), hexagonal diamond (lonsdaleite; carbon-2H), carbynes and fullerenes, are metastable crystalline carbons free of heteroatoms.

Chemical and mineralogical classifications have elements of tradition left over from the time when these disciplines used different analytical techniques with poor instrumental resolution. For example, the geological term “cryptocrystalline” refers to a natural volcanic glass that, viewed in a light-optical microscope, appears to be without structure, *i.e.* is amorphous, but it often shows evidence for ordered entities in an x-ray diffraction (XRD) pattern [2]. Today’s high-resolution transmission electron microscopes (HRTEM) make it possible to view the material properties at the unit-cell level, such as the transition of a single crystal to an amorphous solid, and vice versa. The interface between chemistry and mineralogy, emphasizing transitions from chemical to crystalline bonds, is becoming important to astromineralogy [3] seeking to match infrared (IR) to ultraviolet (UV) spectroscopic and HRTEM information from solid carbon analogs as a proxy of processes in astronomical environments [4,5]. In these environments, amorphous solids quenched from a carbon liquid will be unlikely, but they cannot *a priori* be dismissed. Rather highly disordered, quenched carbon-vapor nanomaterials will be common. The combination of sp-hybridized carbon bond information, structural properties (amorphous or crystalline), IR and UV spectral characterization of condensed carbon nanograins obtained *in situ* in the laboratory, will be an increasingly fertile area of research for direct comparison with remote-sensing data for natural elemental carbon solids (carbynes and fullerenes) in environments that are inaccessible to direct sampling [6,7]. Cross-pollination of disciplines will only bear fruit when interpretations and ideas are challenged. We accept the existence of carbynes as metastable elemental carbon solids when assessing the evidence for natural terrestrial and extraterrestrial carbynes.

16.2 METASTABLE CARBYNES: ARE THEY MINERALS?

A recent book entitled *Carbyne and Carbynoid Structures* [1] makes a strong case that the carbyne forms of carbon *sensu stricto*, *viz.* polyynes with conjugated acetylenic triple bonds, $(-C\equiv C-C\equiv C-)_n$, and (poly)cumulene

isomers with cumulated double bonds, $(=C=C=C=)_n$, are almost exclusively produced by carbon vapor condensation under laboratory conditions. If so, it severely constrains finding natural carbynes because earth sciences must adhere to the Principle of Actualism formulated by James Hutton (1726–1797): “*No powers are to be employed that are not natural to the globe, no action to be admitted except those of which we know the principle*”. That is, accepting that processes operating in Earth’s past proceeded exactly as we can observe them in action today. The second part of the original formulation was amended to include experimental verification under controlled conditions. Nowhere on Earth are carbynes or other pure carbons observed condensing from a natural carbon vapor. Natural carbyne formation will require some geologically acceptable process. When, indeed, carbynes could only be produced in carbon-vapor condensation experiments [1], their formation will be limited to environments conducive to carbon sublimation, which, insofar as we know, would only be in astronomical environments [8] whereof the physiochemical conditions and the gas and solid compositions can only be probed by remote-sensing spectroscopic techniques.

The notion that polyynes could be common carbon dust around young stellar objects (YSOs) that are believed to be in the process of forming a planetary system, such as the solar nebula 4.57 Gyrs ago, is based on the widespread occurrence of acetylene $[H-(C\equiv C)-H]$ as a parent gas for carbyne condensation [9]. It is possible that carbynes could form by extra-terrestrial carbon-vapor condensation. For the solar nebula we have an opportunity to study such carbon dust in the laboratory using collected extraterrestrial materials, *viz.* meteorites from asteroids and interplanetary dust particles (IDPs) from comet nuclei and very primitive asteroids [10]. Earth scientists keep searching for alternative origins or interpretations than condensation. For example, the basal layer thickness ranging from 0.489 nm to 0.363 nm in a sample from the Sri Lanka (formerly Ceylon) graphite type locality covers the full range of c_0 -values reported for carbynes. The layers were interpreted as pre-graphitic carbon with variable admixtures of H, O, and N that are not routinely determined in HRTEM studies [11,12]; certainly not when natural carbynes were first reported in the literature.

The main issue is that carbynes are metastable carbon crystals [13] that:

1. Have no unique P, T constraints or formation modes, (a) flash-heating and carbon vapor sublimation produced by resistive heating or laser ablation using different starting materials (e.g. graphite, glassy carbon), (b) impact compression [14–16] and (c) carbon-rich vapor pyrolysis activated by electrons, ions and near-UV to IR photons [17]
2. Are typically associated with other carbynes, graphite, cubic diamond, amorphous carbon, in random, unpredictable combinations [14, 16, 18–20]

3. Readily suffer decomposition, vesiculation and amorphization when exposed to an incident energy beam, e.g. during TEM analyses, laboratory heat-treatment or irradiation [14,19,21].

The ages of chaoite lamellae in graphite from the 14.7 ± 0.7 Myrs old Ries impact crater [22] and in 60-Myrs old Ticonderoga marble [23] were taken to support the suggestion that chaoite could be a stable natural carbyne [24]. This argument of geologic age tacitly assumes continuous change of mineral properties as a function of “geological time”. Yet, minerals commonly persist outside their thermodynamic stability field as long as there are no activation energies to initiate a reaction. When they are not thermodynamically stable phases, are natural carbynes real minerals? Is chaoite, listed as a mineral by the Committee on New Minerals and Mineral Names of the International Mineralogical Association, the only exception?

According to the *Glossary of Geology* [2], a mineral is a naturally occurring element or chemical compound, usually an inorganic, crystalline substance, with characteristic physical and chemical properties that are due to its atomic arrangement. The keywords are “naturally occurring”, meaning a thermodynamically stable synthetic crystal cannot be a mineral until it is identified in a natural environment with distinct and unique P,T constraints. With this mineral definition, metastable natural carbynes are not minerals and consequently they are not carbon allotropes. Arguments counter to this mineralogical position exist [25].

16.3 THE CARBON PHASE DIAGRAM REVISITED: CARBON “MELTING”

The carbon phase diagram has been modified to accommodate a growing database on metastable carbons [13,26]. It is germane to recall that pure carbon solid reactions will be diffusion-less transformations that occur at the speed of sound. For example, a martensitic transformation (polysynthetic twinning) or a massive transformation (transgression of the new phase across pre-existing grain boundaries); both will be nearly instantaneous at submicron scales. Metastable carbons will respond rapidly to kinetically controlled energy dissipation. One modified version phase diagram includes a high- T /low- P “carbynes” field [27]. This modification presumed that carbynes are equilibrium phases on a par with (hexagonal) graphite and (cubic) diamond. These only true carbon allotropes define a hexagonal graphite \rightleftharpoons cubic diamond phase boundary and allow for reversible metastable conversions more or less along the metastable extension of the diamond-melting curve [26,28]. This led to the proposal of a “vapor-like intermediate” state wherein carbon atoms are disorganized in this metastable region of the phase diagram [29]. We submit an intermediate solid-carbon phase in the formation of metastable carbon solids to bring perhaps

“predictable chaos” to metastable carbon phase relationships. This notion relies on the finding that amorphous silicate nanograins that condensed from “ M ”-SiO-H₂O₂ (M : Al, Fe and/or Mg) “silicate” vapors have discrete compositions when quenched below the glass transition temperature (T_g). These metastable solid compositions are defined by deep metastable eutectics in the equilibrium phase diagram [6,30–34].

A hypothetical high- T /low- P “region of carbynes” with its corrugated vaporus systematically exploited newly reported carbyne properties and their low- P melting behavior (chaoite) to integrate the stability of these peculiar carbons among those of hexagonal graphite and cubic diamond [27]. The corrugated vaporus could lead to narrow carbyne fields centered on a single deep metastable eutectic (Figure 16.1). This topology is not unlike that in *Metal*-O and binary alloy phase diagrams. For example, the Ti-O phase diagram shows narrow composition fields for a sequence of

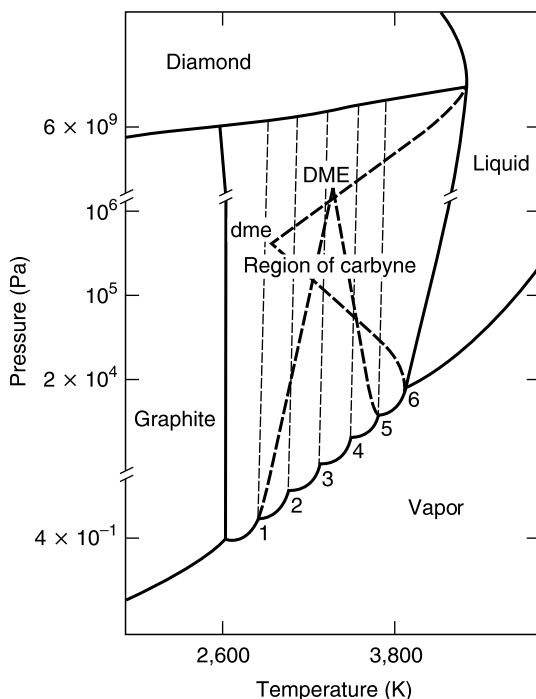


FIGURE 16.1 Modified high-temperature/low-pressure region of the carbon phase diagram [27] and later modified [68] showing a single deep metastable eutectic (DME) in the “region of carbynes” for carbyne condensation across discrete fields corresponding to condensed carbynes with different chain length, C_n ($n=1$ to 6). Another possible deep metastable eutectic (DME) for liquid carbon is shown. The metastable eutectic positions are not fixed within the “region of carbynes”. Their actual positions will be dependent on kinetic factors during carbon formation.

Magnéli phases, $\text{Ti}_2\text{O}_{2n-1}$ ($n=4-10$) [35] between Ti_2O_3 and TiO_2 (a natural mineral with three polymorphs) where the liquidus topology [36] constrains the formation of a deep metastable eutectic. Random combinations of several Magnéli phases co-exist depending on kinetic factors either during quenching or subsequent solid-state heat treatment under laboratory or natural conditions.

A deep metastable eutectic allows the formation of an amorphous compound with an intermediate composition between the eutectics by rapid liquid quenching and thus avoiding the formation of crystalline equilibrium compounds [37]. The deep eutectic temperature has to be below T_g at which the system is configurationally frozen [37] where it will remain amorphous albeit with detectable ordering. Deep eutectic behavior was also observed for co-existing melts in a supercooled liquid above T_g at ambient pressure [38]. The eutectics defining the deep metastable eutectics refer to the melt freezing point rather than the vapor sublimation temperature and composition. Another deep metastable eutectic in the “region of carbyne” is defined by the metastable extension of the diamond liquidus and the triple point (Figure 16.1). This solution, being restricted to carbynes, is not really satisfactory but perhaps this solution describes the highly kinetic behavior of elemental carbons during carbon vapor condensation.

In another revision of the high- T /low- P region in the carbon phase diagram, with the carbyne vaporus shifted from $\sim 2600-4000$ K (see Figure 16.1) to $\sim 4000-5000$ K, the “region of carbynes” is replaced by a low- P field of electrically nonconduction and conducting carbon liquids with a critical point estimated around 0.2 GPa at 6800 K [13]. While carbynes are de-emphasized because their existence is controversial [13], the carbon phase diagram should constrain potential metastable phases such as carbynes and C_{60} fullerene. A field for an intermediate state of “extreme-disordered amorphous carbon” (EDAC) could be a solution to carbon inter-relationships. This EDAC field replaces the low- P fields of carbon liquids [13] and the “region of carbynes” [27]. The formation of an EDAC field in the carbon phase diagram would have to be constrained by low-pressure diamond and superheated graphite “melting”. This particular solution of metastable carbyne formation would describe less-extreme kinetic behavior compared to vapor condensation in natural environments.

First-order solid-state amorphization occurs due to an entropy catastrophe [39] causing “melting” of superheated graphite and decompressed diamond below T_g when the entropy of the ordered crystal would exceed the entropy of the disordered liquid. This condition is resolved with the occurrence of a “kinetic transition” to a (supercooled) glass whereby the exact kinetic conditions during carbon transformation will be critically T_g -dependent [39]. It is important to consider the crystal to liquid transition and the effect of a superheated crystal whereof the ultimate stability is determined by the equality of crystal and liquid entropies [40]. When this condition is met, a solid below its T_g will “melt” to an amorphous solid, particularly

when randomly frozen-in defects are incorporated in the lattice [40]. The positive slope of the equilibrium graphite \leftrightarrow diamond reaction in the carbon P - T diagram will cause diamond to become increasingly sensitive to “melting” and vitrification by decompression towards higher temperatures. When at some pressure the melting curve of a mineral intersects its glass-transition curve, isothermal decompression below T_g will then cross the vitrification curve where the crystal will directly vitrify without melting [41].

An “extreme-disordered amorphous carbon” due to first-order solid-state hexagonal graphite and cubic diamond amorphization (“melting”) yields the EDAC phase field (Figure 16.2) that is also reached by ultra-fast quenching of a carbon melt or vapor. When quenching was the controlling parameter, deep metastable eutectic behavior at $T < T_g$ might favor a specific carbon form, for example, chaoite, as a quenched-melt metastable solid. Amorphous solids formed anywhere within the EDAC field will experience thermal annealing either during initial heat dissipation of the very formation process or during post-formation heat treatment. In both

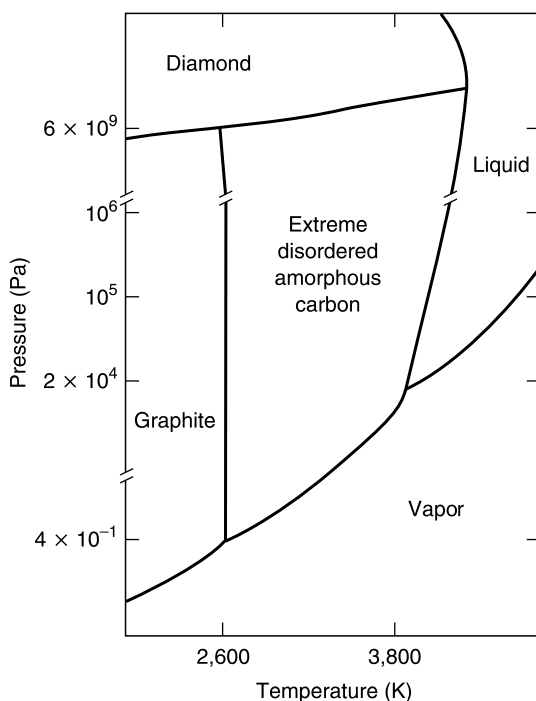


FIGURE 16.2 The proposed “extreme disordered amorphous carbon” field defined by low-pressure diamond “melting” and “melting” superheated graphite in the previously modified [27,68] high-temperature/low-pressure region of the carbon phase diagram.

cases solid-state pure carbon transformations will readily occur. Depending on the time–temperature regime the heat dissipation rate, that could be controlled by the very nature of the experimental set-up, will determine the final carbon assemblages resulting from solid-state transformations of metastable carbon, *viz.* a specific metastable carbon or a mélange of metastable and stable carbon forms. In fact, a role of ultra-rapid solid-state pure-carbon transformations in laboratory experiments, and probably in natural settings too, is still not fully appreciated. Yet, for solids formed in the EDAC field (Figure 16.2), they might link linear carbons (carbynes), carbon rings, graphene sheets, curved sheets, C₂₀ to C₆₀ fullerene and fullerenic carbons.

16.4 TERRESTRIAL CHAOITE: A SPECIAL CASE

The Ries Crater was formed by a hypervelocity meteor impact. The shock-fused graphite gneisses in this impact crater contain hexagonal graphite grains embedded in a glassy (silicate) matrix. The grains are a ~50/50 intergrowth of slightly sigmoidal, thin (0.5–2.5 μm ; measured by the authors from the published image) chaoite and graphite lamellae [22]. This morphology suggests movement along the intergrowth plane. A cryptic statement, “there was no evidence of preferred orientation” [22] probably refers to the crystallographic orientations of chaoite and graphite across the lamella interfaces which appears to be the graphite basal plane.

Meteorites typically have mineral features caused by hypervelocity impacts on the asteroid parent body and from the impact that ejected a meteorite from the parent body. The interstitial spaces between silicate minerals in ureilites, which are differentiated igneous rocks from asteroids that underwent core-mantle separation [42], consist of black polycrystalline inclusions (0.2–0.5 mm) and similar material also forms a rim (~0.1 mm) on these minerals. The inclusions are aggregates of sub-millimeter, angular grains that include 1. cubic diamond <1 μm , 2. hexagonal graphite, 3. chaoite and 4. sub-micron grains of thin hexagonal graphite and hexagonal diamond lamellae [18,43], that were the result of hypervelocity impacts [44].

Graphite crystals in some terrestrial marbles contain narrow intercalated layers that were identified by XRD as α -carbyne, or chaoite, and β -carbyne in the coarse-grained Ticonderoga graphitic marble and as carbon VIII in the Santa Rosa marble [23]. The negative ion spectrum of carbyne from the Santa Rosa marble showed C₁ up to C₁₂ molecules [45]. Similar results were indicated, but not shown, for graphite in other Californian locations and one on Sri Lanka [23]. Not knowing the exact geologic locations makes it difficult to interpret the data.

How could natural chaoite, the only odd-numbered linear carbon [24], form? Hypervelocity impacts are generally treated as vertical impacts described in *P–T*–volume space whereby all energy is dissipated during the

decompression stage [46]. However, an oblique impact includes both shock and high strain-rate shear that, while reducing the peak pressure, will enhance thermal reactions [47,48]. Significant thermal decomposition of target material, e.g. friction melting and vapor decomposition up to ~ 4275 K, will occur through frictional shear heating in addition to shock heating [47–49], including carbon melt formation [50]. It is unknown if the Ries Crater was formed by an oblique impact but localized small-scale shear stresses would be unavoidable.

The graphite unit cell dimensions are $a_0 = 0.246$ nm and $c_0 = 0.673$ nm; for chaoite $a_0 = 0.895$ nm and $c_0 = 1.408$ nm [51]. At room temperature two graphite layers, $2c_0 = 1.346$ nm, are close to the chaoite c -axis suggesting a simple relationship between these carbon crystals. Linear thermal expansion data for graphite are available up to 1273 K and show a 2.2% expansion parallel to its c -axis [52]. Extrapolation of these data to the graphite melting temperature (~ 4475 K) show a $\sim 12\%$ expansion to $c_0 = 0.754$ nm. There is a slight contraction of the basal plane [52]. Static compression data (at room temperature) parallel to the c -axis [53] show a reduced graphite cell volume of $\sim 13\%$ at 9.8×10^9 Pa. Assuming compression is entirely accounted for by c -axis reduction, this compressed unit cell axis, $c_0 = 0.586$ nm, would be reminiscent of the “anomalous graphite” phase in shock-compression experiments [54]. For non-hydrostatic compression during an impact, unit cell compression would probably be less than and thermal expansion and only 5% thermal expansion would yield (superheated) graphite $2c_0 = 1.414$ nm that compares to chaoite $c_0 = 1.408$ nm. During the Ries crater formation shear-stress heating raised the temperature of existing graphite grains in the EDAC field wherein two adjacent superheated graphite unit-cell layers “melted” (Figure 16.2) and subsequently crystallized as a chaoite lamella. Fitting the graphite and chaoite unit cells across the crystallographic ab -plane requires a slight rotation that is expressed by the slightly sigmoidal shape of the lamellae

Impact conditions on the ureilite parent bodies are unknown in terms of purely shock compression or shear stress regimes. From the original reports [18,43] it is unclear whether chaoite and graphite formed individual crystals or had a lamellar inter-relationship. When the former, even weak shock loading (compression) at projectile velocities of 0.655 to 1.88 km/s on a target of amorphous or glassy carbon yield polycrystalline assemblages of graphite, lonsdaleite and chaoite [55]. Hypervelocity impacts on the ureilite parent bodies might have been conducive to the transformation of “melted” graphite in the EDAC field (Figure 16.2) to chaoite.

The graphite-rich marbles formed during regional metamorphism at increasing pressure and temperatures of sedimentary carbonate rocks. The Ticonderoga and Santa Rosa marble quarries are located in tectonic terrains that are defined by large-scale thrust zones, *i.e.* the Appalachian thrust belt in the northeastern US (Ticonderoga) and the Californian strike-slip terrain (Santa Rosa). In deep-seated, tectonically dynamic, geologic terrains, shear

stresses over geological short time (< 1 m.y.) along major fault zones could cause thermal spikes in the thermal regime of regional metamorphism but such thermal spikes are modest at < 1000 K [56,57]. Such frictional shear heating in regionally metamorphic rocks was proposed for the graphitization of anthracite [58]. Higher transient temperatures were inferred for the formation of pseudotachylites, rocks that resemble volcanic glass. These rocks are formed during shear heating along tectonic fault movements when crustal rocks are melted by shear-stress release, although the exact temperatures are unknown. We submit that depending on the amount of shear-stress energy built-up and the rates of catastrophic heat release and dissipation during an earthquake on a tectonic fault line could spike temperatures high enough to “melt” graphite in the EDAC field (Figure 16.2). Here too, graphite expansion will be more dominant than compression during solid-state transformation of graphite to thin α -carbyne or carbon VIII lamellae when two adjacent, thermally expanded (10–15%) graphite layers “melted” in the EDAC field to match carbon VIII, $c_0 = 1.482$ nm, and α -carbyne, $c_0 = 1.536$ nm. The required percentage of linear graphite expansion is very high and unrealistic considering the general equilibrium temperatures during regional metamorphism. Graphite superheating would be possible during catastrophic shear-stress release in an earthquake event. The co-occurrence of α - and β -carbynes in the marbles [23] supports geologic annealing of metastable α -carbyne to more stable, denser β -carbyne, which is consistent with results of thermobaric treatment (5 min; 2073 K; 9 GPa) of α -carbyne [19].

Chaoite, α -carbyne and carbon VIII lamellae in natural graphite are a unique indicator for heat dissipation from catastrophic shear energy release in hypervelocity shock events and during earthquake events on regional geologic scale. The carbynes formed during kinetically controlled solid-state transformations from a “melted” carbon phase in the EDAC field. To the best of our knowledge this is the only natural carbyne-forming process on Earth. The suggestion that chaoite in the Ries crater was unrelated to the impact event [23] is not supported. There are other ways to produce carbynes, e.g. chaoite via graphite pyrolysis at high temperature from 2600 to 3000 K in a low-pressure (0.01 Pa) argon atmosphere [59] but such conditions were not yet observed in natural terrestrial environments.

16.5 CARBYNE IDENTIFICATION

Carbyne identification is still a matter of contention since not all identifications are complete and rigorous. They are generally identified by color, hardness, fracture surface, density and XRD, a bulk technique that produces a list of interplanar (hkl) or d -values [23]. Subtle combinations of d -values and x-ray line intensity are used for carbyne identification [23] but this approach will fail when using electron diffraction data with an up to

$\pm 5\%$ error of measurement. The carbon nature for selected carbyne grains with a hexagonal unit cell based on a *c*-axis electron diffraction pattern was established by electron microprobe analyses [14], negative ion spectroscopy [21] and energy dispersive spectroscopy (EDS) in the TEM for *in situ* determination of impurity elements [24]. Ideally, all crystallographic and chemical properties are obtained on the same carbyne grain, including sp-hybridized bonds using electron energy-loss spectroscopy, which is possible on grains of a few nanometers using state-of-the-art HRTEM [20,60], and new techniques such as scanning transmission x-ray microscopy and micro-Raman and infrared micro-spectroscopy [61].

Since the first report of carbynes in meteorites, the simple question: Carbyne forms of carbon: Do they exist? [62], initiated an enduring discussion on the state of natural extraterrestrial carbynes. There is no need to recapitulate this particular chapter in carbyne history [1] except to say that Smith and Buseck [62] justifiably questioned the robustness of carbyne identifications. Vesiculation and amorphization are known experimental artifacts during HRTEM analysis of single-crystal layer silicate grains (Figure 16.3). Similar behavior for carbynes cannot be a diagnostic feature unless a putative carbyne grain is first identified as a pure elemental carbon solid. It was confusing that EDS spectra for representative carbyne crystals showed distinct Al and Si peaks [Reference 24, Figure 5] and yet were apparently not kaolinite, a layer silicate mineral [60,63]. It was recognized

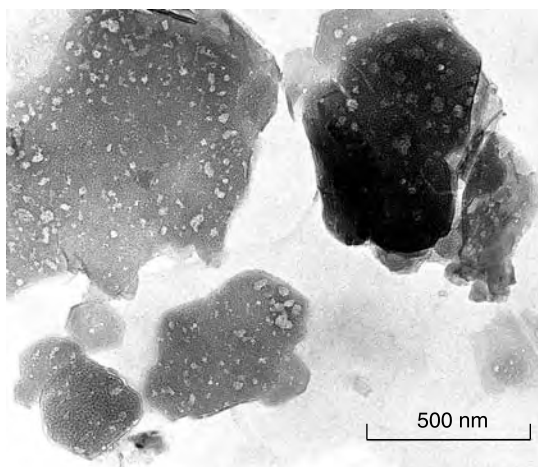


FIGURE 16.3 Transmission electron microscope (TEM) image showing seven hexagonal kaolinite, $[\text{Al}_2\text{Si}_2\text{O}_5(\text{OH})_4]$ single-crystal grains in IDP U2011C2. The crystals show the vesicular texture of heated kaolinite, for example when exposed to the incident electron beam in the TEM. An embedding epoxy (gray background) was applied to prepare this ultrathin section (modified after Rietmeijer and Mackinnon).

that Mg and Si peaks in EDS spectra of putative carbyne crystals indicated that these crystals were layer silicate minerals, e.g. talc $[\text{Mg}_6\text{Si}_8\text{O}_{20}(\text{OH})_4]$ or chrysotile $[\text{Mg}_3\text{Si}_2\text{O}_5(\text{OH})_4]$ asbestos. The problem was exacerbated by the fact that carbyne (*110*) *d*-values from 0.413 nm (β -carbon) to 0.49 nm (carbon XIII) overlap with the range of (*020*) *d*-values, 0.445–0.477 nm, for the most common layer silicate minerals [60]. In layer silicates the length of the crystallographic *c*-axis is determined by composition, structure and water content that can vary in systematic and transitional ways leading to complex polytypism.

Carbyne mineralogy was “plagued” by the presence of minor amounts of impurity elements. When graphite with 0–2.5 wt% Si was used to produce a carbon vapor, the condensed crystals were chaoite plus minor α -SiC [59]. That metal impurities from a graphite target or from the equipment could react with carbon vapor to form carbides was recognized in the earliest carbon condensation experiments [64,65]. However, minor amounts of impurity elements in carbynes are thought to be present at interstitial sites accommodated by the kinked, zigzag structure of the linear carbyne chains [66]. The commonality of a two-dimensional hexagonal carbyne lattice supports “in-plane” organization of carbon atoms and impurities [66]. If so, ordered impure (metal-bearing) carbynes should develop superlattice structures, which were not reported, at least not to the best of our knowledge. It was noted that the typical thin (*001*)-platey hexagonal carbyne morphology seems at odds with the carbyne “pencil-in-box” chain structure [60,66] parallel to the crystallographic *c*-axis and held together by van der Waals forces [25].

Many carbynes were identified by the a_0 -value only. The a_0 -values for carbynes produced by different techniques using a variety of starting materials show a range from 0.460 nm to 1.03 nm [67] but with no apparent correlation to preparation techniques or starting material. Some unidentified a_0 -values (Table 16.1) might be due to carbyne heating, viz. $a_0 = 0.901$ nm (973 K) decreased to $a_0 = 0.840$ nm (1023 K) and back to 0.901 nm at 1073 K, or responded to increasing Ar ion energy bombardment from 30 eV to 150 eV caused the a_0 -value to decrease from 1.03 nm to 0.831 nm [67]. The apparent thermal sensitivity of carbyne *ab*-plane dimensions suggests that a_0 values are an unreliable diagnostic feature.

The two smallest values, $a_0 = 0.476$ nm (C_6 ; polycumulene) and $a_0 = 0.508$ nm (C_{18} ; polyyne) are grains from a sample that also contained an amorphous phase, and was produced by “passing acetylene through a heated solution of copper chloride in a mixture of pyridine and methyl alcohol” [67]. However, using the unified linear carbon polytype equations for the number of carbon atoms in a polyyne or cumulene chain [51], these a_0 values (Table 16.1) do not yield a solution. Perhaps they refer to (*110*) *d*-values of hexagonal carbyne in which case the recalculated a_0 -values become 0.952 nm and 0.984 nm. Using these equations the “new” a_0 -values indicate cumulene chains with 16 and 19 carbon atoms, respectively. Considering

TABLE 16.1

Carbyne a_0 and c_0 values [67] and matching carbynes [51]. Values after heat treatment are in italics. Note: the originally listed value of 10.3Å was incorrectly converted to 103 pm during editing (Fitzgerald, written comm. 2004)

a_0 (nm)	c_0 (nm)	Carbyne
0.476	0.258	
0.508	0.780	
0.824	—	β -carbyne
<i>0.831</i>	—	
<i>0.840</i>	—	
0.870	—	Carbon XIV
0.880	—	
0.886	1.600	
0.892/0.894	—	α -carbyne; chaoite
<i>0.901</i>	—	Carbon VIII
0.942	—	Carbon IX
0.956	—	
1.030	—	<i>See caption note</i>

reasonable errors of measurement they could both be C_{18} polycumulene with six chains, each of three carbon atoms, but it would be inconsistent with their different c_0 values (Table 16.1). With acetylene as the starting material one would expect a polyyne chain structure. Yet, the “new” a_0 -values would make these grains the thinnest carbyne plates found yet. A question arises about the reliability of linear carbon chain identification using the unit cell dimensions.

The unit cell dimensions for a carbyne crystal with a specific number of carbon atoms, $n = 6, 8, 10$ or 12 , are used to identify a cumulene or polyyne chain [51]. In the a_0 vs n diagram the polyyne and cumulene correlation lines are distinctly different but, considering the limited diagnostic value of a_0 values, the use of this particular correlation as an identifying tool is doubtful. Parallel polyyne and cumulene linear correlation lines in the c_0 vs n diagram are separated by $\sim 2\%$ of measured c_0 values that, without consideration given to errors of measurement of diffraction analyses, leaves chain identification open to criticism [68]. Ignoring the cumulene or polyyne identifications for these carbynes [51] the calculated linear correlation coefficient, $r^2 = 0.99$, suggests that $c_0 = 0.128n - 0.029$ is an equally good fit to the data. Unit cell data alone are not reliable for carbyne chain identification.

16.6 CARBYNES IN METEORITES

The primitive carbonaceous meteorites, which include the hydrated CI and CM meteorites and mostly-anhydrous meteorites such as the Allende CV meteorite [69], reach Earth from the asteroid belt between Mars and Jupiter. Asteroid reflectance properties display a remarkably systematic distribution as a function of heliocentric distance for asteroids in this belt, and hence meteorite types, with the most primitive ones located farthest from the sun. Asteroid hydration occurred when internal heating melted (water) ice that had co-accreted with dust, chondrules and refractory inclusions in the solar nebula. These asteroids form the IR spectroscopic C-class with “clays, carbon and organics” at the surface similar to CI and CM meteorite parent bodies [70]. They and the Allende CV parent body, which apparently did not accrete (much) ice, are from the same zone of the asteroid belt. Even more primitive asteroids closer to Jupiter still contain co-accreted ices, organic materials and silicate dust. They define the IR spectroscopic primitive (P)- and dark (D)-class [70] bodies that include comet nuclei and many near-Earth asteroids [10].

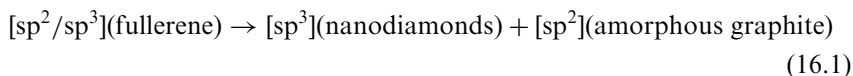
Non-volatile materials in asteroids included 1. presolar (interstellar) dust, and 2. dust condensed from a chondritic vapor in the inner solar system where presolar silicate and carbon dusts had evaporated at ~ 2000 K during a thermal flare-up phase of the young Sun [71]. Evidence for both dust sources can be found in carbonaceous meteorites albeit they were modified by aqueous alteration below ~ 400 K, or thermal alteration up to ~ 800 K in their parent bodies [69,72,73]. When metastable carbynes were not obliterated by parent body alteration, these particular meteorites would be candidates for searches of carbynes formed (probably by condensation) around C-rich YSOs (interstellar dust), in the inner solar system, or both.

In the quest to find the carrier phases of interstellar stable-isotope signatures, a volume of carbonaceous meteorite was dissolved in HCl–HF and concentrated in an acid-resistant residue of carbonaceous matter, spinel (MgAl_2O_4), chromite (FeCr_2O_4) and hibonite ($\text{CaAl}_{12}\text{O}_{19}$). Such residues of the Allende and Murchison meteorites reportedly contained single-crystal grains of carbon VI, -VIII, -X, -XI, -XII and -IX [21,74]. Carbon XII (maximum d -spacing: 0.453 nm) in the Murchison residue might be α -carbyne or chaoite, (110) = 0.447 nm [21]. The identifications were mostly based on the maximum d -value in single-crystal c -axis electron diffraction patterns. There is no quantitative data information on individual carbyne abundances in the residues. Irregular angular grains were ~ 40 to 750 nm in size with a conchoidal (glassy) fracture surface in the Allende sample but they were porous with a “loose structure” in the Murchison sample [21]. Typical faceted, *i.e.* euhedral hexagonal, platy carbyne crystals were rare. Some became quickly amorphized when placed in the incident TEM electron beam. The metastable nature itself was used to distinguish different carbynes. Of two crystals with near identical maximum spacing (0.464 ;

0.466 nm) in the Allende sample one “reacted very slowly” when exposed to the electron beam, the other transformed to rhombohedral graphite while yet other grains were amorphized [21]. The “pencil-in-box” carbyne structure [25] implies a diagnostic correspondence between carbyne c_0 and the full length of the kinked linear chain [24,51,66]. Carbyne dimensions in the crystallographic basal plane will have limited diagnostic value. Thus, carbon X, -XI and -XII identifications are uncertain; no c_0 values were reported for these carbynes and carbon XIII [24].

A HRTEM study of 16 acid-resistant residues of the Allende meteorite did not find carbynes but only carbonaceous matter that was mostly a variety of turbostratic carbon with random, three-dimensional stacking of sp^2 hybridized layers [63]. Another HRTEM study analyzed one of the original samples [21] but found only poorly graphitized or glassy carbon with lattice fringes of 0.35 nm to 0.40 nm; no carbyne-like diffraction patterns [60]. The different carbon identifications [60,63] are a matter of terminology rather than substance, *i.e.* the material is structurally disordered, poorly graphitized carbon. But Smith and Buseck [60] used only a few droplets of a suspension of acid-resistant residue for analysis and thus, yet with an extreme low probability, it remains possible that a few carbyne crystals might exist in this sample.

Yet another HRTEM study of a Murchison acid-resistant residue (MIL) showed, for the first time, carbyne in a petrographic context. An amorphous carbon matrix contained scattered 1. single-crystal cubic nanodiamonds (3–4 nm) identified by the 0.2 nm (*111*) *d*-spacing and in polycrystalline (“ring”) electron diffraction patterns ($\pm 5\%$ error of measurement), and 2. very thin (< 20 nm) well-ordered carbon plates [20]. The electron beam-sensitive plates are chaoite [20] that have a diffuse interface with the matrix. The matrix shows ordering in proto-fringes adjacent to the plates. Although petrographic textures contain a wealth of information on probable formation modes for the elements in a given texture, the interpretation of such textures can be ambiguous. In this residue cubic diamond and carbyne are “swimming” in an amorphous matrix. It would be tempting to conclude that pre-existing nanodiamonds and carbyne plates were incorporated in a later-formed amorphous carbon matrix [75] but an identical texture would result when cubic nanodiamond and carbyne had nucleated *in situ* in amorphous carbon during heat treatment. The amorphous MIL matrix (Reference 20; Figures 2 and 3) shows close-packed rings that resemble dense agglomerations of C_{60} and larger fullerenes of soot grains condensed under controlled laboratory conditions [76], leading to a possible sequence of solid-state transformations in this residue described as



Followed by sp^1 linear carbon growth in “amorphous graphite” which brings us to graphynes in the ternary chemical, carbon classification diagram [1]. Cluster-assembled sp^2 carbon films deposited by supersonic carbon cluster beam deposition in ultrahigh vacuum at room temperature contained embedded sp^1 -hybridized (polyyne and polycumulene) chains [77]. The sp^1 -hybridized carbon rapidly disappeared during thermal annealing up to 473 K and was easily oxidized when exposed to dry air; it did not react with He, H and N [77]. Under high vacuum at room temperature the sp^2 - sp^1 network of this pure carbon solid is very stable showing that cluster-cluster interactions might lead to the formation of larger solid carbons [78]. When amorphous graphite (Eq. 16.1) had similar sp^2/sp^1 hybridized carbon bond distributions, it would offer a self-consistent model for the formation of scarce carbynes in primitive meteorites and aggregate interplanetary dust particles (IDPs).

What are the meteorite data telling us? The original claim that the Murchison and Allende meteorites contained a substantial number of individual crystalline carbyne grains [21] was almost certainly incorrect. In yet another ultrathin section and acid-resistant residue of the Murchison meteorite C=C functional groups were identified but they were linked to aromatic carbons [61]. The only reliable evidence for carbyne (*i.e.* chaoite) in meteorites [20] suggests it formed *in situ* by solid-state carbon annealing that is an acceptable geological process. A tenet of cosmochemistry is that all solids initially formed by condensation from a cooling vapor phase. Whether condensation proceeded at (near) thermodynamic equilibrium, kinetically controlled, metastable equilibrium, or a combination, remains open to debate. Kinetically controlled, metastable condensation is likely for silicates [6,79] and was proposed for carbyne condensation from interstellar polycyanoacetylenes [80].

16.7 COMETS

Information on the chemical composition of active comets is available from two different “reservoirs”, *viz.* solid debris and sublimated volatile species. The former is extracted by IR spectroscopy of the dust tail and dust trails in the comet’s orbit, from collected IDPs, possibly a fraction of CI carbonaceous meteorites, and from meteor data. Information on species in the comet coma and plasma tail is obtained by UV-VIS-IR spectroscopy and radio astronomy.

Comet nuclei range from homogeneous dirty snowballs to rubble piles that are held together by self-gravitation and dirty-ice/icy-dirt “glue” [81–85]. The building blocks include:

1. Giant boulders, km-size to hundreds of meters, of probably ice-free materials similar to CI carbonaceous meteorites and anhydrous, Si-rich proto-CI material.

2. Meter- and centimeter-sized pebbles of compacted, massive dust–ice mixtures with variable degrees of hydration of the embedded dust.
3. Dust in the “glue” matrix.

So far, no carbynes were reported in the completely hydrated CI carbonaceous meteorites. It is likely that pervasive hydration had destroyed metastable carbons originally present. If so, they should still be present in the anhydrous proto-CI materials, which are not yet recognized among the collected meteorites.

The generally carbon-rich aggregate IDPs (10–15 μm) and cluster IDPs ($\sim 100 \mu\text{m}$) are in all of their mineralogical, textural, chemical and spectral properties completely different from any of the collected meteorites [86]. These IDPs are solid debris of the very primitive, IR-spectroscopic P- and D-class bodies. The matrix of IDPs is an aggregate of $\sim 100 \text{ nm}$ to $\sim 1000 \text{ nm}$ sized principal components (PCs):

1. Carbonaceous PCs of refractory hydrocarbons, amorphous organic carbons [61], pure amorphous carbon, poorly graphitized and pre-graphitic turbostratic carbons.
2. Carbon-bearing ferromagnesiosilica PCs of ultrafine (2 to $\sim 50 \text{ nm}$) Fe,Mg-silicate, Fe,Ni-sulfide and Fe-oxide grains in a refractory hydrocarbon and amorphous carbon matrix.
3. Pure ferromagnesiosilica PCs with either a Mg-rich smectite-dehydroxylate $[(\text{Mg,Fe})_6\text{Si}_8\text{O}_{22}]$ or a Fe-rich serpentine-dehydroxylate $[(\text{Mg,Fe})_3\text{Si}_2\text{O}_7]$, metastable eutectic composition.

The chemical analyses and mass measurements of dust released from the nucleus of comet Halley showed a mixture of these PCs [82] although it was proposed [87] that silicates and organic materials were mostly interspersed in dust resembling C-bearing ferromagnesiosilica PCs. There is no mineralogical evidence for carbynes in the matrix of aggregate IDPs, wherein most of the carbon resides, or in cluster IDPs. The lack of evidence cannot be accepted as proof that carbynes do not exist in these very primitive particles. All collected IDPs have experienced flash-heating (5–15 s) that raised the temperature of the entire particle to between $\sim 600 \text{ K}$ and $\sim 1200 \text{ K}$ [82]. Indigenous metastable carbons would probably not survive this thermal event but perhaps vestiges might survive “shielded” inside another carbon phase.

Evidence for carbynes in comets might come from remote-sensing analyses of the volatile species in the coma of active comets, in particular from the study of carbon-chain molecules abundances [88]. Using narrowband filter photometry, C_3 and C_2 were detected in amounts that are classified as being “typical” in comets Hale–Bopp and Halley [89] and as “being depleted in carbon-chain molecules” in comet 67P/Churyumov–Gerasimenko, the new target of the ESA ROSETTA mission, and comet LINEAR 1999

TABLE 16.2

Production rates for C_2 and C_3 (molecules s^{-1}) and dust $A(\theta)f\rho$ in comets Hale-Bopp, Halley and Linear 1999 S4 (no current data for comet 67P/Churyumov-Gerasimenko).

	Hale-Bopp	Halley	Linear 1999 S4
C_3	1.7×10^{27}	1.0×10^{26}	1.0×10^{23}
C_2	1.6×10^{28}	1.0×10^{27}	1.0×10^{24}
$A(\theta)f\rho$	1.0×10^6	2.5×10^3	1.0×10^2

The parameter $A(\theta)f\rho$ is a proxy for dust production, where $A(\theta)$ is the albedo at the particular phase angle of the solar illumination at the time of the observation, f is the filling factor of the grains within the field of view of the photometer entrance aperture, and ρ is the projected radius of the aperture. The quantity $A(\theta)f\rho$ is aperture-independent for dust having a canonical $1/\rho$ spatial distribution, and is independent of wavelength for grains that are gray in color

S4 [90,91] (Table 16.2). A “typical” comet composition is based on the relative amounts of the different gas species measured in the coma of comets from the Oort cloud, an immense spherical cloud surrounding the solar system and extending from approximately 5000 to 100,000 AU. About half of the short-period comets are from the Kuiper Belt, a disk-shaped region containing many small icy bodies extending beyond Neptune’s orbit from 30 to 50 AU, which are depleted in carbon-chain molecules. The other short-period comets have the “typical” composition of Oort cloud comets. So far, carbyne molecules detected in the coma of active comets are very short chains unlike the longer chains characteristic of natural carbyne crystals such as chaoite in the Murchison meteorite [20,67].

16.8 CARBYNE CRYSTALS: WHAT LINK TO CUMULENE AND POLYNE GAS MOLECULES?

Mass spectrometric analyses of Allende meteorite identified a large number of triple-bonded carbon species and yet no carbyne crystals were found in its acid-resistant residues [80]. Similarly, a study of organic matter in IDPs reported $C=C$ functional groups but they were probably from polycyclic aromatic hydrocarbons (PAHs) [61]. It was noted though that the possibility remained that these groups might be associated with an amorphous carbon phase other than the amorphous carbon that was used as a standard [61]. There is no strong evidence from the natural carbyne data to indicate a straightforward correlation between the presence of double- and triple-bonded carbon precursor gas molecules and the presence of carbyne

crystal grains. A synthesis of available data [20,61,77] suggests carbyne nanocrystals, specifically chaoite, could exist in meteorites after thermal annealing of a pure carbon, amorphous precursor with disseminated sp^1 -hybridized entities.

16.9 LABORATORY CARBON CONDENSATION EXPERIMENTS

Chaoite, possibly carbon VI, α -carbyne, β -carbyne and carbon VIII were reported among carbynes that condensed in carbon vapors produced by resistive heating and high-energy laser irradiation of a carbon starting material [92]. Except chaoite and carbon VI, carbynes in the experiments were identified by the a_0 value [92]. In general, low-number (< 22) elemental carbon crystals are defined by default as being a carbyne when the hexagonal unit cell dimensions are larger than those of hexagonal graphite ($a_0 = 0.246$ nm; $c_0 = 0.670$ nm). This is fair practice but whether distinctions within a broad “carbyne group” are possible remains questionable.

Are carbynes produced in laboratory carbon and $C-H_2-Ar$ vapors designed to simulate the properties carbon dust in astrophysical environments? Field-emission scanning electron microscope (FESEM) and HRTEM studies of vapor-condensed carbon smokes showed a wide range of carbon morphologies that were free of metal impurities (at EDS detection limits), *viz.* 1. C_{60} and higher fullerenes that agglomerated into amorphous soot grains, 2. fullerene nanotubes and onions, 3. amorphous carbon sheets, 4. individual poorly-graphitized carbon loops or clusters on the sheets, and 5. pre-graphitic carbon ribbons [4,76]. A thermally annealed (1073 K; 3 h) condensed carbon sample showed clusters of very thin, hexagonal plates (Figure 16.4) with a maximum d -value of 0.53 nm in hexagonal single-crystal c -axis electron diffraction patterns. This d -value was probably not a_0 but the (110) hexagonal plane. These plates with $a_0 = 1.06$ nm are indeed very thin. While C_{60} fullerene was confirmed by high-performance liquid chromatography and mass spectrometry [76], no independent data are available to confirm a carbyne nature of the plates. Assuming the plates are carbyne they might have formed by a solid-state transformation of condensed amorphous carbon sheets, which should then have contained sp^1 -hybridized linear carbon domains. But, there could be an alternative.

A laser ablation experiment using a target of amorphous carbon with carbyne “nanodomains” found that the presence of sp^1 -hybridized carbon inhibited C_{60} fullerene formation but promoted the formation of higher fullerenes, C_{74} to C_{160} , by the step-wise addition of discrete $[C\equiv C]$ units [93]. The target used in the carbon-vapor condensation experiments [4] was apparently carbyne-free since abundant C_{60} did form and agglomerated into amorphous soot grains [76]. Higher fullerenes in the soot grains could have formed according to the fullerene growth reaction that introduces C_2 molecules into the gas phase [94]. When, in that case, the gas molecules were



FIGURE 16.4 Transmission electron microscope (TEM) image of a cluster of thin hexagonal plates formed after thermal annealing (8 h at 1073 K) in a sample of condensed carbons that included fullerenes in amorphous soot grains, carbon nanotubes and anions, amorphous carbon, poorly graphitized carbon loops and pre-graphitic carbon ribbons [4].

in the form of $[C\equiv C]$ and/or $[C=C]$ units, or as larger $(-C\equiv C-C\equiv C-)_n$, and/or $(=C=C=C=)_n$, chains, these units and chains incorporated in an amorphous (sp^2) carbon matrix might bridge two graphene sheets during thermal annealing to form hexagonal carbyne crystals.

16.10 A NEW CARBYNE STRUCTURE

The c -axis dimension of graphite defines the separation of two parallel graphene sheets determined by the size of the carbon atoms and inter-atomic interactions between stacked carbon atoms in a hexagonal arrangement. Increasing the distance between two adjacent graphene sheets could be achieved by “in-plane” addition of heteroatoms (H, N, O, S). The carbyne c_0 dimension appears to be determined by the length of a linear chain of 6 up to 12 carbon atoms [51]. An interesting situation emerges when two adjacent graphene units were to be bridged by a polyyne or cumulene chain determining the separation of the units. Such a chain connecting to the center of each sheet would lead to an “empty” crystal without a physical meaning. For the sake of argument, assuming a molecular chain of eight carbon atoms would yield a carbon solid with twenty C atoms. All carbynes

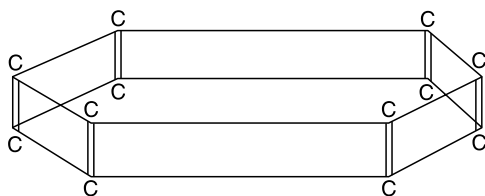


FIGURE 16.5 Cartoon showing the new carbyne (cumulene, C_{12}) structure of two hexagonal graphene sheets that are linked by six linear carbon chains parallel to the crystallographic c -axis. The c -axis is larger than this unit cell axis of graphite. This very thin elemental carbon crystal will be rigid and have considerable hardness.

have a hexagonal symmetry in common [66]. In the new carbyne structure two graphene units are connected by six chains each one terminating in these sheets. The smallest (cumulene) carbyne, C_{12} , consists of two graphene sheets connected by $C=C$ units (Figure 16.5); the smallest (polyyne) carbyne, C_{24} , has six $-C\equiv C-$ chains connecting two graphene units. Kinks in longer chains and alternating cumulene and polyyne chains along the c -axis could potentially lead to carbyne polytypism. The new carbyne structure predicts that most carbynes will be thin hexagonal plates, even at high carbon numbers.

What is the supporting data for this new carbyne structure? The most common natural carbynes are chaoite (C_{11}), α -carbyne (C_{12}) and carbon VIII (C_{12}) that are the smallest predicted carbynes. According to the new model, β -carbon is not carbyne but an “expanded graphite” phase. The notion of thermally “expanded graphite” was invoked to explain the formation of chaoite layers in graphite (Section 16.4). Sinuous lattice fringes of expanded HOPG graphite showed a set of perpendicularly oriented (relative to the graphite c -axis) lattice fringes of a hexagonal carbon, $a_0 = 0.82$ nm and $c_0 = 0.77$ nm, that was probably β -carbyne [95]. Raman and electron-energy loss spectroscopy confirmed its sp^1 -hybridized bond character [95]. In this sample the carbyne plates formed pillars “supporting” the expanded graphite structure.

Soot condensed in a carbon vapor produced in an electric arc technique contained C_{60} and C_{70} fullerene and linear carbon crystals, $(110) = 0.435$ nm, with 60 to 80 (probably 70) carbon atoms [96]. The new carbyne model suggests they are hexagonal crystals with six C_{11} or C_{12} chains but unfortunately there are no TEM images of these crystals [96]. Amorphous carbon was produced containing both sp^2 and sp^1 bonds [77]. While the VIS-IR spectrum of “carbonaceous matter containing carbyne” did not resemble “Astronomical carbon spectra” [97], the notion of carbyne-containing amorphous carbons as precursors in extraterrestrial environments is supported by the meteorite data [67] and laboratory experiments [4]. The original

carbyne chain lengths in the amorphous carbon matrix are unknown. The thinness of the plates suggests the breakdown of cumulene and polyyne chains to their smallest units that locally reorganized to bridge graphene sheets to form carbyne single crystals.

Carbynes are extremely rare in meteorites. The main issue to emerge is that platey carbyne crystals in these extraterrestrial materials were formed by solid-state transformations of amorphous sp^2 -hybridized carbon with embedded carbyne chain molecules during thermal annealing inside a parent body (asteroid; comet nucleus) with a sustained thermal regime. Pervasive hydration of CI and CM meteorites and flash-heating of IDPs during atmospheric entry might have erased most or all of their metastable carbon minerals. Such amorphous carbons could have formed within the solar system or around other stars, and after surviving sojourn through the interstellar medium (ISM), might then be incorporated as so-called presolar dust in meteorites and IDPs. What then is the evidence for carbyne formation in circumstellar environments?

16.11 CIRCUMSTELLAR DUST

Circumstellar regions range from the winds of very young stars to dust envelopes around highly evolved stars. Stars of a few solar masses develop extended atmospheres that, when drifting outwards, will generate warm (~ 1000 K) and relatively dense circumstellar envelopes wherein interesting chemistry and dust formation occur. Carbon-rich envelopes show a particularly rich chemistry. A plethora of carbon-chain molecules take a prominent place in circumstellar envelopes. Vibration-rotation lines of the pure carbon chain molecule C_3 , a potential building block for carbon grains, have been identified in the circumstellar spectrum of the obscured carbon star IRC + 10216 [98]. In the circumstellar shell of the same source C_5 was also detected [99]. In this well studied, nearby envelope of high mass-loss rate, the family of carbon chain molecules $HC_{2n+1}N$ ($n = 1-5$), C_nH ($n = 2-6$) and C_nS ($n = 1-3$) has attracted much attention. It was proposed that the large cyanopolyyne, $HC_{2n+1}N$, were formed in radical reactions of C_3N and C_5N with acetylene [100]. As abundance calculations using a photochemical model of the envelope demonstrate that chains will be efficiently produced in outer circumstellar envelopes [101], within which dust might form and be ejected in to the ISM. The dust, distributed throughout the IS with the gas, extinguishes starlight rising almost monotonically with photon energy from the near IR to far UV. The extinction curve is interpreted as due to grains with a distribution of dust grains sizes ranging from about 3 nm to 300 nm, being the smallest in the “molecular” regime. However, the interpretation of interstellar polarization requires the presence of macroscopic dust [102]. The chemical pathways towards carbonaceous grains, starting from very small radical clusters, such as C_2 , C_3 , C_2H

or C_3H , as well as the structure of these medium-sized circumstellar clusters, is still largely unknown. Depending on the number of C atoms they can be arranged in linear chains, rings and fullerenes that can co-exist in various proportions and that can pass from one to the other in the ambient radiation field because of small energetic separations (less than 1–2 eV) between these carbon molecules. Hydrogenated carbon cluster growth in carbon-rich stellar atmospheres is simulated by a model that considers the simultaneous formation of compounds with carbon atoms of various hybridization: sp^1 , sp^2 and sp^3 [103]. They showed that a mixture of differently hybridized species could appear depending on the relative carbon to hydrogen abundance, $(n_C/n_H)=1$, and the star's temperature. The calculations showed that the distribution of carbon clusters in carbon-rich stellar atmospheres would depend on the relative energies of the clusters and growth kinetics. When the C to H abundance ratio is high (>0.1), medium-sized species molecules of various types will be produced, *viz.* chains (C_nH or C_nH_2), carbon monocycles (C_n) and PAHs that might be accompanied by their corresponding dehydrogenated forms. Carbon chains or monocycles will predominate over dehydrogenated (regular and relatively small) PAHs at 2000 K. In contrast between 5000 K and 7000 K, for example in the vicinity of the star, large PAHs are formed at a much higher rate in competition with cumulenenic chain structures. The models and astronomical observations support that alternating single- and triple-bonded carbons are present in circumstellar environments.

Carbon clusters produced in the inner regions of circumstellar envelopes when driven in the outermost regions are very likely to be reprocessed by the interstellar UV radiation field. The C_n chains that are the structural units in carbynes are very unstable and can easily lead to the creation of sp^2 sites [103]. Benzene rings are formed from the linear C_6 structure to the corresponding cyclic isomer, *i.e.* a fully dehydrogenated benzenic ring. Such rings and linear carbyne molecules could combine to form nanocarbyne crystals as described above. The calculated activation barrier for conversion of the C_6 linear into the cyclic form results smaller than 1.11 eV, on the other hand subsequent hydrogen addition stabilizes the cycle with the creation of sp^2 sites [103]. Gradual sticking of such segments and sp^2 bonded entities would ultimately lead to a very intricate and strongly dehydrogenated network of mixed sp^2 - and sp^1 -hybridized amorphous carbons. The sp^3 -hybridized structures could possibly compete with sp in the inner region of circumstellar envelopes, but they would become more and more graphitized when in the outermost regions of the circumstellar envelope by interstellar UV radiation [103]. Amorphous solids with these mixed hybridization states, either as interstellar dust or formed in the solar nebula, could have survived in CM meteorites wherein they became the precursor of chaoite [67].

In summary, the assembly of benzene and carbyne molecules in circumstellar environments could potentially lead to formation of nanocrystals with the new carbyne structure (Figure 16.5). Still, a more likely scenario

might be the formation of amorphous carbon with multiple hybridization states. This circumstellar carbon dust would be the precursor material for the solid-state formation of platy carbyne crystals when thermally annealed.

16.12 INTERSTELLAR DUST

In the cold (10–30 K) interstellar clouds the detection of carbon clusters is still incomplete but the centro-symmetric carbon chain could possibly be detected by their far-IR bending–rotation transitions. The C_3 molecule was recently detected in one cold dust cloud [104]. The observations of hydrogen-containing polar chain molecules towards star ζ -Ophiuchi and laboratory studies of the electronic transitions of a number of homologous series lead to an important conclusion on the role of carbon chains as potential molecules in the so-called diffuse interstellar bands (DIBs). These carbon-chain molecules would have to be very long, e.g. HC_nH , C_{2n} , C_nH neutral chains, HC_nH^+ cations or $(C_n)^-$ anions (except for odd-numbered carbon chains [105]. Carbon chain species, as a family, have abundances in the diffuse ISM on the order of 10^{-10} (relative to H) that is consistent with their abundances in dense molecular clouds [106]. Assuming an average length of 10 carbon atoms per chain, this abundance implies that roughly a millionth of all cosmically available carbon could occur in the form of these chains. The discovery that carbon chain molecules are abundant in various interstellar regions poses a major problem. Their existence and abundances in the ISM would imply the operation of a facile synthesis process, but it is unclear how such long carbon chains could be synthesized efficiently from smaller units by the ion–molecule processes, by gas-phase chemistry [107,108] or via grain disruption by shock waves that periodically traverse the ISM [109].

Lacking an experimentally verified explanation for carbon chain formation at 10–30 K suggests that carbyne crystals will probably not form in the ISM that is generally characterized by dust destruction and little condensation [110]. Yet, polyyynes are abundantly and efficiently formed in the circumstellar environments, at relatively high pressures and temperatures (see Section 16.11). Stars continuously interact with the ISM. In its early stage a young star will expel much of its enveloping dust and gas. Even when hydrostatic equilibrium is reached as the star settles onto the main sequence of the Hertzsprung–Russell diagram, its stellar winds keep supplying some matter to ISM. The star–ISM interaction becomes dramatic towards the end of stellar evolution when roughly a half of the stellar mass could be injected into the ISM. The most massive stars explode as supernovae thereby rapidly returning their matter, now converted by the nucleosynthesis, to the ISM. In the asymptotic giant branch (AGB) stage of stellar evolution a star gradually loses its outer shells until only a small, extremely dense core is exposed. This particular evolutionary stage is generally believed to be the

main source of dust in the ISM. Eventually, such ejected dust will form a circumstellar envelope, which finally gives rise to a planetary nebula that with time is dispersed as part of a continuous process of dust formation and recycling.

Carbon chains would thus be produced by carbon-rich stars and subsequently expelled into the ISM included in other dust grains. In the millions of years between circumstellar dust formation and the appearance of carbon chains in cold interstellar molecular clouds such chain molecules are unlikely to survive photodissociation when not protected by carbon grains. There remains a remote possibility that polyne molecules associated with interstellar grains could yield carbyne crystal grains when interacting with supernova-generated shock waves via carbon condensation when precursor molecules were evaporated. Considering that the pressure for grain shattering in grain-grain collision is on the order 10^{10} Pa, which is considerably lower than the pressure for grain vaporization (5×10^{11} Pa) [111], there could be another potential pathway for interstellar carbyne crystal formation. The x-ray pattern of graphite produced by arc discharge of a CH_4/CO mixture samples treated at 10^9 Pa pressure showed maxima that were attributed to metastable chaoite suggesting it had a modified graphite structure rather than a chain structure [112], which would be consistent with the new carbyne model (Figure 16.5). Perhaps the high collision energies in the cold ISM could produce a kinetically controlled environment wherein linear C_6 molecules included in carbon grains would not convert to the cyclic form but rather form benzene rings. Smaller linear carbyne molecules could then connect two such rings to form a carbyne crystal (see Section 16.10). However, when carbynes crystals are not formed in the ISM but only sojourn through the ISM to developing circumstellar dust environments, the linear carbon molecules have to be locked within amorphous carbon grains. These carbon grains might resemble the amorphous carbon-nanodiamond-carbyne association in the Murchison meteorite [20]. The conjectural nature of the sections dealing with carbyne crystals among the dust in circumstellar and interstellar environments in part reflects the inability to uniquely constrain the exact form of solid carbons by remote sensing techniques.

16.13 CONCLUSIONS

This review of natural carbynes took a mineralogical approach by accepting carbyne crystals only as metastable forms of purely elemental carbon. Carbynes appear to be almost exclusively produced synthetically as the condensation products of carbon vapors but carbon vapors are not part of the geological processes on Earth. Natural terrestrial carbynes, with chaoite as the preferred natural carbyne, only occur as lamellae in graphite crystals superheated in dynamic environments characterized by the catastrophic

frictional shear-energy releases. To conceptually accommodate this origin a revised carbon P,T diagram has a low- P /high- T field of “extreme-disordered amorphous carbon”. Carbynes are extremely rare in collected meteorites and interplanetary dust particles but the main issue to emerge is that carbynes in extraterrestrial materials formed by solid-state transformations of amorphous carbon with embedded carbyne chain molecules during thermal annealing inside a parent body with a sustained thermal regime. Pervasive hydration meteorites or thermal heating of interplanetary dust particles might have erased most or all metastable carbon minerals. The collected samples do not support a simple correlation between the presence of cumulene and polyyne gas molecules and the presence of carbyne minerals. Linear carbon chains are present in the coma of comets, in circumstellar environments and in some DIBs but the presence of carbyne crystal grains in these environments is not yet confirmed. The identifications of chaoite, carbon VIII and α -carbyne as being different crystals are ambiguous when based mostly on electron diffraction analyses. A new carbyne structure is presented that is consistent with the thin platey (001) hexagonal grains of carbyne crystals. Future research should emphasize well-documented carbon–vapor condensation experiments with special consideration given to heat dissipation rates.

ACKNOWLEDGMENTS

We thank Dieter Heymann and an anonymous colleague for reviewing this paper and Jane Selverstone and Karl Karlstrom, both at UNM, for information on the tectonic settings of the graphite marbles. The TEM images were obtained in the Electron Microbeam Analyses Facility of the Department of Earth and Planetary Sciences (UNM) where Fleur Rietmeijer-Engelsman provided technical support. F.J.M.R was supported by grant NAG5-11762 from the National Aeronautics and Space Administration; A.R. received support from ASI and MURST.

REFERENCES

- [1] Heimann, R.B.; Evsyukov, S.E.; Kavan, L., Eds. *Carbyne and Carbynoid Structures*. Kluwer Academic Publishers, Dordrecht, Boston, London, 1999.
- [2] Gary, M.; McAfee, Jr., R.; Wolf, C.L., Eds. *Glossary of Geology*. American Geological Institute, Washington, DC, 1974.
- [3] Molster, F.J.; Waters, L.B.F.M.; Tielens, A.G.G.M. Crystalline silicate dust around evolved stars. II. The crystalline silicate complexes. *Astron. Astrophys.* **2002**, *382*, 222–240.
- [4] Rotundi, A.; Rietmeijer, F.J.M.; Colangeli, L.; Mennella, V.; Palumbo, P.; Bussoletti, E. Identification of carbon forms in soot materials of astrophysical interest. *Astron. Astrophys.* **1998**, *329*, 1087–1096.

- [5] Rotundi, A.; Rietmeijer, F.J.M.; Brucato, J.R.; Colangeli, L.; Mennella, V.; Palumbo, P.; Bussoletti, E. Refractory comet dust analogues by laser bombardment and arc discharge production: A reference frame for “dusty experiments” on-board ROSETTA. *Planet. Space Sci.* **2000**, *48*, 371–384.
- [6] Nuth, III, J.A.; Rietmeijer, F.J.M.; Hill, H.G.M. Condensation processes in astrophysical environments: The composition and structure of cometary grains. *Meteoritics Planet. Sci.* **2002**, *37*, 1579–1590.
- [7] Rotundi, A.; Brucato, J.R.; Colangeli, L.; Ferrini, G.; Mennella, V.; Palomba, E.; Palumbo, P. Production, processing and characterization techniques for cosmic dust analogues. *Meteoritics Planet. Sci.* **2002**, *37*, 1623–1635.
- [8] Rietmeijer, F.J.M.; Nuth, III, J.A. Experimental astromineralogy: Circumstellar ferromagnesiosilica dust in analogs and natural samples. In *Dust in the Solar System and Other Planetary Systems*. COSPAR Colloquia Series 15. Green, S.F.; Williams, I.P., McDonnell, J.A.M., McBride, N., Eds. Pergamon Elsevier Science, 2002, 333–339.
- [9] Henning, Th.; Salama, F. Carbon in the universe. *Science* **1998**, *282*, 2204–2210.
- [10] Shearer, C.K.; Papike, J.J.; Rietmeijer, F.J.M. The planetary sample suite and environments of origin. In *Planetary Materials, Revs. Mineral.* 36. Papike, J.J., Ed. The Mineralogical Society of America, Washington, DC, 1998, 1–1–1.28.
- [11] Rietmeijer, F.J.M. Mixed layering in disordered Sri Lanka graphite. *Carbon* **1991**, *29*, 669–675.
- [12] Rietmeijer, F.J.M. Are crystalline C–(H–O–N) carbons the elusive meteoritic carbynes? *Meteoritics* **1993**, *28*, 242–245.
- [13] Bundy, F.P.; Bassett, W.A.; Weathers, M.S.; Hemley, R.J.; Mao, H.K.; Goncharov, A.F. The pressure–temperature phase diagram and transformation diagram for carbon: Updated through 1994. *Carbon* **1996**, *34*, 141–153.
- [14] Whittaker, A.G.; Wolten, G.M. Carbon: A suggested new hexagonal crystal form. *Science* **1972**, *178*, 54–56.
- [15] Nelson, L.S.; Whittaker, A.G.; Tooper, B. The formation of new polymorphs of carbon and fluid flow patterns by irradiating solid carbons with a CO₂ laser. *High Temp. Sci.* **1972**, *4*, 445–477.
- [16] Setaka, N.; Sekikawa, Y. Chaoite, a new allotropic form of carbon, produce by shock compression. *J. Am. Ceram. Soc.* **1980**, *63*, 238–239.
- [17] Sokolowska, A.; Olszyna, A. Decomposition of hydrocarbons. In *Carbyne and Carbynoid Structures*. Heimann, R.B.; Evsyukov, S.E.; Kavan, L., Eds. Kluwer Academic Publishers, Dordrecht, Boston, London, 1999, 117–131.
- [18] Vdovkin, G.P. Ureilites. *Space Sci. Revs* **1970**, *10*, 483–510.
- [19] Kasatochkin, V.I.; Korshak, V.V.; Kudryavtsev, Yu.P.; Sladkov, A.M.; Sterenberg, I.E. On crystalline structure of carbyne. *Carbon* **1973**, *11*, 70–72.
- [20] Gilkes, K.W.R.; Pillinger, C.T. Carbon — How many allotropes associated with meteorites and impact phenomena? In *Carbyne and Carbynoid Structures*. Heimann, R.B.; Evsyukov, S.E.; Kavan, L., Eds. Kluwer Academic Publishers, Dordrecht, Boston, London, 1999, 17–30.
- [21] Whittaker, A.G.; Watts, E.J.; Lewis, R.S.; Anders, E. Carbynes: Carriers of primordial noble gases in meteorites. *Science* **1980**, *209*, 1512–1514.
- [22] El Goresy, A.; Donnay, G. A new allotropic form of carbon from the Ries Crater. *Science* **1968**, *161*, 363–364.

- [23] Whittaker, A.G. Carbon: Occurrences of carbyne forms of carbon in natural graphite. *Carbon* **1979**, 17, 21–24.
- [24] Heimann, R.B.; Kleiman, J.; Salansky, N.M. Structural aspects and conformation of linear carbon polytypes (carbynes). *Carbon* **1984**, 22, 147–155.
- [25] Heimann, R.B. The nature of carbyne-pros and cons. In *Carbyne and Carbynoid Structures*. Heimann, R.B.; Evsyukov, S.E.; Kavan, L., Eds. Kluwer Academic Publishers, Dordrecht, Boston, London, 1999, 7–15.
- [26] Bundy, F.P. The P,T phase and reaction diagram for elemental carbon, 1979. *J. Geophys. Res.* **1980**, 85(B12), 6930–6936.
- [27] Whittaker, A.G. Carbon: A new view of its high-temperature behavior. *Science* **1978**, 200, 763.
- [28] Kleiman, J.; Heimann, R.B.; Hawken, D.; Salansky, N.M. Shock compression and flash heating of graphite/metal mixtures at temperatures up to 3200 K and pressures up to 25 GPa. *J. Appl. Phys.* **1984**, 56, 1440–1454.
- [29] Jayaraman, A.; Chen, L.W. Phase diagrams in high-pressure research. In *Phase Diagrams, Materials Science and Technology*, v6-1. Alper, A.M., Ed. Academic Press, New York, London, 1970, 245–293.
- [30] Rietmeijer, F.J.M.; Karner, J.M. Metastable eutectics in the Al_2O_3 – SiO_2 system explored by vapor phase condensation. *J. Chem. Phys.* **1999**, 110, 4554–4558.
- [31] Rietmeijer, F.J.M.; Nuth, III, J.A.; Karner, J.M. Metastable eutectic gas to solid condensation in the FeO – Fe_2O_3 – SiO_2 system. *Phys. Chem. Chem. Phys.* **1999**, 1, 1511–1516.
- [32] Rietmeijer, F.J.M.; Nuth, III, J.A.; Karner, J.M. Metastable eutectic condensation in a Mg – Fe – SiO – H_2 – O_2 vapor: Analogs to circumstellar dust. *Astrophys. J.* **1999**, 527, 395–404.
- [33] Rietmeijer, F.J.M.; Nuth, III, J.A.; Karner, J.M.; Hallenbeck, S.L. Gas to solid condensation in a Mg – SiO – H_2 – O_2 vapor: Metastable eutectics in the MgO – SiO_2 phase diagram. *Phys. Chem. Chem. Phys.* **2002**, 4, 546–551.
- [34] Nuth, III, J.A.; Hallenbeck, S.L.; Rietmeijer, F.J.M. Laboratory studies of silicate smokes: Analog studies of circumstellar materials. *J. Geophys. Res.* **2000**, 105(A5), 10,387–10,396.
- [35] Wahlbeck, P.G.; Gilles, P.W. Reinvestigation of the phase diagram for the system titanium-oxygen. *J. Am. Ceram. Soc.* **1966**, 49, 180–183.
- [36] DeVries, R.C.; Roy, R. A phase diagram for the system Ti – TiO_2 constructed from data in the literature. *Am. Ceram. Soc. Bull.* **1954**, 33, 370–372.
- [37] Highmore, R.J.; Greer, A.L. Eutectics and the formation of amorphous alloys. *Nature* **1989**, 339, 363–365.
- [38] Aasland, S.; McMillan, P.F. Density-driven liquid–liquid phase separation in the system Al_2O_3 – Y_2O_3 . *Nature* **1994**, 369, 633–636.
- [39] Tallon, J.L. A hierarchy of catastrophes as a succession of stability limits for the crystalline state. *Nature* **1989**, 342, 658–660.
- [40] Fecht, H.J. Defect-induced melting and solid-state amorphization. *Nature* **1992**, 356, 133–135.
- [41] Richet, P. Superheating, melting and vitrification through decompression of high-pressure minerals. *Nature* **1988**, 331, 56–58.
- [42] Mittlefehldt, D.W.; McCoy, T.J.; Goodrich, C.A.; Kracher, A. Non-chondritic meteorites from asteroidal bodies. In *Planetary Materials, Revs. Mineral.* 36. Papike, J.J., Ed. The Mineralogical Society of America, Washington, DC, 1998, 4-1–4-195.

- [43] Vdovykin, G.P. Forms of carbon in the new Haverö ureilite of Finland. *Meteoritics* **1972**, 7, 547–552.
- [44] Nakamuta, Y.; Aoki, Y. Mineralogical evidence for the origin of diamond in ureilites. *Meteoritics Planet. Sci.* **2000**, 35, 487–493.
- [45] Whittaker, A.G.; Kintner, P.L. Carbon: Analysis of spherules and splats formed from the liquid state and of the forms produced by quenching gas and solid. *Carbon* **1985**, 23, 255–262.
- [46] Stöffler, D.; Bischoff, A.; Buchwald, V.; Rubin, A.E. Shock effects in meteorites. In *Meteorites and the Early Solar System*. Kerridge, J.F.; Matthews, M.S., Eds. The University of Arizona Press, Tucson, 1988, 165–202.
- [47] Schultz, P.H. Effect of impact angle on vaporization. *J. Geophys. Res.* **1996**, 101(E9), 21,117–21,136.
- [48] Sugita, S.; Schultz, P.H. Spectroscopic characterization of hypervelocity jetting: Comparison with standard theory. *J. Geophys. Res.* **1999**, 104(E12), 30,825–30,845.
- [49] van der Bogert, C.H.; Schultz, P.H.; Spray, J.G. Experimental frictional heating of dolomitic marble: New insights for Martian meteorite Allan Hills 84001 (abstract). *Lunar Planet. Sci.* **1999**, XXX, CD-ROM #1970, Lunar and Planetary Institute, Houston (TX).
- [50] Rietmeijer, F.J.M.; Schultz, P.H.; Bunch, T.E. Carbon calabashes in a shock-produced carbon melt. *Chem. Phys. Lett.* **2003**, 374, 464–470.
- [51] Heimann, R.B.; Kleiman, J.; Salansky, N.M. A unified structural approach to linear carbon polytypes. *Nature* **1983**, 306, 164–167.
- [52] Skinner, B.J. Thermal Expansion. In *Handbook of Physical Constants — revised edition*. Geol. Soc. Am. Memoir 97, Clark, Jr., S.P., Ed. Geological Society of America Inc., New York, 1966, 75–96.
- [53] Birch, F. Compressibility; elastic constants. In *Handbook of Physical Constants — revised edition*. Geol. Soc. Am. Memoir 97, Clark, Jr., S.P., Ed. Geological Society of America Inc., New York, 1966, 97–173.
- [54] Bundy, F.P.; Kasper, J.S. Hexagonal diamond — A new form of carbon. *J. Chem. Phys.* **1967**, 46, 3437–3446.
- [55] Sekine, T.; Akaishi, M.; Setaka, N.; Kondo, K. Diamond synthesis by weak shock loading. *J. Materials Sci.* **1987**, 22, 3615–3619.
- [56] England, P.; Molnar, P. The interpretation of inverted metamorphic isograds using simple physical calculations. *Tectonics* **1993**, 12, 145–158.
- [57] Graham C.M.; England, P.C. Thermal regimes and regional metamorphism in the vicinity of overthrust faults: An example of shear heating and inverted metamorphic zonation from Southern California. *Earth Planet. Sci. Lett.* **1976**, 31, 142–152.
- [58] Ross, J.V.; Bustin, R.M. The role of strain energy in creep graphitization of anthracite. *Nature* **1990**, 343, 58–60.
- [59] Whittaker, A.G.; Kintner, P.L. Carbon: Observation on the new allotropic form. *Science* **1969**, 165, 589–591.
- [60] Smith, P.P.K.; Buseck, P.R. Carbon in the Allende meteorite: Evidence for poorly graphitized carbon rather than carbyne. *Proc. Lunar Planet. Sci.* **1981**, 12B, 1167–1175.
- [61] Flynn, G.J.; Keller, L.P.; Feser, M.; Wirick, S.; Jacobsen, C. The origin of organic matter in the solar system: Evidence from the interplanetary dust particles. *Geochim. Cosmochim. Acta* **2003**, 67, 4791–4806.

- [62] Smith, P.P.K.; Buseck, P.R. Carbyne forms of carbon: Do they exist? *Science* **1982**, *216*, 984–986.
- [63] Lumpkin, G.R. Electron microscopy of carbonaceous matter in Allende acid residues. *Proc. Lunar Planet. Sci.* **1981**, *12B*, 1153–1166.
- [64] Seal, M. Graphitization of diamond. *Nature* **1960**, *185*, 522–523.
- [65] Raal, F.A. Alleged formation of an intermediate diamond structure on heating diamond. *Nature* **1960**, *185*, 523.
- [66] Udod, I.A. Carbyne intercalation compounds. In *Carbyne and Carbynoid Structures*. Heimann, R.B.; Evsyukov, S.E.; Kavan, L., Eds. Kluwer Academic Publishers, Dordrecht, Boston, London, 1999, 269–294.
- [67] Fitzgerald, A.G. Electron diffraction and microscopy. In *Carbyne and Carbynoid Structures*. Heimann, R.B.; Evsyukov, S.E.; Kavan, L., Eds. Kluwer Academic Publishers, Dordrecht, Boston, London, 1999, 195–308.
- [68] Heimann, R.B. Diamond synthesis from carbyne. In *Carbyne and Carbynoid Structures*. Heimann, R.B.; Evsyukov, S.E.; Kavan, L., Eds. Kluwer Academic Publishers, Dordrecht, Boston, London, 1999, 409–425.
- [69] Brearley, A.J.; Jones, R.H. Condritic meteorites. In *Planetary Materials*. Revs. Mineral. 36, Papike, J.J., Ed. The Mineralogical Society of America, Washington, DC, 1998, 3-1–3-398.
- [70] Bell, J.F.; Davis, D.R.; Hartmann, W.K.; Gaffey, M.J. Asteroids: The big picture. In *Asteroids II*. Binzel, R.P.; Gehrels, T.; Matthews, M.S., Eds. The University of Arizona Press, Tucson, 1989, 921–945.
- [71] Jones, R.H.; Lee, T.; Connolly, Jr., H.C.; Love, S.G.; Shang, H. Formation of chondrules and CAIs: Theory vs. observation. In *Protostars and Planets IV*. Mannings, V.; Boss, A.P.; Russell, S.S., Eds. The University of Arizona Press, Tucson, 2000, 927–962.
- [72] Brearley, A.J. Origin of graphitic carbon and pentlandite in matrix olivines in the Allende meteorite. *Science* **1999**, *285*, 1380–1382.
- [73] McSween, H.Y., Jr. Petrographic variations among carbonaceous chondrites of the Vigarano type. *Geochim. Cosmochim. Acta* **1977**, *41*, 1777–1790.
- [74] Whittaker, A.G.; Neudorffer, M.E.; Watts, E.J. Carbon: a rhombohedral carbyne form. *Carbon* **1983**, *21*, 597–599.
- [75] Dai, Z.R.; Bradley, J.P.; Joswiak, D.; Brownlee, D.E.; Hill, H.G.M.; Genge, M.M. Possible *in situ* formation of meteoritic nanodiamonds in the early solar system. *Nature* **2002**, *418*, 157–159.
- [76] Rietmeijer, F.J.M.; Rotundi, A.; Heymann, D. C₆₀ and giant fullerenes in soot condensed in vapors with variable C/H₂ ratio. *Full., Nanotubes, Carb. Nanostructures* **2004**, *12*, 659–680.
- [77] Casari, C.S.; Li Bassi, A.; Ravagnan, L.; Siviero, F.; Lenardi, C.; Piseri, P.; Bongiorno, G.; Bottani, C.E.; Milani, P. Chemical and thermal stability of carbyne-like structures in cluster-assembled carbon films. *Phys. Rev.* **2004**, *B69*, 075422.
- [78] Ravagnan, L.; Siviero, F.; Lenardi, C.; Piseri, P.; Barborini, E.; Milani, P.; Casari, C.S.; Li Bassi, A.; Bottani, C.E. Cluster-beam deposition and *in situ* characterization of carbyne-rich carbon films. *Phys. Rev. Lett.* **2002**, *89*, 285506(1-4).
- [79] Nuth, III, J.A.; Hallenbeck, S.L.; Rietmeijer, F.J.M. Interstellar and interplanetary grains. Recent developments and new opportunities for experimental chemistry. *Earth, Moon, Planets* **1998**, *80*, 73–112.

- [80] Hayatsu, R.; Scott, R.G.; Studier, M.H.; Lewis, R.S.; Anders, E. Carbynes in meteorites: Detection, low-temperature origin, and implications for interstellar molecules. *Science* **1980**, *209*, 1515–1518.
- [81] Rietmeijer, F.J.M. Interrelationships among meteoric metals, meteors, interplanetary dust, micrometeorites, and meteorites. *Meteoritics Planet. Sci.* **2000**, *35*, 1025–1041.
- [82] Rietmeijer, F.J.M. The earliest chemical dust evolution in the solar nebula. *Chemie der Erde* **2002**, *62*, 1–45.
- [83] Rietmeijer, F.J.M. Interplanetary dust particles. In *McGraw-Hill Yearbook of Science & Technology 2001*. The McGraw-Hill Companies Inc., 2000, 208–211.
- [84] Rietmeijer, F.J.M.; Nuth, III, J.A. Collected extraterrestrial materials: Constraints on meteor and fireball compositions. *Earth, Moon, Planets* **2000**, *82/83*, 325–350.
- [85] Rietmeijer, F.J.M.; Mackinnon, I.D.R. Cometary evolution: Clues from chondritic interplanetary dust particles. In *Symposium on the Diversity and Similarity of Comets, European Space Agency SP-278*. Rolfe E.J.; Battrick, B., Eds. ESTEC, Noordwijk, The Netherlands, 1987, 363–367.
- [86] Mackinnon, I.D.R.; Rietmeijer, F.J.M. Mineralogy of chondritic interplanetary dust particles. *Revs. Geophys.* **1987**, *25*, 1527–1553.
- [87] Lawler, M.E.; Brownlee, D.E. CHON as a component of dust from comet Halley. *Nature* **1992**, *359*, 810–812.
- [88] A'Hearn, M.F.; Millis, R.C.; Schleicher, D.O.; Osip, D.J.; Birch, P.V. The ensemble properties of comets: Results from narrowband photometry of 85 Comets, 1976–1992. *Icarus* **1995**, *118*, 223–270.
- [89] Schleicher, D.G.; Lederer, S.M.; Millis, R.L.; Farnham, T.L. Photometric behavior of Comet Hale-Bopp (C/1995 O1) before perihelion. *Science* **1997**, *275*, 1913–1915.
- [90] Schleicher, D.G.; Millis, R.L. Results from narrowband photometry of ROSETTA's new target Comet 67P/Churyumov-Gerasimenko. DPS 35th Meeting, **2003**, on-line abstract.
- [91] Farnham, T.L.; Schleicher, D.G.; Woodney, L.M.; Birch, P.V.; Eberhardy, C.A.; Levy, L. Imaging and photometry of Comet C/1999 S4 (LINEAR) before perihelion and after breakup. *Science* **2001**, *292*, 1348–1353.
- [92] Heimann, R.B. Resistive heating and laser irradiation. In *Carbyne and Carbynoid Structures*. Heimann, R.B.; Evsyukov, S.E.; Kavan, L., Eds. Kluwer Academic Publishers, Dordrecht, Boston, London, 1999, 139–148.
- [93] Cataldo, F.; Keheyan, Y. Generation of higher fullerenes from laser ablation of carbyne and C₆₀ photopolymer astrophysical implications. *Full. Nanotubes Carb. Nanostructures* **2002**, *10*, 99–106.
- [94] Yeretzian, C.; Hansen, K.; Diederich, F.; Whetten, R.L. Coalescence reactions of fullerenes. *Nature* **1992**, *359*, 44–47.
- [95] Li, S-Y.; Zhou, H-H.; Gu, J-L.; Zhu, J. Does carbyne really exist? Carbynes in expanded graphite. *Carbon* **2000**, *38*, 934–937.
- [96] Spitsina, N.G.; Boiko, G.N.; Kudryavisev, Yu. P.; Babuev, V.G.; Guseva, M.B.; Evsyukov, S.E. Concerning the existence of linear carbon molecules in soot obtained in an electric arc. *Russian Chem. Bull.* **1995**, *44*, 1339–1341.
- [97] Cataldo, F. An investigation of the optical properties of carbon black, fullerite, and other carbonaceous materials in relation to the spectrum of interstellar extinction of light. *Full. Nanotubes Carb. Nanostructures* **2002**, *10*, 155–170.

- [98] Hinkle, K.H.; Keady, J.J.; Bernath, P.F. Detection of C₃ in the circumstellar shell of IRC+10216. *Science* **1988**, *241*, 1319–1322.
- [99] Bernath, P.F.; Hinkle, K.H.; Keady, J.J. Detection of C₅ in the circumstellar shell of IRC+10216. *Science* **1989**, *244*, 562–564.
- [100] Cherchneff, I.M.; Glassgold, A.E.; Mamon, G.A. The formation of cyano-polyne molecules in IRC+10216. *Astrophys. J.* **1993**, *410*, 188–201.
- [101] Cherchneff, I.M.; Glassgold, A.E. The formation of carbon chain molecules in IRC+10216. *Astrophys. J.* **1993**, *419*, L41–L44.
- [102] Williams, D.A. Recent developments in astrochemistry. In *AIP Conf. Proc.* **312**, Nenner, I., Ed. Am. Inst. Physics, New York, New York, 1994, 3–23.
- [103] Pascoli G.; Polleux, A. Condensation and growth of hydrogenated carbon clusters in carbon-rich stars. *Astron. Astrophys.* **2000**, *359*, 799–810.
- [104] Cernicharo, J.; Goicoechea, J.R.; Caux, E. Far-infrared detection of C₃ in Sagittarius B2 and IRC +10216. *Astrophys. J.* **2000**, *534*, L199.
- [105] Maier, J.P.; Walker, G.A.H.; Bohlender, D.A. On the possible role of carbon chains as carriers of diffuse interstellar bands. *Astrophys. J.* **2004**, *602*, 286–290.
- [106] Allamandola, L.J.; Hudgins, D.M.; Bauschlicher Jr., C.W.; Langhoff, S.R. Carbon chain abundance in the diffuse interstellar medium. *Astron. Astrophys.* **1999**, *352*, 659–664.
- [107] Freed, K.F.; Oka, T.; Suzuki, H. On the *n*-dependence of the reaction rate for C+ + C/*n*/yields C+/*n* + 1/ in interstellar space. *Astrophys. J.* **1982**, *263*, 718–722.
- [108] Leung, C.M.; Herbst, E.; Huebner, W.F. Synthesis of complex molecules in dense interstellar clouds via gas-phase chemistry — A pseudo time-dependent calculation, *Astrophys. J. Suppl.* **1984**, *56*, 231–256.
- [109] Duley, W.W.; Williams, D.A. Interstellar polyynes from the disruption of carbon grains. *Monthly Note Royal Astron. Soc.* **1984**, *211*, 97–103.
- [110] Tielens, A.G.G.M.; Allamandola, L.J. Evolution of interstellar dust. In *Physical Processes in Interstellar Clouds*. Morfill, G.E.; Scholer, M., Eds. D. Reidel Publishing Company, 1987, 333–375.
- [111] Jones A.P.; Tielens, A.G.G.M.; Hollenbach, D.J.; McKee, C.F. The shattering of grains in the interstellar shock waves. *Am. Astron. Soc* **1994**, 1355 (abstract).
- [112] Nemoitin M.A.; Fridlyand, M.G.; Shipove, G.S. Some features of the X-ray diffraction patterns of graphite produced in an arc discharge and containing a carbene phase. *High Energy Chemistry* **1979**, *13*, 244–245.

17 Structures and Other Properties of Polyynes and their Isomers: Theoretical and Experimental Results

Dieter Heymann and Franco Cataldo

CONTENTS

17.1	Introduction	372
17.2	C ₂ H ₂ Isomers	374
17.2.1	Introduction	374
17.2.2	Vibrational, UV, and Rotational Data	374
17.2.3	Isomerization	376
17.3	C ₃ H ₂ Isomers	377
17.3.1	Introduction	377
17.3.2	Vibrational Data	378
17.3.3	Structure of 3OI(t)	379
17.3.4	Electronic Spectra	381
17.3.5	Rotational Data and Isomerization	384
17.4	C ₄ H ₂ Isomers	384
17.4.1	Introduction	384
17.4.2	Energies and Dipole Moments of the Open Molecules	384
17.4.3	Vibrational Data	385
17.4.4	Electronic Spectra	387
17.4.5	Rotational Data	388
17.5	C ₅ H ₂ Isomers	389
17.5.1	Introduction	389
17.5.2	Comments	390
17.5.3	Electronic Spectra and Rotational Data	390

17.6	C_6H_2 Isomers.....	391
17.6.1	Introduction	391
17.6.2	Comment.....	395
17.6.3	Electronic Spectra and Rotational Data	395
17.7	C_7H_2 Isomers.....	396
17.7.1	Introduction	396
17.7.2	Relative Energies, Zero Point Vibrational Energies and Dipole Moments of the C_7H_2 Molecules	401
17.7.3	Vibrational Frequencies, Electronic Spectra, and Rotational Data	402
17.8	Isomers of C_8H_2 , $C_{10}H_2$, $C_{12}H_2$, $C_{14}H_2$, and $C_{16}H_2$	403
17.8.1	Isomers of C_8H_2	403
17.8.1.1	Vibrational Data	404
17.8.1.2	Electronic Spectra and Rotational Data	405
17.8.2	Isomers of $C_{10}H_2$	405
17.8.2.1	Vibrational Data, Electronic Spectra, and Rotational Data.....	405
17.8.3	Isomers of $C_{12}H_2$	406
17.8.4	Isomers of $C_{14}H_2$ and $C_{16}H_2$	408
17.9	Isomers of C_9H_2 , $C_{11}H_2$, $C_{13}H_2$, and $C_{15}H_2$	408
17.10	Summary	410
	References	414
Appendix 17.1	Constructs of All Molecules Presented in this Chapter.....	422
Appendix 17.2	Calculations Carried out for this Chapter Using the Spartan 02 and 04 Programs.....	423

17.1 INTRODUCTION

Astrochemists can only deduce the presence of a specific molecule in the environment of interest from that molecule's absorption or emission of electromagnetic radiation. This belief has resulted in a long-standing collaboration of astronomers, astrophysicists, and chemists to develop libraries of electromagnetic frequencies at which specific molecules might be detected in nature. In this paper we bring together experimental and theoretical data for polyyynes, the linear organic molecules of the general formula $H(CC)_mH$ ($m=2,4,\dots$), some of which have been detected in circumstellar media, interstellar media, planetary atmospheres, and cometary tails. The interest in polyyynes has also been greatly increased by the recent discovery by Cataldo [1,2] that certain of these molecules can be easily synthesized in an electrical arc discharge between graphite electrodes submerged in various solvents and can be subsequently purified by high-performance liquid chromatography. Although C_mH_2 molecules with m =odd numbered are

not considered to be polyynes, we shall include these in this paper as well as acetylene $\text{HC}\equiv\text{CH}$ because several of these molecules are chemically interesting and have been observed in astronomical environments.

All of these molecules have at least one structural isomer. Arguably the best-known examples are vinylidene (H_2CC) and acetylene (HCCH). Many investigators have studied the mean lifetime of vinylidene, either experimentally or theoretically. Some have concluded that its lifetime is essentially zero, but the most recent studies suggest a much longer lifetime of a few microseconds [3–5]. The number of possible isomers increases greatly with increasing number of carbon atoms of the molecule. Many of these isomers, whether short- or long-lived, are very important because they are highly reactive and may well form, even if only transiently, in chemically active but non-equilibrium carbon and hydrogen-rich natural environments, as Sattelmeyer and Stanton have stressed [6].

Throughout this paper we shall use the term “construct” for any “on paper” bonding arrangement of carbon and hydrogen atoms before treatment with quantum chemical calculations. The term “molecule” is reserved for entities with true energy minima on potential energy surfaces. The term “intermediary” refers to entities with one imaginary vibrational frequency, but computational results with imaginary vibrational frequencies are not reported.

One practical problem facing us was the realization that the number of constructs increases swiftly with increasing number of carbon atoms. C_2H_2 has two constructs; C_3H_2 has six, C_4H_2 eighteen, C_5H_2 forty-nine, counting all unbranched and branched, open as well as cyclical carbon constructs. To illustrate the great variety of resulting molecules we have treated all possible C_mH_2 constructs for $m=2, 3, 4$, and 5 but report data only for molecules that have true energy minima on potential energy surfaces. Beginning with C_6H_2 , we list only molecules reported in the literature and, for our own calculations, a much more restricted set of constructs than for $m=2-5$. For C_8H_2 through C_{16}H_2 we report only the linear HC_mH molecules.

A second practical problem arose from the realization that the molecules of this paper can, in principle, occur in nature and the laboratory in their electronic ground states, in vibrationally and electronically excited states, and as ions. In this paper we report only electronic ground state properties of electrically neutral molecules.

Also, for practical reasons, we have restricted the range of properties reported for all molecules to (a) the energy difference of that molecule with the energy of the isomer having the lowest energy, (b) the dipole moment, (c) the zero point vibrational energy, (d) fundamental vibrational frequencies, (e) infrared intensities, (f) selected values of UV absorption maxima, and (g) rotational lines and constants. Actual values will be listed for properties (a) through (f). However, because the molecules with increasing number of carbon atoms have many IR lines with low intensities, we will only report the three strongest lines beginning with C_8H_2 . Because lists of

rotational data are also usually very lengthy, only literature references will be given.

Acetylene and vinylidene are names that are easily remembered but the names of the various isomers of larger polyyynes are generally long and complicated. For example, the isomers of C_3H_2 are named propargylene, cycloproperylidene, vinylidenecarbene, and cyclopropyne, and that is only a beginning. Seburg et al. [7], in mock despair and probably with tongue in cheek, have proposed to rename 3-(didehydrovinylidene)cyclopropene, a C_5H_2 isomer, to “eiffelene” because its structure resembles that of the famous Parisian landmark. Most authors have therefore used numbered pictures of the molecules in their papers and have referred to these molecules in the text by numbers. We use a slightly more detailed system in which we recognize two clans of molecules. The first is that of “open” molecules, denoted by “O”, in which $n - 1$ is the number of bonds between n carbon atoms. The second clan, denoted by “C”, is that of “cyclical” or “closed” molecules in which the number of bonds between n carbon atoms is n or greater depending on whether the molecule is monocyclic or polycyclic. The “C-clan” also includes ring-chain molecules. We name a given molecule $mXn(y)$. The number m is equal to the number of carbon atoms in the molecule and n is a sequential number. X can be either O or C. Y can be either s (for singlet) or t (for triplet). For example, acetylene in the ground state would be 2O1(s) and vinylidene 2O2(s). In Appendix 17.1 we present the constructs of all molecules reported in this paper. The reader can copy these pages and use these while perusing the text.

The sources for all listed properties are either experimental observations or theoretical computations. We do not include results from semi-empirical calculations. For experimental and computational details of literature values the reader must check the original publications. Details for calculations done by us for this chapter with methods of Spartan-02 and -04 (Wavefunction, Inc., Irvine, CA, USA) are given in Appendix 17.2.

17.2 C_2H_2 ISOMERS

17.2.1 INTRODUCTION

The isomers of C_2H_2 are 2O1(s), acetylene and 2O2(s), vinylidene. Both have singlet ground states. A third isomer was reported to have appeared in a theoretical calculation, but, it turned out to have been a computational artifact [8]. Table 17.1 presents relative self consistent field (SCF) energies, zero point vibrational energies (ZPVE), and dipole moments of the isomers.

17.2.2 VIBRATIONAL, UV, AND ROTATIONAL DATA

The properties of 2O1(s) have been reported in numerous papers and monographs. A complete review of these is outside the scope of our work.

TABLE 17.1
Relative SCF Energies, Zero Point Vibrational Energies (ZPVE), and Dipole Moments of 2O1(s) and 2O2(s)

Data	2O1(s)	2O2(s)	Reference
$\Delta\text{ESCF (kJ mol}^{-1}\text{)}$	0.00	184.1	[9]
$\Delta\text{ESCF (kJ mol}^{-1}\text{)}$	0.00	179.7	[10]
$\Delta\text{ESCF (kJ mol}^{-1}\text{)}$	0.00	184.9	[8]
$\Delta\text{ESCF (kJ mol}^{-1}\text{)}$	0.00	183.7 ± 2.1	[11]
$\Delta\text{ESCF (kJ mol}^{-1}\text{)}$	0.00	~ 180	[12]
$\Delta\text{ESCF (kJ mol}^{-1}\text{)}$	0.00	194.1 ± 23	[13,14]
$\Delta\text{ESCF (kJ mol}^{-1}\text{)}$	0.00	198.3 ± 16.7	[15]
$\Delta\text{ESCF (kJ mol}^{-1}\text{)}$	0.00	181	This work
ZPVE (kJ mol ⁻¹)	69.53	62.01	This work
Dipole (debye)	0.00	2.30	[16]
Dipole (debye)	0.00	2.40	This work

Note: Fan and Pfeiffer [17] have reported calculated total energies for 2O1(s).

TABLE 17.2
Fundamental Vibrational Frequencies of 2O1(s)

F1	F2	F3	F4	F5	F6	F7	Reference
3372.83	3282.50	1973.98	730.29	730.29	612.88	612.88	[19]
3374	3289	1974	730	730	612	612	[20]
3325	3225	2009	788	788	709	709	[21]
3512	3409	2069	757	757	561	561	This work
[0]R	[69]R	[0]R	[101]R	[101]R	[0]R	[0]R	–

We refer the reader to an excellent compilation [18]. In Table 17.2 we reprint the observed fundamental frequencies of gaseous 2O1(s) from that work and report our calculated values. Frequencies entered for the same reference always represent replicate measurements of the same vibrational motion. In this and all subsequent tables, frequency values are never bracketed and are always given in units of cm⁻¹. Data printed in bold characters are experimental results. IR intensities are in [·], {·}, or (·) brackets. Values in [·] are IR intensities in km mol⁻¹. Values in {·} are relative intensities. Values in (·) are in other units as explained in the notes of tables. Intensity values followed by R mean that the vibrational mode is Raman active.

TABLE 17.3
Fundamental Vibrational Frequencies of 2O2(s)

F1	F2	F3	F4	F5	F6	Reference
3050 ^a	3025 ± 30	1635 ± 10	1165 ± 10	835 ^a	320 ^a	[13]
—	—	1650 ± 120	1120 ± 100	—	—	[15]
3391	3301	1837	1363	928	559	[13]
3312	3217	1719	1289	800	422	[13]
3325	3225	2009	—	788	709	[21]
—	3133	1671	1205	809	473	[4]
3192	3117	1709	1228	741	382	This work
[13]R	[37]R	[87]R	[26]R	[96]R	[4.2]R	—

^a = Estimates for unobserved transitions from Franck–Condon simulations.

The near-ultraviolet absorption of 2O1(s) begins just below 250 nm and increases strongly down-wavelength until about 210 nm, where a strong band system of the vacuum UV begins to dominate the absorption. Details of the UV absorption spectrum as well as rotational constants of 2O1(s) can be found in Miller [18].

Much less is known about the short-lived and very reactive 2O2(s) molecule. Its existence was established experimentally [13,14,22] and several of its fundamental vibrational frequencies were determined [13,15] (Table 17.3.)

17.2.3 ISOMERIZATION

Numerous studies were devoted to the vinylidene to acetylene isomerization [3–5,8–10,22–35]. They deal with the energy barrier of the isomerization, hence with the mean lifetime of 2O2(s). In Table 17.4 we list the reported barrier energies, energy of isomerization, and lifetimes of 2O2(s) and one case of the lifetime of 2O2(t), a triplet state of vinylidene. Notice the huge range of the reported ground state-to-ground state lifetimes: from 10^{-14} to 10^{-6} s. Although the longer lifetime seems to be favored now, this issue needs more study before any lifetime value can be definitely accepted. Significant amounts of 2O2(s) can only be expected to survive in environments in which 2O1(s) is exposed to electromagnetic radiation and/or electron and H or H⁺ collisions to produce vinylidene in the triplet excited state. Because of the highly reactive chemical nature of 2O2(s), this species could be a very important participant in the formation of polycyclic aromatic hydrocarbons (PAHs) and other C-bearing substances in natural environments.

TABLE 17.4

Experimental and Calculated Barrier Values and Mean Lifetimes of the Isomerization 2O2(s) to 2O1(s)

Barrier, Experimental (kJ mol ⁻¹)	Barrier, Calculated (kJ mol ⁻¹)	Lifetime, Experimental (s)	Lifetime, Calculated (s)	Reference
—	11.7	—	—	[9]
—	5.9–8.6	—	from 2.9×10^{-14}	[4]
—	—	—	to 8.8×10^{-10}	—
—	—	$> 1 \times 10^{-12}$	—	[5]
—	—	3.5×10^{-6}	—	[3]
—	6.3	—	—	[10]
—	11	—	—	[8]
—	9.03 ± 2.1	—	—	[11]
—	~ 12	—	—	[12]
—	8.4–16.8	$0.24\text{--}4.6 \times 10^{-12}$	—	[32]
~ 8.5	—	4×10^{-14} to 2×10^{-13}	—	[13–15]
—	3.8	—	—	[34]
—	$\sim 230^a$	—	—	[35]
—	33.5	—	—	[36]

^aFrom the triplet state.

17.3 C₃H₂ ISOMERS

17.3.1 INTRODUCTION

Isomers of C₃H₂ are of great interest because of their unique chemical properties and because at least two of these are known to occur abundantly in interstellar molecular clouds [37–42]. Several investigators have studied properties of C₃H₂ isomers both experimentally and theoretically (references in remainder of text). Three isomers have been synthesized, namely triplet propenylidene (also known as propargylene) 3O1(t), singlet cyclopropenylidene 3C1(s), and singlet propadienylidene (also known as vinylidenecarbene) 3O2(s) [43–45]. Theoretical calculations have shown that a fourth isomer triplet, *trans*-propenediylidene 3O3(t) (*trans* with regards to the hydrogen atoms), has a true minimum energy on the C₃H₂ potential surface but it is much less stable than the other isomers [46]. Several investigators have studied cyclopropyne, the cyclical C₃H₂ molecule with both hydrogen atoms bonded to the same carbon atom of the ring [43–50]. However, neither a singlet, nor a triplet ground state of cyclopropyne has a true minimum energy on the C₃H₂ potential. A fourth open construct with both

hydrogen atoms bonded to the central carbon atom also has two imaginary frequencies in the singlet ground state but none in the triplet ground state. The six possible constructs produce only four molecules on the potential energy surface of C_3H_2 .

There has been much debate about the symmetry of 3O1(t). Is its ground-state symmetry $D_{\infty h}$ or C_2 ? A consensus has emerged that the ground-state symmetry is “M-shaped C_2 ” (or “W-shaped” when one rotates the printed page 180°). Seburg and McMahon [51] have commented emphatically: “The conventional wisdom that ‘triplet acetylenic carbenes are linear’ is thus incorrect in the case of the parent system” (in this case C_3H_2). However, later in this section we shall present evidence which suggests a fluxional molecule involving both $D_{\infty h}$ and C_2 geometries.

Absolute values of SCF energies vary somewhat depending on the computational method used, hence will not be reported here. However, the energy difference between two isomers should be less method-dependent. Table 17.5 reports these ΔE_{SCF} values from various sources including our own data. Qualitatively, there is agreement among all results that isomer 3C1(s) has the lowest energy on the C_3H_2 potential surface and that 3O1(t), 3O2(s), and 3O3(t) are the next lowest in that order. The table also reports zero point vibrational energies (ZPVE), and dipole moments.

17.3.2 VIBRATIONAL DATA

Fundamental vibrational frequencies were measured or calculated by many investigators. We begin by reporting the data for 3O1(t) in Table 17.6. Entries from the literature are exact copies of data in references. When more than one set of values is entered for a given reference, the results had been obtained by various computational methods. The reader is referred to the original publications for details [7,51,60]. Here we report only the data for the configurations of lowest energies.

We now turn to the vibrational frequencies of 3O2(s), listed in Table 17.7. The vibrational spectrum of this isomer is obviously dominated by the CC stretches near 2000 cm^{-1} . Overall, the computed frequencies, especially the more recent data, are within a few percent of the experimentally observed values.

Next we report in Table 17.8 the vibrational frequencies of isomer 3O3(t). Only few results are available because this isomer has not been intensely studied. Hehre et al. [52] and Mebel et al. [65] have discussed the isomer but have not calculated its vibrational frequencies. There are significant differences between the results of Ochsenfeld et al. [46] and ours. We find that the CC stretch/scissor frequency is nearer 1300 cm^{-1} than 2000 cm^{-1} . Whereas the spectrum of Ochsenfeld et al. [46] is dominated by the intensity of the line at $\sim 650\text{ cm}^{-1}$, we find that the strongest line is at $\sim 750\text{ cm}^{-1}$ and that five other lines have intensities greater than 10 km mol^{-1} .

TABLE 17.5
Relative SCF Energies, Zero Point Vibrational Energies (ZPVE), and Dipole Moments

Data	3O1(t)	3O2(s)	3O3(t)	3C1(s)		Reference
ΔE_{SCF} (kJ mol ⁻¹)	—	—	—	—	0.00	All references below
ΔE_{SCF} (kJ mol ⁻¹)	—	—	72.0	—	—	[52]
ΔE_{SCF} (kJ mol ⁻¹)	—	93.3	60.7	—	—	[53]
ΔE_{SCF} (kJ mol ⁻¹)	—	96.2	70.7	—	—	[50]
—	94.0	54.8	—	—	—	—
—	54.4	54.8	—	—	—	—
—	36.8	51.9	—	—	—	—
—	94.1	59.4	—	—	—	—
—	54.0	59.4	—	—	—	—
—	36.4	56.5	—	—	—	—
—	22.3	60.7	—	—	—	—
ΔE_{SCF} (kJ mol ⁻¹)	—	58.6	60.0	—	—	[54]
—	33.0	42.2	—	—	—	—
—	26.8	31.4	—	—	—	—
ΔE_{SCF} (kJ mol ⁻¹)	—	0.0 ^a	134.9 ^a	250.8 ^a	—	[46]
ΔE_{SCF} (kJ mol ⁻¹)	—	38.9	44.8	289	—	[55]
ΔE_{SCF} (kJ mol ⁻¹)	—	32.7	45.63	578	—	This work
ZPVE (kJ mol ⁻¹)	—	68.02	81.17	68.11	84.03	This work
Dipole (debye)	—	4.29/4.19	—	—	—	[16]
Dipole (debye)	—	—	—	0.85 to 3.57	—	[49]
Dipole (debye)	0.7	4.1	—	3.4	—	[53]
Dipole (debye)	—	—	—	3.32	—	[56]
Dipole (debye)	—	—	—	3.07	—	[57]
Dipole (debye)	—	4.05 to 4.36	—	3.05 to 3.36	—	[58]
Dipole (debye)	—	—	—	3.27	—	[59]
Dipole (debye)	0.46	4.25	3.11	3.35	—	This work

^aComparison of triplet states only. E_{SCF} of 3C1(s): −115.378639 hartree (this work). Multiple entries were obtained by different computational methods. Fan and Pfeiffer [17] have reported calculated total energies for 3O1(t).

Table 17.9 presents the vibrational frequencies of 3C1(s), the most stable isomer with C₃H₂ composition.

17.3.3 STRUCTURE OF 3O1(t)

We digress to consider the issue of the symmetry of the ground state of 3O1(t). As mentioned above, the current “conventional wisdom” is that the point group of the ground state is C₂. In our calculations we found that both

TABLE 17.6
Fundamental Vibrational Frequencies of 3O1(t)

F1	F2	F3	F4	F5	F6	F7	F8	F9	Reference
–	3266.0	1619.4	–	547.3	401.5	402.6	–	245.9	[61]
3273	3257	1612	–	547	–	402	–	247	[51] ^a
{10}	{57}	{7}	–	{36}	–	{23}	–	{100}	–
3273	3257	1612	–	547	–	402	–	247	[60]
{10}	{57}	{7}	–	{36}	–	{23}	–	{100}	–
–	3265	1621	–	550	403	–	–	249	[54] ^b
–	{71}	{7}	–	{50}	{21}	–	–	{100}	–
3156	3153	1480	1081	510	379	348	337	278	[53]
3561	3452	1679	1226	575	561	477	389	343	[62]
(2599)	(654)	(2250)	(871)	(824)	(2201)	(681)	(739)	(1812)	–
3274.1	3265.3	1610.9	1074.8	547.9	–	401.9	302	245.9	[61]
3156	3153	1480	1081	510	380	348	338	278	[50]
[6.3]	[21.2]	[36.2]	[0.1]	[20.6]	[69.7]	[22.0]	[26.7]	[3.6]	–
3424	3410	1618	1244	502	425	423	361	297	[51] ^a
[18]	[29]	[29]	[0]	[33]	[7]	[24]	[20]	[103]	–
3424	3410	1618	1244	503	425	413	–	–	–
{1.00}	{1.71}	{1.67}	{0.01}	{1.91}	{0.43}	{1.43}	–	–	[60]
3538	3421	1663	1207	553	529	472	–	–	–
{3.38}	{0.97}	{3.09}	{1.16}	{1.31}	{3.08}	{0.96}	–	–	–
3524	3433	1637	1225	557	527	473	–	–	–
{3.40}	{0.98}	{3.16}	{1.06}	{1.15}	{3.29}	{0.95}	–	–	–
3416.7	3410.8	1622.6	1261.7	469.3	401.1	396.5	332.0	221.1	[46]
[6.0]	[57.6]	[16.2]	[0.0]	[38.4]	[21.3]	[10.2]	[1.3]	[95.3]	–
3416.4	3409.8	1610.5	1257.4	450.3	398.8	391.8	324.5	215.2	–
[4.4]	[60.4]	[12.8]	[0.1]	[47.1]	[27.0]	[14.2]	[3.2]	[98.6]	–
3431	3422	1712	1280	426	424	339	193	145	This work
[2.6]R	[79]R	[6.3]R	[0.1]R	[4.7]R	[12]R	[89]R	[74]R	[0.2]R	–

Note: Values in (·) are IR intensities in cm^{−2} L mol^{−1}.

^aWe report data only for the isomer labeled 1a.

^bWe report data only for the isomer labeled 1.

the H-C-C angle α_1 and the C-C-C angle α_2 increased almost systematically with the number of basis functions of the density functional method used for the computation. Figure 17.1 shows the unmistakable trends towards 180° in both angles. Although this does not prove that there exists a “competing” stable energy state with D_{∞h} symmetry, the trend suggests that the energy difference between C₂ and D_{∞h} might be so small that 3O1(t) is a “fluxional” molecule with a considerably smaller dipole moment than 0.46 debye.

TABLE 17.7
Fundamental Vibrational Frequencies of 3O2(s)

F1	F2	F3	F4	F5	F6	F7	F8	F9	Reference
–	3059.6	1963.2	1449.3	–	1025.0	1004.8	–	–	[45]
–	{< 0.01}	{0.32}	{0.05}	–	{< 0.01}	{0.05}	–	–	–
–	3049.5	1952.2	1446.9	–	1004.8	999.5	–	–	–
–	{0.02}	{1.00}	{0.14}	–	{0.05}	{0.10}	–	–	–
–	3049.5^a	1952.0^a	1446.8^a	–	1003.0^a	992.2^a	–	–	[61]
–	–	1952	1446	–	–	1002	–	–	[54] ^b
–	–	{100}	{16}	–	–	{17}	–	–	–
3034	2959	1946	1448	1111	1038	1021	300	269	[53]
3382	3300	2204	1643	1251	1183	1210	340	337	[45]
(118)	(543)	(15776)	(494)	(40)	(172)	(926)	(294)	(10)	–
3389	3302	2188	1615	1247	1139	1164	339	303	–
(64)	(488)	(16700)	(534)	(15)	(172)	(781)	(122)	(17)	–
3304	3206	2075	1542	1152	1080	1051	262	225	–
(64)	(457)	(16970)	(310)	(5)	(160)	(772)	(126)	(15)	–
3035	2960	1946	1448	1111	1038	1021	301	269	[50]
[1.8]	[12.3]	[389.6]	[10.5]	[0.5]	[17.8]	[3.9]	[2.7]	[0.4]	–
3249.8	3137.5	2009.6	1495.9	1133.4	1014.1	1003.8	294.5	175.7	[63]
3210	3146	2019	1503	1125	1057	1049	276	240	[54] ^b
{0.2}	{5}	{248}	{11}	{2}	{3}	{19}	{1}	{3}	–
3240.6	3177.1	2066.3	1521.9	1154	1077.1	1070.6	291.1	271	[64]
3239.2	3176.7	2060.2	1250.1	1155.9	1074.5	1069	293.6	257.9	–
3211.4	3148	2019.4	1503.5	1124.9	1048.4	1056.6	275.3	239.5	–
3212	3123.2	1997.9	1495.2	1118.5	1020.4	1052	275.3	216.9	–
3094	3019	2019	1491	1118	1050	985	236	223[3]	[55]
[2]	[12]	[263]	[5]	[2]	[6]	[14]	[2]	–	–
3176	3099	2044	1496	1147	1060	1032	288	228	This work
[3.0]R	[13]R	[282]R	[8.0]R	[0.3]R	[1.6]R	[21]R	[2.1]R	[2.2]R	–

Note: Values in (–) are IR intensities in cm^{–2} L mol^{–1}.
^aSatellite band at higher frequency.
^bWe report data only for the isomer labeled 2 in the reference.

17.3.4 ELECTRONIC SPECTRA

Isomers of C₃H₂ participate in a rich photochemistry, both as reactants and products [43–46,51,54,60,62,65–67]. Several investigators have computed electronic spectra of C₃H₂ isomers. Values of λ_{max} are listed in Tables 17.10 and 17.11. These are the first tables in which we report UV literature data. Many papers report large numbers of UV peaks. In our tables we focus on selected sets of peaks in the range 150–300 nm, except in cases where strong peaks with wavelengths greater than 300 nm are present. Because all data

TABLE 17.8
Fundamental Vibrational Frequencies of 3O3(t)

F1	F2	F3	F4	F5	F6	F7	F8	F9	Reference
3297.8	3186.9	1962.9	1475.5	1107.3	992.1	661.5	391.7	210.6	[46]
[0.2]	[2.1]	[1.0]	[0.0]	[5.7]	[5.5]	[50.4]	[1.9]	[0.4]	–
3272.1	3170.5	1953.5	1484.6	1094.1	996.9	649.5	374.9	221.8	–
[0.4]	[3.3]	[0.6]	[0.0]	[5.6]	[7.0]	[61.2]	[2.7]	[0.4]	–
3266	3072	1319	1220	1052	743	696	362	228	This work
[5.6]R	[12]R	[30]R	[9.8]R	[1.5]R	[72]R	[36]R	[45]R	[11]R	–

TABLE 17.9
Fundamental Vibrational Frequencies of 3C1(s)

F1	F2	F3	F4	F5	F6	F7	F8	F9	Reference
–	–	–	1279	1063	–	–	888	789	[44]
3457	3418	1759	1419	1191	1071	998	983	854	–
–	–	–	1279	1064	–	–	887	788	[61]
–	–	–	1279	–	–	–	–	–	–
–	–	–	1268	–	–	–	888	781	[51] ^a
–	–	–	{ 100 }	–	–	–	{ 114 }	{ 77 }	–
–	–	–	1278	–	–	895	883	783	[60] ^b
–	–	–	{ 100 }	–	–	{ 14 }	{ 35 }	{ 54 }	–
3457	3418	1759	1419	1191	1071	998	983	854	[49] ^c
3104	3070	1583	1272	1064	975	895	890	774	[53]
3104	3070	1583	1273	1064	976	895	890	774	[50]
[0.0]	[0.0]	[0.0]	[56.4]	[21.6]	[0.0]	[0.8]	[16.0]	[24.3]	–
3108	3074	1563	1267	1054	973	894	892	774	[51] ^a
[0]	[0]	[0]	[56]	[22]	[0]	[3]	[13]	[25]	–
3307	3259	1635	1316	1089	998	914	914	800	[60] ^b
[0.6]	[0.7]	[0.4]	[48]	[9]	[0]	[4]	[19]	[20]	–
3182	3144	1612	1343	1177	983	948	912	784	[55]
[< 1]	[1]	[1]	[47]	[6]	[0]	[4]	[14]	[19]	–
3255	3218	1649	1311	1066	992	888	884	786	This work
[0.2]R	[0.7]R	[0]R	[49]R	[12]R	[0]R	[24]R	[4.1]R	[21]R	–

^aWe report data for isomer labeled 3 in the reference only.

^bWe report data for isomer labeled 3a in the reference only.

^cDZ+P calculation only.

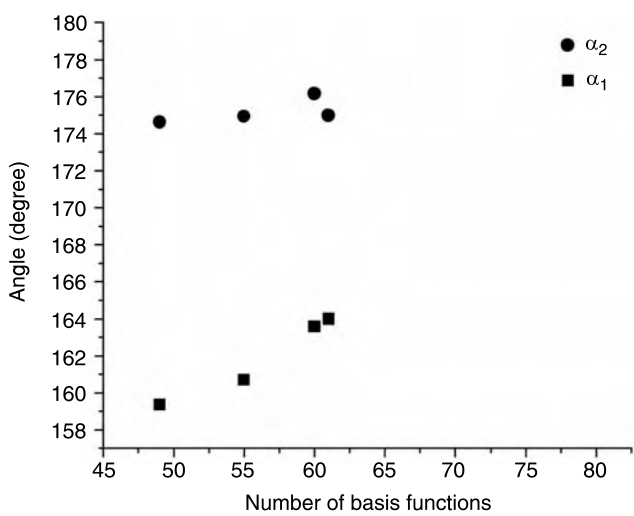


FIGURE 17.1 H-C-C (α_1) and C-C-C (α_2) angles of 3O1(t) as a function of the number of basis functions of the density functional method used.

TABLE 17.10
Selected Bands of the UV Absorption Spectra of 3O1(t)

	-	-	-	-	-	-	-	Reference
λ_{max} (nm)	210	236	240	247	252	260	~315	[51]

TABLE 17.11
Selected Bands of the UV Absorption Spectra of 3O2(s)

	-	-	-	-	-	-	-	-	-	-	Reference
λ_{max} (nm)	213.0	218.0	222.0	227.0	231.0	236.0	240.0	246.0	252	259	[66]
λ_{max} (nm)	213.1	217.6	222.2	227.0	231.0	235.0	240.4	246.1	252	-	[65]
λ_{max} (nm)	212	216	220	224	229	232	237	242	248	250	[67]
-	(1764)	(2520)	(3640)	(5216)	(6300)	(6875)	(7613)	(6857)	(4196)	(4032)	-

Note: (·):extinction coefficient in M⁻¹ cm⁻¹.

reported in this paper for UV absorption spectra are observational, these numbers are not printed in bold face letters.

17.3.5 ROTATIONAL DATA AND ISOMERIZATION

Rotational data are reported in References 37, 38, 53, 59, 63, 64, and 68–70.

Isomerizations involving isomers of C_3H_2 are outside the objectives of this paper. However, because the isomerization of 3O1(t) to the more stable 3C1(s) is of great interest, we refer the reader to the following papers in which the issue is discussed: [46,54,65,71–73].

17.4 C_4H_2 ISOMERS

17.4.1 INTRODUCTION

C_4H_2 isomers are of great interest to astronomers because some of these molecules occur in the atmospheres of Titan [74] (and references therein), Jupiter [75] (and references therein), possibly Pluto [76] in a comet [77], and in circumstellar and interstellar media [42,78–80]. Quantum chemical treatments of the 18 possible constructs, which included branched open constructs, produced 10 molecules of which four were open and six were cyclical. All have singlet ground states. Several investigators have synthesized 4O1(s) in the gas phase and in solvents. Goldberg et al. [81] have synthesized 4O2(s) in the gas phase.

Ramos and Ferreira [82] have reported dipole moment derivatives but only for the Σ_u^+ and Π_u symmetry species of C_4H_2 . Collins et al. [83] have reported dipole moments and vibrational frequencies for 4C3(s), cyclopropenylidenecarbene only. Fowler and Dierksen [84] have published dipole moment and SCF energy for 4O1(s). Toto et al. [85] have reported bond distances and polarizabilities for 4O1(s). Deng et al. [21] have reported rotational constants and vibrational frequencies for 4O1(s). Karpfen [86] has published total energy, bond distances, rotational constants, quadrupole moments, polarizabilities and vibrational frequencies, but again only for 4O1(s). Vila et al. [87] have reported optimized geometries and vibrational frequencies 4O1(s). Basiuk et al. [88] have reported simulated IR spectra for 4O1(s).

17.4.2 ENERGIES AND DIPOLE MOMENTS OF THE OPEN MOLECULES

In Table 17.12 we show relative SCF energies, zero point vibrational energies, and dipole moments of the open molecules. The quantum chemical treatments of the three open but branched constructs did not generate additional molecules.

TABLE 17.12**Relative SCF Energies, Zero Point Vibrational Energies (ZPVE), and Dipole Moments of the Open C₄H₂ Molecules**

Data	4O1(s)	4O2(s)	4O3(s)	4O4(s)	Reference
ΔE_{SCF} (kJ mol ⁻¹)	0.00	170	220	418	This work
ΔE_{SCF} (kJ mol ⁻¹)	0.00	—	—	—	[84]
ZPVE (kJ mol ⁻¹)	96.84	93.2	89.35	86.83	This work
Dipole (debye)	—	4.53	—	—	[16]
Dipole (debye)	0.00	—	—	—	[84]
Dipole (debye)	0.00	4.47	2.3	0.00	This work

Note: E_{SCF} of 4O1(s): -153.522698 hartree (this work). Fan and Pfeiffer [17] have reported calculated total energies for 4O1(s).

TABLE 17.13**SCF Energy Differences, Zero Point Vibrational Energies (ZPVE), and Dipole Moments of the Cyclic Molecules**

Data	4C1(s)	4C2(s)	4C3(s)	4C4(s)	4C5(s)	4C6(s)	Reference
ΔE_{SCF} (kJ mol ⁻¹)	266	270	301	313	317	404	This work
ZPVE (kJ mol ⁻¹)	91.81	99.30	93.19	96.91	95.01	92.79	This work
Dipole (debye)	—	—	4.69 to 5.12	—	—	—	[83]
Dipole (debye)	3.08	4.06	4.99	2.88	3.5	2.73	This work

The same data for the cyclic molecules are shown in Table 17.13. Obviously 4O1(s) is the most stable of all isomers.

17.4.3 VIBRATIONAL DATA

In [Tables 17.14](#) and [17.15](#) we present experimental and theoretical values of the fundamental vibrational frequencies of the C₄H₂ isomers 4O1(s) and 4C3(s). Multiple entries in one row are results from several computational methods. There are significant differences between the frequencies reported by [83] and our results for 4C3(s). The reasons for the differences are not understood at this time. Apparently no experimental vibrational frequencies were determined or calculated for the other isomers. Our theoretical results for these isomers are compiled in [Table 17.16](#).

TABLE 17.14
Fundamental Vibrational Frequencies of 4O1(s)

F1	F2	F3	F4	F5	F6	F7	F8	F9	F10	F11	F12	Reference
3329	3329	2184	2020	874	—	630	627	482	—	—	—	[89]
—	—	—	—	—	—	—	—	—	482.13	—	220.139	[90]
3331	3328	—	2020	—	—	628	627	482	—	—	221.5	[91]
3329	3329	2184	2022.288	—	—	628.04	624.9	482.13	—	—	220.139	[92]
3333.666	—	—	—	—	—	—	—	—	—	—	—	[93]
—	—	2187	—	874	—	630	627	482	—	—	—	[94]
3333.6	3332.1	2188.9	2022.2	871.9	—	628	625.6	482.7	—	—	220.123	[95]
7	1	5	5	2	—	9	6	8	—	—	6	—
3333	3332	2186	2020	874	—	628	628	482	—	—	220	[96]
[136]	—	—	[1.84]	—	—	[172]	—	—	—	—	[6.2]	—
—	—	—	—	—	—	627.894	—	—	—	—	219.97713	[97]
3478	3478	2185	2001	897	—	618	614	460	—	—	218	[86]
3632	3631	2152	918	646	646	570	570	529	529	221	221	[87]
3354	—	—	2197	848	—	659	—	—	—	—	—	[88]
3348	—	—	2238	830	—	—	—	—	—	—	—	—
3682	—	—	2208	902	—	—	—	—	—	—	—	—
3803	—	—	—	—	—	—	—	—	—	—	—	—
3469	3466	2289	2111	918	614	600	600	538	514	239	239	A
[149]R	[0]R	[0]R	[1.1]R	[0]R	[0]R	[91]R	[91]R	[0]R	[0]R	[5.4]	[5.4]	—

Note: A: This work. Khanna et al. [98] have measured infrared band extinctions of crystalline C₄H₂. Materny and Kiefer [99] have determined the Raman spectrum of 4O1(s) crystals. Cernicharo et al. [79] have observed the 628 cm^{−1} band in the proto-planetary nebula CRL 618.

TABLE 17.15
Fundamental Vibrational Frequencies of 4C3(s)

F1	F2	F3	F4	F5	F6	F7	F8	F9	F10	F11	F12	Reference
3330	3276	1866	1604	981	972	828	794	727	649	375	177	A
[6.6]R	[16]R	[18]R	[82]R	[22]R	[1.2]R	[3.2]R	[0]R	[0.2]R	[64]R	[5.3]R	[3.9]R	—
3510	3457	1952	1647	1125	1081	974	929	913	754	449	252	[83]
[11]	[26]	[1]	[23]	[21]	[< 1]	[1]	[0]	[< 1]	[67]	[9]	[4]	—
3448	3395	1899	1621	1045	1032	877	824	870	678	396	198	—
[10]	[25]	[9]	[81]	[19]	[< 1]	[< 1]	[0]	[< 1]	[62]	[9]	[4]	—
3376	3325	1835	1579	1003	1002	810	749	836	624	360	179	—
[9]	[20]	[17]	[107]	[18]	[2]	[< 1]	[0]	[< 1]	[60]	[8]	[3]	—
3497	3444	1945	1641	1132	1080	950	926	903	759	449	251	—
[11]	[25]	[< 1]	[26]	[21]	[< 1]	[< 1]	[0]	[< 1]	[62]	[6]	[6]	—

TABLE 17.16**Fundamental Vibrational Frequencies of the Remaining C₄H₂ Isomers (All This Work)**

Isomer	F1	F2	F3	F4	F5	F6	F7	F8	F9	F10	F11	F12
4O2(s)	3213	3135	2163	1745	1386	963	925	769	513	419	204	155
–	[5.3]R	[27]R	[770]R	[2.2]R	[18]R	[6.4]R	[0.1]R	[81]R	[0]R	[0.9]R	[0.2]R	[3.5]R
4O3(s)	3465	2930	2230	1768	1007	883	663	631	584	364	315	99.7
–	[68]R	[38]R	[2.8]R	[46]R	[0.9]R	[3.6]R	[44]R	[5.5]R	[53]R	[11]R	[9.3]R	[18]R
4O4(s)	3087	3083	1758	1669	1119	949	942	722	618	224	181	167
–	[45]	[0]R	[0]R	[90]	[0]R	[12]	[0]R	[0]R	[56]	[0]R	[22]	[51]
4C1(s)	3239	3150	1780	1489	1382	980	960	794	509	429	387	251
–	[2.4]R	[13]R	[86]R	[2.8]R	[7.3]R	[1.3]R	[14]R	[70]R	[22]R	[2.3]R	[1.1]R	[6.0]R
4C2(s)	3183	3106	1530	1505	1229	1119	1065	1018	965	952	494	435
–	[0.6]R	[6.9]R	[31]R	[9.6]R	[3.6]R	[10]R	[2.5]R	[0]R	[4.6]R	[9.2]R	[72]R	[0]R
4C4(s)	3205	3198	1353	1335	1175	1057	1018	996	943	696	615	609
–	[0.3]R	[0.3]	[43]	[1.2]R	[1.0]	[0]R	[35]R	[21]	[2.3]	[0.6]	[11]	[0]R
4C5(s)	3228	3212	1412	1288	1248	1044	1033	920	791	613	559	536
–	[0]R	[0.1]R	[0.2]R	[2.5]R	[17]R	[2.8]R	[7.9]R	[53]R	[41]R	[2.5]R	[0.1]R	[29]R
4C6(s)	3193	3100	1831	1460	1166	1036	965	890	812	676	220	10.7
–	[0.1]R	[0.6]R	[322]R	[5.9]R	[19]R	[15]R	[0.7]R	[28]R	[8.0]R	[80]R	[11]R	[20]R

17.4.4 ELECTRONIC SPECTRA

Selections of bands from reported UV spectra are listed in [Table 17.17](#). The UV spectrum of 4O1(s) was measured as early as 1935 in which the following progressions (in cm^{-1}) in the vibronic spectrum of 4O1(s): 2132, 2114, 2105, 2102, 2092, 2084, 2080, 2073, 2067, 2065, 2061, 2057, and 2035 were reported [100]. Woo and Chu [101] determined a total of 460 bands of 4O1(s) from 263.32 to 297.00 nm. Because of this large number, the reader is referred to the original publication. Eastmond et al. [102] have determined λ_{max} values for the triethylsilyldiyne-endcapped derivative in methanol and hexane. Their results are very useful for HPLC work because they have also determined molar absorption coefficients. Kloster-Jensen et al. [103] reported 130 bands between 121.9 and 275.7 nm. Okabe [104] reported 28 bands between 121.1 and 172.7 nm. Chang and Graham [94] studied the vibrational structures of the band systems at 246.6 and 247.0 nm in an Ar matrix at 9 K. From the results they deduced fundamental vibrational frequencies of 2187, 874, 627, and 482 cm^{-1} . Fahr and Nayak [105] determined the UV absorption spectrum of 4O1(s) from 160 to 260 nm in intervals of 0.2 nm at seven different temperatures, but have tabulated selected absorption cross sections at 5 nm intervals only. The cross sections listed in the table are not at wavelengths of absorption maxima. The strongest

TABLE 17.17
Selected Bands of the UV Absorption Spectra of 4O1(s)

—	—	—	—	—	—	—	Reference
λ_{\max}	239.3	240.35	240.77	242.20	242.95	—	[100]
—	(6)	(5)	(5)	(5)	(10)	—	—
λ_{\max}	144.6	164.5	—	—	—	—	[107]
λ_{\max}	236	249.5	263.5	279.5	—	—	[102] ^{a,c}
—	2.36	2.57	2.66	2.51	—	—	—
λ_{\max}	237	250	264	280	—	—	[102] ^{b,c}
—	2.28	2.54	2.64	2.49	—	—	—
λ_{\max}	144.6	164.5	211.1	220.7	231.4	243.4	[103]
—	(100)	(73.9)	(42.4)	(83.4)	(100)	(58.0)	—
λ_{\max}	211.1	220.7	231.4	243.4	247.1	248.7	[108]
λ_{\max}	159.0	164.2	—	—	—	—	[104]
—	[1720]	[2120]	—	—	—	—	—
λ_{\max}	246.6 ^d	247.0	—	—	—	—	[94] ^e
λ_{\max}	185	229	254	—	—	—	—
λ_{\max}	160.0	165.0	170.0	175.0	—	—	[105] ^b
—	[2454]	[3574]	[127.9]	[97.14]	—	—	—
λ_{\max}	—	—	—	—	—	211.18	[106]
—	—	—	—	—	—	—	[23]
λ_{\max}	180	—	—	—	—	215	[2] ^f
λ_{\max}	200	—	—	—	—	—	[2] ^a
λ_{\max}	197	—	—	—	—	—	[2] ^b

^aIn methanol.

^bIn hexane.

^cTriethylsilyldyne-endcapped derivative.

^dFor C₄D₂.

^eFor more details see original paper.

^fIn acetonitrile.

{·}: cm⁻¹ amagat⁻¹ [·]: 10⁻¹⁹ cm². (·): relative intensity.

Italics: log ϵ .

absorption peak was at 164.6 nm, whose cross section at 333 K was 4.12×10^{-16} cm². The associated C \equiv C stretching vibration of the vibronic spectrum had the ground state frequency of 2184 cm⁻¹. Smith et al. [106] have pointed out that an impurity of C₄H₃Cl can strongly influence measured absorption coefficients.

17.4.5 ROTATIONAL DATA

Rotational data are reported in References 21, 37, 69, 78, 83, 89, 93, and 110–112.

17.5 C₅H₂ ISOMERS

17.5.1 INTRODUCTION

Whereas C₃H₂ and C₄H₂ molecules have been found in interstellar media and in atmospheres of the giant planets of the Solar System and their satellites, this is not the case for C₅H₂. Only an upper limit of its abundance in the pre-protostellar core TMC-1 was reported [113]. However, the open molecule 5O1(s) and the highly polar ring-chain molecule 5C9(s) were detected in the laboratory in a diacetylene–neon discharge [114]. Experimental evidence for the existence of three isomeric C₅H₂ molecules was reported [115]. Results of theoretical calculations for C₅H₂ isomers are available [7,17,115]. Rotational constants for 5O2(s) are available [69].

As stated in the introduction, we have treated with quantum mechanical calculations all but the branched open constructs of the formula C₅H₂. These 41 constructs produced 16 molecules of which five are open and 11 cyclic. Because of this large number we present our results and literature data in a different format as follows: 1. open molecules, Tables 17.18 and 17.19; 2. cyclic molecules with one five-ring, Tables 17.20 and 17.21; 3. cyclic molecules with one four-ring, Tables 17.22 and 17.23; 4. cyclic molecules

TABLE 17.18

Relative SCF Energy, Zero Point Vibrational Energy (ZPVE), and Dipole Moment of the Open C₅H₂ Molecules

Molecule	ΔE_{SCF} (kJ mol ⁻¹)	ZPVE (kJ mol ⁻¹)	Dipole (debye)	Reference
5O1(t)	0.00	96.75	0.00	This work
5O1(t)	0.00	93.847	–	[7]
5O1(t)	0.00	103.13	–	[115]
5O2(s)	56.3	107.99	6.05	This work
5O2(s)	–	–	5.9	[69]
5O2(s)	63.0	106.69	5.584	[7]
–	74.4	–	5.792	–
–	57.8	–	5.829	–
5O2(s)	29.3 ^a	109.92	–	[115]
5O3(s)	84.7	108.39	5.27	This work
5O3(s)	58.33	107.53	4.461	[7]
–	69.54	–	4.616	–
–	70.21	–	4.787	–
5O3(s)	33.5 ^a	110.43	–	[115]
5O4(s)	274	104.44	3.14	This work
5O5(s)	232	103.06	5.11	This work

Note: E_{SCF} of 5O1(t): –191.560863 hartree (this work).

^aIncludes zero-point energy correction. Fan and Pfeiffer [17] have reported calculated total energies for 5O1(t) only.

with one three-ring, [Tables 17.24](#) and [17.25](#); and 5. cyclic molecules with two three-rings, [Tables 17.26](#) and [17.27](#). The presentation will be followed by comments and references to rotational data.

17.5.2 COMMENTS

A surprisingly large number of C_5H_2 molecules have true minima on the potential energy surface. Several of these, such as 5O1(t), 5O2(s), and 5C8(s) are analogs of molecules that we encountered among the C_3H_2 and C_4H_2 species. As expected, the ground state of 5O1(t) is a triplet state and this molecule has the lowest energy followed by 5C8(s). Several of the “out-landish” molecules are seen to lie far above 5O1(t) but that should not preclude their formation and transient existence in non-equilibrium environments. Nothing is known about the mean lifetimes with regards to 5O1(t) of any of the molecules that are intrinsically unstable.

Where comparisons can be made between the results of Seburg et al. [7] and our data, the agreements are mostly quite close. The most notable exception is the relative energy for 5C8(s), which is considerably smaller in the results of [7].

17.5.3 ELECTRONIC SPECTRA AND ROTATIONAL DATA

Selected bands from reported UV Spectra are listed in [Table 17.28](#).

Rotational data are reported in References 7, 69 and 114.

TABLE 17.19
Fundamental Vibrational Frequencies of the Open C_5H_2 Molecules

Molecule	F1	F2	F3	F4	F5	F6	F7	F8	Reference
5O1(t)	3457	3450	1964	1734	1568	766	447	445	This work
–	[0]R	[178]R	[0]R	[8.3]R	[2.1]R	[0]R	[26]R	[29]R	–
5O1(t)	3473.3	3467.2	1926.1	1578.8	1503.2	737.1	439.4	433.1	[7]
–	–	[184.2]	–	[1.0]	[11.2]	–	[173.4]	–	–
5O2(s)	3182	3106	2215	1976	1519	1374	1041	960	This work
–	[1.3]R	[5.6]R	[822]R	[200]R	[11]R	[9.5]R	[0]R	[34]R	–
5O2(s)	3279.4	3178.1	2179.8	1938.7	1523.1	1361.5	1031.1	910.6	[7]
–	[0.1]	[0.8]	[664.7]	[270.8]	[9.6]	[16.0]	[0.2]	[36.1]	–
5O3(s)	3458	3097	2189	2035	1409	1171	968	891	This work
–	[51]R	[3.3]R	[81]R	[700]R	[3.9]R	[9.8]R	[40]R	[3.1]R	–
5O3(s)	3475.3	3194.0	2169.7	2001.4	1392.5	1162.0	952.5	859.8	[7]
–	[58.5]	[1.8]	[77.7]	[611.9]	[4.7]	[1.4]	[58.5]	[1.5]	–
5O4(s)	3140	3090	2038	1684	1408	1191	1093	910	This work
–	[0.5]R	[25]R	[693]R	[320]R	[1.7]R	[28]R	[14]R	[22]R	–
5O5(s)	3257	3253	1675	1609	1073	1038	974	974	This work
–	[0.2]R	[4.5]R	[1.6]R	[28]R	[10]R	[16]R	[0.4]R	[34]R	–

(Continued)

TABLE 17.19
Continued

Molecule	F9	F10	F11	F12	F13	F14	F15	Reference
5O1(t)	416	410	367	365	361	298	127	This work
–	[0]R	[3.23]R	[78]R	[58]R	[0]R	[17]R	[3.7]R	–
5O1(t)	not	not	not	not	323.2	268.6	39.5	[7]
–	rep.	rep.	rep.	rep.	–	[16.7]	[11.3]	–
5O2(s)	768	616	480	279	266	141	132	This work
–	[0.1]R	[5.8]R	[1.9]R	[8.1]R	[7.3]R	[0]R	[2.5]R	–
5O2(s)	753.3	526.6	410.6	251.5	225.3	137.6	129.8	[7]
–	[0.9]	[5.2]	[1.5]	[5.1]	[6.1]	[0.0]	[1.9]	–
5O3(s)	699	635	591	315	308	218	135	This work
–	[32]R	[52]R	[4.9]R	[14]R	[1.7]R	[2.0]R	[3.6]R	–
5O3(s)	669.6	633.6	560.8	296.1	277.3	214.8	121.6	[7]
–	[37.4]	[49.0]	[4.3]	[12.3]	[2.1]	[1.0]	[2.3]	–
5O4(s)	906	717	521	265	221	149	128	This work
–	[2.5]R	[44]R	[6.4]R	[0]R	[9.8]R	[25]R	[23]R	–
5O5(s)	798	765	586	441	320	263	203	This work
–	[63]R	[0]R	[15]R	[4.1]R	[15]R	[2.2]R	[0]R	–

Note: Lamotte et al. [91] have determined vibrational frequencies for $\text{CH}_3\text{-C}\equiv\text{C-C}\equiv\text{CH}$. The results are not included in this table.

TABLE 17.20
Relative SCF Energy, Zero Point Energy (ZPE), and Dipole Moment of the C_5H_2 Five-Rings (All This Work)

Molecule	ΔE_{SCF} (kJ mol ⁻¹)	ZPVE (kJ mol ⁻¹)	Dipole (debye)
5C1(s)	273	111	2.39
5C2(s)	331	110.56	3.02

17.6 C_6H_2 ISOMERS

17.6.1 INTRODUCTION

Like C_4H_2 , C_6H_2 has been observed in astronomical objects [75,79,117]. Cyclic isomers of C_6H_2 are of particular interest because of the preponderance of six-membered carbon rings in organic chemistry. Moriyama et al. [118] have synthesized a derivative of 6C1(s) with H-atoms substituted by CF_3 groups. Other C_6H_2 isomers were synthesized for a variety of experimental objectives [103,108,117,119–124]. Zahradnik et al. [125] have

TABLE 17.21**Fundamental Vibrational Frequencies of the C₅H₂ Five-Rings (All This Work)**

Molecule	F1	F2	F3	F4	F5	F6	F7	F8
5C1(s)	3216	3200	1364	1324	1254	1186	1180	1017
–	[6.5]R	[4.3]R	[8.2]R	[13]R	[110]R	[6.9]R	[25]R	[30]R
5C2(s)	3188	3119	1789	1599	1445	1153	1080	1009
–	[0.8]R	[2.0]R	[136]R	[28]R	[2.8]R	[12]R	[5.1]R	[28]R
Molecule	F9	F10	F11	F12	F13	F14	F15	
5C1(s)	931	870	852	790	669	392	312	
–	[99]R	[16]R	[30]R	[54]E	[17]R	[7.89]R	[53]R	
5C2(s)	910	873	794	603	454	382	86	
–	[13]R	[0.3]R	[2.0]R	[64]R	[61]R	[84]R	[15]R	

TABLE 17.22**Relative SCF Energy, Zero Point Energy (ZPE), and Dipole Moment of the C₅H₂ Four-Rings (All This Work)**

Molecule	ΔE_{SCF} (kJ mol ⁻¹)	ZPVE (kJ mol ⁻¹)	Dipole (debye)
5C3(s)	147	109.9	4.05
5C4(s)	274	111.29	0.00
5C5(s)	279	108.17	4.23
5C6(s)	498	102.19	2.78

published results of semi-empirical calculations for some C₆H₂ tetra-dehydrobenzenes. Bettinger et al. [126] have computed energy separations and vibrational frequencies of three cyclic C₆H₂ isomers. Sattelmeyer and Stanton [6] have computed equilibrium structures and properties of nine C₆H₂ molecules, four open and five cyclic. Their results offer a good opportunity for comparison with computations for the same molecules with our program. Obviously many more constructs of six carbon and two hydrogen atoms are possible. A potentially interesting one can be derived from 3C1(s) cyclopropenylidene by the substitution of –C₃H for one of the hydrogen atoms. However, the quantum chemical treatment of this construct results in an open molecule with hydrogen atoms bonded to C2 and C6 and $\Delta E_{\text{SCF}} = 224 \text{ kJ mol}^{-1}$ above 6O1(s).

Tables 17.29, 17.30 and 17.31 list energy data for the C₆H₂ isomers.

TABLE 17.23
Fundamental Vibrational Frequencies of the C₅H₂ Four-Rings (All This Work)

Molecule	F1	F2	F3	F4	F5	F6	F7	F8
5C3(s)	3264	3170	1824	1459	1422	1087	1065	914
–	[0]R	[0.83]R	[41]R	[13]R	[63]R	[11]R	[2.3]R	[4.9]R
5C4(s)	3316	3315	1321	1286	1132	1130	1021	1020
–	[0.2]R	[3.0]	[0]R	[24]R	[10]R	[10]R	[0]R	[0]R
5C5(s)	3271	3144	1794	1438	1278	1180	1040	983
–	[0.9]R	[5.1]R	[216]R	[14]R	[9.5]R	[6.3]R	[4.8]R	[4.8]R
5C6(s)	3136	3074	1645	1419	1160	1098	993	919
–	[12]R	[16]R	[199]R	[23]R	[12]R	[30]R	[7.3]R	[27]R
Molecule	F9	F10	F11	F12	F13	F14	F15	
5C3(s)	883	798	712	597	590	334	255	
–	[54]R	[0]R	[0]R	[4.6]R	[48]R	[1.0]R	[2.1]R	
5C4(s)	851	848	837	739	737	528	526	
–	[17]R	[16]R	[0]R	[0]R	[0]R	[42]R	[42]R	
5C5(s)	862	804	671	629	538	251	201	
–	[51]R	[34]R	[5.3]R	[27]R	[18]R	[0.3]R	[13]R	
5C6(s)	875	744	603	510	490	256	163	
–	[43]R	[0.8]R	[11]R	[34]R	[17]R	[28]R	[5.4]R	

TABLE 17.24
Relative SCF Energy, Zero Point Energy (ZPE), and Dipole Moment of the C₅H₂ Three-Rings

Molecule	ΔE_{SCF} (kJ mol ^{−1})	ZPVE (kJ mol ^{−1})	Dipole (debye)	Reference
5C7(s)	99.5	110.45	8.02	This work
5C7(s)	84.5	110.50	8.130	[7]
–	98.8	110.50	8.207	–
–	88.4	110.50	8.156	–
5C8(s)	33.5	109.20	3.55	This work
5C8(s)	0.50	109.54	3.499	[7]
–	12.4	109.54	3.567	–
–	8.41	109.54	3.535	–
5C9(s)	160	104.13	4.68	This work
5C10(s)	344	105.46	2.92	This work

TABLE 17.25
Fundamental Vibrational Frequencies of the C₅H₂ Three-Rings

Molecule	F1	F2	F3	F4	F5	F6	F7	F8	Reference
5C7(s)	3273	3234	2089	1680	1467	1112	965	942	This work
–	[5.4]R	[1.7]R	[923]R	[26]R	[152]R	[17]R	[2.1]R	[0]R	–
5C7(s)	3329.2	3291.5	2045.3	1673.9	1460.0	1150.8	979.3	950.1	[7]
–	[19.0]	[9.0]	[1309.0]	[41.1]	[235.1]	[9.8]	[1.6]	[15.2]	–
5C8(s)	3464	3235	2197	1724	1274	1096	939	715	This work
–	[71]R	[0.4]R	[5.9]R	[4.0]R	[34]R	[6.5]R	[3.6]R	[31]R	–
5C8(s)	3478.9	3298.9	2194.0	1743.7	1290.4	1130.1	943.9	880.5	[7]
–	[68.4]	[1.1]	[10.3]	[6.7]	[52.7]	[8.9]	[2.7]	[18.0]	–
5C9(s)	3171	3098	2000	1568	1438	1286.55	1009.59	932.17	This work
–	[0.1]R	[1.7]R	[8.1]R	[10]R	[0]R	[0.744]R	[0.005]R	[42.3]R	–
5C10(s)	3223	3119	1926	1691	1469	1055	1004	985	This work
–	[0.1]R	[3.7]R	[91]R	[313]R	[1.0]R	[1.4]R	[0]R	[0.9]R	–

Molecule	F9	F10	F11	F12	F13	F14	F15	Reference
5C7(s)	9189	760	738	499	462	172	153	This work
–	[12]R	[53]R	[0.3]R	[0.1]R	[10]R	[0.2]R	[1.0]R	–
5C7(s)	912.3	747.5	732.3	472.4	451.2	149.2	128.8	[7]
–	–	[55.8]	[1.6]	[1.2]	[5.8]	[0.0]	[0.2]	–
5C8(s)	715	703	559	536	516	215	197	This work
–	[31]R	[1.1]R	[55]R	[0.9]R	[5.8]R	[0.9]R	[5.7]R	–
5C8(s)	696.4	690.2	604.3	507.3	474.2	204.0	178.1	[7]
–	[31.3]	[1.9]	[51.6]	[0.8]	[2.1]	[0.8]	[5.3]	–
5C9(s)	719	600	563	455	343	205	21.1	This work
–	[0.4]R	[2.9]R	[6.8]R	[0]R	[13]R	[0.1]R	[1.3]R	–
5C10(s)	957	753	681	339	219	153	57.7	This work
–	[0]R	[0]R	[75]R	[0]R	[0.5]R	[12]R	[19]R	–

TABLE 17.26
Relative SCF Energy, Zero Point Energy (ZPE), and Dipole Moment of the C₅H₂ Two Three-Rings (This Work)

Molecule	ΔE_{SCF} (kJ mol ^{−1})	ZPVE (kJ mol ^{−1})	Dipole (debye)
5C11(s)	214	103.60	0.00

TABLE 17.27
Fundamental Vibrational Frequencies the C₅H₂ Two Three-Rings (This Work)

Molecule	F1	F2	F3	F4	F5	F6	F7	F8	F9	F10	F11	F12	F13	F14	F15
5C11(s)	3268	3265	1712	1616	1159	1069	975	840	827	756	533	448	427	231	192
–	[12]	[0]R	[4.4]	[0]R	[28]	[0]R	[10]	[0]R	[65]	[0]R	[0]R	[448]	[34]	[22]	[46]

TABLE 17.28
Selected Bands of the UV Absorption Spectra of 5O1(t) $\lambda_{\text{max}} > 140$ nm

–	–	–	–	–	Reference
λ_{max}	390.9	402.4	420.5	434.2	[116]
–	–	–	–	–	–
$\Delta\nu$ cm ^{–1}	2551	1817 ^a	751	0.00	[116]
–	–	–	–	–	–

^aC≡C symmetrical stretch. Data were obtained in a neon matrix at 5 K.

17.6.2 COMMENT

Sattelmeyer and Stanton [6] have speculated that 6O4(s), a “branched” open molecule, may not have a true minimum on the potential energy surface, but, instead, is a metastable intermediate towards 6O1(s). We have found that in three attempts to treat the initial construct with the B3LYP/6-311G* method only one result had zero imaginary frequencies.

17.6.3 ELECTRONIC SPECTRA AND ROTATIONAL DATA

One hundred and eleven bands of 6O1(s) were observed [103]. The strongest of these bands are listed in Table 17.32. Lamotte et al. [91] have reported only a few bands in the very narrow range 235–250 nm for CH₃-substituted hexadiyne. Bénilan et al. [123] report absolute absorption coefficients for bands in the 200–300 nm range. Shindo et al. [117] have re-examined these absorption coefficients in the range 185–300 nm and have deduced absolute intensities for the strongest bands of [103].

Rotational data are reported in References 6, 69, 120, 123, and 124.

TABLE 17.29**Relative SCF Energies, Zero Point Vibrational Energies (ZPVE), and Dipole Moments of C₆H₂ Molecules**

Molecule	ΔE_{SCF} (kJ mol ⁻¹)	ZPVE (kJ mol ⁻¹)	Dipole (debye)	Reference
6O1(s)	0.00	123.22	0.00	[6]
6O1(s)	0.00	121.39	0.00	This work
6O2(s)	210.4	120.33	6.098	[6]
6O2(s)	175.39	120.14	6.20	This work
6O3(s)	226.3	121.17	3.947	[6]
6O3(s)	364.0	122.21	3.88	This work
6O4(s)	259.0	118.45	2.034	[6]
6O4(s)	278.8	116.9	2.23	This work
6C1(s)	235.1	144.05	0.00	[6]
6C1(s)	0.00 ^a	—	—	[126]
6C1(s)	258.9	132.11	0.00	This work
6C2(s)	193.7	133.01	1.151	[6]
6C2(s)	-41.4 ^a	—	—	[126]
6C2(s)	218.5	129.53	1.09	This work
6C3(s)	164.8	130.71	1.427	[6]
6C3(s)	-29.3 ^a	—	—	—
6C4(s)	315.0	121.08	.936	[6]
6C4(s)	301.6	120.66	8.20	This work
6C5(s)	320.5	119.24	4.877	[6]
6C5(s)	325.6	118.45	5.00	This work

^aRelative to 6C1 = 0 kJ mol⁻¹; only the B3LYP results are listed. Fan and Pfeiffer [17] have reported calculated total energies for 6O1(s) only. E_{SCF} for 6O1(s) -229.303033 hartree [6] and -229.699581 hartree (this work).

17.7 C₇H₂ ISOMERS

17.7.1 INTRODUCTION

Although C₇H₂ has not yet been observed in nature, comprehensive studies were made of several isomers of this composition. Cooper and Murphy [58] have calculated energy, dipole moment, and geometry for low-lying electronic states of 7O1-C₇H₂. Fan and Pfeiffer [17] have calculated the energy of the ground state of 7O1(t). Aoki and Ikuta [128] have calculated rotational constants, dipole moments and energies of eight stationary points for C₇H₂. Fulara et al. [116] have determined the electronic absorption spectrum of 7O1(t) in the range 411.6 to 505.8 nm. Dua et al. [129,130] have reported properties of four C₇H₂ isomers. McCarthy et al. [131] have measured rotational constants of the ring-chain carbene C₇H₂.

TABLE 17.30
Fundamental Vibrational Frequencies of the Open C₆H₂ Molecules

Molecule	F1	F2	F3	F4	F5	F6	F7	F8	F9	Reference
6O1(s)	3328	<i>3313</i>	<i>2201</i>	2125	<i>2019</i>	1115	<i>625</i>	<i>625</i>	622	[119] ^a
6O1(s)	3328.76	–	–	2128.91	–	–	–	–	621.33	[127]
6O1(s)	3332	–	–	2121	–	1115	–	–	623	[121]
–	{434}	–	–	{6.6}	–	{0.2}	–	–	{312}	–
6O1(s)	3332	3322	–	2121	–	1123/1113	–	–	628	[117]
6O1(s)	3478	3478	2354	2212	2102	1157	–	–	652	[6]
–	[194]	[–]	[–]	[1]	[–]	[1]	–	–	[172]	–
6O1(s)	3353	–	2359	–	–	1337	–	–	852	[88] ^b
–	[151.2]	–	[15.3]	–	–	[1.3]	–	–	[36.0]	–
6O1(s)	3465.53	3464.9	2308.82	2223.35	2105.8	1209.62	636.37	605.32	594.96	This work
–	[212.3]R	[0.117]R	[0.00]R	[1.13]R	[0.00]R	[3.30]R	[0.00]R	[0.00]R	[93.4]R	–
6O2(s)	3282	3184	2186	2078	1751	1459	1210	1013	850	[6]
–	[5]	[21]	[1937]	[304]	[203]	[1]	[0]	[0]	[56]	–
6O2(s)	3206.49	3129.31	2209.48	2108.10	1771.63	1421.79	1220.32	977.30	795.38	This work
–	[1.88]R	[17.2]R	[1856]R	[124]R	[214]R	[2.08]R	[0.007]R	[2.71]R	[71.4]	–
6O3(s)	3479	3201	2196	2132	1713	1312	1051	891	735	[6]
–	[81]	[24]	[4]	[742]	[50]	[1]	[2]	[2]	[12]	–
6O3(s)	3493.40	3134.86	2227.98	2159.30	1729.18	1309.65	1071.35	891.58	739.22	This work
–	[85.3]R	[15.3]R	[47.5]R	[634]R	[25.1]R	[0.072]R	[2.82]R	[0.560]R	[17.1]R	–
6O4(s)	3479	3478	2203	2191	1634	1162	740	694	694	[6]
–	[27]	[115]	[0]	[0]	[18]	[12]	[7]	[53]	[14]	–
6O4(s)	3464.83	3462.84	2228.31	2165.76	1651.60	1133.25	746.19	729.00	669.00	This work
–	[45.5]R	[87.1]R	[0.327]R	[11.3]R	[16.7]R	[7.17]R	[13.1]R	[23.8]R	[38.0]R	–
6O1(s)	–	–	–	491	443	–	258	105	–	[119]
6O1(s)	–	–	–	–	–	–	–	–	–	[127]

(Continued)

TABLE 17.30
Continued

Molecule	F10	F11	F12	F13	F14	F15	F16	F17	F18	Reference
6O1(s)	—	—	—	—	444	—	—	—	—	[121]
—	—	—	—	—	{15}	—	—	—	—	—
6O1(s)	622/617	—	—	—	444	—	—	—	—	[117]
6O1(s)	652	612	—	495	443	—	253	108	—	[6]
—	[·]	[·]	—	[·]	[4]	—	[·]	[9]	—	—
6O1(s)	—	—	—	—	533	—	—	—	—	[88] ^b
—	—	—	—	—	[3.9]	—	—	—	—	—
6O1(s)	594.95	591.38	539.78	520.68	462.44	462.43	270.90	119.13	119.13	This work
—	[93.4]R	[0.020]R	[0.001]R	[0.001]R	[0.448]R	[0.449]R	[0.00]R	[3.74]R	[3.74]R	—
6O2(s)	650	552	472	452	363	223	197	102	91	[6]
—	[0]	[4]	[0]	[3]	[0]	[5]	[7]	[0]	[2]	—
6O2(s)	657.11	579.80	504.02	474.11	387.47	234.80	212.85	103.39	93.02	This work
—	[0.138]R	[4.49]R	[0.851]R	[2.20]R	[0.174]R	[5.56]R	[7.46]R	[0.390]R	[1.78]R	—
6O3(s)	685	638	591	468	363	333	186	179	—	[6]
—	[38]	[48]	[2]	[0]	[5]	[16]	[0]	[5]	—	—
6O3(s)	656.51	607.06	574.69	528.03	400.18	373.70	224.41	215.53	94.71	This work
—	[40.7]R	[0.158]R	[54.1]R	[1.03]R	[1.77]R	[7.19]R	[6.83]R	[1.22]R	[3.18]R	—
6O4(s)	639	633	581	534	344	342	202	131	120	[6]
—	[94]	[·]	[0]	[12]	[9]	[·]	[2]	[4]	[2]	—
6O4(s)	618.26	561.97	531.65	511.09	350.76	317.08	204.55	125.75	73.01	This work
—	[59.1]R	[4.60]R	[10.4]R	[41.6]R	[0.010]R	[4.01]R	[0.675]R	[5.20]R	[0.728]R	—

Note: [·]: IR inactive.

^aEntries in italics are Raman frequencies of C₆H₂ in pentane at −20 to −30°C.

^bOnly PM3 results are listed. Matsumura et al. [120] and Haas et al. [122] have published high-resolution IR spectra. Cernicharo et al. [79] have observed the 622 cm^{−1} band in the proto-planetary nebula CRL 618. Lamotte et al. [91] have determined vibrational frequencies for CH₃-C≡C-C≡C-CH₃. The results are not listed in this table.

TABLE 17.31
Fundamental Vibrational Frequencies of the Cyclic C₆H₂ Molecules

Molecule	F1	F2	F3	F4	F5	F6	F7	F8	F9	Reference
6C1(s)	3231	3227	2040	1858	1342	1310	1287	1211	1097	[126]
–	[0]	[6]	[0]	[0.3]	[0]	[0]	[1]	[0]	[0]	–
6C1(s)	3273	3269	1963	1766	1396	1332	1297	1228	1097	[6]
–	[–]	[4]	[0]	[2]	[ñ]	[0]	[3]	[ñ]	[ñ]	–
6C1(s)	3218.69	3215.70	2040.07	1854.70	1345.76	1310.55	1294.00	1215.03	1098.84	This work
–	[0.00]R	[16.9]	[0.00]R	[0.181]	[0.00]R	[0.142]	[1.03]	[0.00]R	[0.00]R	–
6C2(s)	3267	3250	1913	1780	1405	1367	1289	1152	1065	[6]
–	[4]	[0]	[0]	[12]	[1]	[4]	[3]	[24]	[1]	–
6C2(s)	3213.57	3195.38	1895.88	1719.58	1442.05	1378.38	1234.76	1168.50	1108.99	This work
–	[8.86]R	[1.00]R	[11.0]R	[16.9]R	[1.69]R	[7.85]R	[9.85]R	[46.9]R	[8.91]R	–
6C3(s)	3322	3321	1739	1607	1277	1269	1235	1104	997	[6]
–	[1]	[4]	[137]	[1]	[1]	[1]	[0]	[16]	[45]	–
6C3(s)	3295.11	3257.09	1752.90	1621.90	1282.48	1245.93	1232.26	1110.49	975.93	This work
–	[0.001]R	[0.006]R	[130]R	[1.32]R	[0.378]R	[0.003]R	[2.45]R	[14.5]R	[75.3]R	–
6C4(s)	3349	3301	2123	1847	1621	1210	1050	977	900	[6]
–	[17]	[21]	[440]	[235]	[20]	[1]	[20]	[8]	[0]	–
6C4(s)	3307.83	3258.59	2133.08	1864.76	1637.32	1210.48	1012.87	954.79	844.18	This work
–	[9.08]R	[11.5]R	[340]R	[184]R	[7.38]R	[0.084]R	[22.7]R	[5.02]R	[0.919]R	–
6C5(s)	3475	3341	2213	1887	1644	1027	942	858	723	[6]
–	[81]	[25]	[8]	[22]	[143]	[9]	[23]	[6]	[40]	–
6C5(s)	3 461.39	3287.54	2211.89	1903.99	1663.47	1028.19	907.03	860.44	634.17	This work
–	[88.7]R	[13.9]R	[5.83]R	[29.4]R	[126]R	[3.36]R	[4.09]R	[28.1]R	[34.2]R	–

(Continued)

TABLE 17.31
Continued

Molecule	F1	F2	F3	F4	F5	F6	F7	F8	F9	Reference
6C1(s)	977	902	846	690	584	547	418	336	237	[126]
–	[48]	[0]	[30]	[0]	[0]	[270]	[0]	[13]	[0]	–
6C1(s)	959	905	847	687	633	591	571	520	350	[6]
–	[43]	[·]	[34]	[·]	[149]	[·]	[·]	[·]	[13]	–
6C1(s)	980.81	892.91	829.06	688.14	575.98	541.38	415.20	334.92	235.56	This work
–	[50.9]	[0.00]R	[34.9]	[0.00]R	[0.001]R	[255]	[0.00]R	[12.7]	[0.00]R	–
6C2(s)	1039	936	772	732	549	469	464	416	369	[6]
–	[15]	[·]	[51]	[15]	[·]	[3]	[67]	[·]	[98]	–
6C2(s)	1015.56	904.24	748.94	724.02	552.30	526.69	489.80	233.10	104.02	This work
–	[0.625]R	[0.001]R	[58.9]R	[23.8]R	[38.2]R	[0.005]R	[2.33]R	[0.025]R	[246]R	–
6C3(s)	972	790	771	617	616	606	572	567	469	[6]
–	[1]	[·]	[58]	[11]	[56]	[77]	[·]	[·]	[1]	–
6C3(s)	974.42	767.81	750.14	611.04	610.18	580.82	568.33	559.32	449.75	This work
–	[1.39]R	[0.00]R	[59.4]R	[9.35]R	[133]R	[45.8]R	[0.00]R	[0.963]R	[0.965]R	–
6C4(s)	824	651	625	569	400	327	237	137	108	[6]
–	[·]	[62]	[0]	[3]	[0]	[9]	[5]	[0]	[3]	–
6C4(s)	836.01	649.35	630.02	582.95	410.82	327.26	253.94	144.75	113.69	This work
–	[0.00]R	[66.0]R	[0.004]R	[3.67]R	[0.177]R	[11.6]R	[7.68]R	[0.067]R	[2.27]R	–
6C5(s)	677	672	630	500	480	344	222	195	107	[6]
–	[38]	[27]	[0]	[6]	[0]	[0]	[6]	[7]	[7]	–
6C5(s)	647.53	634.17	582.58	486.78	481.78	357.95	233.54	211.82	113.96	This work
–	[44.8]R	[34.2]R	[1.24]R	[1.70]R	[1.76]R	[0.513]R	[5.02]R	[7.05]R	[5.62]R	–

TABLE 17.32
Selected Bands of the UV Absorption Spectra of 6O1(s). $\lambda_{\text{max}} > 175 \text{ nm}$

	–	–	–	–	–	–	–	–	–	Reference
λ_{max}	211	221	230	270	274	291	310.5	320	332	[102] ^c
–	4.65	4.95	5.04	2.08	2.3	2.48	2.52	1.6	2.32	–
λ_{max}	211.5	211	231.5	270	274.5	291.5	311	332	–	[102] ^c
–	4.64	4.99	5.11	2.08	2.2	2.42	2.49	2.26	–	–
λ_{max}	176.1	179.3	183.1	185.0	186.3	260.6	275.8	293.3	–	[103]
–	(61.0)	(95.4)	(100)	(85.1)	(80.9)	(82.0)	(100)	(53.4)	–	–
λ_{max}	209.2	230.5	234.9	–	–	–	–	–	–	[103]
–	(0.4)	(9.3)	(18.5)	–	–	–	–	–	–	–
λ_{max}	246.9	260.6	275.8	293.3	–	–	–	–	–	[108]
–	186.3	260.6	275.8	293.3	–	–	–	–	–	[117]
λ_{max}	{4579.4}	{17}	{30.4}	{26}	–	–	–	–	–	–
–	176.1	179.3	183.1	185.0	186.3	–	–	–	–	[117]
λ_{max}	{3387.9}	{5236}	{5399}	{4750}	{4446.9}	–	–	–	–	–
	scaled (see notes)									
λ_{max}	198	208	228	235	–	–	–	–	–	[2] ^d
λ_{max}	–	208	218	225	–	–	–	–	–	[2] ^a
λ_{max}	–	210	216	233	–	–	–	–	–	[2] ^b

^aIn methanol.
^bIn hexane.
^cTriethylsilyldiyne-endcapped derivative.
^dIn acetonitrile.
Note: (–): relative intensity; {–}: absolute intensity in amagat^{−1} cm^{−1} at 300 K. Relative intensities taken from [103] scaled to the spectrum of [117] by a least-squares fit.
Italics: log ϵ .

Because we report the results of our calculations for only three isomers, 7O1(t), 7O2(s), and 7C1(s), we compare in Table 17.33 the nomenclatures for the reported molecules.

17.7.2 RELATIVE ENERGIES, ZERO POINT VIBRATIONAL ENERGIES
AND DIPOLE MOMENTS OF THE C₇H₂ MOLECULES

In Table 17.34 we make an exception by presenting the calculated SCF energies from various sources alongside the customary data of this table because this is the only case in which there is a disagreement among authors as to which molecule has the lowest energy. According to Cooper and Murphy [58] and Aoki and Ikuta [128], that molecule is the “three-membered ring with one side chain” or 7C1(s). According to Dua et al. [130] and our own work, 7O1(t) is the molecule with the lowest energy. In the case of C₅H₂, there is full agreement that 5O1(t) is the molecule with the lowest

TABLE 17.33**Nomenclatures for C₇H₂ Molecules Treated by Various Investigators Compared to our Names**

Our	[58]	[17]	[128]	[116]	[130]	[131]
name	—	—	—	—	—	—
7O1(t)	³ Σ [−]	C ₇	8'	HC ₇ H	5	—
7O2(s)	c	—	7'	—	6	—
7O3(s)	—	—	5'	—	7	—
7O4(s)	—	—	3'	—	8	—
7O5(s)	—	—	6'	—	4	—
7O6(t)	—	—	—	—	9t	—
7O7(s)	—	—	4'	—	—	—
7C1(s)	c	—	1'	—	2	C ₇ H ₂
7C2(s)	d	—	2'	—	1	—
7C3(s)	—	—	—	—	3	—
7C4(s)	—	—	—	—	9s	—

energy [7,115, this work]. Both 5O1(t) and 7O1(t) have D_{∞h} symmetry and since it is not obvious why ring-closing with its extra C–C bond would lower the energy of 7C1(s) much more than of 5C9(s), we surmise that 7O1(t) is the most stable of the C₇H₂ isomers.

This issue is of considerable interest because McCarthy et al. [131], using the results of Aoki and Ikuta [128], have argued that the ring-chain molecule 7C1(s) should be the most abundant C₇H₂ in astronomical settings. The results of Dua et al. [130] and our own results imply that the zero-dipole 7O1(t) molecule could be the more abundant species and this molecule cannot be detected by radio astronomy techniques.

17.7.3 VIBRATIONAL FREQUENCIES, ELECTRONIC SPECTRA, AND ROTATIONAL DATA

Fundamental vibrational frequencies of C₇H₂ molecules are listed in [Table 17.34](#).

Fulara et al. [116] are the only investigators who have reported electronic spectra for 9O1(t) in a neon matrix at 5 K in the range 411.6 to 505.8 nm. The three strongest “pairs” occur at 505.8 + 504.7, and 458.3 + 457.3 nm.

Rotational data are reported in References 69 and 131.

TABLE 17.34
Relative SCF Energies, Zero Point Vibrational Energies (ZPVE), and Dipole Moments of the C₇H₂ Molecules

Molecule	ΔE_{SCF} (kJ mol ⁻¹)	ZPVE (kJ ΔE_{SCF} (kJ mol ⁻¹)	Dipole (debye) ^a	<i>E</i> (hartree)	Reference
7O1(t)	24.42	—	—	−264.4794	[58]
7O1(t)	20.5	—	0.0000	−266.84395	[128] ^a
7O1(t)	0	130.7	0	−267.71051	[130]
7O1(t)	0	123.1	0.00	−267.74888	This work
7O2(s)	44.37	—	7.8	−264.4718	[58]
7O2(s)	91.63	—	3.1984	−266.8169	[128] ^a
7O2(s)	92.75	139	7.33	−267.67825	[130]
7O2(s)	84.38	133.9	7.70	−267.71674	This work
7O3(s)	87.86	—	2.5707	−266.81835	[128] ^a
7O3(s)	110.3	137.3	6.69	−267.67097	[130]
7O4(s)	72.38	—	2.0625	−266.82427	[128] ^a
7O4(s)	111.5	137.9	5.93	−267.67072	[130]
7O5(s)	89.12	—	2.0350	−266.81792	[128] ^a
7O5(s)	146.9	34.3	5.58	−267.6559	[130]
7O6(t)	444.05	129.6	4.08	−267.54284	[130]
7O7(s)	74.47	—	0.9078	−266.82348	[128] ^a
7C1(s)	0	—	—	−264.4887	[58]
7C1(s)	0	—	1.4959	−266.85183	[128] ^a
7C1(s)	57.11	138.1	3.63	−267.69151	[130]
7C1(s)	63.61	135.3	3.74	−267.72465	This work
7C2(s)	37.02	—	3.37	−264.4746	[58]
7C2(s)	7.53	—	1.5538	−266.84902	[128] ^a
7C2(s)	73.26	138.1	3.74	−267.69151	[130]
7C3(s)	142.2	139.7	10.88	−267.65971	[130]
7C4(s)	359.4	134.6	3.88	−267.5751	[130]

Note: All entries for [58] are for 3-21G CASSCF4 calculations. All entries for [128] are for ACPF calculations. All entries for [130] are for B3LYP/aug-cc-pVDZ//B3LYP/6-31G(d) calculations and relative energies ΔE_{SCF} include ZPE corrected by 0.9804.
^aThe dipole moments of [128] are given in atomic units.

17.8 ISOMERS OF C₈H₂, C₁₀H₂, C₁₂H₂, C₁₄H₂, AND C₁₆H₂

17.8.1 ISOMERS OF C₈H₂

In this section we present all of the remaining C_{*m*}H₂ molecules with even *m*-values.

C₈H₂ occurs in the atmosphere of Titan [132,133]. The compound was recently synthesized in solutions by Cataldo [1,2], who also determined its UV–vis absorption spectrum. We will consider only the two open molecules

TABLE 17.34B
Fundamental Vibrational Frequencies of the C₇H₂ Molecules (All This Work)

Molecule	F1	F2	F3	F4	F5	F6	F7	F8	F9	F10
7O1(t)	3458	3455	2051	2014	1682	1657	1081	561	489	489
–	[0.1]R	[251]R	[0]R	[1.1]R	[0]R	[15]R	[6.1]R	[0]R	[0.5]R	[4.1]R
7O2(s)	3185	3109	2188	2173	1947	1573	1435	1079	1031	927
–	[0.7]R	[2.7]R	[1932]R	[96]R	[343]R	[23]R	[9.0]R	[0.1]R	[0]R	[40]R
7C1(s)	3465	3235	2275	2156	1723	1262	1196	989	911	841
–	[109]R	[0.8]R	[13]R	[3.7]R	[5.0]R	[32]R	[3.7]R	[3.4]R	[4.3]R	[18]R

Molecule	F11	F12	F13	F14	F15	F16	F17	F18	F19	F20	F21
7O1(t)	487	480	431	430	398	384	378	286	192	96.7	78.8
–	[53]R	[53]R	[45]R	[40]R	[0]R	[1.4]R	[1.8]R	[0.7]R	[0]R	[2.8]R	[2.8]R
7O2(s)	590	571	545	487	444	296	278	193	179	76.9	76.3
–	[6.3]R	[0.6]R	[0.5]R	[2.1]R	[1.0]R	[0]R	[0.4]R	[8.2]R	[10]R	[1.1]R	[0.1]R
7C1(s)	669	571	567	537	523	500	469	268	240	99.3	97.1
–	[39]R	[50]R	[1.3]R	[2.5]R	[0.9]R	[0.1]R	[1.5]R	[1.9]R	[4.4]R	[0.3]R	[3.4]R

TABLE 17.35
Relative SCF Energies, Zero Point Vibrational Energies (ZPVE), and Dipole Moments of C₈H₂ Molecules (All This Work)

Molecule	ΔE_{SCF} (kJ mol ^{−1})	ZPVE (kJ mol ^{−1})	Dipole (debye)
8O1(s)	0.00	148.46	0.00
8O2(s)	180	146.31	7.85

E_{SCF} of 8O1(s)=−305.877583 hartree (this work). Fan and Pfeiffer [17] have reported calculated total energies for 8O1(s).

of C₈H₂, 8O1(s) and 8O2(s). Table 17.35 presents their relative energies, zero point vibrational energies and dipole moments of the molecules. The three strongest vibrational frequencies are presented in [Table 17.36](#).

17.8.1.1 Vibrational Data

Because we report only selected frequencies of high intensitiy, the F-numbering shows “gaps”. For example, in Table 17.36 F1 is missing

TABLE 17.36**Three Strongest Vibrational Frequencies of 8O1(s) and 8O2(s)**

Molecule	F2	F3	F4	F5	F8	F10	Reference
8O1(s)	3332.2(R)	—	—	1232.6(R)	—	621.5	[133]
—	{595}	—	—	{256}	{496}	—	—
—	3326.6(P)	—	—	1226(P)	—	—	—
—	{595}	—	—	{256}	—	—	—
8O1(s)	3386	—	—	955	—	600	[133]
—	[454.93]	—	—	—	[7.61]	[91.3]	—
8O1(s)	3466	—	—	943	—	599	This work
—	[274]R	—	—	[6.2]R	[93]R	—	—
—	—	2218	2163	2040	—	—	This work
—	—	[659]R	[2228]R	[1415] R	—	—	—

(R) and (P) after frequencies denote band systems.

for 8O1(s), which means that its intensity is lower than that of the three frequencies actually listed.

17.8.1.2 Electronic Spectra and Rotational Data

UV–vis absorption spectra have been determined for 8O1(s). Because Eastmond et al. [102] have measured the spectra for C_8H_2 we will report these data only and not the results for the triethylsilyldiyne-endcapped derivative. Observed values of λ_{\max} are listed in Tables 17.36 and 17.37.

Rotational data are reported in Reference 69.

17.8.2 ISOMERS OF $C_{10}H_2$

We will consider only two open molecules of $C_{10}H_2$, 10O1(s) and 10O2(s). Table 17.38 presents their relative energies, zero point vibrational energies and dipole moments.

17.8.2.1 Vibrational Data, Electronic Spectra, and Rotational Data

The three strongest vibrational frequencies are presented in Table 17.39.

UV–vis absorption spectra have been determined for 10O1(s), including spectra for triethylsilyldiyne-endcapped derivatives. Observed values of λ_{\max} are listed in Table 17.40.

No rotational data were found.

TABLE 17.37
Selected Values of the UV Absorption Spectra of 8O1(s)

—	—	—	—	—	—	—	Reference
B-bands only							
λ_{max}	215	222.5	281.5	297.5	316	337.5	[102] ^a
—	<i>5.06</i>	<i>5.25</i>	—	—	—	—	—
λ_{max}	215.5	226	—	—	—	—	[102] ^a
—	<i>5.12</i>	<i>5.28</i>	—	—	—	—	—
λ_{max}	184.1	190.8	198.7	207.3	—	—	[103] ^c
—	{13.9}	{24.1}	{56.2}	{100}	—	—	—
λ_{max}	197.4	206.0	215.4	225.6	—	—	[103] ^d
—	{16.0}	{31.4}	{71.2}	{99.4}	—	—	—
λ_{max}	200	218	227	—	—	—	[2] ^e
λ_{max}	200	218	227	—	—	—	[2] ^a
λ_{max}	200	218	227	—	—	—	[2] ^b
A-Bands only							
λ_{max}	283.5	301.4	321.7	336.9	340.2	345.1	[103] ^a
—	{45.5}	{55.0}	{56.1}	{12.6}	{20.4}	{34.2}	—

^aIn methanol.
^bIn hexane.
^cHigh-intensity transitions in the gas phase.
^dB-band in *n*-pentane at 25°C.
^eIn acetonitrile.
Note: Italics: log ϵ

TABLE 17.38
Relative SCF Energies, Zero Point Vibrational Energies (ZPVE), and Dipole Moments of C₁₀H₂ Molecules (All This Work)

Molecule	ΔE_{SCF} (kJ mol ^{−1})	ZPVE (kJ mol ^{−1})	Dipole (debye)
10O1(s)	0.00	175.08	0.00
10O2(s)	185.5	172.20	9.44

E_{SCF} of 10O1(s) = −382.056283 hartree (this work). Fan and Pfeiffer [17] have reported calculated total energies for 10O1(s).

17.8.3 ISOMERS OF C₁₂H₂

We will consider only two open molecules of C₁₂H₂, 10O1(s) and 10O2(s). Table 17.41 presents their relative energies, zero point vibrational energies and dipole moments. The three strongest vibrational frequencies are

TABLE 17.39
Three Strongest Vibrational Frequencies of 10O1(s) and 10O2(s) (All This Work)

Molecule	F2	F3	F5	F7	F13	F14
10O1(s)	3465	—	—	—	601	601
—	[335]R	—	—	—	[92]R	[92]R
10O2(s)	—	2230	2072	1804	—	—
—	—	[922]R	[5852]R	[392]R	—	—
—	—	—	—	—	—	—

TABLE 17.40
Selected Values of the UV Absorption Spectra of 10O1(s)

—	—	—	—	—	—	—	Reference
λ_{max}	226	238	250	—	—	—	[102] ^a
—	(0.33)	(0.7)	(1.0)	—	—	—	—
λ_{max}	227.5	239	251.5	—	—	—	[102] ^b
λ_{max}	211	217.3	227.7	238.7	244.2	251.3	[103] ^c
—	(3.3)	(10.6)	(30.8)	(74.6)	(13.1)	(100)	—
λ_{max}	227.5	237.6	251.4	—	—	—	[134] ^b
λ_{max}	218	227	239	251	—	—	[2] ^d
λ_{max}	218	227	239	251	—	—	[2] ^a
λ_{max}	218	227	239	251	—	—	[2] ^b

^aIn methanol.
^bIn hexane.
^cIn *n*-pentane at 25°C.
^dIn acetonitrile.

TABLE 17.41
Relative SCF Energies, Zero Point Vibrational Energies (ZPVE), and Dipole Moments of C₁₂H₂ Molecules (All This Work)

Molecule	ΔE_{SCF} (kJ mol ^{−1})	ZPVE (kJ mol ^{−1})	Dipole (debye)
12O1(s)	0.00	201.69	0.00
12O2(s)	616.8	197.93	11.01

Note: E_{SCF} of 12O1(s) = −458.234937 hartree (this work).

TABLE 17.42
Vibrational Frequencies of 12O1(s) and 12O2(s) (All This Work)

Molecule	F2	F3	F5	F7	F13	F14
10O1(s)	3465	—	—	—	602	602
—	[394]R	—	—	—	[92]R	[92]R
10O2(s)	—	2225	2019	1971	—	—
—	—	[1347]R	[3215]R	[5954]R	—	—

TABLE 17.43
Selected Values of the UV Absorption Spectra of 12O1(s)

—	—	—	—	—	—	Reference
λ_{max}	225	235	246.5	259.5	273.5	[102] ^a
—	<i>4.51</i>	<i>4.69</i>	<i>4.49</i>	<i>5.38</i>	<i>5.47</i>	—
λ_{max}	225.5	236	247.5	260.5	275	[102] ^b
—	<i>4.59</i>	<i>4.74</i>	<i>5.02</i>	<i>5.41</i>	<i>5.51</i>	—
λ_{max}	—	—	246.4	258.6	273.3	[134] ^b
λ_{max}	—	237	248	260	273	[2] ^d
λ_{max}	—	237	248	260	273	[2] ^a
λ_{max}	—	237	248	260	273	[2] ^b

^aIn methanol.

^bIn hexane.

^cIn *n*-pentane at 25°C.

^dIn acetonitrile.

Note: Italics: log ϵ .

presented in Table 17.42. Selected values for the UV absorption spectra are listed in Table 17.43.

17.8.4 ISOMERS OF C₁₄H₂ AND C₁₆H₂

We restrict the report to 14O1(s) and 16O1(s). [Tables 17.44](#) to [17.47](#) speak for themselves.

17.9 ISOMERS OF C₉H₂, C₁₁H₂, C₁₃H₂, AND C₁₅H₂

Almost nothing is known of these molecules. McCarthy et al. [135] have determined rotational properties of the carbon ring-chain C₉H₂. Fulara

TABLE 17.44
SCF Energies, Zero Point Vibrational Energies (ZPVE), and Dipole Moments of 14O1(s) and 16O1(s) (All This Work)

Molecule	E_{SCF} (kJ mol ⁻¹)	ZPVE (kJ mol ⁻¹)	Dipole (debye)
14O1(s)	-534.413808	227.01	0.00
16O1(s)	-610.592734	252.67	0.00

TABLE 17.45
Three Strongest Vibrational Frequencies of 14O1(s) and 16O1(s) (All This Work)

Molecule	F2	F15	F16
14O1(s)	3464	604	604
—	[432]R	[90]R	[89]R
16O1(s)	3464	605	604
—	[434]R	[90]R	[77]R

TABLE 17.46
Selected Values of the UV Absorption Spectra of 14O1(s)

—	—	—	—	—	—	Reference
λ_{max}	295	279	264	252	236	[102] ^a
—	(1.0)	(0.85)	(0.48)	(0.17)	(0.12)	—
λ_{max}	297	281	266	253	237	[102] ^b
λ_{max}	297	280	268	253	237	[134] ^b
λ_{max}	297	280	268	253	237	[2] ^d
λ_{max}	297	280	268	253	237	[2] ^a

^aIn methanol.

^bIn hexane.

^cIn *n*-pentane at 25°C.

^dIn acetonitrile.

Note: (·): relative intensities.

TABLE 17.47
Selected Values of the UV Absorption Spectra of 16O1(s)

—	—	—	—	—	—	Reference
λ_{max}	255	267	281	297	315	[102] ^a
—	<i>4.30</i>	<i>4.60</i>	<i>5.01</i>	<i>5.36</i>	<i>5.48</i>	—
λ_{max}	255.5	268	281.5	298	316	[102] ^b
—	<i>4.51</i>	<i>4.72</i>	<i>5.19</i>	<i>5.44</i>	<i>5.54</i>	—
λ_{max}	255	268	281	298	318	[134] ^b
λ_{max}	255	268	281	298	318	[2] ^d
λ_{max}	255	268	281	298	318	[2] ^a

^aIn methanol.

^bIn hexane.

^cIn *n*-pentane at 25°C.

^dIn acetonitrile.

Note: Italics: log ϵ .

TABLE 17.48
SCF Energies, Zero Point Vibrational Energies (ZPVE), and Dipole Moments of Isomers of C₉H₂, C₁₁H₂, C₁₃H₂, and C₁₅H₂ (All This Work)

Molecule	ESCF (hartree)	ZPVE (kJ mol ^{−1})	Dipole (debye)
9O1(t)	−343.933701	151.23	0.00
9O2(s)	−343.894088	159.71	9.29
11O1(t)	−420.116803	177.50	0.00
11O2(s)	−420.071440	185.40	10.86
13O1(t)	−496.298803	203.29	0.00
13O2(s)	−496.248803	210.95	12.40
15O1(t)	−572.4801733	232.16	0.00

et al. [116] have measured absorption spectra of C₉H₂, C₁₁H₂, and C₁₃H₂ in neon matrices at 5 K. We present here the results of our quantum chemical calculations for all of these molecules (Tables 17.48 and 17.49).

17.10 SUMMARY

1. We have confirmed that the ground states of the C_{*m*}H₂ molecules with *m* = even numbers are singlets and that the ground states of the C_{*m*}H₂ molecules with *m* = odd numbers are triplets.

TABLE 17.49**Three Strongest Vibrational Frequencies of Isomers of C_9H_2 , $C_{11}H_2$, $C_{13}H_2$, and $C_{15}H_2$ (All This Work)**

Molecule	F2	F3	F5	F6	F10	F11	F12	F13
9O1(t)	3458	—	—	—	523	523	—	—
—	[326]R	—	—	—	[78]R	[79]R	—	—
9O2(s)	—	2220	2671	1930	—	—	—	—
—	—	[1157]R	[1453]R	[348]R	—	—	—	—
11O1(t)	3460	—	—	—	—	—	546	546
—	[402]R	—	—	—	—	—	[75]R	[75]R
13O1(t)	F2	—	—	—	—	—	F14	F17
—	3460	—	—	—	—	—	562	561
—	[471]R	—	—	—	—	—	[75]R	[88]R
13O2(s)	—	F3	F5	F7	—	—	—	—
—	—	2227	2158	1956	—	—	—	—
—	—	[1118]R	[2538]R	[6362]R	—	—	—	—
15O1(t)	F2	—	—	—	—	—	F19	F20
—	3489	—	—	—	—	—	552	552
—	[623]R	—	—	—	—	—	[96]R	[96]R

- The only exception to the rule that the HC_mH molecules (the $mO1$ molecules) have the lowest energy is 1C3(s), cyclopropenylidene.
- Figure 17.2 shows an interesting trend among the intensities of the strongest IR lines of the HC_mH molecules, which is always due to the asymmetric C–H stretch. The intensities increase with increasing chain length and in the case of the $m = \text{even}$ molecules appears to level off near $m = 18$.
- There is also a drift of the wavelengths of the strongest IR lines as shown in Figure 17.3.
- There is a subtle trend among the C–C bond lengths of the $m = \text{even}$ molecules as shown in Figure 17.4.
- The change of C–C bond lengths of the $m = \text{odd}$ molecules is much more pronounced as shown in Figure 17.5. Data for C_2H_2 and C_3H_2 are not entered because these bond lengths do not fit the trends. Clearly C_2H_2 and C_3H_2 are exceptional molecules.
- The C–H bond lengths remain essentially constant near 0.1064 nm in all HC_mH molecules.

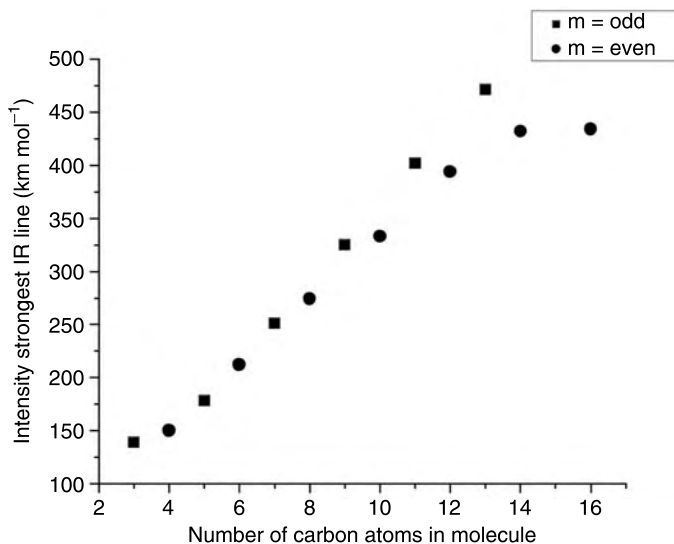


FIGURE 17.2 Intensities of the strongest IR lines which in all HC_mH molecules are due to the asymmetric C–H stretch.

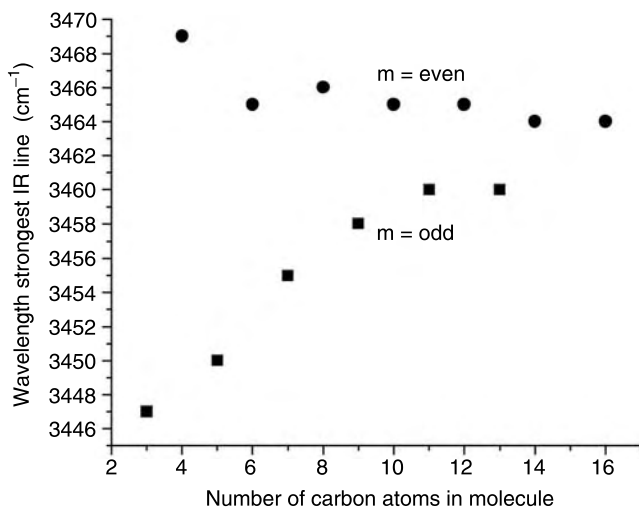


FIGURE 17.3 Drift of the wavelengths of the strongest IR line of the HC_mH molecules.

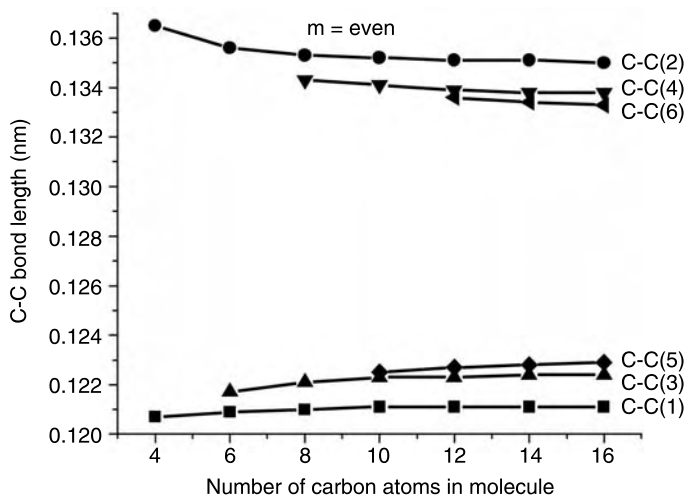


FIGURE 17.4 Change of C-C bond lengths with m for the $m = \text{even}$ molecules.

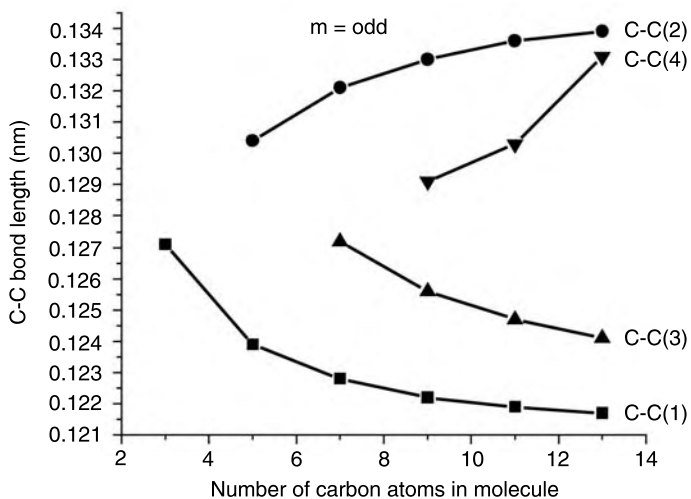


FIGURE 17.5 Change of C-C bond lengths with m for the $m = \text{odd}$ molecules.

REFERENCES

- [1] Cataldo, F. Simple generation and detection of polyynes in an arc discharge between graphite electrodes submerged in various solvents. *Carbon* **2003**, *41*, 2653–2689.
- [2] Cataldo, F. Synthesis of polyynes in a submerged electric arc in organic solvents. *Carbon* **2004**, *42*, 129–142.
- [3] Levin, J.; Feldman, H.; Baer, A.; Ben-Hamu, D.; Heber, O.; Zajfman, D.; Vager, Z. Study of unimolecular reactions by Coulomb explosion imaging: The nondecaying vinylidene. *Phys. Rev. Lett.* **1998**, *81*, 3347–3350.
- [4] Schork, D.; Köppel, H. Barrier recrossing in the vinylidene–acetylene isomerization reaction: A five-dimensional ab initio quantum dynamical investigation. *J. Chem. Phys.* **2001**, *115*, 7907–7923.
- [5] Hayes, R.L.; Fattal, E.; Govind, N.; Carter E.A. Long live vinylidene! A new view of the $\text{H}_2\text{C}=\text{C}:$ to $\text{HC}\equiv\text{CH}$ rearrangement from ab initio molecular dynamics. *J. Am. Chem. Soc.* **2001**, *123*, 641–657.
- [6] Sattelmeyer, K.W.; Stanton, J.F. Computational studies of C_6H_2 isomers. *J. Am. Chem. Soc.* **2000**, *122*, 8220–8227.
- [7] Seburg, R.A.; McMahon, R.J.; Stanton J.F.; Gauss, J. Structures and stabilities of C_5H_2 isomers: Quantum chemical studies. *J. Am. Chem. Soc.* **1997**, *119*, 10838–10845.
- [8] Smith, B.J.; Smernik, P.; Radom, L. The vinylidene–acetylene rearrangements. A phantom minimum on the MP2 potential energy surface. *Chem. Phys. Lett.* **1992**, *188*, 589–594.
- [9] Zou, S.L.; Bowman, J.M. A new ab initio potential energy surface describing acetylene/vinylidene isomerization. *Chem. Phys. Lett.* **2003**, *368*, 421–424.
- [10] Chang, N.Y.; Shen, M.Y.; Yu, C.H. Extended ab initio studies of the vinylidene–acetylene rearrangement. *J. Chem. Phys.* **1997**, *106*, 3237–3242.
- [11] Petersson, G.A.; Tensfeldt, T.G.; Montgomery, J.A., Jr. Vinylidene and the Hammond postulate. *J. Am. Chem. Soc.* **1992**, *114*, 6133–6138.
- [12] Gallo, M.M.; Hamilton, T.P.; Schaefer, H.F., III. Vinylidene: the final chapter? *J. Am. Chem. Soc.* **1990**, *112*, 8714–8719.
- [13] Ervin, K.M.; Ho, J.; Lineberger, W.C. A study of the singlet and triplet-states of vinylidene by photoelectron-spectroscopy of $\text{H}_2\text{C}=\text{C}^-$, $\text{D}_2\text{C}=\text{C}^-$, and $\text{HDC}=\text{C}^-$, vinylidene acetylene isomerization. *J. Chem. Phys.* **1989**, *91*, 5974–5992.
- [14] Ervin, K.M.; Gromet, S.; Barlow, S.E.; Gilles, M.K.; Harrison, A.G.; Bierbaum, V.M.; De Puy, C.H.; Lineberger, W.C.; Ellison, G.B. Bond strengths of ethylene and acetylene. *J. Am. Chem. Soc.* **1990**, *112*, 5750–5759.
- [15] Burnett, S.M.; Stevens, A.E.; Feigerle, C.S.; Lineberger, W.C. Observation of X1A1 vinylidene by photoelectron-spectroscopy of the C_2H_2^- ion. *Chem. Phys. Lett.* **1983**, *100*, 124.
- [16] Dykstra, C.E.; Parsons, C.A.; Oates, C.L. Structures and energies of cumulene carbenes. *J. Am. Chem. Soc.* **1979**, *101*, 1962–1965.
- [17] Fan, Q.; Pfeiffer, G.V. Theoretical study of linear C_n ($n=6-10$) and HC_nH ($n=2-10$) molecules. *Chem. Phys. Lett.* **1989**, *162*, 472–478.

- [18] Miller, S.A. *Acetylene: its Properties, Manufacture, and Uses*. Academic Press, New York, 1965.
- [19] Herzberg, G. *Infrared and Raman Spectra of Polyatomic Molecules*. Van Nostrand, NY, 1945.
- [20] Shimanouchi, T. *Tables of Molecular Vibrational Frequencies Consolidated*. Vol 1, Natl. Bureau Stand., Vol 39. US GPO, Washington, DC, 1972.
- [21] Deng, W.Q.; Han, K.L.; Zhan, J.P.; He, G.Z. Ab initio and RRKM calculations of *o*-benzyne pyrolysis. *Chem. Phys. Lett.* **1998**, 288, 33–36.
- [22] Chen, Y.Q.; Jonas, D.M.; Kinsey, J.L.; Field, R.W. High-resolution spectroscopic detection of acetylene–vinylidene isomerization by spectral cross-correlation. *J. Chem. Phys.* **1989**, 91, 3976–3985.
- [23] Zou, S.L.; Bowman, J.M. Full dimensionality quantum calculations of acetylene/vinylidene isomerization. *J. Chem. Phys.* **2002**, 117, 5507–5510.
- [24] Zou, S.L.; Bowman, J.M. Reduced dimensionality quantum calculations of acetylene to vinylidene isomerization. *J. Chem. Phys.* **2002**, 116, 6667–6673.
- [25] Schork, R.; Köppel, H. Unexpected stability of vinylidene from 5D ab-initio quantum-dynamical calculations. *Chem. Phys. Lett.* **2000**, 326, 277–282.
- [26] Jacobson, M.P.; Field, R.W. Acetylene at the threshold of isomerization. *J. Phys. Chem. A* **2000**, 104, 3073–3086.
- [27] Field, R.W.; Jacobson, M.P. Order out of chaos: Local bends above the energy of the acetylene–vinylidene isomerization barrier. In *Abstracts of papers of the American Chemical Society* 217, 141-PHYS Part 2, Mar 21, 1999.
- [28] Stanton, J.F.; Gauss, J. An estimation of the isomerization energy of acetylene. *J. Chem. Phys.* **1999**, 110, 1831–1832.
- [29] Chen, Y.; Pique, J.P.; Field, R.; Kinsey, J.L. A spectroscopic study of acetylene–vinylidene isomerization. In *Abstracts of papers of the American Chemical Society* 193, 117-PHYS, Apr 5, 1987.
- [30] Chen, Y.Q.; Jonas, D.M.; Kinsey, J.L.; Field, R.W. High-resolution spectroscopic detection of acetylene–vinylidene isomerization by spectral cross-correlation. In *Abstracts of papers of the American Chemical Society* 199, 58-PHYS Part 2, Apr 22, 1990.
- [31] Field, R.W.; Jonas, D.M.; Kinsey, J.L.; Chen, Y.Q. Acetylene to vinylidene isomerization — tunneling resonances in eigenstate resolved spectra. In *Abstracts of papers of the American Chemical Society* 199, 156-PHYS Part 2, Apr 22, 1990.
- [32] Carrington, T., Jr.; Hubbard, L.M.; Schaefer, H.F., III; Miller, W.H. Vinylidene: potential energy surface and unimolecular reaction dynamics. *J. Chem. Phys.* **1984**, 80, 4347–4354.
- [33] Kasai, P.H. ESR study of sodium atom–acetylene complex: evidence for acetylene–vinylidene rearrangement. *J. Phys. Chem.* **1982**, 86, 4092–4094.
- [34] Krishnan, R.; Frisch, M.J.; Pople, J.A. von R.; Schleyer, P. The vinylidene–acetylene isomerization barrier. *Chem. Phys. Lett.* **1981**, 79, 408–411.
- [35] Conrad, M.P.; Schaefer, H.F., III. Absence of an energetically viable pathway for triplet 1,2 hydrogen shifts. A theoretical study of the vinylidene–acetylene isomerization. *J. Am. Chem. Soc.* **1978**, 100, 7820–7823.

- [36] Dykstra, C.E.; Schaefer, H.F. The vinylidene–acetylene rearrangement: A self-consistent electron pairs study of a model unimolecular reaction. *J. Am. Chem. Soc.* **1978**, *100*, 1378–1382.
- [37] Matthews, H.E.; Irvine, W.M. The hydrocarbon ring C_3H_2 is ubiquitous in the Galaxy. *Astrophys. J. Lett.* **1985**, *298*, L61–L65.
- [38] Thaddeus, P.; Vrtilek, J.M.; Gottlieb, C.A. Laboratory and astronomical identification of cyclopropenylidene, C_3H_2 . *Astrophys. J.* **1985**, *299*, L63–L66.
- [39] Thaddeus, P.; McCarthy, M.C.; Travers, M.J.; Gottlieb, C.A.; Chen, W. New carbon chains in the laboratory and in interstellar space. *Faraday Discuss.* **1998**, *109*, 121–135.
- [40] Yamamoto, S.; Saito, S.; Ohishi, M.; Suzuki, H.; Ishikawa, S.I.; Kaifu, N.; Murakami, A. Laboratory and astronomical detection of the cyclic C_3H radical. *Astrophys. J. Lett.* **1987**, *322*, L55–L58.
- [41] Cernicharo, J.; Kahane, C.; Guélin, M.; Gomez-Gonzalez, J. Tentative detection of CH_3NC towards Sgr B2. *Astron. Astrophys.* **1988**, *189*, L1–L2.
- [42] Turner, B.E.; Herbst, E.; Terzieva, R. The physics and chemistry of small translucent molecular clouds. VIII. The basic hydrocarbon chemistry. *Astrophys. J. Suppl.* **2000**, *126*, 427–460.
- [43] Bernheim, R.A.; Kempf, R.J.; Gramas, J.V.; Skell, P.S. Electron paramagnetic resonance of triplet alternant methylenes. Propargylene and homologs. *J. Chem. Phys.* **1965**, *43*, 196–200.
- [44] Reisenauer, H.P.; Maier, G.; Riemann, A.; Hoffmann, R.W. Cyclopropenylidene. *Angew. Chem. Int. Ed. Engl.* **1984**, *23*, 641.
- [45] Maier, G.; Reisenauer, H.P.; Schwab, W.; Čársky, P.; Hess, B.A.; Schaad, L.J. Vinylidenecarbene: A new C_3H_2 species. *J. Am. Chem. Soc.* **1987**, *109*, 5183–5188.
- [46] Ochsenfeld, C.; Kaiser, R.I.; Lee, Y.T.; Suits, A.G.; Head-Gordon, M. A coupled-cluster *ab initio* study of triplet C_3H_2 and the neutral–neutral reaction to interstellar C_3H . *J. Chem. Phys.* **1997**, *106*, 4141–4151.
- [47] Saxe, P.; Schaefer, H.F., III. Can cyclopropyne really be made? *J. Am. Chem. Soc.* **1980**, *102*, 3239–3240.
- [48] Yamaguchi, Y.; Osamura, Y.; Fitzgerald, G.; Schaefer, H.F., III. Analytic force constants for post-Hartree–Fock functions: The simplest case. *J. Chem. Phys.* **1983**, *78*, 1607–1608.
- [49] Lee, T.J.; Bunge, A.; Schaefer H.F., III. Toward the laboratory identification of cyclopropenylidene. *J. Am. Chem. Soc.* **1985**, *107*, 137–142.
- [50] Jonas, V.; Böhme, M.; Frenking, G. Structures and energies of the lowest lying singlet and triplet states of C_3H_2 and C_3F_2 . A theoretical–study. *J. Phys. Chem.* **1992**, *96*, 1640–1648.
- [51] Seburg, R.A.; McMahon, R.J. Auto- und Isomerisierungen im System Propinyliden ($HCCCH$), Propadienyliden (H_2CCC) und Cyclopropenyliden ($c-C_3H_2O$) *Angew. Chem.* **1995**, *107*, 2198–2201.
- [52] Hehre, W.J.; Pople, J.A.; Lathan, W.A.; Radom, L.; Wasserman, E.; Wasserman, Z.R. Molecular orbital theory of the electronic structure of organic compounds 28. Geometries and energies of singlet and triplet states of the C_3H_2 hydrocarbons. *J. Am. Chem. Soc.* **1976**, *98*, 4378–4383.

- [53] DeFrees, D.J.; McLean, A.D. Ab initio molecular orbital studies of low-energy, metastable isomers of the ubiquitous cyclopropenylidene. *Astrophys. J.* **1986**, *308*, L31–L35.
- [54] Seburg, R.A.; Patterson, E.V.; Stanton, J.F.; McMahon, R.J. Structures, automerizations, and isomerizations of C_3H_2 isomers. *J. Am. Chem. Soc.* **1997**, *119*, 5847–5856.
- [55] Rubio, M.; Stålring, J.; Bernhardsson, A.; Lindh, R.; Roos, B.O. Theoretical studies of isomers of C_3H_2 using a multiconfigurational approach. *Theor. Chem. Acc.* **2000**, *105*, 15–30.
- [56] Brown, R.D.; Godfrey, P.D.; Bettens, R.P.A. The dipole moment of C_3H_2 . *Roy. Astron. Soc. Monthly Notices* **1987**, *227*, 19P–20P.
- [57] Bofill, J.M.; Farràs, J.; Olivella, S.; Solé, A.; Vilarassa, J. Molecular and electronic structure of the low-lying electronic states of cycloalkenylidenes: cyclopropenylidene. *J. Am. Chem. Soc.* **1988**, *110*, 1694–1700.
- [58] Cooper, D.L.; Murphy S.C. Ab initio geometries for $C_{2n+1}H$, $C_{2n+1}H^+$, and $C_{2n+1}H_2$ species for $n = 1, 2, 3$. *Astrophys. J.* **1988**, *333*, 482–490.
- [59] Lovas, F.J.; Suenram, R.D.; Ogata, T.; Yamamoto, S. Microwave spectra and electric dipole moments for low- J levels of interstellar radicals: SO, C_2S , C_3S , c- HC_3 , CH_2CC , and c- C_3H_2 . *Astrophys. J.* **1992**, *399*, 325–329.
- [60] Seburg, R.A.; DePinto, J.T.; Patterson, E.V.; McMahon, R.J. Structure of triplet propynylidene. *J. Am. Chem. Soc.* **1995**, *117*, 835–836.
- [61] Huang, J.W.; Graham, W.R.M. Fourier transform infrared study of tricarbon hydride radicals trapped in Ar at 10 K. *J. Chem. Phys.* **1990**, *93*, 1583–1596.
- [62] Maier, G.; Reisenauer, H.P.; Schwab, W.; Čársky, P.; Špirko, V.; Hess, B.A., Jr.; Schaad, L.J. Propargylene: A C_3H_2 isomer with unusual bonding. *J. Chem. Phys.* **1989**, *91*, 4763–4773.
- [63] Gottlieb, C.A.; Killian, T.C.; Thaddeus, P.; Botschwina, P.; Flügge, J.; Oswald, M. Structure of propadienylidene, H_2CCC . *J. Chem. Phys.* **1993**, *98*, 4478–4485.
- [64] Gauss, J.; Stanton, J.F. The equilibrium structure of propadienylidene. *J. Mol. Struct.* **1999**, *486*, 43–50.
- [65] Mebel, A.M.; Jackson, W.M.; Chang, A.H.H.; Lin S.H. Photodissociation dynamics of propyne and allene: A view from ab initio calculations of the C_3H_n ($n = 1–4$) species and the isomerization mechanism for C_3H_2 . *J. Am. Chem. Soc.* **1998**, *120*, 5751–5763.
- [66] Stanton, J.F.; DePinto, J.T.; Seburg, R.A.; Hodges, J.A.; McMahon, R.J. Electronic spectrum of propadienylidene ($H_2C=C=C$). *J. Am. Chem. Soc.* **1997**, *119*, 429–430.
- [67] Hodges, J.A.; McMahon, R.J.; Sattelmeyer, K.W.; Stanton, J.F. Electronic spectrum of propadienylidene ($H_2C=C=C$) and its relevance to the diffuse interstellar bands. *Astrophys. J.* **2000**, *544*, 838–842.
- [68] Vrtilik, J.M.; Gottlieb, C.A.; Thaddeus, P. Laboratory and astronomical spectroscopy of C_3H_2 , the first interstellar organic ring. *Astrophys. J.* **1987**, *314*, 716–725.
- [69] Maluendes, S.A.; McLean, A.D. Ab initio predictions on the rotational spectra of carbon-chain carbene molecules. *Chem. Phys. Lett.* **1992**, *200*, 511–517.

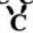

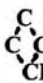

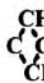
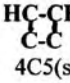
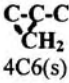
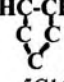
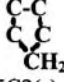
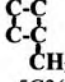
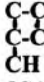
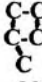
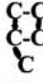


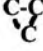
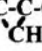
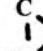
- [70] Mollaaghababa, R.; Gottlieb, C.A.; Vrtilek, J.M.; Thaddeus, P. Millimeter-wave spectrum of vibrationally excited cyclopropenylidene, $c\text{-C}_3\text{H}_2$. *J. Chem. Phys.* **1993**, *99*, 890–896.
- [71] Kaiser, R.I.; Ochsenfeld, C.; Head-Gordon, M.; Lee, Y.T.; Suits, A.G. A combined experimental and theoretical study on the formation of interstellar C_3H isomers. *Science* **1996**, *274*, 1508–1511.
- [72] Kaiser, R.I.; Ochsenfeld, C.; Head-Gordon, M.; Lee, Y.T.; Suits, A.G. Crossed-beam reaction of carbon atoms with hydrocarbon molecules. III: Chemical dynamics of propynylidyne ($l\text{-C}_3\text{H}; X^2\Pi_j$) and cyclopropynylidyne ($c\text{-C}_3\text{H}; X^2B_2$) formation from reaction of $\text{C}(^3P)$ with acetylene, $\text{C}_2\text{H}_2(X^1\Sigma_g^+)$. *J. Chem. Phys.* **1997**, *106*, 1729–1741.
- [73] Takahashi, J.; Yamashita, K. *Ab initio* studies on the interstellar molecules C_3H_2 and C_3H and the mechanism for the neutral–neutral reaction $\text{C}(^3P) + \text{C}_2\text{H}_2$. *J. Chem. Phys.* **1996**, *104*, 6613–6627.
- [74] Lebonnois, S.; Bakes, E.L.O.; McKay, C.P. Atomic and molecular hydrogen budget in Titan's atmosphere. *Icarus* **2003**, *161*, 474–485.
- [75] Moses, J.I.; Bezard, B.; Lellouch, E.; Gladstone, G.R.; Feuchtgruber, H.; Allen, M. Photochemistry of Saturn's atmosphere — I. Hydrocarbon chemistry and comparisons with ISO observations. *Icarus* **2000**, *143*, 244–298.
- [76] Krasnopolsky, V.A. Middle ultraviolet spectroscopy of Pluto and Charon. *Icarus* **2001**, *153*, 277–284.
- [77] Magee-Sauer, K.; Dello Russo, N.; DiSanti, M.A.; Gibb, E.; Mumma, M.J. CSHELL observations of Comet C/2002 C1 (Ikeya-Zhang) in the 3.0-micron region. *Bull. Am. Astronom. Soc.* **2000**, *34*, 868.
- [78] Cernicharo, J.; Gottlieb, C.A.; Guélin, M.; Killian, T.C.; Thaddeus, P.; Vrtilek, J.M. Astronomical detection of H_2CCCC . *Astrophys. J.* **1991**, *368*, L43–L45.
- [79] Cernicharo, J.; Heras, A.M.; Tielens, A.G.G.M.; Pardo, J.R.; Herpin, F.; Guélin, M.; Waters, L.B.F.M. Infrared space observatory's discovery of C_4H_2 , C_6H_2 , and benzene in CRL 618. *Astrophys. J.* **2001**, *546*, L123–L126.
- [80] Cernicharo, J.; Goicoechea, J.R.; Benilan, Y. A new infrared band in interstellar and circumstellar clouds: C_4 or C_4H ? *Astrophys. J.* **2002**, *580*, L157–L160.
- [81] Goldberg, N.; Stülzle, D.; Schwarz, H. The gas-phase generation and characterization of butatrienylidene H_2CCCC : by neutralization–reionization mass spectrometry. *Chem. Phys. Lett.* **1993**, *213*, 593–596.
- [82] Ramos, M.N.; Ferreira, M.M.C. Infrared intensity parameters of the diacetylene and acidity of acetylenic hydrogens. *Spectrochim. Acta A* **1987**, *43*, 345–348.
- [83] Collins, C.L.; Meredith, C.; Yamaguchi, Y.; Schaefer, H.F. III. Advancing the search for cyclopropenylidenecarbene, the exocyclic ring isomer of diacetylene. *J. Am. Chem. Soc.* **1992**, *114*, 8694–8696.
- [84] Fowler, P.W.; Dierksen, G.H.F. Polarizabilities of triply bonded molecules: the 14- and 26-electron systems CN^- , N_2 , HCN , C_2H_2 , C_2N_2 , HC_3N and C_4H_2 . *Chem. Phys. Lett.* **1990**, *167*, 105–110.

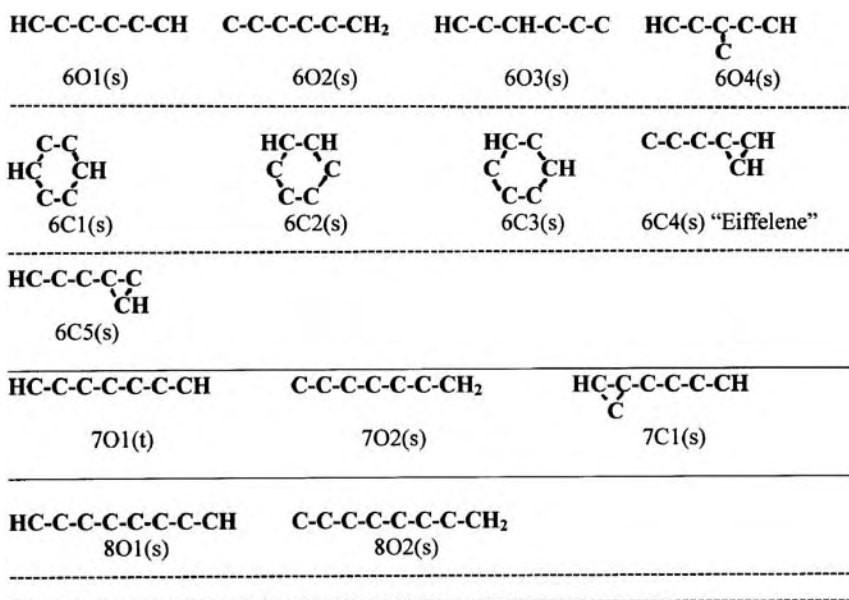
- [85] Toto, J.L.; Toto, T.T.; de Melo, C.P.; Kirtman, B.; Robins, K. Hartree–Fock static longitudinal (hyper)polarizability of polyyne. *J. Chem. Phys.* **1996**, *104*, 8586–8592.
- [86] Karpfen, A. The dimer of acetylene and the dimer of diacetylene: A floppy and a very floppy molecule. *J. Phys. Chem. A* **1999**, *103*, 11431–11441.
- [87] Vila, F.; Borowski, P.; Jordan, K.D. Theoretical study of the low-lying electronically excited states of diacetylene. *J. Phys. Chem. A* **2000**, *104*, 9009–9016.
- [88] Basiuk, V.A.; Navarro-González, R.; Bénilan, Y.; Raulin, F. PM3, AM1, MNDO and MINDO3 semi-empirical IR spectra simulations for compounds of interest for Titan's chemistry: diazomethane, methyl azide, methyl isocyanide, diacetylene and triacetylene. *Spectrochim. Acta A* **2001**, *57*, 505–511.
- [89] Jones, V.A. Rotation–vibration spectra of diatomic and simple polyatomic molecules with long absorbing paths. VIII The spectra of trideutero-methylacetylene and diacetylene from 1.2 μ to 0.7 μ . *J. Chem. Phys.* **1952**, *20*, 860–868.
- [90] Winther, F. The high resolution far infrared spectrum of diacetylene, obtained with a Michelson interferometer. *Z. Naturforsch. A* **1973**, *28*, 1179–1185.
- [91] Lamotte, J.; Binet, C.; Romanet, R. Structure vibrationnelle des spectres d'absorption ultraviolette de quelques hydrocarbures α -diyniques et homologues deutériés. *J. Chimie Physique* **1977**, *74*, 577–585.
- [92] Hardwick, J.L.; Ramsay, D.A.; Garneau, J.M.; Lavigne, J.; Cabana A. The infrared spectrum of diacetylene. *J. Mol. Spectrosc.* **1979**, *76*, 492–505.
- [93] Buijs, H.L.; Ramsay, D.A. The ν_4 band of diacetylene near 3 microns. *Astrophys. J.* **1980**, *235*, L115–L117.
- [94] Chang, K.W.; Graham, W.R.M. The near-ultraviolet spectrum of diacetylene trapped in solid argon at 9 K. *J. Mol. Spectrosc.* **1982**, *94*, 69–78.
- [95] Guelachvili, G.; Craig, A.M.; Ramsay, D.A. High-resolution Fourier studies of diacetylene in the regions of the ν_4 and ν_5 fundamentals. *J. Mol. Spectrosc.* **1984**, *105*, 156–192.
- [96] Koops, Th.; Visser, T.; Smit, W.M.A. The harmonic force field and absolute infrared intensities of diacetylene. *J. Mol. Struct.* **1984**, *125*, 179–196.
- [97] Arié, E.; Johns, J.W.C. The bending energy levels of C_4H_2 . *J. Mol. Spectrosc.* **1992**, *155*, 195–204.
- [98] Khanna, R.K.; Ospina, M.J.; Zhao, G. Infrared band extinctions and complex refractive indices of crystalline C_2H_2 and C_4H_2 . *Icarus* **1988**, *73*, 527–535.
- [99] Materny, A.; Kiefer, W. Absorption, luminescence, resonance Raman, and resonance CARS spectroscopy on FBS diacetylene single crystals with color zones. *Macromolecules* **1992**, *25*, 5074–5080.
- [100] Woo, S.C.; Chu, T.C. The absorption spectrum of diacetylene in the near ultraviolet. *J. Chem. Phys.* **1935**, *3*, 541–543.
- [101] Woo, S.C.; Chu, T.C. The absorption spectrum of diacetylene in the near ultraviolet. II. *Chem. Phys.* **1937**, *5*, 786–791.

- [102] Eastmond, R.; Johnson, T.R.; Walton, D.R.M. Silylation as a protective method for terminal alkynes in oxidative couplings. General synthesis of the parent polyyynes $\text{H}(\text{C}\equiv\text{C})_n\text{H}$ ($n=4-10, 12$). *Tetrahedron* **1972**, *28*, 4601–4616.
- [103] Kloster-Jensen, E.; Haink, H.J.; Christen, H. The electronic spectra of unsubstituted mono- to penta-acetylene in the gas phase and in solution in the range 1100–4000 Å. *Helvetica Chimica Acta* **1974**, *57*, 1731–1744.
- [104] Okabe, H. Photochemistry of acetylene at 1470 Å. *J. Chem. Phys.* **1981**, *75*, 2772–2778.
- [105] Fahr, A.; Nayak, A.K.; Temperature dependent ultraviolet absorption cross sections of 1,3 butadiene and butadiyne. *Chem. Phys.* **1994**, *189*, 725–731.
- [106] Smith, N.S.; Bénilan, Y.; Bruston, P. The temperature dependent absorption cross sections of C_4H_2 at mid ultraviolet wavelengths. *Planet. Space. Sci.* **1998**, *46*, 1215–1220.
- [107] Price, W.C.; Walsh, A.D. The absorption spectra of triple bond molecules in the vacuum ultra violet. *Trans. Faraday Soc.* **1945**, *41*, 381–388.
- [108] Haink, H.J.; Jungen, M. Excited states of the polyacetylenes. Analysis of the near ultraviolet spectra of diacetylene and triacetylene. *Chem. Phys. Lett.* **1979**, *61*, 319–322.
- [109] Glicker, S.; Okabe, H. Photochemistry of diacetylene. *J. Phys. Chem.* **1987**, *91*, 437–440.
- [110] Hardwick, J.L.; Ramsay, D.A. The near ultraviolet band system of diacetylene. *Chem. Phys. Lett.* **1977**, *48*, 399–401.
- [111] Matsumura, K.; Etoh, T.; Tanaka, T. Microwave spectroscopy of the $\nu_8-\nu_6$ band of diacetylene. *J. Mol. Spectrosc.* **1981**, *90*, 105–115.
- [112] Matsumura, K.; Tanaka, T. Microwave vibration rotation spectrum of diacetylene. *J. Mol. Spectrosc.* **1982**, *96*, 219–233.
- [113] Dickens, J.E.; Langer, W.D.; Velusamy, T. Small scale abundance variations in TMC-1. *Bull. Am. Astron. Soc.* **2000**, *32*, 1415.
- [114] Travers, M.J.; McCarthy, M.C.; Gottlieb, C.A.; Thaddeus, P. Laboratory detection of the ring-chain molecule C_3H_2 . *Astrophys. J.* **1997**, *438*, L135–L138.
- [115] Blanksby, S.J.; Dua, S.; Bowie, J.H.; Schröder, D.; Schwarz, H. Gas-phase syntheses of three isomeric C_5H_2 radical anions and their elusive neutrals. A joint experimental and theoretical study. *J. Phys. Chem. A* **1998**, *102*, 9949–9956.
- [116] Fulara, J.; Freivogel, P.; Forney, D.; Maier, J.P. Electronic absorption spectra of linear carbon chains in neon matrices. III. HC_{2n+1}H . *J. Chem. Phys.* **1995**, *103*, 8805–8810.
- [117] Shindo, F.; Bénilan, Y.; Guillemin, J.C.; Chaquin, P.; Jolly, A.; Raulin, F. Ultraviolet and infrared spectrum of C_6H_2 revisited and vapor pressure curve in Titan's atmosphere. *Planet. Space Sci.* **2003**, *51*, 9–17.
- [118] Moriyama, M.; Ohana, T.; Yabe, A. Direct observation of benzydyne: Photolysis of 1,4-Bis(trifluoromethyl)-2,3,5,6-benzenetetracarboxylic dianhydride in an argon matrix. *J. Am. Chem. Soc.* **1997**, *119*, 10229–10230.
- [119] Bjarnov, E.; Christensen, D.H.; Nielsen, O.F.; Augdahl, E.; Kloster-Jensen, E.; Rogstad, A. Vibrational spectra and force field of triacetylene. *Spectrochim. Acta A* **1974**, *30*, 1255–1262.

- [120] Matsumura, K.; Kawaguchi, K.; McNaughton, D.; Bruget, D.N. High-resolution infrared spectroscopy of the ν_5 band of triacetylene. *J. Mol. Spectrosc.* **1993**, *158*, 489–493.
- [121] Delpech, C.; Guillemin, J.C.; Paillous, P.; Khelifi, M.; Bruston, P.; Raulin F. Infrared spectra of triacetylene in the 4000–220 cm^{-1} region: absolute band intensity and implications for the atmosphere of Titan. *Spectrochim. Acta A* **1994**, *50*, 1095–1100.
- [122] Haas, S.; Winnewisser, G.; Yamada, K.M.T.; Matsumura, K.; Kawaguchi, K. The high-resolution spectra of the ν_{11} band of triacetylene near 622 cm^{-1} : revised assignments for hot bands. *J. Mol. Spectr.* **1994**, *167*, 176–90.
- [123] Bénilan, Y.; Bruston, P.; Raulin, F.; Courtin, R.; Guillemin, J. C. Absolute absorption coefficient of C_6H_2 in the mid-UV range at low temperature; implications for the interpretation of Titan atmospheric spectra. *Planet. Space Sci.* **1995**, *43*, 83–89.
- [124] McCarthy, M.C.; Thaddeus, P. Laboratory detection of a bent-chain carbene isomer of C_6H_2 . *Astrophys. J.* **2002**, *569*, L55–L58.
- [125] Zahradnik, R.; Hobza, P.; Burcl, R.; Hess, B.A.; Radziszewski, J. Strained unsaturated molecules. Theoretical study of acyclic and cyclic cumulenes and acetylenes. *J. Mol. Struct.* **1994**, *313*, 335–349.
- [126] Bettinger, H.F.; Schleyer, P.v.R.; Schaefer, H.F., III. Tetrahydrobenzenes: singlet-triplet separations and vibrational frequencies. *J. Am. Chem. Soc.* **1999**, *121*, 2829–2835.
- [127] McNaughton, D.; Bruget, D.N. The high-resolution infrared spectrum of triacetylene. *J. Mol. Spectrosc.* **1991**, *150*, 620–634.
- [128] Aoki, K.; Ikuta, S. The singlet with a C_3 ring: the probable candidate of HC_6N and C_7H_2 . *J. Mol. Struct. (Theochem)* **1994**, *310*, 229–238.
- [129] Dua, S.; Blanksby, S.J.; Bowie, J.H. The syntheses of C_6CH_2^- and the corresponding carbenoid cumulene C_6CH_2 in the gas phase. *Chem. Commun.* **1998**, 1767–1768.
- [130] Dua, S.; Blanksby, S.J.; Bowie, J.H. Formation of neutral C_7H_2 isomers from four isomeric C_7H_2 radical anion precursors in the gas phase. *J. Phys. Chem. A* **2000**, *104*, 77–85.
- [131] McCarthy, M.C.; Travers, M.J.; Gottlieb, C.A.; Thaddeus, P. Laboratory detection of the carbon ring chain C_7H_2 . *Astrophys. J.* **1997**, *483*, L139–L142.
- [132] Shindo, Fr.; Bénilan, Y.; Guillemin, J.C.; Chaquin, P.; Jolly, A.; Raulin, F. Spectroscopy of two organic compounds involved in Titan's atmosphere chemistry: Tetracetylene (C_8H_2) and Vinylacetylene (CH_2CHCCH). *Bull. Am. Astron. Soc.* **2001**, *33*, 1109.
- [133] Shindo, Fr.; Bénilan, Y.; Chaquin, P.; Guillemin, J.C.; Jolly, A.; Raulin, Fr. IR spectrum of C_8H_2 : Integrated band intensities and some observational implications. *J. Mol. Spectrosc.* **2001**, *210*, 191–195.
- [134] Tsuji, M.; Kuboyama, S.; Matsuzaki, T.; Tsuji, T. Formation of hydrogen-capped polyynes by laser ablation of C_{60} particles suspended in solution. *Carbon* **2003**, *41*, 2141–2148.
- [135] McCarthy, M.C.; Travers, M.J.; Chen, W.; Gottlieb, C.A.; Thaddeus, P. Laboratory detection of the carbon ring chain C_9H_2 . *Astrophys. J.* **1998**, *498*, L89–L92.

APPENDIX 17.1 CONSTRUCTS OF ALL MOLECULES PRESENTED IN THIS CHAPTER

HC-CH 201(s)	C-CH₂ 202(s)		
HC-C-CH 301(t)	C-C-CH₂ 302(s)	C-CH₂-C 303(t)	HC-CH  3C1(s)
HC-C-C-CH 401(s)	C-C-C-CH₂ 402(s)	C-CH-C-CH 403(s)	C-CH-CH-C 404(s)
 4C1(s)	 4C2(s)	 4C3(s)	 4C4(s)
 4C5(s)	 4C6(s)		
HC-C-C-C-C 501(t)	C-C-C-C-CH₂ 502(s)	HC-C-CH-C-C 503(s)	C-C-CH-CH-C 504(s)
C-CH-C-CH-C 505(s)	 5C1(s)	 5C2(s)	 5C3(s)
 5C4(s)	 5C5(s)	 5C6(s)	 5C7(s)
HC-C-C-C  5C8(s)	 5C9(s)	 5C10(s)	 5C11(s)



The equilibrium geometries of 10O1(s), 12O1(s), 14O1(s), and 16O1(s) are analogous to the equilibrium structure of 8O1(s).

The equilibrium geometries of 10O2(s), 12O2(s), 14O2(s), and 16O2(s) are analogous to the equilibrium structure of 8O2(s).

The equilibrium geometries of 9O1(t), 11O1(t), 13O1(t), and 15O1(t) are analogous to the equilibrium structure of 7O1(t).

The equilibrium geometries of 9O2(s), 11O2(s), 13O2(s), and 15O2(s) are analogous to the equilibrium structure of 7O2(s).

APPENDIX 17.2 CALCULATIONS CARRIED OUT FOR THIS CHAPTER USING THE SPARTAN 02 AND 04 PROGRAMS

Our quantum chemical calculations were carried out with the Spartan 02 and Spartan 04 programs by Wavefunction, Inc., Irvine, California, USA. Spartan 02 was used only to obtain the Raman spectra. All other calculations were done with Spartan 04 using the RB3LYP method with the 6-311G* base set. In most cases, the final geometry was computed directly from the initial construct. In other cases, the final calculation was preceded by MMFF molecular mechanics and PM3 semi-empirical treatments.

Here is the example of the setup for the geometry optimization of 4O1(s):

Method: RB3LYP; basis set: 6-311G*; number of shells: 26; number of basis functions: 78.

Properties available: Energy; HOMO energy; LUMO energy; Dipole moment; Area of molecule; Volume of molecule.

Printed outputs: Cartesian Coordinates of Atoms; Molecular Orbital Energies and Eigenfunctions; Mulliken Population Analysis; Atom Occupancies and Charges; Vibrational Frequencies and Intensities; Raman Active, yes/no; Zero Point Energy; Enthalpy; Entropy; Gibbs Free Energy, C_v .

Visuals: Vibrational Modes; UV-vis Spectra; Molecular Orbitals; Charge Densities.

18 Polyynes: Possible Bulk Synthesis and Chemical Properties

Franco Cataldo

CONTENTS

18.1	Introduction	425
18.1.1	Some Notes on Polyynes in Nature and their Biological Activity.....	426
18.2	Possible Scale-Up Synthesis of Polyynes with the Submerged Carbon Arc Technique	426
18.2.1	Preparation of Concentrated Solutions of Polyynes by Distillation	426
18.2.2	Polyynes: Isolation as Acetylides	428
18.3	Hydrogenation of Polyynes to Ene-Ynes: An Easy Access to Biologically Active Molecules	434
18.4	Oxidative Degradation and Photolysis of Polyynes	443
18.4.1	Stability of Polyne Solutions in Air	443
18.4.2	Oxidation of Polyynes with Ozone	444
18.4.3	Addition of Bromine to Polyynes	445
18.4.4	Polyne Photolysis in Air (Low Pressure Hg Lamp)	445
18.4.5	Polyne Photolysis in Nitrogen (High Pressure Hg Lamp)	447
18.5	Conclusions	448
	References	450

18.1 INTRODUCTION

In this chapter we will discuss some chemical properties of polyynes obtained from the electric arc and the possible application of the submerged electric carbon arc technique as a tool for the low-cost synthesis of polyynes. In fact, the polyynes cannot be easily synthesized and in general are also

of low stability. The use of the submerged electric arc is a promising easy route to these molecules, which can be used as building blocks in chemical synthesis. The main application of polyyne is in synthetic chemistry where molecules with biological activity and which can be used as drugs can be designed. The research on naturally occurring acetylenes has shown the enormous potential of these and related molecules containing the polyyne moieties, as will be discussed in [Chapter 19](#).

18.1.1 SOME NOTES ON POLYYNES IN NATURE AND THEIR BIOLOGICAL ACTIVITY

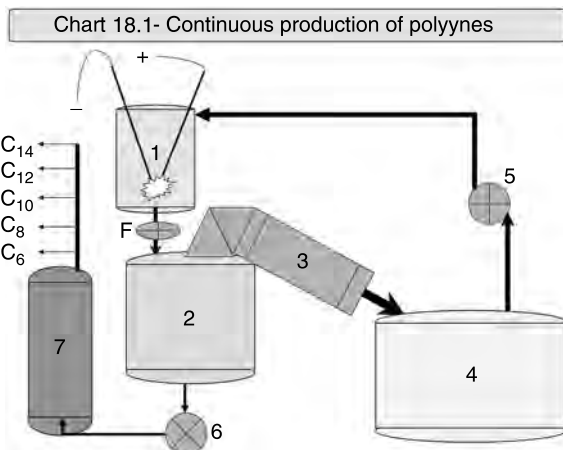
Polyyne, known also as polyacetylenes, are widespread in nature as metabolites of plants, microorganisms, fungi, marine organisms, and even animals. They exert some kind of protection of the living organisms against the aggression of pathogens and disease. Furthermore, the biological activity of naturally occurring polyacetylenes as fungicides, nematocides, and as antibiotic, antiseptic and even as anticancer agents is widely recognized [1–4]. Excellent reviews are available on the specific subject of naturally occurring polyyne [1–4] and their pharmacological activity [5] so that we refer to those works for comprehensive and updated reviews. One of the most promising application of polyyne and derivatives are as building blocks in the pharmaceutical industry. In [Chapter 19](#) Guanti and co-workers have reviewed the pharmacological applications of the ene-diyne, but the topic of pharmaceutical application is not limited to the class of molecules known as ene-diyne because many other naturally occurring polyacetylenes exert a biological and potentially pharmaceutical activity [5].

18.2 POSSIBLE SCALE-UP SYNTHESIS OF POLYYNES WITH THE SUBMERGED CARBON ARC TECHNIQUE

18.2.1 PREPARATION OF CONCENTRATED SOLUTIONS OF POLYYNES BY DISTILLATION

Prolonged arcing seems to be an attractive route for the preparation of bulk quantities of polyyne in solution. In [Chapter 8](#) we have shown that polyyne accumulate linearly with arcing time into organic solvents. The best solvents for rapid polyyne formation appear to be hydrocarbons rather than alcohols, but the latter offer the advantage of forming a very low level of polycyclic aromatic hydrocarbons (PAHs) as secondary products.

In principle, polyyne solutions can be concentrated simply by distilling off the solvent. This process is illustrated in the flow [chart 18.1](#), where we have provided a scheme for (1, [Chart 18.1](#)) the reactor with the graphite electrodes. After arcing, the solvent with the polyyne solution is transferred into the distillation unit (2, [Chart 18.1](#)). Before passing into the distillation



unit, the solution is filtered through a 0.45 micron PVDF membrane (F, Chart 18.1) to take away the carbon particles formed during arcing. The solvent is distilled off by using moderate heat and reduced pressure through the refrigerated arm (3, Chart 18.1) into the recovery tank (4, Chart 18.1) and recycled with the pump (5, Chart 18.1) to the arc reactor. After distillation, the concentrated volume of the polyynes solution is pumped through (6, Chart 18.1) into the tank (7, Chart 18.1). In this way a crude, concentrated polyne solution is obtained. Such technical solution may be already useful for some synthetic purposes but it still contains polycyclic aromatic hydrocarbons as secondary products. Otherwise, for pharmaceutical purposes the components of the mixtures can be separated with preparative liquid chromatographic techniques. With adequate equipment it is possible to separate almost pure fractions of the C_8H_2 polyne which represents the $>70\%$ by mol of the polyne mixture (see [Chapter 8](#)). Of course, other important polyynes like $C_{10}H_2$ can be isolated as well with the same technique.

We have carried out some experiment in the concentration of various solutions of polyynes prepared by arcing. For example, we have verified that 100 ml of a polyne solution in methanol having the absorbance $A = 2.5$ a.u. at 225 nm can be concentrated to only 3 ml without any side reaction and significant polyne loss, provided that heating is conducted in a warm water bath under reduced pressure. This has been verified by HPLC analysis. Polyne solutions in methanol with concentrations as high as $\approx 10^{-2}$ M have been achieved in our laboratory and probably it is possible to reach 0.1 M concentrations with appropriate methods.

The concept of concentration by distillation under reduced pressure is illustrated in [Figure 18.1](#) and [18.2](#). In [Figure 18.1](#) is reported the chromatogram of the polyne mixture produced by the carbon arc in methanol and

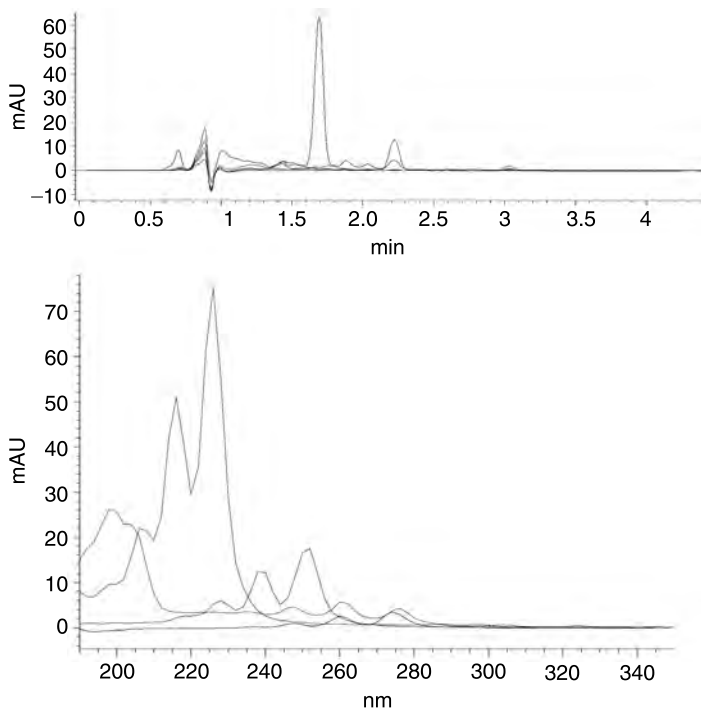


FIGURE 18.1 Polyynes in methanol produced by graphite arcing. Top: Chromatogram of the mixture. Bottom: Overlapped absorption spectra of the polyynes series. The peak at 223 nm is due to C_8H_2 . The concentration is approximately 3.9×10^{-6} M.

the relative electronic absorption spectra (overlapped) of all the detected polyynes. It can be observed that the most abundant polyne, C_8H_2 , reaches an A value of 75 mAU. Using the Lambert-Beer law and knowing that the molar extinction coefficient of this molecule is $190,546 \text{ L mol}^{-1} \text{ cm}^{-1}$, it can be calculated a concentration of 3.9×10^{-6} M. If 100 ml of this solution are concentrated by evaporation under reduced pressure to about 9 ml, then a concentration of 4.5×10^{-5} M for the same molecular species can be easily achieved as shown in [Figure 18.2](#).

18.2.2 POLYINES: ISOLATION AS ACETYLIDES

Polyynes prepared in decalin solution by arcing offer the advantage to start from relatively highly concentrated solutions, which can be further concentrated by low pressure distillation. However, the drawback of decalin is that it is a relatively viscous and high boiling liquid which is filtered with more difficulty in comparison to methanol or ethanol and requires higher

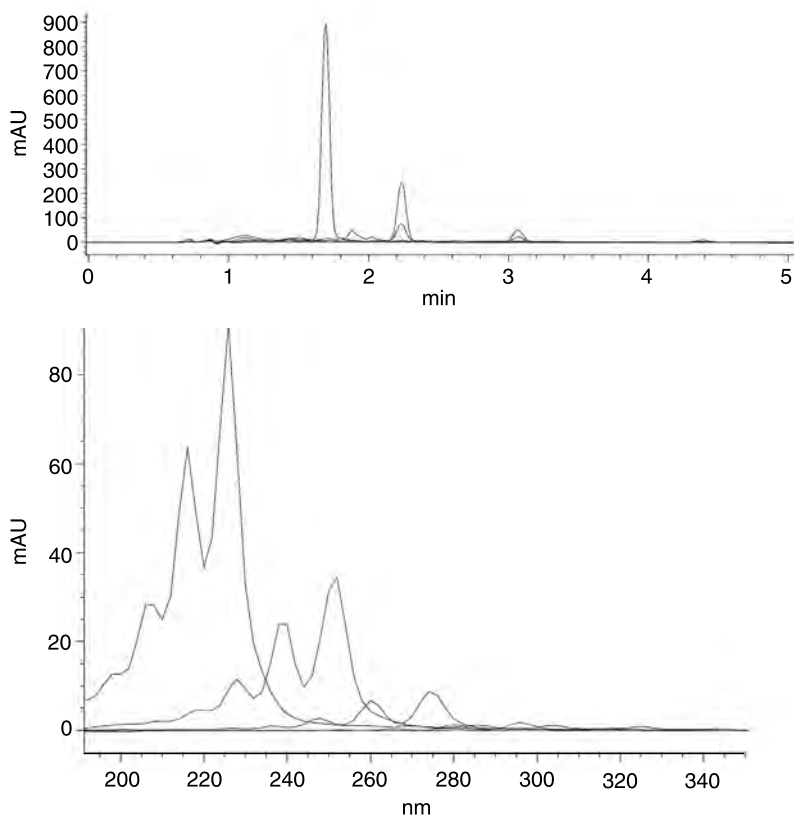


FIGURE 18.2 The same polyynine mixture of [Figure 18.1](#) after concentration by distillation at reduced pressure in a water bath. Now, the C_8H_2 concentration is 4.5×10^{-5} M. The original solution of 100 ml was reduced to 10 ml and the polyynine concentration increased by an order of magnitude. Top: Chromatogram of the polyynine mixture. Bottom: overlapped absorption spectra of the polyynine series.

temperature for distillation and this may negatively affect the stability of the polyynes during the work-up. Furthermore, arcing in decalin also produces a relatively abundant mixture of PAHs as secondary products which may be the source of difficulties in polyynine separation.

The simplest approach to avoid the distillation and to separate the polyynes from PAHs and carbon is to precipitate them as copper salts, taking advantage of a particular property of the hydrogen-terminated acetylenes to react with Cu(I) salt solutions to produce acetylides. Thus, the polyynine acetylides precipitate as brown powders by stirring a concentrated solution of these molecules in decalin with a Cu(I) solution in ammonia. The filtration permits the recovery of these molecules as the copper salts.

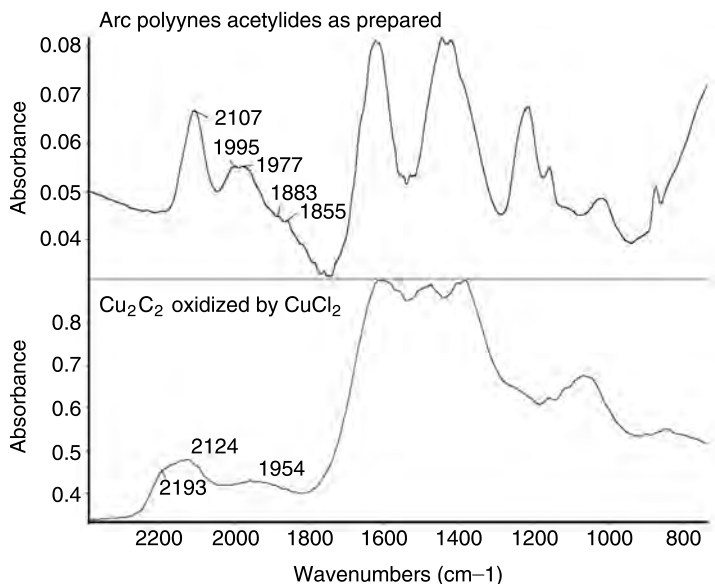


FIGURE 18.3 FT-IR spectra. Top: Polyynes prepared with the arc in decalin and precipitated as copper acetylides. Bottom: spectrum of oxidized copper acetylide, Cu_2C_2 .

The FT-IR spectra of the polyynes acetylides is shown in Figure 18.3 where it is possible to appreciate the triple bonds stretching band at 2107 cm^{-1} followed by another band at $1995\text{--}1977\text{ cm}^{-1}$. In normal conditions the latter band can be attributed to allene or cumulene moieties and it is possible that the polyynes combination with copper causes partial isomerization on the chains due to the interaction with copper atoms. In any case, HPLC analysis has not revealed any allene or cumulene derivatives in the products of the carbon arc. Therefore, the band at $1995\text{--}1977\text{ cm}^{-1}$ appears more a special feature of the copper acetylides.

In a series of studies [6–13] we have shown that copper acetylide ($\text{Cu-C}\equiv\text{C-Cu}$) and copper diacetylide ($\text{Cu-C}\equiv\text{C-C}\equiv\text{C-Cu}$) can be used to produce polyynes. Their ageing under the action of air or under the action of other oxidizing agents, for instance hydrogen peroxide, causes the coupling reaction of the acetylide moieties with the formation of polyynes and a carbonaceous solid containing also carbynoid structures [6–13] and with the release of copper ions, which can be washed out with the aid of ammonia or amines. The FT-IR spectrum of aged copper acetylide is shown in Figure 18.3. In comparison to the polyynes acetylides spectrum the differences are evident but depending on the ageing degree of the acetylide the differences can be less striking. In any case, for copper acetylide it is

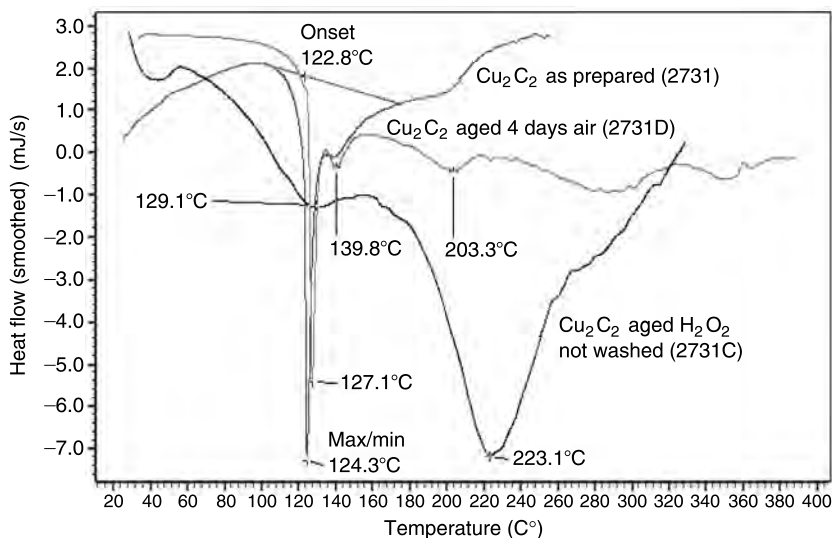


FIGURE 18.4 DSC traces. Top: Freshly prepared Cu_2C_2 , which explodes at 124°C , is shown by the sharp exothermal peak. Middle: Cu_2C_2 after 4 days. Bottom: Cu_2C_2 oxidized with H_2O_2 . It is no longer explosive and shows an exothermal rearrangement at 223°C .

possible to observe a broad band at 2124 cm^{-1} accompanied by a shoulder at 2193 cm^{-1} and by a weaker and broader band at 1954 cm^{-1} .

A specific feature of copper acetylide and the diacetylide is the thermal instability. When heated (or under a mechanical shock) they explode. This is well illustrated in Figure 18.4 which shows a DSC (differential scanning calorimeter) trace of freshly prepared $\text{Cu}-\text{C}\equiv\text{C}-\text{Cu}$ in comparison to aged samples of the same substance. The DSC trace is characterized by a sharp exothermal peak at 124°C which is due to the explosion of the sample. When copper acetylide is aged, *i.e.* it is oxidized in air or under the action of H_2O_2 , depending on the degree of oxidation reached, the exothermal peak shifts at higher temperature. For instance in Figure 18.4 after 4 days ageing the decomposition appears at 127°C and is accompanied by another exothermal transition at 203°C with a reduced explosive violence. However, the strong oxidation of the acetylide sample which corresponds to its conversion to a mixture of polyynes and carbonaceous matter containing carbynyd structures, causes the disappearance of the explosive behaviour. This is shown in Figure 18.4 where the oxidized sample with H_2O_2 does not show anymore the sharp explosion at about $124\text{--}127^\circ\text{C}$. In place of this transition, only a very small and broad transition is observed at about 130°C which is not accompanied by any explosion. This transition is followed by another broader exothermal transition with a peak at 223°C (Figure 18.4). Thus,

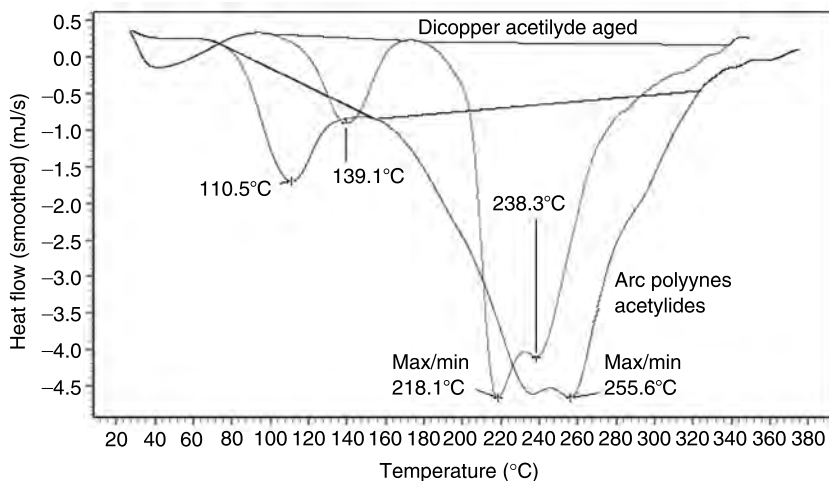


FIGURE 18.5 DSC traces. Top: Aged Cu_2C_2 , which is no longer explosive, and shows an exothermal peak at 218°C followed by another peak at 238°C . Bottom: Copper acetylides of the polyynes mixture prepared by the electric arc. They are not explosive and show broad exothermal peak at 238° and 255°C .

based on these experimental data, it is possible to affirm that oxidized dicopper acetylide is stable and can be safely handled without the risk of accidents.

The polyynes produced with the carbon arc in decalin and precipitated as acetylides show a DSC which resembles that of oxidized copper acetylide (see Figure 18.5). The freshly prepared polyynes acetylides are safer than copper acetylides because their first exothermal transition appears at 110°C but it is not explosive. The energy is released more gradually as shown by the broad peak (see Figure 18.5). Furthermore the polyynes acetylides display a DSC trace which is comparable to that offered by oxidized copper acetylide as shown in Figure 18.5. In fact both samples are not explosive and show a very broad and intense transition above 218°C . In the case of copper acetylide this transition shows two peaks at 218 and 238°C while the polyynes acetylides are peaking at 238° and 255°C . During these transitions essentially the polyyne chains end-capped with copper undergo a cross-linking reaction. This reaction is suggested by the disappearance of the triple bonds stretching bands after thermal annealing (see Figure 18.6) and justifies the considerable amount of the released heat which is more than 4 kJ/g .

Another feature of the polyyne acetylides is the fact that by acid hydrolysis they again release the free polyynes and these can be collected into a solvent. This has been demonstrated and discussed in previous studies [7–12].

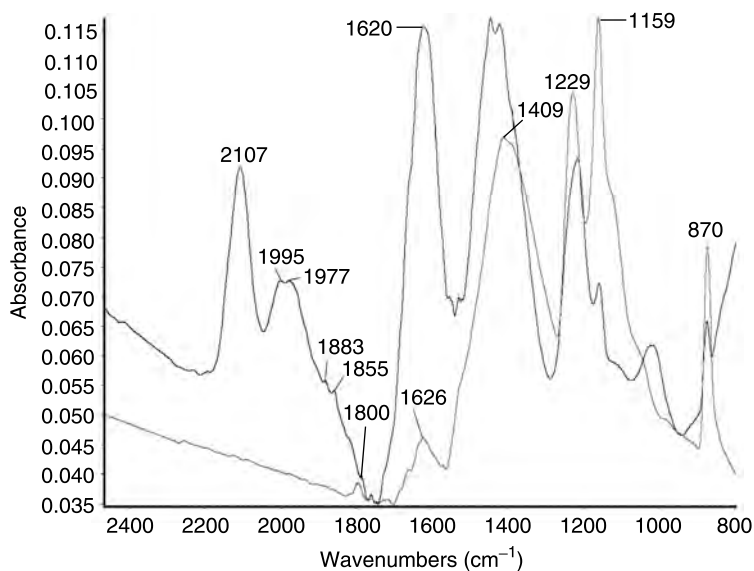
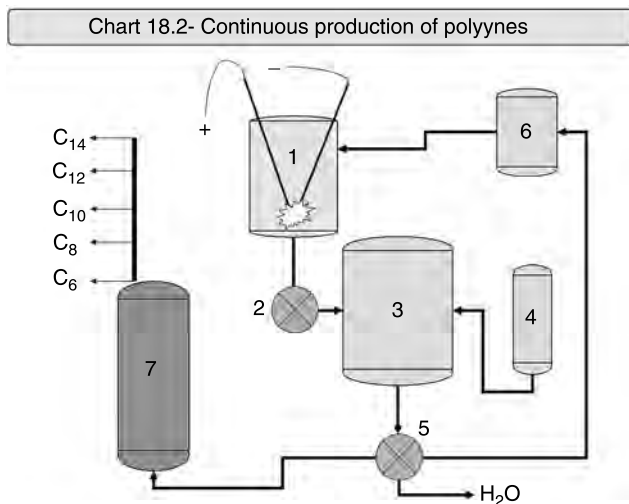


FIGURE 18.6 FT-IR spectra. Top: Copper polyynes prepared from the electric arc. Bottom: After annealing at 300°C. All the triple bond stretching bands have disappeared.

Based on the above knowledge on the behaviour of polyynes, a new flow chart can be designed showing the possible scaling up of the process as shown in Chart 18.2. In (1, Chart 18.2) decalin is arced with graphite electrodes and is filtered in (2, Chart 18.2) to remove the carbon particles formed during arcing. In the precipitation tank (3, Chart 18.2), the polyynes



solution in decalin is treated with a CuCl solution in aqueous ammonia taken from (4, Chart 18.2). After the complete precipitation, the polyyynes acetylides are recovered in the filter (5, Chart 18.2) while the purified decalin is sent to a storage tank (6, Chart 18.2) in order to be recycled into the process. If needed, decalin can be distilled at this stage without any problem to separate the PAHs accumulated. The polyyynes acetylides in (7, Chart 18.2) are hydrolized with diluted hydrochloric acid solution (or diluted sulphuric acid) with the release of the free polyyynes [7–10]. The hydrolysis is conducted by stirring the polyyynes acetylides with the acid solution in presence of a solvent, for instance *n*-hexane, in order to collect the purified polyyynes, which can be used as a technical mixture or can be separated into the components by preparative liquid chromatographic techniques.

18.3 HYDROGENATION OF POLYYNES TO ENE-YNES: AN EASY ACCESS TO BIOLOGICALLY ACTIVE MOLECULES

The polyyynes produced by the submerged electric arc in *n*-hexane show the typical band pattern in the UV spectrum that we have discussed elsewhere [14–18]. The spectrum of the polyyynes in *n*-hexane is shown in Figure 18.7(A). When the polyyynes solution is shaken with a mixture of zinc dust and hydrochloric acid, a reagent which is able to hydrogenate fullerene to fullerenes [19], in a few minutes the UV spectrum changes radically as shown in Figure 18.7(B). The changes in the band pattern are so radical that they can be interpreted only in terms of formation of completely new chemical species. The other aspect emerging from Figure 18.7(B–D) is that the hydrogenation practically stops at this stage, although prolonged shaking with Zn/HCl causes a certain reduction in the intensity of the bands at about 217 nm, which appears less intense and shifted at 220 nm (compare Figure 18.7(B) with 18.7(C)), the other bands are not affected at all. If the hexane solution is left stirring overnight with the mixture of Zn/HCl, again only the part of the spectrum around 220 nm is affected and appears with reduced intensity (compare Figure 18.7(C) with Figure 18.7(D)). The curve in Figure 18.7(E) is the difference spectrum between the ene-yne solution and the pristine polyyne solution: the bands pointing upward are the new bands formed as a consequence of the hydrogenation reaction while the bands pointing downward are those disappeared because of the transformation of polyyynes to ene-yynes.

Fortunately, the ene-yynes are easily recognizable because of their peculiar electronic absorption spectra. In the past we have produced ene-yynes by dehydrohalogenation reactions of chlorinated paraffins [20–22], hence we have acquired a certain specific experience in the field. Furthermore, the spectra of ene-yynes are well known in literature [23–25] starting from the spectrum of mycomycin and its isomer isomycomycin. In the context of the spectra of Figure 18.7(B–D), particularly interesting is

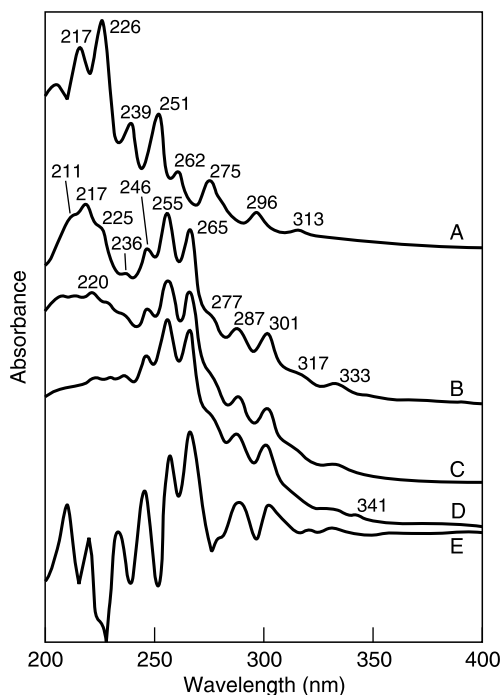
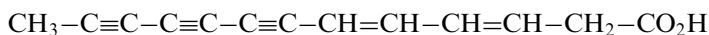


FIGURE 18.7 Electronic absorption spectra in *n*-hexane. (A) Polyynes solution as prepared. (B) Ene-yne solution after 5 min reduction of polyynes with Zn/HCl. (C) Ene-yne solution after prolonged treatment with Zn/HCl. (D) Ene-yne solution left overnight in contact with Zn/HCl solution. (E) Difference spectrum between ene-yne solution and original polyynes solution.

the electronic absorption spectrum of isomycomycin [23,26] which is a diene-tryne with the structure [26]



whose spectrum is characterized by three intense bands at 246, 258, and 267 nm followed by other four less intense bands at 288, 306, 324, and 347 nm. If we compare the position of these bands with those reported in Figure 18.7(B), we can see that the agreement of the first three with those in Figure 18.7(B) is good (246, 255, and 265 nm) while it is less good for the other four bands at longer wavelengths. Thus, we can deduce that one of the main components of the ene-yne mixture produced by the polyynes reduction is made by a chromophore similar to that present in isomycomycin and composed of three acetylenic bonds and two ethylenic bonds or

something similar. In other words, isomycomycin can be used as a model compound which reflects the structures of the ene-yne present in the reduced mixture. The electronic absorption spectrum of mycomycin appears instead different from those of Figure 18.7(B–D).

Further arguments in favour of the ene-yne nature of the hydrogenation products can be inferred from the FT-IR spectra [15], by the development of the ethylenic stretching band at 3119 cm^{-1} , and the simultaneous disappearance of the acetylenic $\equiv\text{C-H}$ stretching at 3312 cm^{-1} as hydrogenation proceeds, suggesting that the hydrogenation is directed preferentially towards the chain ends. Additionally, the shift of the residual acetylenic triple bonds stretching to 2250 cm^{-1} is observed [15], while originally the triple bond stretching was located at 2190 and 2096 cm^{-1} . This is due to the change in conjugation and by the formation of allenic groups, underlined by the development of a new band at 1957 cm^{-1} , which is in fact due to allenic groups.

The complete separation and identification of the mixture of ene-yne was achieved by HPLC analysis using a diode array detector. All the results of the chromatographic analysis are summarized in Table 18.1. As reported in the experimental section, the analysis of the ene-yne solution in hexane was made in comparison with the original polyyne solution in hexane. In Table 18.1 are compared the retention time of the molecules detected in the ene-yne solution in comparison to the retention time of the molecules detected in the polyyne solution before the hydrogenation reaction. Furthermore, in the same table are compared the electronic absorption bands of the polyyne and the hydrogenated counterpart having approximately the same retention time. It can be observed that, in all cases, the spectra of each individual chemical species changed completely after the hydrogenation although in some cases the retention time was affected only slightly. This is essentially due to the fact that the partial hydrogenation of an unsaturated molecule changes only slightly its molecular weight and these changes are practically negligible in practice. It is quite obvious to observe that in the case of complete hydrogenation instead of the partial hydrogenation, no electronic absorption spectra could be expected (with $\lambda > 200\text{ nm}$) because the final products will be saturated paraffins which in fact are not able to show any electronic transition in the usual spectral window used by the spectrophotometers.

In the first column of Table 18.1 are reported the chain length of the polyyne with a given retention time. This assignment was made on the basis of the electronic spectrum of each polyyne which was separated chromatographically as discussed previously [14–18]. In some cases, the first column of Table 18.1 does not report any number of the corresponding chain length. In such cases, judging from the retention time, it could be reasonably assumed that we are dealing with chains having length comprised between the preceding and the following fully identified compound. Probably, the compounds without indication of the chain length in the first column of

TABLE 18.1
Summary Data for Hydrogenated Polyynes in Hexane

Number of Carbon Atoms		Solvent, Hexane	Retention Time (min)	Wavelengths											
4		Hydrogenated Pristine	1.351		218	230									
		Hydrogenated Pristine	1.471	197											
		Hydrogenated Pristine	1.556		197	222	231								
		Hydrogenated Pristine	1.538		197			247	262	275		298			
		Hydrogenated Pristine	1.649	197	200		235	245							
		Hydrogenated Pristine	1.685	194	205	218		247		285					
6		Hydrogenated Pristine	1.743				225		253	265					
		Hydrogenated Pristine	1.804		210	216		233	247	260	275	300	320	340	
8	Main component	Hydrogenated	1.943	190	209			248	257	267					
	Main component	Hydrogenated Pristine	1.951		200	218	227								
	Relat. Abundant	Hydrogenated	2.103			224		238		267	278	303			
		Hydrogenated Pristine	2.244	190	211	220	230				273	288	308	328	352

(Continued)

TABLE 18.1
Continued

Number of Carbon Atoms		Solvent, Hexane	Retention Time (min)	Wavelengths											
10	Main component	Hydrogenated	2.303	190	225				266	276	287	303			
		Pristine	2.338	190		230		255			288	305	325	343	352
		Hydrogenated	2.57			225	241	253		273	295	310			
		Pristine	2.698		220	227	237	250	259		285	300 / 308	320	345	362
	Main component	Hydrogenated	2.783			228		255	269	278	283	306	318	335	
	Main component	Pristine	2.778		218	227	239	251							
	Main component	Hydrogenated	3.396	195			230	260	259		280	300	310	342	
		Pristine	None												
		Hydrogenated	4.183			230			260	275	286	300	313	330	345
	Main component	Pristine	4.098				237	248	260	273					
14		Hydrogenated	None												
	Main component	Pristine	6.4			237		253	268		280	297			
16		Hydrogenated	None												
		Pristine	10.911					255	268		281	298	318		

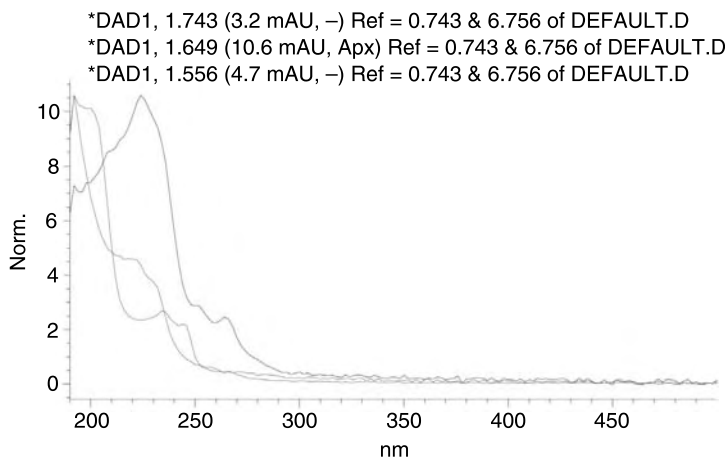


FIGURE 18.8 Electronic absorption spectra recorded by a diode-array detector of the HPLC showing two dienes and a triene ($R_t = 1.743$ min) present in the reduced mixture of polyynes.

Table 18.1 are molecules that are not end capped with hydrogen atoms but capped by other adventitious groups which are essentially alkyl groups in hexane. Furthermore, the electric arc in hexane gives also polycyclic aromatic compounds (PAHs) as secondary products [27]. Some of the compounds in Table 18.1 without a number in the first column may belong to the class of PAHs molecules.

In Table 18.1 are hence reported the complete set of polyynes identified (from 4 to 16 carbon atoms), the alkyl-capped analogs and other secondary products. As stated, the partial hydrogenation changes the absorption spectra completely. The spectra of the main components detected by the chromatographic analysis of the ene-yne mixture are shown in Figure 18.8–18.10 with their retention time. In Figure 18.8 are shown the spectra of the three lower molecular weight compounds having relatively short retention time corresponding to polyynes with C₄ ($R_t = 1.556$ and 1.649 min) and C₆ carbon atoms ($R_t = 1.743$ min). Judging from their spectra, also in comparison to the spectra of their polyyne counterpart (see Table 18.1), we may conclude that we are dealing with simple polyenes (dienes for the C₄ and trienes for the C₆) in this specific case. In fact the spectrum of vinylacetylene (the C₄ ene-yne) is rather peculiar [28] and does not correspond to the spectra reported in Figure 18.8. The spectrum of the C₆ compound (having $R_t = 1.743$) is clearly the spectrum of a higher homolog of that at $R_t = 1.649$ min. In fact it is characterized by a maximum at 225 nm and two shoulders at 253 and 265 nm while the preceding compound has a maximum at about 200 nm and two shoulders at 235 and 245 nm (note

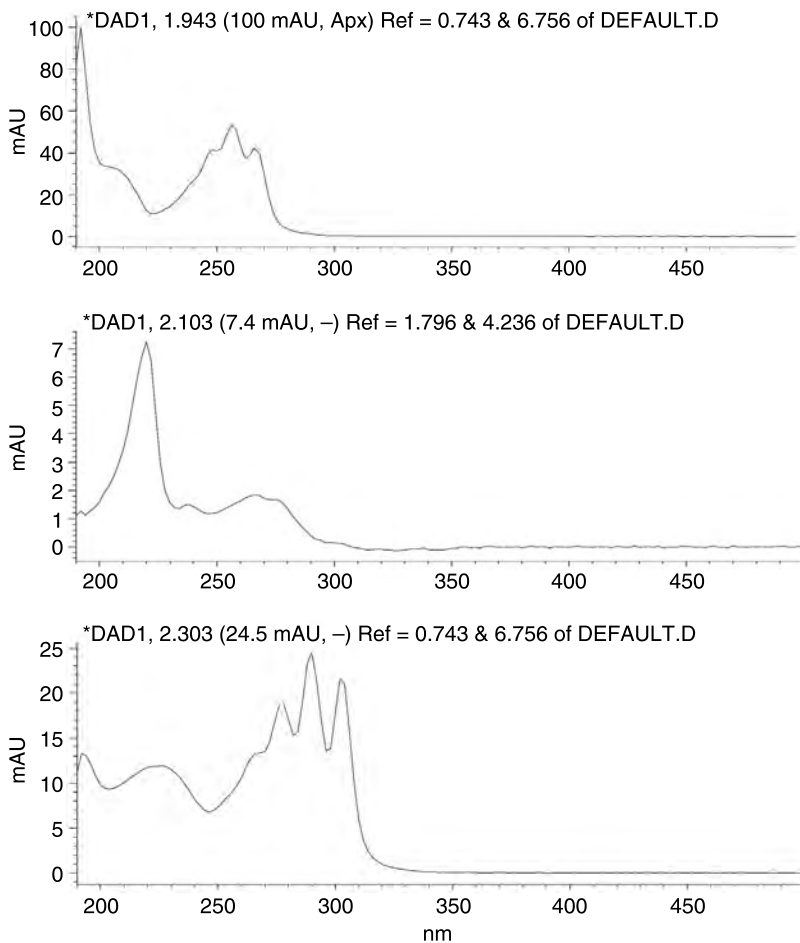


FIGURE 18.9 Electronic absorption spectra recorded by the diode-array detector of the HPLC. Top: $C_8 \rightarrow R-(C \equiv C)-(CH=CH)-(C \equiv C)-CH_2-CH_2-R'$. Middle: The pattern resembles naphthalene. Bottom: $C_8 \rightarrow R-CH=CH-C \equiv C-C \equiv C-CH=CH-R'$ (allene moiety possibly present).

the approximate constancy of 20 nm in the band difference between the two compounds). Hence, C_6 may reasonably be a triene.

The spectrum shown in Figure 18.9 (top) and corresponding to the compounds with retention time of 1.943 min can be assigned to a C_8 chain having an yne-ene-yne, *i.e.* $R-(C \equiv C)-(CH=CH)-(C \equiv C)-R'$ moiety. This assignment is based on the match between the spectrum of Figure 18.3 (top)

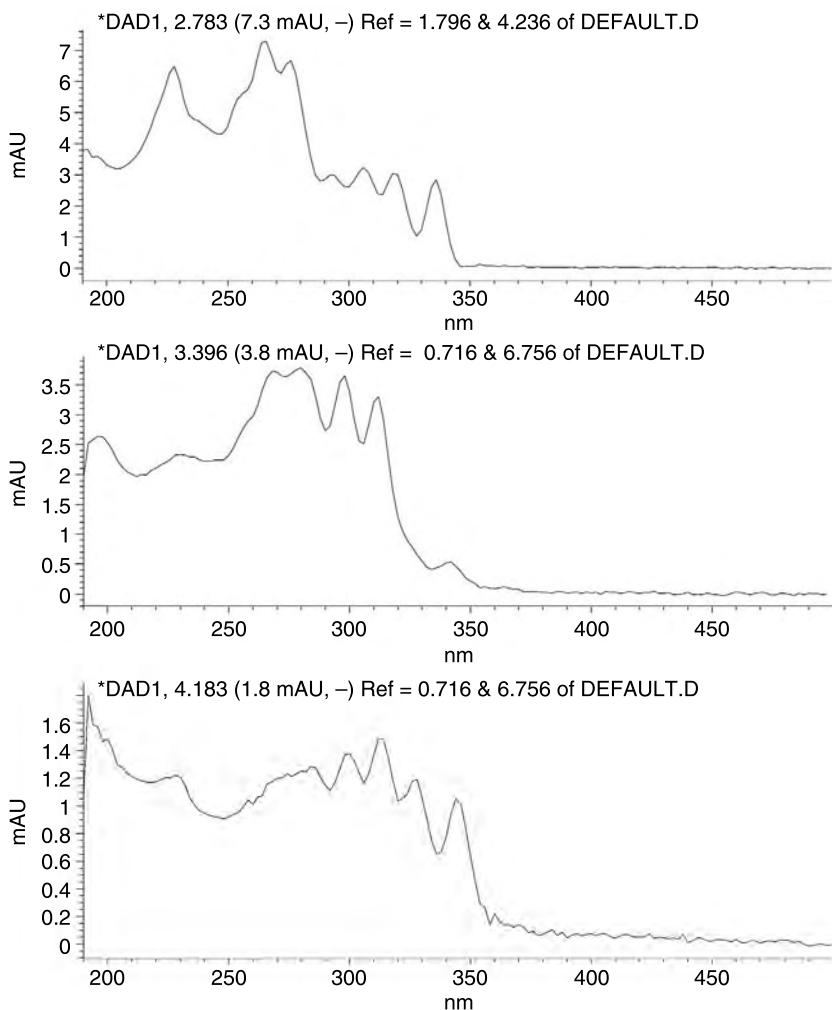


FIGURE 18.10 Electronic absorption spectra recorded by the diode-array detector of the HPLC. Top: $C_{10} \rightarrow R-CH=CH-(C \equiv C)_3-CH=CH-R'$ or $R-(CH=CH)_2-(C \equiv C)_3-R'$. Middle: $C_{10} \rightarrow R-(CH=CH)_2-(C \equiv C)_2-(CH=CH)-R'$. Bottom: $C_{12} \rightarrow R-(CH=CH)_3-(C \equiv C)_3-R'$ or $R-(CH=CH)_2-(C \equiv C)_2-(CH=C)_2-R'$.

with a published spectrum of a compound having this moiety [1]. For the compound with retention time 2.103 min (again a C_8), whose spectrum is reproduced in [Figure 18.9](#) (middle) we have not found any reasonable match with the reference spectra at our disposition. It appears that we are dealing again with a chromophore relatively similar to that of the preceding

compound, probably with an additional “ene” or “yne” group extending conjugation and causing a longer wavelength absorption in comparison to the preceding compound. The spectrum in Figure 18.9 (middle) resembles that of naphthalene, a $C_{10}H_8$ molecule. There is a good band pattern match between this spectrum and the spectrum of naphthalene even if the retention times are not the same. Thus the uncertainty of assignment remains.

A clearly peculiar ene-yne spectrum is that shown in Figure 18.9 (bottom) with a $R_t = 2.303$ min. This spectrum suggests that the C_8 compound (with alkyl end groups) should possess the ene-diyne-ene moiety, *i.e.* $R-CH=CH-C\equiv C-C\equiv C-CH=CH-R'$. The assignment is based on the table of ene-ynes published by Bohlmann [1] and on the ene-ynes reference spectra [24,25].

The following two eluted compounds with $R_t = 2.783$ and 3.396 min are both C_{10} chains and display relatively similar spectra (Figure 18.10 (top) and 18.10 (middle)). The most reasonable assignment for the first compound is a ene-tryne-ene *i.e.* $R-CH=CH-(C\equiv C)_3-CH=CH-R'$; alternatively a diene-tryne, $R-(CH=CH)_2-(C\equiv C)_3-R'$, structure is also possible. The other compound with $R_t = 3.396$ min is a diene-diyne-ene, *i.e.* $R-(CH=CH)_2-(C\equiv C)_2-(CH=CH)-R'$.

The latest detectable compound had a retention time of 4.183 min. Its spectrum can be assigned either to a triene-triyne, *i.e.* $R-(CH=CH)_3-(C\equiv C)_3-R'$ or to a diene-diyne-diene, *i.e.* $R-(CH=CH)_2-(C\equiv C)_2-(CH=CH)_2-R'$. In both cases a C_{12} chromophoric chain. In all the latest cases the spectral assignments are based on the Bohlmann tables [1,25] and Perkampus' atlas [24] on ene-yne reference compound spectra.

It is remarkable that in practically all cases the electronic absorption spectra are able to confirm the chain length of the ene-ynes. When we are dealing with a C_8 we have found a chromophore having exactly eight carbon atoms; similar considerations can be applied for C_{10} and C_{12} chains. The “R” we have put at the end of each chain refers either to H end groups or to alkyl end groups. We have used R and R' in all cases. This means that the end groups may be equal or different to each other.

It must be emphasized that our assignments are based only on the electronic spectra and are restricted by the number of reference spectra available to make a comparison and the assignment. In all cases each assignment was made using the best reasonable match in the band pattern but this does not imply that the assignment we have made is 100% certain. For instance none of the proposed assignments presents an allene moiety although we know from the FT-IR of the crude ene-yne mixture that this moiety must be present. This again is due to the lack of availability of a sufficient number of reference electronic absorption spectra useful to make the precise assignment.

In any case, the hydrogenation of polyynes represents an easy tool to convert these molecules into ene-ynes which are known to display extremely interesting biological and pharmacological properties [3,5].

18.4 OXIDATIVE DEGRADATION AND PHOTOLYSIS OF POLYINES

18.4.1 STABILITY OF POLYNE SOLUTIONS IN AIR

Polyyne are thought to be unstable in air and there is a general agreement on this idea. Proper end capping with opportune bulky groups instead ensures the stability of these long carbon chains [29,30]. For instance, Eastmond and colleagues [31] have clearly reported the difficulty in the isolation of the polyyne prepared by a long and relatively complicated synthetic strategy. In a recent study on carbyne by Ravagnan and colleagues [32] (see also [Chapter 3](#)) it was shown by Raman spectroscopy that the carbyne chains deposited on a cooled surface are rapidly destroyed when exposed to air. However, in the latter case it was highly probable that the carbyne chains were not capped, *i.e.* the chain ends were terminated by free radicals. Therefore, the high reactivity with oxygen was quite expected. We have shown with four different analytical approaches (electronic, FT-IR, HPLC and assay with Ilosvay's reagent) that the polyyne produced by the submerged electric arc are hydrogen capped. These conclusions are in line with the results of Tsuji and colleagues [33,34] who have shown that hydrogen-capped polyyne are formed also by laser ablation of graphite or C_{60} particles in a solvent.

In Figure 18.11, we show that the solution of polyyne in DHNP (decahydronaphthalene) left in air at room temperature (in the dark) for 1 week does not show any substantial changes in the band pattern of the

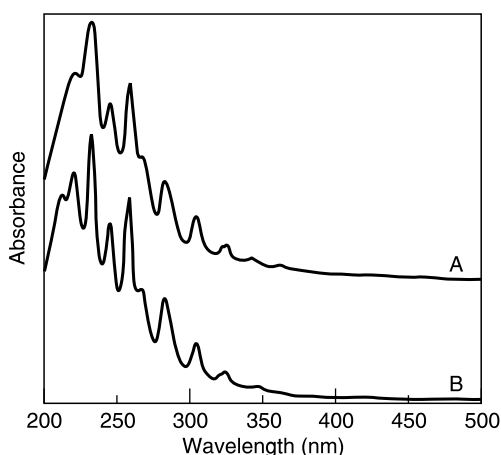


FIGURE 18.11 Electronic absorption spectra of polyyne in DHNP. A study of the stability in air. (A) A Freshly prepared solution of polyyne. (B) The same solution after 1 week's exposure to air in the dark.

absorption spectrum in comparison to the pristine solution. This is quite surprising but it is an experimental fact and we have repeated the experiment twice in *n*-hexane and also in acetonitrile confirming the result. Thus, our knowledge in this field must now be revolutionized: at least in dilute solution, polyyynes having chains composed by 16 carbon atoms ($m=8$) and end capped with hydrogen atoms, are completely stable. In Chapter 15 we discussed the instability of the monocyanopolyyynes and dicyanopolyyynes.

18.4.2 OXIDATION OF POLYYNES WITH OZONE

Once we have verified that the polyyynes in dilute solution are stable to air oxidation, we studied the effect of a more powerful oxidizing agent: ozone. Figure 18.12(A) (bottom curve) shows the electronic absorption spectrum of the polyyynes solution in DHNP. The addition of O_3 to this solution causes an increase in the intensity of the bands at 220 and 232 nm (Figure 18.12A, top curve); this increase in the absorption intensity is due to ozone dissolved in DHNP which has an absorption maximum just in this wavelength range. However, a reduction in intensity can be observed in Figure 18.12(A) for the other bands at 257, 245, 282, 303, and 322 nm as a consequence of the ozone treatment. This fact can be better appreciated by the spectrum difference

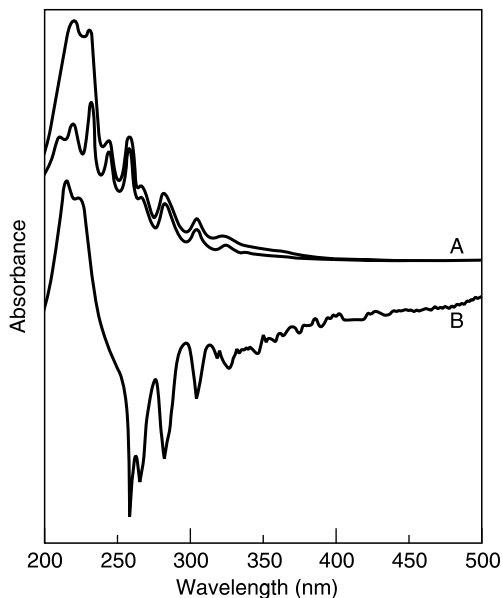


FIGURE 18.12 Electronic absorption spectra in DHNP. A study of the O_3 (A). Bottom curve: Pristine solution of polyyynes. Top curve: Solution of polyyynes after the addition of ozone. (B) Difference spectrum.

between the pristine spectrum and the spectrum of the ozonized polyyne solution (Figure 18.12(B)). In Figure 18.12(B) the bands pointing downwards are the bands which were reduced in intensity due to the reaction with ozone of the associated molecular species, while the bands pointing upward are due to the ozone excess in DHNP solution, as stated before. Figure 18.12(B) demonstrates that the polyyne is reacting with ozone, although the reaction kinetics does not appear particularly fast. This deserves a further detailed investigation, but it can be anticipated that, as in the case of conjugated polyene polymers [35–37], the polyyne may form charge transfer complexes with ozone and show a slower reaction kinetics than that expected for a highly unsaturated compound. It is also possible that the polyyne is reacting with ozone more slowly than polyenes, but this needs to be verified.

18.4.3 ADDITION OF BROMINE TO POLYINES

Being highly unsaturated, it is expected that the polyyne should react quite promptly with an electrophilic agent like bromine. In fact, the addition of Br_2 to a solution of polyyne in DHNP causes the disappearance of the original band pattern in a few minutes due to the polyyne mixture [38]. If the solution is left overnight, all free bromine is added and all absorption bands due to polyyne are lost. The addition product is a mixture of highly brominated hydrocarbon chains that still bear some residual double bond which explains the peak at 235 nm and the tail at longer wavelengths in the absorption curve.

18.4.4 POLYNE PHOTOLYSIS IN AIR (LOW PRESSURE Hg LAMP)

The first photolysis study was conducted on a polyyne solution in a mixture of acetonitrile/water, 80/20, v/v [38]. It is well known that both solvents are very transparent to UV radiation, hence all UV radiation was available for the polyyne. The peculiarity of a low pressure mercury lamp is that it emits an almost monochromatic light at 254 nm. Thus, it is not surprising if the polyyne absorbing around the mentioned wavelength is consumed more quickly than the others. This is illustrated in Figure 18.13: the pristine spectrum (Figure 18.13(A)) is changed into Figure 18.13(B) after 90 min photolysis. It can be observed that the polyyne having an absorption maximum at 244 and 257 nm have been destroyed more rapidly and completely than the polyyne having their maximum of absorption at shorter or longer wavelengths than those mentioned. The phenomenon can be easily appreciated by the difference spectrum between the pristine and the photolyzed polyyne solution (Figure 18.13(C)): the bands which were destroyed more efficiently are those at 244 and 257 nm; those closer to the emission line of the low pressure mercury lamp (254 nm).

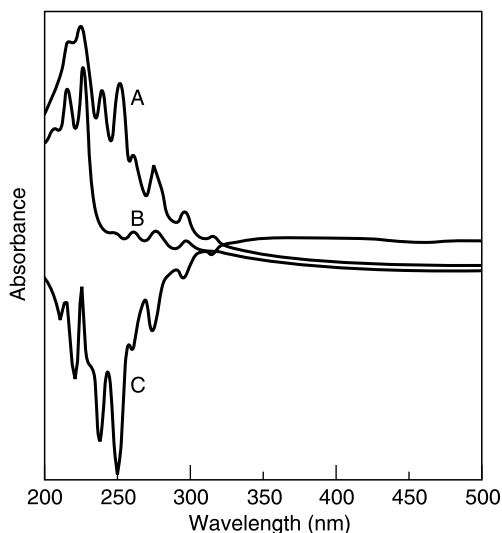


FIGURE 18.13 Electronic absorption spectra in $\text{CH}_3\text{CN}/\text{H}_2\text{O}$ of polyynes photolyzed with a low pressure Hg lamp in air. (A) Pristine solution of polyynes. (B) Solution of polyynes after 90 min photolysis. (C) Difference spectrum.

Completely analogous behavior was found in the photolysis of the polyynes in *n*-hexane. Also, *n*-hexane is a solvent transparent to UV radiation. In this solvent, the rapid and selective photolysis of the polyynes absorbing at 239 and 251 nm can be observed, those absorbing closer to the emission line of the lamp at 254 nm (see Figure 18.14 and the kinetic plot of Figure 18.15). The spectra of Figure 18.14(A) were taken after 21, 47, and 83 min of photolysis; the respective difference spectra (versus the pristine spectrum) are shown in Figure 18.14(B–D). It can be observed that the first to be photolyzed are the compounds at 239 and 251 nm, but the polyynes absorbing at longer wavelengths (namely at 262, 275, and 296) also follow the same trend of the two mentioned bands. Instead, the bands at shorter wavelength, those at 217 and 226 nm, are photolyzed only when all the bands at 239 and 251 nm have been completely photolyzed. Thus, they need a much longer exposure time to react, and the reaction starts only when the “protection” of the other species absorbing at longer wavelengths has vanished. This can be easily appreciated in the kinetic graph of Figure 18.15. This result opens the door to a simple technique for the selective degradation of polyynes from a mixture. In other words, if the polyynes are or will be produced in mixture through, for instance, the submerged electric arc, some of them can be selectively photolyzed by a selected monochromatic radiation, leaving the other(s) almost untouched.

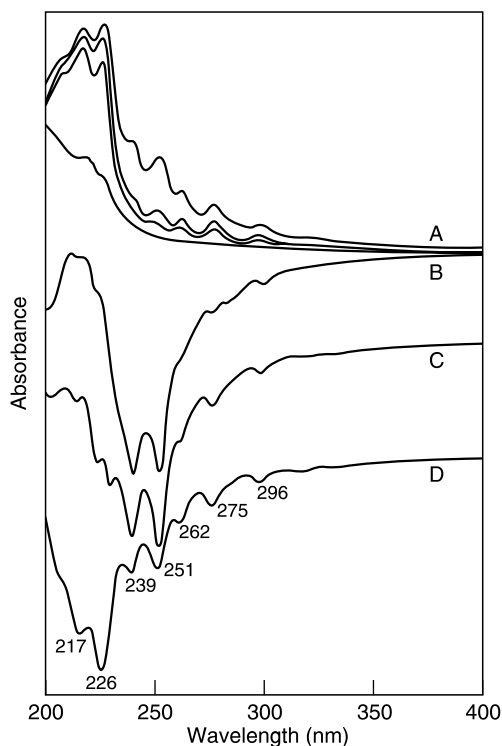


FIGURE 18.14 Electronic absorption spectra in *n*-hexane of polyynes photolyzed with a low pressure Hg lamp in air. (A) From top to bottom: Absorption spectra taken before and after 21, 27, and 83 min photolysis. (B to D) Difference spectra (with respect to the spectrum of the pristine solution) after 21, 27, and 83 min photolysis.

18.4.5 POLYNE PHOTOLYSIS IN NITROGEN (HIGH PRESSURE Hg LAMP)

The photolysis of the polyynes produced in *n*-hexane was also studied under the action of the UV radiation generated by a high pressure mercury lamp under N_2 [38]. The polyne solution was photolyzed after the solution was blown into the reactor with a stream of N_2 to eliminate O_2 from air. The spectrum of the pristine solution is shown in [Figure 18.16\(A\)](#) together with the spectra taken after 26, 50, 75, and 160 min of photolysis. It is evident the gradual reduction of the intensity of the bands and after 160 min all polyynes have been destroyed. In [Figure 18.16\(B–E\)](#) are reported the difference spectra taken at the named photolysis time. It is not possible to discuss photolytic selectivity as we did in the case of the low pressure Hg lamp because high pressure Hg lamp is not monochromatic [39]. The high pressure lamp emits in the UV at 200–270 nm and also at longer

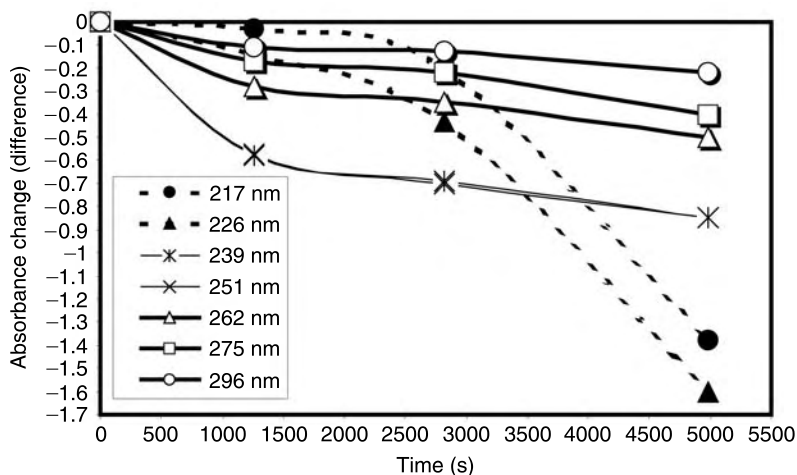


FIGURE 18.15 The data from [Figure 18.14](#). The decay of the absorption bands of the spectrum of the pristine solution as a function of photolysis time.

wavelengths [39]. Hence, its action cannot be selective and, in fact, we confirm in [Figure 18.16\(B–E\)](#) the general photolysis of the polyyne mixture. The kinetic plot of [Figure 18.16\(B–E\)](#) shows that the decay of the intensity has the same shape for all bands (see [Figure 18.17](#)). In particular, all bands show an initial slope which suggests a rapid photolysis followed by a change of slope after a certain irradiation time, suggesting a slow down of the photolytic process. This change in the photolysis speed is reached in about 1500 s for the bands at 200, 239, and 251 and probably also by the other peaks at longer wavelengths (too weak) which lie at 262 and 275 nm. On the other hand, the photolysis speed for the bands at 217 and 226 nm slows down only after 3800 s irradiation ([Figure 18.17](#)). Probably this different behavior of the two most intense bands is linked to various factors such as the main emission of the lamp which has a peak at 222 nm [39], the higher concentration of the polyyne associated with these two bands and the specific molar extinction coefficient.

18.5 CONCLUSIONS

The possible bulk production of polyyne can be achieved either by prolonged arcing followed by low pressure distillation of the resulting solution. The feasibility of this approach has been demonstrated experimentally. The drawback is the fact that the polyyne are produced in the presence of a mixture of PAHs formed as secondary products. To obtain pure polyyne solutions it is possible to precipitate the polyyne, which are

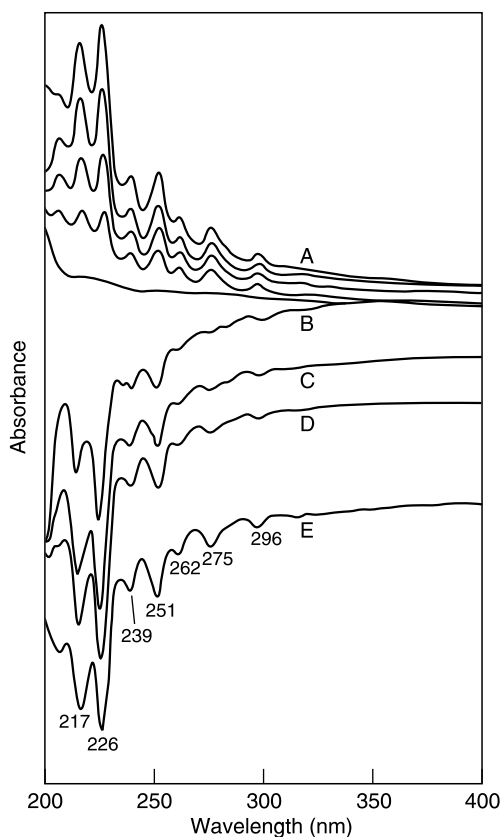


FIGURE 18.16 Electronic absorption spectra in *n*-hexane of polyynes photolyzed with a high pressure Hg lamp in N_2 . (A) From top to bottom: Absorption spectra taken before and after 26, 50, 75, and 160 min photolysis. (B to D) Difference spectra (with respect to the spectrum of the pristine solution) after 26, 50, 75, and 160 min photolysis.

obtained by arcing, as copper acetylides. With this approach the PAHs remain in solution while the polyynes are separated from the solution and are regenerated from the corresponding acetylides by treatment with HCl. The possible flow charts of this synthesis has been reported together with the spectral features of polyynes acetylides and their thermal stability in comparison to the common (explosive) dicopper acetylide. It has been found that the polyynes acetylides are not as explosive as the dicopper acetylide.

Concerning the chemical properties of polyynes in diluted solutions, a simple approach has been discussed for the hydrogenation of polyynes to ene-yne by using zinc dust and HCl.

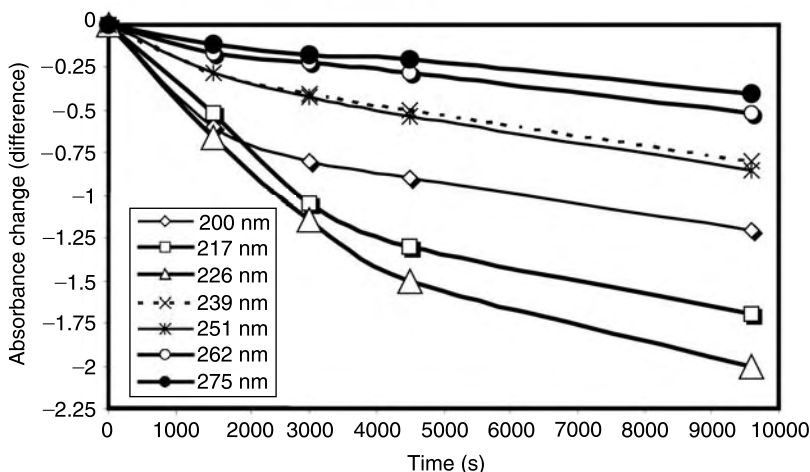


FIGURE 18.17 The data of Figure 18.16. The decay of the absorption bands of the spectrum of the pristine solution as a function of photolysis time.

Ene-ynes are important polyyne derivatives from the hydrogenation reaction and are useful as building blocks in organic synthesis or for their interesting biological properties.

The stability of polyynes in solution has been checked over a period of weeks and it has been found to be surprisingly stable even in contact with air.

Polyynes react easily with ozone and with bromine, giving degradation products with the former reagent and addition products with the latter. The photolysis of polyynes has been explored by using both a high pressure and a low pressure mercury lamp as the UV source either in air or under an atmosphere of nitrogen. The polyynes undergo relatively slow photolysis. Further work is needed in this field to clarify further the nature of the resulting products.

REFERENCES

- [1] Bohlmann F.; Burkhardt T.; Zdero C. *Naturally Occurring Acetylenes*. Academic Press, London, 1973.
- [2] Jones, E.R.H.; Thaller, V. Natural acetylenes. Chapter 14 in *The Chemistry of the Carbon-Carbon Triple Bond*, Part 2, edited by S. Patai. J. Wiley & Sons, Chichester, 1978.
- [3] Banthorpe D.W. Biochemistry of triple-bonded functional groups. Chapter 12 in *The Chemistry of Triple-Bonded Functional Groups*, Suppl. C2, edited by S. Patai. J. Wiley & Sons, Chichester, 1994.
- [4] Steglich, W.; Fugmann, B.; Lang-Fugmann, S. *Rompp Encyclopedia of Natural Products*, Georg Thieme Verlag, Stuttgart, 2000.

- [5] Ben-Zvi Z.; Danon A. Pharmacology of acetylenic derivatives. Chapter 13 in *The Chemistry of Triple-Bonded Functional Groups*, Suppl. C2, edited by S. Patai, J. Wiley & Sons, Chichester, 1994.
- [6] Cataldo F. Synthesis of carbonaceous material rich in carbyne, a carbon allotrope, by coupling reaction of Cu_2C_2 . *Eur. J. Solid State Inorg. Chem.* **1997**, *34*, 53–63.
- [7] Cataldo F. A study on the structure and electrical properties of the IV carbon allotrope: carbyne. *Polymer International* **1998**, *44*, 191–200.
- [8] Cataldo F. Structural relationships between dicopper diacetylide and dicopper acetylide. *Eur. J. Solid State Inorg. Chem.* **1998**, *35*, 281–291.
- [9] Cataldo F. From dicopper diacetylide to carbyne. *Eur. J. Solid State Inorg. Chem.* **1998**, *35*, 293–304.
- [10] Cataldo F.; From dicopper acetylide to carbyne. *Polymer International* **1999**, *48*, 15–22.
- [11] Cataldo F. Spectroscopical characterization of carbonaceous matter prepared through Glaser coupling reaction route. *Carbon* **1999**, *37*, 161–163.
- [12] Cataldo F.; Capitani D. Preparation and characterization of carbonaceous matter rich in diamond-like carbon and carbyne. *Mater. Chem. Phys.* **1999**, *59*, 225–231.
- [13] Cataldo F.; Raman scattering investigation of carbynoid and diamond-like carbon. *Fullerene Science & Technology* **2001**, *9*, 153–160.
- [14] Cataldo, F. Simple generation and detection of polyyynes in an arc discharge between graphite electrodes in various solvents. *Carbon* **2003**, *41*, 2671–2674.
- [15] Cataldo, F. Synthesis of polyyynes in a submerged electric arc in organic solvents. *Carbon* **2004**, *42*, 129–142.
- [16] Cataldo, F. Polyyynes production in a solvent-submerged electric arc between graphite electrodes. Part 1: synthesis and spectroscopy. *Fullerenes, Nanotubes and Carbon Nanostructures* **2004**, *12*, 603–617.
- [17] Cataldo, F. Polyyynes production in a solvent-submerged electric arc between graphite electrodes. Part 2: Analysis by Liquid Chromatography. *Fullerenes, Nanotubes and Carbon Nanostructures* **2004**, *12*, 619–631.
- [18] Cataldo, F. Submerged electric arc between graphite electrodes: a one-pot tool for the synthesis of long chain polyyynes in solution. *Tetrahed. Lett.* **2004**, *45*, 141–144.
- [19] Cataldo, F. Fullerane, the hydrogenated fullerene: properties and astrochemical considerations. *Fullerenes Nanotubes and Carbon Nanostructures* **2003**, *11*, 295–316.
- [20] Cataldo, F. Synthesis of polyyynes by dehydrochlorination of chlorinated paraffins. *Angew. Makromol. Chem.* **1999**, *264*, 65.
- [21] Cataldo, F. Synthesis of polyyynes (and ene-yynes) segments by dechlorination reaction of chlorinated polyethylene wax and chlorinated docosane. *J. Mater. Sci.* **2000**, *35*, 2413.
- [22] Cataldo, F. Raman spectra and thermal analysis on polyyne and polyene-yne chain segments. *J. Macromol. Sci. Pure Appl. Chem.* **2000**, *A37*, 881.
- [23] Rao, CNR. *Ultraviolet and Visible Spectroscopy. Chemical Applications*. Butterworths, London, 1961, p. 65.
- [24] Perkampus, H.H. *UV-VIS Atlas of Organic Compounds*, 2nd edition. VCH-Weinheim, 1992.
- [25] Bohlmann, F. *Fortschr. Chem. Forsch.* **1962**, *4*, 138.

- [26] Budavari, S (editor). *The Merck Index. An Encyclopedia of Chemicals. Drugs and Biologicals*. 12th Ed. Merck & Co. Inc, Whitehouse Station, NJ, 1996, abstract 6407.
- [27] Cataldo, F. Polyyynes and cyanopolyyynes synthesis from the submerged electric arc. About the role played by the electrodes and solvents in polyyynes formation. *Tetrahedron* **2004**, *60*, 4265–4274.
- [28] Gillam, A.E.; Stern, E.S.; Jones, E.R.H. *An Introduction to Electronic Absorption Spectroscopy in Organic Chemistry*. Edward Arnold Publishers Ltd, London, 1954, pp. 78–79.
- [29] Gbitter, Th.; Hampel, F.; Gisselbrecht, J.P.; Hirsch, A. End-cap stabilized oligoynes: model compounds for the linear sp carbon allotrope carbyne. *Chem. Eur. J.* **2002**, *8*, 408 (and ref. cited therein).
- [30] Hlavaty, J.; Kavan, L.; Kubitsa, J. Carbonaceous materials from end-capped carbynes. *Carbon* **2002**, *40*, 345.
- [31] Eastmond, R.; Johnson, T.R.; Walton, D.R.M. Silylation as a protective method for terminal alkynes in oxidative couplings. A general synthesis of the parent polyyynes $\text{H}(\text{C}\equiv\text{C})_n\text{H}$ ($n = 4\text{--}10, 12$). *Tetrahedron* **1972**, *28*, 4601.
- [32] Ravagnan, L.; Siviero, F.; Lenardi, C.; Piseri, P.; Barborini, E.; Dilani, P. Cluster-beam deposition and in situ characterization of carbyne-rich carbon film. *Phys. Rev. Lett.* **2002**, *89*, 285506.
- [33] Tsuji, M.; Kuboyama, S.; Matsuzaki, T.; Tsuji, T. Formation of hydrogen-capped polyyynes by laser ablation of C_{60} particles suspended in solution. *Carbon* **2003**, *41*, 2141.
- [34] Tsuji, M.; Tsuji, T.; Kuboyama, S.; Yoon, S.H.; Korai, Y.; Tsujimoto, T.; Kubo, K.; Mori, A.; Mochida, I. Formation of hydrogen-capped polyyynes by laser ablation of graphite particles suspended in solution. *Chem. Phys. Lett.* **2002**, *355*, 101.
- [35] Cataldo, F. On the action of polymers having unconjugated and cross or linearly conjugated unsaturations: chemistry & technological aspects. *Polym. Deg. Stab.* **2001**, *73*, 511.
- [36] Cataldo, F. Ozone interaction with conjugated polymers. Part 1: polyacetylene. *Polym. Deg. Stab.* **1998**, *60*, 223.
- [37] Cataldo, F. Ozone interaction with conjugated polymers. Part 2: polyphenylacetylene. *Polym. Deg. Stab.* **1998**, *60*, 233.
- [38] Cataldo, F. Polyyynes production in a solvent-submerged electric arc between graphite electrodes part 3: chemical reactivity and stability toward air, ozone and light. *Fullerenes, Nanotubes and Carbon Nanostructures* **2004**, *12*, 633.
- [39] Ninomiya, I.; Naito, T. *Photochemical Synthesis*. Academic Press, London, 1989, p. 212.

19 From Natural to Rationally Designed Artificial Eneidyne: Towards New Anticancer Antibiotics Activable at Will

*Giuseppe Guanti, Luca Banfi, Andrea Basso
and Renata Riva*

CONTENTS

19.1	Introduction	454
19.1.1	The Natural Eneidyne	454
19.1.2	The Natural Eneidyne of Type I	455
19.1.3	Mechanism of Action of Type I Eneidyne	457
19.1.4	Rational Design of Artificial Eneidyne	458
19.1.5	Preliminary Testing of Artificial Eneidyne	460
19.2	Synthetic Methodologies for the Construction of Cyclic 10-Membered Eneidyne	460
19.2.1	Cyclization after Eneidyne Construction.....	461
19.2.2	Double-Bond Formation During or After Cyclization ..	462
19.3	Monocyclic or Ortho-Fused Artificial Eneidyne	464
19.3.1	Monocyclic Carba Eneidyne	464
19.3.2	Cyclic Eneidyne Fused with Arenes Through the Double Bond	466
19.3.3	Aza, Oxa, and Thia Eneidyne, Monocyclic or Fused with Arenes Through the Double Bond.....	467
19.3.4	Cyclic Eneidyne Fused with Other Rings Through Carbons 7–10.....	468

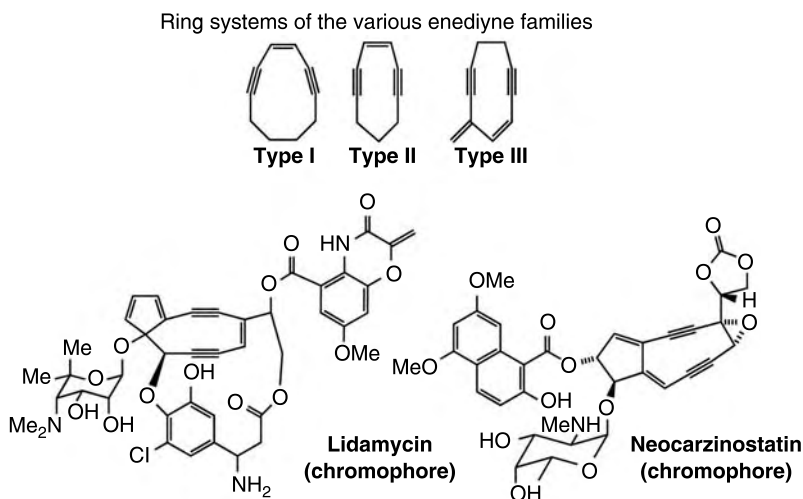
19.4	Bridged Polycyclic Enediynes	469
19.4.1	Compounds with a Double Bond as a Safety Catch	470
19.4.2	Compounds with an Epoxide as a Safety Catch	472
19.4.3	Compounds Where the Enediyne Double Bond is Formed by a Suitable Reaction	476
19.4.4	Miscellaneous.....	476
19.5	Acyclic Enediynes	478
19.5.1	Influence of Substituents	479
19.5.2	Metal-Ion Coordination	480
19.5.3	The Myers–Saito Cycloaromatization	481
19.5.4	Photochemical Cycloaromatization Reaction	482
References	483

19.1 INTRODUCTION

19.1.1 THE NATURAL ENEDIYNES

The enediyne antitumor antibiotics^{1,2} are a small family of natural compounds, composed by only nine members to date. Although one of them (neocarzinostatin) had been already isolated in the 1960s, the enediyne antibiotic story should be considered starting only around 1985–1987, when the structures of neocarzinostatin³ and calicheamicin⁴ were disclosed. The novel molecular architecture of these compounds was intriguing, since conjugated enediynes were considered to be rather unstable structures, and they were not expected to be found in nature. But the interest of the scientific community was not attracted only by this unusual structure: natural enediynes were found to be highly cytotoxic and endowed with a potent antitumor activity. Of equal importance to these astonishing properties, the enediynes also offered a distinct opportunity to study the unparalleled biosyntheses of their molecular scaffolds as well as previously unknown modes of self-resistance by microorganisms to highly reactive natural products.⁵ Finally their unprecedented mode of action opened the door to the development of several artificial enediynes endowed with interesting biological properties.

In all natural enediynes, the conjugated system is embedded in a ring. They may be divided in three classes, depending on the size and nature of this ring. In type I enediynes (Scheme 19.1) a 3-ene-1,5-diyne system is embedded in a 10-membered ring. This family is represented by calicheamicins, esperamicins, namenamicin, shishijimicins, and dynemicins. In type II enediynes the 3-ene-1,5-diyne system is included in a 9-membered ring. These compounds include maduropeptin,⁶ lidamycin (C-1027)⁷ and kedarcidin.⁸ Finally, neocarzinostatin^{3,9} and N-1999A2¹⁰ belong to a third class, being characterized by a 9-membered cyclic dienediyne of type III (Scheme 19.1). With the exception of N-1999A2, all type II and type III

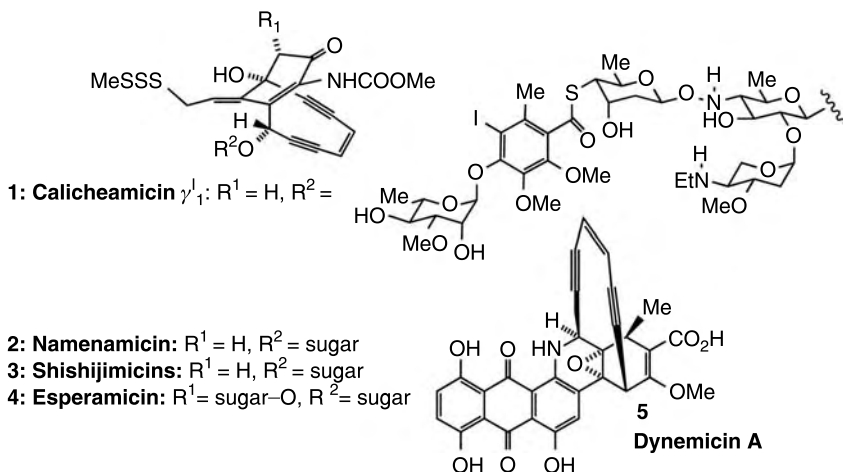


SCHEME 19.1

enediynes are chromoproteins, being formed by a complex between a protein and an unstable chromophore containing the enediyne moiety. Probably, another four natural chromoproteins (largomycin, sporamycin, actinoxanthin, and auromomycin) belong to the type III family, but their structure has not been yet elucidated. Scheme 19.1 shows the structure of the chromophores of lidamycin and neocarzinostatin, as examples of type II and type III enediynes. In this chapter we will, however, discuss mainly of type I natural enediynes and their artificial analogs.

19.1.2 THE NATURAL ENEDIYNES OF TYPE I

Calicheamicin γ_1^I (Scheme 19.2) from *Micromonospora echinospora calichensis* is the most prominent of the type I enediynes.^{4,11} There are currently about 15 different calicheamicins, characterized by small variations on the tetrasaccharide part. Apart from the enediyne moiety, these molecules contain several unusual structural features, such as the acyl enamine and the trisulfide in the aglycon, and the hexasubstituted aryl ring and the thioester and hydroxylamine glycosidic linkages in the saccharide. Namenamicin **2**,¹² and the shishijimicins **3**,¹³ from the thin encrusting orange ascidians *Polysyncraton lithostrotum* and *Didemnum proliferum*, have the same aglycon, while in the esperamicins **4**,¹⁴ isolated from *Actinomadura verrucosospora*, the aglycon is quite similar, having only an additional hydroxy group. On the other hand, the saccharide portions of **2**, **3**, and **4** are much more different from that of **1**. The last member of this family, dynemicin **5**^{15,16} from *Micromonospora chersina*, contains a novel



SCHEME 19.2

combination of an anthraquinone moiety fused with a 10-membered bridged enediyne ring.

All these compounds are extremely cytotoxic and cause both *in vitro* single- and double-stranded DNA cuts of supercoiled plasmids. For example calicheamicin γ_1^I (in the presence of a reducing thiol) afforded about 50% total cut at 5–25 nM concentration, with a double to single cleavage ratio of 2:1.^{17,18} By comparison, bleomycin has the same activity only at 160 nM and with a double to single cut ratio of 1:9. The high activity of calicheamicin was demonstrated to be strongly dependent on the presence of the tetrasaccharide unit. Actually, the aglycone of **1** was about 1000 times less active, with a 1:30 ratio of double to single scission.¹⁷ Obviously the damage caused to the cell by double cut is by far more fatal than that caused by a single cut. The DNA cleavage by enediynes was demonstrated to be oxygen-dependent (it does not occur under anaerobic conditions).¹⁹

Although four very ingenious total syntheses of calicheamicin or its aglycone have been achieved,^{15,20–22} its microbiological synthesis is far more practical, especially after bioengineering improvements based on expression of a self-resistance aiding protein.²³

Although calicheamicin is more potent than any other known compound as anticancer agent (for example it is 1000 times stronger than adriamycin in murine tumor models),¹¹ it lacks significant specificity for tumor cells. Therefore, a way to deliver it selectively was sought. Very promising results have been obtained by conjugating it with monoclonal antibodies.²⁴ The resulting conjugate gemtuzumab ozogamicin (called MylotargTM and produced by Wyeth–Ayerst) is currently on the market and has led to valuable results against acute myeloid leukemia.

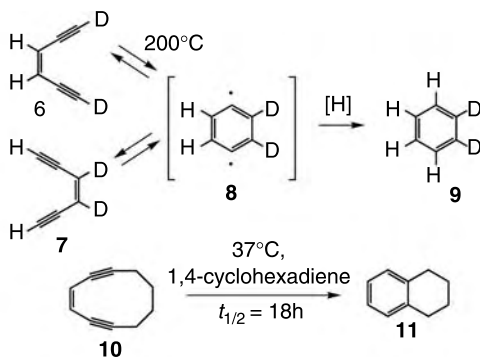
19.1.3 MECHANISM OF ACTION OF TYPE I ENEDIYNES

Calicheamicin is a masterpiece of nature's ingenuity. It has been compared to a smart bomb equipped with:

1. a *delivery system* which is responsible for a strong and specific complexation with DNA. This system is represented by the oligosaccharide unit.
2. a *warhead* (the enediyne moiety) that is able to attack simultaneously the two complementary DNA strands, causing the lethal double cut.
3. a *safety catch* that prevents the enediyne reaction, by imposing a structural restraint to its reaction. In this way the warhead does not explode until a particular chemical event takes place. In calicheamicin the *safety catch* is represented by the enamine double bond.
4. a chemical *trigger* that mediates the removal of the *safety catch* and therefore unleashes the high reactivity of the enediyne. In **1** the *trigger* is the trisulfide group.

The key transformation of 3-ene-1,5-diynes is a thermal rearrangement that was disclosed in the early 1970s by Darby et al.²⁵ and Lockhart and Bergman,²⁶ and which is commonly called the Bergman cycloaromatization (Scheme 19.3). In the classical Bergman experiment, the deuterated enediyne **6** was transformed into the isomer **7** or, in the presence of a hydrogen donor, into deuterated benzene **9**. This reaction is believed to proceed through a diradical benzenoid species (a *p*-benzyne).²⁷

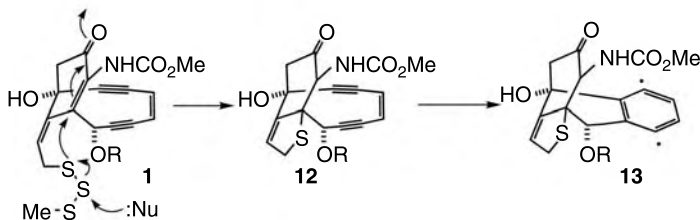
Acyclic *Z* 3-ene-1,5-diynes, such as **6**, undergo the classical Bergman thermal cycloaromatization only at elevated temperatures (a photochemical promoted Bergman-type cycloaromatization of acyclic enediynes can take place under milder conditions on particular substrates).²⁸ However,



SCHEME 19.3

Nicolaou et al. have shown that, by including the enediyne in a ring, the steric strain in the substrate may lower the activation energy to such a point that cycloaromatization takes place even at room temperature. Not surprisingly, the crucial ring size was found to be 10: compound **10** undergoes cycloaromatization at 37°C with a $t_{1/2}$ of 18 h, while larger rings were completely stable.²⁹ From this evidence all type I enediynes, where the unsaturated moiety is included in a 10-membered ring, should be expected to be poorly stable at room temperature. However, as already anticipated above, in natural enediynes a structural bias acting as a *safety catch* is present. Thus only after a suitable *triggering* event the cycloaromatization is allowed to take place. The di-radical then attacks the DNA at the deoxyribose, through a complex oxygen-dependent pathway. The bifunctional nature of the di-radical allows not only a single-strand cleavage, but even double cleavage if the geometry of the complex DNA–enediyne allows that.³⁰

The cascade of events that leads to DNA cleavage by calicheamicin is shown in Scheme 19.4. It is initiated by attack on the central atom of the trisulfide by a nucleophile (probably glutathione), that causes the formation of a thiolate which is in a perfect position for adding intramolecularly to the α,β -unsaturated ketone to form **12**. Now the bridgehead carbon atom is no longer sp^2 hybridized and therefore cycloaromatization is not any more impeded by Bredt's rule. The reactivity of **12** is even higher than that of **10** and rapid formation of the diradical **13** takes place.



SCHEME 19.4

While obviously natural enediynes **2–4** behave in the same way, in dynemicin the cascade of events is different. However, this molecule also displays a delivery unit (the anthraquinone), a *safety catch* (the epoxide) and a *trigger* (the quinone). Bioreduction of the quinone unleashes two lone pairs (one on the nitrogen and one on the upper hydroquinone oxygen) which bring about intramolecular epoxide opening.¹

19.1.4 RATIONAL DESIGN OF ARTIFICIAL ENEDIYNES

Although conjugation of the natural enediynes with monoclonal antibodies has led to important clinical results, the quest for more selective analogs is

still an important issue. However, the structural complexity of the natural substances makes *de novo* total synthesis, as well as semisynthesis, of analogs, rather difficult. On the other hand, the knowledge of the chemical foundations of their unique mode of action (based on the triad *warhead*, *safety catch*, *trigger*) enables, in principle, the rational design of simpler artificial analogs based on the same general concept.³¹ These simpler analogs may be then coupled with several DNA-complexing agents (the *delivery unit*) in order to assemble enediyne prodrugs endowed with the desired potency and selectivity. For this goal it is important to be able to predict the reactivity of a particular cyclic enediyne towards cycloaromatization. The most precise way to do that is by theoretical *ab initio* calculations of the strain energies of both ground and transition state.³² These calculations are rather sophisticated and thus a simplified procedure has been devised.³¹ By the reasonable assumption that the transition state is product-like and that the steric strain of the di-radical is similar to that of the final product coming from hydrogen addition to the diradical, the reactivity of a particular system may be related to the difference in steric strain between the starting enediyne and the cycloaromatized product (Δ SE). Common desktop molecular mechanic programs may be used by anybody to evaluate this difference. As a standard for comparison it is useful to adopt the parent 10-membered enediyne **10**. For a given system one can predict a higher reactivity when the resulting Δ SE is lower (more negative or less positive) than that calculated with the same program for the couple **10–11**, and vice versa.

An ideal artificial enediyne prodrug should be stable toward cycloaromatization. Therefore the Δ SE must be considerably higher than that calculated for **10–11**. This can be realized by designing structural constraints that increase the steric strain of the product much more than that of the enediyne. Simple substituents are not, in general, able to diminish the reactivity adequately; thus, stabilized enediyne analogs are typically ortho-fused or bridged bicyclic or polycyclic compounds.

However, a suitable transformation must be devised in order to convert, under physiological conditions, the enediyne prodrug³³ into the active drug. An alternative strategy is to use, as enediyne prodrug, a 1,5-diyne equipped with functional groups that allow the introduction of the missing double bond under appropriate conditions.

Another important feature of designed enediyne prodrugs is the presence of attachment points to be used for joining DNA-complexing substructures. The dramatic importance of the *delivery unit* in calicheamicin indicates that it is probably very difficult to achieve nanomolar potencies without a fitting DNA-complexing agent.

Finally, a not trivial issue is the stability in the dry state. It is actually known that, often, enediyne compounds tend to undergo radical polymerization in the dry state. It is clear that, for potential development as a drug, full stability is essential.

In general, designed enediynes are directed against DNA as a target. However, recently, some artificial enediynes have been shown to possess interesting biological activity not directly related to DNA damage,³⁴ but rather to interactions with proteins.^{34,35} The knowledge of these interactions is still very preliminary and does not allow a rationale design for these “new” prospective applications of enediyne chemistry.

19.1.5 PRELIMINARY TESTING OF ARTIFICIAL ENEDIYNES

When a new artificial enediyne is prepared, usually the first property to be analyzed is its propensity to undergo cycloaromatization. This is typically done in solution by simply measuring the rate of disappearance in the presence of a hydrogen donor (usually 1,4-cyclohexadiene), but also, in the solid state, by differential scanning calorimetry.³⁶ Then its activity towards DNA is tested by incubating different concentrations of the enediyne with a supercoiled plasmid DNA (pBR322 or ϕ X174). A single cut is evidenced by conversion of form I (supercoiled circular) into form II (relaxed circular), while a double cut causes formation of form III (linear). It is worth noting that the probability of a double cleavage deriving from two distinct single cleavages is nearly negligible.¹⁷ These three forms can easily be separated by agarose gel electrophoresis and quantitated by UV in the presence of ethidium bromide. In this chapter, in order to compare the various compounds, we use the term EC_{50} to indicate the effective concentration that provokes about 50% overall cut of form I, and D/S ratio to indicate the approximate double to single cut ratio. Since, in most papers, only photographs of the gels are reported, these values have been determined by rule of thumb and therefore should be considered approximate. For calicheamicin γ_1^I (the most potent of the enediynes so far) the EC_{50} is about 25 nM, and D/S 2:1.¹⁸ Since, in this experiment the plasmid is always the limiting agent, the potency depends not only on the rate of cycloaromatization, but also on the affinity of the enediyne for DNA.

19.2 SYNTHETIC METHODOLOGIES FOR THE CONSTRUCTION OF CYCLIC 10-MEMBERED ENEDIYNES

It is impossible to describe in detail in this chapter all the formidable synthetic efforts that have been dedicated to the total synthesis of natural and artificial enediynes. However, we will try to summarize here the main strategies that have been employed in the preparation of cyclic enediyne rings. In most cases complex bicyclic or polycyclic compounds have been prepared by one of these methodologies.

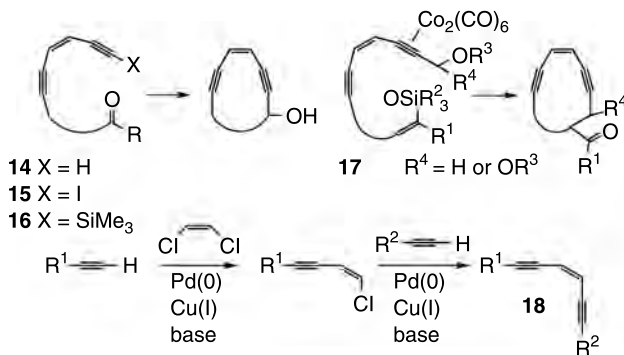
First, the synthetic strategies may be divided into three categories:

1. Those that form the enediyne moiety first at the acyclic level and then perform a suitable cyclization.

2. Those where cyclization is simultaneous to the generation of the enediyne at the double bond site (there are no examples of generation of the enediyne upon cyclization at the triple bond site).
3. Those that form the double bond after cyclization.

19.2.1 CYCLIZATION AFTER ENEDIYNE CONSTRUCTION

As far as the first strategy is concerned, the method most widely applied involves the intramolecular nucleophilic addition of an acetylide onto a carbonyl compound (Scheme 19.5). This cyclization has been realized starting from terminal alkynes **14** by treatment with a base such as lithium or potassium hexamethyldisilazide.^{15,22,37} The use of CeCl_3 as additive may be beneficial.³⁸ This method, however, affords poor results when the carbonyl compound is an enolizable aldehyde and is also not compatible with several functional groups. The most general and widely used procedure is a variation of the Nozaki reaction and starts from iodoalkynes **15**.^{31,39} Treatment with stoichiometric CrCl_2 and catalytic NiCl_2 furnishes the desired enediynic alcohol, through the intermediacy of an alkynyl chromium species. This reaction gives moderate to good yields also for enolizable aldehydes. An alternative methodology involves the fluoride mediated cyclization of silylated alkynes **16**.^{40,41}



SCHEME 19.5

A second, less used, strategy encompasses the Lewis acid catalyzed intramolecular reaction of a silyl enol ether with a propargyl cation. The latter can be conveniently generated by a cobalt complexed propargyl ether.^{31,42} This complexation strongly helps the carbocation formation. By using cobalt complexation, intramolecular aldol type reactions (for $\text{R}^4 = \text{OR}^3$) have been accomplished.⁴³

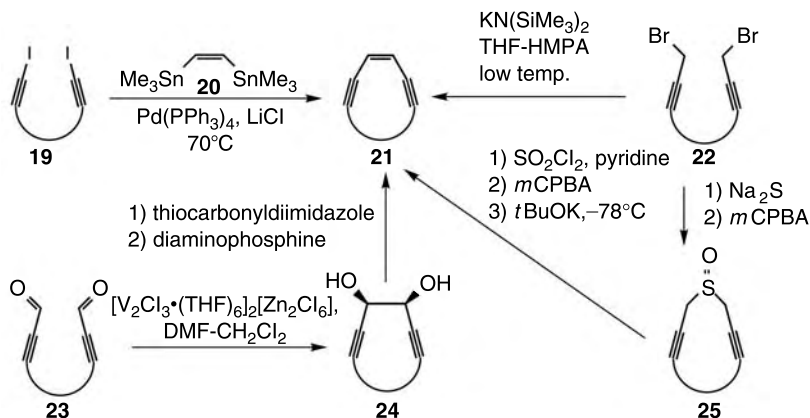
For the construction of the required acyclic enediyne, the method of choice is the Sonogashira coupling of terminal alkynes with *Z* dichloroethylene. The complete stereoselectivity for the *Z* double bond and the mild

reaction conditions, compatible with most functional groups, are the main advantages. For unsymmetrical enediynes, two sequential cross-coupling reactions are performed. The choice of the palladium catalyst and the base depends upon the electrophile; when this is dichloroethylene (first step), $\text{Pd}(\text{PPh}_3)_4$ and *n*-butylamine are the best, whereas $\text{Pd}(\text{PhCN})_2\text{Cl}_2$ and piperidine are better suited for the second step.⁴⁴ When enediynes **14–16** are desired, R^1 is usually $=\text{Me}_3\text{Si}$. The resulting silylated enediynes can be converted into the unsubstituted alkynes by the use of fluorides, Na_2CO_3 , or AgNO_3 .⁴⁵ These can be, in turn, iodinated by the complex iodine–morpholine.⁴⁵ Alternatively, the silyl alkynes have been transformed in one step into their iodinated counterparts by the use of AgNO_3 –*N*-iodosuccinimide.³⁹

19.2.2 DOUBLE-BOND FORMATION DURING OR AFTER CYCLIZATION

This strategy is probably the most convergent. In principle, the most obvious way would be a cross-coupling reaction between a dialkyne and a suitable ethylene unit. Although the Sonogashira reaction cited above seemed perfect for this goal, its intramolecular version^{6,46} has failed so far to afford cyclodeca-3-ene-1,5-diynes.⁴⁷ After having screened without success several organometal catalyzed cross-coupling reactions, Danishefky eventually succeeded in obtaining the desired ring by a modification of the Stille reaction involving a diiodoalkyne **19** as electrophile and *Z* stannylene **20** as nucleophile (Scheme 19.6). This method has already been employed for the synthesis of polyfunctionalized enediynes, including calicheamicinone,²¹ dynemicin A¹⁵ and simplified dynemicin analogues.^{48,49} The use of LiCl as additive has been shown to improve the yields.^{48,50}

A three-step methodology, starting from a propargylic dialdehyde, takes advantage of the Pedersen reductive pinacol reaction.⁵¹ This method is

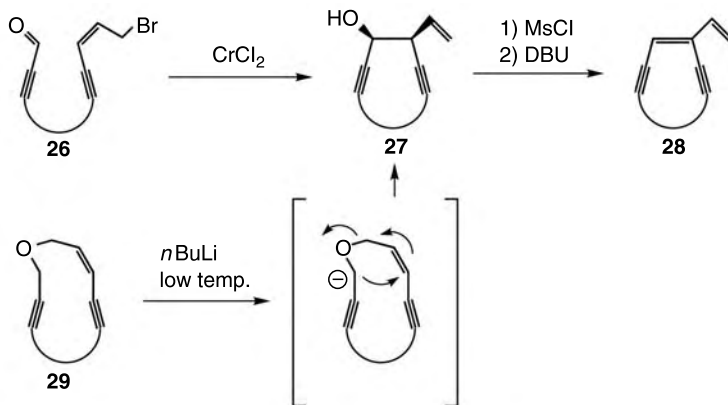


SCHEME 19.6

particularly mild and tolerant of functionalities and affords the diols **24** with a moderate to good stereoselection favouring the *cis* isomers.^{52,53} This is very important, since only the *cis* adducts can undergo Corey–Winter reduction (via a thionocarbonate) to the desired cyclic enediyne.^{52,53} The required diols for this elimination have also been obtained by alternative routes.⁵⁴ Particularly interesting is the double addition of a diacetylide to a diketone.⁵⁵

Two routes starting from a propargylic dibromide have been developed. Both have been used especially for unfunctionalized enediynes, since the conditions are poorly compatible with several functional groups. The most concise one involves carbenoid cyclization under the action of a strong base.^{56,57} The second, longer route, is based on a Ramberg–Bäcklund rearrangement of an alpha chlorosulphone.²⁹ Unfortunately, direct chlorination of the sulphone does not work efficiently and so the oxidation of the cyclic sulfide has to be carried out stepwise, passing through the sulfoxide **25**.

Cyclic enediynes have been obtained also by elimination of a suitable propargylic alcohol on a preformed cyclic diyne.⁵⁸ An example is shown in Scheme 19.7, where the cyclization was accomplished through a Nozaki–Hiyama intramolecular allyl bromide addition to an aldehyde.⁵⁹ This method proved successful for the synthesis of a particular enediyne that, because of conformational biases, could not be obtained by the strategies described above.



Scheme 7

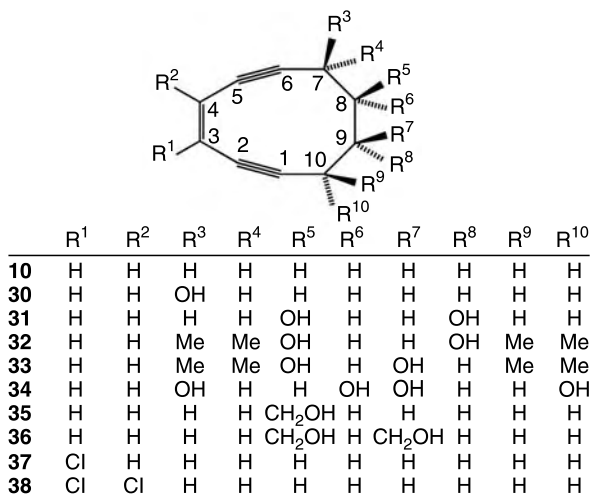
SCHEME 19.7

Alcohols of general formula **27** may also be obtained by base-promoted [2,3] Wittig sigmatropic rearrangement. This method has been applied for the synthesis of 9-membered cyclic enediynes.⁶⁰

19.3 MONOCYCLIC OR ORTHO-FUSED ARTIFICIAL ENEDIYNES

19.3.1 MONOCYCLIC CARBA ENEDIYNES

Apart from the parent compound **10**,²⁹ several cyclodeca-3-ene-1,5-diyne variously substituted at all possible positions have been prepared and studied (Scheme 19.8). These simple systems are useful in order to evaluate the steric and electronic effects of the substituents as well as to explore the effect of conjugation with DNA complexing substructures.

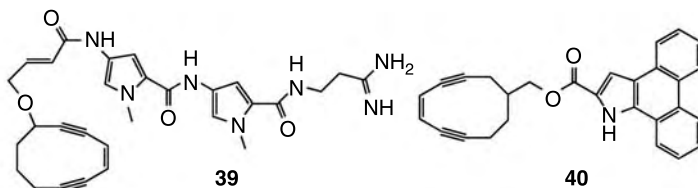


SCHEME 19.8

The presence of hydroxy groups at the 7 and 10 positions, as in **30**^{54,61} and **34**⁶², provokes an increase of the cycloaromatization rate. For example **30** has a $t_{1/2}$ of 4.5 h at 37°C (it is 18 h for **10**). A similar acceleration is observed for *trans* diol **31** ($t_{1/2}$ = 2 h at 50°C) where the hydroxy groups are in position 8 and 9 instead.⁵³ An analogous result was obtained by the *trans* tetramethylated diol **32**.⁶³ On the contrary, the *trans* isomer **33** was less reactive than **10**, and the diketone derived from **32** or **33** was even less prone to cycloaromatization.⁶³ Finally, the presence of one or two hydroxymethyl groups, as in **35**⁵⁶ or **36**,²⁹ has no appreciable influence on the reactivity.

On the other hand, the introduction of halogen atoms on the double bond was demonstrated to have an inhibitory effect on the Bergman reaction.⁶⁴ In particular, compound **38** has a half-life of 60 h at 100°C. Thus the two chlorine atoms may be considered efficient blocking devices. However, efficient triggering devices for such stabilized enediyne have not been yet devised.

The cleavage activity of the monocyclic compounds listed in [Scheme 19.8](#) against DNA is generally only moderate, with EC_{50} around $500\text{ }\mu\text{M}$ and with D/S ratios $<1:15$. In order to increase the potency, the hydroxy substituted derivatives **30** and **35** have been extensively used for the preparation of conjugated compounds where a DNA complexing subunit is attached to the OH group.

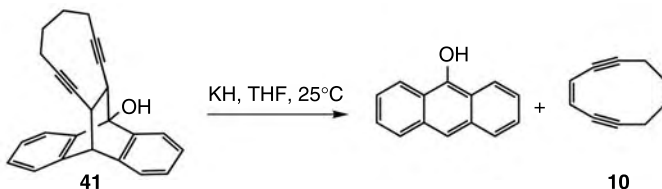


SCHEME 19.9

The best results have been obtained so far with compounds **39** and **40** (Scheme 19.9). In the first one, the enediyne is bonded to the minor groove binder netropsin through a semirigid linker. It displays a 2000-fold increase in activity compared to the parent alcohol. With an EC_{50} of about 200 nM , it is probably the most potent artificial enediyne prepared so far. However, it is still 10 times less active than calicheamicin and, most of all, no double strand cleavage was detected.⁶⁵ Compound **40** contains a DNA intercalator and has an EC_{50} of $80\text{ }\mu\text{M}$ and a D/S ratio of 1:18.⁶⁶

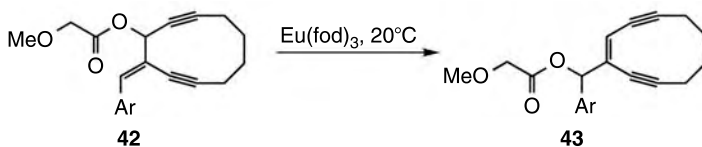
Monocyclic enediynes are not ideal prodrugs, because they generally lack a blocking device (*safety catch*) that prevents cycloaromatization, and when such device is present (*i.e.* in compounds **37** and **38**) it is not easily removable under physiological conditions.

A possible way to overcome this drawback involves generation of the monocyclic enediyne *in vivo*. Nicolaou and co-workers have shown that the parent compound **10** may be obtained from the polycyclic precursor **41** through a *retro*-Diels–Alder reaction (Scheme 19.10). While the thermal reaction requires a temperature of 150°C , formation of the alkoxide allows the cycloreversion to take place at room temperature.⁶⁷



SCHEME 19.10

The monocyclic enediyne **43** has been generated under mild conditions by Lewis acid catalyzed allylic rearrangement of the precursor **42** ([Scheme 19.11](#)).



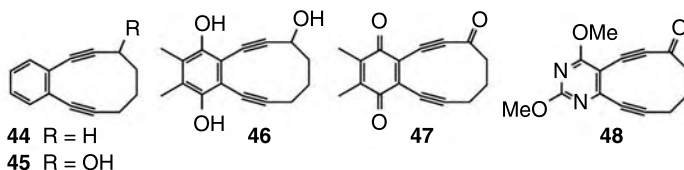
SCHEME 19.11

In order for the rearrangement to take place, the presence of an alkoxy group at the α position of the ester or, alternatively, the presence of an ortho hydroxymethyl group in the aryl group is essential.⁶⁸

Prodrugs **42** exhibit DNA cleaving properties and cytotoxicity *in vitro* indicating that the allylic rearrangement may occur also in aqueous buffer, without Lewis acid catalysis. Interestingly, in this case also the free alcohols are active. In particular, for Ar = 2-naphthyl, compounds with EC_{50} around 1–10 μM were obtained. They also were demonstrated to be cytotoxic on cancer cell lines.⁶⁸

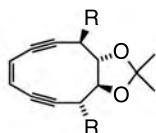
19.3.2 CYCLIC ENEDIYNES FUSED WITH ARENES THROUGH THE DOUBLE BOND

The fusion of the 10-membered enediyne ring with a benzene ring brings about a marked decrease of the cycloaromatization rate, probably because of the lower gain in aromatic stabilization (Scheme 19.12). Thus compound **44** is stable for more than 1 week at 37°C, undergoing appreciable Bergman reaction only at 84°C. Moreover, the rate is dependent on the concentration of 1,4-cyclohexadiene.⁶⁹ This fact seems to be due to a change in the rate limiting step, with the hydrogen abstraction by the di-radical becoming the slow one.⁷⁰ A similar behavior was shown by **45**.⁷¹ Interestingly, the corresponding ketone reacted slightly faster.

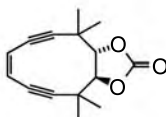


SCHEME 19.12

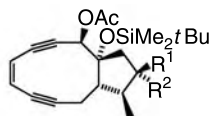
A strong difference between hydroquinone **46** and quinone **47** has been observed. The former is quite stable up to 100°C, whereas **47** undergoes cycloaromatization at 55°C with a $t_{1/2}$ of 32 min. This result opens the way for conceivable hydroquinone prodrugs to be activated upon an oxidative process.⁷² Actually, despite its stability, the hydroquinone **46** induced *in vitro*



58 R: H

59 R: OSiMe₂tBu

60

61 R¹, R²: = O62 R¹: H, R²: OSiMe₂tBu

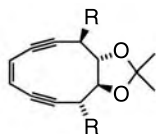
19.3.4 CYCLIC ENEDIYNES FUSED WITH OTHER RINGS THROUGH CARBONS 7–10

The fusion of a 10-membered cyclic enediyne with another ring is expected to stabilize it against cycloaromatization provided that:

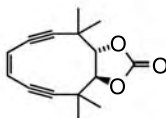
1. The fusion involves the carbons 7 to 10
2. The stereochemistry of ring junction is *trans*
3. The fused ring is small enough.

As far as this latter point is concerned, there is evidence that 6- or 7-membered rings are too large to function as blocking devices.^{47,77} On the other hand, fusion with 3-membered rings has not yet been explored. So, the most useful cases regard 5- or 4-membered rings.

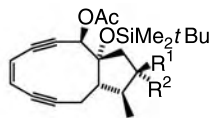
Trans fused dioxolanes **58**⁵³, **59**,⁶² and **60**⁶³ (Scheme 19.15) were indeed completely stable toward cycloaromatization, whereas the already cited corresponding diols **31** and **32** did react smoothly at 37°C. Conditions for an *in vivo* transformation of **58–60** (Scheme 19.15) into the corresponding diols have not yet been devised. On passing from dioxolanes to 5-membered carbocycles, the stabilizing effect may be dramatically reduced. Thus, ketone **61**⁷⁸ is even more reactive than the monocyclic compound **10**, showing a *t*_{1/2} of only 14 h at 25°C! The corresponding protected alcohol **62** is much more stable (*t*_{1/2} = 0.5 h at 90°C) indicating that subtle conformational effects can be crucial. Oxidation of deprotected **62** can therefore be viewed as a possible triggering event for prodrug activation. The results obtained so far with fused carbocyclic 5-membered rings indicate that subtle changes in hybridization within the [8.3.0] framework led to changes in reactivity.⁷⁹ As expected, when 5-membered rings are fused with a *cis* junction, no particular stabilization was observed.⁸⁰



58 R: H

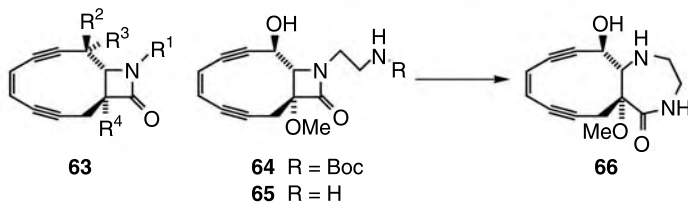
59 R: OSiMe₂tBu

60

61 R¹, R²: = O62 R¹: H, R²: OSiMe₂tBu

SCHEME 19.15

The most interesting results in this field have been obtained with enediynes *trans* fused with a β -lactam. When the fusion involves carbons 3 and 4 of the latter, cycloaromatization is completely prevented, because of the rigid planar structure of the azetidinone. Several compounds of general formula **63** ($R^2, R^3 = H$ or OH ; $R^4 = H$ or OR ; $R^1 = H$, Me , $SiMe_2tBu$ or various activating substituents), called “lactenediynes”, were prepared and found to be highly stable at the dry state and therefore easily manipulated (Scheme 19.16).^{45,52,81,82}



SCHEME 19.16

Opening of the β -lactam leads to monocyclic enediynes that undergo smooth cycloaromatization. When $R^1 = H$ or Me the conditions required for the azetidinone hydrolysis are too harsh to be used *in vivo*. However, by inserting activating substituents at R^1 , derivatives able to induce single and double cut on plasmid DNA were obtained.⁸³ Taking advantage of the various attachment points present in the basic formula, these activated lactenediynes have been conjugated to DNA complexing subunits, leading to compounds that give double-strand scission at concentrations as low as $1 \mu M$. As far as the double scission activity is concerned, these compounds are among the most potent artificial enediynes prepared so far.

Intramolecular opening of the β -lactam may be a way to selectively control the triggering mechanism. For example, the protected amine **64** was completely ineffective toward DNA. However, the free amine **65** undergoes an intramolecular transacylation forming **66**, which is no longer stabilised toward cycloaromatization. Therefore **66** is active, although only moderately, against DNA.⁸² Enzymatically removable protecting groups have been already explored⁷⁷ as a way of utilizing enzyme prodrug therapies.⁸⁴

Also fusion of a β -lactam involving the nitrogen atom and C-4 was explored.⁸⁵ The resulting bicyclic azaenediynes are also stabilized toward cycloaromatization. However, they are somehow less stable in the dry state, and are therefore less useful.

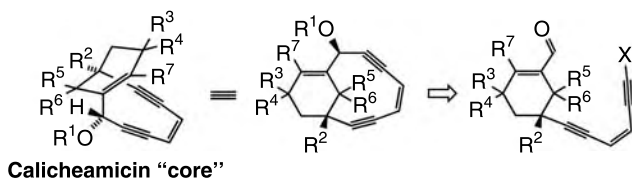
19.4 BRIDGED POLYCYCLIC ENEDIYNES

The main representatives of this group are simplified analogs of calicheamicins/esperamicins aglycons or dynemicin A, respectively characterized

by a double bond and an epoxide as safety catch. However, as described in the following paragraphs, different safety catches have also been proposed.

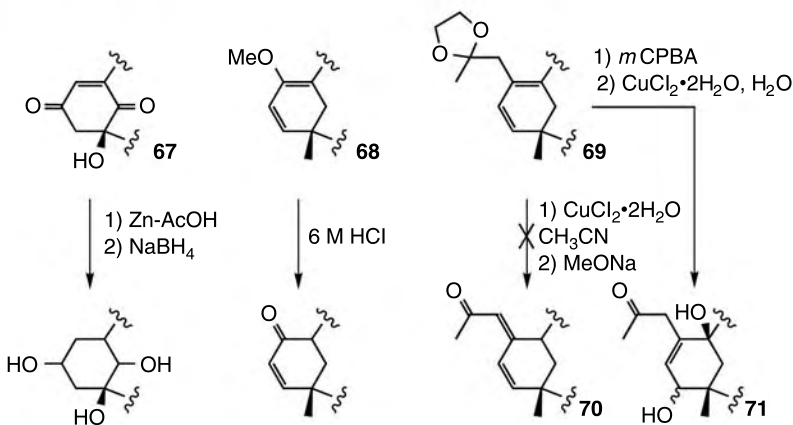
19.4.1 COMPOUNDS WITH A DOUBLE BOND AS A SAFETY CATCH

This family of compounds, constituted mainly by a series of [7.3.1] derivatives,⁸⁶ but including also [7.4.1], [8.3.1] and [9.3.1] polycyclic compounds, is characterized by the fact that the same synthetic strategy was followed for their preparation. That is, the formation of the cyclic enediyne system was achieved by the attack of the acyclic enediyne onto an aldehyde by one of the methods described above and illustrated in Scheme 19.17 for the formation of [7.3.1] systems.



SCHEME 19.17

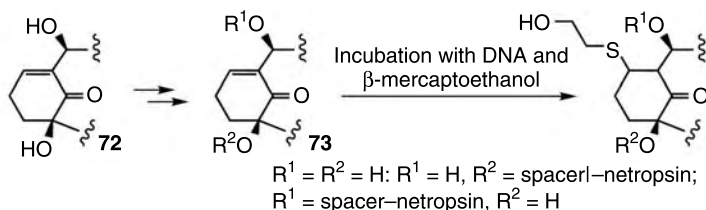
Apart from R^1 , which can be either a hydrogen or an alcohol protecting group, the difference in the [7.3.1] analogs lies only in the nature of the substituents in the 6-membered ring. For derivative **67**, the triggering event is the reduction of the $C=C$ double bond to give a 1,4-diketone, which shows interesting DNA cleavage activity that has been enhanced when the incubation was performed in the presence of $NaBH_4$, as a result of the additional reduction of the two carbonyl groups (Scheme 19.18).⁸⁶



SCHEME 19.18

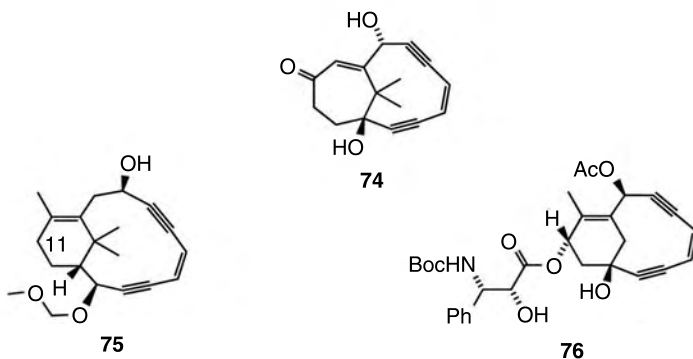
On the other hand, in compound **68** an enol–keto trigger, which is easily activated under acidic conditions, is operating.⁸⁷ While in the previous cases the bridgehead double bond was completely removed, as in calicheamicin itself, Semmelhack et al. studied the possibility to activate the prodrug by shifting the double bond to another position. An attempt to cause *endo*-to-*exo* base-promoted isomerization of **69** to give **70** failed because the double bond prefers to remain in the more strained bridgehead position. Therefore, **69** was activated in a more conventional way by a selective epoxidation followed by solvolytic opening of the oxyrane. The resulting diol **71** underwent easy cycloaromatization.⁸⁸

The enediyne **72**, having the carbonyl group on the shortest bridge of the bicyclic derivative, was conjugated, through an appropriate spacer, with netropsin, a well known minor-groove DNA binder, alternatively through the propargylic or the tertiary alcoholic function (Scheme 19.19).⁸⁹ In particular, the hybrid of **72** with netropsin bonded to the propargylic alcohol, showed an enhanced activity against plasmid DNA with respect to **72**. It resulted comparable to the one of esperamicin; unfortunately, the cytotoxicity against human colon tumor cells was unexpectedly low.



SCHEME 19.19

Scheme 19.20 summarizes some examples of bicyclic derivatives with ring sizes different from calicheamicin.⁹⁰ Compound **74**, with a 7-membered



SCHEME 19.20

ring and a configuration at the propargylic stereogenic centre opposite with respect to calicheamicin, exhibited poor DNA cleavage activity, while a weak cytotoxicity against human colon tumoral cells was displayed.

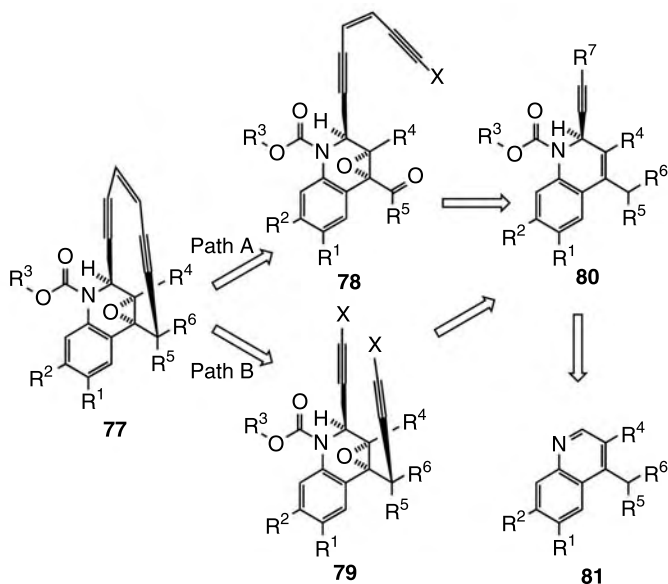
An interesting family of possible antitumoral agents is represented by taxamycins, a group of taxoid–calicheamicin hybrids, projected with the aim of achieving a synergic combination of the tubulin binding ability, peculiar of taxoids, with DNA damage properties, typical of enediynes.⁹¹ Compound **75**, the closest to Taxol[®] (Bristol-Myers Squibb), however, lacks the oxygenated group at C₁₁, since the authors were unable to introduce it. This compound underwent the cycloaromatization only under harsh conditions without triggering devices, probably due to the too large ring size of the cyclic enediyne (12-membered instead of the usual 10). On the other hand **76**, with a structure more similar to calicheamicin, and also bearing the side chain of Taxol[®], showed a negligible tubulin binding activity, although a weak cytotoxicity against HT-29 cancer cell line was observed. The latter should probably be enhanced by removing the bridgehead double bond.

19.4.2 COMPOUNDS WITH AN EPOXIDE AS A SAFETY CATCH

This important family of compounds is constituted mainly by dynemicin A analogs, which have been summarized in a recent review.⁹² These analogs typically lack the anthraquinone moiety and are protected at nitrogen. Actually, while in dynemicin the electron poor anthraquinone system makes this nitrogen poorly nucleophilic, in these truncated compounds the lone pair is able to assist epoxide solvolytic opening, inducing spontaneous cycloaromatization at room temperature. Therefore, a removable carbamate is used as a secondary safety catch. The synthetic approaches utilized so far for the preparation of derivatives **77** are summarized in [Scheme 19.21](#): the formation of the 10-membered enediyne cycle can be performed either by the cyclization of an acyclic enediyne like **78** (path A) or by ring closure at the double bond site starting from diyne **79** (path B). In all cases, however, an important feature is represented by the diastereoselective functionalization of a functionalized quinoline precursor such as **81** by means of a suitable acetylenic derivative to give intermediate **80**.

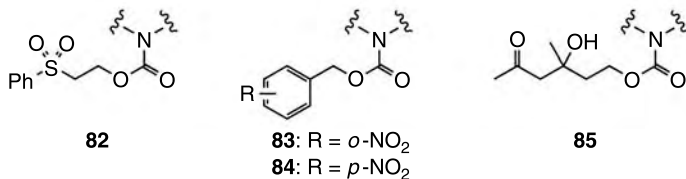
In **77** R¹ is usually hydrogen; although also OR groups have been placed there, their effect is negligible.⁹² R² is usually a hydrogen atom. Nevertheless, when R² is an *o*-nitrobenzyloxy group, readily cleaved to give the corresponding phenol upon irradiation, it has been exploited as the triggering device.⁹³

In the first reported simplified dynemicin analogs a carbamate, which is not easily removable, was present (R³ = Me, Ph etc), thus requiring a hydride-promoted reduction as the triggering event. However, the employment of a moiety that is easily removed, possibly under physiological conditions, spread rapidly. This substructure is usually introduced at the end of the synthesis, by an exchange reaction on the carbamate best suited



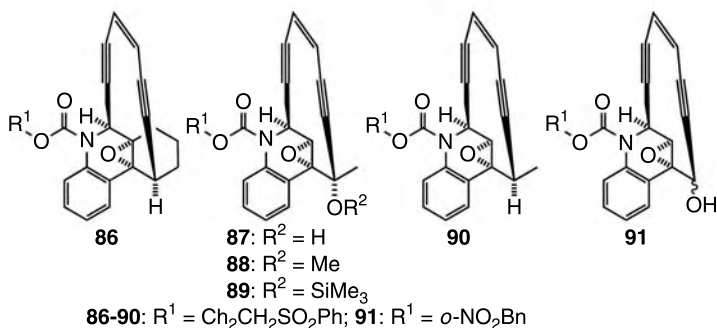
SCHEME 19.21

for the whole synthetic pathway. In particular an interesting urethane is represented by sulfone **82** (Scheme 19.22), which is easily removed under nearly physiological conditions in aqueous medium at pH 7.4–8.5, through a β -elimination process.^{48,93,94} Another possibility is represented by *o*-nitrobenzyl carbamate **83**, which can be easily cleaved by photoactivation, under irradiation at $\lambda > 300$ nm.⁴⁰ The corresponding *p*-nitrobenzyl carbamate **84** has been removed by means of enzyme nitroreductase NR2 from *Escherichia coli* B, while the *o*-isomer is unaffected under the same conditions.⁹⁵ This approach therefore represents a new entry to EPT-based (enzyme prodrug therapy) cancer therapies. Very recently, the first aldolase-mediated removal of carbamate **85**, involving a retro-aldol and an oxa-Michael reaction, has been reported as a new entry to ADEPT (antibody directed enzyme prodrug therapy).⁹⁶



SCHEME 19.22

As far as it concerns groups R^4 – R^6 , different compounds have been synthesized and some selected examples are reported in Scheme 19.23.^{40,48,49,93,94} These compounds all show interesting DNA cleaving activity, but only compounds **86**⁹³ and **90**⁴⁸ showed an appreciable amount of the more efficient double-strand break (single:double-strand break ratio for 1000 μ mol solutions is about 80:20 for **86** and 70:30 for **90** respectively).

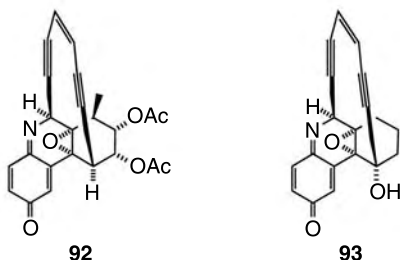


SCHEME 19.23

By comparing the activity of the structurally related compounds reported in Scheme 19.23 it seems that the highest DNA cleavage ability is showed by those compounds bearing a tertiary and not a quaternary carbon in the propargylic position α to the benzylic terminus of the epoxide. Moreover, a hydroxy (and an alkoxy even more) group is usually responsible for a lower activity, while the combination of a quaternary carbon with an alkoxy group represents the worst situation. It is noteworthy that the presence of this alkoxy or hydroxy group is a consequence of the strategy employed for the formation of the 10-membered enediyne. This problem can be overcome either by employing a strategy passing through path **B** (Scheme 19.21), as done for the synthesis of **90**, or removing reductively the hydroxyl after the cyclization, as done for compound **86**.

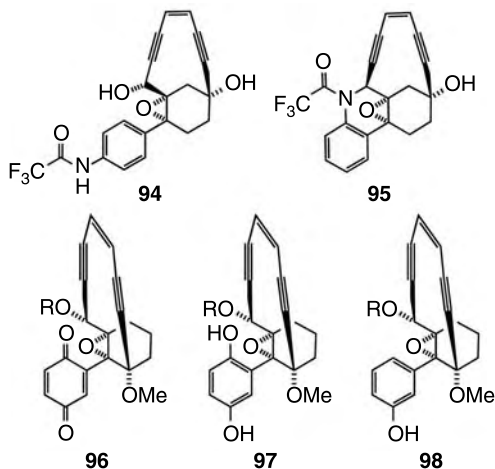
When the double bond of the 3-ene-1,5-diyne system is part of a benzene or a naphthalene ring, a lowered activity resulted, in agreement with the lower activity of benzo-fused enediyne already cited in Section 19.3.2.⁹⁷ Finally, the activity both *in vitro* (human carcinoma KB cells) and *in vivo* (mice inoculated with murine P338 leukemia) of **87–89** was tested.⁹⁴ Interestingly, while the phenyl carbamates have no detectable *in vitro* activity against plasmid DNA and were less cytotoxic *in vitro* than **87–89**, an opposite behavior was observed *in vivo*. Thus the phenyl carbamates showed an interesting activity, while the sulfones showed little or no activity, probably due to the fact that they are quite unstable and they are not able to reach tumor cells before cycloaromatization begins.

Another possibility is the synthesis of derivatives equipped with a quinone trigger, which are able to match the natural leads. Compounds **92** and **93**, synthesized by Shair et al.⁹⁸ display (Scheme 19.24) impressive *in vivo* activity with a reduction of tumor volume which is superior to the one showed in the same experiment by clinically used mitomycin C.



SCHEME 19.24

Two derivatives, compound **94**, which bears an esperamicin core with an epoxide trigger,⁹⁹ and **95**, which is a hybrid between esperamicin and dynemicin A cores,¹⁰⁰ have been reported (Scheme 19.25). Both compounds, after trifluoroacetamide removal, underwent cycloaromatization and showed an interesting antitumor activity *in vivo* in mice.



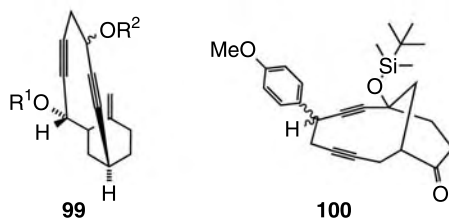
SCHEME 19.25

Finally, the dynemicin A analog lacking the heterocyclic nitrogen **96** was designed by Maier et al.⁹² In this case the triggering device is the quinone: upon its reduction, the hydroquinone **97** was expected to undergo

easy epoxide opening. However, this quinone **96** could be obtained only in low yield by oxidation of the phenol **98** (Scheme 19.25).

19.4.3 COMPOUNDS WHERE THE ENEDIYNE DOUBLE BOND IS FORMED BY A SUITABLE REACTION

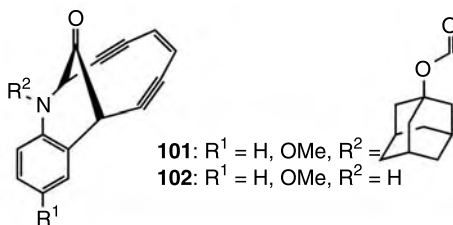
Only few examples of bridged polycyclic enediynes belonging to this family are known and they cannot be assimilated to specific natural derivatives. However, they have the same safety catch, that is the absence of the double bond conjugated with the two triple bonds. In order to prevent cycloaromatization the double bond had to be introduced as the last step by a suitable reaction. This can be done by the action of a base, causing an elimination reaction as in compound **99** (when $R^2 = \text{SO}_2\text{Me}$)¹⁰¹ or by a DDQ-mediated benzylic oxidation as in compound **100**³¹ (Scheme 19.26). The latter compound cycloaromatizes when heated at 80°C and shows some cytotoxicity with respect to rat embryo fibroblast cells.



SCHEME 19.26

19.4.4 MISCELLANEOUS

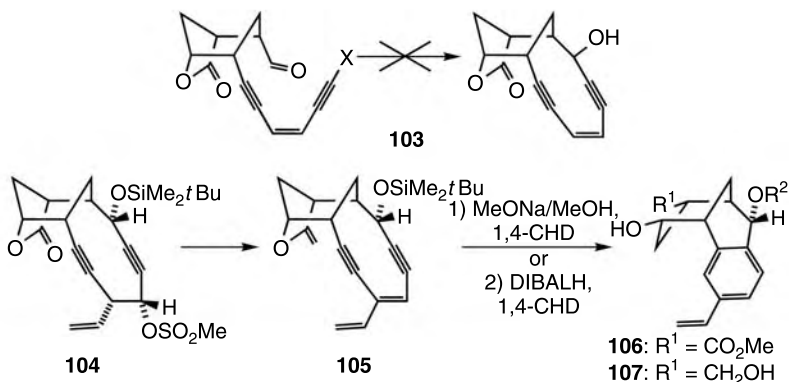
A dynemicin A analog resembling also the calicheamicin structure has been synthesized by Magnus et al.¹⁰² In this case the epoxide is not present and the role of safety catch is played by the carbonyl on the shortest bridge. The synthesis of **101** (Scheme 19.27) is achieved exploiting the reaction



SCHEME 19.27

illustrated above on compound **17** (Scheme 19.5). Azabicyclo[7.3.1]enediynes **102**, obtained after adamantyl carbamate removal under acidic conditions, exhibits an interesting antitumor activity both *in vitro* (HCT116 human colon carcinoma cells) and *in vivo* (P388 leukemia assays using CDF1 mice).¹⁰³ Differently from the other cases, the cycloaromatization is supposed to follow here a polar, nonradical pathway.

A more recent approach to simplified enediynes has been proposed by Semmelhack et al. (Scheme 19.28).⁵⁹ In this case a very simple bicyclic[7.3.1] enediyne was designed: in the prodrug, however, it was planned to introduce a third ring (a γ -lactone) in such a position that the 6-membered ring connected with the enediyne is forced to assume a boat conformation, thus creating a situation unsuitable for cycloaromatization. The triggering event is then the opening of the lactone, which will permit the boat-to-chair conversion of the 6-membered ring, thus allowing the enediyne to assume a conformation favourable to the cycloaromatization.

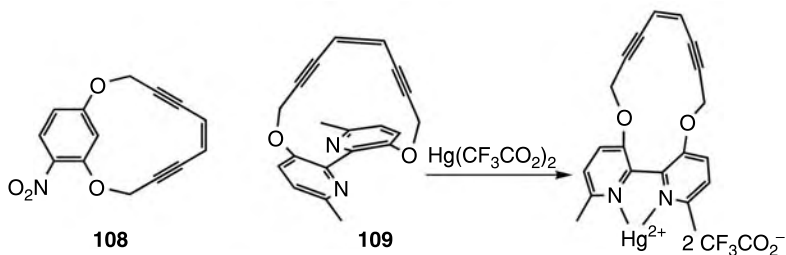


SCHEME 19.28

The simpler enediyne **103** could not be synthesized, since any attempt to exploit the usual cyclization of an acetylide onto a carbonyl moiety failed, giving a dimeric derivative arising from an intramolecular double coupling as the only product. This problem was solved using a different chromium(II)-mediated cyclization, followed by the base-induced elimination of mesylate **104** to introduce the conjugated double bond during the last step. Derivative **105** showed, as expected, an appreciable stability with a $t_{1/2} > 100$ h when heated to 74°C, while, when the same compound was treated with MeONa/MeOH in the presence of 1,4-cyclohexadiene as hydrogen donor, the only isolated product was cycloaromatized ester **106** (with an estimated half life time of the hydroxy ester equipped with the enediyne moiety of less than about 2 h at 23°C), thus supporting the working hypothesis of the authors. The same behaviour was observed upon reduction of the lactone with

diisobutylaluminum hydride to give **107** (with an estimated half life time of the diol equipped with the enediyne moiety of around 40 min at 24.5°C).

In addition, enediyne macrocycles, belonging to the family of cyclophanes, have been developed. Usually, they have been designed for different applications, such as the use as intermediates for fullerenes synthesis. However, studies of their propensity to undergo cycloaromatization have been performed for compounds **108** and **109** (Scheme 19.29). The first one is stable towards Bergman cycloaromatization up to 100°C and decomposes beyond this temperature, confirming molecular dynamics predictions.¹⁰⁴ The second one undergoes the same reaction at 237°C, but, when treated with $\text{Hg}(\text{CF}_3\text{CO}_2)_2$, the same reaction started at 145°C: this is probably due to the intervention of a double coordination of the two pyridine nitrogens with mercury(II) which causes important conformational changes in the macrocycle.¹⁰⁵



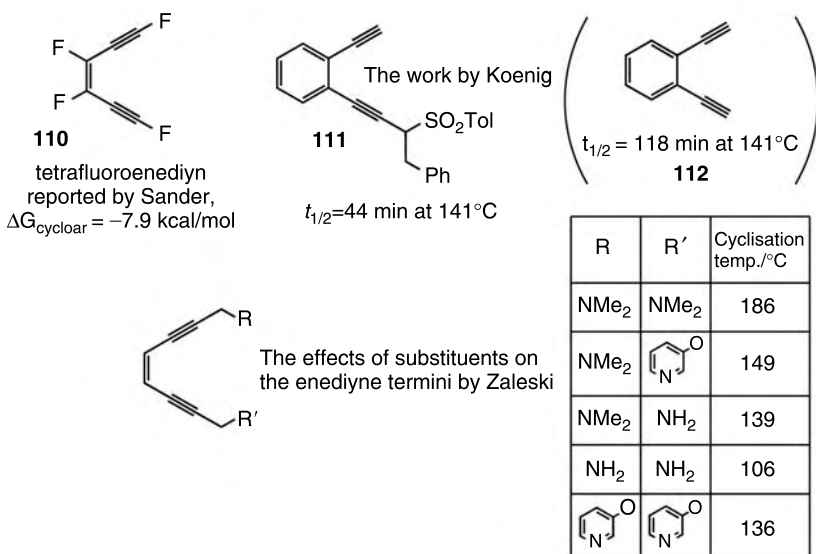
SCHEME 19.29

19.5 ACYCLIC ENEDIYNES

The thermal Bergman rearrangement of the unconstrained (*Z*)-hex-3-ene-1,5-diyne system to give a 1,4-didehydrobenzene diradical usually occurs above 400 K and therefore cannot take place in biological environments. Many research groups have devoted their attention to studying the factors influencing the cycloaromatization process of acyclic enediyne systems, in order to synthesize molecules that can cycloaromatize at physiological temperatures and ultimately find pharmacological applications. The final goal is the discovery of a blockbuster drug: the main advantage of acyclic systems over their mono- or polycyclic counterparts would be, of course, a more easily achievable synthesis, especially on large scale. The two main approaches that have been followed in this field are (a) the substitution of the terminal *sp* carbons of simple enediyne systems with opportune functional groups; and (b) the coordination of the enediyne molecule with metal ions.¹⁰⁶

19.5.1 INFLUENCE OF SUBSTITUENTS

The Bergman cyclization is quite sensitive to substituent effects, and substituents at the alkyne termini are generally the most effective. It has been demonstrated that electron acceptor substituents,¹⁰⁷ and more in particular σ -acceptors and/or π -donors,¹⁰⁸ can facilitate the thermal cyclization, but apart from the work reported by Sander¹⁰⁹ for the tetrafluoro-substituted enediyne **110** (which undergoes an exothermic Bergman cyclization), so far this approach has not produced particularly promising results (Scheme 19.30).

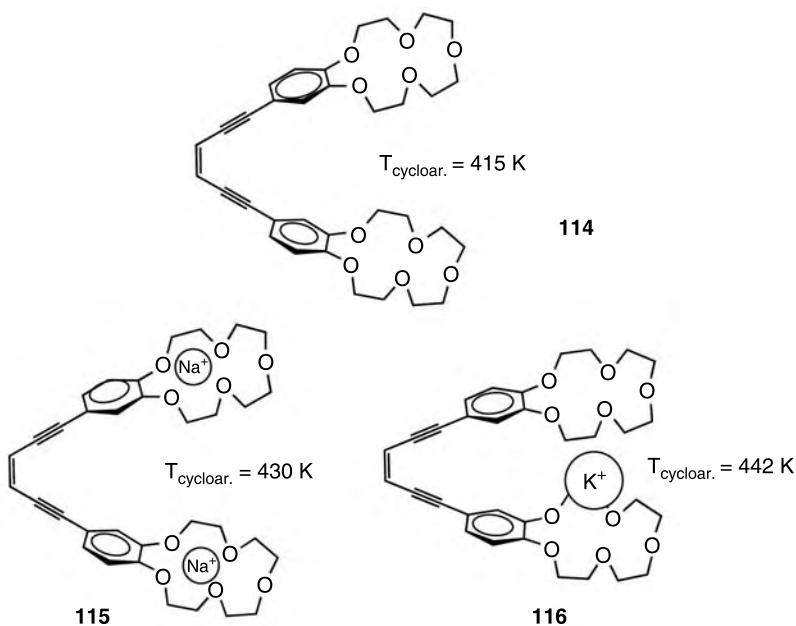


SCHEME 19.30

Klein and König,¹¹⁰ for example, have reported the synthesis of a sulfonamide substituted 1,2-aryldiyne **111**, where the sulfonamide group, being a σ -acceptor, should facilitate the Bergman cycloaromatization. However, as reported by Zaleski for a series of 1,8-*bis* substituted oct-4-ene-2,6-diyne derivatives **113**,¹¹¹ steric hindrance and hydrogen bond formation between the terminal substituents can influence the temperature of the cyclization, and therefore the reactivity of the sulfonamide compound **111** is comparable with the one of the unsubstituted analog **112**, since the electron withdrawing effect of the substituent is compensated by its steric hindrance (Scheme 19.30).

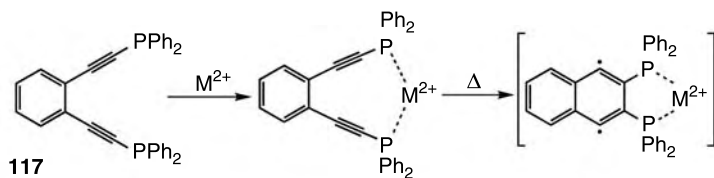
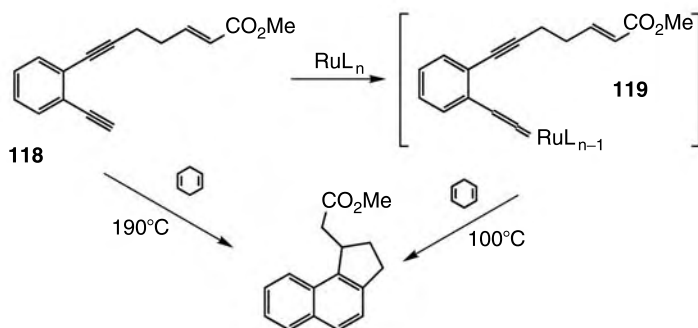
19.5.2 METAL-ION COORDINATION

The design of enediyne systems stable and unreactive until activated by a metal ion is extremely intriguing from a pharmaceutical point of view. Various research groups have found that the coordination of metal ions to suitable substituted enediynes can modulate their reactivity due to conformational and electronic changes in their structure. Conformational changes are observed, for example, in the work by König and Rutters,¹¹² where the enediyne system **114**, equipped with two crown ether moieties, is alternatively transformed in a bis sodium complex **115** or in a sandwich potassium complex **116**, and the effects of the coordination on the cycloaromatization process is investigated. However, the results are disappointing, since the cycloaromatization process begins at temperatures higher than the metal-free counterpart (Scheme 19.31).



SCHEME 19.31

Conformational changes are observed also in the 1,2-aryldiyne system **117** bearing two phosphine groups at its extremities synthesized by Warner et al.¹¹³ in this case the complexation to ions such as Pd^{2+} and Pt^{2+} activates the Bergman rearrangement, while Hg^{2+} stabilizes the aryldiyne moiety (Scheme 19.32). The author proposes that not only conformational changes, but also electronic effects, may contribute to the reactivity. Electronic effects are observed in a third example by Wang and Finn:¹¹⁴

The *bis* phosphinoenediyne by Buchwald

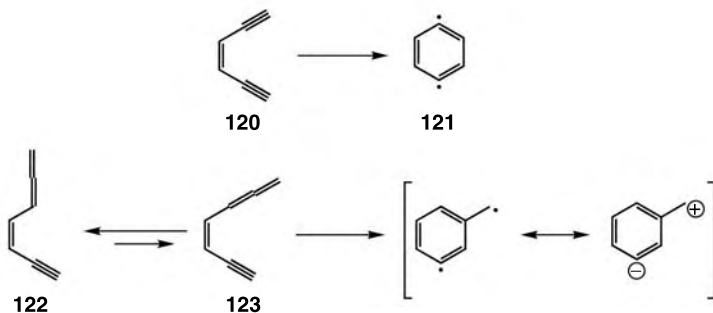
The activation by ruthenium complexation by Wang and Finn

SCHEME 19.32

they report the great enhancement of reactivity of the 1,2-aryldiyne system **118** when converted into a vinylidene complex **119** with ruthenium (Scheme 19.32). The increased thermal reactivity after the electronic structure modification is due to the possibility of the vinylidene complex **119** to give another type of cycloaromatization, named Myers–Saito, which will be illustrated in the following paragraph.

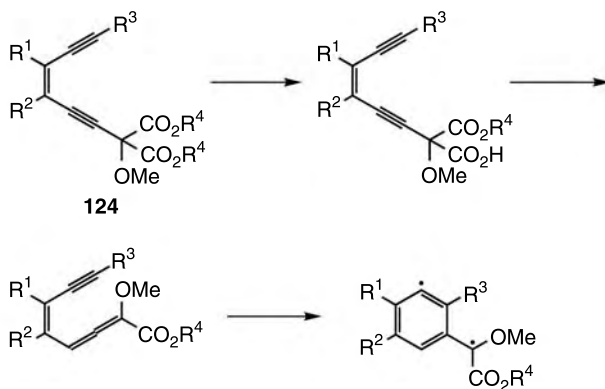
19.5.3 THE MYERS–SAITO CYCLOAROMATIZATION

While the rearrangement of acyclic (*Z*)-hex-3-ene-1,5-diynes **120** requires thermal activation, the cycloaromatization of (*Z*)-1,2,4-heptatrien-6-yne derivatives **123** proceeds under relatively mild conditions.¹¹⁵ The natural compound neocarzinostatin undergoes this type of cycloaromatization at physiological temperatures, when the steric impediment is removed. However, the reaction of acyclic enyne–allene derivatives requires higher temperatures, because the *s-trans* conformer **122** is generally more stable than the *s-cis* **123** conformer, which is indispensable for this reaction (Scheme 19.33). For the above-mentioned reasons efforts to prepare biologically relevant molecules have been oriented to the synthesis of compounds *forced* in the *s-cis* conformation, for example via the introduction of a benzene ring as part of the molecule, and with a triggering device able to block the aromatization process, that would take place even at room temperature on



SCHEME 19.33

the *s-cis* derivative. The main approach that has been followed is to generate the allene functionality from an opportunely functionalized alkyne moiety, for example from a propargyl dicarboxylate **124** as illustrated in Scheme 19.34.¹¹⁶

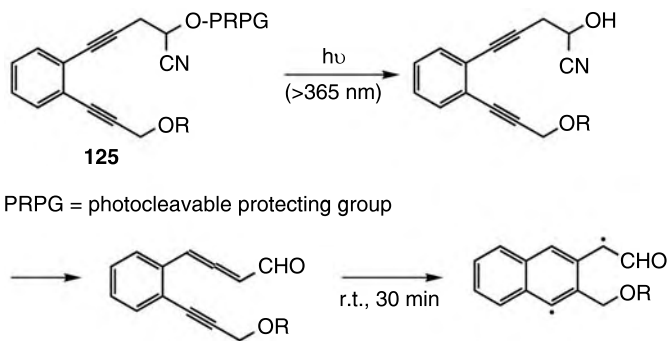


SCHEME 19.34

In contrast to di-radicals such as **121** (Scheme 19.33), di-radicals originated by the Myers–Saito rearrangement are known to have an ionic character in protic solvents and this nature is thought to reduce their DNA damaging ability. However, it has been shown by Shibuya¹¹⁷ that the presence of an electron withdrawing group in the benzylic position produces a dehydrotoluene species with an enhanced diradical character.

19.5.4 PHOTOCHEMICAL CYCLOAROMATIZATION REACTION

An alternative to thermal cycloaromatization is represented by photoactivable enediyne systems, where a stable enediyne molecule is activated



SCHEME 19.35

upon irradiation. The irradiation process can either remove a protecting group, like for compound **125**, triggering an alkyne-allene isomerization¹¹⁸ (Scheme 19.35), or cause a *trans/cis* isomerization,¹¹⁹ or directly produce a Bergman-type di-radical.¹²⁰ Only preliminary results have appeared so far in the literature, but the concept of photoactivation is of extreme relevance, considering the recent progress of optical fiber techniques and therefore the possibility of directing an intense beam of activating radiation into the depths of the human body in a very narrow localized area, thus minimizing side effects generally associated with chemotherapies.

REFERENCES

- [1] Nicolaou, K. C. Chemistry and biology of the enediyne anticancer antibiotics. *Angew. Chem., Int. Ed. Engl.* **1991**, 32, 1387–1416.
- [2] Smith, A.L.; Nicolaou, K.C. The enediyne antibiotics. *J. Med. Chem.* **1996**, 39, 2103–2117.
- [3] Edo, K.; Mizugaki, M.; Koide, Y.; Seto, H.; Furihata, K.; Otake, N.; Ishida, N. The structure of neocarzinostatin chromophore possessing a novel bicyclo-[7,3,0]dodecadiene system. *Tetrahedron Lett.* **1985**, 26, 331–340.
- [4] Thorson, J.S.; Sievers, E.L.; Ahlert, J.; Shepard, E.; Whitwam, R.E.; Onwueme, K.C.; Ruppen, M. Understanding and exploiting nature's chemical arsenal: the past, present and future of calicheamicin research. *Curr. Pharm. Design* **2000**, 6, 1841–1879.
- [5] Thorson, J.S.; Shen, B.; Whitwam, R.E.; Liu, W.; Li, Y.; Ahlert, J. Enediyne biosynthesis and self-resistance: a progress report. *Bioorg. Chem.* **1999**, 27, 172–188.
- [6] Kato, N.; Shimamura, S.; Khan, S.; Takeda, F.; Kikai, Y.; Hirama, M. Convergent approach to the maduropeptin chromophore: aryl ether formation of (*R*)-3-aryl-3-hydroxypropanamide and cyclization of macrolactam. *Tetrahedron* **2004**, 60, 3161–3172.

- [7] Wang, Z.; He, Q.Y.; Liang, Y.Y.; Wang, D.S.; Li, Y.Y.; Li, D.D. Non-caspase-mediated apoptosis contributes to the potent cytotoxicity of the enediyne antibiotic lidamycin toward human tumor cells. *Biochem. Pharmacol.* **2003**, *65*, 1767–1775.
- [8] Myers, A.G.; Hurd, A.R.; Hogan, P.C. Evidence for facile atropisomerism and simple (non-nucleophilic) biradical-forming cycloaromatization within kedarcidin chromophore aglycon. *J. Am. Chem. Soc.* **2002**, *124*, 4583–4585.
- [9] Hwang, G.S.; Jones, G.B.; Goldberg, I.H. Stereochemical control of small molecule binding to bulged DNA: Comparison of structures of spirocyclic enantiomer-bulged DNA complexes. *Biochemistry* **2004**, *43*, 641–650; Myers, A.G.; Glatthar, R.; Hammond, M.; Harrington, P.M.; Kuo, E.Y.; Liang, J.; Schaus, S.E.; Wu, Y.S.; Xiang, J.N. Development of an enantioselective synthetic route to neocarzinostatin chromophore and its use for multiple radioisotopic incorporation. *J. Am. Chem. Soc.* **2002**, *124*, 5380–5401.
- [10] Miyagawa, N.; Sasaki, D.; Matsuoka, M.; Imanishi, M.; Ando, T.; Sugiura, Y. DNA cleavage characteristics of non-protein enediyne antibiotic N1999A2. *Biochem. Biophys. Res. Commun.* **2003**, *306*, 87–92; Bertus, P.; Zhang, J.H.; Sir, G.; Weibel, J.M.; Pale, P. Asymmetric synthesis of the cyclopentanones related to NCS and N1999A2 antitumor antibiotics. *Tetrahedron Lett.* **2003**, *44*, 3391–3395.
- [11] Lee, M.D.; Ellestad, G.A.; Borders, D.B. Calicheamicins: discovery, structure, chemistry, and interaction with DNA. *Acc. Chem. Res.* **1991**, *24*, 235–243.
- [12] Weinstein, D.S.; Nicolaou, K.C. Synthesis of the namenamicin A–C disaccharide: towards the total synthesis of namenamicin. *J. Chem. Soc., Perkin Trans. 1* **1999**, 545–547.
- [13] Oku, N.; Matsunaga, S.; Fusetani, N. Shishijimicins A–C, novel enediyne antitumor antibiotics from the Ascidian *Didemnum proliferum*. *J. Am. Chem. Soc.* **2003**, *125*, 2044–2045.
- [14] Prabhakaran, J.; Lhermitte, H.; Das, J.; Sasi-Kumar, T.K.; Grierson, D.S. The synthesis of a sulfone containing analogue of the esperamicin-A(1) aglycone: A hetero Diels–Alder approach. *Synlett* **2000**, 658–662.
- [15] Danishefsky, S.; Shair, M.D. Observations in the chemistry and biology of cyclic enediyne antibiotics: Total syntheses of calicheamicin γ_1^I and dynemicin A. *J. Org. Chem.* **1996**, *61*, 16–44.
- [16] Myers, A.G.; Tom, N.J.; Fraley, M.E.; Cohen, S.B.; Madar, D.J. A convergent synthetic route to (+)-dynemicin A and analogs of wide structural variability. *J. Am. Chem. Soc.* **1997**, *119*, 6072–6094.
- [17] Drak, J.; Iwasawa, N.; Danishefsky, S.; Crothers, D.M. The carbohydrate domain of calicheamicin γ_1^I determines its sequence specificity for DNA cleavage. *Proc. Natl. Acad. Sci. USA* **1991**, *88*, 7464–7468.
- [18] Walker, S.; Landovitz, R.; Ding, W.D.; Ellestad, G.A.; Kahne, D. Cleavage behavior of calicheamicin γ_1 and calicheamicin T. *Proc. Natl. Acad. Sci. USA* **1992**, *89*, 4608–4612.
- [19] Batchelder, R.M.; Wilson, W.R.; Hay, M.P.; Denny, W.A. Oxygen dependence of the cytotoxicity of the enediyne anti-tumour antibiotic esperamicin A(1). *Br. J. Cancer* **1996**, *74*, S52–S56.
- [20] Nicolaou, K.C.; Hummel, C.W.; Nakada, M.; Shibayama, K.; Pitsinos, E.N.; Saimoto, H.; Mizuno, Y.; Baldenius, K.-U.; Smith, A.L. Total synthesis

- of calicheamicin γ_1^I 3. The final stages. *J. Am. Chem. Soc.* **1993**, *115*, 7625–7635.
- [21] Clive, D.L.J.; Tao, Y.; Bo, Y.X.; Hu, Y.Z.; Selvakumar, N.; Sun, S.Y.; Daigneault, W.S.; Wu, Y.J. Synthetic studies on calicheamicin γ_1 — synthesis of (–)-calicheamicinone and models representing the four sugars and the aromatic system. *Chem. Commun.* **2000**, 1341–1350.
- [22] Churcher, I.; Hallet, D.; Magnus, P. Synthesis of the enediyne aglycon (+/–)-calicheamicinone. *J. Am. Chem. Soc.* **1998**, *120*, 3518–3519.
- [23] Whitwam, R.E.; Ahlert, J.; Holman, T.R.; Ruppen, M.; Thorson, J.S. The gene *calC* encodes for a non-heme iron metalloprotein responsible for calicheamicin self-resistance in *Micromonospora*. *J. Am. Chem. Soc.* **2000**, *122*, 1556–1557.
- [24] Hamann, P.R.; Hinman, L.M.; Beyer, C.F.; Lindh, D.; Upeslakis, J.; Flowers, D.A.; Bernstein, I. An anti-CD33 antibody–calicheamicin conjugate for treatment of acute myeloid leukemia. Choice of linker. *Bioconjugate Chem.* **2002**, *13*, 40–46; Hamann, P.R.; Hinman, L.M.; Hollander, I.; Beyer, C.F.; Lindh, D.; Holcomb, R.; Hallett, W.; Tsou, H.-R.; Upeslakis, J.; Shochat, D.; Mountain, A.; Flowers, D.A.; Bernstein, I. Gemtuzumab ozogamicin, a potent and selective anti-CD33 antibody–calicheamicin conjugate for treatment of acute myeloid leukemia. *Bioconjugate Chem.* **2002**, *13*, 47–58.
- [25] Darby, N.; Kim, C.U.; Salaün, J.A.; Shelton, K.W.; Takada, S.; Masamune, S. Concerning the 1,5-didehydro[10]annulene system. *J. Chem. Soc., Chem. Commun.* **1971**, 1516–1518.
- [26] Lockhart, T.P.; Bergman, R.G. Evidence for the reactive spin state of 1,4-dehydrobenzenes. *J. Am. Chem. Soc.* **1981**, *103*, 4091–4096.
- [27] Stahl, F.; Moran, D.; Schleyer, P.V.; Prall, M.; Schreiner, P.R. Aromaticity of the Bergman, Myers–Saito, Schmittel, and directly related cyclizations of enediynes. *J. Org. Chem.* **2002**, *67*, 1453–1461.
- [28] Jones, G.B.; Wright, J.M.; Plourde II, G.; Purohit, A.D.; Wyatt, J.K.; Hynd, G.; Fouad, F. Synthesis and photochemical activity of designed enediynes. *J. Am. Chem. Soc.* **2000**, *122*, 9872–9873.
- [29] Nicolaou, K.C.; Zuccarello, G.; Riemer, C.; Estevez, V.A.; Dai, W.-M. Design, synthesis, and study of simple monocyclic conjugated enediynes. The 10-membered ring enediyne moiety of the enediyne anticancer antibiotics. *J. Am. Chem. Soc.* **1992**, *114*, 7360–7371.
- [30] Kumar, R.A.; Ikemoto, N.; Patel, D.J. Solution structure of the calicheamicin γ_1^I –DNA complex. *J. Mol. Biol.* **1997**, *265*, 187–201.
- [31] Maier, M.E. Design of enediyne prodrugs. *Synlett* **1995**, 13–26.
- [32] Snyder, J.P. Monocyclic enediyne collapse to 1,4-diyl biradicals — a pathway under strain control. *J. Am. Chem. Soc.* **1990**, *112*, 5367–5369.
- [33] Ettmayer, P.; Amidon, G.L.; Clement, B.; Testa, B. Lessons learned from marketed and investigational prodrugs. *J. Med. Chem.* **2004**, *47*, 2393–2404.
- [34] Hakimelahi, G.H.; Gassanov, G.S.; Hsu, M.-H.; Hwua, J.R.; Hakimelahi, S. A novel approach towards studying non-genotoxic enediynes as potential anticancer therapeutics. *Bioorg. Med. Chem.* **2002**, *10*, 1321–1328.
- [35] Lin, C.F.; Hsieh, P.C.; Lu, W.D.; Chiu, H.F.; Wu, M.J. A series of enediynes as novel inhibitors of topoisomerase I. *Bioorg. Med. Chem.* **2001**, *9*, 1707–1711; Plourde, G.W.I.; El-Shafey, A.; Fouad, F.S.; Purohit, A.S.; Jones, G.B.

- Protein degradation with photoactivated enediyne-amino acid conjugates. *Bioorg. Med. Chem. Lett.* **2002**, 12, 2985–2988.
- [36] Basak, A.; Mandal, S.; Kumar Das, A.; Bertolasi, V. Benzene fused monocyclic enediynyl amides: synthesis, reactivity and DNA-cleavage activity in comparison to the corresponding sulfonamides. *Bioorg. Med. Chem. Lett.* **2002**, 12, 873–877.
- [37] Nicolaou, K.C.; Maligres, P.; Suzuki, T.; Wendeborn, S.V.; Dai, W.M.; Chadha, R.K. Molecular design and chemical synthesis of potent enediynes. 1. Dynamicin model systems equipped with N-tethered triggering devices. *J. Am. Chem. Soc.* **1992**, 114, 8890–8907.
- [38] Sato, I.; Akahori, Y.; Iida, K.; Hiram, M. Efficient synthesis of a carbocyclic core moiety with the stereochemistry of the C-1027 chromophore. *Tetrahedron Lett.* **1996**, 37, 5135–5138.
- [39] Nishikawa, T.; Shibuya, S.; Hosokawa, S.; Isobe, M. One-pot synthesis of haloacetylenes from trimethylsilylacetylenes. *Synlett* **1994**, 485–486.
- [40] Wender, P.A.; Zercher, C.K.; Beckham, S.; Haubold, E.M. A photochemically triggered DNA-cleaving agent — synthesis, mechanistic and DNA cleavage studies on a new analog of the antitumor antibiotic dynemicin. *J. Org. Chem.* **1993**, 58, 5867–5869.
- [41] Nishikawa, T.; Shibuya, S.; Isobe, M. Cesium fluoride promoted cyclization in the synthesis of enediyne antibiotics. *Synlett* **1994**, 482–484.
- [42] Magnus, P.; Carter, P.; Elliott, J.; Lewis, R.; Harling, J.; Pitterna, T.; Bauta, W.E.; Fortt, S. Synthetic and mechanistic studies on the antitumor antibiotics esperamicin A1 and calicheamicin γ_1 - synthesis of 2-ketobicyclo[7.3.1] enediyne and 13-ketocyclo[7.3.1] enediyne cores mediated by η -2 dicobalt hexacarbonyl alkyne complexes — cycloaromatization rate studies. *J. Am. Chem. Soc.* **1992**, 114, 2544–2559.
- [43] Magnus, P.; Carter, R.; Davies, M.; Elliott, J.; Pitterna, T. Studies on the synthesis of the core structures of the antitumor agents neocarzinostatin, kedarcidin, C-1027 and maduropeptin. *Tetrahedron* **1996**, 52, 6283–6306.
- [44] Chemin, D.; Linstrumelle, G. Palladium-catalyzed reaction of (*E*) and (*Z*)-dichloroethenes with 1-alkynes. An efficient stereospecific synthesis of (*E*) and (*Z*)-enediynes. *Tetrahedron* **1994**, 50, 5335–5344.
- [45] Banfi, L.; Basso, A.; Guanti, G. Rational design, synthesis, and reactivity of lactendiynes, a new class of cyclic enediynes ortho-fused with the β -lactam ring. *Tetrahedron* **1997**, 53, 3249–3268.
- [46] Dai, W.M.; Wu, A. First synthesis of a highly strained cyclodeca-1,5-diyne skeleton via intramolecular Sonogashira cross-coupling. *Tetrahedron Lett.* **2001**, 42, 81–83.
- [47] Jones, G.B.; Wright, J.M.; Hynd, G.; Wyatt, J.K.; Warner, P.M.; Huber, R.S.; Li, A.W.; Kilgore, M.W.; Sticca, R.P.; Pollenz, R.S. Oxa-enediynes: Probing the electronic and stereoelectronic contributions to the Bergman cycloaromatization. *J. Org. Chem.* **2002**, 67, 5727–5732.
- [48] Guanti, G.; Riva, R. Simplified dynemicin analogues: diastereoselective synthesis and evaluation of their activity against plasmid DNA. *Org. Biomol. Chem.* **2003**, 1, 3967–3976.
- [49] Banfi, L.; Basso, A.; Gandolfo, V.; Guanti, G.; Riva, R. Asymmetric synthesis of a new simplified dynemicin analogue equipped with a handle. *Tetrahedron Lett.* **2004**, 45, 4221–4223.

- [50] Moss, D.K.; Spence, J.D.; Nantz, M.H. Effects of propargylic substitution and annelation on the cycloaromatization of a bicyclo[7.3.1]enediyne. *J. Org. Chem.* **1999**, *64*, 4339–4343.
- [51] Myers, A.G.; Dragovich, P.S. Design and synthesis of a system for enediyne formation by anthraquinone reductive activation. *J. Am. Chem. Soc.* **1992**, *114*, 5859–5860.
- [52] Banfi, L.; Basso, A.; Guanti, G. New approach to β -lactam-fused enediynes (“lactenediynes”) by stereoselective pinacol coupling. *Eur. J. Org. Chem.* **2000**, 939–946.
- [53] Pitsch, W.; Klein, M.; Zabel, M.; König, B. Synthesis and structure of a stabilized 10-membered cyclic enediyne. *J. Org. Chem.* **2002**, *67*, 6805–6807.
- [54] Semmelhack, M.F.; Gallagher, J. Cyclic conjugated enediynes via elimination of a thionocarbonate in a latent *Z*-hex-3-ene-1,5-diyne unit. *Tetrahedron Lett.* **1993**, *34*, 4121–4124.
- [55] Crich, D.; Pavlovich, A.B.; Wink, D.J. Synthesis of fully-substituted enediynes by the Corey–Winter reaction. *Synth. Commun.* **1999**, *29*, 359–377.
- [56] Jones, G.B.; Huber, R.S.; Mathews, J.E. Towards enediyne libraries: cyclic enediynes via an intramolecular carbenoid coupling protocol. *J. Chem. Soc., Chem. Commun.* **1995**, 1791–1792.
- [57] McPhee, M.M.; Kerwin, S.M. Synthesis and metal ion binding studies of enediyne-containing crown ethers. *J. Org. Chem.* **1996**, *61*, 9385–9393.
- [58] Iida, K.; Hiram, M. Synthesis and characterization of nine-membered cyclic enediynes, models of the C-1027 and kedarcidin chromophores: equilibration with a *p*-benzyne biradical and kinetic stabilization. *J. Am. Chem. Soc.* **1995**, *117*, 8875–8876.
- [59] Semmelhack, M.F.; Wu, L.; Pascal, R.A.J.; Ho, D.M. Conformational control in activation of an enediyne. *J. Am. Chem. Soc.* **2003**, *125*, 10496–10497.
- [60] Takahashi, T.; Tanaka, H.; Yamada, H.; Matsumoto, T.; Sugiura, Y. DNA cleavage by a nine-membered masked enediyne, an analogue of the kedarcidin and C-1027 chromophores. *Angew. Chem., Int. Ed. Engl.* **1996**, *35*, 1835–1836.
- [61] Crévisy, C.; Beau, J.-M. The esperamicin–calicheamicin aglycones: ring closure of a simple strained system mediated by chromium(II)–nickel(II) salts. *Tetrahedron Lett.* **1991**, *32*, 3171–3174.
- [62] Klein, M.; Zabel, M.; Bernhardt, G.; König, B. Tetrahydroxy 10-membered cyclic enediynes. *J. Org. Chem.* **2003**, *68*, 9379–9383; Comanita, B.M.; Heuft, M.A.; Rietveld, T.; Fallis, A.G. A mild route to α -alkoxyacetylenes mediated by Lewis acids and synthetic routes to 10-, 11- and 12-membered ring enediyne carbocycles. *Israel J. Chem.* **2000**, *40*, 241–253.
- [63] Nicolaou, K.C.; Sorensen, E.J.; Discordia, R.; Hwang, C.-K.; Minto, R.E.; Bharucha, K.N.; Bergman, R.E. Ten-membered ring enediynes with remarkable chemical and biological profiles. *Angew. Chem., Int. Ed. Engl.* **1992**, *31*, 1044–1046.
- [64] Plourde, G.W.I.; Warner, P.M.; Parrish, D.A.; Jones, G.B. Halo-enediynes: Probing the electronic and stereoelectronic contributions to the Bergman cycloaromatization. *J. Org. Chem.* **2002**, *67*, 5369–5374.
- [65] Semmelhack, M.F.; Gallagher, J.J.; Ding, W.D.; Krishnamurthy, G.; Babine, R.; Ellestad, G.A. The effect on DNA cleavage potency of tethering a simple cyclic enediyne to a netropsin analog. *J. Org. Chem.* **1994**, *59*, 4357–4359.

- [66] Jones, G.B.; Mathews, G.E. Bifunctional antitumor agents: a DNA interactive enediyne from the pyrrolo[9,10-b]phenanthrene template. *Bioorg. Med. Chem. Lett.* **1997**, *7*, 745–748; Jones, G.B.; Mathews, J.E. Bifunctional antitumor agents. Derivatives of pyrrolo[9,10-b]phenanthrene — A DNA intercalative delivery template. *Tetrahedron* **1997**, *53*, 14599–14614.
- [67] Bunnage, M.E.; Nicolaou, K.C. The oxide anion accelerated retro-Diels–Alder reaction. *Chem. Eur. J.* **1997**, *3*, 187–192.
- [68] Dai, W.M.; Lai, K.W.; Wu, A. X.; Hamaguchi, W.; Lee, M.Y. H.; Zhou, L.; Ishii, A.; Nishimoto, S. DNA cleavage potency, cytotoxicity, and mechanism of action of a novel class of enediyne prodrugs. *J. Med. Chem.* **2002**, *45*, 758–761.
- [69] Semmelhack, M.F.; Neu, T.; Foubelo, F. Arene 1,4-Diradical formation from o-dialkynylarenes. *Tetrahedron Lett.* **1992**, *33*, 3277–3280.
- [70] Taneko, T.; Takahashi, M.; Hiram, M. Benzannulation alters the rate limiting step in enediyne cycloaromatization. *Tetrahedron Lett.* **1999**, *40*, 2015–2018.
- [71] Boger, D.L.; Zhou, J. CDPI₃-enediyne and CDPI₃-EDTA conjugates: a new class of DNA cleaving agents. *J. Org. Chem.* **1993**, *58*, 3018–3024.
- [72] Nicolaou, K.C.; Liu, A.; Zeng, Z.; McComb, S. Redox-controlled Bergman cycloaromatizations. Designed enediynes with DNA-cleaving properties and antitumor activity. *J. Am. Chem. Soc.* **1992**, *114*, 9279–9282.
- [73] Choy, N.; Blanco, B.; Wen, J.; Krishnan, A.; Russell, K.C. Photochemical and thermal Bergman cyclization of a pyrimidine enediynol and enediynone. *Organic Lett.* **2000**, *2*, 3761–3764.
- [74] Singh, R.; Just, G. The synthesis of a 10-membered benzo-oxadiyne ring. *Tetrahedron Lett.* **1990**, *31*, 185–188.
- [75] Basak, A.; Bdour, H.M.; Shain, J.C.; Mandal, S.; Rudra, K.R.; Nag, S. DNA-cleavage studies on N-substituted monocyclic enediynes: Enhancement of potency by incorporation of intercalating or electron poor aromatic ring and subsequent design of a novel phototriggerable acyclic enediyne. *Bioorg. Med. Chem. Lett.* **2000**, *10*, 1321–1325.
- [76] Suzuki, I.; Shigenaga, A.; Manabe, A.; Nemoto, H.; Shibuya, M. Synthesis, reactions and DNA damaging abilities of 10-membered enediyne-sulfone and related compounds. *Tetrahedron* **2003**, *59*, 5691–5704.
- [77] Banfi, L.; Guanti, G.; Rasparini, M. Intramolecular opening of β -lactams with amines as a strategy toward enzymatically or photochemically triggered activation of lactenediyne prodrugs. *Eur. J. Org. Chem.* **2003**, 1319–1336.
- [78] Semmelhack, M.F.; Gu, Y.; Ho, D.M. A new framework for the cycloaromatization of enediynes under mild conditions. *Tetrahedron Lett.* **1997**, *38*, 5583–5586.
- [79] Semmelhack, M.F.; Jaskowski, M.; Sarpong, R.; Ho, D.M. A simple synthesis and evaluation of the bicyclo[8.3.0]enediyne framework. *Tetrahedron Lett.* **2002**, *43*, 4947–4950.
- [80] Wang, J.; De Clercq, P.J. Estramycins: a new diyl precursor family derived from estradiol. *Angew. Chem., Int. Ed. Engl.* **1995**, *34*, 1749–1752.
- [81] Banfi, L.; Guanti, G. Synthesis of a new lactenediyne scaffold equipped with three handles. *Tetrahedron Lett.* **2002**, *43*, 7427–7429.
- [82] Banfi, L.; Guanti, G. Synthesis of intramolecularly activated lactenediynes and evaluation of their activity against plasmid DNA. *Eur. J. Org. Chem.* **2002**, 3745–3755.

- [83] Banfi, L.; Guanti, G. *Trans* 11-azabicyclo[8.2.0]dodec-5-ene-3,7-diin-12-*oni* con attività citotossica e antitumorale: procedimento per la loro preparazione e composizioni terapeutiche che li contengono. Italian Patent No. TO2002A000716, 12-8-2002.
- [84] Eisenbrand, G.; Lauck-Birkel, S.; Tang, W.C. An approach towards more selective anticancer agents. *Synthesis* **1996**, 1246–1258; Niculescu-Duvaz, I.; Springer, C.J. Antibody-directed enzyme prodrug therapy (ADEPT): a review. *Adv. Drug Delivery Rev.* **1997**, 26, 151–172.
- [85] Basak, A.; Khamrai, U.K.; Mallik, U. The synthesis and reactivity of novel azetidiny enediynes. *J. Chem. Soc. Chem. Commun.* **1996**, 749–750; Basak, A.; Mandal, S. A carbene insertion route to β -lactam fused cyclic enediynes. *Tetrahedron Lett.* **2002**, 43, 4241–4243; Banfi, L.; Guanti, G. Synthesis of N-fused “Lactendiynes”. *Eur. J. Org. Chem.* **1998**, 1543–1548.
- [86] Mantlo, N.B.; Danishefsky, S.J. A core system that simulates the cycloaromatization and DNA cleavage properties of calicheamicin–esperamicin: a correlation experiment. *J. Org. Chem.* **1989**, 54, 2781–2783.
- [87] Semmelhack, M.F.; Gallagher, J.J.; Minami, T.; Date, T. The enol–keto trigger in initiating arene diradical formation in calicheamicin/esperamicin analogs. *J. Am. Chem. Soc.* **1993**, 115, 11618–11619.
- [88] Semmelhack, M.F.; Sarpong, R.; Bergman, J.; Ho, D.M. Evaluation of alkene isomerization as a trigger for enediyne activation. *Tetrahedron Lett.* **2002**, 43, 541–544.
- [89] Wittman, M.D.; Kadow, J.F.; Langley, D.R.; Vyas, D.M.; Rose, W.C.; Solomon, W.; Zein, N. The synthesis and biological activity of enediyne minor groove binding hybrids. *Bioorg. Med. Chem. Lett.* **1995**, 5, 1049–1052.
- [90] Lee, S.; Bain, A.; Sulikowski, G.A.; Solomon, W.; Zein, N. Synthesis and biological evaluation of a bicyclo[7.4.1]enediyne. *Bioorg. Med. Chem. Lett.* **1996**, 6, 1261–1264.
- [91] Fallis, A.G. 1998 Alfred Bader award lecture. Tangents and targets: the synthetic highway from natural products to medicine. *Can. J. Chem.* **1999**, 77, 159–177.
- [92] Maier, M.E.; Bosse, F.; Niestroj, A.J. Design and synthesis of dynemicin analogs. *Eur. J. Org. Chem.* **1999**, 1–13.
- [93] Nicolaou, K.C.; Dai, W.-M.; Wendeborn, S.V.; Smith, A.L.; Torisawa, Y.; Maligres, P.; Hwang, C.-K. Eneidyne compounds equipped with acid-, base, and photo-sensitive triggering devices. Chemical simulation of the dynemicin A reaction cascade. *Angew. Chem., Int. Ed. Engl.* **1991**, 30, 1032–1036.
- [94] Unno, R.; Michishita, H.; Inagaki, H.; Baba, Y.; Jomori, T.; Nishikawa, T.; Isobe, M. Synthesis and biological evaluation of novel cyclic enediyne compounds related to dynemicin A as antitumor agents. *Chem. Pharm. Bull.* **1997**, 45, 125–133.
- [95] Hay, M.P.; Wilson, W.R.; Denny, W.A. A novel enediyne prodrug for antibody-directed enzyme prodrug therapy (ADEPT) using *E. coli* B nitroreductase. *Bioorg. Med. Chem. Lett.* **1995**, 5, 2829–2834.
- [96] Sinha, S.C.; Li, L.-S.; Miller, G.P.; Dutta, S.; Rader, C.; Lerner, R.A. Prodrugs of dynemicin analogs for selective chemotherapy mediated by an aldolase catalytic Ab. *Proc. Natl. Acad. Sci. USA* **2004**, 101, 3095–3099.
- [97] Nicolaou, K.C.; Hong, Y.-P.; Torisawa, Y.; Tsay, S.-C.; Dai, W.-M. Novel enediynes equipped with triggering and detection devices. Isolation of

- cis*-diol models of the dynemicin cascade. *J. Am. Chem. Soc.* **1991**, *113*, 9878–9880.
- [98] Shair, M.D.; Yoon, T.; Chou, T.-C.; Danishefsky, S. J. Eneidyne quinone imines: truncated biologically active dynemicin congeners. *Angew. Chem., Int. Ed. Engl.* **1994**, *33*, 2477–2479; Shair, M.D.; Yoon, T.Y.; Mosny, K.K.; Chou, T.C.; Danishefsky, S.J. The total synthesis of dynemicin A leading to development of a fully contained bioreductively activated enediyne prodrug. *J. Am. Chem. Soc.* **1996**, *118*, 9509–9525.
- [99] Mastalerz, H.; Doyle, T.W.; Kadow, J.F.; Vyas, D.M. Synthesis of an esperamicin core analog with an epoxide trigger. *Tetrahedron Lett.* **1996**, *37*, 8683–8686.
- [100] Mastalerz, H.; Doyle, T.W.; Kadow, J.F.; Vyas, D.M. Synthesis of a hybrid analog of the esperamicin and dynemicin cores. *Tetrahedron Lett.* **1996**, *37*, 8687–8690.
- [101] Audrain, H.; Skrydstrup, T.; Ulibarri, G.; Riche, C.; Chiaroni, A.; Grierson, D.S. Application and mechanistic studies of the [2,3]-Wittig rearrangement: an approach to the bicyclic core structure of the “enediyne” antitumor antibiotics calicheamicin γ_1^1 and esperamicin-A₁. *Tetrahedron* **1994**, *50*, 1469–1502.
- [102] Magnus, P.; Eisenbeis, S.A.; Fairhurst, R.A.; Iliadis, T.; Magnus, N.A.; Parry, D. Synthetic and mechanistic studies on the azabicyclo[7.3.1]enediyne core and naphtho[2,3-*h*]quinoline portions of dynemicin A. *J. Am. Chem. Soc.* **1997**, *119*, 5591–5605.
- [103] Magnus, P.; Eisenbeis, S.A.; Rose, W.C.; Zein, N.; Solomon, W. Studies on dynemicin. A nonradical cycloaromatization pathway for the azabicyclo [7.3.1]enediyne core structure initiated by thiolate addition. *J. Am. Chem. Soc.* **1993**, *115*, 12627–12628.
- [104] Suffert, J.; Raepfel, S.; Raepfel, F.; Didier, B. Straightforward access to [6]metacyclophe-ene-based enynes by an inter-intramolecular tandem etherification through a one-pot double S_NAr reaction. *Synlett* **2000**, 874–876.
- [105] König, B.; Pitsch, W.; Thondorf, I. Synthesis, structure and reactivity of enediyne macrocycles. *J. Org. Chem.* **1996**, *61*, 4258–4261.
- [106] König, B. Changing the reactivity of enediynes by metal-ion coordination. *Eur. J. Org. Chem.* **2000**, 381–385; Basak, A.; Mandal, S.; Bag, S.S. Chelation control in Bergman cyclization. Synthesis and reactivity of enediynyl ligands. *Chem. Rev.* **2003**, *103*, 4077–4094.
- [107] Koga, N.; Morokuma, K. Electron acceptor substituents at terminal alkyne carbons. *J. Am. Chem. Soc.* **1991**, *113*, 1907–1911.
- [108] Prall, M.; Wittkopp, A.; Fokin, A.A.; Schreiner, P.R. Substituent effects on the Bergman cyclization of (*Z*)-1,5-hexadiyne-3-enes: A systematic computational study. *J. Comput. Chem.* **2001**, *22*, 1605–1614.
- [109] Wenk, H.H.; Balster, A.; Sander, W.; Hrovat, D.A.; Borden, W.T. Matrix isolation of perfluorinated *p*-benzynes. *Angew. Chem., Int. Ed. Engl.* **2001**, *40*, 2295–2298.
- [110] Klein, M.; König, B. Synthesis and thermal cyclization of an enediyne-sulfonamide. *Tetrahedron* **2004**, *60*, 1087–1092.
- [111] Rawat, D.S.; Zaleski, J.M. Syntheses and thermal reactivities of symmetrically and asymmetrically substituted acyclic enediynes: steric control of Bergman cyclization temperatures. *Chem. Commun.* **2000**, 2493–2494.

- [112] Konig, B.; Rutters, H. Synthesis and reactivity of the first bis(crown ether) enediyne. *Tetrahedron Lett.* **1994**, 35, 3501–3504.
- [113] Warner, B.P.; Millar, S.P.; Broene, R.D.; Buchwald, S.L. Controlled acceleration and inhibition of Bergman cyclization by metal chlorides. *Science* **1995**, 269, 814–816.
- [114] Wang, Y.; Finn, M.G. An organometallic diradical cycloaromatization reaction. *J. Am. Chem. Soc.* **1995**, 117, 8045–8046.
- [115] Myers, A.G.; Kuo, E.Y.; Finney, N.S. Thermal generation of α ,3-dehydrotoluene from (Z)-1,2,4-heptatrien-6-yne. *J. Am. Chem. Soc.* **1989**, 111, 8057–8058; Nagata, R.; Yamanaka, H.; Okazaki, E.; Saito, I. Biradical formation from acyclic conjugated eneyne–allene system related to neocarzinostatin and esperamicin–calicheamicin. *Tetrahedron Lett.* **1989**, 30, 4995–4998.
- [116] Shibuya, M.; Wakayama, M.; Naoe, Y.; Kawakami, T.; Ishigaki, K.; Nemoto, H.; Shimizu, H.; Nagao, Y. Cycloaromatization of enediyne model compounds via a reaction cascade triggered by hydrolysis of the α -alkynylmalonates. *Tetrahedron Lett.* **1996**, 37, 865–868.
- [117] Suzuki, I.; Shigenaga, A.; Nemoto, H.; Shibuya, M. Acid-catalysed cycloaromatization of enediyne model compounds via enyne–allene intermediates. *Heterocycles* **2001**, 54, 571–576.
- [118] Suzuki, I.; Uno, S.; Tsuchiya, Y.; Shigenaga, A.; Nemoto, H.; Shibuya, M. Synthesis and DNA damaging ability of enediyne model compounds possessing photo-triggering devices. *Bioorg. Med. Chem. Lett.* **2004**, 14, 2959–2962.
- [119] Kagan, J.; Wang, X.; Xu, C.; Lau, K.Y.; Batac, I.V.; Tuveson, R.W.; Hudson, J.B. DNA cleavage, antiviral and cytotoxic reactions photosensitized by simple enediyne compounds. *J. Photochem. Photobiol. B: Biol.* **1993**, 21, 135–142.
- [120] Turro, N.J.; Evenzahav, A.; Nicolaou, K.C. Photochemical analogue of the Bergman cycloaromatization reaction. *Tetrahedron Lett.* **1994**, 35, 8089–8092.

20 Polyynes: Simple Synthesis in Solution Through the Glaser Reaction

Franco Cataldo and Yeghis Keheyan

CONTENTS

20.1	Introduction	493
20.2	Experimental	494
20.2.1	Typical Synthesis of Polyynes by Glaser Reaction	494
20.2.2	Liquid Chromatographic Analysis.....	494
20.2.3	Stability of Polyynes in Concentrated Solutions	495
20.3	Results and Discussion	495
	References	498

20.1 INTRODUCTION

The synthetic approach presented here is a development of our earlier observation that dicopper acetylide (Cu_2C_2) and dicopper diacetylide (Cu_2C_4), left to age in humid air, undergo a slow coupling reaction [1–3]. The coupling reaction is the well-known Glaser reaction, an oxidative carbon-carbon bond formation of acetylenic species mediated by copper ions [4]. When copper acetylide or dicopper acetylide are hydrolyzed with hydrochloric acid, they release polyynes in an extracting hydrocarbon medium [1–3] and a carbonaceous residue containing carbynoid structures [5–7]. The drawback of the described synthetic approach involved the handling of almost dry and more or less aged dicopper acetylide and dicopper diacetylide, both proven to be explosive. Instead, the synthetic approach proposed in this chapter is completely safe because the acetylides are formed in situ in an aqueous solution. When dispersed in water solution the acetylides are completely safe and not explosive. They are oxidized and hydrolyzed, always in water solution in a completely safe procedure, which is in contrast to

our old approach, which involved necessarily the isolation of the acetylides. Furthermore, in [Chapter 18](#) we have shown that the polyynides, i.e. the copper salts of polyyne, are already much less explosive and dangerous than the corresponding acetylides.

Therefore, the synthetic procedure reported here represents a simple alternative to the carbon arc for the synthesis of polyyne in solution.

20.2 EXPERIMENTAL

20.2.1 TYPICAL SYNTHESIS OF POLYYNES BY GLASER REACTION

NH_4Cl (7.5 g) was dissolved in 200 ml of distilled water in a thick-walled conical flask with glass stopper equipped with a valve. $\text{CuCl}_2 \cdot 2\text{H}_2\text{O}$ (10.3 g) and CuCl (5.2 g) were added to the ammonium chloride solution and stirred to ensure the dissolution (may remain undissolved matter). Heptane (50 ml) is added to the solution, followed by calcium carbide (CaC_2 , 3.5 g) in small portions. After the addition of CaC_2 the flask fitted with the stopper is hand-shaken for few seconds and then the excess of acetylene is released by opening the valve. The operation is repeated several times until all calcium carbide has been added. When the first portion of CaC_2 is added the solution turns into a violet color but on further CaC_2 addition it becomes dark-brown. The reaction mixture is further shaken for about 2 mins and 35 ml of conc. hydrochloric acid were added to cause the hydrolysis of the acetylides. Shaking is prolonged for another 2 mins and then the crude mixture is filtered with the aid of a water pump. A dark precipitate is collected on the filter paper. The filtrate consists of a green aqueous phase and the heptane layer containing the polyyne dissolved therein. The heptane solution is collected with the aid of a separatory funnel. If an assay of the polyyne heptane solution (0.1 ml) is diluted 25 times with pure heptane it displays the following electronic absorption spectrum (in nm) 200 (s), 207 (sh), 216 (ms), 227 (s), 239 (m), 252 (m), 261 (w), 275 (mw), 297 (w).

Similar results as just described can be obtained by changing the ratio of $\text{Cu}^+/\text{Cu}^{2+}$ or even by using only Cu^+ or only Cu^{2+} , as outlined in [Table 20.1](#), although some change in the distribution of the products has been observed. If the polyyne solution in heptane is left in contact with the aqueous solution of copper chlorides under acidic conditions for one week, a plethora of new products can be detected by HPLC analysis. Probably, coupling reactions and intramolecular cyclization as well as addition reactions have taken place.

20.2.2 LIQUID CHROMATOGRAPHIC ANALYSIS

HPLC analysis was conducted on an Agilent Technologies liquid chromatograph. An assay of the heptane solution recovered was diluted at least

TABLE 20.1 - Polyynes in mol%

Cu species	Data from HPLC-DAD analysis					
	ARC	RUN 1	RUN 2	RUN 3	RUN 4	RUN 5
	None	from CaC ₂ Cu(I)/Cu(II)	from CaC ₂ Cu(I)/Cu(II)	from CaC ₂ Cu(I)/Cu(II)	from CaC ₂ Cu(II)	from CaC ₂ Cu(I)
POLYKYNE						
C ₆ H ₂	20.3	56.8	48.7	67.4	80.9	83.3
C ₈ H ₂	61.2	35.8	49.1	31.2	18.7	15.6
C ₁₀ H ₂	14.8	6.6	2.2	1.2	0.4	1.1
C ₁₂ H ₂	2.9	0.7	Traces	0.2	0.0	0.0
C ₁₄ H ₂	0.6	0.1	0.0	0.0	0.0	0.0
C ₁₆ H ₂	0.2	0.0	0.0	0.0	0.0	0.0
	100	100	100	100	100	100
total conc.	0.01 mM	85.5 mM	53.4 mM	97.7 mM	56.1 mM	28.7 mM

15 times with pure heptane and 25 microL were injected. The diodes of the detector were set at 202, 225, 250, 295 and 350 nm. Use was made of a C-8 column for the separation under isocratic conditions with a mobile phase of acetonitrile/water 80:20 vol/vol (see [Chapter 8](#) for further details). Polyynes were identified on the basis of their retention times and on the basis of their characteristic electronic absorption spectra (see [Chapter 8](#)).

20.2.3 STABILITY OF POLYKYNES IN CONCENTRATED SOLUTIONS

All the solution reported in Table 20.1 on standing, even when left in closed glass flasks in the dark or in diffuse light, leave a thick brown deposit on the walls and at the bottom of the flask resembling cork for its color and its consistency. There are no doubts that the precipitate is the result of a crosslinking reaction. The brown material can be recovered by decantation of the solution. It is insoluble in all common solvents and the FT-IR spectrum in KBr is as follows (absorption peaks in cm⁻¹): 3294 (s), 2956 (sh), 2929 (m), 2859 (mw), 2180 (m) 2100 (mw), 1773 (sh), 1714 (sh), 1617 (s), 1384 (ms), 1213 (s), 1122 (s), 978 (sh), 877 (w), 757 (w), 662 (mw).

20.3 RESULTS AND DISCUSSION

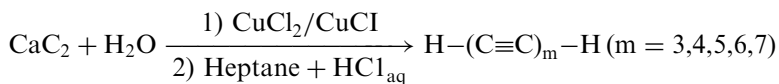
One of the drawbacks of the synthesis of the polyynes with the submerged carbon arc is the simultaneous formation of a mixture of PAHs (polycyclic aromatic hydrocarbons) and soot (see [Chapter 8](#)). Apparently the PAHs

and soot are formed mainly by the plasmalysis of the solvent caused by the arc. In any case, the HPLC analysis has shown that the PAHs concentration is two orders of magnitude lower than the polyyne concentration and for some synthetic purposes this could be a sufficient condition. It is possible to purify the polyyne, separating them from the PAHs and the soot by precipitation as acetylides, but this operation is relatively complex and not completely satisfactory (see Chapter 18). The best purification way remains the preparative HPLC [8].

Another drawback suffered by the polyyne solution prepared by the submerged electric arc technique is the relatively low concentration achievable. Usually, concentrations as high as 10^{-5} – 10^{-6} M can be reached. Higher concentrations can be reached by prolonging arcing for hours [8]. Alternatively, it is also possible to concentrate the solutions by distillation under reduced pressure (see Chapter 18). Under these circumstances it is also possible to increase the relative concentration of C_8H_2 and higher polyyne chains at the expenses of C_6H_2 which, being more volatile, distills away with the solvent.

The synthesis of polyyne by arcing graphite electrodes remains a very simple synthetic approach and has also many implications in different fields of science from astrochemistry to soot formation mechanism, as already discussed in other chapters of this book.

As an alternative to the submerged electric arc, the polyyne can be produced simply by hydrolizing calcium carbide (CaC_2) into an NH_4Cl aqueous solution of $CuCl/CuCl_2$, followed by acid hydrolysis of the resulting oxidized acetylides. The hydrolysis of calcium carbide produces *in situ* acetylene which, by reacting with $Cu(I)$, forms dicopper acetylide Cu_2C_2 . The latter compound is then oxidized by the action of Cu^{2+} , causing the coupling reaction. It has been observed that the presence of Cu^{2+} is not essential, since the polyyne are formed even when only Cu^+ ions are present. This is due to the fact that even the atmospheric oxygen is sufficient to cause the oxidative coupling reaction. It is also possible to start from $CuCl_2$ solutions; the addition of CaC_2 and the resulting acetylene produced causes the reduction of Cu^{2+} to Cu^+ so that the formation of Cu_2C_2 precipitate is observed. In any of the above mentioned cases, the liberation of the polyyne is caused by the addition of hydrochloric acid after the complete hydrolysis of calcium carbide. Schematically, the reactions involved can be represented as follows:



The polyyne liberated from their Cu^+ salts by the acid hydrolysis are trapped into hydrocarbon solvents by shaking the solution with n-hexane, n-heptane or n-octane. The polyyne are easily detected by HPLC analysis

of the resulting hydrocarbon solution using a diode-array detector and also by electronic absorption spectroscopy of the resulting hydrocarbon solutions (see [Chapter 8](#)).

As expected, the hydrolysis of calcium carbide in an aqueous solution of NH_4Cl in the complete absence of copper ions does not produce any detectable amount of polyyne. Thus, the copper ions are involved in the coupling reaction and polyyne synthesis as it happens in a typical Glaser reaction [4].

[Table 20.1](#) shows the distribution of polyyne formed with the electric arc synthesis in comparison with the polyyne produced by the calcium carbide hydrolysis and copper-based coupling. The relative concentration of each individual polyyne species has been measured using a diode array detector in HPLC analysis and the molar extinction coefficients reported in literature. Arcing graphite electrodes in hydrocarbon solvents produces a quite constant distribution of polyyne with C_8H_2 species dominant, followed by C_6H_2 and C_{10}H_2 with still appreciable or detectable amounts of the higher homologs. Instead, the distribution of polyyne produced by the calcium carbide hydrolysis in presence of copper ions varies according to the conditions adopted and is always characterized by a dominant level of C_6H_2 .

When Cu^+ and Cu^{2+} ions are present in solutions simultaneously, the concentration of C_8H_2 appears high, although C_6H_2 remains dominant, but also C_{10}H_2 is present in the solution. When instead the calcium carbide hydrolysis is conducted in aqueous solutions containing only Cu^+ or only Cu^{2+} ions, the coupling reaction appears less effective and the concentration of C_8H_2 appears much lower in comparison to C_6H_2 and C_{10}H_2 concentration is very low.

In any case, one of the major advantages offered by the synthetic method presented in this chapter, apart from the simplicity and the rapidity, is represented by the high concentration reached in a few minutes by the polyyne in the solution. As shown in [Table 20.1](#), the total polyyne concentration obtained by arcing 5–10 minutes is about 10^{-5} M, while, with the new method just reported, at the same time it is possible to prepare solutions having a total polyyne concentration as high as 0.1 M.

By extrapolating his data on the thermal stability of polyyne in solution and especially on C_8H_2 polyyne, Heymann [8] concluded that the threshold of the instability of polyyne solution should lie at 10^{-3} M. In fact, the relatively concentrated polyyne solutions prepared through the Glaser reaction are all unstable and separate a brown polymeric material on standing. Particularly remarkable are the residual acetylenic bands at 3294 and 2180 and 2100 cm^{-1} , testifying that it is a three-dimensional polymer derived from the crosslinking reaction of the polyyne species. Furthermore, bands due to oxidation can be observed in the brown precipitate 1773, 1714 and 1122 cm^{-1} . Since oxygen from air has appreciable solubility in heptane [8] and since the polyyne solutions were always prepared and

exposed to air, it is clear that the oxidation occurred from the reaction between polyyynes and oxygen directly in solution.

REFERENCES

- [1] Cataldo, F. Structural relationships between dicopper diacetylide and dicopper acetylide. *Eur. J. Solid State Inorg. Chem.* **1998**, 35, 281.
- [2] Cataldo, F. From dicopper diacetylide to carbyne. *Eur. J. Solid State Inorg. Chem.* **1998**, 35, 293.
- [3] Cataldo, F. From dicopper acetylide to carbyne. *Polym. Int.* **1999**, 48, 15.
- [4] Siemsen, P, Livingston, RC, Diederich, F. Acetylenic coupling: a powerful tool in molecular construction. *Angew. Chem. Int. Ed.* **2000**, 39, 2632.
- [5] Cataldo, F. Spectroscopical characterization of carbonaceous matter prepared through Glaser coupling reaction route. *Carbon* **1999**, 37, 161.
- [6] Cataldo F, Capitani, D. Preparation and characterization of carbonaceous matter rich in diamond-like carbon and carbyne. *Mater. Chem. Phys.* **1999**, 59, 225.
- [7] Cataldo, F. Raman scattering investigation of carbynoid and diamond-like carbon. *Fullerene Sci. Technol.* **2001**, 9, 153.
- [8] Heymann, D. *Carbon* **2005**, in press.

Abbreviations

ADEPT	antibody-directed enzyme prodrug therapy
AES	atomic emission spectroscopy or Auger electron spectroscopy
AFM	atomic force microscopy
AGB	asymptotic giant branch
AO	atomic orbital
ATD	arrival time distribution
CARS	coherent antistokes Raman spectroscopy
CCD	charge-coupled device
CI	configuration interaction
CLARA	cluster assembling roaming apparatus
CMB	crossed molecular beam
CP MAS	cross-polarization magic angle spinning
CVD	chemical vapor deposition
DAD	diode array detector
DDQ	2,3-dichloro-5,6-dicyano-1,4-benzoquinone
DFT	density functional theory
DHNP	decahydronaphthalene
DIB	diffuse interstellar band
DIBALH	diisobutylaluminum hydride
DME	deep metastable eutectic
DTA	differential thermal analysis
DOVS	density of valence electron states
EA	electron affinity
EDS	energy dispersive spectroscopy
EDX	energy dispersive x-ray
EELS	electron energy loss spectroscopy
EPT	enzyme prodrug therapy
ESCA	electron spectroscopy for chemical applications
FOJT	first-order Jahn–Teller
FT	Fourier transform

GC/MS	gas chromatography/mass spectrometry
GIXD	grazing incidence x-ray diffraction
HOMO	highest occupied molecular orbital
HOPG	highly oriented pyrolytic graphite
HPLC	high-performance liquid chromatography
IPDs	interplanetary dust particles
IPHAC	ion-produced hydrogenated amorphous carbon
ISM	interstellar medium
ITO	indium tin oxide
LCAO	linear combination of atomic orbitals
LD TOF	laser-desorption time-of-flight
LECBD	low energy cluster beam deposition
LED	light-emitting diode
LIF	laser-induced fluorescence
LUMO	lowest unoccupied molecular orbital
MALDI	matrix-assisted laser desorption/ionization
MCPs	multi-channel plates
MO	molecular orbital
MPI	multi-photon ionization
MWNT	multiwalled carbon nanotube
NMR	nuclear magnetic resonance
OJDS	optical joint density state
PAH	polycyclic aromatic hydrocarbon
PES	potential energy surface
PTFE	poly(tetrafluoroethylene)
PVD	physical vapor deposition
PVDF	poly(vinylidene difluoride)
QMS	quadrupole mass spectrometer
REMPI	resonant-enhanced multiphoton ionization
RRKM	Rice–Ramsberg–Kassel–Marcus (theory)
SCBD	supersonic carbon cluster beam deposition
SCF	self consistent field
SEM	scanning electron microscope
SOJT	second-order Jahn-Teller effect
STM	scanning tunneling microscopy

TEM	transmission electron microscopy (microscope)
TG	thermogravimetry
TOF/MS	time-of-flight mass spectrometer (or spectrometry, depending on context)
UH	ultra-high vacuum
UPS	ultraviolet photoelectron spectroscopy
UV-vis	ultraviolet-visible
XRD	x-ray diffraction
XPS	x-ray photoelectron spectroscopy
YSO	young stellar object
ZPE	zero point energy
ZPVE	zero point vibrational energies